Imperial College London
Department of Chemistry

Structural and Dynamical Analysis of Ionic Liquids in Electric Fields

Ryan Ashley Arthur Clark

This thesis is presented for the degree of
Doctor of Philosophy

Declaration

The work described within this thesis was, unless clearly stated and referenced, undertaken by me between October 2016 - June 2020.

Copyright

Abstract

Ionic liquids are a relatively new field of study, and there remain many mysteries in their behaviour and properties. One of these that is not fully understood is the behaviour of the ions around an electrode, and more generally in an electric field.

In this thesis, molecular rotors are used to study the the mid- and long-range effects of applying a potential to an electrode on the viscosity of an ionic liquid (1-butyl-3-methylimidazolium bis-(trifluoromethylsulfonyl)imide, $[C_4C_1im][NTf_2]$). This is supplemented by molecular dynamics simulations investigating how the structure of the ionic liquid changes in an electric field, in terms of both the bulk structuring of the ionic liquid, as well as the structures of the ions themselves.

In order to understand what the results upon application of a potential mean, first a study on the environment in which the molecular rotors used lie in ionic liquids was performed. This showed that the positively charged dye (3,3'-diethylthiacarbocyanine iodide, Cy3) is mainly surrounded by the anions of the ionic liquid, and is very sensitive to changes in the anion. When keeping the anion constant, Cy3 is mainly surrounded by anions but has to sample some of the other parts of the ionic liquid, unless the ions are large enough that the dye can fully surround itself with anions.

The neutral dye (8-[4-decyloxyphenyl]-4,4-difluoro-4-bora-3a,4a-diaza-*s*-indacene, a.k.a boron-dipyrromethene C10, BODIPY-C10) was found to prefer to partition into the non-polar alkyl chain environment, which leads to two trends in the lifetime of the dye: one when it could fully partition into the alkyl chains, and one when it also sampled polar moieties.

When looking at these dyes upon application of a potential, there are two different effects of the potential. For Cy3 in positive potentials and BODIPY-C10 in negative potentials, there is electrophoresis of the dyes towards the electrodes. This was so strong that in both of these samples there was no dye left to report on the viscosity. For Cy3, the rate at which this occurred, and the extent of the effect was found to be concentration- and potential-dependent effect. This was hypothesised to be due to a free energy minima at a cathode for Cy3 and a similar free energy minima at an anode for BODIPY-C10.

For Cy3 at an anode and BODIPY-C10 at a cathode, changes to the counts are seen, but there remains enough of the dye to extract the lifetime of the dye, and thus viscosity. In both of these cases, changes to the viscosity of the ionic liquid are observed up to 25 μm away from the electrode, which is an unusually long distance. Due to the different environments of the dyes, the increase in viscosity reported by Cy3 was hypothesised to be due to a constriction

of the polar region and an increase in the density of the ionic liquid. The increase in viscosity reported by BODIPY-C10 was hypothesised to be due to a rotational alignment of the ions that is somewhat meta-stable.

The molecular dynamics simulations showed large changes in the structure of the ionic liquid, as well as to the dynamics of the ions. In low electric field strengths no changes were seen in the structure of the ionic liquid, and a linear relationship between diffusive changes and electric field strength is seen. As the electric field strength increases, larger changes are seen in the diffusion, with a non-linear response seen. The structure and orientation of individual ions was found to be the first structure to change in low electric fields, followed by changes to the bulk ionic liquid structure in stronger electric field strengths.

The change in the structure of the ions was found to be be able to be described by the charge arm of the ions. This is the vector from the centre of mass to the centre of charge, and was found to be a good indicator as to why the structure of the ions change as they do in an electric field. There was also a competition found in an electric field when the most favourable charge arm orientation clashed with the most favourable orientation for diffusion. The similarities and differences between charge arms and dipoles were also found to show that while charge arms do not act like dipoles, there can be some dipole-like local orientation effect.

Acknowledgements

First, I have to thank my main supervisor, Prof. Tom Welton, for all of his support, guidance, encouragement, and enthusiasm throughout the years. I genuinely don't think I could have asked for a better supervisor for a PhD, due to his invaluable advice with my project, his patience and understanding as I was going through struggles, and for being a generally joyous and friendly person. For all of this, I am grateful and it has been a joy to be your PhD student. Secondly, I must thank Dr. Alastair McIntosh. Despite jumping ship shortly before the move to White City (for which I do not blame him), his expertise and aid whilst I was getting up to speed with the project and learning new skills is much appreciated.

I also want to thank my other two supervisors, Prof. Joshua Edel, and Dr. Marina Kuimova. To Joshua, thank you for allowing me to use (substantial amounts of) time on the FCS/lifetime laser set-up, for helping when there were invariably problems, and for the help with the data analysis and interpretation. To Marina, if not for the fruitful discussions with you on interpretation of the results and the nuances of the analysis I have no doubt the results would be much more difficult to understand, and the next steps much less clear. I should also thank Dr. Alex Ivanov for his help with setting up the lifetime card, and advice on experimental set-ups and data interpretation.

I would like to thank all of the other past and present members of the Welton group, not just for their help, but for also making my time within the group such an enjoyable experience. Cameron, Eduards, Tommy, Marianne (2017, it was a very good year), Raquel, David, Jay, Olga, Azizi, Frederik, Spiros, Julian, Hanim, Mikkaila, Nik, Rafiq, Ivan, Qingshan, Yongji, Clara, Lottie, Madaleine, Alfie, Ana, Demetrious, Danae, Steph, and Antonio. There are so many of you, and the group has changed so much during my time! I hope you've all enjoyed your time with the group, and I wish you all the best of luck in your future endeavours.

Lastly, but certainly not least, I would like to thank all of my other friends, and my family who have supported be throughout the years. Especially to my parents and brothers, for supporting me and listening to me talk about what must seem like nonsense most of the time, to Diana for your support and proofreading my entire thesis(!!), and to all of my friends from my undergraduate degree at Nottingham for all of the good times during these last 4 years.

'If it wasn't for bad luck, you would have no luck at all.'

Tom Welton

Publications

Work presented in this thesis also appears in the publications listed below

- *The Effect of Structural Heterogeneity upon the Microviscosity of Ionic Liquids* R. Clark, A. Nawawi, A. Dobre, D. Pugh, Q. Liu, A. P. Ivanov, A. J. P. White, J. Edel, M. K. Kuimova, A. J. S. McIntosh and T. Welton, *Chem. Sci.*, 2020, **11**, 6121 - 6133.[1] Chemical Science Pick of the Week 17-24th June 2020, part of the 2020 Chemical Science HOT Article Collection, and back cover feature.
- *Effect of an External Electric Field on the Dynamics and Intramolecular Structures of Ions in an Ionic Liquid* R. Clark, M. von Domaros, A. J. S. McIntosh, A. Luzar, B. Kirchner and T. Welton, *J. Chem. Phys.*, 2019, **151**, 164503.[2]

Other publication not related to this thesis:

- *Structure and lifetimes in ionic liquids and their mixtures* S. Gehrke, M. von Domaros, R. Clark, O. Hollóczki, M. Brehm, and T. Welton, *Faraday Discussion*, 2017, **206**, 219-245.[3]

Contents

List of Figures

List of Tables

Chapter 1

Introduction

The study of electricity and electrical potentials has a long and storied history, beginning with historic experiments such as those performed by the likes of Luigi Galvani on frogs legs, Alessandro Volta and the voltaic pile battery or Charles-Augustin de Coulomb's studies on electric currents and wires.

From this work, a push to understand the physics of electric fields and how they affect and are affected by other species has been explored, and many equations and theories have been created.

One relatively new source of these studies are ionic liquids, which have opened the door to studying how concentrated electrolytes behave in an electric field. Ionic liquids have been used to push the boundaries of established theories explaining electrochemical properties of salt solutions, by enabling studies of highly concentrated salts. Properties studied have included impedance, dielectric constants, screening lengths, and layering structures at electrodes. Some remarkable results have been observed, which have challenged and expanded the current theories on how ions behave in electric fields.

In this thesis, the viscosity and behaviour of ions near an electrode is studied to ascertain the extent to which an electric potential can effect ionic liquids. These are complemented by molecular dynamics simulations, which give an indication as to the behaviour of ions in an electric field, which can aid in the understanding of the experimental results.

1.1 Outline

Previous work performed by Alastair McIntosh and Azizi Nawawi (PhD students in Tom Welton's group) showed that when applying a potential to an ionic liquid, effects of that potential on multiple fluorescent dyes could be seen at 50 μm from the electrode, far beyond what theories and other types of measurement could see. These effects also persisted for much longer time-scales than the theories predict as well (see Section 2.2.2 for a summary of their work). This project is a continuation of their work. It involves re-analysing their data with a new outlook, then looks at some of the same effects using a different dye. To aid the understanding of what is occurring, molecular dynamics simulations have also been performed looking at how uniform electric fields can affect the ionic liquid structure. In particular, the intramolecular structure of the ions is considered and how this affects an ionic liquid.

Chapter 2 introduces the field briefly. It includes an introduction to ionic liquids, an overview of why an understanding of ionic liquids in electric fields is important, and highlights some of the more important fundamental properties of ionic liquids. The chapter concludes with the current theories on the behaviour of ionic liquids in electric fields and provides an outline on some of the more impactful and unusual work to progress the understanding of ionic liquids in electric fields.

Chapter 3 contains all of the synthetic procedures employed during this PhD.

Chapter 4 contains all of the simulation protocols employed during this PhD.

Chapter 5 contains the analysis of measurements of the fluorescence lifetime of two molecular rotors (Cy3 and BODIPY-C10) in various ionic liquids, as well as temperature dependent measurements, to study the environment in which these dyes reside in various ionic liquids.

Chapter 6 contains the analysis of measurements of ionic liquids in electric fields. This involves measurements and analysis of fluorescence lifetime decay experiments of the aforementioned dyes in 1-butyl-3-methylimidazolium bis(trifluoromethylsulfonyl)imide at various distances from an electrode under the effect of an electric field.

Chapter 7 contains the results from molecular dynamics simulations on 1-butyl-3-methylimidazolium bis(trifluoromethylsulfonyl)imide and 1-octyl-3-methylimidazolium bis(trifluoromethylsulfonyl)-imide to study how the structures within the ionic liquids, as well as the dynamics of the ions, are affected by electric fields. This includes the development of a methodology to accurately simulate particles in an electric field.

Chapter 8 contains the analysis of the charge arms of the ionic liquids, a relatively new and unexplored analysis which can explain a lot of the results seen in Chapter 7.

This thesis is structured so that Chapters 5-8 each have their own introduction, highlighting the most relevant literature to that specific topic but and the discussion also links to general ionic liquid knowledge introduced in Chapter 2.

Chapter 2

Introduction to Ionic Liquids

2.1 Ionic Liquids

Ionic liquids are a class of compounds which differ from most 'conventional' chemicals in that they are liquids composed entirely of ions. They contain large and often asymmetric or flexible ions which lower the lattice energy, and hence the melting point to the point where many are liquids at or near room temperature. This has led to many names for ionic liquids such as 'liquid salts', 'molten salts', 'room temperature ionic liquids' etc. In this thesis, the term ionic liquid will be used ubiquitously to refer to an organic-based, large salt that is above its melting temperature.

The first published record of a molten salt was recorded in 1914 by Paul Walden, who synthesised ethylammonium nitrate ($[EtNH_3][NO_3]$) and discovered it had a melting point of 12 °C. At the time not much interest was paid, with very few studies conducted on this and similar compounds.

In the early 1980's, John Wilkes and others "re-popularised" the field by discovering chloroaluminate ionic liquids, and introduced the now very popular 1-alkyl-3-methylimidazolium cation ($[C_nC_1im]^+$, Figure 2.1).[4]

Later, Wilkes introduced the first air and water stable ionic liquids in the form of 1-alkyl-3-methylimidazolium nitrate($[C_nC_1im][NO_3]$), 1-alkyl-3-methylimidazolium sulfate ($[C_nC_1im][SO_4]$) and 1-alkyl-3-methylimidazolium tetrafluoroborate ($[C_nC_1im][BF_4]$),[5] although the latter was later shown to react with water under ambient conditions so is not considered stable anymore.[6]

These seminal papers sparked a lot of interest in ionic liquids, especially their potential use as 'designer solvents', a concept touted as the ability to tune the properties of an ionic liquid to a

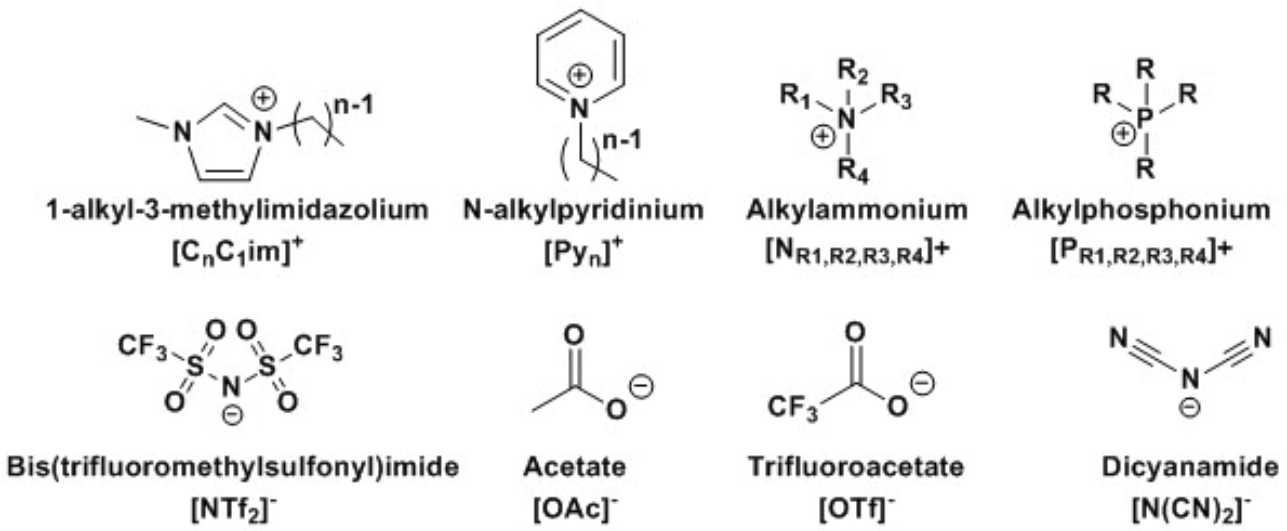

Figure 2.1: *Examples of some of the most common cations and anions used to make ionic liquids.*

specific use by changing the cation and anion.[7] Some of the most common ions used in current research are shown in Figure 2.1.

Since these early reports, many studies have looked into the fundamentals and the applications of ionic liquids. Investigation into fundamental properties very quickly showed many unique properties of ionic liquids, including low (but measurable) vapour pressure,[8,9] large electrochemical window[10] and very high solubilities of many substances, most interestingly gases and metals.[11,12]

This has led to a large and varied list of speculated uses for ionic liquid including replacements for traditional organic solvents,[13] media for electrodeposition,[12] flue gas capture,[11] electrolytes, nuclear fuel processing, creating biofuel from lignin, and fine chemicals processing amongst many others.[14]

There have been some attempts to describe and characterise properties of ionic liquids using theories developed based upon studies of molecular solvents or dilute electrolytes, however these often fail. This is usually attributed to the difference in the dominant interactions between these systems and ionic liquids. The intermolecular forces in dilute electrolytes and molecular solvents are weak dispersion forces, however as ionic liquids are purely ionic, the inter-particle interactions are dominated by strong coulombic forces. The difficulty arises in separating the properties of ionic liquids caused by the structure and flexibility of the ions from those caused by simply having a highly concentrated charged system.

2.1.1 Micro-heterogeneity in Ionic Liquids

One very important property of ionic liquids is that they they are structured at the nano-scale. Referred to as micro-heterogeneity or nano-structure, it is understood that the different regions in an ionic liquid aggregate to form distinct nano-domains within the macroscopically homogeneous liquid.

The presence of nano-structure was first indirectly measured and hypothesised by Schröder *et al.* on electrochemical studies of water diffusion in ionic liquids.[15] This theory was later reinforced based upon measurements of physical properties of 1-alkyl-3-methylimdazolium bis-(trifluoromethylsulfonyl)imide ($[C_nC_1im][NTf_2]$) ionic liquids with various alkyl chain lengths,[16] as well as simulations on the rotational dynamics and red-edge effect of a fluorescent dye in 1-butyl-3-methylimidazolium hexafluorophosphate ($[C_4C_1im][PF_6]$).[17]

Coarse grain molecular dynamics simulations from Urahata and Ribeiro were beginning to explore this effect by looking at how changing chain length of the $[C_nC_1im]^+$ cation affected the structure with various anions (F^-, Cl^-, Br^-, PF_6^-).[18] They saw that the anion always remained around the imidazolium ring (although occupied different positions due to steric effects). When simulating a butyl- chain the alkyl chains were found to be dispersed, however, when simulating an octyl- chain the alkyl chains aggregated together.[18]

Around a similar time Margulis calculated the radial distribution functions of $[C_nC_1im][PF_6]$ (n = 6, 8, 10 or 12).[19] This study showed that as the alkyl chain length increased, the cation and anion radial distribution functions became more structured, and the diffusion of the cation and anion became much more correlated.

Further coarse grain simulations from Wang and Voth on $[C_nC_1im][NO_3]$ directly observed the aggregation of the alkyl chains of the cation above a butyl chain ($[C_nC_1im]^+$, $n > 4$).[20]

These observations were all built upon by Canongia Lopes *et al.* who showed using molecular dynamics simulations[21,22] and cohesive energy determination[23] on $[C_nC_1im][NTf_2]$ and $[C_nC_1im][PF_6]$ that not only did the alkyl chains aggregate when sufficiently long enough, but the ionic domains also formed a continuous polar domain (see Figure 2.2).

By labelling the alkyl chains as the non-polar domain and the imidazolium head group and anion as the polar domain, there was distinct nano-segregation of these domains when the alkyl chains reached a certain length.

With alkyl chains shorter than hexyl- chains ($[C_nC_1im]^+$, $n < 6$), for all anions they studied there existed a continuous polar domain with a dispersed non-polar domain. When increasing the alkyl chain beyond this, these non-polar domains grew in size to a point where when $n \geq$

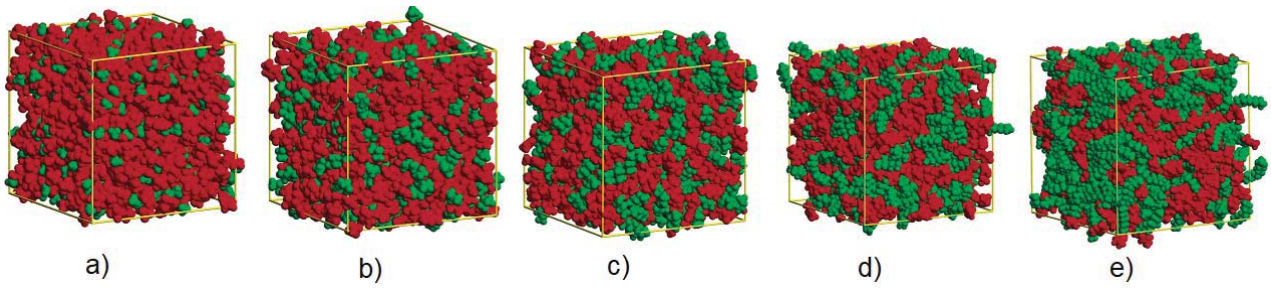

Figure 2.2: *Simulation snapshot of: a) [C_2C_1im][PF_6], b) [C_4C_1im][PF_6], c) [C_6C_1im][PF_6], d) [C_8C_1im][PF_6], e) [$C_{12}C_1$im][PF_6]. Simulation boxes coloured so the alkyl chains (non-polar domains) are coloured in green and the polar domains are coloured in red. Reprinted with permission from J. N. Canongia Lopes and A. A. Pádua, Journal of Physical Chemistry B, 2006,* ***110****, 3330-3335.*[21] *Copyright 2006 American Chemical Society.*

6 the alkyl chains aggregated into a single, continuous non-polar domain within the liquid.[21,22] Since these seminal papers, there have been many more simulations confirming this observation using simulations of a large variety of ionic liquids.[24–26] There have also been many experiments that confirm the existence of this nano-structure.

Experimental micro-heterogeneity was first observed by Triolo *et al.* using x-ray scattering on 1-alkyl-3-methylimidazolium chloride and tetrafluoroborate ionic liquids.[27] The “pre-peak" in the x-ray scattering profile around 2-3 nm^{-1} indicating the presence of structures around 3-5 Å in size, and this peak was only present in ionic liquids with hexyl- or larger alkyl chains. They also observed a temperature dependence of this in [C_8C_1im][BF_4], with the position of the peak decreasing and the intensity of the signal increasing with decreasing temperature.

Further x-ray scattering measurements from Triolo *et al.* on ionic liquids with the $[NTf_2]^-$ anion confirmed these structures in [$C_nC_1$im][NTf_2] ionic liquids, and showed the same order of structuring for one ammonium (N-trioctylethylammonium NTf_2, [N_{8882}][NTf_2]) and one phosphonium (P-trioctylethylphosphonium NTf_2, [P_{8882}][NTf_2]) ionic liquid.[28] They also observed that analogous ionic liquids, with ether chains instead of alkyl chains, did not show the same structural peaks in the x-ray scattering. Therefore, it was determined that ionic liquids with ether chains instead of alkyl chains were less structured on the nano-scale.[27]

Other x-ray scattering measurements by Shen *et al.* showed that a similar structuring could be observed for ionic liquids with fluorinated alkyl chains.[29] The fluorinated alkyl chains also appeared to aggregate into a separate domain, even when there was also an alkyl domain, leading to three domains in the liquid: a polar, a non-polar and a fluorous domain. The presence of a separate fluorous domain and triphilic ionic liquid mixtures was later confirmed by molecular dynamics simulations.[30]

Rocha *et al.* observed this micro-heterogeneity when they measured the enthalpy and entropy

of vaporisation for $[C_nC_1im][NTf_2]$ (n = 2, 3, 4, 5, 6, 7, 8, 10, 12). They observed two trends for the series, one for n = 2-6 where adding one extra CH_2 group to the alkyl chain increased the enthalpy of vaporisation by 5.5 $kJmol^{-1}$ and the entropy of vaporisation by 11.8 $JK^{-1}mol^{-1}$. Above n = 6, adding extra CH_2 groups to the alkyl chain only increased the enthalpy of vaporisation by 3.7 $kJmol^{-1}$ and the entropy by 6.1 $JK^{-1}mol^{-1}$.[31] The decrease in entropy gain above n = 6 was attributed to the nano-segregated alkyl chains not gaining as much entropy going into the gas phase due to more freedom to rotate in the liquid phase.

Moschovi and Dracopoulos saw differences between the polar and non-polar regions in the infrared and Raman spectra of 1-alkyl-3-methylimidazolium and 1-alkyl-3-H-imidazolium $[NTf_2]$ based ionic liquids.[32] They observed a change in the *cis*/*trans* ratio of the anion which they attribute to different interactions between the cation and anion when the polar and non-polar regions separate into different domains. They also observed that the alkyl chains contained more gauche bonds at low alkyl chain length, indicating the chains were more 'curled up' when there was no micro-heterogeneity. Conversely, when the nano-structure was present the alkyl chains took more anti bond configurations, indicating a preference for a stretching of the alkyl chain, likely in order to maximise the interactions between them.[32]

This structural micro-heterogeneity has been used to aid in the explanation of the dynamics of the ions within the ionic liquid, as well as solutes in ionic liquids.

Kaintz *et al.* investigated dynamic heterogeneity by observing the diffusion of various size tracer species within pyrrolidinium and phosphonium ionic liquids.[33] They discovered that neutral and charged species behaved differently when comparing the ratio of the probe volume to the ionic liquid ion volume, and the ratio between the the observed and theoretical friction coefficients (see Figure 2.3).

They investigated how the ratio between the size of the solute and the average size of the ions in the ionic liquid affected the effective friction on the solute. The observed friction coefficient was calculated from the Einstein relation

$$\zeta_{\text{obs}} = k_B T / D \tag{2.1}$$

where ζ_{obs} is the observed friction coefficient, k_B is the Boltzmann constant, T is the temperature, and D is the diffusion coefficient calculated from pulsed-field-gradient NMR.

The theoretical friction coefficient was calculated from the Stokes-Einstein equation

$$\zeta_{\text{SE}} = 6\pi\eta R \tag{2.2}$$

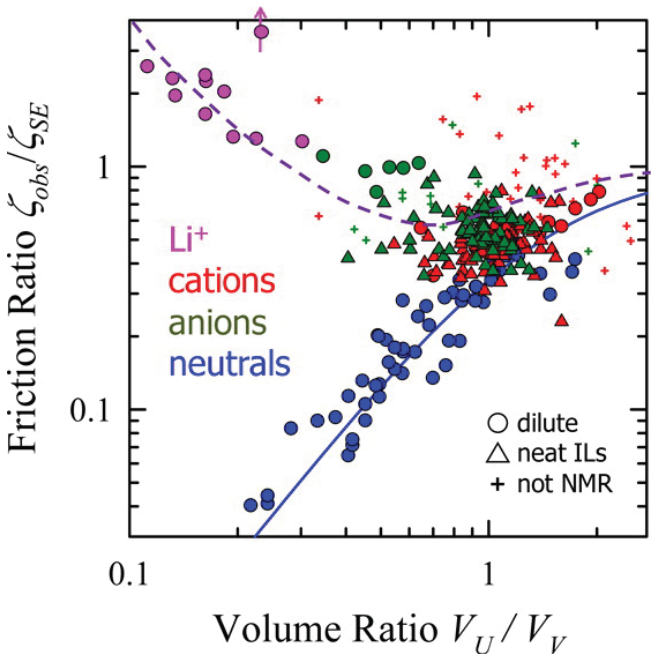

Figure 2.3: *Ratio of observed to Stokes-Einstein friction plotted versus the ratio of solute-to-solvent volumes for ionic and neutral solutes in ionic liquids. The neutral solute data (blue) are from the referenced work, and the blue curve is the fit. Circles are tracer diffusion data, and triangles are self-diffusion data. Reprinted with permission from Anne Kaintz, Gary Baker, Alan Benesi and Mark Maroncelli, Journal of Physical Chemistry B, 2013,* ***117****, 11697-11708.*[33] *Copyright 2013 American Chemical Society.*

where ζ_{SE} is the calculated friction coefficient, η is the viscosity, and R is the hydrodynamic radius of the solute.

For both charged and neutral solutes, when the volume of the solute was greater than the average volume of the ions, ζ_{obs} was similar to ζ_{SE}. However when the volume of the solute was equivalent or lower than the average volume of the ions, there were large differences between charged and neutral solutes.[33]

When decreasing the relative volume of a neutral solute, the diffusion was much greater than expected, leading to ζ_{obs} being much lower than ζ_{SE}. This effect was independent of the dipole, indicating that it was the overall charge on the solute that caused this effect. The trend for neutral solutes was contrasted by charged solutes, whose ζ_{obs} was larger than predicted from the hydrodynamic radius at equivalent or smaller solute volume ratios.[33]

This was studied using molecular dynamics by Araque *et al.* who modelled the diffusion of a selection of charged and neutral solutes in the same ionic liquid that Kaintz *et al.* investigated. From this, they discovered that the diffusion of ions consists of two modes, a 'jump' and a 'cage' trajectory.

The jump trajectory involves the motion of the solute through 'soft' non-polar regions, and solutes undergo fast diffusion. In contrast, the cage trajectory involves motion of the solute

through 'stiff' polar regions, where little net diffusion of the solute is observed.

From the molecular dynamics analysis it was determined that the difference in the diffusion of the charged and neutral solutes was due to a difference in the amount of time they spent in the different trajectories/regions. For both neutral and charged species, the majority of diffusion was found to occur during the jump trajectory (i.e. within the soft non-polar region). The differences in diffusion for charged and neutral solutes was found to come from the amount of time the solutes spent within the jump and cage trajectories.

Although both charged and uncharged solutes spent the majority of their time within an ion cage, uncharged solutes moved into the jump region significantly more often than the charged solutes. It was determined that it was differences in the temporal distribution of solutes between the cage and jump regions which resulted in the deviation of the observed frictional forces from the predicted frictional forces. The physical process which caused these temporal differences was changes in the interactions of the solutes with the different regions of the ionic liquids.[34]

For charged solutes with a large relative volume compared to the ionic liquid ions, there existed a weakly coordinated ion cage around the solute, comprised mainly of counter ions to the solute charge. A similar cage was found to exist for relatively large neutral solutes, comprised mainly of cations (which contain the non-polar region of the alkyl chains) with a small number of anions. The diffuse nature of the ion cage meant that disruption of the ion cage to allow access to the jump region, and therefore greater diffusion, was relatively easy and similar for both charged and neutral solutes.

Decreasing the solute volume to a similar or smaller volume than the ionic liquid ions leads to differences in the mechanism of motion for both charged and uncharged solutes. The frictional coefficients of neutral solutes decrease below what is expected, as with decreasing relative volume the first solvation shell of neutral solutes comprises increasing amounts of alkyl chains, which make up the soft non-polar region. Therefore they are inherently more associated to the soft region, meaning their diffusion will necessarily increase. Conversely, decreasing the relative volume of charged solutes led to more ions in the first solvation shell and therefore more association with the stiff polar region of the ionic liquid. This lead to the small charged solutes becoming

> *not an innocent spectator of stiff and soft solvent regions but instead a participant in creating the electrostriction it experiences*[34]

This cage/jump model has since been studied in neat ionic liquids, and has been shown to be an

appropriate model for describing the motion of the ions themselves.[35,36] Feng *et al.* investigated the dynamics of the ions in $[C_4C_1im][NTf_2]$ with respect to what they describe as 'free' and 'bound' states, which are analogous to the jump and cage trajectories described by Araque *et al.*. They found that both the cation and the anion were bound within ion cages composed of counter-ions, with the percentage of ions bound to a cage and the average time spent in an ion cage decreasing with temperature, though remaining approximately equal for both cation and anion.[35]

Diffusion coefficients for both the free and bound states showed conclusively that the diffusion was faster in the free state, and experimental measurements are the average of the two. They also demonstrated the applicability of these results to calculations of conductivity. By modifying the Nernst-Einstein equation to account for the ions in the ionic liquid which were bound within the ion cage, and thus cannot diffuse and contribute to the conductivity, they found much better agreement between their predicted conductivity and measured conductivity.[35]

Another temperature dependant study on the ion cages of $[C_4C_1im][NTf_2]$ was performed by Sha *et al.* They also confirmed that the average time spent in the ion cage for both the cation and the anion was approximately the same, regardless of temperature, and average retention time of both ions within their ion cage decreased with increasing temperature. They also found an inverse relationship between the ion retention time and the diffusion coefficient, providing further evidence that retention of the ions within the ion cage decreases net diffusion.[36]

Very recently, a link between the micro-heterogeneity and bulk properties of the ionic liquids have been observed. Amith *et al.* have drawn a link between the rate at which the polar and non-polar domains 'mix' i.e. swap over time, and the correlation function of the stress tensor which can be used to calculate viscosity.[37] These results indicate that the malleability of the polar network (polarity blurring), and how quickly the non-polar network can fill in the voids which are generated upon polarity blurring (apolar flooding) could have a profound impact on the bulk viscosity.[37] However, the recency of these results means that this has not been fully explored yet.

All of these results combined show that the nano-structure of ionic liquids is not only a very interesting property, but can be the explanation, or part of the explanation, behind a number of interesting phenomena seen in ionic liquids.

2.2 Ionic Liquids in Electric Fields

As mentioned in Section 2.1, one of the proposed applications of ionic liquids is as replacement electrolytes in batteries, supercapacitors, fuel cells etc.[10,14] It was hypothesised that because ionic liquids have a high ion concentration, they would be good electrolytes for these applications. This combined with their large electrochemical window (>8 V in some ionic liquids), low flammability and relative safety compared to currently used electrolytes led many researchers to attempt to develop an ionic liquid battery.

However, these attempts to use pure ionic liquids as electrolytes in batteries have failed due to many factors. These include the high viscosity of ionic liquids leading to poor lithium transport numbers, formation of a solid electrolyte interface that impedes conducting ions from reaching the electrode and low cyclability.[38]

Proposed solutions to these problems are to use sodium instead of lithium,[39] to add a small amount of molecular solvent to reduce viscosity[10] or to instead investigate "solvate ionic liquids", These use cation-glyme complexes which share many of the same properties of ionic liquids but which incorporate the charge carrying ion (usually lithium) into the electrolyte.[40]

Similar to this is the use of ionic liquids in supercapacitors as they both benefit from many of the same advantages of ionic liquid properties, such as larger electrochemical windows and low flammability.

In the case of supercapacitors, these devices are not limited by poor ion conductivity. Indeed, ionic liquids have been shown to posses a much larger capacitance than conventional electrolytes.[41]

The energy stored in a capacitor can be calculated by

$$W = \frac{1}{2}CV^2 \tag{2.3}$$

where W is the energy stored in a capacitor, C is the capacitance and V is the voltage difference across a capacitor. Therefore ionic liquids having a large capacitance and wide electrochemical window means they could be ideal solvents for use in capacitors.

Despite the advantages of using ionic liquids as capacitor electrolytes, a working commercial capacitor using an ionic liquid has not yet been made as there are some difficulties in building such a device.

The electrochemical window of ionic liquids can be decreased significantly by impurities which, as discussed in Chapter 5, are abundant and difficult to remove or prevent from forming.

Practically, electrochemical windows of ionic liquids are closer to 4 V, not much large than the 3.6 V of aqueous electrolytes which are easier to handle and very well characterised.[42]

Another problem is that ionic liquids can be corrosive to certain metals that are commonly used as electrodes (e.g. aluminium).[42] This can be rectified by changing the electrode material, for example $[C_2C_1im][BF_4]$ is corrosive to aluminium but performs very well using a graphene electrode.[43] However, the electrode material needs to be carefully chosen, as a material suitable for one ionic liquid may not be suitable for another, similar ionic liquid. For example in 1-ethyl-3-methylimidazolium tetracyanoborate ($[C_2C_1im][B(CN)_4]$), the $[B(CN)_4]$ anion was found to react with the surface forming an insulating layer of polycyanoborani at the cathode.[44] This reaction was proposed as a safety mechanism as it only occurred at voltages greater than 2.2 V, nevertheless it highlights the differences that can occur when changing one ion in an ionic liquid.

Part of the reason behind this, and the final problem as to why ionic liquid capacitors are not yet functional, is that the electrode surface-ionic liquid interface is poorly understood. While some things are known e.g. the formation of layers of ions directly at the electrode, enough remains a mystery that hinders the development of an effective capacitor.

If ionic liquids are to be used as electrolytes in capacitors, then the structure and dynamics at an electrode need to be understood.

2.2.1 Ionic Liquids at Electrified Interfaces

Atomic force microscopy (AFM) measurements by Hayes *et al.* and Atkin *et al.* showed distinct layering of ions at a gold electrode, even in the absence of an applied potential, for both N-ethyl-N-methylpyrrolidinium and N-butyl-N-methylpyrrolidinium with the tris(pentafluoroethyl)trifluorophosphate anion. The observed ion layering became more pronounced at greater potentials (both positive and negative) with both the number of ion layers, along with the force required to disrupt these layers increasing with potential.[45,46]

They also found that when applying negative potentials, the structure they measured at the electrode required less force to disrupt it and less layers were formed (6 layers for -2 V, 8 layers for +2 V). They concluded that this meant the structure of the anions at a cathode was less effective at propagating structure into the bulk than cations at an anode.[45] This was backed by the discovery of a 'herringbone' structure on the electrode with negative potentials, but no such structure being seen at positive potentials.[46]

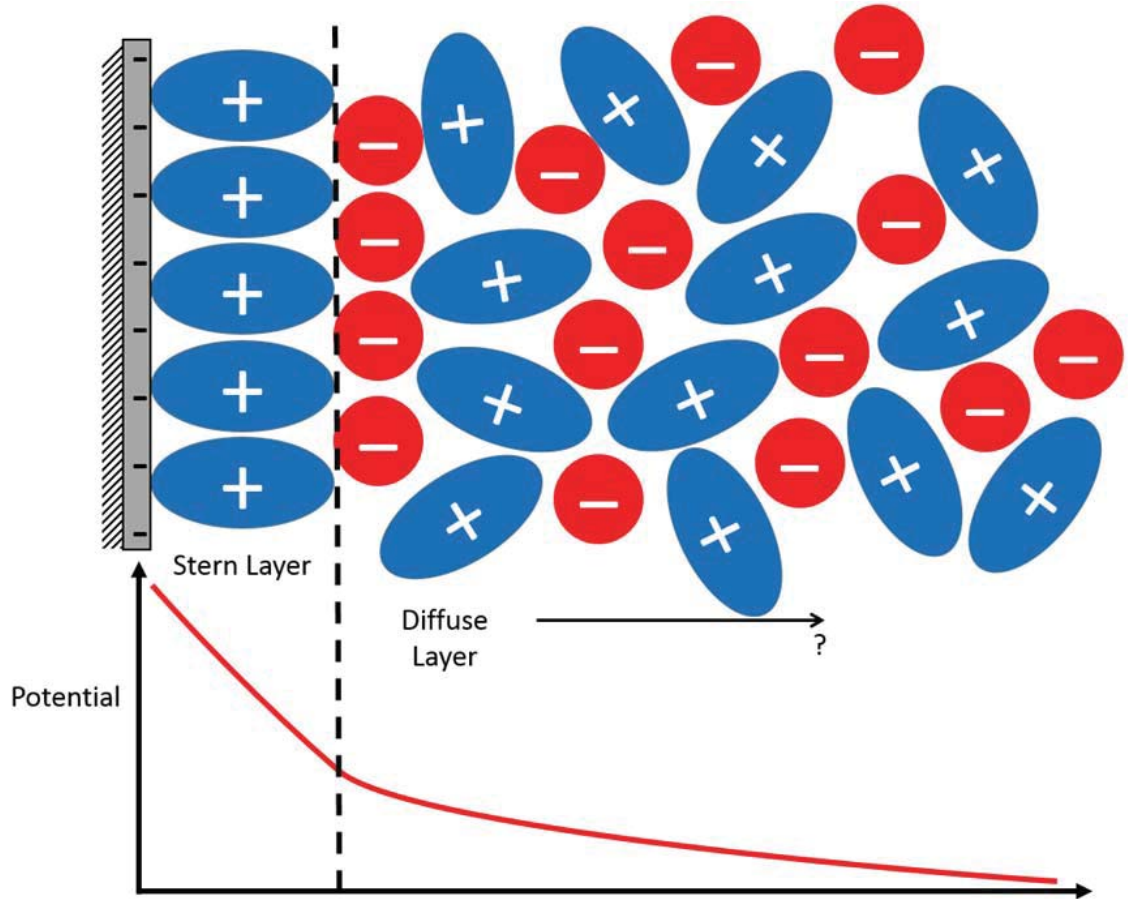

Figure 2.4: *Top: Schematic diagram of the Stern-Gouy-Chapman model for the structure of electrolytes at an electrode, using a negative electrode as an example. The Stern layer is highlighted, and the propagation of the diffuse layer pointed out. Bottom: Representation of how the potential from the surface propagates from into the liquid.*

Hayes *et al.* found no evidence of a diffuse layer, thus postulated that the structure of the ionic liquid at the electrode should be similar to that of a Helmholtz model, which involves the formation of layers of opposite polarity at the surface: the classic electrical double layer theory.[47]

Later surface force balance (SFB) measurements showed the presence of a force at distances where Helmholtz layers were not present, showing evidence for a diffuse layer extending into the bulk.[48–52] This has led to the current most popular model for the structure of ionic liquids at electrodes being the Stern-Gouy-Chapman model, of which a simplified representation is shown in Figure 2.4.

The Stern-Gouy-Chapman model involves an extension of the Gouy-Chapman model to include Helmholtz layers. The Gouy-Chapman model proposed that application of a potential to an electrode causes ions of opposite charge to cluster closer to the electrode and ions of the same charge to be repelled from it. This leads to a concentration gradient of ions from the electrode into the bulk, known as a diffuse layer.[47]

The Gouy-Chapman model itself fails to account for the fact that a highly charged electrode will strongly attract ions of opposite charge to itself causing a very steep concentration gradient, especially at higher electrolyte concentrations. Therefore, the modification proposed by Stern was to expand the model to include a Helmholtz layer of ions with opposite polarity to the electrode at the surface, which then turned into a Gouy-Chapman diffuse layer when moving farther from the electrode.[47]

This leads to a model which can account for both the high electrode concentration leading to 'overcrowding' at the electrode as well as the structure that propagates from the electrode. The AFM measurements show that while the Stern layer thickness is very dependant on the potential at the surface, it always remains $\lesssim$10 nm.[45,46] This was shown even to be the case for very large ions e.g. the AFM profile of 1-butyl-3-methylimdazolium 1,4-bis(2-ethylhexoxy)-1,4-dioxobutane-2-sulfonate shows that, despite the large anion, the Stern layer structure persists for 7.5 nm.[53] Instead of increasing the size of the Stern layer, larger ions simply led to the presence of fewer Stern layers.

Beyond the Stern layers, SFB measurements have shown that there is a measurable force from diffuse layers at up to 50 nm from the surface, though this is also potential- and liquid-dependant.[48–50,54] The same long range forces were also measured on concentrated salt solutions (e.g. 2 M NaCl in water), indicating that this is not necessarily a property unique to ionic liquids, but instead is a property of concentrated salt solutions.[50]

On the topic of the measurements of the diffuse layer, initially there was a debate about a consequence of these measurements in the literature, which was started due to a rather interestingly titled paper: "*Ionic Liquids Behave as Dilute Electrolytes*".[48] In this paper the exponential decay profile of the Stern layer structure from SFB measurements was used to calculate a Debye screening length (the distance the effect of charge propagates), found to be 11 nm for $[C_4C_1im][NTf_2]$.[55] From the Debye length the ion concentration can be determined from the Debye-Hückel equation (Equation 2.4)

$$\kappa^{-1} = \sqrt{\frac{\epsilon k_B T}{4\pi q^2 I(m)}} \tag{2.4}$$

where κ^{-1} is the Debye length, ϵ is the dielectric constant of the medium, k_B is the Boltzmann constant, T is the temperature, q is the ion charge, and $I(m)$ is the molar concentration in mol/L.

Using the measured screening length to calculate the concentration of ions in $[C_4C_1im][NTf_2]$ a concentration of $\approx$0.75 mM was calculated, which is not correct as the concentration of ions

in neat $[C_4C_1im][NTf_2]$ is ≈3.4 M. The screening length suggests that the concentration of ions was nearly 5000× lower than it was.

Further experimental results were obtained which showed the screening lengths were correct, therefore the interpretation of the results must have been flawed. An important result was that this effect was not unique to ionic liquids and was a feature of all concentrated electrolytes.[50]

The overall conclusion of these papers was that while the Debye/screening length of an electrolyte initially decreases with increasing concentration, there is a concentration at which the Debye/screening length then increases with concentration.[50,56–58] While this occurred in all electrolytes measured, the point at which this reversal occured was different for each electrolyte.

Smith *et al.* quantified this increase via the relationship between two parameters. The deviation from the Debye length was quantified by the ratio between the measured screening length (λ_{exp}) and the theoretical Debye length, $\lambda_{exp}/\kappa^{-1}$. They correlated this to a 'dielectric-scaled ion density' which is represented by the ratio between the diameter of the ion (d) and the theoretical Debye length, d/κ^{-1}.[50]

They found that when $d/\kappa^{-1} < 1$, then $\lambda_{exp}/\kappa^{-1} = 1$ meaning that the classical Debye-Hückel theory predicted the measured screening lengths very well. However, once the diameter of the ion became greater than the calculated Debye length, from Debye-Hückel theory, the theory breaks down and the screening length increases with increasing ion diameter.

Later work showed that the Bjerrum length was a good predictor of screening lengths when the ion diameter is greater than the Debye length.[57] The Bjerrum length is the distance at which the interaction energy between two ions is equal to the thermal energy. Lee *et al.* showed that this occurred with a direct dependence upon the Bjerrum length, ion concentration and the cube of the ion diameter.[57]

In summary, the screening length of electrolytes was found to be equal to the Debye length when the ion diameter was less than the Debye length. In this regime, increasing concentration leads to a decrease in Debye length, as per the Debye-Hückel theory. At the point at which the Debye length decreases below the ion diameter, the screening length increases, and this can be predicted from the ion diameter, concentration, and the Bjerrum length.

Importantly for ionic liquids, as they have a high concentration and large ions, they are within this regime wherein the Debye length is less than the ion diameter. This means that the screening lengths of the ions within an ionic liquid will be much larger than Debye length, which will have consequences upon the length scales on which interactions occur within ionic liquids.

2.2.2 Ionic Liquids in Electric Fields - Long Distances and Long Times

Despite all of the theory and literature described in the previous section, which seems to indicate relatively 'normal' behaviour of ionic liquids, there are some results from the study ionic liquids at electrode which would suggest otherwise. The literature results will be discussed here, and the work carried out by previous members of the Welton/McIntosh research group (which forms the basis of this thesis) is summarised below.

As discussed in the previous section, it was deduced from AFM, SFB and electrochemical measurements[43,45] that the structure of the ionic liquid/electrode interface is a Stern-Gouy-Chapman double layer structure (Figure 2.4). This has a Stern layer of oppositely charged ions (with respect to the electrode) on the electrode surface, followed by a diffuse layer into the bulk. This diffuse layer is made up of alternating layers of cations and anions, with the concentration of the ions in the layers decreasing until unity is reached and the liquid is 'bulk' liquid. From the AFM measurements, the Stern layer was determined to be around 10 nm at most, with the thickness of the repeating layers decaying with voltage. The diffuse layer was measured by SFB measurements and this structure was proposed to propagate in the order 10's of nm at most away from the electrode, which is still a relatively long distance compared to the lengths of these layers in conventional electrolytes (<10 nm).

Likewise, the time required to charge a capacitor and create this structure, the cell time constant, for ionic liquids at electrodes was considered to be very long. A calculation of the time constant of an ionic liquid cell (also known as the RC constant) determined that the charging and discharging time of an ionic liquid capacitor should be <1 s.

With respect to both the time of the charging dynamics and the distance these structures propagate over, there have been some interesting results which suggest these could be even longer. Nishi *et al.* used surface plasmon resonance measurements to study the adsorption of methyltrioctylammonium bis(nonafluorobutanesulfonyl)imide ions on a platinum electrode, and found that the times associated with the adsorption and desorption of the ions had characteristic lifetimes of 100's of seconds, despite a calculated RC time giving a lifetime of 0.1 s. These effects were independent of the potential step applied i.e. the magnitude of change in potential and whether the potential went from positive to negative or *vice versa.*[59]

Chu *et al.* measured x-ray reflectivity of the ionic liquid methyltrioctylammonium bis(trifluoromethylsulfonyl)imide at a silica electrode as a function of potential, and found that the reflectivity profile required >3000 s to equilibrate after a change in potential. As seen by Nishi

et al., this was found to be independent of the potential step.[60]

Uysal *et al.* measured a slow response of 1-nonyl-3-methylimidazolium bis(trifluoromethylsulfonyl)imide at a graphene electrode. Their measurements showed a slow response of the change in the interfacial structure to the the applied potential, although their time-scales were relatively short compared other measurements discussed here (>10 s). They also saw a "path-dependent manner" in the change in structure, essentially a structural hysteresis.[61]

When measuring how the surface tension and current changed in methyltrioctlyammonium bis(nonafluorobutanesulfonyl)imide at an electrode, Yasui *et al.* also saw very long relaxation times for the surface tension with a change in the potential of over 100 s.[62] Also reported, but not discussed in this paper, was that the change in current was of a similar, but slightly slower time-scale to that of the surface tension.

Perez-Martinez and Perkin used a surface force balance to investigate the change in distance between two electrodes, either conductive or non-conductive, in an AC field with various liquid mediums between the electrodes. Based upon calibrations in air and PDMS, the behaviour of the balance was calibrated and found to be theoretically predictable. However, when swapping out the medium for an ionic liquid, either 1-ethyl-3-methylimidazolium bis(trifluoromethylsulfonyl)imide or N-butyl-N-methylpyrollidinium bis(trifluoromethylsulfonyl)imide, a very different behaviour was observed.[63]

Upon application of a field with an ionic liquid as the medium, there was a much larger than predicted change in the distance between the plates, up to 50× greater, with these changes taking a long time to occur, much slower than predicted. Given the initial calibrations, the distance between the electrodes should have fully changed over ≈ 1 s then equilibrated, given the viscosity of the ionic liquid. Instead, the distance between the electrodes required over 1000 s to fully equilibrate in the field independent of the voltage, initial separation of the plates and frequency of the AC field.[63]

Perhaps the most unusual of this phenomena was that the force profile consisted of either: an initial repulsion, followed by a quick attraction, then a final much longer repulsion, or for some unexplainable reason, *the exact opposite profile was observed.* A swapping between a positive then negative response to a potential has been observed before by Yasui *et al.*[62] in surface tension measurements, although they also simply acknowledge the existence of such a switch, and cannot rationalise an explanation.

Another unusual phenomenon described in the literature comes from an investigation by Anaredy and Shaw on the structure of various ionic liquids near a rotating, *uncharged* silver disc. They saw that when studying the structure of the ionic liquid near the rotating silver disc, ordered

structures were seen extending *ca.* 2 μm from the disc, and these took between 30 to 120 minutes to form, scaling linearly with the viscosity.[64] The formation of this structure was found to be independent of the substrate material, cation structure, overlying vapour phase, and presence of water impurities. From their analysis they determined that this structure forms from a reorientation of the $[NTf_2]^-$ anion throughout the entire thickness of this film, though they ruled out that this causes a crystallisation of their ionic liquids.[64]

This result is unusual as there was no potential applied to the silver surface from which structure formed. Although there was no potential applied, there is evidence that structuring exists at ionic liquid/electrode interfaces without the presence of a potential.[46] However, if there is no potential applied there is no force for forming a structure, therefore the observation of such a force, especially one that persists across such long times and distances, is peculiar indeed.

It should be noted that simulations of ionic liquids at electrodes have, so far, been unable to replicate these experimental results,[65,66] although some relatively long time-scale process (>10 ns, which is long for molecular dyanmics simulations) have been observed.[67]

Explanations for the unusually long time-scale and distance experimental results could be aided by considering other results in the literature. For example, Comtet *et al.* showed that capillary freezing in ionic liquids could occur at a longer range when using a more polarisable confinement material e.g. platinum (high polarisability) could force capillary freezing at a separation of ≈ 170 nm compared to ≈ 20 nm for mica (low polarisability).[68]

Another interesting and possibly related result was seen by Kong *et al.*, who observed that the contact angle decreased and friction force increased on a tribometer measuring an ionic liquid sample when an electric field was applied between the ball and pad.[69]

There have also been many observations of hysteresis in cyclic voltammetry measurements, which show a slow change in the ion composition and/or orientation at an electrode, as well as a dependence on the direction which the voltage is changing.[70–75] Given the diverse range of ionic liquids and electrodes that have been used in these studies of long time-scale and long distance effects, the presence of these appears to not be related to any specific properties of an electrode, but is instead related to the ionic liquids.

Long Distances and Long Times - Previous PhD theses

As part of his work into ion dynamics across ionic liquid interfaces, Alastair McIntosh performed some fluorescence correlation spectroscopy experiments on a dye (Rhodmaine 123, Rh123) in $[C_4C_1im][NTf_2]$ at an electrified interface. This was to aid the understanding of how ion dy-

namics change across an ionic liquid/liquid interface and how an electric field could affect this. It was discovered that when applying a potential of +2 V or +3 V to an electrode, the ion dynamics at the electrode/liquid interface slowed drastically, which was an expected result.

When profiling how the potential at the electrode affected the diffusion of the dye into the 'bulk' of the ionic liquid, this decrease in the diffusion of Rh123 was found to extend up to at least 50 μm from the electrode into the liquid. Measurements beyond 50 μm could not be performed dye to limitations in the microscope objective used.

This was surprising as 50 μm is far, far beyond anything that should be seen, especially considering that the recently reported effects of 30 nm were considered long range.[49]

Alongside the long range, the time-scales upon which onset and recovery occurred where much longer than anticipated. Although slow, it was accepted that the dynamics of ionic liquid ions at interfaces was of the order of a few seconds.[76] It was seen that close to the electrode, the dynamics did change very rapidly upon potential application.

However, when considering the onset of the reduced dynamics at greater distances from the electrode, as well as the recovery of the system after returning to zero potential, this was far from the case. It took up to a minute of holding the potential at a constant voltage for the decrease in diffusion of the dye to be observed at 50 μm.

More evidence of long time-scale effects were seen when removing the potential and returning to the potential of zero current. After returning to 0 V the low diffusion of the dye was found to persist for at least 10 minutes at all distances from the electrode.

These results showed effects of an electrified interface on an ionic liquid that were over 3 orders of magnitude larger in scale, both in terms of distance and time, than anything that had previously been reported at the time.

Since these results were found and presented, others have seen similarly long range and long time-scale results in ionic liquids at interfaces, although not all electrified.[63,64]

After Alastair's work Azizi Nawawi began working on the project and confirmed these results in the same ionic liquid. Alongside this, Azizi also measured the same effect in another ionic liquid, N-butyl-N-methylpyrrolidinium bis(trifluoromethylsulfonyl)imide ($[C_4C_1pyrr][NTf_2]$).

Azizi also worked on the hypothesis that this decrease in diffusion was caused by an increase in viscosity by using molecular rotors (Chapter 5) to try to measure the viscosity of ionic liquids and observe how the viscosity of $[C_4C_1im][NTf_2]$ and $[C_4C_1pyrr][NTf_2]$ changed at the same long distances from an electrode when a potential was applied.

Changes in the viscosity of both of these ionic liquids were observed, with a tripling of the viscosity from ≈50 cP to ≈150 cP. This was a huge change, and the first task of my part of the

project was to confirm and/or replicate these results.

Although the results and analysis in this thesis show that the large changes in the viscosity are not the correct interpretation, the increase in viscosity is still believed to be true. Chapter 6 has the full details of this.

Chapter 3

Synthetic Procedures

To ensure that the glassware used was free of contaminants, all glassware used was washed with ethanol, followed by washing with a 5 % (v/v) Decon 90 solution in distilled water, then rinsed with distilled water until bubbles from the Decon 90 ceased.

The glassware was subsequently rinsed with piranha solution (1:3, 30 % hydrogen peroxide: 95-98 % sulphuric acid) a minimum of four times or until effervescence from organic residues ceased. This was followed by at least four rinses with distilled water to remove piranha residue. The glassware was then dried overnight in a clean oven operating at 120 °C. If any contaminants were observed on the glassware then this procedure was repeated until the glassware was residue free after being in the oven.

To minimise the introduction of contaminants during synthesis, thick-walled PTFE sleeves were used instead of grease. These were also rinsed with Decon 90, piranha solution and distilled water following the same procedure as for the glassware.

Any stirring bars, Rotaflo stopcocks, spatulas or any other glassware/equipment involved in the synthetic procedure were also washed with Decon 90, piranha solution and distilled water and dried before being used.

All starting materials were purchased from Sigma Aldrich at the highest purity possible. Solvents were used as received, but most starting materials were purified before use (with the exception of lithium bis(trifluoromethylsulfonyl)imide which was used as received).

Toluene (99.85 %), ethyl acetate (99.9 %), acetonitrile (99.9 %) and hexane (99.9 %) were purchased from Sigma Aldrich as AcroSeal solvents. These are extra dry solvents stored under dry nitrogen over molecular sieves and were used without further purification.

Dichloromethane (99.9 %) was purchased from VWR at HPLC grade and was used without

further purification.

Water was distilled using a D4000 distinction water still.

3.1 Synthesis of 1-butyl-3-methlimidazolium chloride

This synthetic procedure was performed by Mohd Azizi Nawawi.[77]

1-chlorobutane (Sigma Aldrich, $\geq$ 99 %) was purified by washing with concentrated (96-98 %) sulfuric acid ($\approx$1 mL H_2SO_4 per 5 mL of 1-chlorobutane) until the acid layer remained colourless. The organic layer was then neutralised by washing with a saturated solution of sodium bicarbonate in distilled water until the aqueous layer was slightly basic (pH $\approx$ 8) followed by a final rinse with distilled water. The organic layer was then dried with magnesium sulfate overnight. The magnesium sulfate was then removed via filtration and the organic layer further dried with phosphorus pentoxide overnight. The 1-chlorobutane was then distilled from phosphorus pentoxide to give the purified 1-chlorobutane used in this synthesis.

1-methylimidazole (Sigma Aldrich, $\geq$ 99.5 %) was stirred with potassium hydroxide pellets overnight followed by distillation. This was followed by stirring with freshly cut sodium metal overnight and a further distillation.

1-chlorobutane (340 mL, 3.26 mol, 1.1 eq) was added drop-wise to a cooled, stirred solution of 1-methylimidazole (235 ml, 2.96 mol, 1 eq) in 200 mL ethyl acetate. Whilst stirring, the reaction mixture was allowed to warm up to room temperature then continued to be stirred for 1 week at room temperature. The temperature was increased by 10 °C every 4 days until the reaction reached 60 °C and the reaction mixture was then held at 60 °C for 3 weeks. The reaction mixture was then cooled to -20 °C for 2 days affording white crystals. Excess solvent was decanted, and the crystals washed with extra dry ethyl acetate (2 x 150 mL) then recrystallised twice from acetonitrile:ethyl acetate (1:5) and then dried *in vacuo* yielding white crystals. (295.41 g, 57 % yield).

^{1}H NMR (400 MHz, DMSO-d6) δ 9.22 (1H, s, NC*H*N), 7.80 (1H, s, NC*H*CHN), 7.73 (1H, s, NCHC*H*N), 4.18 (2H, t, J = 7.2 Hz, NCH_2CH$_2$CH$_2$CH$_3$), 3.86 (3H, s, NCH_3), 1.77 (2H, quintet, J = 7.4 Hz, NCH$_2$CH_2CH$_2$CH$_3$), 1.27 (2H, m, NCH$_2$CH$_2$CH_2CH$_3$), 0.91 (3H, t, J = 7.4 Hz, N(CH$_2$)$_3$CH_3).

^{13}C NMR (101 MHz, DMSO-d6) δ 137.16 (N*C*HN), 124.09 (N*C*HCHN), 122.75 (NCH*C*HN), 48.94(N*C*H$_2$CH$_2$CH$_2$CH$_3$), 36.21 (N*C*H$_3$), 31.83 (NCH$_2$*C*H$_2$CH$_2$CH$_3$), 19.24 (s, NCH$_2$CH$_2$*C*H$_2$ CH$_3$), 13.75 (s, N(CH$_2$)$_3$*C*H$_3$).

3.2 Synthesis of 1-butyl-3-methylimidazolium bis(trifluoromethylsulfonyl)imide

Solid lithium bis(trifluoromethylsulfonyl)imide ($\geq$ 99.95 %, Sigma Aldrich) (71.15 g, 0.25 mol, 1 eq) was added to a stirred solution of 1-butyl-3-methylimidazolium chloride (43.29 g, 0.25 mol, 1 eq) in 300 mL dichloromethane. The mixture was stirred for 24 hours at room temperature then filtered to remove the lithium bromide precipitate. The filtrate was washed with distilled water (8 x 50 mL) until the aqueous phase was halide free, confirmed by silver nitrate test. Excess solvent was removed on the rotary evaporator and the resulting liquid was washed with 150 mL n-hexane before removing excess solvent *in vacuo*. The crude oily liquid was stirred with activated charcoal overnight and filtered through filter paper followed by a sterile 0.2 µm PTFE membrane filter. The resulting liquid was dried *in vacuo* at 55 °C for 2 days to give clear colourless viscous liquid (60.77 g, 58 % yield).

^{1}H NMR (400 MHz, DMSO-d6 capillary) δ 8.01 (1H, s, NC*H*N), 6.92 (1H, s, NC*H*CHN), 6.85 (1H, s, NCHC*H*N), 3.62 (2H, t, J = 7.4 Hz, NC*H*$_2$CH$_2$CH$_2$CH$_3$), 3.35 (3H, s, NC*H*$_3$), 1.30 (2H, quintet, J = 7.6 Hz, NCH$_2$C*H*$_2$CH$_2$CH$_3$), 0.78 (2H, hextet, J = 7.5 Hz, NCH$_2$CH$_2$C*H*$_2$CH$_3$), 0.35 (3H, t, J = 7.4 Hz, N(CH$_2$)$_3$C*H*$_3$).

^{13}C NMR (101 MHz, DMSO-d6 capillary) δ 135.42 (s, N*C*HN), 122.89 (s, N*C*HCHN), 121.63 (s, NCH*C*HN), 119.30 (quartet, $^{1}J_{CF}$ = 320.7 Hz, *C*F$_3$), 48.85 (s, N*C*H$_2$CH$_2$CH$_2$CH$_3$), 34.96 (s, N*C*H$_3$), 30.99 (s, NCH$_2$*C*H$_2$CH$_2$CH$_3$), 18.34 (s, NCH$_2$CH$_2$*C*H$_2$CH$_3$), 11.85 (s, N(CH$_2$)$_3$*C*H$_3$).

ES MS +ve mode: m/z 139 (M^+, 100). ES MS -ve mode: m/z 281 (M^-, 100).

Found: C, 28.8; H, 3.7; N, 10.2. Calc. for $C_{10}H_{15}F_6N_3O_4S_2$: C, 28.6; H, 3.6; N, 10.0 %

3.3 Synthesis of 1-octyl-3-methylimidazolium chloride

1-chlorooctane (Sigma Aldrich, $\geq$ 99.5 %) was purified by washing with concentrated (96-98 %) sulfuric acid ($\approx$1 mL H_2SO_4 per 5 mL of 1-chlorooctane) until the acid layer remained colourless. The organic layer was then neutralised by washing with a saturated solution of sodium bicarbonate in distilled water until the aqueous layer was slightly basic (pH $\approx$ 8) followed by a final rinse with distilled water. The organic layer was then dried with magnesium sulfate overnight. The magnesium sulfate was then removed via filtration and the organic layer further dried with phosphorus pentoxide overnight. The 1-chlorooctane was then distilled from

phosphorus pentoxide to give the purified 1-chlorooctane used in this synthesis.

1-methylimidazole (Sigma Aldrich, $\geq$ 99.5 %) was stirred with potassium hydroxide pellets overnight followed by distillation. This was followed by stirring with freshly cut sodium metal overnight and a further distillation.

1-chlorooctane (410.3 g, 2.76 mol) was added drop-wise to a solution of 1-methylimidazole (206.0 g, 2.51 mol) in toluene (200 mL) at room temperature with stirring. The temperature was gradually increased to 40 °C over 6 hours and the mixture was left to stir at this temperature for 50 days. After this the temperature was decreased to 35 °C for a further 14 days. The reaction mixture was washed with ethyl acetate (3 $\times \approx$ 50 mL) affording a clear, colourless oil. The crude was purified by dissolving in a small amount of acetonitrile ($\approx$ 40 mL) and precipitating with ethyl acetate, followed by multiple washes with ethyl acetate (5 $\times \approx$ 250 mL). Excess solvent was removed *in vacuo* overnight (at 30°C) to give the product as a clear, very slightly yellow oil (383.68 g, 66 % yield).

^{1}H NMR (400 MHz, DMSO-d6) δ 9.38 (1H, s, NC*H*N), 7.83 (1H, t, J = 1.7 Hz, NC*H*CHN), 7.76 (1H, t, J = 1.7 Hz, NCHC*H*N), 4.17 (2H, t, J = 7.2 Hz, NCH_2CH$_2$(CH$_2$)$_5$CH$_3$), 3.86 (3H, s, NCH_3), 1.77 (2H, q, J = 7.4 Hz, NCH$_2$CH_2(CH$_2$)$_5$CH$_3$), 1.35 – 1.14 (10H, m, NCH$_2$CH$_2$(CH_2)$_5$ CH$_3$), 0.85 (3H, t, J = 6.9 Hz, MCH$_2$CH$_2$(CH$_2$)$_5$CH_3).

^{13}C NMR (101 MHz, DMSO-d6) δ 136.62 (N*C*HN), 123.54 (N*C*HCHN), 122.23 (NCH*C*HN), 48.68 (octyl-C(1)), 35.69 (N-CH$_3$), 31.13 (octyl-C(2)), 29.38 (octyl-C(3)), 28.45 (octyl-C(4)), 28.32 (octyl-C(5)), 25.47 (octyl-C(6)), 22.02 (octyl-C(7)), 13.91 (octyl-C(8)) (Note: The peaks at 48.68 and 35.69 were confirmed by DEPT-135 ^{13}C NMR).

3.4 Synthesis of 1-octyl-3-methylimidazolium bis(trifluoromethylsulfonyl)imide

To a solution of 1-octyl-3-methylimidaozlium chloride (57.93 g, 0.251 mol) in distilled water was added a solution of lithium bis(trifluoromethylsulfonyl)imide ($\geq$ 99.95 %, Sigma Aldrich) (72.11 g, 0.251 mol) in distilled water at room temperature. The resulting cloudy solution was left stirring at room temperature for 5 days. The ionic liquid layer was isolated and washed with water (5 $\times \approx$ 50 mL) until the aqueous layer was halide free, confirmed by silver nitrate test. The ionic liquid layer was then collected, and washed with hexane (150 mL). Acetonitrile ($\approx$ 20 mL) was added to the ionic liquid to reduce the viscosity and this solution was stirred

for 3 days with activated charcoal. This was then filtered through filter paper followed by a sterile 0.2 μm PTFE membrane filter and dried *in vacuo* overnight at room temperature to give a crystal clear liquid as product (89.00 g, 89% yield).

^{1}H NMR (400 MHz, DMSO-d6) δ 9.09 (1H, s, NC*H*N), 7.75 (1H, t, J = 1.8 Hz, NC*H*CHN), 7.69 (1H, t, J = 1.8 Hz, NCHC*H*N), 4.14 (2H, t, J = 7.2 Hz, NC*H*$_2$CH$_2$(CH$_2$)$_5$CH$_3$), 3.84 (3H, s, NC*H*$_3$), 1.77 (2H, p, J = 7.3 Hz, NCH$_2$C*H*$_2$(CH$_2$)$_5$CH$_3$), 1.36 – 1.10 (10H, m, NCH$_2$CH$_2$(C*H*$_2$)$_5$ CH$_3$), 0.86 (3H, t, J = 7.0 Hz, imCH$_2$CH$_2$(CH$_2$)$_5$C*H*$_3$).

^{13}C NMR (101 MHz, DMSO-d6) δ 136.45 (s, N*C*HN), 123.56 (s, N*C*HCHN), 122.22 (s, NCH*C*HN), 119.46 (q, J = 323.2 Hz, CF3), 48.77 (s, octyl-C(1)), 35.70 (s, N-CH$_3$), 31.11 (s, octyl-C(2)), 29.34 (s, octyl-C(3)), 28.42 (s, octyl-C(4)), 28.29 (s, octyl-C(5)), 25.45 (s, octyl-C(6)), 22.00 (s, octyl-C(7)), 13.85 (s, octyl-C(8)) (Note: The peaks at 48.68 and 35.69 were confirmed by DEPT-135 ^{13}C NMR).

ES MS +ve mode: m/z 195 (M^+, 100). ES MS -ve mode: m/z 280 (M^-, 100).

Elemental Analysis: Found: C, 35.55; H, 4.82; N, 8.99. Calc. for $C_{14}H_{23}F_6N_3O_4S_2$: C, 35.36; H, 4.88; N, 8.84 %

Chapter 4

Simulation Protocols

4.1 Simulations of 1-butyl-3-methylimidazolium bis(trifluoromethylsulfonyl)imide in electric fields

The force field used in the experiments is a polarisable, thermalised Drude oscillator method, implemented into the simulation using the method developed by Dequidt, Devémy and Pádua for LAMMPS.[78]

The OPLS-AA force field parameters from the widely used Canongia-Lopes and Padua force field were used as the initial parameters.[21,79] The Drude particle spring constants and masses were taken from Lamoureux and Roux,[80] and additive polarisabilites from Bernardes *et al.*[81] All simulations were run using LAMMPS.[82]

In this force field, the Drude particles were assigned a mass of 0.4 amu, a half spring constant (K/2) of 500 kcal mol^{-1} Å^{-2} and an equilibrium position of zero with respect to the Drude core atom. The electrostatic potential between the Drude particle and the Drude core were dampened using a Thole function. The Drude cores were thermalised at 1 K using a seperate Nosé-Hoover thermostat with a time constant of 2.5 fs. This thermostat is decoupled from the thermostat of the Drude cores, and the temperature of the Drude particles are calculated from the kinetic energy of the Drude particles using the Drude cores as the reference frame.

For hydrogen and fluorine atoms the polarisability is accounted for on the direct neighbour atom, rather than assigning a Drude particle to these atoms.

All simulations described here are run in a canonical ensemble (fixed NVT) with a timestep of 0.5 fs. Periodic boundary conditions were applied and long-range interactions were treated

with a particle-particle particle-mesh solver method (PPPM) with a relative error in forces of 1×10^{-6}. Short-range Coulomb interactions were damped by Thole functions with a damping parameter of 2.6.[78] Lennard-Jones interactions where cut off after 12 Å; whereas Coulomb interactions were treated in reciprocal space beyond that distance.

Two thermostats were employed to run parallel trajectories under the same electric field conditions to check consistency of the results. The first is a Nosé-Hoover thermostat which uses non-Hamiltonian equations of motion to generate positions and velocities and performs both thermostatting and time integration.[83] The second is a CSVR thermostat which adjusts the temperature in a canonical ensemble using global velocity rescaling with Hamiltonian dynamics.[84]

It should be noted that this thermostat does not perform time integration, i.e. the CSVR thermostat controls temperature only each time step and does not progress the simulation through time. Therfore, the time integration was performed using the `fix nve` command, and the thermostatting modified to use the temperature from the CSVR thermostat. Therefore in this simulation, the NVE time integration equations are used to progress the simulation, and the CSVR thermostat used to control the temperature.[84]

Initially, 256 ion pairs of $[C_4C_1im][NTf_2]$ were placed in a simulation box with all sides of size 5426.8 pm using the fftool[85] and PACKMOL[86] algorithms. This matches the theoretical density predicted by Vranes et al.[87] at 600 K (theoretical as $[C_4C_1im][NTf_2]$ decomposes at approx. 450 K). When changing temperature, the box size was also changed so at any temperature the density matches the prediction found by Vranes et al.[87]

Drude particles were added to all atoms in the simulation box except for hydrogen and fluorine using the `polarizer` addon in fftool.[85] Charges of the Drude particles were assigned according to the polarisabilties in Table 4.1 and Equation 4.1.

Table 4.1: *Polarisabilites of the atoms used in these simulations.*[81]

Atom	H	C (sp^2)	C (sp^3)	N	S	F	O
Polarisability (Å^3)	0.389	1.290	1.081	1.085	2.771	0.346	0.354

$$q = \sqrt{\frac{K}{\alpha}} \tag{4.1}$$

Charges and masses on the Drude core atoms were adjusted so the charge and mass of an atom-Drude particle pair was the same as the charge and mass of the initial atom.

Equilibration of the simulations was performed using the following procedure:

1. Unfavourable initial configurations were relaxed by a short (1000 step) conjugate gradient energy minimisation and subsequent thermalisation at 600 K over 500 ps using a Nosé-Hoover thermostat with a time constant of 20 fs.

2. The minimised box was cooled to 400 K over 500 ps using a Nosé-Hoover thermostat with a time constant of 20 fs.

3. This simulation box was then held at 400 K to thermally equilibrate the system at this temperature using a Nosé-Hoover thermostat with a time constant of 100 fs.

4. Separate trajectories were then equilibrated with the Nosé-Hoover thermostat and CSVR thermostat at 400 K for 500 ps from the end configuration of the previous simulation with a time constant for both thermostats of 100 fs.

5. Electric fields of strength described below were then applied to each of the end points of the previous two trajectories. Electric fields were applied along the z vector of the simulation box. At this point, the thermostats were modified to only take into account temperature in the xy plane to avoid interference between the thermostat and electric field. These simulations were equilibrated with the electric field for 1 ns.

6. For static structure analysis, 1 ns production runs were run with coordinates output every 50 fs. Convergence of these trajectories was checked by calculating properties for the whole trajectory, the first half of the trajectory, and the second half of the trajectory. These were then compared within the same simulation and between trajectories run with the same electric field but with different thermostats for consistency. All simulations had converged when analysing static properties.

7. For dynamic property analysis, 10 ns production runs from starting points of the end of the static analysis trajectories were run with trajectory coordinates output every 500 fs.

The electric fields investigated were static fields of strengths: 0.000 VÅ^{-1}, 0.001 VÅ^{-1}, 0.002 VÅ^{-1}, 0.005 VÅ^{-1}, 0.010 VÅ^{-1}, 0.020 VÅ^{-1}, 0.050 VÅ^{-1}, 0.100 VÅ^{-1}, 0.200 VÅ^{-1}, 0.300 VÅ^{-1}, 0.400 VÅ^{-1} and 0.500 VÅ^{-1}. Electric fields were applied by applying a force to each particle in the simulation equal to $F = EQ$ where F is force, E is electric field strength and Q is the charge on the particle.

A separate simulation was performed with the same protocol as above, but without any electric field and with the thermostat always applied in all directions. This was obtained to test the

assumption that taking into account temperature in only two directions (xy plane) in the thermostat doesn't change the result (See Section 7.2.1 for this analysis).
Analysis of the resulting trajectories was performed using TRAVIS[88] and python. Pictures of the ions were created using the VMD package.[89]

4.2 Simulations of 1-octyl-3-methylimidazolium bis(trifluoromethylsulfonyl)imide in electric fields

The same force field described in Section 4.1 was used for the simulations of $[C_8C_1im][NT_2]$ using the OPLS-AA force field parameters from the widely used Canongia-Lopes and Padua force field for the atoms charges and Lennard Jones parameters,[21,79] Drude particle spring constants and masses from Lamoureux and Roux,[80] and additive polarisabilites from Bernardes *et al.*[81]
All simulations were run in LAMMPS[82] using a time step of 0.5 fs. Periodic boundary conditions were applied and long-range interactions were treated with a particle-particle particle-mesh solver method (PPPM) with a relative error in forces of 1×10^{-6}. Short-range Coulomb interactions were damped by Thole functions with a damping parameter of 2.6.[78] Lennard-Jones interactions where cut off after 12 Å; whereas Coulomb interactions were treated in reciprocal space beyond that distance.
For these simulations, 256 ion pairs of $[C_8C_1im][NTf_2]$ were used to build the simulation box, which was then relaxed by a 1000 step conjugate gradient energy minimisation. The box was then relaxed using a 2 ns isothermal–isobaric ensemble (NPT, fixed number of atoms, pressure and temperature) at 400 K. The average box size over the final 500 ps was then used to fix the box size for a 2 ns canonical/NVT equilibration. Due to the analysis presented in Section 7.2 and 7.3, all of the canonical simulations of $[C_8C_1im][NTf_2]$ used a Nosé-Hoover thermostat.
The end configuration of this simulation was then used to run 12 parallel simulations to investigate the same electric fields as before: 0.000 VÅ^{-1}, 0.001 VÅ^{-1}, 0.002 VÅ^{-1}, 0.005 VÅ^{-1}, 0.010 VÅ^{-1}, 0.020 VÅ^{-1}, 0.050 VÅ^{-1}, 0.100 VÅ^{-1}, 0.200 VÅ^{-1}, 0.300 VÅ^{-1}, 0.400 VÅ^{-1} and 0.500 VÅ^{-1}. The electric fields were applied along the z vector of the simulation box to the end configuration of the previous 2 ns canonical equilibration, and at this point the thermostat was modified to only consider temperature perpendicular to the electric field (in the xy plane). As before, electric fields were applied by applying a force to each particle in the simulation equal to $F = EQ$ where F is force, E is electric field strength and Q is the charge on the particle.

Each of the simulations was equilibrated for a further 2 ns in the presence of the electric field. For static structure analysis, 1 ns production runs were run with coordinates output every 25 fs. Convergence of these trajectories was checked by calculating properties for the whole trajectory, the first half of the trajectory, and the second half of the trajectory. All simulations had converged when analysing static properties. For dynamic property analysis, 10 ns production runs from starting points of the end of the static analysis trajectories were run with trajectory coordinates output every 500 fs. Analysis of the resulting trajectories was performed using TRAVIS[88] and python. Pictures of the ions were created using the VMD package.[89]

4.3 Simulation of tributylhexylphosphonium bis(trifluoromethylsulfonyl)imide

The same force field described in Section 4.1 was used for the simulations of $[C_8C_1im][NT_2]$ using the OPLS-AA force field parameters from the widely used Canongia-Lopes and Padua force field for the atoms charges and Lennard Jones parameters,[21,79] Drude particle spring constants and masses from Lamoureux and Roux,[80] and additive polarisabilites from Bernardes *et al.*[81] All simulations were run using LAMMPS[82] with a time step of 0.5 fs. Periodic boundary conditions were applied, and long-range interactions were treated with a particle-particle particle-mesh solver method (PPPM) with a relative error in forces of 1×10^{-6}. Short-range Coulomb interactions were damped by Thole functions with a damping parameter of 2.6.[78] Lennard-Jones interactions where cut off after 12 Å; whereas Coulomb interactions were treated in reciprocal space beyond that distance. All simulations were run at 400 K.

To build the simulation box 512 ion pairs of $[P_{4446}][NTf_2]$ were packed into a cubic simulation box using the fftool[85] and PACKMOL[86] algorithms, and any unfavourable initial configurations were relaxed by a short (1000 step) conjugate gradient energy minimization.

The simulation was thermally equilibrated and relaxed by an initial 2.5 ns isobaric-isothermal run, with the average box size from the final 500 ps being used to set the box size for the production canonical run. This gave a final box size of 75.68 Å with a density of 1.113 g/mol, an error of 0.3% from experimental density.[90] The box size was fixed, and a canonical equilibration of 2 ns was performed, followed by a production run of 2 ns, with coordinates output every 100 fs for analysis.

Chapter 5

Molecular Rotors in Ionic Liquids

Some of the work presented in this chapter has already been published in:
The Effect of Structural Heterogeneity upon the Microviscosity of Ionic Liquids R. Clark, A. Nawawi, A. Dobre, D. Pugh, Q. Liu, A. P. Ivanov, A. J. P. White, J. Edel, M. K. Kuimova, A. J. S. McIntosh and T. Welton, *Chem. Sci.*, 2020, DOI: 10.1039/D0SC02009E.[1]

5.1 Introduction

The viscosity of a fluid is a measure of its ability to resist flow or deformation due to the internal forces holding the molecules together. This can be thought of as an internal friction force opposed to motion, usually quantified as a force per unit area which resists uniform flow. It is a fundamental property of fluids, and a large part of fluid dynamics involves understanding how the viscosity of a fluid affects its motion.

The viscosity of a fluid can have many implications on important properties which are related to the flow of individual molecules or the fluid as a whole. Considering bulk motion of the fluid, these are often an engineering problem, such as the ability of a fluid to be pumped, stirred and efficiently mixed.

When considering the ability of a fluid to impede motion on a molecular level, this is referred to as the microviscosity of the fluid. The microviscosity has implications for properties such as the conductivity of a fluid (which is movement of charge carriers through the fluid), mass transport in a solvent during diffusion-controlled processes or any other process which is diffusion-dependent.

Ionic liquids are highly viscous fluids, due to the fact that their components are held together by strong coulombic forces. This high viscosity limits the potential uses for ionic liquids in many diffusion-dependent processes that would otherwise benefit from high ion concentration (i.e. electrolytes, ion conducting fluids).

In order to design ionic liquids with suitable properties for such uses, a knowledge of macroscopic viscosity aids in choosing and designing better ionic liquids. However, the knowledge of the microviscosity of ionic liquids is currently limited to simulations,[16,91,92] and needs to be expanded and complemented by experimental approaches to aid in this goal.

Molecular rotors are a group of fluorescent compounds whose emission profile can be modified by a twisting/rotation around one or more bonds. This can be seen as a reduction in the emission intensity at a specific wavelength, caused by an increase in non-radiative decay by the twisting of the molecule, or a shift in the emission to a different wavelength.[93] Some example rotors are shown in Figure 5.1.

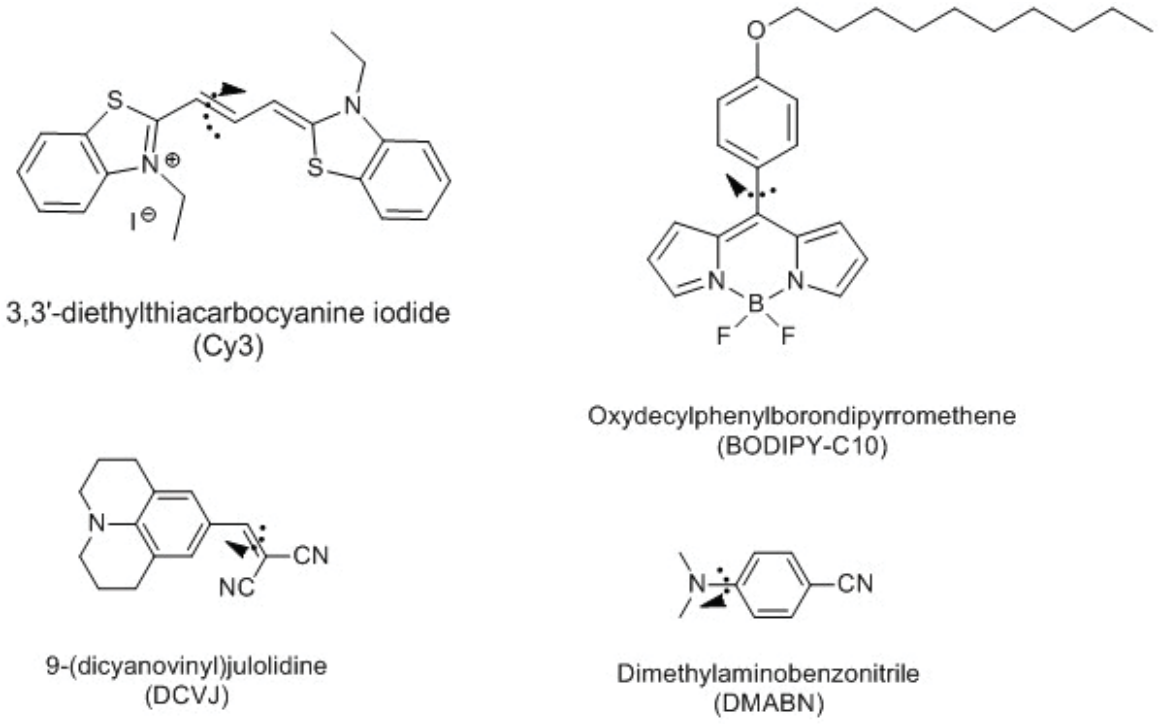

Figure 5.1: *Some example molecular rotors with arrows on the area of the molecule around which rotation leads to non-radiative quenching.*

An important feature of a molecular rotor is that the molecule requires a physical twist (i.e. a change in structure that requires movement through a medium) to quench fluorescence. This means that the emission profile of these rotors is susceptible to the viscosity of the medium in which they are being studied.[93]

The exact mechanism and twisting profile varies from rotor to rotor, however as a general rule

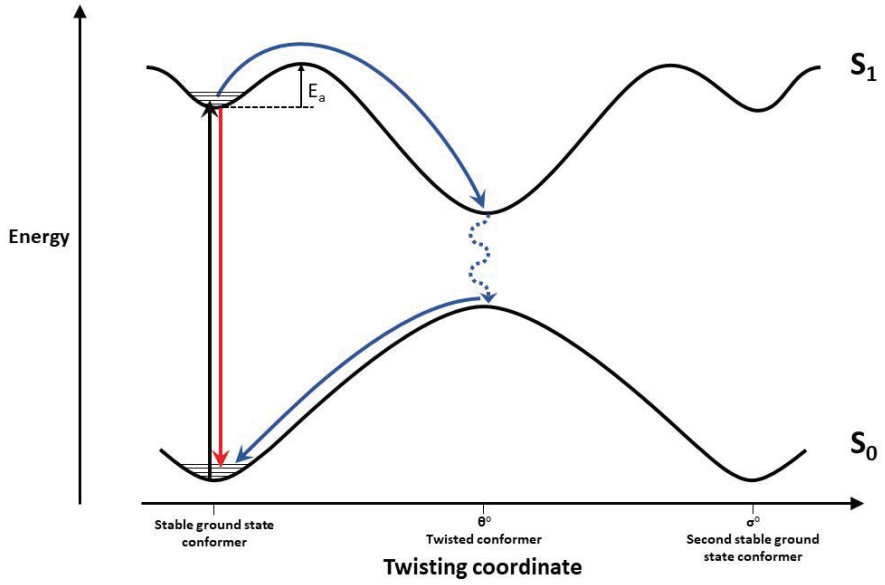

Figure 5.2: *Proposed general decay profile of molecular rotors.*

the rotors have a conjugated ground state, with a potential energy well in one configuration (line S_0 in Figure 5.2).

Upon absorption of a photon of the correct energy, the molecule moves into an excited state (S_1, black line in Figure 5.2). The rotor can relax from its excited state in two ways, the first involving the simple re-emission of a photon (red line in Figure 5.2). During this relaxation pathway, the rotor remains in its excited state for an amount of time related to the inherent lifetime of the excited state in the initial configuration, then emits a photon of similar energy to the one it absorbed. This relaxes the rotor back to its ground state without any change in its conformation. This is the slowest relaxation process in the rotor, hence has the longest lifetime. The lifetime associated with this decay is commonly known as the inherent lifetime.

The other mode of relaxation involves the twisting of the rotor in the excited state (blue lines in Figure 5.2). This occurs because in the excited state, the most stable ground state conformation is not the lowest energy conformation. Instead, the minimum energy conformation is a twisted conformation, with respect to the ground state, which the rotor can reach after overcoming a small activation energy barrier (E_a). In this twisted conformation the energy of the ground state is higher and is similar to that of the excited state, allowing non-radiative relaxation back to the ground state to occur. Once back in the ground state in the twisted conformation, the rotor is in a high-energy configuration and twists back to the most stable ground state conformation.

As this secondary pathway relies upon a change in the structure there are some limitations to

this relaxation pathway. If the viscosity of the medium in which the dye is being studied is too high (e.g. a solid) then this pathway is not accessible. With liquids there is a fairly simple trend in that the greater the viscosity of the liquid, the greater the frictional restriction on twisting of the rotor, and the higher E_a is. This makes it more difficult for the rotor to access the non-radiative decay pathway, a greater amount of the dye undergoes radiative decay, and the closer the lifetime to the inherent lifetime.

It is important to note that there is still some uncertainty behind the angle of rotation needed in order to access this secondary decay pathway. There is no general angle for all rotors, and the angle required changes depending on the rotor being considered.

Because of the uncertainty in how the dye and solvent affect each other, it is important to understand the relationship between the viscosity and the rotor lifetime. This has been shown mathematically to follow the Förster-Hoffman equation, a power law relationship between the viscosity and quantum yield[93,94]

$$log_{10}(\phi_F) = C + mlog_{10}(\eta) \tag{5.1}$$

where ϕ_F is fluorescent quantum yield, η is the viscosity, and C and m are rotor- and dye-based constants which can be determined through a calibration if required. This equation describes the relationship between the fluorescent quantum yield and viscosity, however this can easily be modified to include lifetime, as it is known that fluorescent quantum yield is related to the lifetime of the excited state by

$$\phi_F = \frac{\tau}{\tau_0} \tag{5.2}$$

where τ is the excited state lifetime and τ_0 is the inherent lifetime of the fluorophore. Therefore Equation 5.1 becomes

$$log_{10}\left(\frac{\tau}{\tau_0}\right) = C + mlog_{10}(\eta) \tag{5.3}$$

which can be rearranged to

$$log_{10}(\tau) = C + log_{10}(\tau_0) + mlog_{10}(\eta) \tag{5.4}$$

$$log_{10}(\tau) = x + mlog_{10}(\eta) \tag{5.5}$$

where x is a constant that includes both C in Equation 5.1 and τ_0 from equation 5.2.

While this is the standard equation used for describing the behaviour of molecular rotors, it has been shown that some rotors' behaviour cannot be modelled using this equation, notably

in the case of cyanine-based dyes.[95]

There are a few characteristics required of these pathways of relaxation that are required in a dye to make it a good molecular rotor. The dye must have a stable ground state. Rumble *et al.* showed that 9-(2-carboxy-2-cyanovinyl)julolidine (CCVJ), a negatively charged analogue of DCVJ, would convert between an *E* and *Z* isomer in the presence of high intensity laser light. Each of these isomers has a slightly different absorption and emission profile, making rotor measurements inconsistent, and thus meaning CCVJ is a bad molecular rotor.[96]

The non-radiative relaxation must be a viable, competitive pathway. This involves E_a being large enough that not all of the dye will instantly decay non-radiatively, but small enough that viscosity can affect the rotor lifetime. This can often be achieved by taking a 'standard' fluorescent dye and attaching a functional group to induce a viscosity dependence of the fluorescence. This was recently shown to be possible for Rhodamine B, which Guo *et al.* turned into a molecular rotor by addition of a large imidazole/phenyl moeity via a single bond, which induced a viscosity dependence of the lifetime.[97]

In this thesis, the two dyes used for lifetime measurements are a charged dye, 3,3'-diethylthiacarbocyanine iodide (Cy3, Figure 5.1) and a neutral dye, 8-[4-decyloxyphenyl]-4,4-difluoro-4-bora-3a,4a-diaza-*s*-indacene (a.k.a boron-dipyrromethene C10, BODIPY-C10, Figure 5.1). These dyes were chosen to investigate the different micro-regions within ionic liquids, as Cy3 should have a high affinity to the polar region, and BODIPY-C10 to the non-polar region. The changes in the lifetimes of these dyes are investigated in different ionic liquids and in one ionic liquid at different temperatures in this chapter. These results will then be used to understand changes in one ionic liquid in the presence of an electric field (Chapter 6).

5.1.1 Cyanine Dye Literature

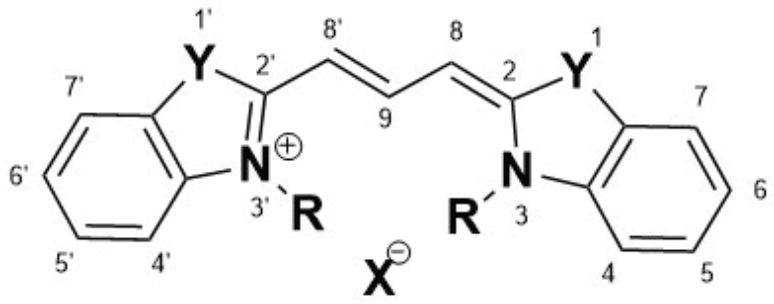

Figure 5.3: *Diagram of the skeleton structure of 3,3'-alkylcarbocyanine based dyes with the labels used in this chapter.*

Cyanine based dyes have been used for a long time, especially in the photographic industry.

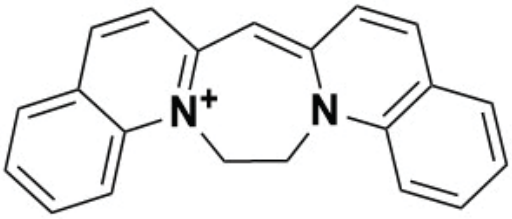

Figure 5.4: *Restricted cyanine dye investigated by West* et al. *using UV-vis spectroscopy.*[99]

It should be noted that when referring to dyes, the label "cyanine" is used to describe many dyes with a rigid alkyl chain with terminal quaternised nitrogen groups.[98] Herein only cyanine based dyes with ring-based quaternised nitrogens are considered.

West *et al.* studied a rigid cyanine dye (Figure 5.4) using UV-vis spectroscopy.[99] Due to the linking ethyl group, this molecule is fixed into one planar configuration and any rotor-based effect can be neglected.

They found evidence of absorption in ground and excited vibrational states in the UV-vis absorption spectra at room temperature and -196 °C due to overtone bands. These were seen at wavenumbers of 540 cm^{-1} and 1370 cm^{-1}, which they had previously assigned to the C=C bending and C=C stretching respectively. These were stronger at low temperatures, aiding in their assignment to some motion based effect in the fixed planar configuration.

A mirroring of these overtones in the emission spectra confirmed that these come from vibrationally excited states.[100]

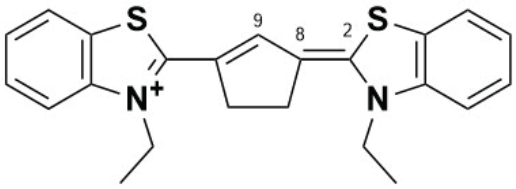

Figure 5.5: *A thiacarbocyanine dye used by O'Brien* et al. *in their study of fluorescence yield.*[101] *This dye has restricted molecular rotation around its 8-9 bond.*

A study by O'Brien *et al.* compared the fluorescence yield of various thiacarbocyanine dyes. They compared the fluorescence yield of Cy3 (Y = sulfur, R = ethyl, Figure 5.3), a partially restricted Cy3 analogue (Figure 5.5), and a fully rigid Cy3 with restriction to the 2-8 and 8-9 bonds.

The fluorescence yield, Φ_F, is defined as the ratio of the molecules in the excited state undergoing fluorescence decay, as opposed to other decay pathways shown in Figure 5.6

$$\Phi_F = \frac{k_F}{k_F + k_S + k_{ST}} \tag{5.6}$$

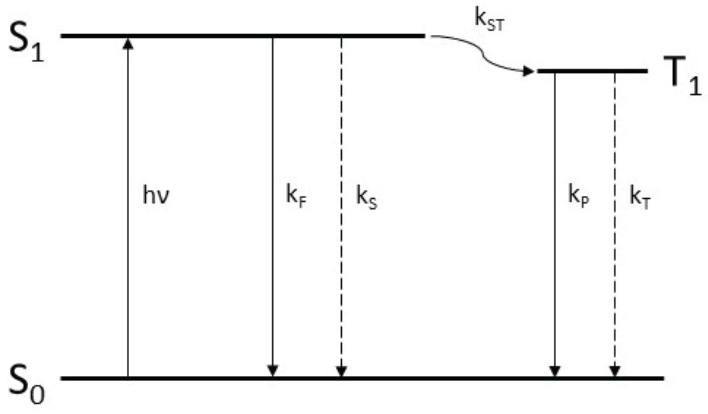

Figure 5.6: *Modes of decay for a first excited state: fluorescence, k_f; non-radiative singlet decay, k_s; singlet-triplet crossing, k_{st}; phosphorescence, k_P; non-radiative triplet decay, k_T.*

where k_F is the rate constant of fluorescence k_S is the rate constant of non-radiative singlet decay, and k_{ST} is the rate constant for singlet-triplet crossing.

They found that for all Cy3 samples the relaxation from the excited state occurred as fluorescence or non-radiative singlet decay, and that phosphorescence had a negligible contribution to their observed decay pathways (i.e. $k_{ST} \approx 0$).[101]

They also observed that Φ_F for unrestricted Cy3 and the 8-9 restricted Cy3 were identical, at 0.02 in their samples. Their Cy3 analogue which had restriction around both 8-9 and 2-8 had a much higher Φ_F, at 0.52.[101] This is strong evidence that non-radiative singlet decay must occur via rotation around the 2-8 bond, not the 8-9 bond, as restricting the 8-9 bond does not change the fluorescence yield, while restricting the 2-8 bond decreased the amount of dye undergoing non-radiative singlet decay.

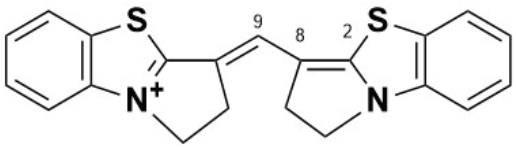

Figure 5.7: *Thiacarbocyanine dye investigated by Cooper* et al. *using absorption/emission spectroscopy.[100] This dye has restricted molecular rotation around its 2-8 bond.*

This is backed up by an earlier study on the fluorescence of a thiacarbocyanine dye with the rotation restricted around the 2-8 bond, shown in Figure 5.7. This restriction was achieved by 'tying' the ethyl groups onto the cyanine bridge.

When studying the emission spectra from various excitation wavelengths, they also observed no phosphorescence at any wavelength, thus showing singlet-triplet crossing in the excited state did not occur for this dye.[100]

What they observed when comparing the 2-8 restricted Cy3 to unrestricted Cy3 was that fluo-

rescence of the 2-8 restricted Cy3 was stronger than that of the unrestricted Cy3.[100] This would mean that the fluorescence yield was higher, and the amount of dye undergoing non-radiative singlet decay was reduced compared to unrestricted Cy3.

Another observation of Cooper *et al.* was a time-dependence of the emission spectra of the 2-8 restricted Cy3, which they described as 'retarded fluorescence'.[100] They saw that when comparing the input and output pulse widths of their laser light, the output laser light had a much larger width for the restricted Cy3 than the unrestricted Cy3, which is the earliest observation of a lifetime for the excited singlet state of Cy3.

Combining the results of the studies by Cooper *et al.* and O'Brien *et al.* it becomes clear that the non-radiative decay of 3,3'-alkylthiacarbocyanine occurs as a twisting of the benzothiazole rings around the 2-8 bond to the cyanine bridge.

This was later confirmed using both NMR and calculations of ground and excited state transitions in isomers of Cy3.

NMR measurements were performed by Ghelli and Ponterini on dyes which were frozen in deuterated methanol at 193 K. In an attempt to observe the photoisomers of the dyes, they performed two measurements of each sample: one sample which was irradiated while freezing, and compared it to another sample which was frozen in the dark.[102]

They saw that the irradiated frozen sample of 3,3'-diethyloxacarbocyanine (Y = oxygen, R = ethyl) showed splitting of the 8 and 8' protons which was not present in the dark frozen sample. Due to the symmetry in the NMR of the frozen dark sample, this was determined to be an all *trans* bond configuration of the cyanine bridge. From the coupling constants and a COSY experiment, the two 8 position proton environments were determined to be one *cis* and one *trans* from the 9 position proton. This showed that the frozen irradiated sample contained some all-*trans* dye and some mono 8,9-*cis* dye.[102]

The same analysis on a sample of 3,3'-diethylthiacarbocyanine (Y = sulfur, R = ethyl) showed a different splitting of the 8 and 8' protons. The irradiated frozen sample also showed two 8 proton environments, and while one could be assigned to being *trans* to the 9 proton, the coupling constant of the other lay intermediary to that expected if it was *cis* or *trans* to the 9 proton.[102]

They deduced that the most likely explanation for this was that the proton remained in a *trans* isomer, but that disruption of the conjugation nearby weakened the coupling. Thus, based upon the literature previously discussed here and their own calculations,[103] they also determined that the thiacarbocyanine dyes rotor motion occurs around the 2-8 bond.[102]

These calculations carried out compared the oscillator strength of various cyanine dyes when

undergoing 2-8 and 8-9 isomerisations and found that the experimentally calculated oscillator strengths for oxacarbocyanines matched the calculations for an 8-9 isomer, and for the thiacarbocyanines, a 2-8 isomer.[103]

In all of these studies, the authors assume that when excited from a planar ground state, these dyes twist a full 180° from the planar ground state minima, through a twisted configuration, into a planar excited state. They then undergo non-radiative decay and twist back through 180° into the most stable ground state configuration. Therefore, in the NMR studies they assume the frozen out excited state must be the planar, 180° twisted configuration.

This is based upon calculations which showed this was the case for isolated, gas phase cyanine dyes.[104] However, within this paper the authors acknowledge the possible existence of 90° twisted excited states when solvent effects are accounted for. They do not believe they can conclude they exist due to limitations of the theories used at the time, and the low energy of the minima observed for these 90° twisted excited states.[104]

A more recent study has investigated this using better computational techniques and found that a 90° twisted excited state was not only possible, but had a significantly deeper potential energy well than the fully planar excited state (over 1 eV lower).[105]

This study also looked at the decay pathway and twist angles in the excited state using solvent models for acetonitrile and benzene.[105] They matched polarity-based spectral changes to experimental values, confirming the accuracy of their models, and then investigated the non-ratiative decay pathway in these models. What they found was that an increase in solvent polarity *decreased* the twist of the molecule in the excited state, with the excited state of Cy3 in acetonitrile having a twist of 76°.[105] A twist of <180° in the excited state matches the NMR results as well. A 180° frozen configuration in NMR would still be conjugated, allowing coupling between the 8 and 9 proton as either *cis* or *trans*. However a 90° configuration could disrupt the conjugation enough to change the coupling between the protons to that of between *cis* and *trans*.

For my studies I have used 3,3'dietheylthiacarbocyanine (Cy3 in Figure 5.1) to probe the charged regions of the ionic liquid. This was chosen as it is commercially available and has a structure which is not too dissimilar to that of 1-alkyl-3-methylimidazolium cations.

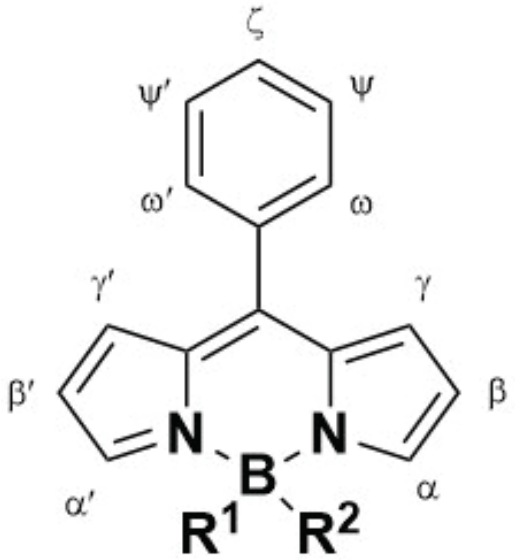

Figure 5.8: *Diagram of the skeleton structure of boron-dipyrromethene based dyes with the labels used in this chapter.*

5.1.2 Boron-Dipyrromethene Dye Literature

A large advantage of BODIPY based rotors is the customisability of the dyes. The R groups can be changed, and substitutions made onto the α, β, γ , ζ, ψ and ω positions (Figure 5.8) to make the most appropriate dye for what is required for the particular study. A disadvantage of this customisability is that literature for a specific rotor is very limited, so structurally analogous BODIPY rotors are also included here.

Because of the wide range of possible structures, there are many uses for BODIPY-based dyes, most of which do not involve the use as a molecular rotor. The non-rotor uses see BODIPY-based dyes employed as a photon harvester for energy capture and transport,[106–109] a molecular sensor for peroxynitrate,[110] cyanide,[111,112] or fluorine[112–115] anions as a chemisorbant; zinc,[116,117] nickel,[118] copper,[119,120] or mercury[121] cations as a complexing agent; as an electrophore for redox flow batteries,[122] or to study the diffusion of electrochemical species at an electrode.[123]

As a rotor, BODIPY has been used to map the viscosity of cell membranes,[124] as well as the viscosity of model lipid bilayers[125–127] and lipid micelles in water.[128] More recently, studies have been performed on the viscosity of various solvents under high pressures using BODIPY rotors as a probe[129,130] as well as to study the viscosity of live cells.[131,132]

An important study into the fundamental behaviour of BODIPY rotors came from Kee *et al.* who used experimental and computational methods to study a few representative rotors. They found that sterically unhindered BODIPY rotors (where α, β, γ, ϵ, ψ, ω = H, R = F, or α, β, γ, ψ, ω = H, R = F, ζ = *iso*-butyl) showed a strong correlation between viscosity and lifetime,

whereas replacement of the hydrogen with a methyl group at the ζ, ω or γ positions led to a loss of the viscosity dependence of the lifetime.[133]

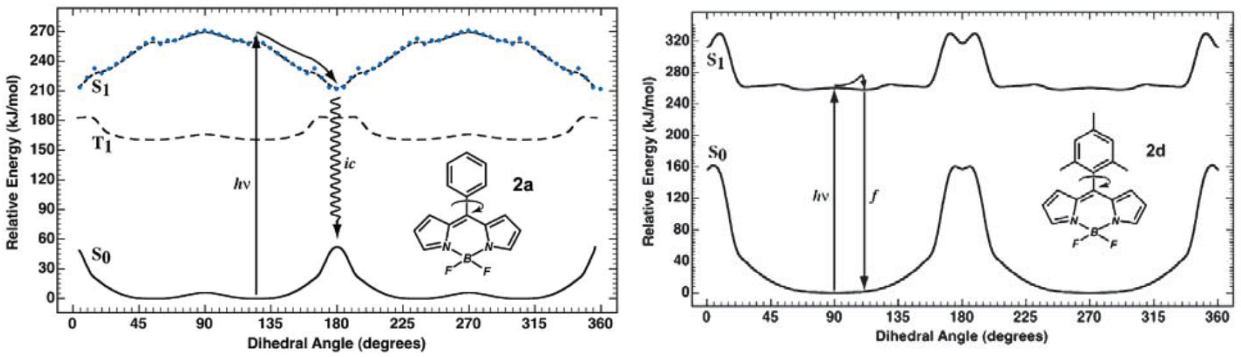

Figure 5.9: *Calculated energy profiles for the singlet and excited state of a sterically unhindered (left) and sterically hindered (right) BODIPY based dye. Reprinted (adapted) with permission from H. L. Kee et. al The Journal of Physical Chemistry B, 2005, 109, 20433-20443. Copyright 2005 American Chemical Society.*

Subsequent computational analysis found that this was due to the energy profile of the ground and first excited states, shown in Figure 5.9. For the sterically unhindered rotor, the ground state minimum occurred at 50° (and 130° due to symmetry). Excitation to the first excited state in this configuration leads to the rotor being at a high energy, which can relax slightly by twisting to a configuration of 180° (or 0°) *with no energy barrier.*[133]

Once in this twisted configuration, the rotor can decay back to the ground state, which is at its maximum energy. Twisting from 180° back to the initial configuration completes the cycle. This was found to be a radiative decay, but to change the wavelength of light from visible light to infrared light.[133] This is ideal rotor behaviour as this twisting allows modification of the accessibility of this pathway through viscosity changes.

The sterically hindered rotor (ω, ω', ζ = Methyl) has its minimum at 90° in the ground state and 120° in the excited state. While the closeness of the angles is not necessarily bad, the energy difference between the ground and excited state at 90° and 120° is almost identical, meaning any twisting that occurs does not change the emitted light enough to modify the measured lifetime. The same was also found to be the case with only one methyl group substituted on the ω position.[133]

This occurs as the methyl groups in the ω position lead to the energy at 180° (minimum in the sterically unhindered analogue) being much higher in the excited (and ground) state. Hence this dyes is a poor molecular rotor as its fluorescence lifetime does not change with viscosity. This was confirmed with various other studies of BODIPY-based rotors with substituents on the ω and γ position causing a loss of the viscosity dependence of the lifetime.[134,135]

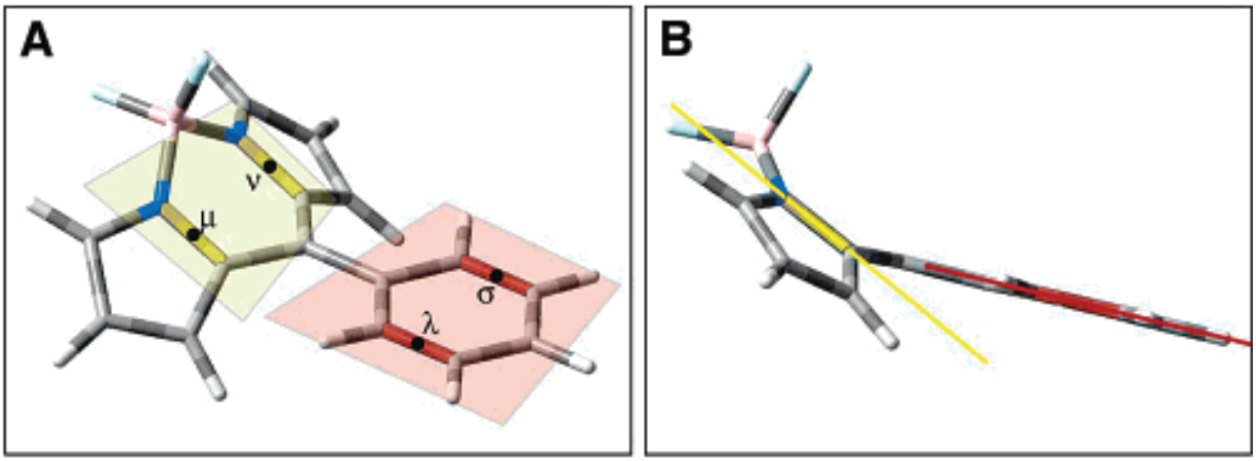

Figure 5.10: *3D model of the BODIPY rotor showing the 'buckling' that occurs as the phenyl group (red plane) rotates into the plane of the boron-dipyrromethene framework (yellow plane). Reprinted (adapted) with permission from H. L. Kee et. al The Journal of Physical Chemistry B, 2005, 109, 20433-20443. Copyright 2005 American Chemical Society.*

This study also observed that a 'buckling' of the rotor in the ground state occurred when the phenyl group rotated towards the plane of the boron-dipyrromethene frame, as shown in Figure 5.10. This was found to to be vital in the activity of rotor.[133]

The importance of this buckling was confirmed in further papers on other BODIPY based rotors,[130,135] with emphasis put onto how this distorts the shape such that the two fluorine atoms on the boron are not equivalent. The reason as to why this was required in the twisting profile is not known.

A more recent study from Polita *et al.* confirmed this pathway during excitation and relaxation, however their calculations show the excited state was more stable in the optimised ground state configuration (Figure 5.11). In toluene, there was a small (≈0.07 eV) potential energy barrier to the twist of the phenyl group, and therefore access to the non-radiative decay pathway. This increased to ≈0.11 eV in a more polar solvent (DMF), which contradicted experimental results that show highly polar solvents pose a lower activation barrier to twisting than non-polar solvents.[136] Therefore, there are clearly still some limitations in the computational models used to study molecular rotors.

For my studies, I have used the BODIPY-10 rotor (oxy-decyl chain group on the ζ position, see Figure 5.1). This rotor was chosen as it has previously been shown to be effective at mapping the viscosity of lipids,[125,127] so I believe it is a good rotor to investigate the non-polar region of ionic liquids.

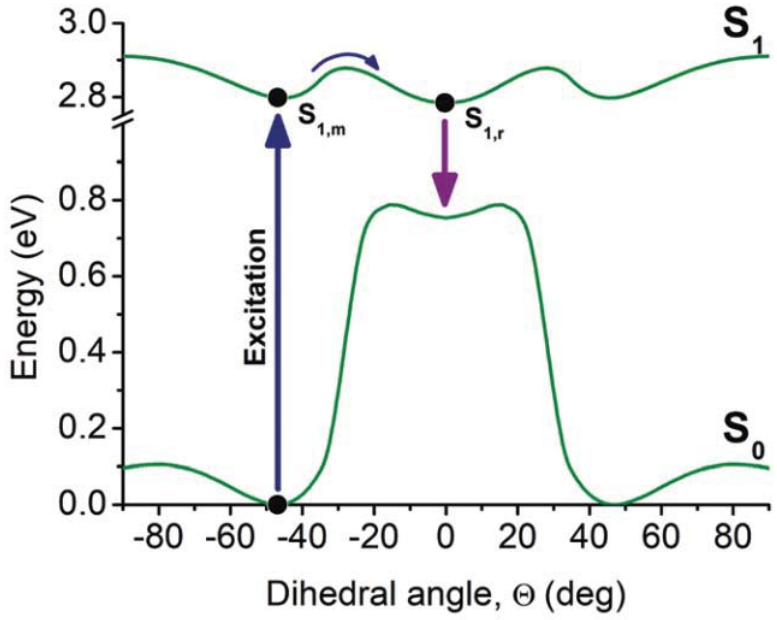

Figure 5.11: *Potential energy curves of the ground (S_0) and the first excited electronic state (S_1) of BODIPY-C10 obtained from time dependent-DFT calculations. Θ is a dihedral angle between a phenyl ring and a BODIPY core. Republished with permission of the PCCP Owner Societies, from The effect of solvent polarity and macromolecular crowding on the viscosity sensitivity of a molecular rotor BODIPY-C10, A. Polita, S. Toliautas, R. Žvirblis, A. Vyšniauskas, Physical Chemistry Chemical Physics, 2020, **22**, 8296-8303; permission conveyed through Copyright Clearance Center, Inc.*

5.1.3 Molecular Rotors in Ionic Liquids

There have been only a few studies on the application of molecular rotors to the measurement of the microviscosities of ionic liquids.[137–140] Scalise *et al.* performed measurements of 1,1-dimethyl-2,3,4,5-tetraphenylsilole (a very large, neutral rotor) in $[C_4C_1im][BF_4]$, $[C_4C_1im][PF_6]$ and $[C_8C_1im][BF_4]$. They found that the measured fluorescence yields of the dye predicted viscosities of around an order of magnitude lower than the measured viscosity when comparing to both polar and non-polar molecular solvents.[137] There was also a lack of viscosity dependence of the quantum yield, with the order of quantum yield being: $[C_4C_1im][BF_4] < [C_8C_1im][BF_4] < [C_4C_1im][PF_6]$, despite the viscosity of $[C_8C_1im][BF_4]$ being greater than that of $[C_4C_1im][PF_6]$.[137]

Singh *et al.* performed measurements of Thioflavin T (a relatively small, positively charged rotor) in $[C_2C_1im][FAP]$ and $[(HO)_2C_2C_1im][FAP]$ (FAP = tris(pentafluoroethyl)trifluorophosphate). They found that they did have the correct relationship between measured fluorescence yield and viscosity, both when comparing the ionic liquids to each other, and when performing temperature-dependent measurements. However, large differences were seen when comparing ionic liquids and molecular solvents once again. Converting their quantum yields into viscosities using molecular solvent calibrations led to a much larger than measured viscosity. This predic-

tion was closer than that predicted by Scalise *et al.* however it was still 40-80% different.[138] Using their temperature-dependent measurements they calculated the activation energy of non-radiative decay and free volume around the rotor. The activation energy of non-radiative decay was found to be lower, and the free volume higher in ionic liquids than glycerol.[138] Therefore, one would expect that the quantum yield of the rotor would be lower in an ionic liquid when compared to a molecular solvent of a similar viscosity. The fact that it was shown not to be the case again reinforces the different behaviour of molecular rotors in ionic liquids and molecular solvents.

Paul and Samanta investigated the fluorescent yield of 9-(dicyanovinyl)julolidine (DCVJ, a small neutral rotor) in $[C_2C_1im][NTf_2]$, $[C_4C_1im][PF_6]$, $[C_4C_1im][NTf_2]$, $[(OH)_2C_2C_1im][NTf_2]$, $[C_2C_1im][EtSO_4]$, $[C_4C_1im][BF_4]$ and $[(OH)_2C_2C_1im][BF_4]$. They found that for all of the ionic liquids the viscosity predicted from the fluorescence yield was significantly different to the viscosity measured by rheometry. For all of the ionic liquids except $[C_4C_1im][PF_6]$, the fluorescence yield predicted a higher than measured viscosity. For $[C_4C_1im][PF_6]$ the predicted viscosity was much lower than the measured value.[139]

They also performed variable temperature experiments in ionic liquids and found that for low viscosity ionic liquids ($[C_2C_1im][NTf_2]$, $[C_2C_1im][EtSO_4]$) these measurements gave clear trends. For high viscosity ionic liquids ($[(OH)_2C_2C_1im][BF_4]$, $[C_4C_1im][PF_6]$) two temperature regions were seen. They concluded this must be due to a change in the partitioning of the dye when the temperature crossed a threshold.[139]

A study by Kimball *et al.* compared the temperature- (and thus viscosity-) dependent lifetime of a di-BODIPY-based dye linked with a double alkyne bridge in different ionic liquids. They found that different trends were observed in different ionic liquids, whereas when comparing the viscosity-dependent trends of the same rotor in molecular solvents, all measurements followed the same trend.[140]

In all of these studies, the differences between the molecular solvent and ionic liquid calibrations were attributed to either the different domains having non-bulk viscosities,[137,139] the changes in the free volume and activation for rotation,[138] or a combination of both of these including the difference in the interactions between the rotor and liquid.[140]

Whatever the true cause, it is clear that when comparing microviscosities, which is the viscosity measured by molecular rotors, and bulk viscosity, which is the viscosity measured by rheometer, there is a complex (if even present) relationship.

Therefore in order to investigate the molecular rotors studied herein (Cy3 and BODIPY-C10), a series of measurements in different ionic liquids, as well as temperature-dependent measure-

ments are performed, before attempting to use these dyes to study the effect of an external electric field on the structure of ionic liquids.

5.2 Experimental

All ionic liquids were synthesised using the same high quality procedure described in Chapter 3 by Azizi Nawawi ($[C_nC_1im][NTf_2]$, n = 2, 3, 4, 6 or 12, $[C_4C_1im][X]$, X = OTf, PF_6, BF_4), Qingshan Liu ($[P_{4446}][NTf_2]$) and myself ($[C_8C_1im][NTf_2]$). Detailed procedures along with analysis is published in the literature.[1]

Cy3 was purchased from either Alfa Aesar or TCI (96% purity) and used without purification. BODIPY-C10 was kindly provided by Marina Kuimova and was synthesised using the procedures in Dent *et al.*[127]

All samples of dyes in ionic liquids in this chapter are at a concentration of 100 nM unless stated.

5.2.1 Custom Confocal Set-up

The lifetimes of the neat ionic liquids and the samples of dyes in different ionic liquids were measured on a custom built confocal microscope using a sub-micrometre precision stage to position the sample in the laser beam. The sample was excited using a 466 nm pulsed diode laser (PicoQuant GmbH, PDL 800-B) operating at a frequency of 20 MHz (50 ns pulse separation) and a power of 1.35 mW. Beam steering mirrors were used to control the laser beam direction and height and a dichroic mirror was used to direct the laser beam into the objective. An infinity corrected, high numerical aperture (NA) microscope objective (Olympus 60x/1.2, water immersion) focuses the laser into a femtolitre volume within the sample. Fluorescence from the sample was collected by the same microscope objective, directed to the same dichroic mirror, then passed through an emission filter (z488lp, Chroma Technology Corp.) to remove residual excitation photons. A plano-convex lens (+50.2 F, Newport Ltd.) focused the filtered light onto a 75 μm pinhole positioned on the confocal plane of the microscope objective. Another dichroic mirror (630dcxr, Chroma Technology Corp.) was then used to split the beam towards two avalanche photodiodes (AQR-141, EG&G, Perkin-Elmer). The light was further filtered by another emission filter (hq 540/80 m, Chroma Technology Corp.) and focused by a plano-convex lens (f=30.0, i.d. 25.4 mm, Thorlabs) onto the first avalanche photodiode (green detector, photons in the range 500-580 nm). The second avalanche photodiode (red detector) was not used in these experiments. The signal from the green detector was coupled to a multifunction DAQ device for data logging (PCI 6602, National Instruments) running on a Pentium PC, as

well as to a time-correlated single-photon counting card (SPC-130 EM, Becker & Hickl GmbH) running on a separate Pentium PC.

The data was collected at 298 K, and the raw data was deconvoluted using the instrument response function (IRF), which was measured using a 15 μM solution of auramine O in distilled water. Auramine O has a lifetime of a few ps, therefore the IRF is dictated by the detector and has a FWHM of ≈0.9 ns.

5.2.2 Fluorescence lifetime measurement of dyes in variable temperature ionic liquid

The lifetimes of the dyes in $[C_4C_1im][NTf_2]$ at various temperatures were measured using a Delta Flex system (Horiba Scientific) using an excitation wavelength of 467 nm. Each measurement was repeated three times, and data presented is the average and error of the fitted lifetimes.

5.2.3 Data Analysis

The data were analysed using a modified version of the JLife program written at Imperial College London written by Joshua Edel and myself, with amplitudes and lifetimes loosely constrained to give positive, non-zero values. Goodness of fit was judged based upon χ^2 values, and all presented data are from fittings with χ^2 values of less than 1.2.

The fluorescence decay was treated as an n component exponential decay of the form shown in equation 5.7, and the IRF was fitted to the measured data using the sequential quadratic programming method with an error tolerance of 10^{-6}.

$$I(t) = bkg + IRF \circledast \sum_{i=1}^{n} \alpha_i \exp(-t/\tau_i) \tag{5.7}$$

where I is fluorescence intensity at time t, bkg is background counts, t is the time vector of the experiment, α_i is amplitude of component i, IRF is the measured instrument response function, $\circledast$ denotes the convolution of the data to the IRF, and τ is lifetime of component i.

5.3 Results and Discussion

5.3.1 Fluorescence in Neat Ionic Liquids

It has been shown before that ionic liquids have an inherent autofluorescence i.e. ionic liquids fluoresce without any added fluorescent compounds.[141–143] This is suspected to be, at least in part, due to impurities in the ionic liquids. This is due to previous investigations showing that rigorous purification of ionic liquids results in lower levels of autofluorescence.[144]

It was found to be impossible to remove all of the autofluorescence and reduce the autofluorescence of ionic liquids to a similar background level of photon counts as deionised water. Therefore, before being able to distinguish between which lifetime components belong to ionic liquids, and which to the dye (which is the intended probe) is important. To achieve this, the autofluorescence of the neat ionic liquids was investigated on the set-up described in Section 5.2.1, and are shown in Table 5.1.

Table 5.1: *Calculated lifetimes and their respective contribution to the overall decay for neat [$C_nC_1$im][NTf_2] (n = 2, 3, 4, 6, 8 or 12), [P_{4446}][NTf_2], [C_4C_1im][OTf], [C_4C_1im][BF_4] and [C_4C_1im][PF_6].*

Ionic liquid	τ_A [ns]	Contribution [%]	τ_B [ns]	Contribution [%]	τ_C [ns]	Contribution [%]
$[C_2C_1im][NTf_2]^\dagger$	6.17 ± 0.53	33.1 ± 3.0	1.52 ± 0.22	21.0 ± 1.9	0.107 ± 0.012	45.9 ± 1.9
$[C_3C_1im][NTf_2]^\dagger$	6.12 ± 0.21	36.9 ± 1.6	1.40 ± 0.09	22.9 ± 1.3	0.115 ± 0.004	40.2 ± 0.4
$[C_4C_1im][NTf_2]^\dagger$	6.27 ± 0.25	38.3 ± 1.6	1.42 ± 0.15	23.9 ± 1.3	0.123 ± 0.019	37.8 ± 1.0
$[C_6C_1im][NTf_2]^\dagger$	6.34 ± 0.31	38.9 ± 0.5	1.32 ± 0.09	25.7 ± 0.8	0.137 ± 0.010	35.4 ± 0.9
$[C_8C_1im][NTf_2]^\dagger$	6.24 ± 0.29	41.2 ± 2.1	1.57 ± 0.16	26.5 ± 1.6	0.125 ± 0.010	32.3 ± 1.1
$[C_{12}C_1im][NTf_2]^\dagger$	6.98 ± 0.20	42.4 ± 0.6	1.61 ± 0.09	31.0 ± 1.5	0.158 ± 0.013	26.5 ± 1.0
$[P_{4446}][NTf_2]^\dagger$	6.85 ± 0.18	43.7 ± 1.6	1.52 ± 0.07	20.7 ± 0.7	0.096 ± 0.006	35.6 ± 1.3
$[C_4C_1im][OTf]$	6.39 ± 1.38	21.5 ± 1.4	1.27 ± 0.15	32.5 ± 4.0	0.065 ± 0.007	46.1 ± 3.1
$[C_4C_1im][BF_4]$	6.41 ± 0.15	22.1 ± 0.7	0.95 ± 0.04	54.6 ± 1.1	0.097 ± 0.018	23.4 ± 1.4
$[C_4C_1im][PF_6]$	6.07 ± 1.11	14.2 ± 2.1	1.60 ± 0.50	20.0 ± 6.0	0.070 ± 0.010	70.5 ± 1.3

†Measurements performed by Azizi Nawawi,[77] however all analysis was performed by myself.

The previous studies of the autofluorescence of ionic liquids involved the study of the fluorescent decays of $[C_4C_1im][BF_4]$, $[C_4C_1im]Cl$ (0.35 M acetonitrile solution), $[C_4C_1im][PF_6]$, $[C_2C_1im][BF_4]$, $[C_2C_1im][NTf_2]$ and $[C_4C_1im][NTf_2]$. The time resolved decays of all of these ionic liquids were fitted by three components. Two components were attributed to 'associated structures' in the ionic liquids (examples given were cation-anion and cation-cation interactions), and one to fluorescence of the imidazolium ring.[141–143]

Here, three components are also seen in the neat ionic liquids. Considering the lifetimes of the components seen previously, the components attributed to associated structures had long lifetimes at ≈ 2 ns and ≈ 9 ns.[141–143] The component assigned to fluorescence of the imidazolium

ring had a short lifetime of ≈ 500 ps.[141–143] The components seen here are of a similar length in all of these ionic liquids, τ_A, τ_B and τ_C in Table 5.1.

The fact that there is a component of similar lifetime to that assigned to the imidazolium in $[P_{4446}][NTf_2]$, which does not contain an imidazolium moiety, brings into question the origin of this component. It cannot be ruled out that that in $[P_{4446}][NTf_2]$ this component originates from a different physical process, and coincidentally has the same lifetime. However it is equally as probable that the source of this component in $[P_{4446}][NTf_2]$ also contributes to the same component in the other ionic liquids.

However, considering the contribution of this component to the decays of $[C_nC_1im][NTf_2]$ (n = 2, 3, 4, 6, 8 or 12) in Table 5.1 it is easy to see why this component was assigned to the imidazolium moiety. Increasing the alkyl chain decreases the concentration of this moiety, and the contribution of this component changes in line with this. Unfortunately, the lifetime of this component is close to the limit of the detection capability of this spectrometer, 0.1 ns. Hence, it is not possible to determine whether this signal arises due to a genuine fluorescence from the ionic liquids, or whether it arises from some other process, such as scattering.

Another difference between these measurements and literature is that the components contribute different fractions of photons to the decay. In literature measurements, the components assigned to associated structures for $[C_4C_1im][BF_4]$, $[C_4C_1im]Cl$, $[C_4C_1im][PF_6]$ and $[C_2C_1im][BF_4]$ contributed 10 % of the total photons to the decay, whereas for $[C_2C_1im][NTf_2]$ and $[C_4C_1im][NTf_2]$ these two components contributed 32-50 % of the photons. The rest of the photons in the decay are attributed to the short lifetime component, which contributed 90 % of the photons to the fluorescent decay of $[C_4C_1im][BF_4]$, $[C_4C_1im]Cl$, $[C_4C_1im][PF_6]$ and $[C_2C_1im][BF_4]$, and 50-68 % of the photons to the fluorescent decay of $[C_2C_1im][NTf_2]$ and $[C_4C_1im][NTf_2]$.[141–143]

In the measurements in Table 5.1 all of the ionic liquids have a lower contribution from the short lifetime component (τ_C) and larger contributions from the component previously assigned to the associated structures. The reasoning behind the assignment of the short component to the imidazolium ring was due to the decrease in the contribution of this component with dilution of samples with a non-fluorescent solvent (methanol or acetonitrile).[141–143] From the measurements of these ionic liquids, along with samples deemed too impure for these measurements, I believe this short component arises from impurities, and is likely scattering.

This is because the measurements in the literature were performed on commercial samples at 95-99% purity. While this is relatively pure, the samples measured here are of a much higher purity, with an estimated purity of ≥99.99%. Thus, the substantially lower contribution of this

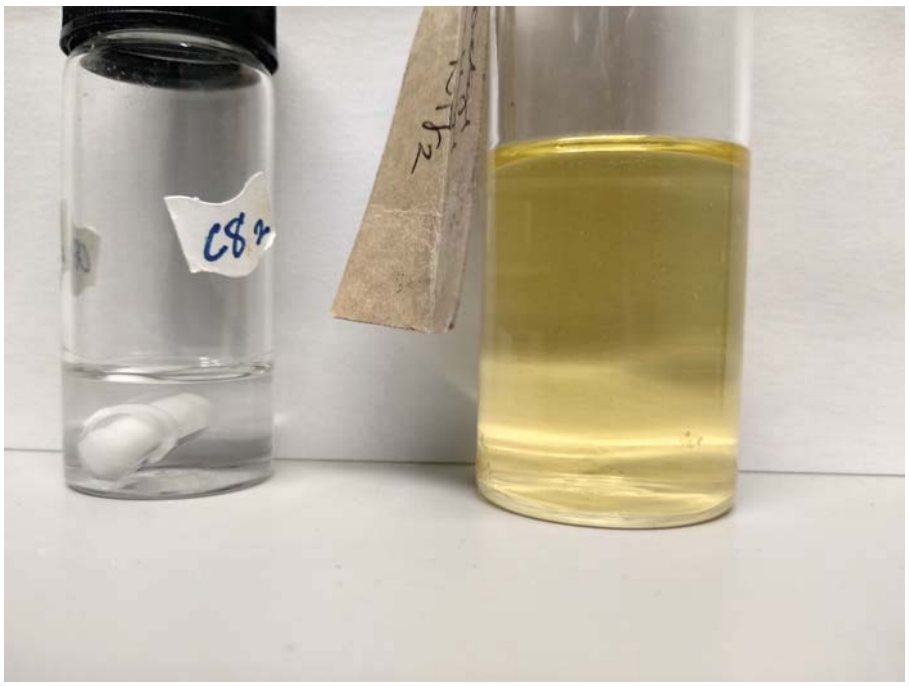

Figure 5.12: *Photo of two samples of the ionic liquid 1-octyl-3-methylimidazolium bis(trifluoromethylsulfonyl)imide. The sample on the left was synthesised as per the ultra-pure methodology in Section 3. The sample on the right was purchased from IoLiTec at >98% purity.*

component to the overall decay in these ionic liquids leads to this conclusion.

Many commercial samples are of high purity and yet are still coloured (see Figure 5.12). It is well known that when synthesising ionic liquids if care is not taken many coloured impurities can form, although the nature of these is not well studied.[145] What is known is that the formation of coloured impurities is exacerbated by high temperatures and impure starting materials. It was found that even if careful synthesis is undertaken to make ionic liquids which are pure by NMR, mass-spectrometry and elemental analysis, there was still an unacceptable amount of background fluorescence in the sample i.e. when adding a rotor to the sample, it was difficult to distinguish the signal from the rotor from the ionic liquids.[144]

This is why the ultra-pure synthesis was developed for this work. As the dyes are dissolved the ionic liquids in such low concentrations, if the fluorescence from the ionic liquid is too high then the signal from the dye gets lost in the noise from the ionic liquid.

Also when considering the set-up for the measurements, there is a very high resolution, with the lowest measurable lifetime on the set-up being ≈100 ps. If this process truly came from autofluorescence, then it lies upon the lowest threshold to be classed as fluorescence, and not scattering.

However, as the lifetime of this component is similar to that of the instrument response, there is a strong indication that it arises due to scattering. This is backed by the large contribution in samples that have higher inherent fluorescence, and the fact that this can be removed

with purification, further indicating scattering from impurities contribute significantly to this component.

5.3.2 BODIPY-C10 in Ionic Liquids

Absorption and Emission

In order to check that there are no major changes in the absorption/emission profiles of the dyes in the conditions in which the lifetime will be investigated, the absorption and emission were measured in all ionic liquids studied, as well as a range of temperatures greater than the temperatures at which the lifetime was recorded.

For all the ionic liquids, there are small differences in the absorption and emission maxima, however these differ by 3 nm at most, therefore it can be reasonably asserted that changing the ionic liquid has no major effect upon the absorption or emission of BODIPY-C10.

The same can be said for the absorption and emission at various temperatures, where there is very little difference in the absorption or emission profiles. There was a difference in the intensities of the emission, with higher temperatures leading to a less intense emission. However this is expected from higher temperature samples with a lower viscosity (see later discussion). Therefore the investigations of the lifetimes could be undertaken.

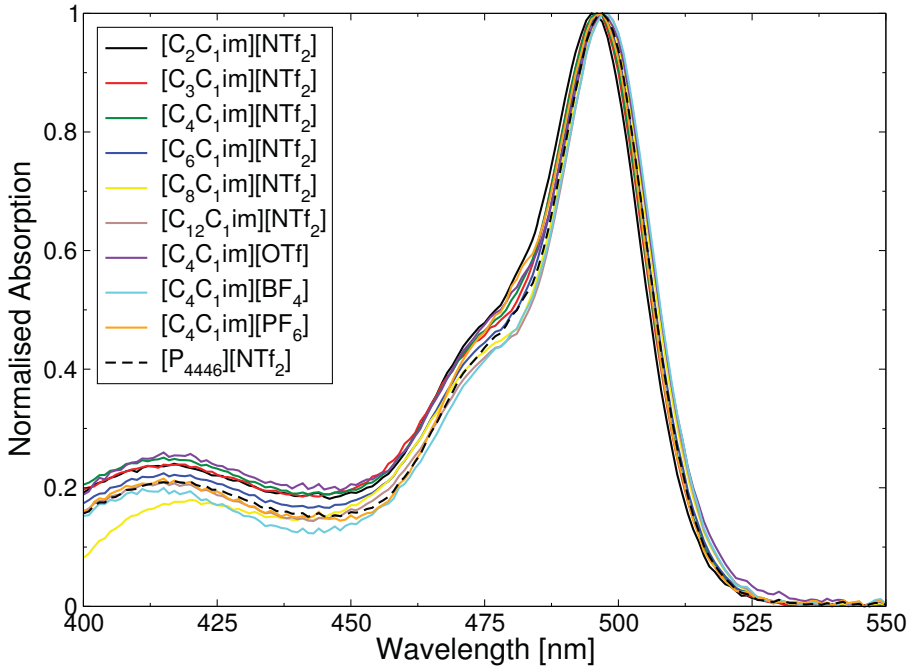

Figure 5.13: *Absorption of BODIPY-C10 in all ionic liquids used here.*

Table 5.2: *Wavelength of the maximum absorption of BODIPY-C10 in the ionic liquids studied.*

Ionic Liquid	λ_{max} [nm]
$[C_2C_1im][NTf_2]$	495
$[C_3C_1im][NTf_2]$	496
$[C_4C_1im][NTf_2]$	496
$[C_6C_1im][NTf_2]$	497
$[C_8C_1im][NTf_2]$	497
$[C_{12}C_1im][NTf_2]$	497
$[P_{4446}][NTf_2]$	497
$[C_4C_1im][BF_4]$	498
$[C_4C_1im][OTf]$	497
$[C_4C_1im][PF_6]$	497

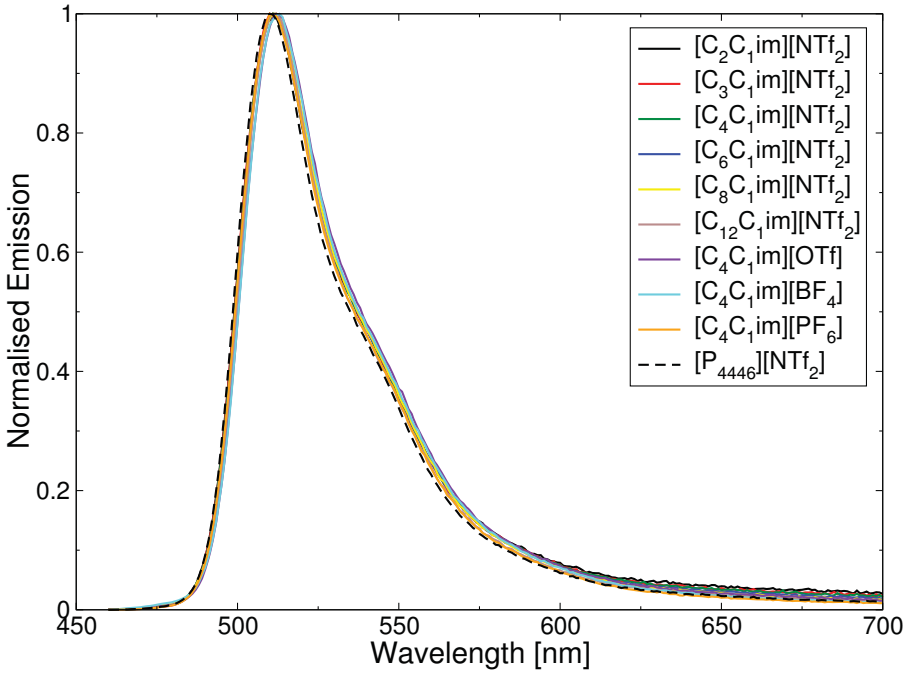

Figure 5.14: *Emission of BODIPY-C10 in all ionic liquids used here. Excitation wavelength was 445 nm.*

Table 5.3: *Wavelength of the maximum emission of BODIPY-C10 in the ionic liquids studied. Excitation wavelength was 445 nm.*

Ionic Liquid	λ_{max} [nm]
$[C_2C_1im][NTf_2]$	511
$[C_3C_1im][NTf_2]$	510
$[C_4C_1im][NTf_2]$	511
$[C_6C_1im][NTf_2]$	511
$[C_8C_1im][NTf_2]$	511
$[C_{12}C_1im][NTf_2]$	512
$[P_{4446}][NTf_2]$	510
$[C_4C_1im][BF_4]$	513
$[C_4C_1im][OTf]$	512
$[C_4C_1im][PF_6]$	510

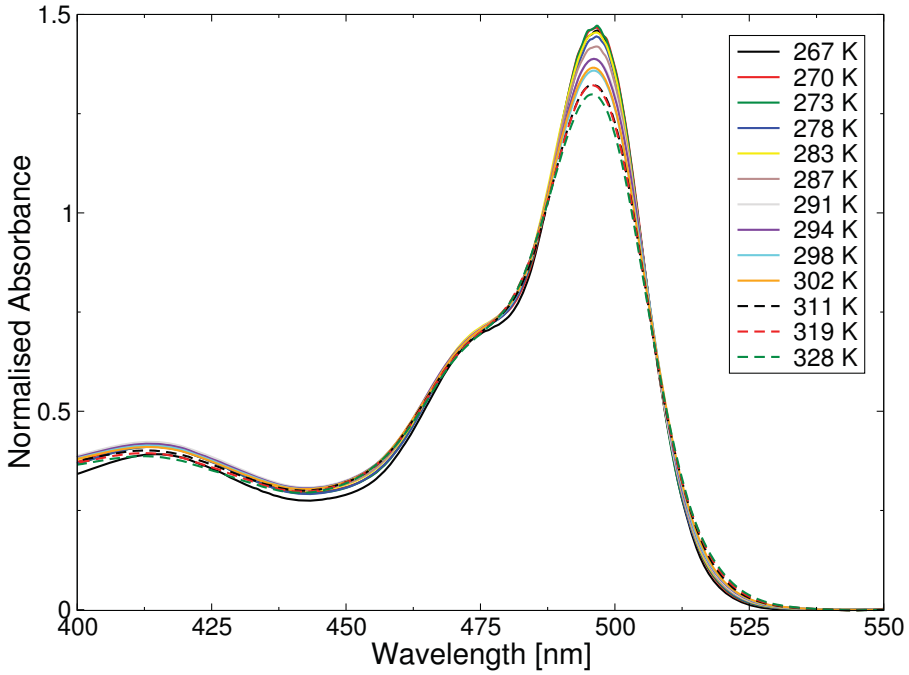

Figure 5.15: *Absorption of BODIPY-C10 in $[C_4C_1im][NTf_2]$ in various temperatures.*

Table 5.4: *Wavelength of the maximum absorption of BODIPY-C10 in $[C_4C_1im][NTf_2]$ in various temperatures.*

Temperature [K]	267	270	273	278	283	287	291	294	298	302	311	319	328
λ_{max} [nm]	497	497	497	497	496	497	496	496	496	496	496	496	496

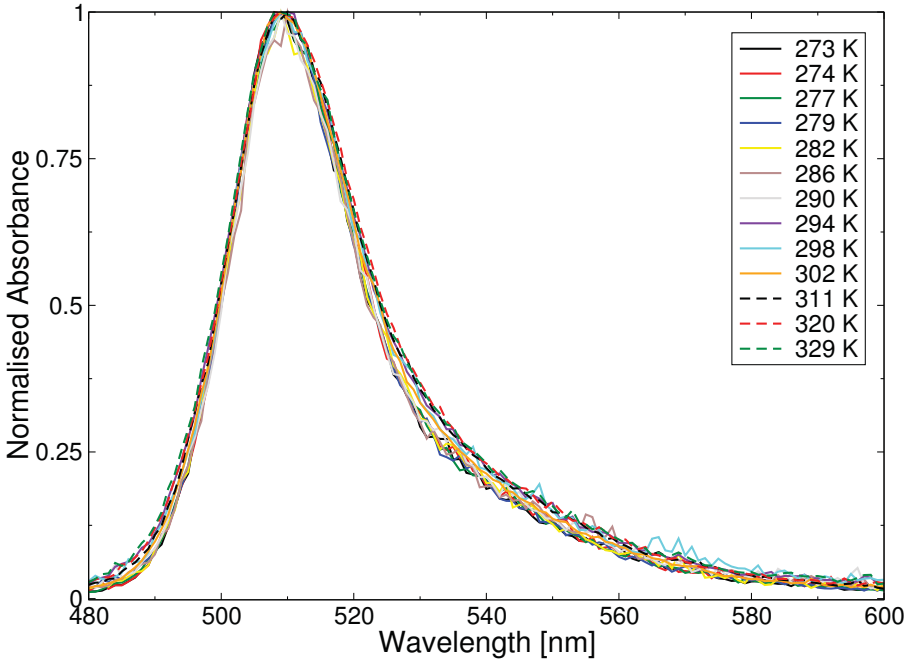

Figure 5.16: *Emission of BODIPY-C10 in $[C_4C_1im][NTf_2]$ in various temperatures. Excitation wavelength used was 467 nm.*

Table 5.5: *Wavelength of the maximum emission of BODIPY-C10 in $[C_4C_1im][NTf_2]$ in various temperatures. Excitation wavelength used was 467 nm.*

Temperature [K]	273	274	277	279	282	286	290	294	298	302	311	320	329
λ_{max} [nm]	509	508	510	510	509	510	509	510	509	509	510	509	509

Components Present for BODIPY-C10 in Ionic Liquids

Before looking at the differences in the rotor lifetimes, the components of each decay will be reported. When reporting these, each component reported is from the lowest number of components that fit the overall decay curve well i.e. the phrase "this decay contains 2 components" means "the decay is best fitted when the IRF is deconvoluted with 2 components".

The time resolved fluorescence decay of BODIPY-C10 was measured in $[C_4C_1im][NTf_2]$ at temperatures of 277-329 K on the set-up described in Section 5.2.2. These temperatures lead to the ionic liquid having viscosities of 17-148 cP,[146] and the results are shown in Table 5.6 (decays shown in Appendix A).

Table 5.6: *Calculated lifetime of BODIPY-C10 (τ_{BDPY}) in the decay profile of BODIPY-C10 at various temperatures in the ionic liquid $[C_4C_1im][NTf_2]$.*

Temperature [K]	τ_{BDPY} [ns]	Temperature [K]	τ_{BDPY} [ns]
277	2.193 ± 0.001	298	1.082 ± 0.001
279	2.015 ± 0.003	302	0.951 ± 0.001
282	1.797 ± 0.001	311	0.757 ± 0.001
286	1.597 ± 0.001	320	0.611 ± 0.001
290	1.398 ± 0.002	329	0.504 ± 0.002
294	1.234 ± 0.001		

The time resolved fluorescence decays for the variable temperature samples of BODIPY-C10 in $[C_4C_1im][NTf_2]$ can all be fitted to 1 component. This component is therefore attributed to the rotor and labelled τ_{BDPY}; no contribution to the decays from the ionic liquids were observed.

To study the fluorescence of BODIPY-C10 in different ionic liquids, the time resolved fluorescence decay was measured in the ionic liquids $[C_nC_1im][NTf_2]$ (n = 2, 3, 4, 6, 8 or 12), $[P_{4446}][NTf_2]$, $[C_4C_1im][OTf]$, $[C_4C_1im][BF_4]$ and $[C_4C_1im][PF_6]$ on the setup described in Section 5.2.1. The components in the decays are shown in Table 5.7 (decays shown in Appendix A).

For all of the measurements of BODIPY-C10 in different ionic liquids, more than one component is needed to fit the fluorescence decay. This seems to arise due to a difference in the set-up used for the variable temperature and the measurements in different ionic liquids. The reason behind this is unknown and could come from a number of factors including: a more efficient photodiode in the custom set-up, more efficient photon harvesting in the custom set-up, or the direction in which the photons are collected (back scatter c.f. perpendicular scatter). However, the difference does not arise from the laser sources, as both set-ups have approximately the same wavelength and power (466 nm and 1.35 mW c.f. 467 nm and ≈1.3 mW).

In all of ionic liquids except for $[C_4C_1im][OTf]$, the time resolved fluorescence decays can be

Table 5.7: *Calculated lifetime of BODIPY-C10 (τ_{BDPY}) and other component in the time resolved fluorescent decay of BODIPY-C10 in all ionic liquids. Contribution is shown in brackets after the lifetime*

Ionic Liquid	τ_{BDPY} [ns]	τ_A [ns]	τ_B [ns]
$[C_2C_1im][NTf_2]$	0.865 ± 0.011 (85%)	0.181 ± 0.019 (15%)	-
$[C_3C_1im][NTf_2]$	1.138 ± 0.022 (90%)	0.203 ± 0.019 (10%)	-
$[C_4C_1im][NTf_2]$	1.282 ± 0.019 (92%)	0.221 ± 0.015 (8%)	-
$[C_6C_1im][NTf_2]$	1.655 ± 0.014 (94%)	0.282 ± 0.015 (6%)	-
$[C_8C_1im][NTf_2]$	1.941 ± 0.018 (92%)	0.422 ± 0.039 (8%)	-
$[C_{12}C_1im][NTf_2]$	2.331 ± 0.015 (92%)	0.674 ± 0.063 (8%)	-
$[P_{4446}][NTf_2]$	2.648 ± 0.014 (93%)	0.532 ± 0.031 (7%)	-
$[C_4C_1im][OTf]$	1.649 ± 0.031 (92%)	0.247 ± 0.022 (6%)	6.57 ± 0.53 (2%)
$[C_4C_1im][BF_4]$	1.868 ± 0.104 (95%)	0.487 ± 0.041 (5%)	-
$[C_4C_1im][PF_6]$	2.780 ± 0.010 (95%)	0.693 ± 0.064 (5%)	-

fitted to 2 components. There is a short lifetime component, τ_A, which has a low contribution to the overall decay ($< 15\%$) and a lifetime similar to τ_3 in the neat samples. Therefore this component is attributed to the ionic liquid. As with τ_3 in Table 5.1, τ_A is below the detection limit for this spectrometer meaning it cannot be assigned with certainty to any process within the ionic liquid and will not be included in this discussion. The second component is present in all samples and has a lifetime around 1-2 ns. This is approximately the lifetime expected from BODIPY-C10 at these viscosities,[95] and, as it was found to contribute over >85% of photons to all of the decays, this component is attributed to the lifetime of the BODIPY-C10 rotor (τ_{BDPY}).

In order to adequately fit the time resolved fluorescence decay in $[C_4C_1im][OTf]$ the same two components were required, as well as an additional third component, τ_B. As the lifetime of τ_B is similar to that of τ_1 in the neat ionic liquids, the contribution is very low (2%), and the lifetime is far too large to be associated with BODIPY-C10, it is also attributed to the ionic liquid and will not be included in the discussion of the rotor.

Viscosity Dependence of τ_{BDPY} in Ionic Liquids

When considering the variable temperature measurements of BODIPY-C10 in $[C_4C_1im][NTf_2]$, τ_{BDPY} can be plotted against the viscosity of the ionic liquid at different temperatures, shown in Figure 5.17. The viscosities of $[C_4C_1im][NTf_2]$ at each temperature were calculated from the relationship found by Tariq *et al.*[146]

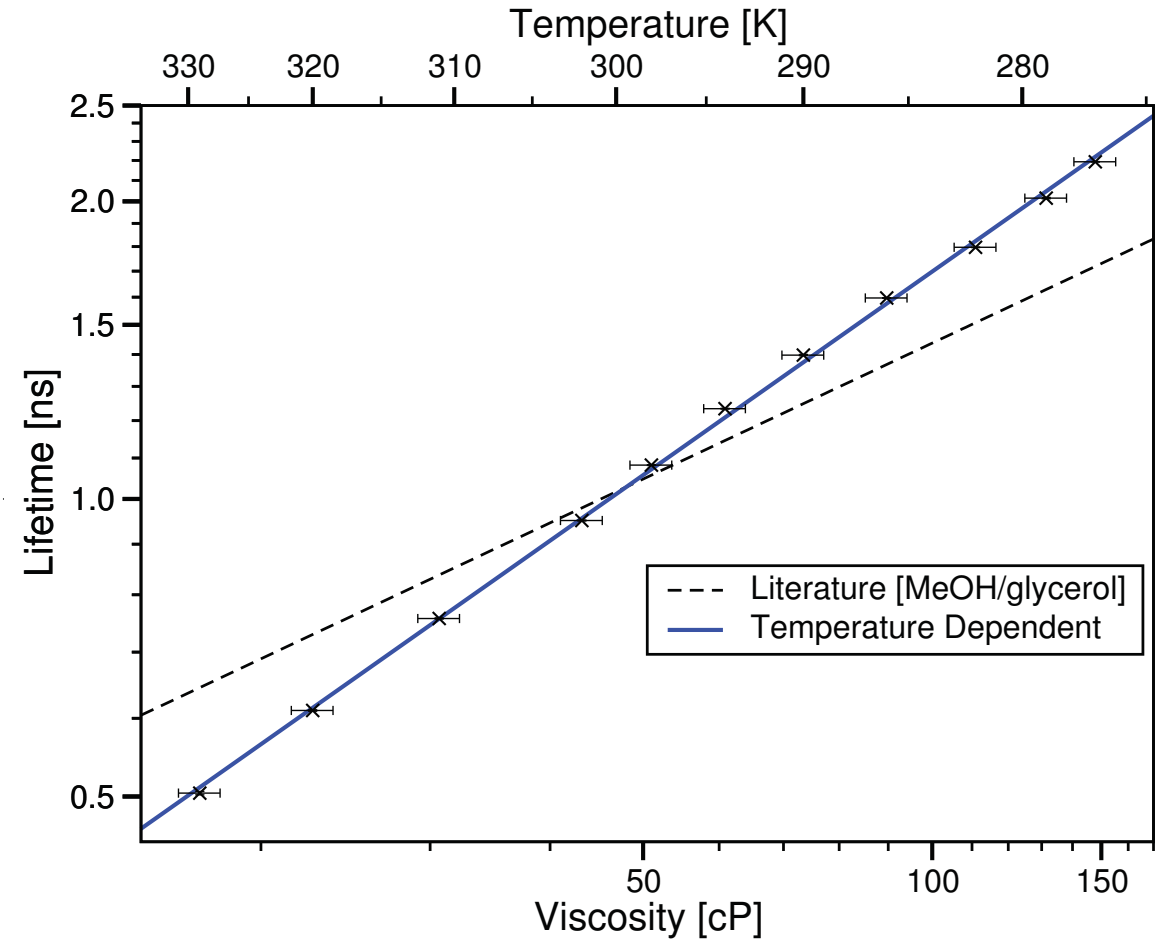

Figure 5.17: *Log-log plot of the temperature dependent fluorescence lifetime of BODIPY-C10 in the ionic liquid $[C_4C_1im][NTf_2]$ against the the viscosity at the corresponding temperature, taken from Ref[146]. The blue line is the best fit to this data (Equation 5.8). The dashed black line is the fit to values derived from the literature methanol/glycerol calibration.*[95]

This figure shows that when changing the temperature of this sample, the lifetime of the rotor clearly increases with increasing viscosity. It is also clear that this trend is different to that of BODIPY-C10 in methanol/glycerol mixtures.[95] The log-log plot shows that the rotor lifetime varies with viscosity as would be expected from the Förster-Hoffmann equation (Equation 5.5). This data can be fitted to the Förster-Hoffmann equation of the form:

$$log_{10}(\tau_{BDPY}) = 0.684 log_{10}(\eta) - 1.138,\ R^2 = 0.9992 \tag{5.8}$$

Considering the ionic liquids with the same cation and various anions, τ_{BDPY} can be plotted against the viscosity, shown in Figure 5.18. The viscosities of these ionic liquids are taken from the measurements by Tokuda *et al.*[91] This trend is compared to the calibration of the lifetime of BODIPY-C10 in methanol/glycerol mixtures,[95] as well as the variable temperature results.

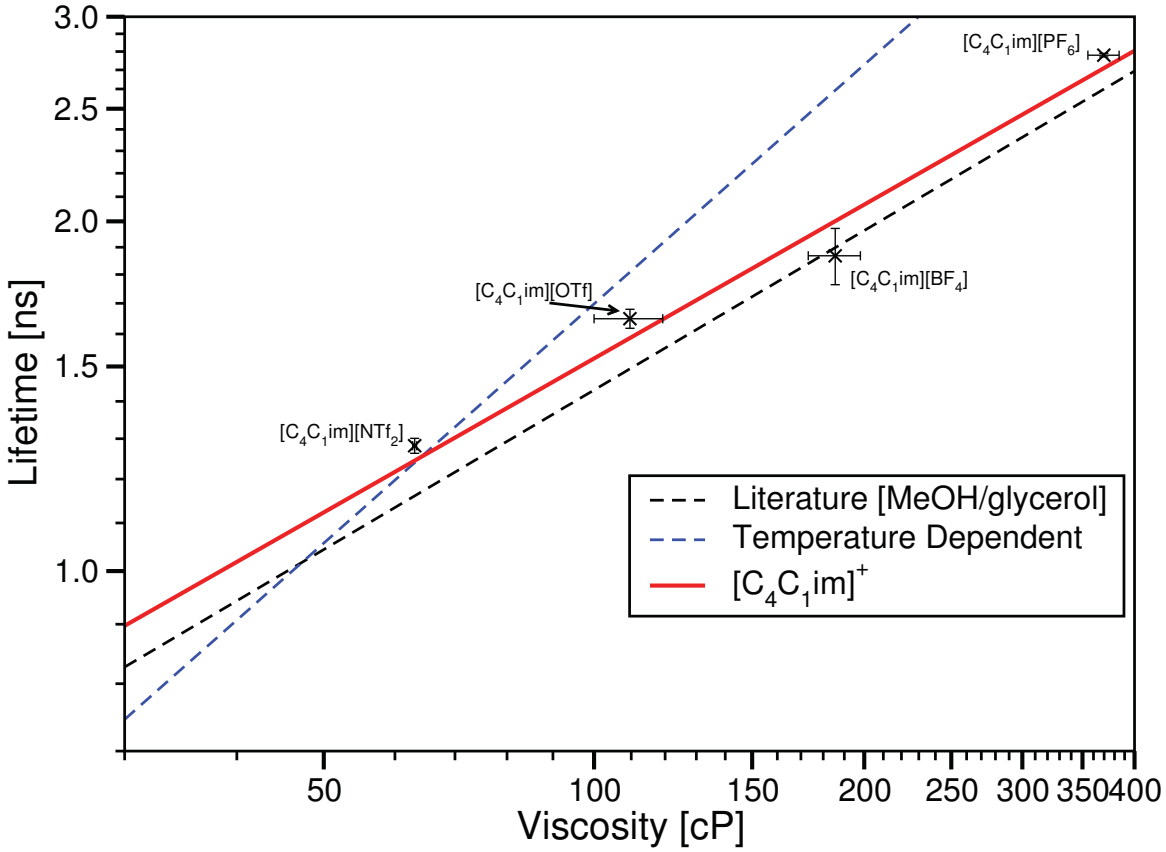

Figure 5.18: *Fluorescence lifetime of BODIPY-C10 in the ionic liquids $[C_4C_1im][NTf_2]$, $[C_4C_1im][OTf]$, $[C_4C_1im][BF_4]$ and $[C_4C_1im][PF_6]$ plotted against the ionic liquid viscosities from Ref[91]. The red line is the best fit to this data (Equation 5.9). The dashed black line is the fit to values derived from the literature methanol/glycerol calibration.[95] The dashed blue line is the best fit to the temperature dependent data in $[C_4C_1im][NTf_2]$.*

In all of these samples, the lifetime of the rotor clearly increases with viscosity as would be expected. When comparing the ionic liquid and molecular solvent data, a molecular solvent with the same bulk viscosity as an ionic liquid presents a slightly lower lifetime of BODIPY-C10. This indicates that the microviscosity of the BODIPY-C10 cybotactic region (the immediate environment surrounding the rotor) is slightly greater in an ionic liquid than in a molecular solvent of the same bulk viscosity. This is not the case for $[C_4C_1im][BF_4]$, however it should be noted that this data point has large error bars for both its viscosity and lifetime.

The data for these ionic liquids can be fitted to the Förster-Hoffmann equation (Equation 5.5) as

$$log_{10}(\tau_{BDPY}) = 0.440 log_{10}(\eta) - 0.697, \; R^2 = 0.9897 \tag{5.9}$$

Considering the ionic liquids which have the same anion and various different cations, τ_{BDPY} is plotted against the ionic liquid viscosities in Figure 5.19. These viscosities are taken from the measurements by Tariq *et al.*[146]

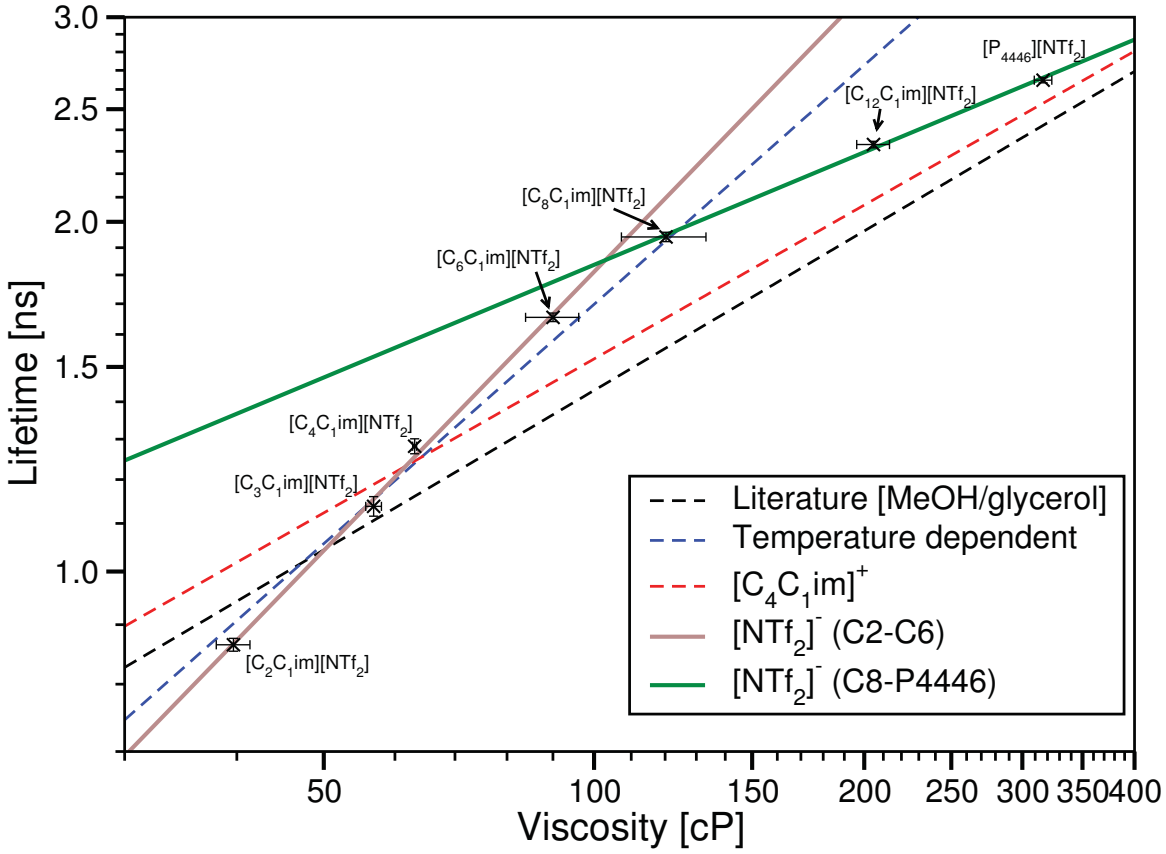

Figure 5.19: *Fluorescence lifetime of BODIPY-C10 in the ionic liquids $[C_nC_1im][NTf_2]$ (n = 2, 3, 4, 6, 8 or 12) and $[P_{4446}][NTf_2]$ plotted against the ionic liquid viscosities on a log-log plot. The brown line is the Förster-Hoffmann equation fitted to the ionic liquids $[C_nC_1im][NTf_2]$ (n = 2, 3, 4 or 6) (Equation 5.10). The green line is the Förster-Hoffmann equation fitted to the ionic liquids $[C_nC_1im][NTf_2]$ (n = 8 or 12) and $[P_{4446}][NTf_2]$ (Equation 5.11). The dashed black line is the fit to values derived from the literature methanol/glycerol calibration.[95] The dashed blue line is the best fit to the temperature dependent data in $[C_4C_1im][NTf_2]$. The dashed red line is the best fit to the variable anion data.*

As before, the lifetime of the rotor clearly increases with viscosity, and the microviscosity of the BODIPY-C10 cybotactic region is greater in an ionic liquid than a molecular solvent of the same bulk viscosity, with the exception of $[C_2C_1im][NTf_2]$.

When attempting to fit the data, it was clear that the whole of this data set cannot be fitted to a single Förster-Hoffmann equation. Careful observation of the graph showed that instead, there are two regions in the log-log plot, each of which can be fitted to a separate Förster-Hoffmann equation.

The relationship between τ_{BDPY} and η for the ionic liquids $[C_nC_1im][NTf_2]$ (n = 2, 3, 4 or 6)

can be fitted to the Förster-Hoffmann equation as

$$log_{10}(\tau_{\mathrm{BDPY}}) = 0.797 log_{10}(\eta) - 1.336,\ R^2 = 0.9968 \tag{5.10}$$

and the data for the ionic liquids $[C_nC_1im][NTf_2]$ (n = 8 or 12) and $[P_{4446}][NTf_2]$ can be fitted as

$$log_{10}(\tau_{\mathrm{BDPY}}) = 0.322 log_{10}(\eta) - 0.380,\ R^2 = 0.9980 \tag{5.11}$$

BODIPY-C10 in Ionic Liquids Discussion

The measurements of BODIPY-C10 in variable temperature, variable anion and variable cation conditions indicates that the lifetime of BODIPY-C10 is indeed sensitive to the viscosity of the ionic liquids. While an overall proportionality between the lifetime of the rotor and viscosity is seen, there are different magnitudes to the change in lifetime upon changing the viscosity in different ways. This indicates that there is some sensitivity of the changes in the lifetime that is related to the environment in which the dye resides. Thus, the make-up of the cybotactic region is vital knowledge to aid in the rationalisation of these results.

As discussed briefly in Section 2.1.1, considerations of the immediate environment around a solute (its cybotactic region) are often studied by looking at the differences in the diffusivities of charged and uncharged species.[147–149] As BODIPY-C10 is a neutral molecule comprised of mainly aliphatic and aromatic moieties, it is therefore expected to partition itself mostly 'soft' non-polar domains generated by the alkyl chains of the ionic liquid cations, with the BF_2 group possibly anchoring itself into the polar region.[150] Due to the large size of the molecule compared to the ionic liquid ions, there is a possibility that BODIPY-C10 may have to stretch between the domains, especially in the ionic liquids with shorter alkyl chains. This is because the completeness of this partitioning is dependent upon the relative sizes of these domains and the solute. What is seen in the literature is that the frictional force against *translational* motion for a neutral molecule is always lower than that for a similarly sized ion.[33] These same effects have also been observed to extend to the rotational dynamics of charged and uncharged solutes, where neutral molecules rotate more freely than charged ions.[151]

As discussed in Section 5.1.2, one must remember that in order for the BODIPY-C10 to undergo non-radiative decay it must change conformer to access the non-radiative decay pathway. This can be accessed by twisting of the phenyl group into the plane of the boraindacene ring and the molecule 'buckling' around the rotor bond, pushing the boraindacene ring out of the

plane of the phenyl group.[133,136] When measuring the lifetime of the BODIPY-C10 rotor in $[C_4C_1im][NTf_2]$ and modifying the viscosity by changing the temperature, the log of the rotor lifetime is proportional to the log of the viscosity. It is known that temperature variations do not have a direct effect on the photophysics of BODIPY-C10, i.e. the lifetimes of this dye respond to viscosity only and the radiative and non-radiative decay pathways are unaffected by changes to the temperature.[152] Therefore this trend in lifetime measurements can be attributed exclusively to the change in viscosity.

Comparing these measurements to the molecular solvent calibration, the ionic liquid trend has a steeper gradient indicating a greater dependence of the lifetime of BODIPY-C10 on the viscosity in the ionic liquid. This indicates that changes in the viscosity of the ionic liquid have a greater effect upon the lifetime of the rotor than changes to the viscosity of a molecular solvent. As this graph is normalised by viscosity, it means that a high viscosity ionic liquid restricts the motion of the rotor more than a similarly viscous molecular solvent. As the interactions in ionic liquids are stronger than those in molecular solvents, it is not necessarily surprising that this occurs. However the fact that a low viscosity ionic liquid is apparently less restrictive to rotor twisting than a similarly viscous molecular solvent is peculiar.

When keeping the cation constant and varying the anion to modify viscosity, the log of the lifetime of the BODIPY-C10 rotor is also directly proportional to the log of the viscosity.

The variable temperature and variable anion measurements show that having a constant cation for measurements of BODIPY-C10 in ionic liquids leads to a change in the rotor lifetime that can be predicted by the Förster-Hoffmann equation. This means that the rotor lifetime is changing in a predictable way with viscosity, and there are no significant changes in the cybotactic region.

However, the difference between the variable temperature measurements and the variable anion measurements highlight that the environment in which the rotor resides is very important. BODIPY-C10 appears to be more sensitive to changes in the bulk viscosity caused by temperature than changes caused by changing the anion when using the $[C_4C_1im]^+$ cation. It is known that this particular molecular rotor is sensitive to polarity only when the overall environment is low polarity.[136,153] Therefore it is unlikely that the difference between these two trends is due to the changing polarities of the ionic liquids with different anions.[154]

Instead, this indicates that the BODIPY-C10 must be sampling some of the anionic region i.e. the polar region of the ionic liquid. This leads to the rotor twisting and buckling sampling, at least partially, some of the anionic region. This in turn means that there is a different trend in the lifetime of the rotor when modifying the viscosity with a different anion, rather than

modifying the viscosity with changes to the temperature.

Keeping the anion constant and varying the cation to change the viscosity, the lifetime of BODIPY-C10 shows a more complex trend with the viscosity. These ionic liquid polarities are as close as possible to each other while allowing for variation of the viscosity.[154] Combined with the high overall polarity of the system means no polarity-based effects are expected.

The relationship between τ_{BDPY} and the ionic liquid viscosity follows two different and distinct trends, one in the ionic liquids $[C_nC_1im][NTf_2]$ (n = 2, 3, 4 or 6) and another in the ionic liquids $[C_nC_1im][NTf_2]$ (n = 8 or 12) and $[P_{446}][NTf_2]$. The crossover for these trends occurs at a viscosity of ≈104 cP, the viscosity of $[C_7C_1im][NTf_2]$.[146] This crossover point, as well as the ionic liquids associated with each trend suggests that the two trends are related to the micro-heterogeneity of the ionic liquids. As BODIPY-C10 is expected to partition into the non-polar domain, the size of this domain needs to be investigated.

It has been shown that for the ionic liquids $[C_nC_1im][NTf_2]$ (n = 6-10) the size of the non-polar domains can be found from the distance between the centres of two imidazolium rings, which are separated by alkyl chains (C-C_{Alkyl}, Figure 5.20). This follows the trend of: C-C_{Alkyl}(Å) = $1.96 \times n_{CH_2} + 3.12$.[155]

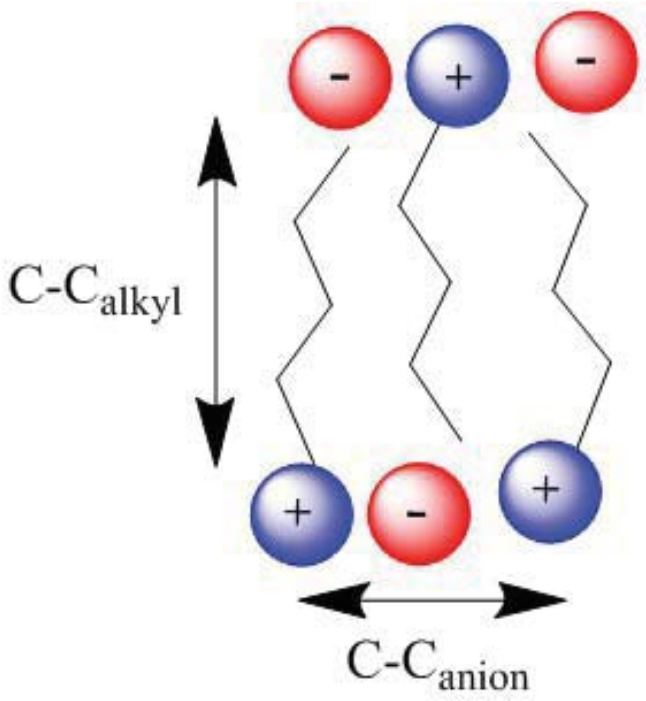

Figure 5.20: *Idealised model illustrating the main structural features of $[C_nC_1im][NTf_2]$ ionic liquids.*

The crystal structure of BODIPY-C10 shows that it adopts a fully extended alkyl chain configuration.[1] In order to maximise the dispersion interactions between the BODIPY-C10 alkyl chain and those of the ionic liquids, it is expected to adopt a similar conformation in the liquid

phase. This gives BODIPY-C10 a length of approximately 21 Å, with the aliphatic region of BODIPY-C10 having a length of approximately 18 Å (see Figure 5.21).

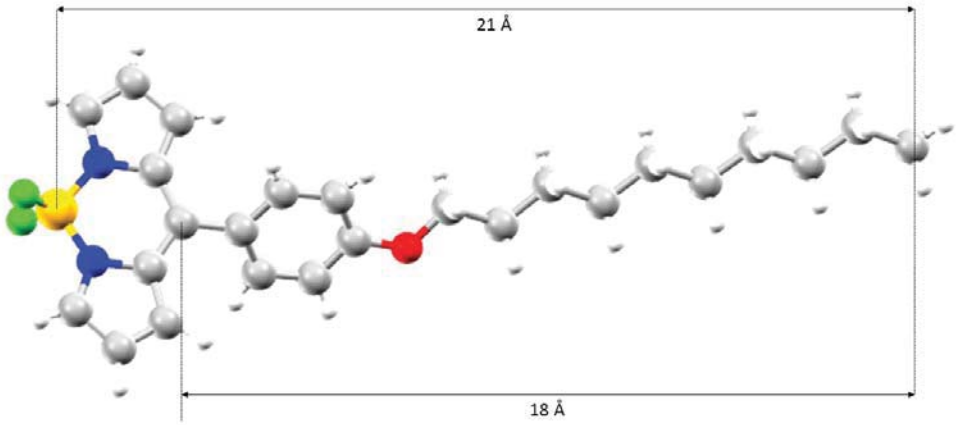

Figure 5.21: *BODIPY-C10 crystal with some lengths labelled.*

Considering the ionic liquids in the first trend ($[C_nC_1im][NTf_2]$ (n = 2, 3, 4 or 6)), these liquids have a continuous polar domain with dispersed non-polar regions within this domain.[21,24,156] In these ionic liquids, the maximum C-C_{Alkyl} distance occurs in $[C_6C_1im][NTf_2]$ at approximately 15 Å. This means that BODIPY-C10 is too large to confine its non-polar moieties entirely in the non-polar alkyl chains between two cations. Therefore the cybotactic region must contain both polar and non-polar moieties.

The fact that this trend is maintained in these ionic liquids indicates that the partitioning of the dye does not change and BODIPY-C10 cannot fit entirely into the non-polar region. This means that changing the length of the alkyl chain within these limits changes the viscosity, and the observed trend is a representation of the viscosity dependent lifetime of BODIPY-C10 when surrounded by both polar and non-polar moieties in ionic liquids.

This also confirms a previous conclusion in the variable anion trend, that BODIPY-C10 must be sampling some of the polar region. Therefore changes to the anion will effect the viscosity in a way that the BODIPY-C10 rotor will report upon.

Considering the ionic liquids in the second trend, τ_{BDPY} in both $[C_nC_1im][NTf_2]$ (n = 8 or 12) is lower than would be expected if the first trend had been maintained for these ionic liquids. This means that while intramolecular rotation is more restricted in these more viscous ionic liquids, this restriction is not as great as expected if the BODIPY-C10 was sampling both polar and non-polar domains. It is known that these ionic liquids have continuous and persistent non-polar domains,[24] alongside the increase in the C-C_{Alkyl} distance.

The C-C_{Alkyl} distances of $[C_8C_1im][NTf_2]$ and $[C_{12}C_1im][NTf_2]$ are 19 Å and 26 Å respectively, much closer to the 21 Å length of BODIPY-C10. This means that BODIPY-C10 can more easily partition its non-polar moieties into the non-polar domains and surround itself mostly with alkyl chains.

Alongside this, the ability of BODIPY-C10 to partition itself in this way could be enhanced by a templating effect of its large, linearlly organised, non-polar groups with a polar terminal BF_2 group. Elfgen *et al.* found that long alkyl chains in alcohols could template an ionic liquids alkyl chains around itself, when the length of the alkyl chain was of similar length to the alkyl chain on the alcohol i.e. ±2 carbons.[157]

The structure of the phosphonium ionic liquid, $[P_{4446}][NTf_2]$, and other phosphonium ionic liquids are less well studied than imidazolium ionic liquids. τ_{BDPY} in $[P_{4446}][NTf_2]$ is below that predicted by the trend for $[C_nC_1im][NTf_2]$ (n = 2, 3, 4 or 6), however it does fit with the same Förster-Hoffmann equation as $[C_8C_1im][NTf_2]$ and $[C_{12}C_1im][NTf_2]$. This indicates that BODIPY-C10 is partitioning itself in a similar manner to these ionic liquids, and thus the relationship of its lifetime top bulk viscosityis similar to these ionic liquids.

Hence, in the ionic liquids in the second trend, BODIPY-C10 is likely to be almost entirely solvated by the alkyl chains of these ionic liquids. This trend is therefore a representation of the viscosity dependent lifetime of BODIPY-C10 when it is partitioned in the most optimal way in ionic liquids.

Simulation of $[P_{4446}][NTf_2]$

To see if it is possible for BODIPY-C10 to partition into the non-polar domain in the way described above, a simulation of $[P_{4446}][NTf_2]$ was run to investigate the sizes of the polar and non-polar domains in this ionic liquid. This is described in Section 4.3.

Domain analysis was performed using the Voronoi tessellation feature of the TRAVIS software package.[88,158] The Drude particles were excluded from the domain Voronoi analysis, the polar domain was assigned to be all of the atoms in the anion, and the phosphorous and adjacent CH_2 groups in the cation as these carry the majority of the charge in this force field. The non-polar domain was assigned to be the rest of the CH_n groups on the alkyl chains. Voronoi parameters are shown in Table 5.8.

The Voronoi analysis indicates that one continuous polar and one continuous non-polar domain are a permanent feature of this ionic liquid. Both of these domains are very large, with the non-polar domain accounting for approximately 55% of the total volume, and the polar domain

Table 5.8: *Average domain properties from the Voronoi analysis of [P_{4446}][NTf_2].*

Domain	No of Domains	Volume [Å^3]	Surface Area [Å^3]
Polar	1.00 ± 0.00	190087 ± 221	153232 ± 513
Non-Polar	1.00 ± 0.00	243372 ± 221	153232 ± 513

accounting for approximately 45% of the total volume. An estimation of the non-polar domain volumes of the imidazolium based ionic liquids can be calculated based upon extrapolation from known values using the numbers of carbons in the alkyl chain. Known non-polar domain volume ratios, calculated to be 22% for [C_4C_1im][NTf_2] and 34% for [C_8C_1im][NTf_2], lead to a non-polar domain accounting for 45% of the total volume in [$C_{12}C_1$im][NTf_2]. Comparing this to non-polar domain volume ratios calculated from the molar volumes of these ionic liquids, these show that the non-polar domain in [C_8C_1im][NTf_2] accounts for 32% of the total volume, and the non-polar domain in [$C_{12}C_1$im][NTf_2] accounts for 43% of the total volume.[159,160] Therefore [P_{4446}][NTf_2] has a larger volume of non-polar moieties (55% of the total volume) than all of the imidazolium based ionic liquids that have BODIPY-C10 fully partitioned. As the polar domains are of a similar size (≈400 Å^3 per ion pair in imidazolium ionic liquids, ≈380 Å^3 per ion pair in phosphonium ionic liquids), it can be deduced that there is likely a much larger non-polar domain for the BODIPY-C10 to partition into. Therefore it can be reasonably assumed that BODIPY-C10 is indeed fully partitioning into the non-polar domain of [P_{4446}][NTf_2].

Summary of BODIPY-C10 in ionic liquids

When comparing the trends seen here, the variable temperature and short chain variable cation trends are very similar. Given the similarity between these ionic liquids, and the conclusion that in all of these ionic liquids BODIPY-C10 samples both polar and non-polar domains, it is not surprising that τ_{BDPY} changes in a similar way with changes to the bulk viscosity.

Comparing the variable anion trend to the short chain variable cation trend, τ_{BDPY} is less dependant upon changes to the bulk viscosity when changing the anion. In all of the ionic liquids in these trends, BODIPY-C10 is sampling both polar and non-polar domains. Therefore, greater changes to τ_{BDPY} upon changes to the cation indicates the stronger association of BODIPY-C10 to this part of the ionic liquid.

Comparing the two variable cation trends, the lifetime of BODIPY-C10 shows a greater dependence upon the bulk viscosity when the BODIPY-C10 is sampling both polar and non-polar domains, than when it is sampling only the non-polar domain. This has been reported before for a different BODIPY dye in variable temperature measurements, where changes to viscosity

in $[C_4C_1im][NTf_2]$ led to greater changes in the lifetime of the BODIPY dye than the same change in viscosity for $[C_{12}C_1im][NTf_2]$.[140]

The fact that τ_{BDPY} is less affected by changes to the viscosity in the longer chain ionic liquids seems counter-intuitive. One might expect that τ_{BDPY} would be more affected by changes to the viscosity in the longer chain ionic liquids, as the added viscosity arises due to addition of more CH_2 groups. These extra CH_2 groups are added into the domain of the ionic liquid in which the dye is residing mostly in, therefore τ_{BDPY} should increase more.

What might be the case is that once the ionic liquids form one distinct non-polar domain, increases in the bulk viscosity lead to an increase in the viscosity of both domains. That is to say that adding more CH_2 groups increases the viscosity of the non-polar regions through a greater number of interactions. This could also increase the viscosity of the polar region by causing a greater segregation between the domains. This would remove non-polar moieties from this domain, increasing the strength of interactions in the polar domain, therefore increasing the viscosity. Both of these could work in tandem to increase the bulk viscosity.

If this were the case, as BODIPY-C10 is expected to be mainly within the non-polar domain it only experiences a part of the increase in the viscosity; that which is associated to the non-polar domain. Therefore there is a lesser increase of τ_{BDPY} with increasing bulk viscosity than when the ionic liquids do not have continuous non-polar domains.

To better understand if this is the case, greater knowledge of how addition of alkyl chains affects the bulk viscosity in ionic liquids is required. This needs a more rigorous model to detail how the polar and non-polar domains are individually affected by the addition of more CH_2 groups. To complement this, molecular dynamics simulations could be employed to study the difference between the cybotactic region of the dye in these different ionic liquids. As the changes in the lifetime are known, these simulations could be directly corroborate the experimental measurements.

5.3.3 3,3'-diethylthiacarbocyanine in Ionic Liquids

Absorption and Emission

In order to check that there are no major changes in the absorption/emission profiles of Cy3 in the conditions in which the lifetime will be investigated, the absorption and emission were measured in all ionic liquids studied, as well as a range of temperatures greater than the temperatures in which the lifetime was recorded.

For all the ionic liquids, there are small differences in the absorption and emission maxima, however these differ by 4 nm at most, therefore it can be reasonably asserted that changing the ionic liquid has no major effect upon the absorption or emission of Cy3.

The same can be said for the absorption and emission in various temperatures, where there is very little difference in the absorption or emission profiles. There was a difference in the intensities of the emission, with higher temperatures leading to a lower emission. However this is expected from higher temperature samples with a lower viscosity (see later discussion).

Therefore the investigations of the lifetimes can proceed.

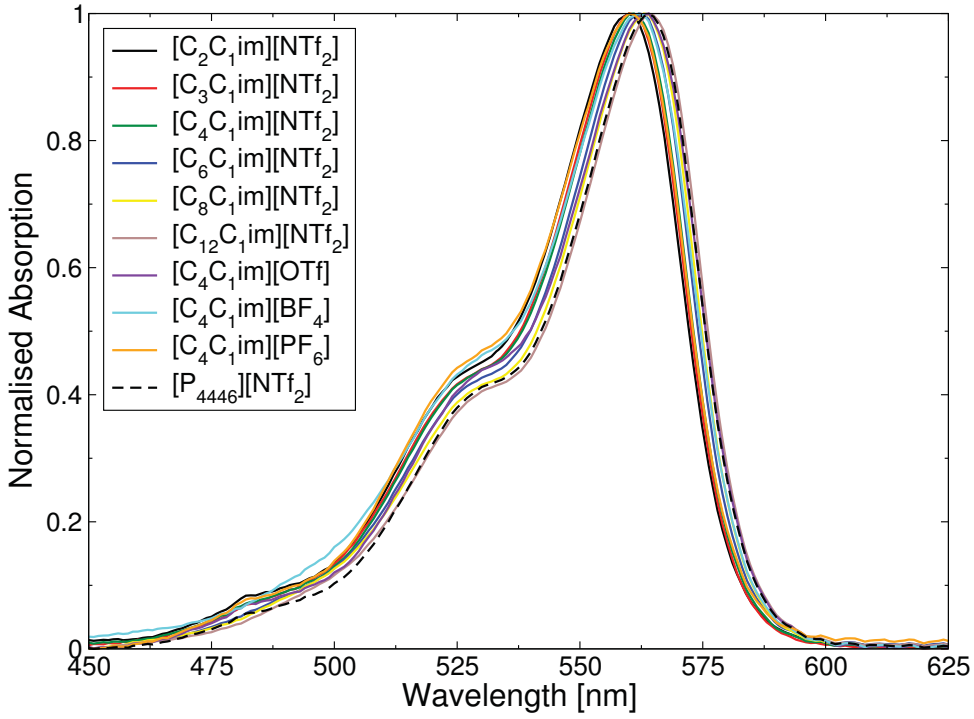

Figure 5.22: *Absorption of Cy3 in all ionic liquids used here.*

Table 5.9: *Wavelength of the maximum absorption of Cy3 in the ionic liquids studied.*

Ionic Liquid	λ_{max} [nm]
$[C_2C_1im][NTf_2]$	560
$[C_3C_1im][NTf_2]$	560
$[C_4C_1im][NTf_2]$	561
$[C_6C_1im][NTf_2]$	562
$[C_8C_1im][NTf_2]$	563
$[C_{12}C_1im][NTf_2]$	564
$[P_{4446}][NTf_2]$	564
$[C_4C_1im][BF_4]$	562
$[C_4C_1im][OTf]$	564
$[C_4C_1im][PF_6]$	560

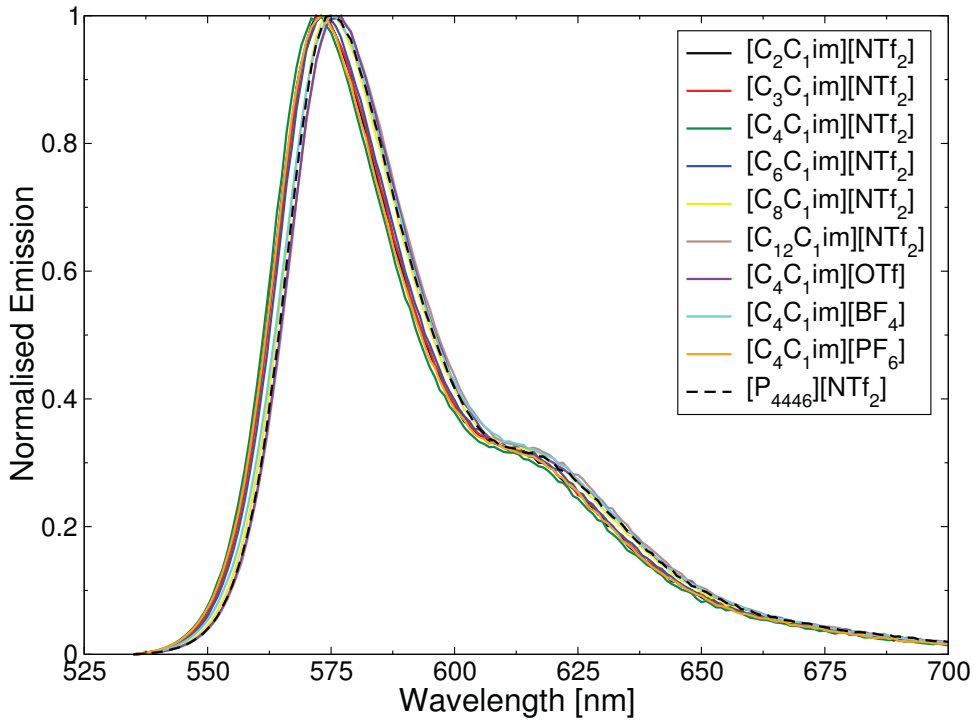

Figure 5.23: *Emission of Cy3 in all ionic liquids used here. Excitation wavelength was 520 nm.*

Table 5.10: *Wavelength of the maximum emission of Cy3 in the ionic liquids studied. Excitation wavelength was 520 nm.*

Ionic Liquid	λ_{max} [nm]
$[C_2C_1im][NTf_2]$	572
$[C_3C_1im][NTf_2]$	572
$[C_4C_1im][NTf_2]$	573
$[C_6C_1im][NTf_2]$	573
$[C_8C_1im][NTf_2]$	574
$[C_{12}C_1im][NTf_2]$	576
$[P_{4446}][NTf_2]$	575
$[C_4C_1im][BF_4]$	575
$[C_4C_1im][OTf]$	577
$[C_4C_1im][PF_6]$	573

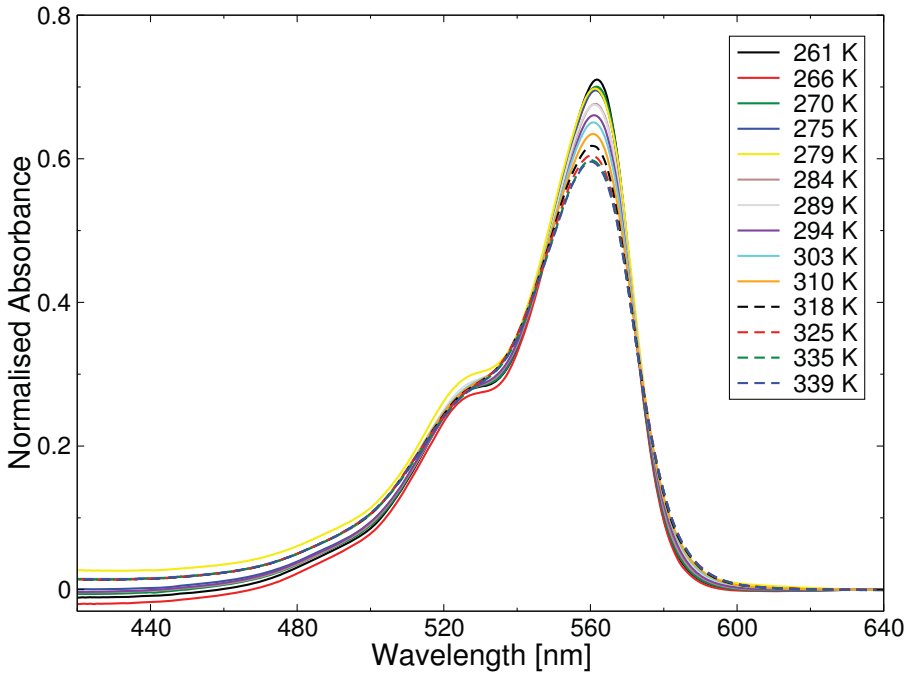

Figure 5.24: *Absorption of Cy3 in $[C_4C_1im][NTf_2]$ in various temperatures.*

Table 5.11: *Wavelength of the maximum absorption of Cy3 in $[C_4C_1im][NTf_2]$ in various temperatures.*

Temperature [K]	261	266	270	275	279	284	289	294	303	310	318	325	335	339
λ_{max} [nm]	562	562	562	561	561	561	561	561	561	561	560	560	560	560

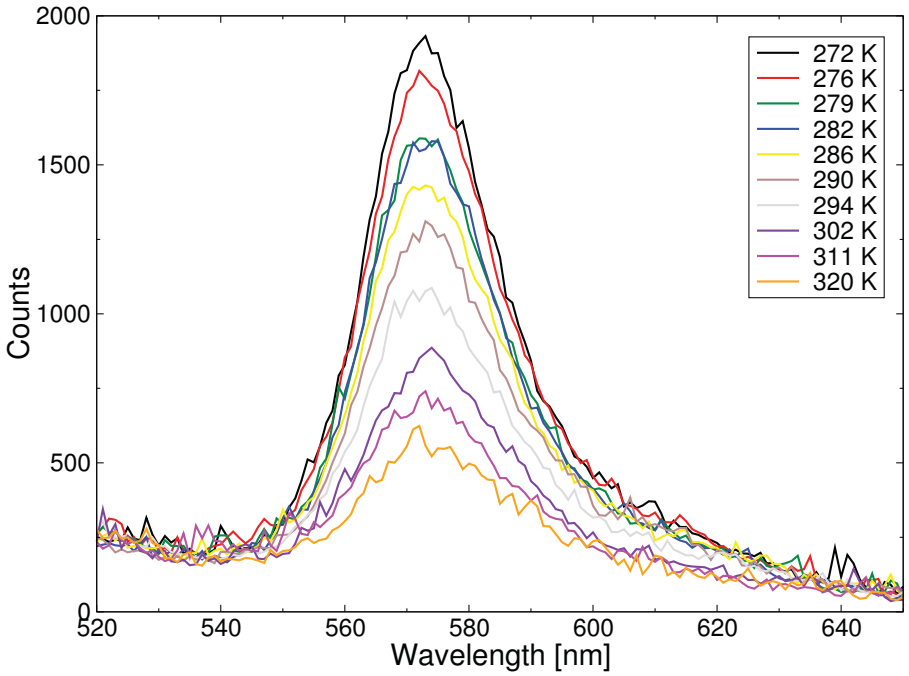

Figure 5.25: *Emission of Cy3 in $[C_4C_1im][NTf_2]$ in various temperatures. Excitation wavelength used was 467 nm.*

Table 5.12: *Wavelength of the maximum emission of Cy3 in $[C_4C_1im][NTf_2]$ in various temperatures. Excitation wavelength used was 467 nm.*

Temperature [K]	272	276	279	282	286	290	294	302	311	320
λ_{max} [nm]	572	572	572	573	573	573	573	574	574	574

Components Present for Cy3 in Ionic Liquids

To study the fluorescence of Cy3 in an ionic liquid when varying the viscosity using temperature, the time resolved fluorescence decay was measured in $[C_4C_1im][NTf_2]$ in temperatures of 276-320 K on the setup described in Section 5.2.2. This corresponds to viscosities of 23-157 cP, and the results are shown in Table 5.13 (decays shown in Appendix A).

Table 5.13: *Calculated lifetime of Cy3 (τ_{Cy3}) in the decay profile of Cy3 at various temperatures in the ionic liquid $[C_4C_1im][NTf_2]$.*

Temperature [K]	τ_{Cy3} [ns]	Temperature [K]	τ_{Cy3} [ns]
276	1.323 ± 0.002	294	0.839 ± 0.002
279	1.244 ± 0.001	302	0.660 ± 0.001
282	1.159 ± 0.001	311	0.519 ± 0.001
286	1.050 ± 0.001	320	0.409 ± 0.002
290	0.942 ± 0.002		

The time resolved decay of Cy3 in these measurements can all be fitted to one component which can be attributed to the lifetime of Cy3 in the solution. As with the BODIPY-C10 variable temperature measurements, no contribution to the decays from the ionic liquids were observed. To study how the fluorescence of Cy3 changes in ionic liquids with different ion combinations, the time resolved fluorescence decay was measured in the ionic liquids $[C_nC_1im][NTf_2]$ (n = 2, 3, 4, 6, 8 or 12), $[P_{4446}][NTf_2]$, $[C_4C_1im][OTf]$, $[C_4C_1im][BF_4]$ and $[C_4C_1im][PF_6]$ on the setup described in Section 5.2.1 (Decays shown in Appendix A).

Table 5.14: *Calculated lifetime of Cy3 (τ_{Cy3}) and other components in the decay profile of Cy3 in $[C_nC_1im][NTf_2]$ (n = 2, 3, 4, 6, 8 or 12), $[P_{4446}][NTf_2]$, $[C_4C_1im][OTf]$, $[C_4C_1im][BF_4]$ and $[C_4C_1im][PF_6]$.*

Ionic Liquid	τ_{Cy3} [ns]	τ_C [ns]	τ_D [ns]
$[C_2C_1im][NTf_2]$	0.727 ± 0.003 (85%)	0.023 ± 0.003 (15%)	-
$[C_3C_1im][NTf_2]$	0.865 ± 0.009 (86%)	0.027 ± 0.004 (14%)	-
$[C_4C_1im][NTf_2]$	0.908 ± 0.003 (86%)	0.020 ± 0.005 (14%)	-
$[C_6C_1im][NTf_2]$	1.090 ± 0.005 (87%)	0.017 ± 0.006 (13%)	-
$[C_8C_1im][NTf_2]$	1.227 ± 0.004 (84%)	0.058 ± 0.005 (11%)	3.75 ± 0.10 (5%)
$[C_{12}C_1im][NTf_2]$	1.352 ± 0.005 (86%)	0.045 ± 0.004 (11%)	4.01 ± 0.22 (3%)
$[P_{4446}][NTf_2]$	1.385 ± 0.005 (86%)	0.039 ± 0.004 (12%)	3.79 ± 0.23 (2%)
$[C_4C_1im][OTf]$	1.189 ± 0.001 (87%)	0.024 ± 0.002 (11%)	6.76 ± 0.32 (2%)
$[C_4C_1im][BF_4]$	1.161 ± 0.005 (82%)	0.026 ± 0.004 (15%)	4.32 ± 0.14 (3%)
$[C_4C_1im][PF_6]$	1.304 ± 0.007 (88%)	0.062 ± 0.004 (12%)	-

As with the measurements of BODIPY-C10 in different ionic liquids, more than one component is needed to fit the fluorescence decay of Cy3 in different ionic liquids. As discussed previously This seems to arise due to a difference in the set-up used for the variable temperature and the

different ionic liquid measurements, however, the reason behind this is unknown.

The time resolved decay of Cy3 in the ionic liquids $[C_nC_1im][NTf_2]$ (n = 2, 3, 4 or 6) and $[C_4C_1im][PF_6]$ can be fitted with two components. Using the same logic as with BODIPY-C10 it can be deduced that the short lifetime component, τ_C, is similar to τ_3 in Table 5.1 seen for the neat ionic liquid sample, and therefore it is assigned to a signal from the ionic liquid of unknown source and not included in this discussion. The longer component around 0.7-1.4 ns has a much higher contribution to all decays (>85% of photons in each decay), so this component can be assigned to the Cy3 rotor (τ_{Cy3}).

For the time resolved decay of Cy3 in $[C_8C_1im][NTf_2]$, $[C_{12}C_1im][NTf_2]$, $[P_{4446}][NTf_2]$, $[C_4C_1im]$ [OTf] and $[C_4C_1im][BF_4]$ a third component, τ_D, is required for an accurate fit. As with τ_B for BODIPY-C10 samples, this is similar to the longer lifetime components that arise from the pure ionic liquids. This similarity along with its minor contribution (<5% of each decay it is present) means it is also expected from the ionic liquid and therefore will not be included in the discussion of the rotor lifetime.

Viscosity Dependence of τ_{Cy3} in Ionic Liquids

When considering the sample of Cy3 in $[C_4C_1im][NTf_2]$ at variable temperatures, τ_{Cy3} was plotted against the viscosity of $[C_4C_1im][NTf_2]$ at each different temperature in Figure 5.26. The viscosity of $[C_4C_1im][NTf_2]$ at each temperature was calculated from the relationship found by Tariq *et al.*[146]

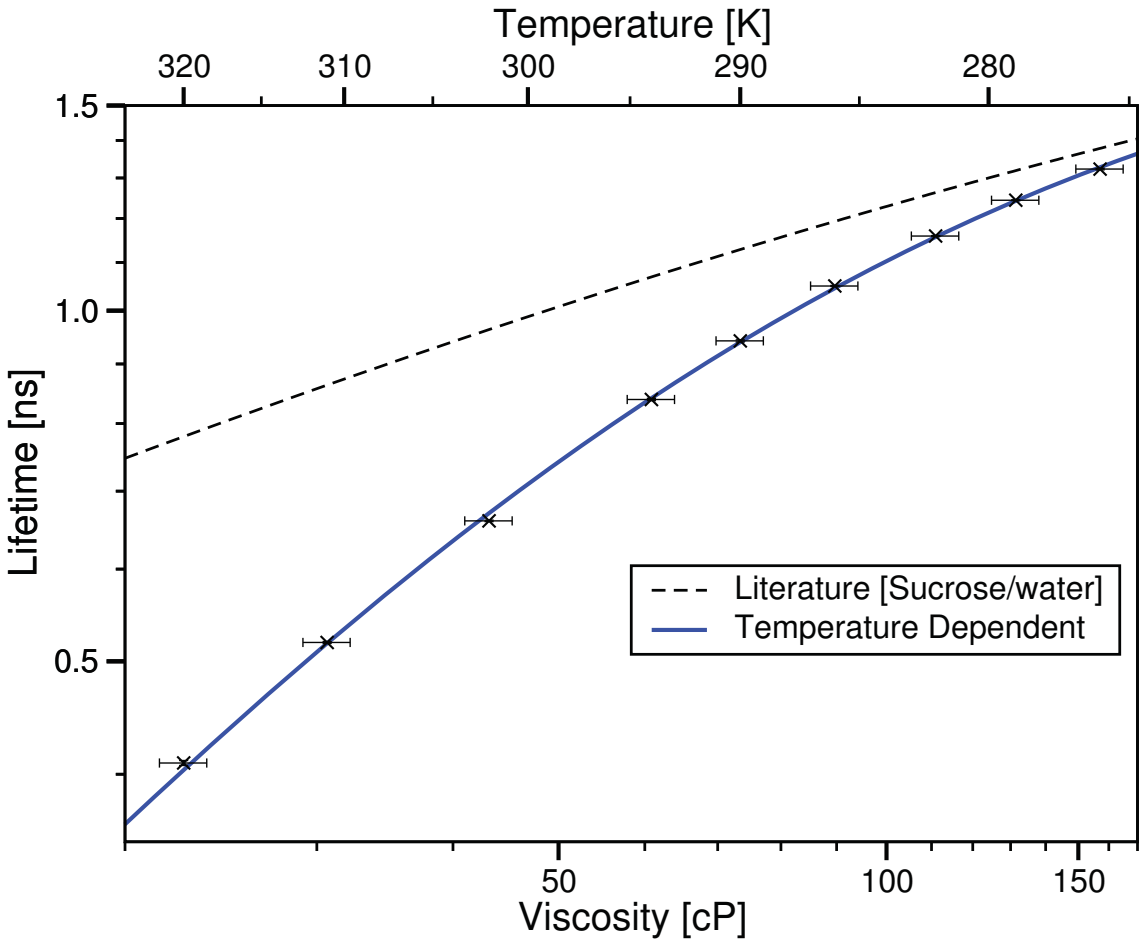

Figure 5.26: *Log-log plot of the temperature dependent fluorescence lifetime of Cy3 in the ionic liquid $[C_4C_1im][NTf_2]$ plotted against the ionic liquid viscosity at the corresponding temperature, taken from Ref[146]. The blue line is the best fit to this data (Equation 5.12). The dashed black line is the fit to values derived from the literature sucrose/water calibration.*[95]

Figure 5.26 shows that the lifetime of Cy3 increases with increasing viscosity of the ionic liquid, as would be expected. An interesting trend when comparing these data to a literature calibration is that for any given viscosity τ_{Cy3} is lower in the ionic liquid than than the sucrose/water mixtures, and this difference decreases with increasing viscosity.

This data set cannot be fitted to a Förster-Hoffmann equation, which is behaviour that has been seen for this rotor before.[95] Hosny *et al.* found that Cy3 data could be fitted to a Hill function instead, and the same function can be used to fit this temperature dependent Cy3

data to the equation

$$\tau = \frac{1.971\eta^{1.075}}{111.14 + \eta^{1.075}}, \; R^2 = 0.9998 \tag{5.12}$$

Considering τ_{Cy3} in ionic liquids with the same anion, these are plotted against the ionic liquid viscosities measured by Tariq *et al.*[146] in Figure 5.27.

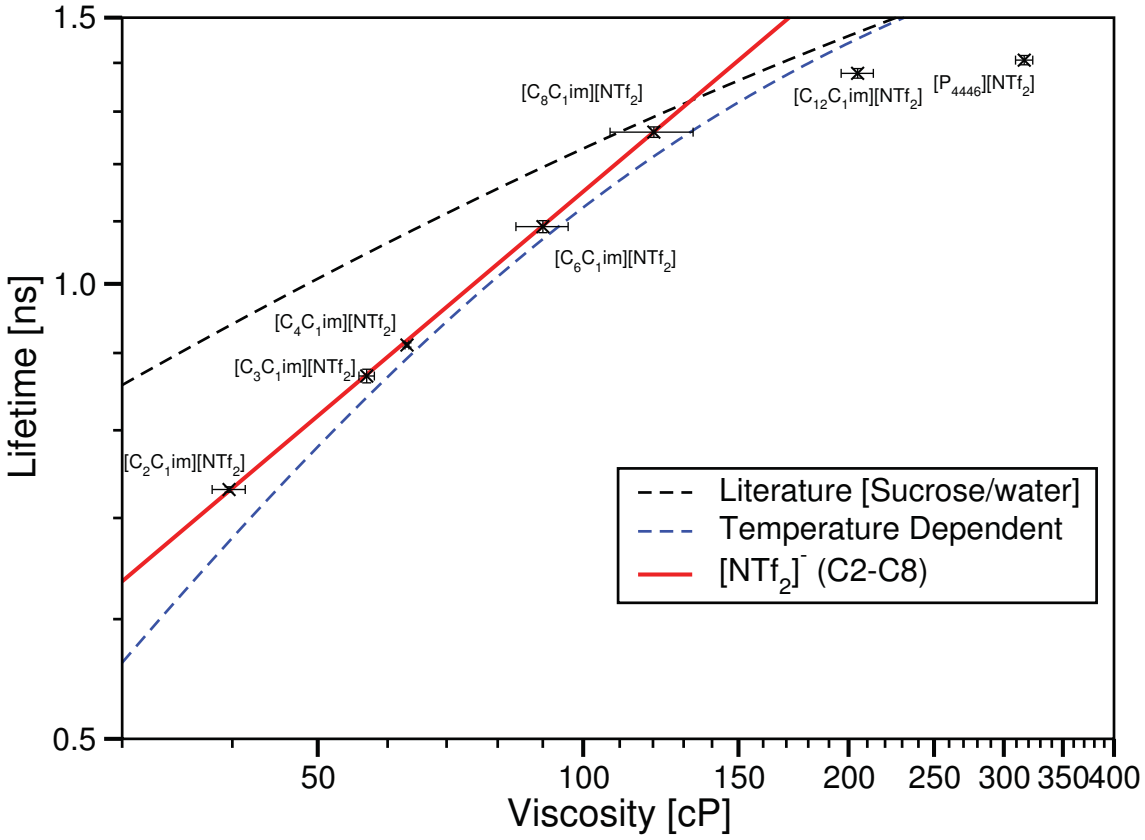

Figure 5.27: *Log-log plot of the fluorescence lifetime of Cy3 in the ionic liquids $[C_nC_1im][NTf_2]$ (n = 2, 3, 4, 6, 8 or 12), $[P_{4446}][NTf_2]$ plotted against the ionic liquid viscosities taken from Ref*[146]*. The red line is the Förster-Hoffmann equation fitted to the ionic liquids $[C_nC_1im][NTf_2]$ (n = 2, 3, 4, 6 or 8, Equation 5.13). The dashed black line is the fit to values derived from the literature sucrose/water calibration.*[95] *The dashed blue line is the best fit to the temperature dependent data in $[C_4C_1im][NTf_2]$.*

As with the temperature dependent measurements, the lifetime of Cy3 in these ionic liquids increases with viscosity for all ionic liquids. When drawing comparisons between these data and the literature calibration, as with the variable temperature measurements, at any given viscosity τ_{Cy3} is lower in the ionic liquid than than the sucrose/water mixtures, and this difference mostly decreases with increasing viscosity, with the exception of $[C_{12}C_1im][NTf_2]$ and $[P_{4446}][NTf_2]$. When considering the ionic liquids $[C_nC_1im][NTf_2]$ (n = 2, 3, 4, 6 or 8) a clear trend can be seen for τ_{Cy3} against η. This can be fitted to the Förster-Hoffmann equation as

$$log_{10}(\tau_{Cy3}) = 0.493 log_{10}(\eta) - 0.925, \; R^2 = 0.9998 \tag{5.13}$$

The ionic liquids $[C_{12}C_1im][NTf_2]$ and $[P_{4446}][NTf_2]$ do not fit this trend, and there are not enough ionic liquids in this region to attempt to fit these data to an alternative curve.

Considering the ionic liquids with a constant cation and various anions, Figure 5.28 shows a plot of τ_{Cy3} against the viscosity taken from Tokuda *et al.*[91]

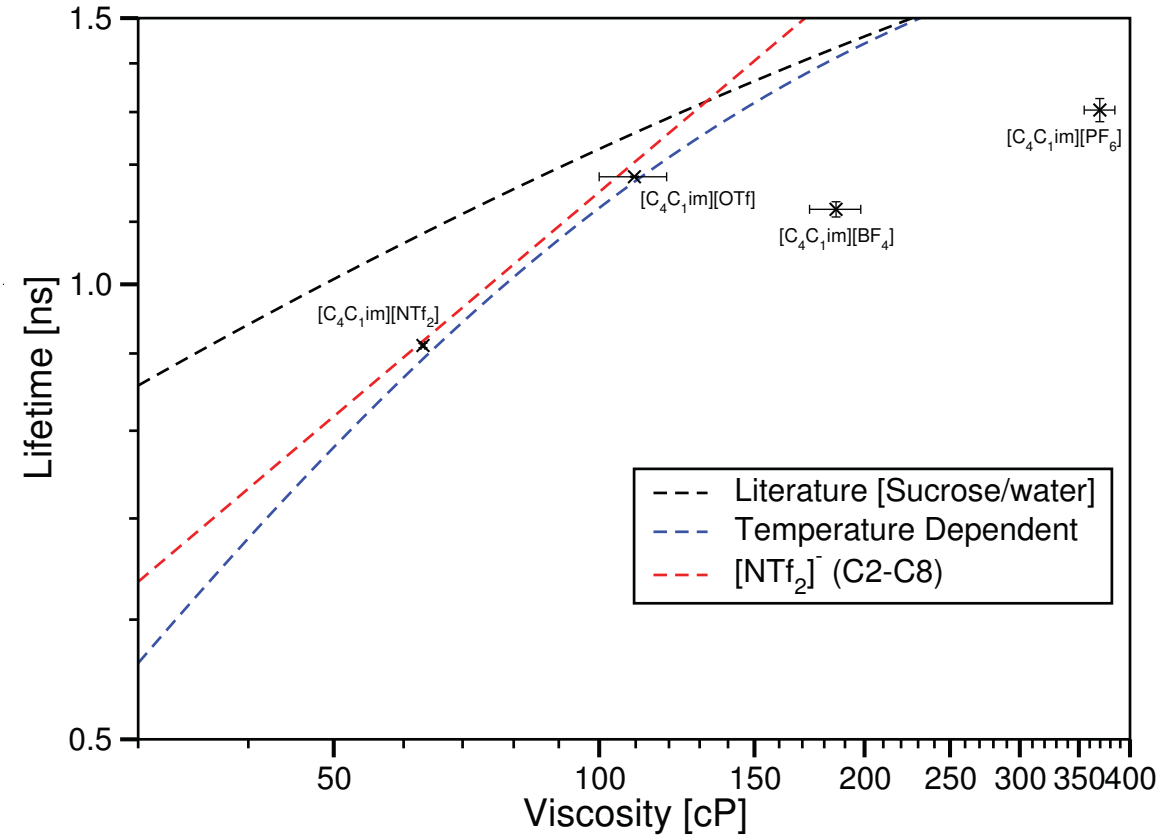

Figure 5.28: *Log-log plot of the fluorescence lifetime of Cy3 in the ionic liquids $[C_4C_1im][NTf_2]$ $[C_4C_1im][OTf]$, $[C_4C_1im][BF_4]$ and $[C_4C_1im][PF_6]$ plotted against the ionic liquid viscosities taken from Ref[91]. The dashed black line is the fit to values derived from the literature sucrose/water calibration.[95] The dashed blue line is the best fit to the temperature dependent data in $[C_4C_1im][NTf_2]$. The dashed red line is the fit to the ionic liquids $[C_nC_1im][NTf_2]$ (n = 2, 3, 4, 6 or 8).*

As with the previous Cy3 measurements, for any given viscosity, η_{Cy3} is lower in the ionic liquid than than the sucrose/water mixture.

However, here the lifetime of Cy3 is no longer dominated by viscosity, unlike the BODIPY-C10 data and the temperature and cation variation data sets for Cy3. τ_{Cy3} in $[C_4C_1im][OTf]$ is greater than τ_{Cy3} in $[C_4C_1im][BF_4]$, despite the viscosity of $[C_4C_1im][OTf]$ being lower than that of $[C_4C_1im][BF_4]$. Along with this, when comparing these data to the constant anion data, $[C_4C_1im][PF_6]$ has a higher viscosity than all the $[NTf_2]^-$ ionic liquids, yet shows a lower τ_{Cy3} value than both $[C_{12}C_1im][NTf_2]$ and $[P_{4446}][NTf_2]$.

These results suggest that there is a difference in the interaction between Cy3 and different anions which affects its lifetime. To understand how the anion interactions affect the ground state of Cy3, crystals of Cy3 with these and other anions were grown and their structures

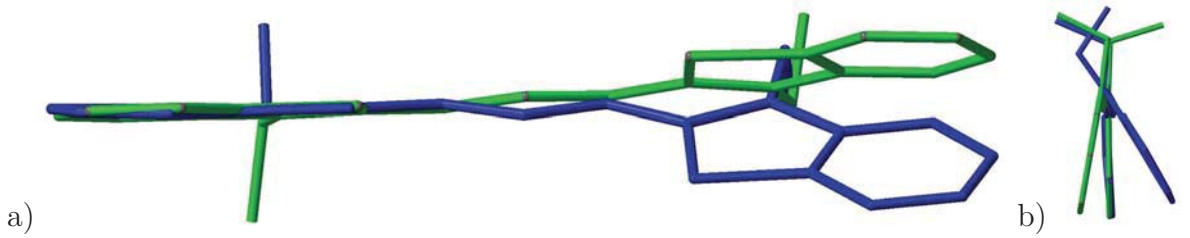

Figure 5.29: *The two different structures of the cation in the crystal structure of [Cy3][NTf$_2$], the more twisted in blue and the less twisted in green. a) view of the different twists along the linker b) end-on view of the two structures overlapped.*

studied.[1] All of the bridging bonds were found to be mid-way between a classical C=C double bond (≈1.33 Å) and a C−C single bond (≈1.54 Å), consistent with the notion that there is complete delocalisation across both benzothiazole rings and the C3 linker. These bonds were also all found the be the same length, within experimental error. Hence the interactions between anion and Cy3 do not appear to influence the bonding in the Cy3 cation.[1]

However, notable differences were found in the the twist angle between the benzothiazole rings (θ in Table 5.15). These vary from 3.3° to 26.8° which indicate a large degree of flexibility in the Cy3 cation despite the formal complete delocalisation of the pi-symmetry orbitals. This is especially notable within [Cy3][NTf$_2$] and [Cy3][CHTf$_2$] where each structure contains two symmetry-independent cations with hugely different twist angles in the same structure. This is shown for [Cy3][NTf$_2$] in Figure 5.29. The combined evidence of the Cy3-anion distances indicating only weak interactions, the similarity of the intramolecular bonds across the different structures and yet the significantly different twists around the bonds of the linking conjugated chain in Cy3 indicate the extreme flexibility and ease of distortion of the Cy3 cation.

Table 5.15: *Summary of relevant dihedral angles in the Cy3 structures. Brackets show the angle deviation from a planar molecule. Notes: (a) cation with larger overall twist; (b) cation with smaller overall twist; (c) related by symmetry to C2C8C9C8'; (d) related by symmetry to NC2C8C9; (e) related by symmetry to SC2C8C9.*

Salt	θ	NC2C8C9	SC2C8C9	C2C8C9C8'	C8C9C8'C2'	C9C8'C2'N'	C9C8'C2'S'
BF_4	10.4	175.4 (4.6)	-4.4 (4.4)	-180.0 (0)	177.2 (2.8)	175.8 (4.2)	-5.6 (5.6)
NTf_2[a]	26.8	-170.9 (9.1)	10.7 (10.7)	-174.5 (5.5)	c	d	e
NTf_2[b]	10.4	174.7 (5.3)	-5.2 (5.2)	178.8 (1.2)	c	d	e
$CHTf_2$[a]	21.8	-169.4 (10.6)	11.1 (11.1)	-176.6 (3.4)	-175.1 (4.9)	-174.0 (6.0)	6.4 (6.4)
$CHTf_2$[b]	8.31	-173.2 (6.8)	5.7 (5.7)	-179.9 (0.1)	-178.3 (1.7)	.177.0 (3.0)	3.5 (3.5)
OTf	15.07	179.8 (0.2)	-0.4 (0.4)	178.1 (1.9)	178.2 (1.8)	168.4 (11.6)	-12.7 (12.7)
BF_4/I	9.02	176.0 (4.0)	-4.2 (4.2)	-179.0 (1.0)	176.6 (3.4)	176.5 (3.5)	-5.0 (5.0)
PF_6	5.12	178.2 (1.8)	-3.1 (3.1)	177.7 (2.3)	-179.3 (0.7)	176.6 (3.4)	-3.4 (3.4)
I	3.28	179.8 (0.2)	1.5 (1.5)	-178.3 (1.7)	178.2 (1.8)	-177.8 (2.2)	1.0 (1.0)

Further evidence of this flexibility comes from examination of the 3-bond torsion angles across the conjugated C3 linker (Table 5.15). For an ideal planar molecule, all of these torsion angles should either be 0° or 180°. In most cases the deviation from planarity is small, being 5° or less.

This indicates that the overall twist angle between the benzothiazole rings is comprised of lots of small twists, which sum to a larger twist across the entire delocalised C3 linker. However, the cations with the biggest overall twists ([Cy3][OTf], [Cy3][$CHTf_2$] and [Cy3][NTf_2]) have torsion angles which deviate by 11° or more. These relatively large torsion angles all occur across the C2–C8 bond (or C8'–C2') with only small torsion angles noted across the C8–C9 (or C9–C8') bond, implying that the C2–C8 bond is the most flexible across the entire conjugated linker.

Cy3 in Ionic Liquids Discussion

The variable temperature and variable cation measurements of the Cy3 rotor lifetimes in ionic liquids show that Cy3 can be sensitive to the viscosity of the ionic liquid. However the variable anion measurements show that for this rotor, as opposed to BODIPY-C10, the lifetime is much more sensitive to the anions present in the ionic liquid. Therefore again understanding the cybotactic region and rotor quenching mechanism is vital to help rationalise these results.

As discussed in Section 5.1.1, although the exact mechanism for non-radiative decay of cyanine molecules is not known exactly, the ground and excited states have been studied using NMR and computational methods. These showed that the ground state takes a planar configuration, similar to that seen in some crystal structures. The excited state involves a twist around the C2-C8 bond, which through NMR was identified to be somewhere between a cis and trans isomer.

An especially important result is that calculations by Vladimirova *et al.* showed a lower twist of the benzothiazole rings in the excited state in polar solvents than in non-polar solvents.[105] Both of these were also lower twists than gas phase calculations by Baraldi *et al.*[103]

When considering the crystal structures, these show that the twist of the benzothiazole occurs over multiple dihedrals in the linker chain.[1] This indicates that the excited state twist angles calculated through computation may be misleading, as the calculations all involve a fixed linker chain with rotation around a single bond.[102,105] These crystal structures show that allowing the whole linker to twist is a more realistic model of Cy3 twisting.

While the C2-C8 bond has the largest single twist angle in every crystal structure, the large range of dihedral angles highlights the high degree of flexibility of the Cy3 cation while in its ground state. In the liquid phase, this flexibility could also lead to greater accessibility to the secondary decay pathway.

Returning to the lifetimes of Cy3, these are shorter in all ionic liquids than in molecular solvents of the same bulk viscosity. That is, the microviscosity reported by a dye which is expected to be

mostly partitioned into the 'stiff' polar region of the ionic liquid is *lower* than the microviscosity of the same dye recorded in an aqueous sucrose solution of the same bulk viscosity, opposite to what would be expected.

Considering the environment in which the the dye will reside, as discussed in Section 2.1.1, from the study of the diffusion and rotational dynamics of charged solutes in various ionic liquids, it is known that charged solutes will partition into the 'stiff' polar domain generated by the charge carrying moieties in the cation and anion.[33,147–151] The partitioning into the polar domain is very strong for solutes that are significantly smaller than the ionic liquid ions, while solutes that are larger in comparison to the ionic liquid will partition less strongly.[33]

As Cy3 is a relatively large molecular ion with a single positive charge distributed across its symmetrical structure, it is expected that it will be solvated directly by the anions of the ionic liquid in an ion 'cage' structure.

When diffusion (the method by which solutes are classically studied) occurs, the ion must 'jump' from this cage to a neighbouring cage.[35,161,162] It is this jump that poses a high activation barrier to translation, thus leading to slow diffusion of ions in ionic liquids. In their study of the size, shape, and charge of a solute rotating in $[C_4C_1im][BF_4]$ Rumble *et al.* demonstrated that such diffusive jumps were much more common and of greater amplitude for the smaller probes, where they significantly contributed to rotational diffusion coefficients, but rarer in the case of larger probes.[151] Hence, while one would expect Cy3 to experience a large friction to its diffusive motion, the rotational motion will be dictated more by the nature of the ion cage.

Within the same study, Rumble *et al.* also showed other faster, spatially restricted motions of all of their solutes, regardless of size. These consisted of oscillations within a slowly relaxing environment which, along with other similar motions, are often described as 'rattling' inside the cage.[151,163–165]

This gives rise to the likely explanation for the lower than expected lifetime reported by Cy3, when compared to aqueous sucrose solutions with the same bulk viscosity. Rather than requiring a jump or movement between cages, it appears that sufficient molecular rotation of the dye can occur within its ion cage to allow non-radiative decay to take place.

If the cage contains no other ions other than Cy3, then the cage structure could excluded other ions which could impede the twisting of Cy3, thus allowing easier rotation than would be expected. As no such structure exists in molecular solvents, while twisting to undergo non-radiative decay, a dye in a molecular solvent is required to move past crowded molecules. This would lead to a greater hindrance of non-radiative decay in molecular solvents than ionic liquids, which matches with the results herein.

Considering the temperature dependent measurements, the ion cage flexibility is affected by both the bulk viscosity of the liquid, and short range inter-ionic interactions. As both of these factors change with temperature, it follows that the lifetime of the rotor changes with temperature due to changes in the ionic liquid.

When considering Cy3, there have been no reported studies on the temperature dependence of this rotor i.e. by comparing the lifetime of Cy3 in two solutions which have the same viscosity at different temperatures. The only study of temperature dependent properties of Cy3 involve the binding of Cy3 to DNA.[166] While this shows no effect of temperature, this is not entirely relevant to the effect of temperature on the lifetime of Cy3 in ionic liquids.

This means that there is a possible effect of temperature on the rotor lifetime shown in the trend observed in Figure 5.26. If this were the case, a higher temperature would cause the non-radiative decay pathway to be more easily accessible. This would lead to an additional decrease in Cy3 lifetime, beyond the effect on viscosity of the solution, and one may expect to see lower lifetimes at high temperature if this was the case.

Examining the changes to the fluorescent lifetimes of Cy3 in the different ionic liquids, given the conclusion above that Cy3 resides within an ion cage, these likely reflect the changing flexibility of the anion cages in these liquids and hence the ease of rotation of Cy3 within these cages. This is not the resistance of the cage to diffusive motion of a solute, which is the more common experiment. Given that Cy3 is cationic, the flexibility of the ion cage around this ion is most influenced by a change in the anion of the ionic liquid, however changes of the cation may also affect the flexibility of the anion cage around the dye.

The photophysical properties of Cy3 in different polarity environments have not been rigorously studied previously, therefore it is possible that there is some polarity related contribution to this effect i.e. polarity could affect the radiative and non-radiative decay pathways. As this dye is cationic, the polarity of the anions is the important quantity.

Therefore considering the changes to the ionic liquid that should affect the rotor the most, the ionic liquids with different anions can be examined. For this, the effect of polarity upon the dye also requires consideration. As the ionic liquids have different anions, the difference in polarity is reflected in the β values of the ionic liquids, which is the Kamlet-Taft polarity scale measure of the ability of a solvent to donate electron density to a solute.

The ionic liquids in this trend, $[C_4C_1im][X]$ where X = OTf, PF_6, BF_4 or NTf_2, have very different β values,[154] along with different viscosities. There is a lack of a correlation between the lifetime of Cy3 and viscosities in these ionic liquids. Therefore this is likely due to a complex interplay between bulk viscosity, ion cage strength and flexibility, and polarity. The

direct effect of polarity on the rotor cannot be investigated with these data, and should be investigated separately.

When using different cations to modify the viscosity, there is a correlation between the lifetime of the rotor and the bulk viscosity. When keeping the anions constant, as in these ionic liquids, there is as little as possible difference in their polarities while still allowing variation in their viscosities. Therefore the interactions between the liquid and the dye should remain approximately constant and polarity related spectral changes will not be seen.

For the ionic liquids $[C_nC_1im][NTf_2]$ (n = 2, 3, 4, 6 or 8) a linear trend in the log-log plot is observed and the viscosity dependence of the lifetime can be fitted to the Förster-Hoffmann equation. Given that in these ionic liquids, Cy3 is expected to be surrounded by anions, the large changes in the lifetime of Cy3 suggest that it is more sensitive to the viscosity than it is expected to be.

The hypothesis for this is that Cy3 cannot partition fully into the preferred domain, with its cybotactic region containing only anions. Unlike BODIPY-C10, this cannot be due to the lack of a continuous domain as all imidazolium ionic liquids studied here present a continuous polar domain.[21,24,156]

Instead this is hypothesised to be related to the relative size of the Cy3 cation to the ionic liquid ions. Many studies have shown that the size of a solute, along with its charge, are very important when determining the segregation of the solute into one domain.[33,147–151] When considering the volume of Cy3 (V_{Cy3}), this can be determined from the crystal structure as ≈300 Å^3.[1] The volumes of the ionic liquid ions (V_{IL}) have been calculated by Philippi *et al.* for all even numbered imidazolium cations, $[P_{4446}]^+$ and $[NTf_2]^-$.[167]

Table 5.16: *Cation volumes and ratio of Cy3 volume to average ion volume in $[C_nC_1im][NTf_2]$ (n = 2, 4, 6, 8 or 12) and $[P_{4446}][NTf_2]$. The $[NTf_2]^-$ anion has a volume of 211Å^3. Ionic liquid ion volumes taken from Ref[167].*

Ionic Liquid	Cation Volume [Å^3]	V_{Cy3}/V_{IL}
$[C_2C_1im][NTf_2]$	158	1.7
$[C_4C_1im][NTf_2]$	206	1.5
$[C_6C_1im][NTf_2]$	253	1.3
$[C_8C_1im][NTf_2]$	300	1.2
$[C_{12}C_1im][NTf_2]$	395	1.0
$[P_{4446}][NTf_2]$	470	0.9

Table 5.16 shows that the solute-to-solvent ratio, V_{Cy3}/V_{IL}, for $[C_nC_1im][NTf_2]$ (n = 2, 3, 4, 6 or 8) decreases from 1.7 to 1.2 as n increases. For $[C_{12}C_1im][NTf_2]$ V_{Cy3}/V_{IL} = 1.0 and for $[P_{4446}][NTf_2]$ V_{Cy3}/V_{IL} = 0.9.

It is expected that this decrease in the solute-to-solvent volume ratio will, at some ratio, lead

to a greater partitioning of Cy3 into the polar domain, which will change the cybotactic region and thus the trend in lifetime. This is what could be the cause of the difference of τ_{Cy3} in $[C_{12}C_1im][NTf_2]$ and $[P_{4446}][NTf_2]$ from the trend seen in $[C_nC_1im][NTf_2]$ (n = 2, 3, 4, 6 or 8). It seems that once V_{Cy3}/V_{IL} decreases to 1, there is a strong enough partitioning of the dye into the polar, anionic domain that the lifetime is not greatly affected by changes to the viscosity from the non-polar region.

If this interpretation is correct, then the trend in $[C_nC_1im][NTf_2]$ (n = 2, 3, 4, 6 or 8) reflects the flexibility of the cybotactic region of the dye in methylimidazolium ionic liquids when the Cy3 cannot fully surround itself with anions. Thus changes to the viscosity by adding or removing alkyl chains leads to significant changes in the lifetime of Cy3, as it has to sample some of the non-polar region.

The lifetime of Cy3 in $[C_{12}C_1im][NTf_2]$ and $[P_{4446}][NTf_2]$ are lower than would be predicted by this trend. Therefore it can hypothesised that in $[C_{12}C_1im][NTf_2]$ and $[P_{4446}][NTf_2]$ the ions in the ionic liquid are large enough that Cy3 partitions into the polar domain, and surround itself entirely with anions.

The lower than predicted lifetime fits with the partition hypothesis as the viscosity difference between $[C_8C_1im][NTf_2]$ and $[C_{12}C_1im][NTf_2]$ involves addition of alkyl chains into the non-polar region. If the dye is surrounded entirely by anions, this addition of alkyl chains to increase viscosity is into a domain in the liquid the dye is not directly sampling. Thus the lifetime does not increase as much as expected from the previous trend, with only 0.135 ns increase despite a 80 cP increase in viscosity. This is the same difference in viscosity as that between $[C_2C_1im][NTf_2]$ and $[C_8C_1im][NTf_2]$, where there is a difference of 0.500 ns in τ_{Cy3}.

The data point for $[P_{4446}][NTf_2]$ suggests that the anion cage of Cy3 must be the same in this ionic liquid as that in $[C_{12}C_1im][NTf_2]$, due to τ_{Cy3} being very similar (0.033 ns difference) despite a difference in their viscosities of 112 cP. The aforementioned simulation of $[P_{4446}][NTf_2]$ shows that this ionic liquid contains a continuous polar domain. Therefore it is indeed possible that the Cy3 can fully partition into a domain containing exclusively $[NTf_2]^-$ anions, thus is largely unaffected by the additional viscosity associated to the non-polar region.

Although the ion cage is suspected to be largely unaffected by changes to the bulk viscosity between $[C_{12}C_1im][NTf_2]$ and $[P_{4446}][NTf_2]$, there is a slightly greater lifetime in the higher viscosity $[P_{4446}][NTf_2]$. This implies that changes to the non-polar domain are indirectly (i.e. via cation motion) affecting the flexibility of the anion cage. Confirmation of this will require further study.

Chapter 6

Measurements of Ionic Liquids in Electric Fields

Initially, the central focus of this project was to study ionic liquids in electric fields. As discussed in Section 2.2.2, previous measurements have observed very long time and distance effects from an electrode on an ionic liquids upon application of a potential.

The techniques that have been used previously to observe these are the fluorescence lifetime imaging (molecular rotor measurements) previously discussed in Chapter 5, and fluorescence correlation spectroscopy, FCS.

In this chapter, previously measured fluorescence lifetime results of Cy3 in $[C_4C_1im][NTf_2]$ in electric fields are re-analysed and re-interpreted, and more fluorescence lifetime measurements using BODIPY-C10 in $[C_4C_1im][NTf_2]$ in electric fields are presented and discussed.

Sections which contain previously collected data are marked at the start of the section with the person who measured it.

6.1 Experimental Details

The electrochemical cell used for the measurements of the lifetime of the dyes in ionic liquids is shown in Figure 6.1.

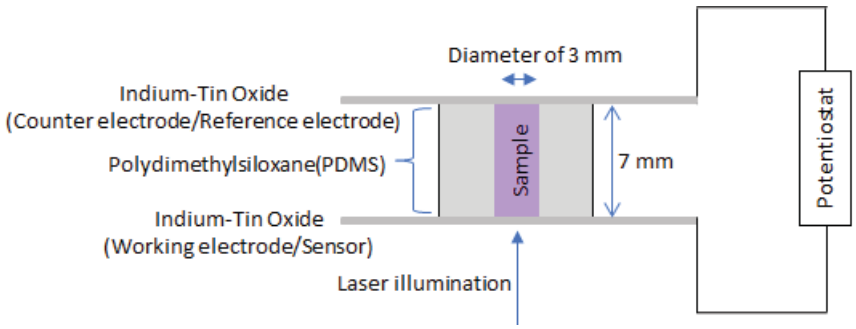

Figure 6.1: *Diagram of the electrochemical cell used for measurements on the confocal microscope.*

In these experiments, a solution of the dye in ionic liquids is placed into the void in the PDMS and sealed by sandwiching between two indium-tin oxide (ITO) coated glass slides. The glass slides adhere to the PDMS, therefore extra adhesive is not required.

The ITO slides have silver 'busbars' for connections. Copper tape is stuck next to these and the connection completed with silver conductive paint. Once mounted on the microscope, the copper tape is connected to the potentiostat using crocodile clips. Due to the persistence of the effects, a new cell was used for each measurement. The connections were checked each time a new cell was mounted.

For the charging cycle, the following standard procedure was used, unless specifically stated. Firstly, the open circuit potential (OCP, also known as the potential of zero charge) was determined. This is the potential applied across the cell at which there is no current, and this is used as the reference point for 0 V. It is important that the cell is fully discharged and there is no static potential across it, so the cell requires shorting before the OCP is measured. This was achieved by connecting the two pieces of copper tape together with crocodile clips for at least 10 minutes.

The OCP was determined by measuring the change in potential difference across the cell with time. When the change in the potential difference was <1 μV/s, the average voltage at this point was used as the OCP. If this criteria was not satisfied after 240 s, the potential differences which gave rise to the lowest change were averaged and used as the OCP.

After determination, the OCP was set to zero volts and the following procedure was applied:

- 0 V for 120 s

- Measurement potential for 120 s
- 0 V for 600 s

The measurement potential was applied to the bottom ITO slide, with the top slide used as the counter/pseudo-reference electrode.

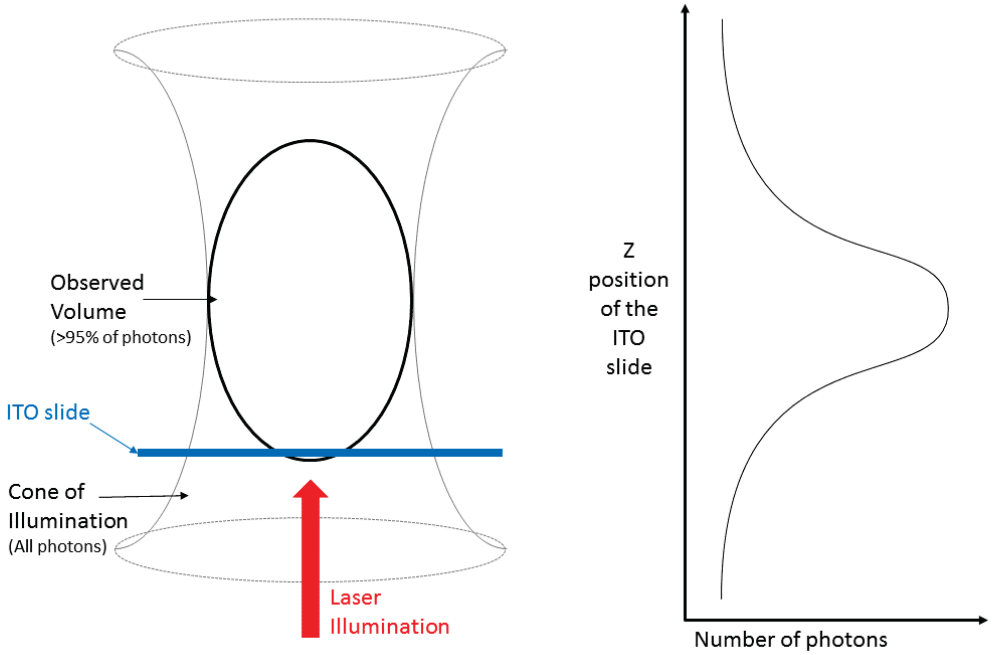

Figure 6.2: *Diagram of the electrochemical cell used for measurements on the confocal microscope.*

Distances from the electrode were determined through scattering of the red laser caused by the ITO slide. When the ITO slide is inside the main focal volume, there is an increase in the number of red photons observed from the focal volume. Shown in Figure 6.2, the number of observed photons changes with different z distances of the ITO slide. This was used to "zero" the focal volume to the distance at which the increase in counts was noticed. The height of the laser focal volume was previously determined to be 1.5 µm,[144] therefore the centre of the focal volume is approximately 0.75 µm above the stated distance.

As there is likely some ITO inside the observed volume at 0 µm, the closest measurement to the electrode was 1 µm higher in the z direction from the zero point. To investigate the behaviour of the dye at various distances, measurements were also performed at 10 µm, 25 µm, and 50 µm.

Considering the electrochemical stability of the dyes chosen, this was investigated by performing CV measurements of the neat ionic liquid, and comparing this to a CV of the ionic liquid with

the dye dissolved in a high concentration. These show that the dyes are both stable within the region of -2 V to +2 V, and are present in Appendix B.

Instrumentation

The lifetimes of dyes in electric fields were measured on a custom built confocal microscope using a sub-micrometre precision stage to position the sample in the laser beam. As the bottom slide is the working electrode, distance from the working electrode can be probed by moving the laser focal volume in the z direction i.e. up and down.

The sample was excited using a 466 nm pulsed diode laser (PicoQuant GmbH, PDL 800-B) operating at a frequency of 20 MHz and a power of 1.35 mW. Beam steering mirrors were used to control the laser beam direction and height and a dichroic mirror used to direct the beam into the objective. An infinity corrected, high numerical aperture microscope objective (Olympus 60x/1.2, water immersion) focuses the laser into a femtolitre volume within the sample. Fluorescence from the sample was collected by the same microscope objective, directed to the same dichroic mirror, then passed through an emission filter (z488lp, Chroma Technology Corp.) to remove any excitation photons. A plano-convex lens (+50.2 F, Newport Ltd.) focused the filtered light onto a 75 μm pinhole positioned on the confocal plane of the microscope objective. Another dichroic mirror (630dcxr, Chroma Technology Corp.) was then used to split the beam towards two avalanche photodiodes (AQR-141, EG&G, Perkin-Elmer). The light was further filtered by another emission filter (hq 540/80 m, Chroma Technology Corp.) and focused by a plano-convex lens (f=30.0, i.d. 25.4 mm, Thorlabs) onto the first avalanche photodiode (green detector, wavelengths of 500-580 nm). The second avalanche photodiode (red detector) was only used to determine the position of the ITO slide. The signal from the green detector was coupled to a multifunction DAQ device for data logging (PCI 6602, National Instruments) running on a Pentium PC, as well as to a time-correlated single-photon counting card (SPC-130 EM, Becker & Hickl GmbH) running on a separate Pentium PC.

The data was collected at 298 K, and the raw data was deconvoluted using the instrument response function (IRF), which was measured using a 15 μM solution of auramine O in distilled water. Auramine O has a lifetime of a few ps, therefore the IRF is dictated by the detector and has a FWHM of ≈0.9 ns.

Data Analysis

During the experiment, the data is all written as delay data, i.e. time between the excitation laser pulse being sent, and the emission laser pulse being received, to one continuous data file that was collected throughout the experiment. To monitor the evolution of the lifetime over the experiment, the data is split into 'bins', which are time-resolved sections of the data. Each bin was 30 seconds wide i.e. bin number 1 contains data from the time interval 0-30 seconds, bin number 2 contains data from 30-60 seconds etc. Therefore, each bin contains the delay data from within one relevant time period, and the fluorescence lifetime decay can be calculated by making a histogram of the delay data within one bin.

The fluorescence lifetime decays were analysed using a modified version of the JLife program written at Imperial College London by Joshua Edel and myself, with amplitudes and lifetimes loosely constrained to give positive, non-zero values. Goodness of fit was judged based upon χ^2 values, and all presented data are from fittings with χ^2 values of less than 1.2.

The fluorescence lifetime decay was treated as an n component exponential decay of the form shown in equation 6.1, and the IRF was fitted to the measured data using the sequential quadratic programming method with an error tolerance of 10^{-6}.

$$I(t) = bkg + IRF \circledast \sum_{i=1}^{n} \alpha_i \exp(-t/\tau_i) \tag{6.1}$$

where I is fluorescence intensity at time t, bkg is background counts, t is the time, α_i is amplitude of component i, IRF is the measured instrument response function, $\circledast$ denotes the convolution of the data to the IRF, and τ is lifetime of component i.

Measurements

From this analysis two quantities can be extracted. Firstly, the total number of photons collected per second can be calculated. Assuming the lifetime of the dye is constant, this gives an indication of any changes in the concentration of the rotor. Even if there is a change to the lifetime of the rotor, this can be seen using the second quantity (discussed below), and then accounted for. This will lead to a general notion behind the concentration change e.g. if the lifetime of the dye decreases, then the dye will emit fewer photons. Therefore, if the number of photons increases despite a decrease in the lifetime, an increase in the concentration can still be deduced.

The second quantity that can be extracted is the lifetime of the dye. This is generated by collecting one bin of data and histogramming all of the delay data within that bin. From this, the data can deconvoluted with the instrument response function (IRF), which is the response of the instrument to a zero lifetime dye. This is the quantity that allows for the investigation of the lifetime, and from the lifetime and pre-exponential factor, the contribution of this component to the overall decay (the yield) can be found from

$$yield = \frac{\tau_i \cdot \alpha_i}{\sum_{j=1}^{n} \tau_j \cdot \alpha_j} \tag{6.2}$$

where τ_i is the lifetime of component i, α_i is the pre-exponential factor of component i and the sum is the sum of τ and α of all components.[93]

6.2 Lifetime of Cy3 in $[C_4C_1im][NTf_2]$

6.2.1 Positive 2 V

Data here was collected by Azizi Nawawi, however all analysis was performed by myself.

Two different data sets were collected for the application of +2 V to Cy3 in $[C_4C_1im][NTf_2]$, one in September 2016, and another in June 2017. In the data set from September 2016, Cy3 was used at a concentration of 10 nM, whereas in the samples from June 2017 Cy3 was used at a concentration of 100 nM. These are both included as the discussion benefits from a comparison of different concentrations.

Another difference between these data is that the 10 nM samples were measured on an older TCSPC capture card (Timeharp 100) than described in the setup. There were some problems with this card in that one of the chips on the board would fail and require shorting before any measurements could be made. In November of 2016 this card failed completely and was replaced by the newer B&H capture card, which the 100 nM data was measured on.

Experiments were repeated 3 times, and usable data is presented below. During analysis it was found that the cells were not shorted before measurements, so some of the samples had very high OCP values. Any measurements which had OCP values of magnitude >250 mV, or whose current trace contained any features which indicated poor connections were discarded. The remaining traces are all displayed below.

1 μm

The initial interpretation of the results measured at 1 μm was that there was an increase in the lifetime of Cy3 from ≈ 0.85 ns to ≈ 1.1 ns. This was correlated to a 25 cP increase in the viscosity of the ionic liquid.[77] However, calculation of the number of emitted photons per second from the samples (Figures 6.3a - 6.3c) indicate that this is not the correct interpretation.

Upon application of the electric field, a clear decrease in the number of emitted photons is observed. This would not be the expected outcome if there were an increase in lifetime, which would lead to an increase in the number of photons being emitted (as less non-radiative decay leads to greater amounts of photons emitted).

The decrease in emitted photons indicates either: a decrease in the lifetime of the dye, a decrease in the concentration of the dye, or a decrease in the amount of fluorescing dye. The blank ionic

liquids were also measured at the same time as the dye samples; for the 10 nM samples the ionic liquid was measured at 10,000 counts per second, and for the 100 nM samples the ionic liquid was measured at 15,000 counts per second.

This means that in both samples, upon application of +2 V, the signal from the dye disappears completely and the only fluorescence is from the ionic liquid. This occurs very quickly upon application of the electric field, regardless of the concentration of dye used. Figures 6.3a - 6.3c show that the decrease in counts occurs within the first 5 seconds of the application of the field. During the application of the potential, the counts initially drop to slightly higher than the counts of the ionic liquid. There is a slight decrease in the counts during the application of the potential, which is especially noticeable in the 100 nM sample.

Similar to the application of the potential, upon removal of the potential there is a fast initial recovery of the counts. However this is much slower than the decrease, as after 10 minutes of 'recovery time', the counts have not increased to the initial level of counts. For example in the 100 nM concentration, only 50% of the original counts have recovered after 10 minutes of 0 V application.

These results suggest that upon application of a positive potential at the electrode, there is a change in the system which decreases the amount of fluorescing dye in the focal volume. No comments can be made about the lifetime of the dye, as there is not enough dye fluorescing in the focal volume.

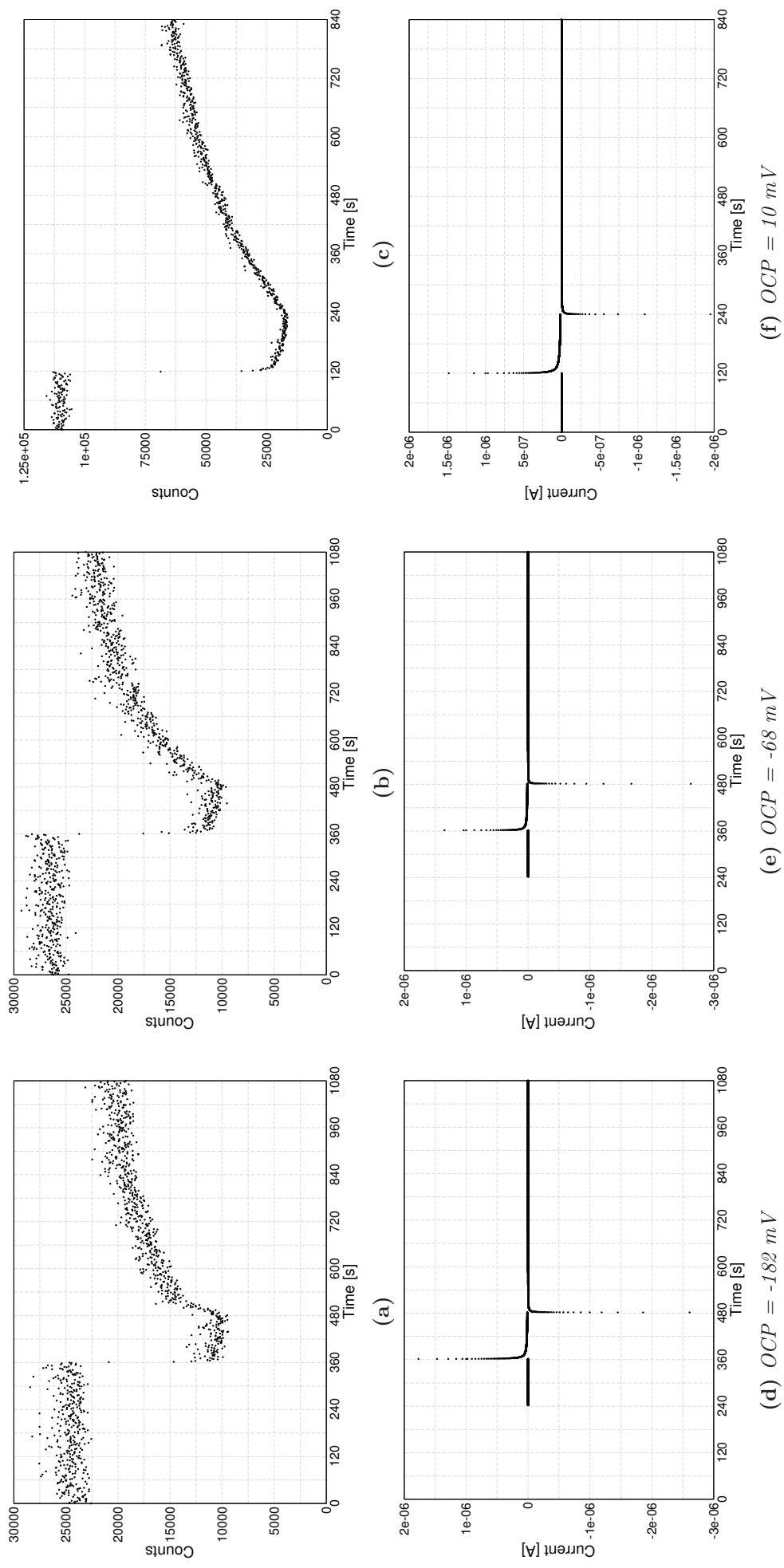

Figure 6.3: *(a) and (b): Counts per second at 1 µm from the electrode during the application of +2 V to a 10 nM solution of Cy3 in $[C_4C_1im][NTf_2]$. (c): Counts per second at 1 µm from the electrode during the application of +2 V to a 100 nM solution of Cy3 in $[C_4C_1im][NTf_2]$. (d) to (g): Current across the cell during the measurements in (a) to (c) respectively. OCP values are in the captions of the current graph.*

10 μm

As with the results recorded at 1 μm, the initial interpretation of the results at 10 μm was an increase in lifetime, and thus viscosity. The increase in lifetime was from ≈ 0.85 ns to ≈ 1.2 ns which corresponded to a 40-50 cP increase in viscosity.[77]

Looking at the emitted photons at this distance from the electrode (Figures 6.4a - 6.4c), a similar picture to that at 1 μm can be seen. Upon application of +2 V there is an almost immediate decrease in the number of emitted photons, down to just above the counts of the ionic liquid in both concentrations.

While the potential is applied the photon count remains low, and there is a slight decrease in the counts over the course of the potential application.

The recovery of the counts upon removal of the field is slightly slower at 10 μm than at 1μm. There is a slight increase upon removal of the potential, followed by a much more gradual recovery over time.

What is interesting is that this recovery is delayed slightly, even though the decrease of the counts occurs as soon as the potential is applied. This is only ≈ 5 seconds for the sample shown in Figure 6.4b, however this is around 30 seconds for the samples shown in Figures 6.4a and 6.4c. The latter is long beyond the point at which the current graphs show that the cell is fully discharged, indicating a disconnect between the current and fluorescence measurements.

As with the data recorded at 1 μm, information about the lifetime of the dye cannot be extracted from this data, as there are not enough photons which come from the dye to extract this information.

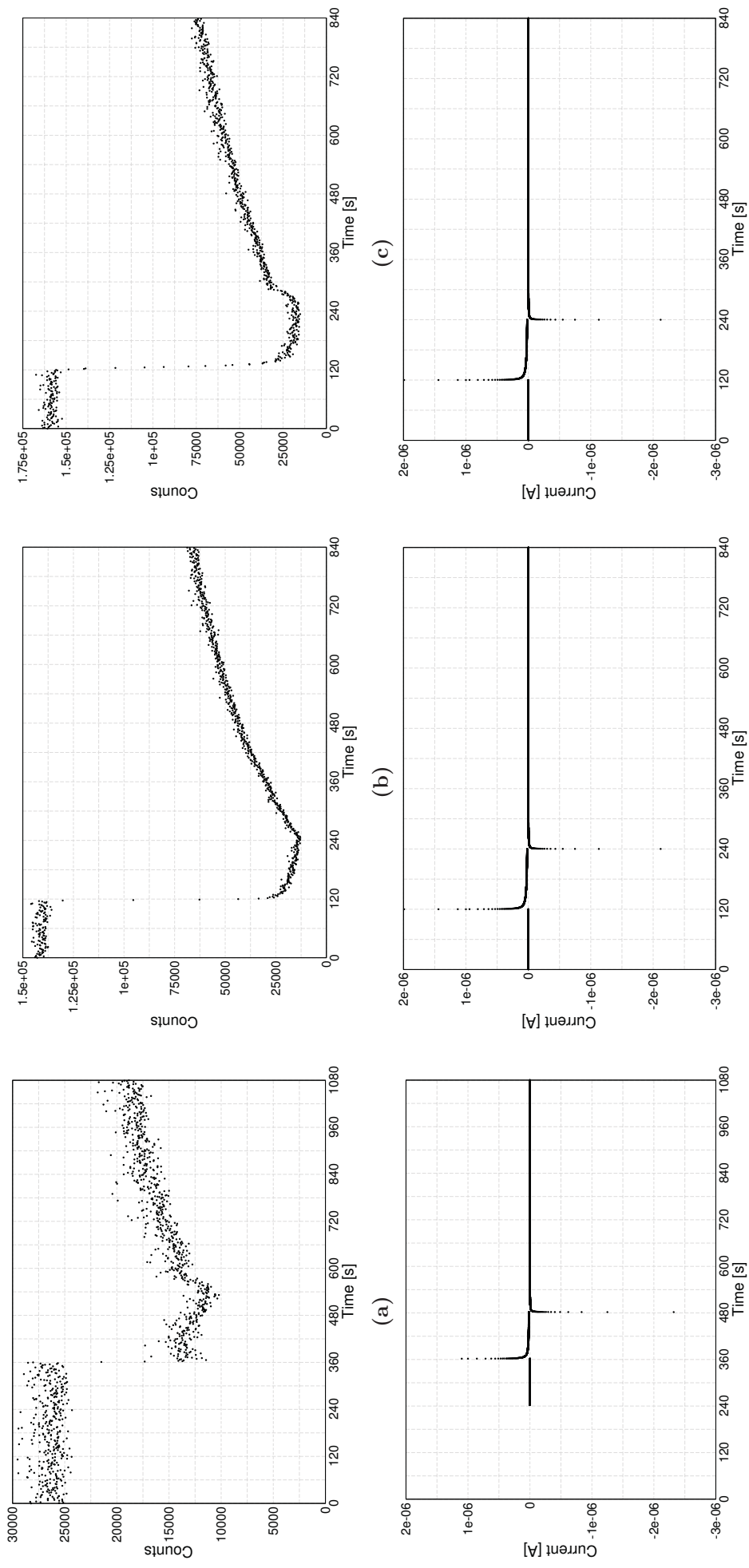

Figure 6.4: *(a): Counts per second at 10 µm from the electrode during the application of +2 V to a 10 nM solution of Cy3 in $[C_4C_1im][NTf_2]$. (b) and (c): Counts per second at 10 µm from the electrode during the application of +2 V to a 100 nM solution of Cy3 in $[C_4C_1im][NTf_2]$. (d) to (f): Current across the cell during the measurements in (a) to (c) respectively. OCP values are in the captions of the current graph.*

25 μm

At 25 μm, the lifetime of Cy3 increased from ≈ 0.85 ns to ≈ 1.4 ns which corresponded to a >60 cP increase in viscosity.[77] Calculations of the emitted photons again show that this was not the correct interpretation of the results, as upon application of the potential the signal drops to around the level of the blank ionic liquid (Figures 6.5a-6.5c).

At these distances from the electrodes, there is a greater delay between the application of the potential and the decrease in the counts. Whereas the previous distances showed an almost immediate decrease in the counts, at 25 μm it takes around 10-20 seconds for the signal to drop to close to the ionic liquid level of counts.

The counts also show a slight decrease during the application of the potential.

The recovery of the counts is very different for the different concentrations at 25 μm. For the 10 nM samples, there is a similar recovery to that of the 1 μm and 10 μm samples, however there is a much greater delay before the counts start to recover. One sample has a delay of nearly 2 minutes between removal of the potential and the counts beginning to recover (Figure 6.5a).

The 100 nM sample has a similar delay between the removal of potential and the beginning of the recovery of the counts as the 10 μm sample. However, the recovery is much slower at 25 μm, and after 10 minutes of 0 V application, the counts are much lower that those at 10 μm.

As with the other distances, no information about the lifetime of the dye can be gained due to the lack of fluorescing dye in the focal volume.

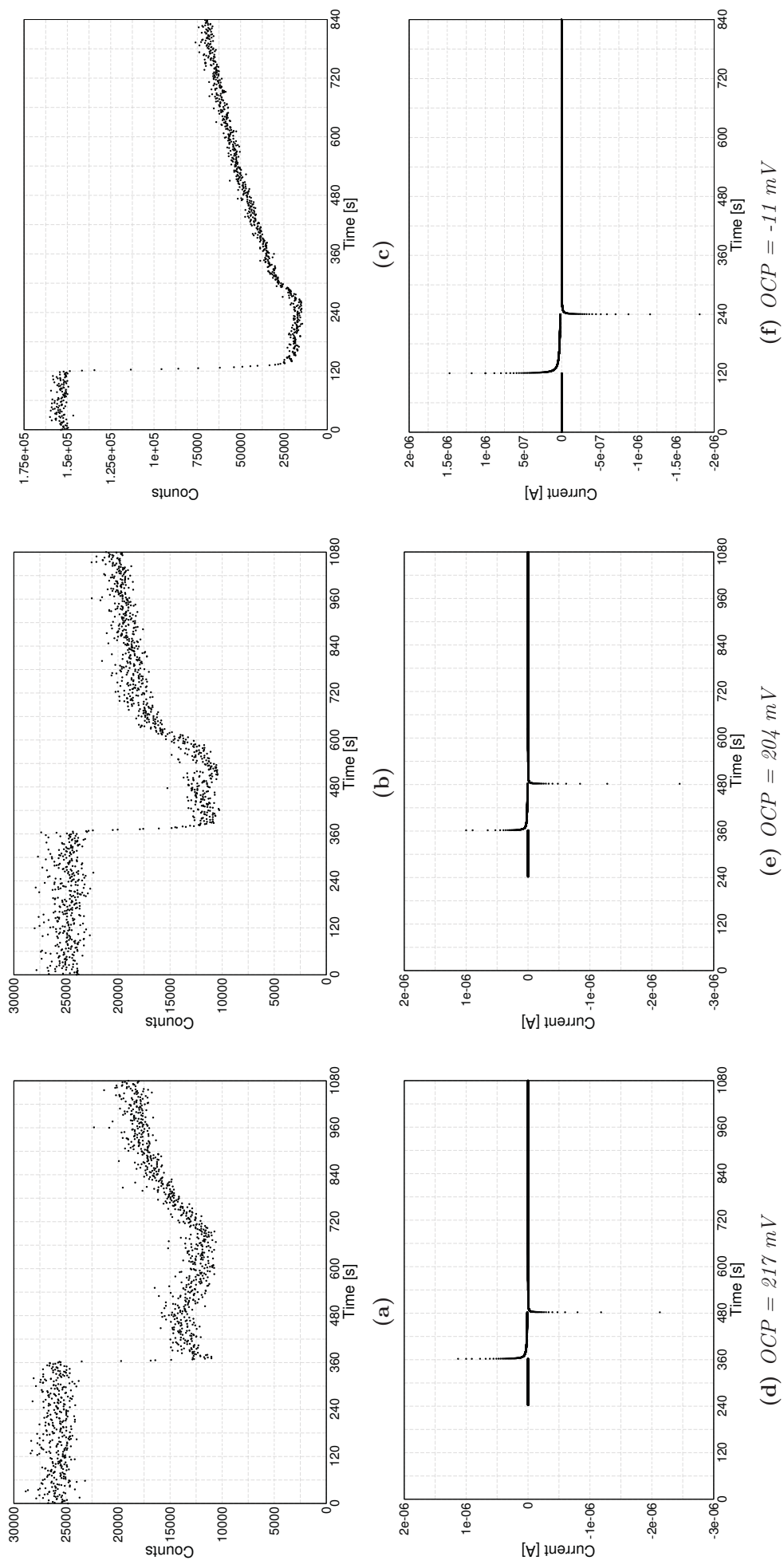

Figure 6.5: *(a) and (b): Counts per second at 25 µm from the electrode during the application of +2 V to a 10 nM solution of Cy3 in $[C_4C_1im][NTf_2]$. (c): Counts per second at 25 µm from the electrode during the application of +2 V to a 100 nM solution of Cy3 in $[C_4C_1im][NTf_2]$. (d) to (f): Current across the cell during the measurements in (a) to (c) respectively. OCP values are in the captions of the current graph.*

50 μm

At 50 μm, the previous interpretation was a small increase in lifetime from ≈ 0.85 ns to ≈ 0.90 ns which corresponded to a 5 cP increase in the viscosity.

The counts show that at this distance there are different behaviours for the 10 nM and the 100 nM samples. Using a concentration of 10 nM, the application of a +2 V potential causes a reduction of the counts to the level of the blank ionic liquid. In the 100 nM samples, while there is a decrease in the counts, the counts do not reach the level of the blank ionic liquid, which indicates there is fluorescing dye within the focal volume.

For the 10 nM samples the decrease in the counts begins almost immediately upon the application of the positive potential, however the counts do not reach the minimum until ≈ 30 seconds after the application of the potential.

Interestingly, the counts remain at their lowest for 120 seconds, the amount of time the potential is applied for. Due to the delay, this means that upon removal of potential, and apparently complete discharge of the cell (from the current traces) the counts remain low at 50 μm from the electrode.

After this delay however, the recovery of the counts seems to proceed in a similar manner to the rest of the samples, with an initial quick increase, followed by a steady climb over the rest of the experiment.

In the 100 nM samples, there is a different behaviour shown in the traces. The first is that the counts do not decrease to the level of the blank ionic liquid. There is a decrease in the counts at this distance, but this does not reach the counts of the ionic liquid.

The two 100 nM samples show different behaviours when it comes to the recovery of the counts. One sample has a steeper decrease in the counts upon application of the potential and a relatively short recovery time (≈ 10 seconds).

The other sample has a greater delay between application of the potential and decrease in the counts (≈ 20 seconds), and a much greater delay between the removal of the potential and the increase in the counts (≈ 240 seconds). This delay means that the counts continue to decrease after the potential was removed.

The cause of the difference between the two 100 nM samples is not entirely clear.

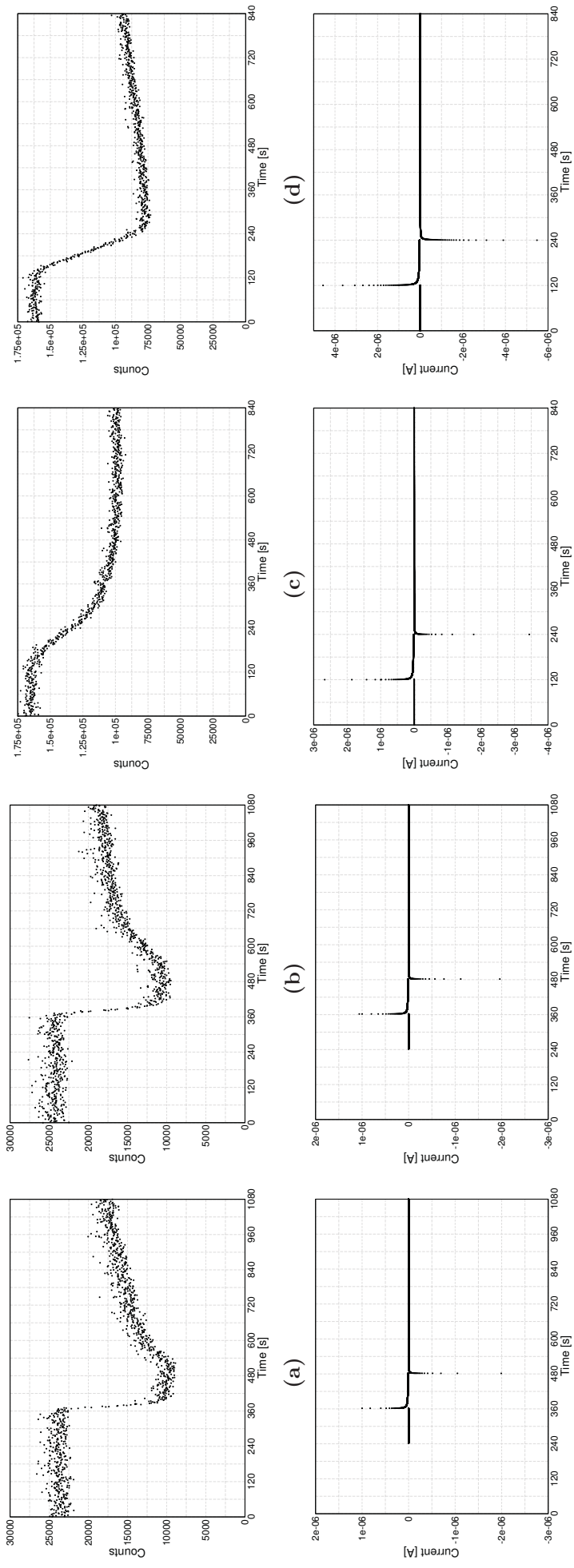

Figure 6.6: *(a) and (b): Counts per second at 50 µm from the electrode during the application of +2 V to a 10 nM solution of Cy3 in $[C_4C_1im][NTf_2]$. (c) and (d): Counts per second at 50 µm from the electrode during the application of +2 V to a 100 nM solution of Cy3 in $[C_4C_1im][NTf_2]$. (e) to (h): Current across the cell during the measurements in (a) to (d) respectively. OCP values are in the captions of the current graph.*

When considering the lifetime of the 100 nM samples, both of these follow a similar trend, indicating that the cause of the different levels of counts does not affect the lifetime of the dye. Calculation of the lifetime from the fluorescence lifetime decay shows that there are two components to the decay (shown in Figure 6.7). One is approximately 0.85 ns, consistent with the lifetime of Cy3 (Section 5.3.3 and Ref[77]), and the other < 0.1 ns, consistent with the short lifetime component seen in neat ionic liquids and the previous measurements of Cy3 (Section 5.3.3). Before the potential application, the Cy3 component contributes 99% of the photons to the decay, and the short lifetime component the remaining 1%.

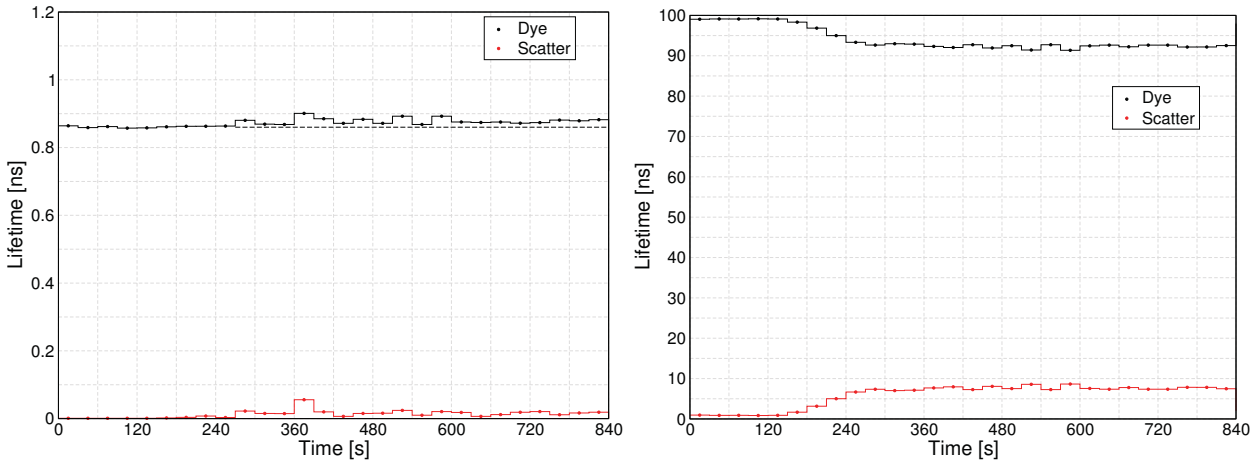

Figure 6.7: *Lifetime (left) and contribution (right) of the components of the fluorescence lifetime decay at 50 µm during application of +2 V to a 100 nM concentration of Cy3 in $[C_4C_1im][NTf_2]$. Dashed black line shows the average lifetime before the application of the electric field. Current graph for potential application is Figure 6.6g.*

Upon application of the potential, the contribution of Cy3 decreases gradually to $\approx 90\%$ at the point at which the counts are the lowest. From the pre-exponential factor, this change in the contributions arises from a reduction in the number of photons emitted by the dye.

Application of the potential increases the lifetime of the Cy3 component to 0.9 ns, even taking the decrease in the counts into account. Therefore the increase in lifetime of Cy3 is an effect of the electric field.

Interestingly, this change in the lifetime does not occur upon application of the electric field. Instead, there is a ≈ 150 second delay until the lifetime increases, and a ≈ 240 second delay until it reaches its maximum.

From the alkyl chain fit in Section 5.3.3, a 0.05 ns increase in lifetime corresponds to a 6 cP increase in the viscosity. This is only a small change, but it indicates that the lifetime of Cy3 could change at other distances. However, Cy3 is not the correct probe to investigate this.

Comparison

When comparing the +2 V results, a clear trend appears as to the onset and recovery of the counts where distances closer to the electrode decrease and recover counts quicker than distances further away. These are consistent between the concentrations, despite the magnitude of the effects being different.

Comparing the 10 nM samples (Figure 6.8), upon application of the potential the counts in the 1 and 10 µm samples decrease immediately to the background counts of the ionic liquid. The counts at 25 µm take slightly longer to decrease to the background of the ionic liquid. At 50 µm there also is a delay between potential application and the start of the decrease in counts, followed by a slower decrease in counts to the level of the blank ionic liquid. The recovery of the counts shows a similar trend where the closer distances to the electrodes increase first upon release of the potential.

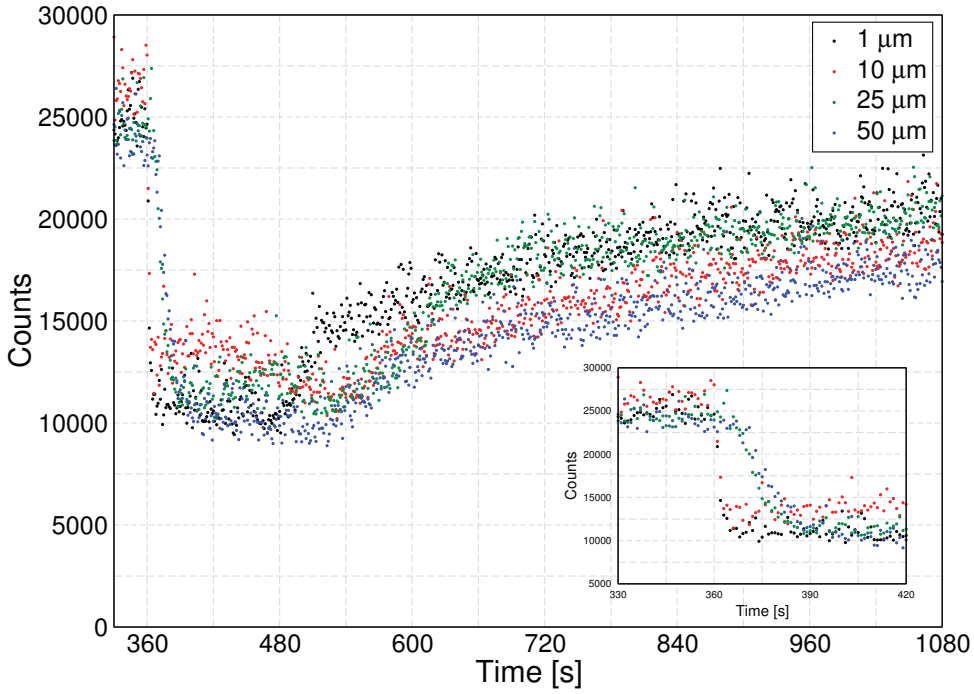

Figure 6.8: *Comparison of the changes to the counts at 1 µm, 10 µm, 25 µm, and 50 µm when applying +2 V to a 10 nM solution of Cy3 in $[C_4C_1im][NTf_2]$. Inset shows a close-up of the decrease in counts upon potential application.*

A similar trend is observed for the 100 nM samples (Figure 6.9) where the counts decrease immediately at 1 µm and 10 µm upon application of the potential. There is a slight delay between application of the potential and decrease of the counts at 25 µm, but within 10 seconds the counts decreased to the level of the background of the ionic liquid.

At 50 µm ,the counts decrease much slower than any other sample at +2 V, and do not de-

crease to the level of the blank ionic liquid. This means there is still fluorescing dye in the focal volume, allowing the lifetime of the dye to be extracted. Calculation of the lifetime of the dye shows a 0.05 ns increase in the lifetime, which can be correlated to a 6 cP increase in viscosity.

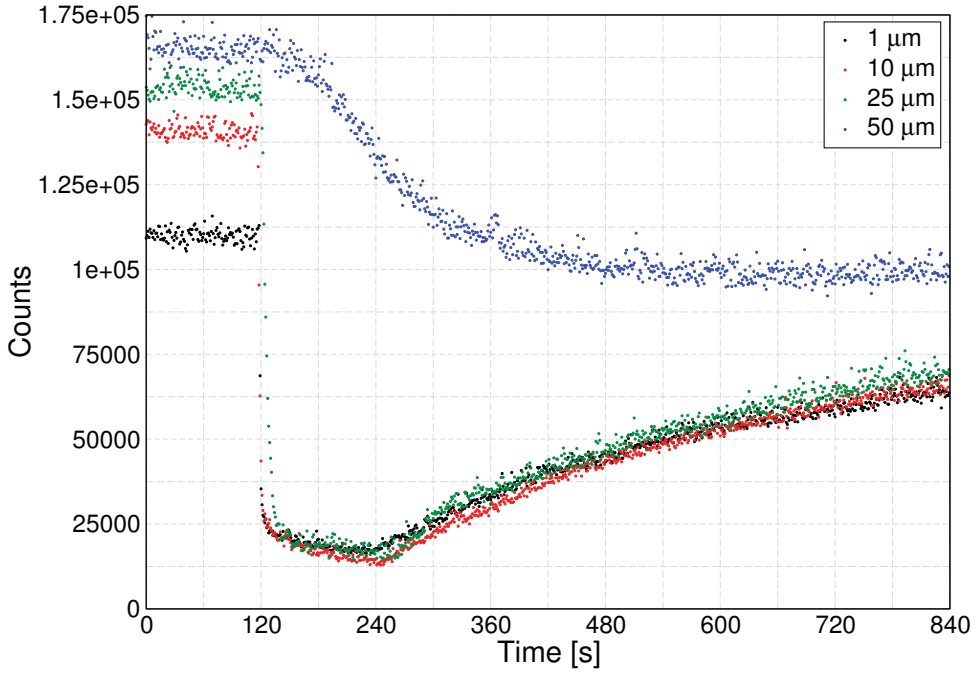

Figure 6.9: *Comparison of the changes to the counts at 1 µm, 10 µm, 25 µm, and 50 µm when applying +2 V to a 100 nM solution of Cy3 in $[C_4C_1im][NTf_2]$.*

This shows that a change in viscosity does occur at this distance from the electrode.

Combined, these results confirms the existence of the remarkably long range effects that were postulated previously from the work of Alastair and Azizi (Section 2.2.2), however these are of a different nature than first anticipated. Between 1-25 µm it is not possible to determine if +2 V causes any change in the viscosity of the ionic liquid as no dye is present to report on the viscosity. At 50 µm, with a 10 nM sample of Cy3, a similar depletion of the dye is observed. With 100 nM of dye however, a change in the lifetime and thus viscosity can be observed.

The measurements at 50 µm are especially interesting as they highlight a concentration dependence of the change in counts. To investigate a possible voltage dependence, measurements applying +1 V were also performed, but had not been analysed prior to this thesis.

6.2.2 Positive 1 V

Data here was collected by Azizi Nawawi in December 2016, however all analysis was performed by myself.

These results were only measured on the older Timeharp 100 card at 10 nM, and were not repeated with the newer card at a higher concentration.

1 μm

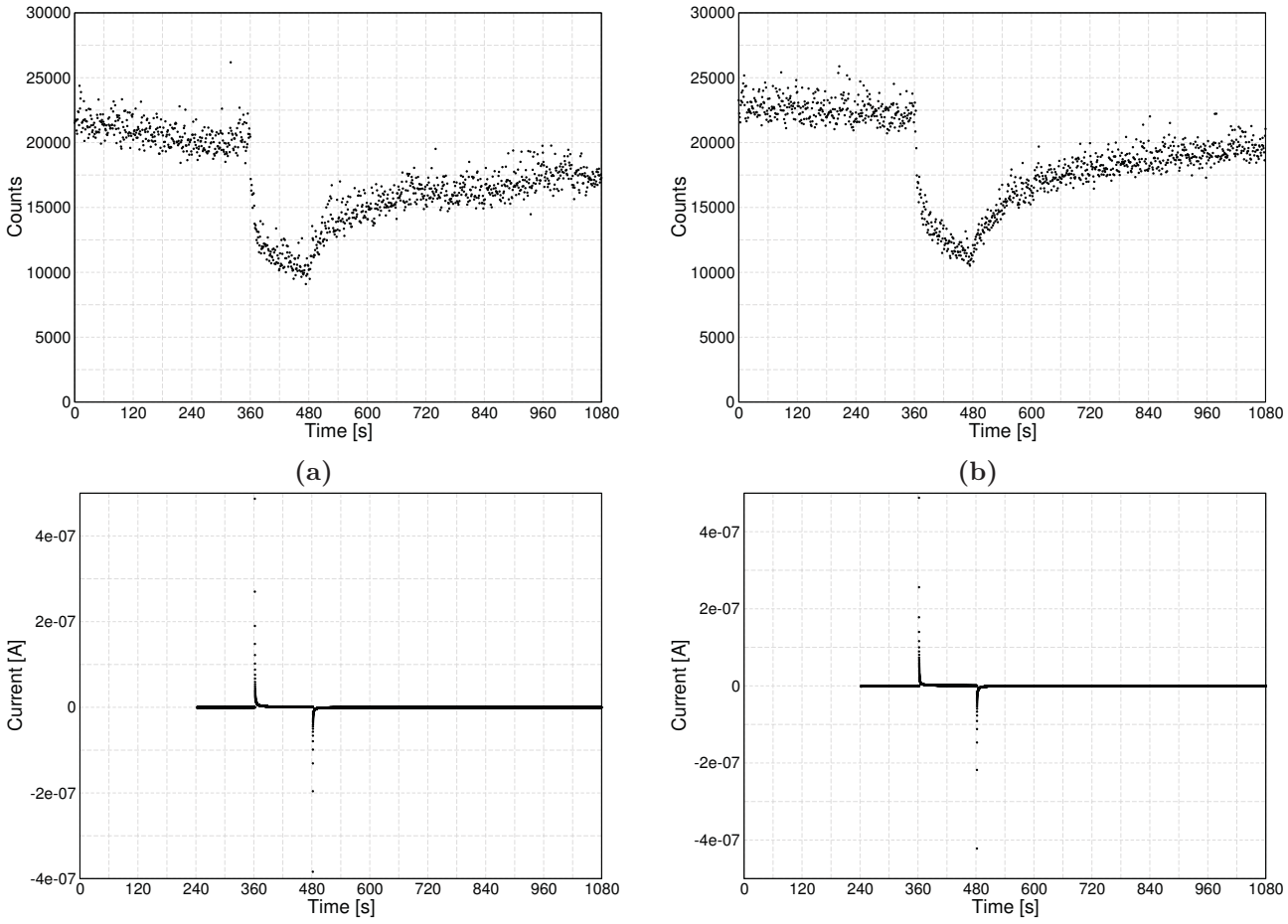

(a) **(b)**

(c) *OCP = 173 mV* **(d)** *OCP = 97 mV*

Figure 6.10: *(a) and (b): Counts per second collected at 1 μm from the electrode during the application of +1 V to a 10 nM solution of Cy3 in $[C_4C_1im][NTf_2]$. (c) and (d): Current across the cell during these measurements. OCP values are in the caption of the current graph.*

It is immediately obvious that at 1 μm, the same decrease in counts to the level of the blank ionic liquid is observed for +1 V as for +2 V.

There is a difference though, as rather than decreasing immediately to the level of the ionic liquid, the +1 V samples require much more time. There is a fast initial decrease of the counts by ≈25-40%, however the final reduction in the counts is much slower, not levelling out across the entire 120 seconds in which the potential is applied.

Upon the release of the potential, the recovery is similar to that of the +2 V sample (Figure 6.11). Both show an immediate commencing of the increase in counts upon removal of the potential, which increases at an approximately consistent rate over the recovery period.

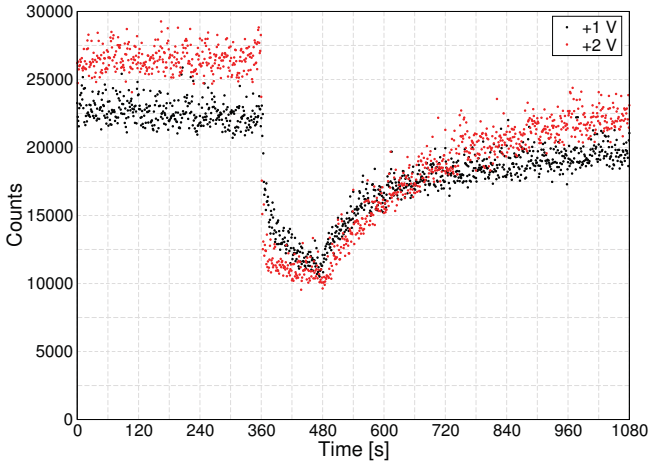

Figure 6.11: *Comparison of the changes in the counts at 1 μm from the electrode when applying +1 V or +2 V to a 10 nM solution of Cy3 in $[C_4C_1im][NTf_2]$.*

10 μm

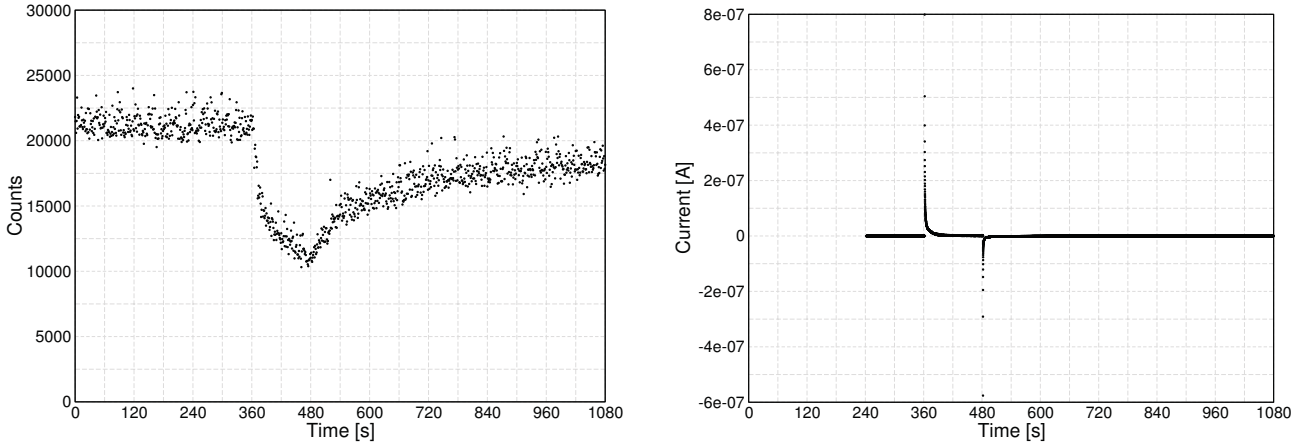

(a) **(b)** *OCP = 61 mV*

Figure 6.12: *(a): Counts per second collected at 10 μm from the electrode during the application of +1 V to a 10 nM solution of Cy3 in $[C_4C_1im][NTf_2]$. (b): Current across the cell during these measurements. OCP values are in the caption of the current graph.*

At 10 μm, there is a similar trend to that of the 1 μm where immediately upon application of the potential there is a rapid decrease in the number of counts. This levels out after 10 seconds and there is a slower decline towards the level of the ionic liquid background.

The recovery of the dye is similar to that of the +2 V samples (Figure 6.13). A slight delay is observed between the samples, but once the recovery begins, the increase proceeds at the same rate.

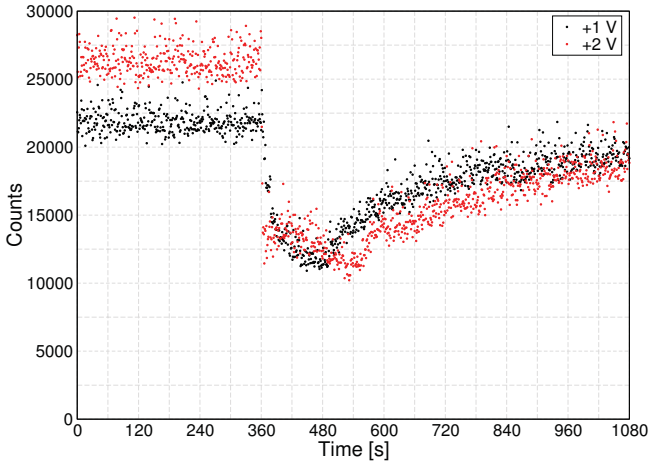

Figure 6.13: *Comparison of the changes in the counts at 10 µm from the electrode when applying +1 V or +2 V to a 10 nM solution of Cy3 in* $[C_4C_1im][NTf_2]$.

25 µm

At 25 µm, there is a major difference between the +1 V and the +2 V samples. While the decrease in the counts seems to begin shortly after a potential of +1 V is applied (Figures 6.14a and 6.14b), this is much slower than that of the +2 V samples. When applying +2 V, the sample at 25 µm decreases to the level of the blank ionic liquid counts within 20 seconds, the +1 V samples only drop by ≈30% over the course of the potential application.

Upon the removal of the potential, there is a very slow increase of the counts. This is much slower than at the distances closer to the electrode at +1 V, and also slower than that of the +2 V samples.

As there is still fluorescing dye within the focal volume, the fluorescence lifetime decay can be analysed. This is comprised of 3 components, one contributes 65% of the photons with a lifetime of ≈ 0.82 ns, thus is assigned to Cy3. Considering the other components, one has a short lifetime of < 0.2 ns and is assigned to scatter, and the other has a long lifetime >5 ns and is assigned to the ionic liquid.

Upon application of the electric field, there is a gradual decrease in the counts from the ionic liquid, thus an increase in the contribution from the background components. Interestingly, the decrease begins 30 seconds after the potential is applied, and the increase upon removal of the potential is similarly delayed by 30 seconds.

The lifetime of the dye remains relatively constant before the application of the potential. Upon application of the potential there is a gradual increase in the lifetime of the dye, up to a maximum of ≈ 0.87 ns, an increase of 0.05 ns. For these lifetimes, this corresponds to a 4 cP increase in the viscosity of the ionic liquid.

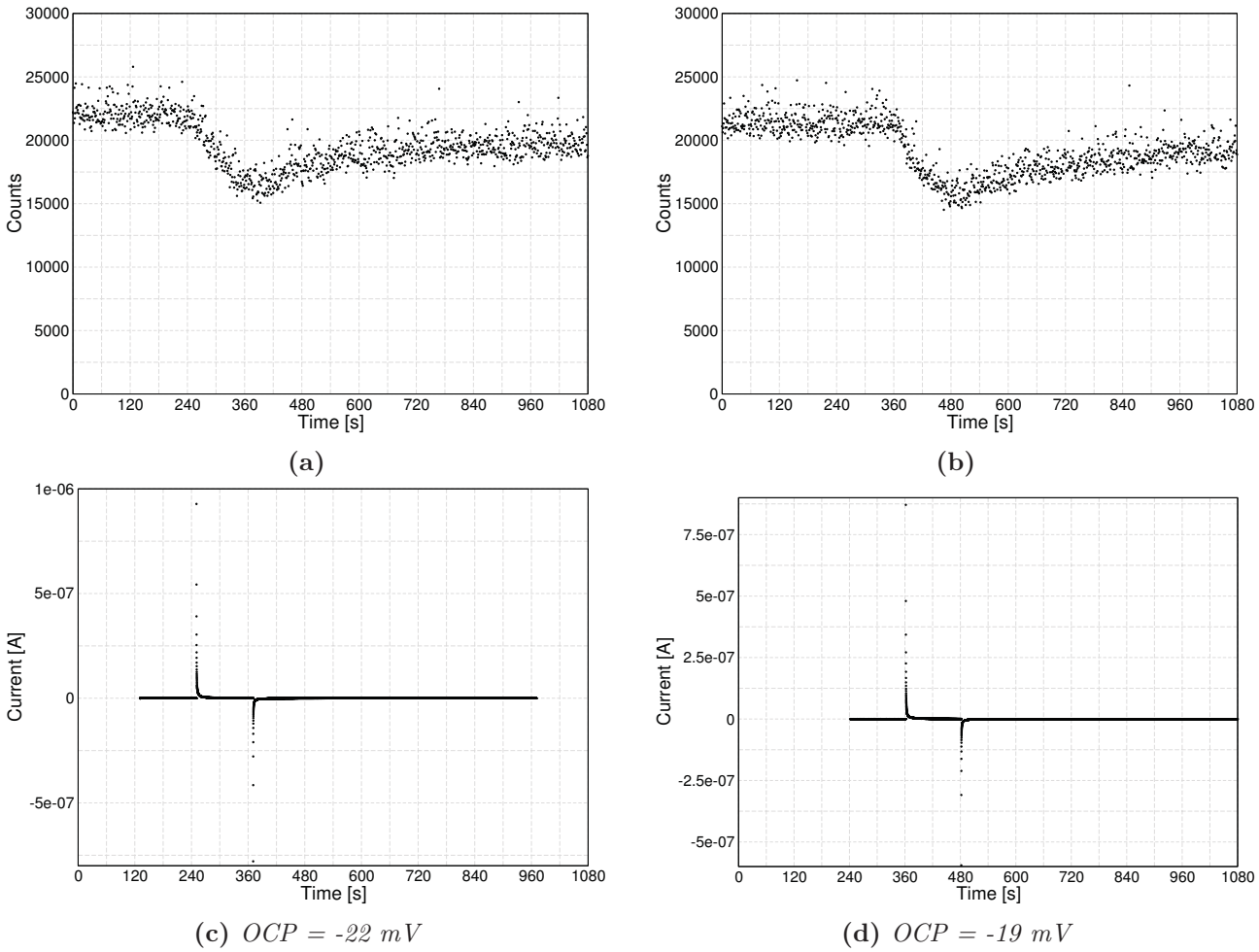

Figure 6.14: *(a) and (b): Counts per second collected at 25 µm from the electrode during the application of +1 V to a 10 nM solution of Cy3 in $[C_4C_1im][NTf_2]$. (c) and (d): Current across the cell during these measurements. OCP values are in the caption of the current graph.*

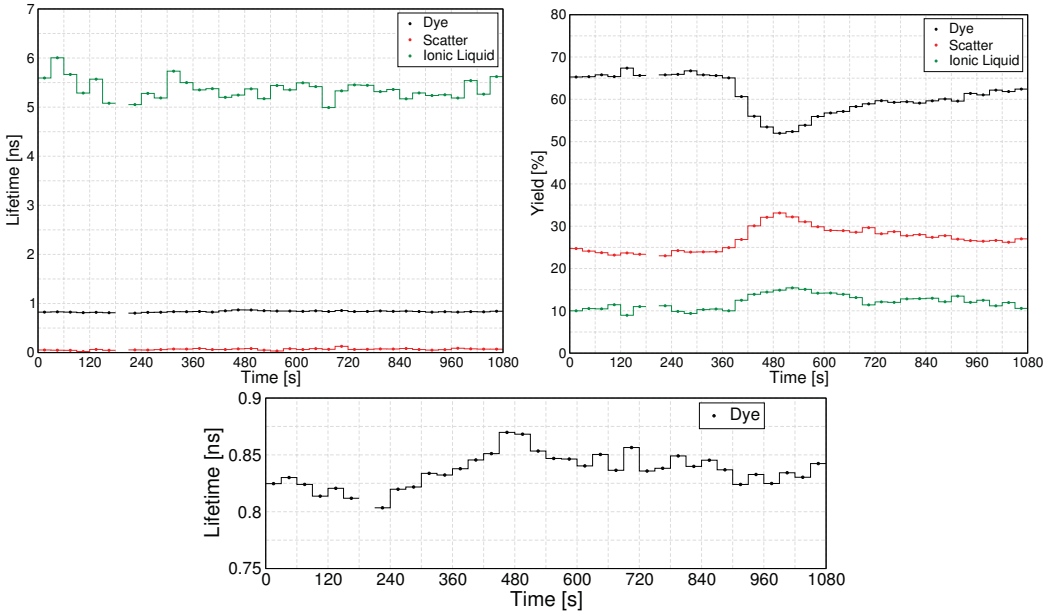

Figure 6.15: *Lifetime (top left) and contribution (top right) of all of the components in the fluorescence lifetime decay at 25 µm during application of +1 V to a 10 nM concentration of Cy3 in $[C_4C_1im][NTf_2]$. Lifetime of the dye (bottom) is shown separately. Current graph for potential application is Figure 6.14d.*

Upon removal of the potential, the lifetime of the dye steadily decreases towards the pre-potential value. However, it does not reach the pre-potential value, even 10 minutes after removal of the potential.

50 μm

When considering the sample at 50 μm, there is only a minor change in the counts during the application of +1 V (Figures 6.16a and 6.16b). There is a slight decrease, beginning ≈ 30 seconds after the application of the potential and decreasing very slowly. Upon removal of the potential, the decrease in the counts begins to slow, however there is a delay of ≈ 60 seconds before they level out. After this, there is a very slow increase in the counts over the rest of the experiment, although not back to pre-potential levels.

This means that the fluorescence lifetime decays can be analysed. This decay is composed of the same three components described for 25 μm, one for the dye at ≈ 0.8 ns, and two from the ionic liquid/scatter at ≈ 5 ns and ≈ 0.1 ns respectively.

Upon application of the potential there is a slight shift in the contributions, with the ionic liquid component slightly reducing its contribution to the overall decay. This decrease begins 30 seconds after application of the potential, in line with the change in the overall counts. The increase in the counts of the ionic liquid after removal of the potential has a 90 second delay after removal of the potential; a disconnect to the overall count trend.

For the lifetime of the dye, there is a possible slight increase in the lifetime of 0.03 ns to 0.83 ns, however this data is too noisy to determine if this is the case or not.

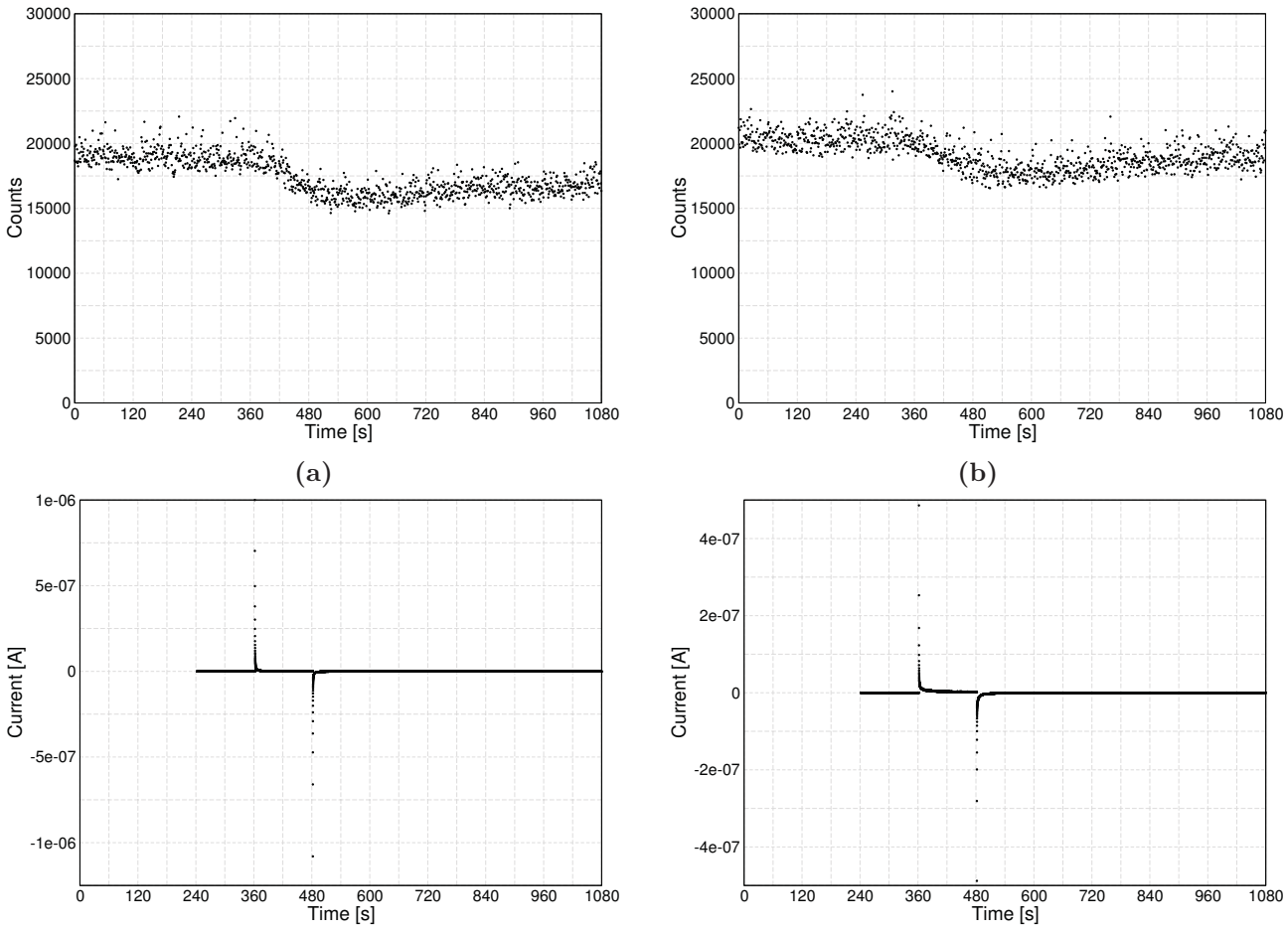

(a) (b)

(c) *OCP = 180 mV* (d) *OCP = 52 mV*

Figure 6.16: *(a) and (b): Counts per second collected at 50 µm from the electrode during the application of +1 V to a 10 nM solution of Cy3 in $[C_4C_1im][NTf_2]$. (c) and (d): Current across the cell during these measurements. OCP values are in the caption of the current graph.*

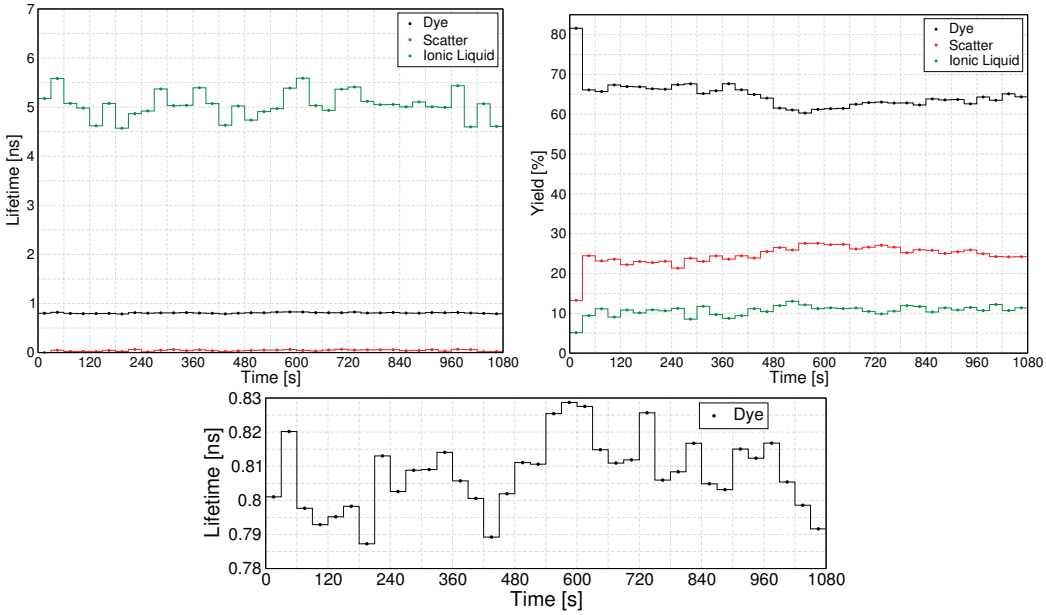

Figure 6.17: *Lifetime (top left) and contribution (top right) of all of the components in the fluorescence lifetime decay at 50 µm during application of +1 V to a 10 nM concentration of Cy3 in $[C_4C_1im][NTf_2]$. Lifetime of the dye (bottom) is shown separately. Current graph for potential application is Figure 6.16d.*

Comparison

Comparing the change in the counts of 10 nM samples upon application of +1 V in Figure 6.18, there is a clear trend between the different distances. Upon application of the potential, there is first a decrease in the counts at 1 µm, followed by 10 µm, then 25 µm and 50 µm. However the longer scale recovery is very similar.

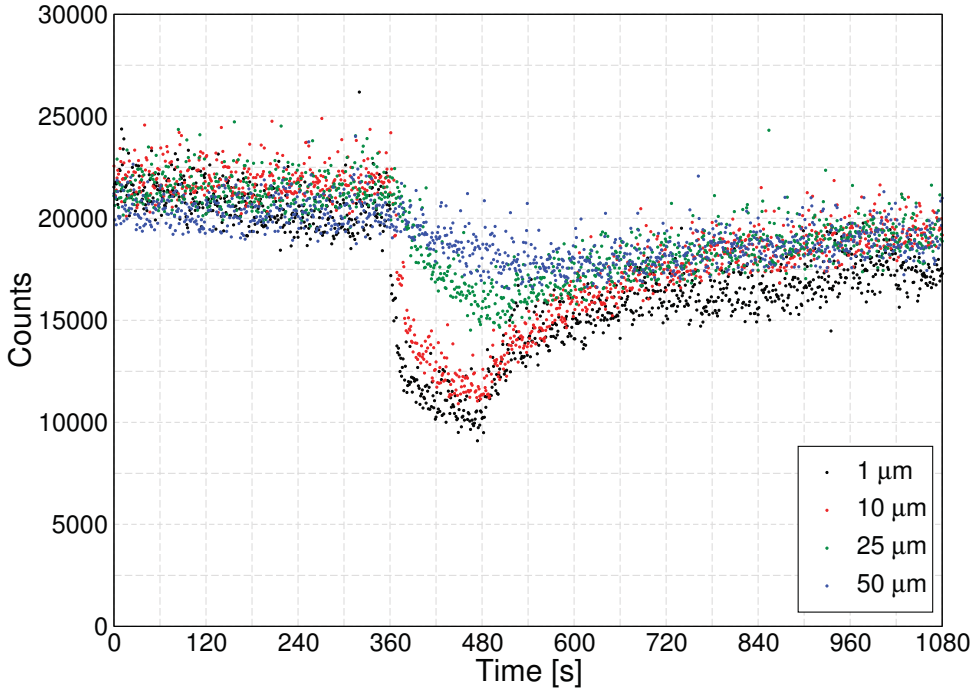

Figure 6.18: *Comparison of the changes to the counts at 1 µm, 10 µm, 25 µm, and 50 µm when applying +1 V to a 10 nM solution of Cy3 in* $[C_4C_1im][NTf_2]$.

The measurements at 25 µm and 50 µm contain fluorescing dye throughout the experiment so the lifetime of the dye can be extracted from the fluorescence lifetime decay. This shows that the at 25 µm, upon application of the potential there is a steady increase in the dye lifetime. This corresponds to an increase in the viscosity of the ionic liquid up to a maximum of 4 cP. At 50 µm the lifetime of the dye can also be found from the fluorescence lifetime decay, and this data suggests a 0.03 ns increase in the lifetime of the dye. However this data is too noisy to determine if this is a true result or not.

Combined, these positive potential results show that upon application of the positive potential to an electrode has effects far into the bulk of the ionic liquid. A discussion of a hypothesis as to why these decreases in the counts occur for Cy3 in positive potentials can be found in Section 6.4.1.

6.2.3 Negative 2 V

Data here was collected by Azizi Nawawi in December 2016, however all analysis was performed by myself.

1 μm

Looking at the counts collected at 1 μm upon application of -2 V to a 10 nM sample of Cy3 in $[C_4C_1im][NTf_2]$ (Figure 6.20a), there is a large increase in the counts upon application of the potential. This reaches a maximum quickly after the potential is applied, and then gradually decreases during the potential application. Upon removal of the potential there is a sharp decrease in the counts, followed by a more gradual decrease over the remaining experiment.
As the counts do not decrease to the level of the blank ionic liquid, the fluorescence lifetime decay can be found and deconvoluted into individual components. Over the entire experiment, there are 3 components in the decay (Figures 6.20c and 6.20d). One component has a lifetime of ≈0.92 ns, another has a lifetime of ≈0.1 ns, and another has a lifetime of ≈5 ns. Given the assignments in Section 5.3.3, the component with a lifetime of ≈0.92 ns is assigned to the rotor, and the latter two to scatter and the ionic liquid respectively.
Considering the large change in the counts, Figures 6.20d and 6.20e show that this is not due to an increase in the signal from the dye. Indeed the pre-exponential factor indicates that, if anything, the signal from the dye actually decreases. Instead, this large increase in the counts seems to be attributed to an increase in the contribution from the long lifetime component assigned to the ionic liquid. The change in the counts appears to almost perfectly follow the change to the pre-exponential factor of this long lifetime component (Figure 6.20e).
This lifetime is certainly far too long to be associated to Cy3 as the maximum lifetime of Cy3, i.e. the lifetime of Cy3 when the dye undergoes exclusively radiative decay, is <3 ns.[95] Therefore this seems to be directly showing a change in the ionic liquid, without the need to indirectly infer a result from changes to the lifetime of Cy3. This does seem to be a real result, as the scatter component remains relatively constant throughout, therefore can be used as a 'pseudo-normalising' component.
Unfortunately, the origin of this component is not known. Experiments from Paul, Samanta, and Mandal did look into an assignment of components present in the fluorescence lifetime decay of neat ionic liquids.[141–143] They reported that a component similar to this one could be assigned to 'associated structures' in the ionic liquid, although the nature of these could not be determined. These were hypothesised to be related to some kind of ion-ion interactions,

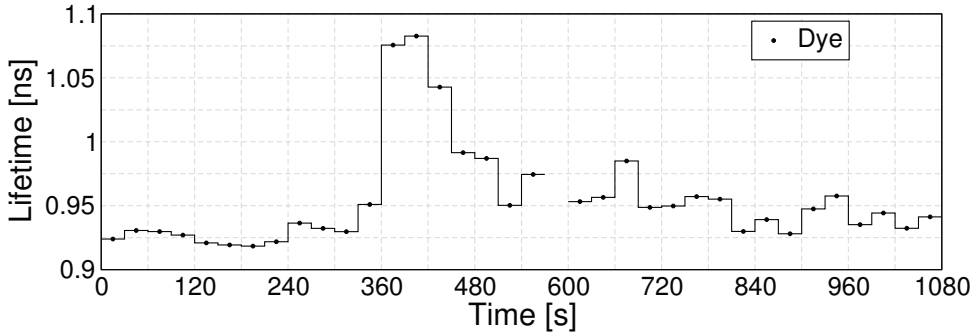

Figure 6.19: *Lifetime of Cy3 at 1 μm from the electrode during the application of -2 V to a 10 nM solution of Cy3 in $[C_4C_1im][NTf_2]$.*

though this could not be confirmed. If the physical cause of this component could be determined through a more rigorous study, then these results could be better interpreted.

Considering only the component associated with Cy3, the lifetime of this component is shown in Figure 6.19.

The lifetime of Cy3 in these experiments does increase dramatically from ≈0.925 ns before the application of the potential, to 1.075 ns immediately after the potential is applied. This decreases during the potential application down to ≈0.99 ns. Both of these represent a significantly large increase in the lifetime of Cy3. After removal of the potential, there is a steady decrease in the lifetime towards the pre-potential value, although this is not reached after 10 minutes of holding the potential at 0 V.

In terms of the viscosity, assuming that the trend seen between the ionic liquids $[C_nC_1im][NTf_2]$ (n = 2, 3, 4, 6 or 8) is followed (Equation 5.13), the initial increase in the lifetime from 0.925 ns to 1.075 ns corresponds to a 22.9 cP increase in the viscosity. The viscosity difference between a lifetime of 0.99 ns and the initial 0.925 ns corresponds to a 9.5 cP increase in the viscosity.

The magnitude of this increase does raise some concerns. As there are large changes to the lifetime and pre-exponential factors of the components in a relatively short period of time (1 histogram bin), there is a possibility that the components have not been deconvoluted correctly. These results definitely show that something is happening, however in order to confirm the change in the lifetime of the dye and the contribution of the ionic liquid component, more experiments need to be performed. This would involve repeating the same measurements on a more concentrated sample of Cy3, to minimise any impact of the ionic liquid components in order to confirm if the change in lifetime is this large. An experiment should also be performed looking at the blank ionic liquids upon application of a potential of -2 V to confirm if this component increase does indeed come from the ionic liquid.

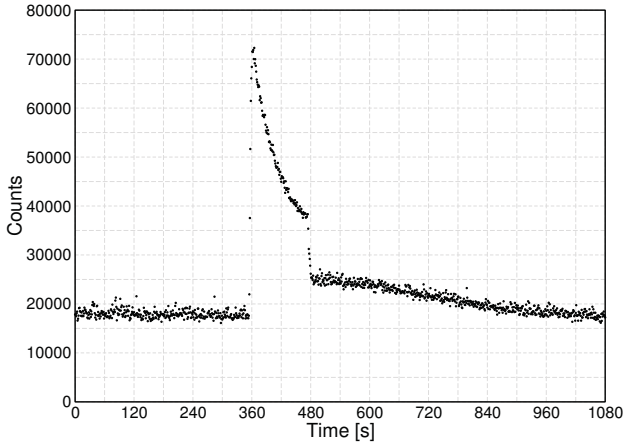

(a) *Counts collected at 1 µm from the electrode during the application of -2 V to a 10 nM sample of Cy3 in* $[C_4C_1im][NTf_2]$.

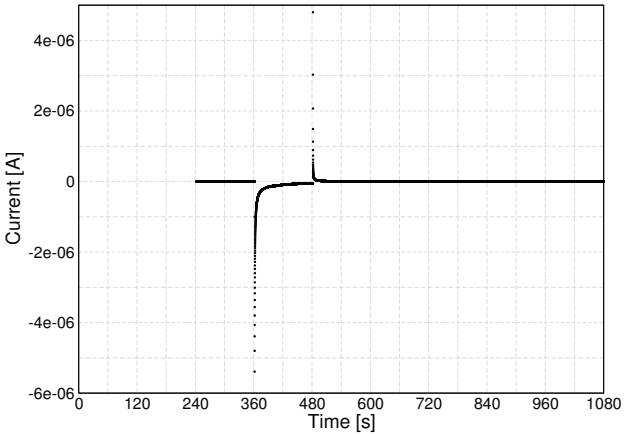

(b) *Current measured across the cell during the measurement of Cy3 at 1 µm from the electrode during the application of -2 V to a 10 nM sample of Cy3 in* $[C_4C_1im][NTf_2]$. *The OCP across the cell before the measurement was 19 mV*

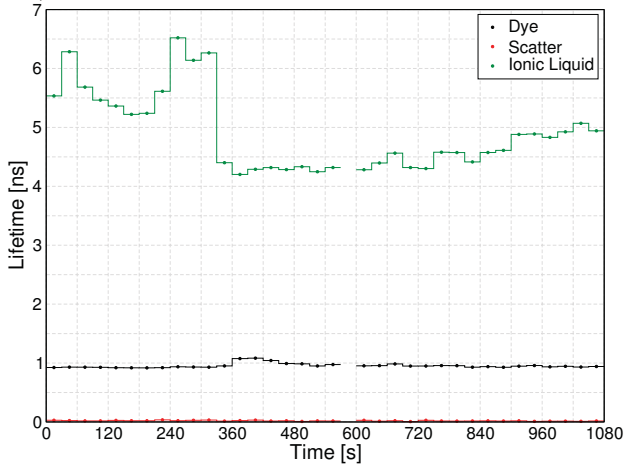

(c) *Lifetime of all of the components in the fluorescence decay at 1 µm from the electrode during the application of -2 V to a 10 nM sample of Cy3 in* $[C_4C_1im][NTf_2]$.

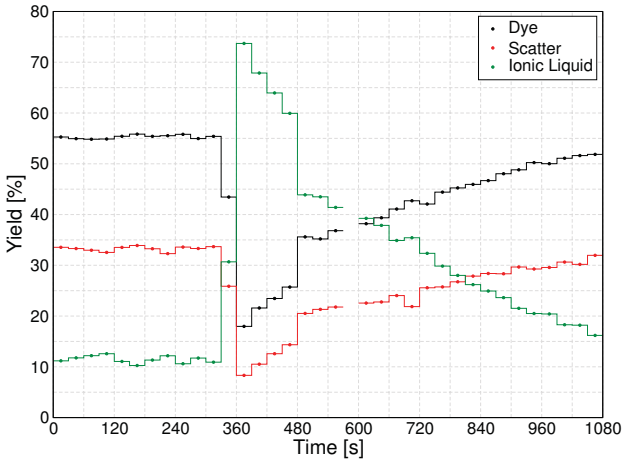

(d) *Contribution (yield) of all of the components within the fluorescence lifetime decay measured at 1 µm from the electrode during the application of -2 V to a 10 nM sample of Cy3 in* $[C_4C_1im][NTf_2]$.

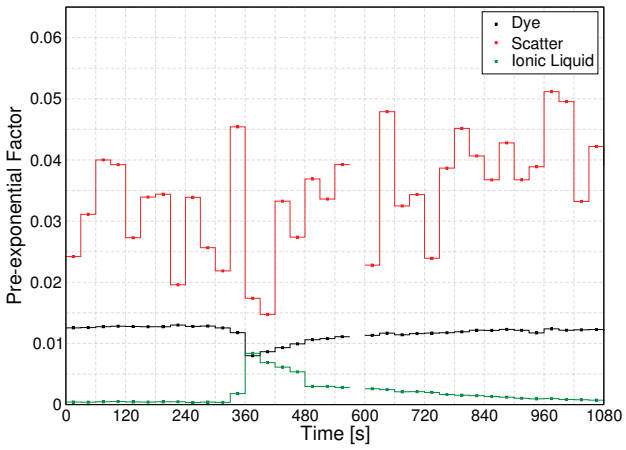

(e) *Pre-exponential factor of all of the components within the fluorescence lifetime decay measured at 1 µm from the electrode during the application of -2 V to a 10 nM sample of Cy3 in* $[C_4C_1im][NTf_2]$.

Figure 6.20: *Results from the fluorescence lifetime decay analysis of data collected at 1 µm from the electrode during the application of -2 V to a 10 nM solution of Cy3 in* $[C_4C_1im][NTf_2]$.

10 μm

The results 10 μm from the electrode upon the application of -2 V to a 10 nm solution of Cy3 in $[C_4C_1im][NTf_2]$ are similar to those at 1 μm, although of a lesser magnitude.

Considering the counts collected, there is a large increase in the counts reaching a maximum very quickly after the application of the potential. After reaching this maximum, there is a gradual decrease while the potential is being held. Upon removal of the potential there is an initial quick decrease, followed by a more gradual decrease over the remaining experiment.

Again, as the counts do not decrease to the level of the blank ionic liquids, the fluorescence lifetime decays can be found and the components calculated. These show the same 3 components as before, one with a lifetime of ≈0.92 ns which is assigned to Cy3, one with a lifetime of ≈0.1 ns which is assigned to scatter, and one with a lifetime of ≈5 ns which is assigned to the ionic liquid.

As with the counts at 1 μm, the change in the counts seem to be related entirely to a change to the long lifetime ionic liquid component, with the Cy3 components pre-exponential factor decreasing and the scatter component remaining approximately the same. As the nature of this component is not known, these results cannot be well interpreted.

The lifetime of the component which was associated with the Cy3 is shown in Figure 6.21.

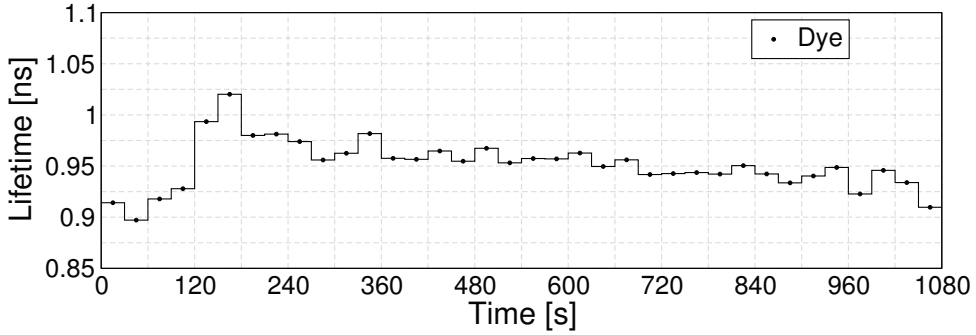

Figure 6.21: *Lifetime of Cy3 at 10 μm from the electrode during the application of -2 V to a 10 nM solution of Cy3 in $[C_4C_1im][NTf_2]$.*

The lifetime of Cy3 also increases 10 μm away from the electrode upon application of the potential. This increases from 0.925 ns pre-potential to 1.025 ns shortly after application of the potential, which then decreases to 0.975 ns when the potential is held. Upon removal of the potential there is no immediate decrease in the lifetime, instead there is a gradual decrease over the remaining time in the experiment.

Using the trend between the ionic liquids $[C_nC_1im][NTf_2]$ (n = 2, 3, 4, 6 or 8), Equation 5.13, the initial increase in lifetime from 0.925 ns to 1.025 ns corresponds to a 14.9 cP increase in

viscosity. The viscosity difference between the initial lifetime of 0.925 ns and the final lifetime during the potential application of 0.975 ns corresponds to a 7.2 cP increase in viscosity.
As with the results at 1 µm, the magnitude and speed of the changes raise concerns as to whether the components have been correctly deconvoluted. Therefore additional experiments are needed to confirm these results.

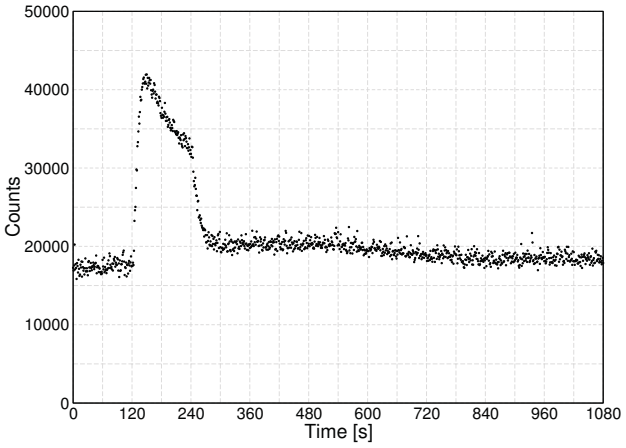

(a) *Counts collected at 10 µm from the electrode during the application of -2 V to a 10 nM sample of Cy3 in $[C_4C_1im][NTf_2]$.*

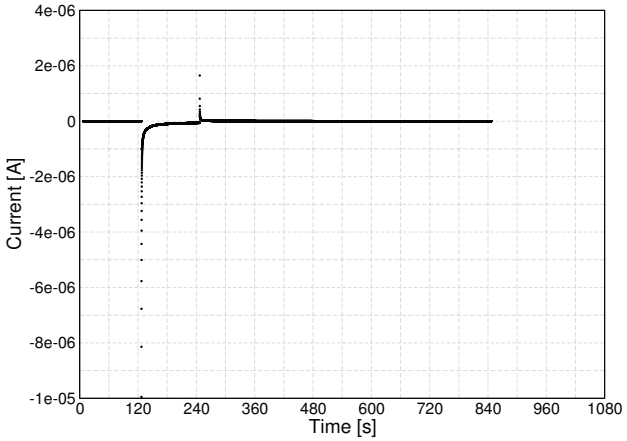

(b) *Current measured across the cell during the measurement of Cy3 at 10 µm from the electrode during the application of -2 V to a 10 nM sample of Cy3 in $[C_4C_1im][NTf_2]$. The OCP across the cell before the measurement was 11 mV*

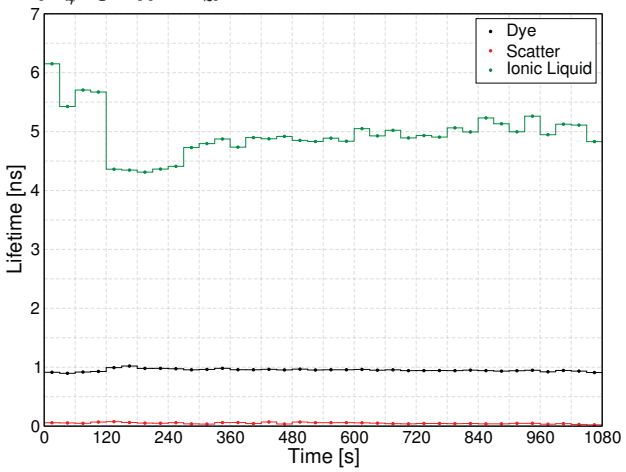

(c) *Lifetime of all of the components in the fluorescence decay at 10 µm from the electrode during the application of -2 V to a 10 nM sample of Cy3 in $[C_4C_1im][NTf_2]$.*

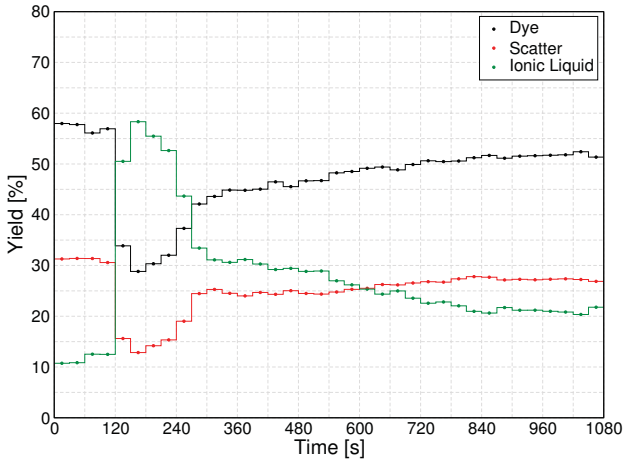

(d) *Contribution (yield) of all of the components within the fluorescence lifetime decay measured at 1 µm from the electrode during the application of -2 V to a 10 nM sample of Cy3 in $[C_4C_1im][NTf_2]$.*

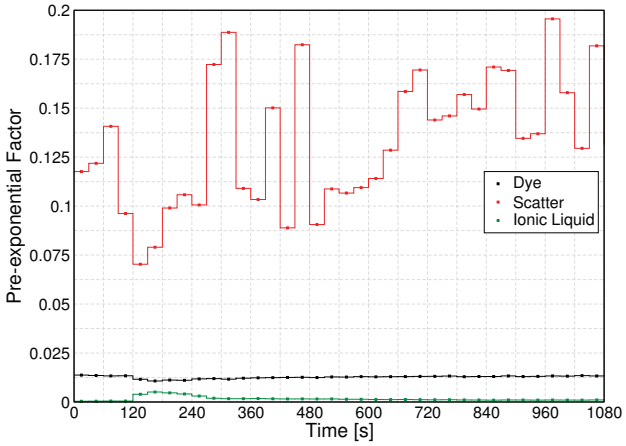

(e) *Pre-exponential factor of all of the components within the fluorescence lifetime decay measured at 10 µm from the electrode during the application of -2 V to a 10 nM sample of Cy3 in $[C_4C_1im][NTf_2]$.*

Figure 6.22: *Results from the fluorescence lifetime decay analysis of data collected at 10 µm from the electrode during the application of -2 V to a 10 nM solution of Cy3 in $[C_4C_1im][NTf_2]$.*

25 μm

The counts 25 μm from an electrode upon application of -2 V to a 10 nM solution of Cy3 in $[C_4C_1im][NTf_2]$ also show an increase in the counts, as at 1 μm and 10 μm, but this is less dramatic than at the closer distances.

Upon application of the potential, there is a steady increase in the counts over the first 60 seconds, and a steady decrease over the second 60 seconds. Upon removal of the potential there is also a steady decrease in the counts.

As the counts do not decrease, the fluorescence lifetime decay can be found and the components present calculated. These are a similar three components as before, one with a lifetime of ≈0.85 ns which is assigned to Cy3, one with a lifetime of ≈0.1 ns which is assigned to scatter, and one with a lifetime of ≈5 ns which is assigned to the ionic liquid.

As the change in counts is lower than before, there is not as great a change in the pre-exponential factors. However it does seem that this increase in counts can still be attributed to an increase in the contribution of the ionic liquid component.

The lifetime of the component associated to Cy3 is shown in Figure 6.23.

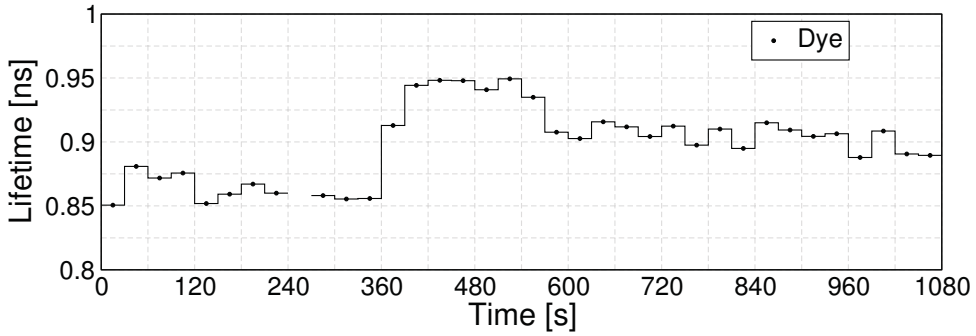

Figure 6.23: *Lifetime of Cy3 at 25 μm from the electrode during the application of -2 V to a 10 nM solution of Cy3 in $[C_4C_1im][NTf_2]$.*

This lifetime does increase upon the application of the potential, and this is more consistent that that at 1 μm and 10 μm. The pre-potential lifetime is lower in this measurement than the ones at the other distances, and the reason for this is unknown.

Before the potential is applied, the lifetime of the component attributed to Cy3 is ≈0.85 ns, and upon application of the potential this increases to ≈ 0.95 ns. This component remains at this lifetime for 60 seconds after the removal of the potential, then gradually decreases towards the pre-potential value.

Using the trend between the ionic liquids $[C_nC_1im][NTf_2]$ (n = 2, 3, 4, 6 or 8), Equation 5.13, the initial increase in lifetime from 0.85 ns to 0.95 ns corresponds to a 13.7 cP increase in

viscosity.

While the final lifetime is lower than the closer distances, the lower starting value leads to a greater increase in the viscosity at the point at which the potential is removed. To investigate if the viscosity should increase by as much as it does in the this experiment, this measurement should be repeated.

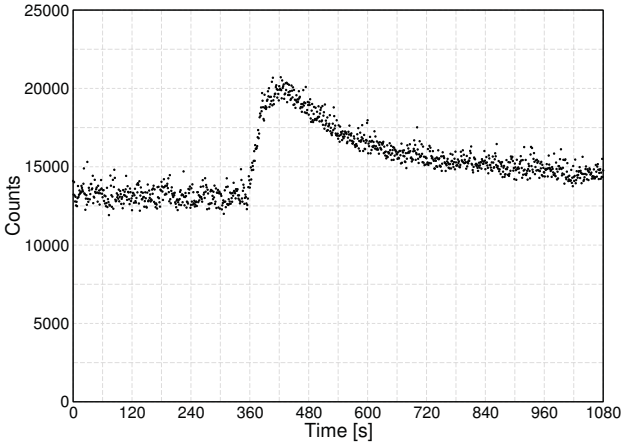

(a) *Counts collected at 25 µm from the electrode during the application of -2 V to a 10 nM sample of Cy3 in $[C_4C_1im][NTf_2]$.*

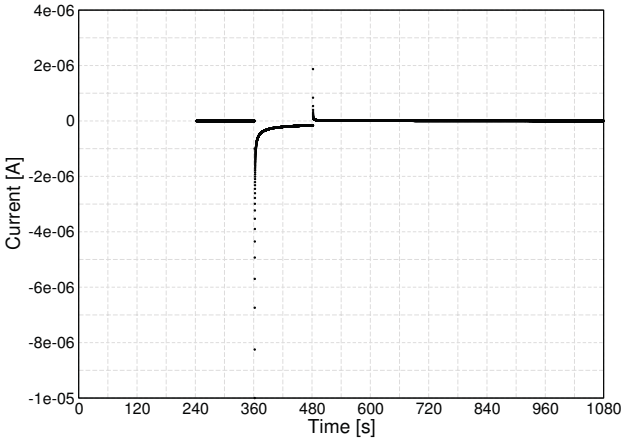

(b) *Current measured across the cell during the measurement of Cy3 at 25 µm from the electrode during the application of -2 V to a 10 nM sample of Cy3 in $[C_4C_1im][NTf_2]$. The OCP across the cell before the measurement was 6 mV*

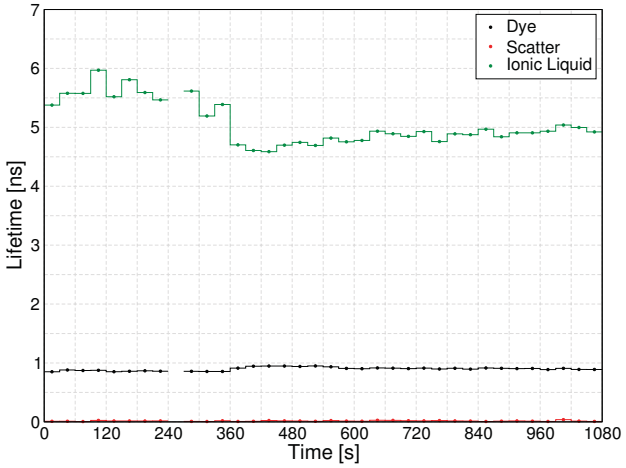

(c) *Lifetime of all of the components in the fluorescence decay at 25 µm from the electrode during the application of -2 V to a 10 nM sample of Cy3 in $[C_4C_1im][NTf_2]$.*

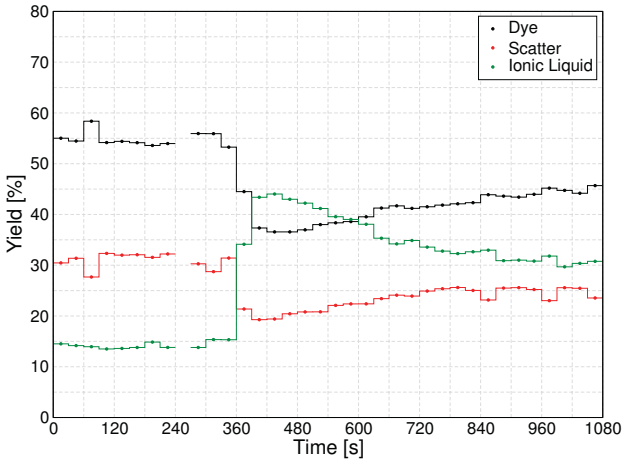

(d) *Contribution (yield) of all of the components within the fluorescence lifetime decay measured at 25 µm from the electrode during the application of -2 V to a 10 nM sample of Cy3 in $[C_4C_1im][NTf_2]$.*

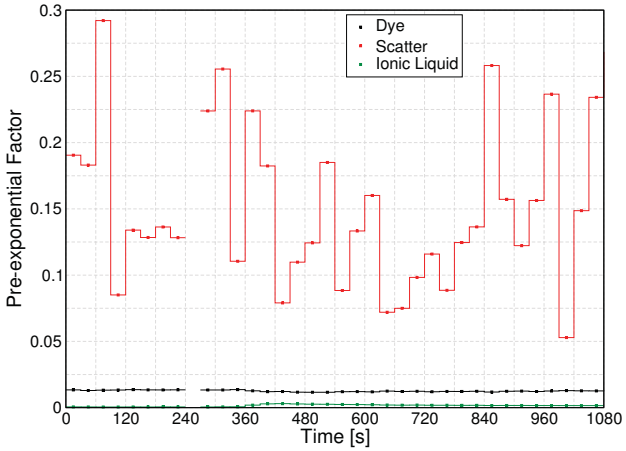

(e) *Pre-exponential factor of all of the components within the fluorescence lifetime decay measured at 25 µm from the electrode during the application of -2 V to a 10 nM sample of Cy3 in $[C_4C_1im][NTf_2]$.*

Figure 6.24: *Results from the fluorescence lifetime decay analysis of data collected at 25 µm from the electrode during the application of -2 V to a 10 nM solution of Cy3 in $[C_4C_1im][NTf_2]$.*

50 μm

The counts from a 10 nM solution of Cy3 in $[C_4C_1im][NTf_2]$ 50 μm from the electrode increase upon the application of -2 V. Upon application of the potential there is a slow increase in the counts, although this begins to occur ≈30 s after the potential is applied. This increase is fast at first, but slows down over the potential application. Upon removal of the potential the counts continue to increase for another ≈120 s before levelling out and then gradually decreasing over the remaining time in the measurement. The total increase in the counts at 50 μm is the smallest change in the counts out of all of the distances.

As with the other distances, the fluorescence lifetime decay can be found and the components present calculated. In these measurements, there are initially only two components present in the decay. One of the components has a lifetime of ≈0.9 ns therefore is assigned to Cy3, and the other component has a lifetime of ≈0.1 ns and is assigned to scatter. The other lifetime component, with a lifetime of ≈5 ns and is assigned to the ionic liquid, does not feature in the fluorescence lifetime decays before the potential application. However, after the application of the potential this component *is* required to fit the lifetime decay. Over the counts of the experiment, this component increases its contribution to the overall decay (Figure 6.26d) following the same trend as the counts. Therefore, as with the data at 25 μm, there is not as greater overall change in the pre-exponential factors. However it does seem that the increase in counts can still be attributed to an increase in the contribution of the ionic liquid component. The lifetime of the component associated to Cy3 is shown in Figure 6.23.

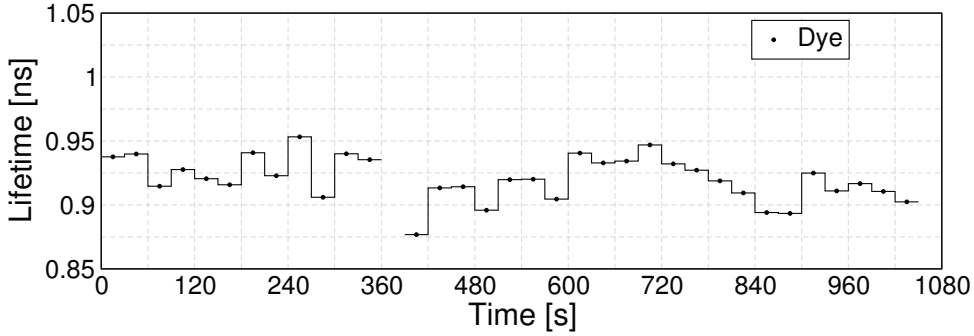

Figure 6.25: *Lifetime of Cy3 at 50 μm from the electrode during the application of -2 V to a 10 nM solution of Cy3 in $[C_4C_1im][NTf_2]$.*

This seems to show that the lifetime of Cy3 does not substantially change at 50 μm from the electrode upon application of -2 V. If there is any change, then this seems to be a decrease in the lifetime, however this is not significant enough to conclude this is occurring, especially because the data is very noisy.

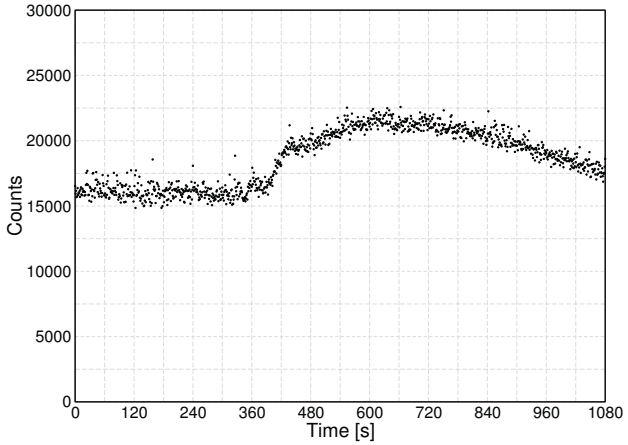

(a) *Counts collected at 50 µm from the electrode during the application of -2 V to a 10 nM sample of Cy3 in $[C_4C_1im][NTf_2]$.*

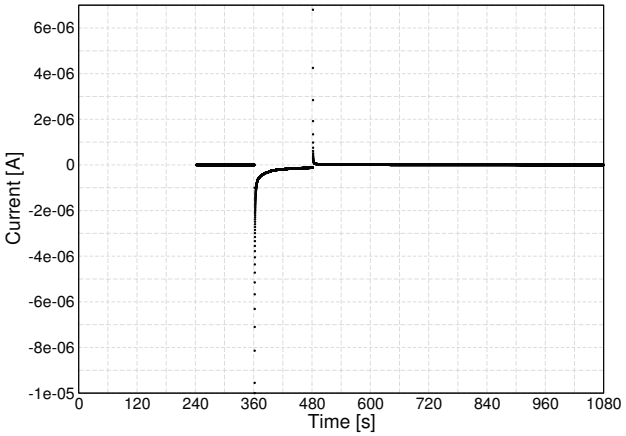

(b) *Current measured across the cell during the measurement of Cy3 at 50 µm from the electrode during the application of -2 V to a 10 nM sample of Cy3 in $[C_4C_1im][NTf_2]$. The OCP across the cell before the measurement was -20 mV*

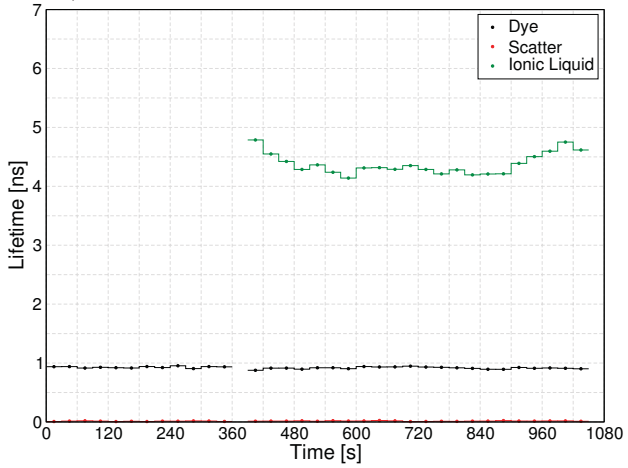

(c) *Lifetime of all of the components in the fluorescence decay at 50 µm from the electrode during the application of -2 V to a 10 nM sample of Cy3 in $[C_4C_1im][NTf_2]$.*

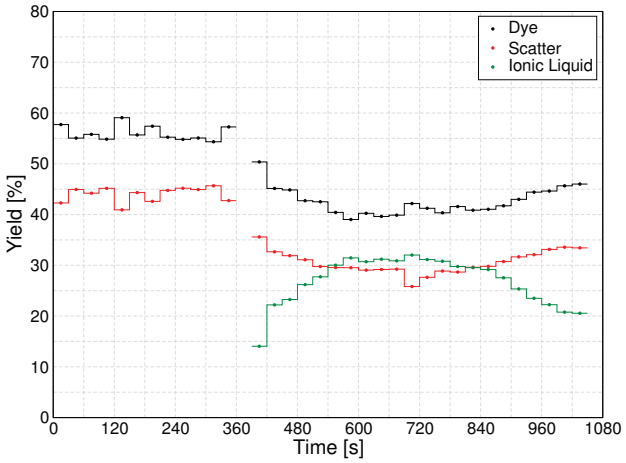

(d) *Contribution (yield) of all of the components within the fluorescence lifetime decay measured at 50 µm from the electrode during the application of -2 V to a 10 nM sample of Cy3 in $[C_4C_1im][NTf_2]$.*

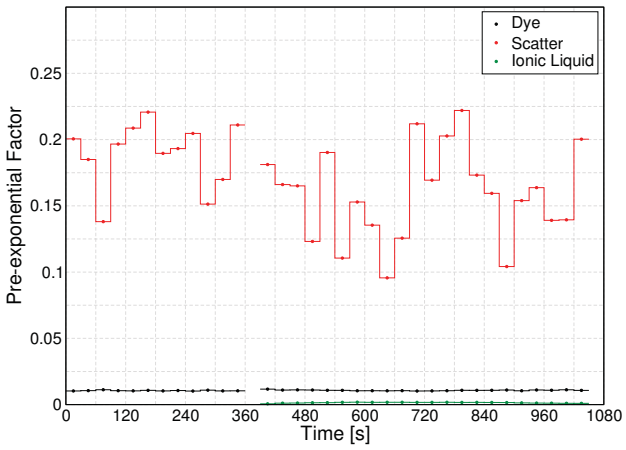

(e) *Pre-exponential factor of all of the components within the fluorescence lifetime decay measured at 50 µm from the electrode during the application of -2 V to a 10 nM sample of Cy3 in $[C_4C_1im][NTf_2]$.*

Figure 6.26: *Results from the fluorescence lifetime decay analysis of data collected at 50 µm from the electrode during the application of -2 V to a 10 nM solution of Cy3 in $[C_4C_1im][NTf_2]$.*

Comparison

The samples of Cy3 after application of -2 V are compared in Figure 6.27. It should be noted that to better compare these, the data at 10 µm has been shifted in time so that the application of the potential in all samples begins at 360 s.

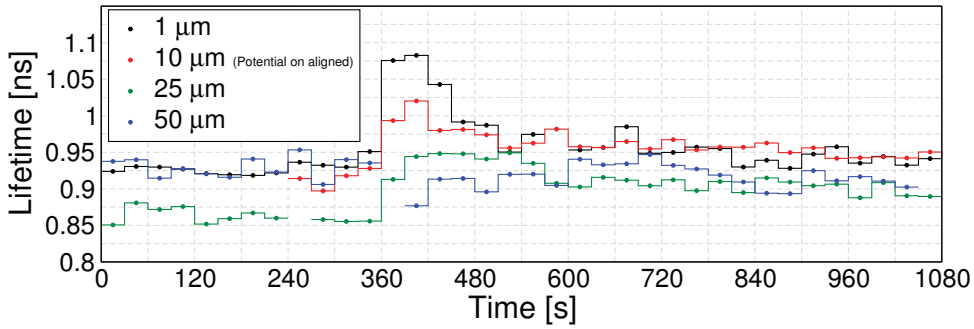

Figure 6.27: *Comparison of the changes to the lifetime of Cy3 at 1 µm, 10 µm, 25 µm, and 50 µm when applying -2 V to a 10 nM solution of Cy3 in* $[C_4C_1im][NTf_2]$.

When comparing the changes in the lifetime of Cy3 at different distances during the potential application, these follow the trend that closer to the electrode there are greater changes in the lifetime of the rotor. Over the duration of the potential application, the lifetime increases the most at 1 µm (0.15 ns), followed by 10 µm (0.10 ns) and 25 µm (0.10 ns), and there is no significant change at 50 µm.

One would expect the dye and ionic liquid closer to the electrode to be more affected by the application of the potential, however large changes to the lifetime, and thus viscosity, at 25 µm from the electrode are peculiar. A discussion as to the hypothesis behind the long range viscosity changes seen here are presented in Section 6.4.2.

The decrease in the lifetimes post-potential application at the different distances are all of approximately the same magnitude at the distances of 1-25 µm. This is despite the large difference in the counts, and the lifetime during the potential application. It is also difficult to differentiate between the samples, due to the large amount of noise within these values. Therefore, while a change in the lifetime and thus viscosity can be concluded to occur, the magnitude of this effect, and the difference between different distances from the electrode cannot be determined from these measurements. Further measurements with a different dye, or a higher concentration of Cy3, are needed to determine the extent of these effects.

Another conclusion from this chapter is that upon application of a potential of -2 V there is an increase in the counts that seems to be related to an increase in one of the components related to the ionic liquid. The exact reason behind this is unknown, as the nature of the process

that leads to this component is unknown. Determination of this would require a study of the fluorescence lifetime decays in neat ionic liquids in a negative potential.

6.3 Lifetime of BODIPY-C10 in $[C_4C_1im][NTf_2]$

6.3.1 Positive 2 V

1 μm

From the data collected at 1 μm (Figure 6.29), a decrease in the number of photons collected can be seen to begin upon application of the potential (Figure 6.29a). This decrease continues during the potential application, and immediately reverses into an increase upon removal of the potential.

Calculation of the lifetimes present in the fluorescence lifetime decay show that before application of the potential, the decay can be adequately fitted by one component. This component has a similar lifetime to that of the BODIPY-C10 in Section 5.3.2 therefore it is determined to belong to the dye.

Upon application of the field, a second component is required to adequately fit the decay. This component has a very long lifetime, similar to that of the long lifetime component in blank ionic liquids in Table 5.1, therefore it is assigned to the ionic liquid.

While there is a significant decrease to the counts, extraction of the contribution of each component (a.k.a. the yield, Figure 6.29d) from the fluorescence lifetime decay shows that the dye component is still the dominant component. Alongside this, a calculation of the estimated concentration of the dye in the focal volume shows that there is still a significant concentration of the dye within the focal volume (Figure 6.29f). This is achieved by taking the total number of counts and multiplying by the yield of the lifetime component.

Combined, these analyses show that looking at the lifetime of the dye is a valid analysis, as there is enough fluorescing dye within the focal volume. The lifetime of the dye is shown in Figure 6.28.

A clear increase in the lifetime of the dye can be seen upon application of +2 V. This is not exactly aligned with the application of the potential, however this is probably due to the fact that the potential is applied in the middle of one of the 30 second bins, which the decay data is required to be split into.

However, the first bin in which the potential is applied throughout does have a significant increase in the lifetime, from ≈1.13 ns to ≈1.18 ns. Using the variable temperature calibration in Section 5.3.2 this corresponds to a 18.5 cP increase in viscosity, and using the variable cation calibration in Section 5.3.2 this corresponds to a 9.0 cP increase in the viscosity of the ionic

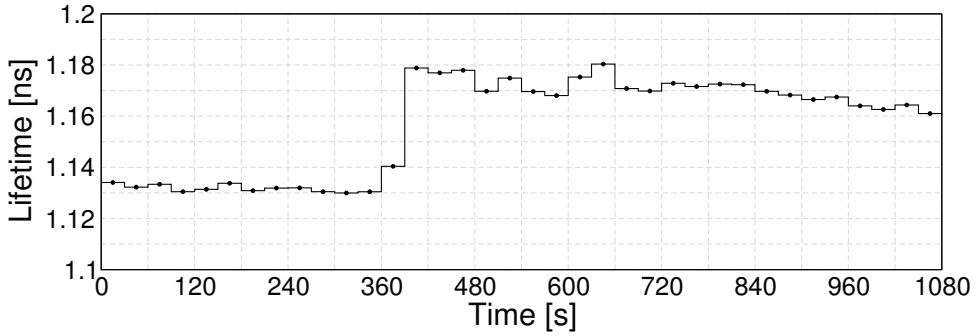

Figure 6.28: *Lifetime of BODIPY-C10 at 1 μm from the electrode during the application of +2 V to a 100 nM solution of BODIPY-C10 in $[C_4C_1im][NTf_2]$.*

liquid.

There is a significant difference in these calibrations, highlighting the problems with assessing which is the correct calibration. However, a significant increase in the viscosity is a definite observation.

The increase in the lifetime persists for a long time, with the lifetime remaining approximately consistent for 270 seconds. After this, there is a steady decrease in the lifetime over the remaining experiment, however 10 minutes after the removal of the potential the lifetime has only decreased to ≈1.16 ns. This is much higher than the pre-potential values, indicating that the viscosity has not fully recovered, even 10 minutes after the removal of the potential.

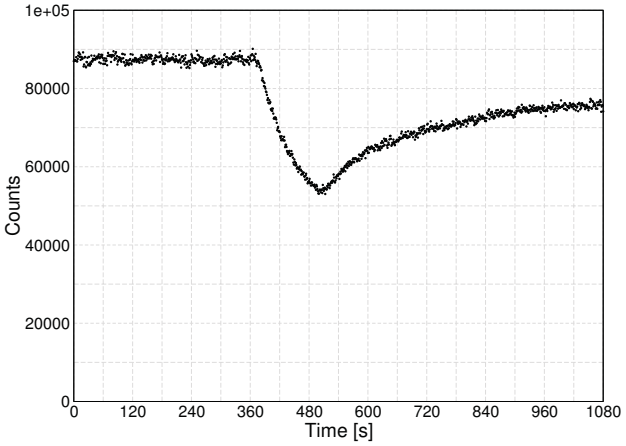

(a) *Counts collected at 1 µm from the electrode during the application of +2 V to a 100 nM sample of BODIPY-C10 in* $[C_4C_1im][NTf_2]$.

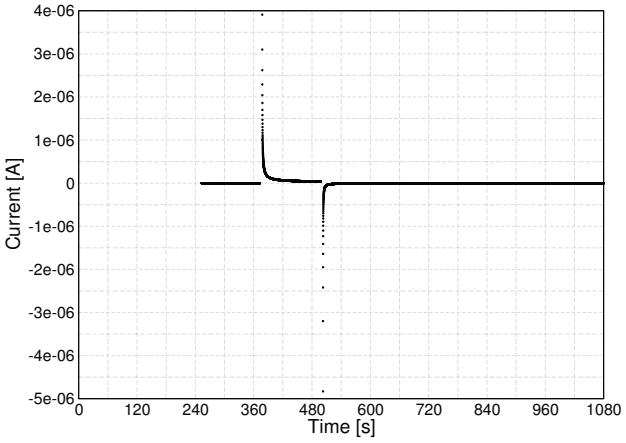

(b) *Current measured across the cell during the measurement of BODIPY-C10 at 1 µm from the electrode during the application of +2 V to a 100 nM sample of BODIPY-C10 in* $[C_4C_1im][NTf_2]$. *The OCP across the cell before the measurement was -46 mV.*

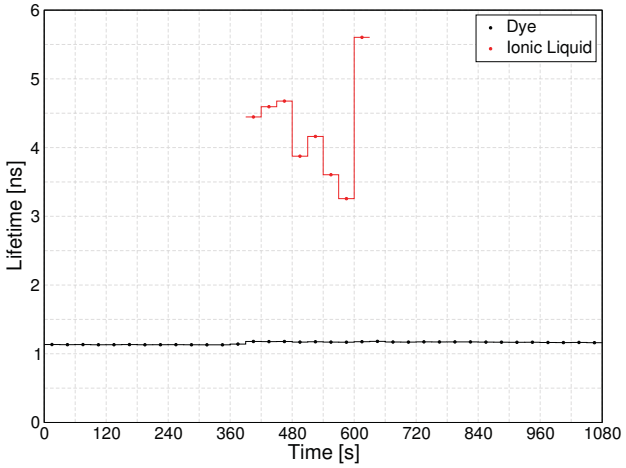

(c) *Lifetime of all of the components in the fluorescence decay at 1 µm from the electrode during the application of +2 V to a 100 nM sample of BODIPY-C10 in* $[C_4C_1im][NTf_2]$.

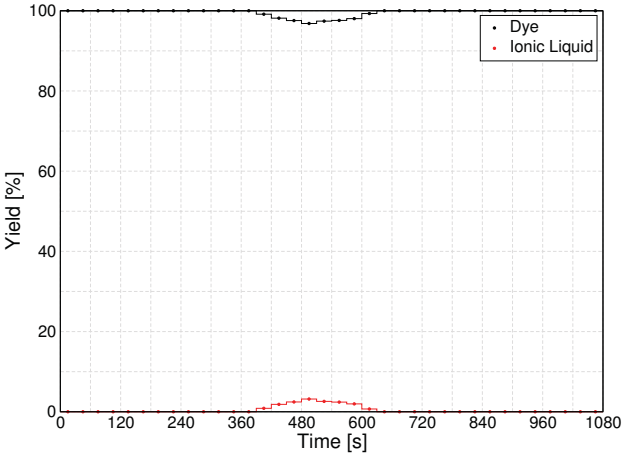

(d) *Contribution (yield) of all of the components within the fluorescence lifetime decay measured at 1 µm from the electrode during the application of +2 V to a 100 nM sample of BODIPY-C10 in* $[C_4C_1im][NTf_2]$.

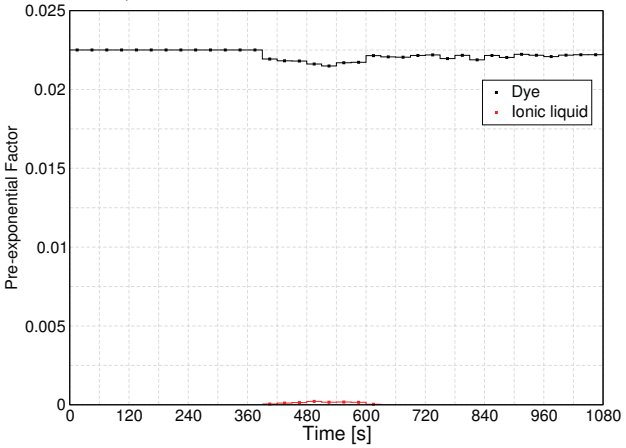

(e) *Pre-exponential factor of all of the components within the fluorescence lifetime decay measured at 1 µm from the electrode during the application of +2 V to a 100 nM sample of BODIPY-C10 in* $[C_4C_1im][NTf_2]$.

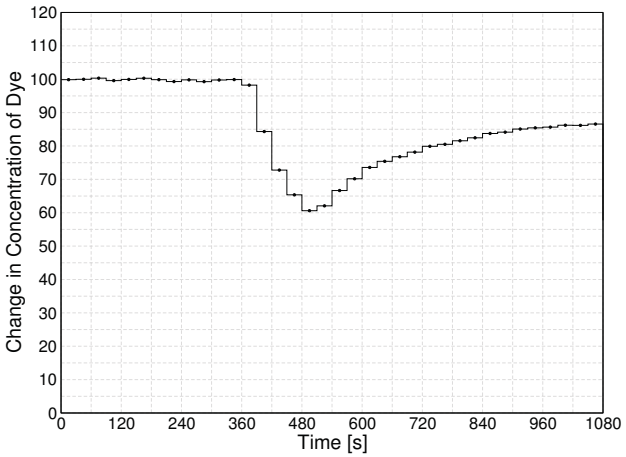

(f) *Concentration of the dye, calculated from the counts and contribution, measured at 1 µm from the electrode during the application of +2 V to a 100 nM sample of BODIPY-C10 in* $[C_4C_1im][NTf_2]$.

Figure 6.29: *Results from the fluorescence lifetime decay analysis of data collected at 1 µm from the electrode during the application of +2 V to a 100 nM solution of BODIPY-C10 in* $[C_4C_1im][NTf_2]$.

10 μm

From the counts collected at 10 μm (Figure 6.31a), a similar trend to that observed at 1 μm can be seen. There is a decrease in the counts seen immediately upon application of the potential, and removal of the potential causes a reversal and increase in the counts again.

Calculation of the fluorescence lifetime decay, and the components within the decay, shows that at all points within this experiment there is only one component present. This component has a similar lifetime to that of the BODIPY-C10 in Section 5.3.2 and at 1 μm, therefore it is assigned to the dye.

From the presence of only one component, as well as the concentration (Figure 6.31d) of the dye still being significant, this component can reasonably be analysed. This component is shown in Figure 6.30.

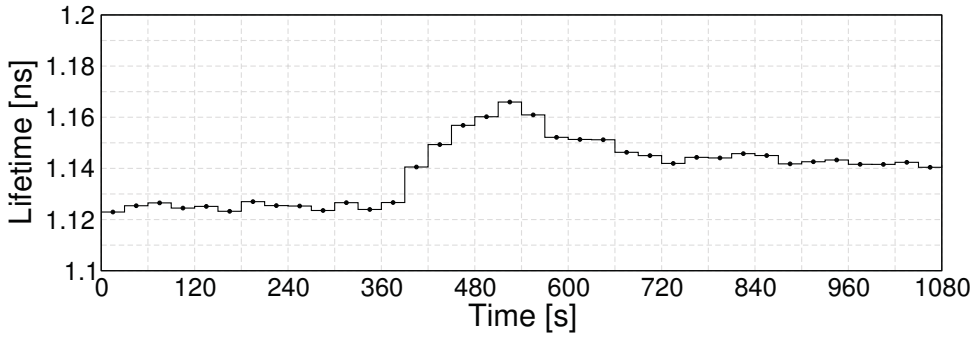

Figure 6.30: *Lifetime of BODIPY-C10 at 10 μm from the electrode during the application of +2 V to a 100 nM solution of BODIPY-C10 in $[C_4C_1im][NTf_2]$.*

A clear increase in the lifetime of BODIPY-C10 can be seen at 10 μm. Rather than an immediate increase, there is a gradual increase in the lifetime of the dye for 6 bins (180 seconds) after the application of the potential. This is unexpected as the potential is only applied for 120 seconds, and after removal of the potential, there is still an increase in the lifetime, even while the counts have begun to increase again.

At its maximum, the lifetime of the dye has increased to ≈1.175 ns from ≈1.125 ns. Using the variable temperature calibration in Section 5.3.2 this corresponds to a 18.2 cP increase in viscosity, and using the variable cation calibration in Section 5.3.2 this corresponds to a 8.9 cP increase in viscosity. These are slightly lower increases in viscosity than those seen at 1 μm.

After the lifetime has reached its maximum (with the potential being removed), there is a fairly significant immediate decrease in the lifetime over the next 60 seconds to ≈1.15 ns. However, over the remaining experiment, the lifetime decreases much slower, decreasing to 1.14 ns at the end of the 10 minute application of 0 V of potential. This is still higher than the pre-potential

lifetime so it does not constitute a full recovery of the lifetime.

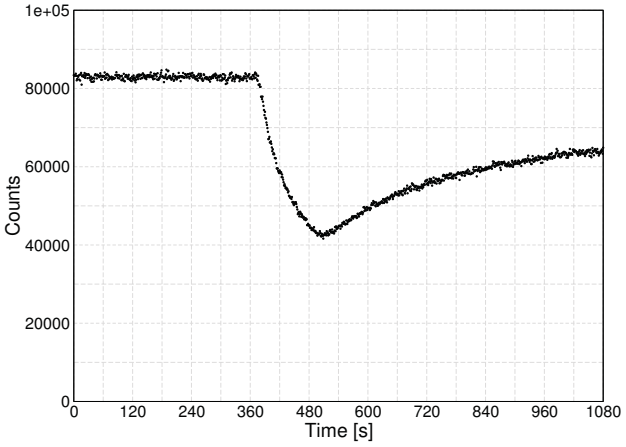

(a) *Counts collected at 10 µm from the electrode during the application of +2 V to a 100 nM sample of BODIPY-C10 in* $[C_4C_1im][NTf_2]$.

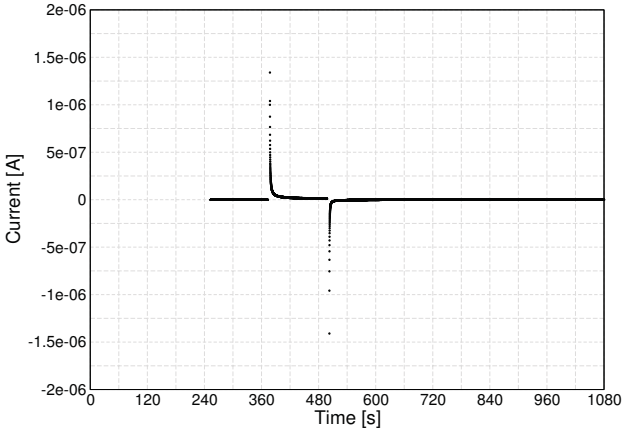

(b) *Current measured across the cell during the measurement of BODIPY-C10 at 10 µm from the electrode during the application of +2 V to a 100 nM sample of BODIPY-C10 in* $[C_4C_1im][NTf_2]$. *The OCP across the cell before the measurement was 20 mV.*

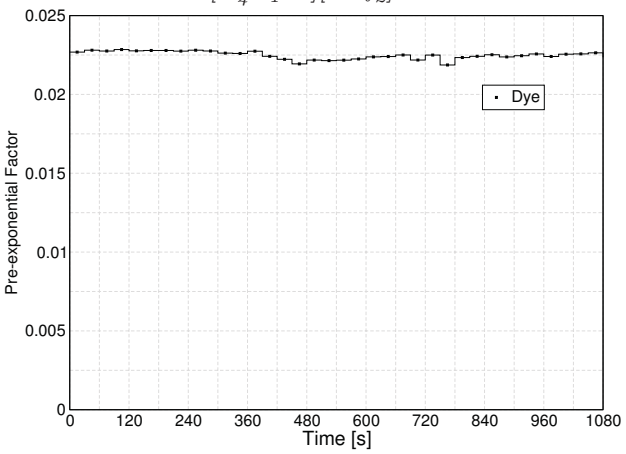

(c) *Pre-exponential factor of all of the components within the fluorescence lifetime decay measured at 10 µm from the electrode during the application of +2 V to a 100 nM sample of BODIPY-C10 in* $[C_4C_1im][NTf_2]$.

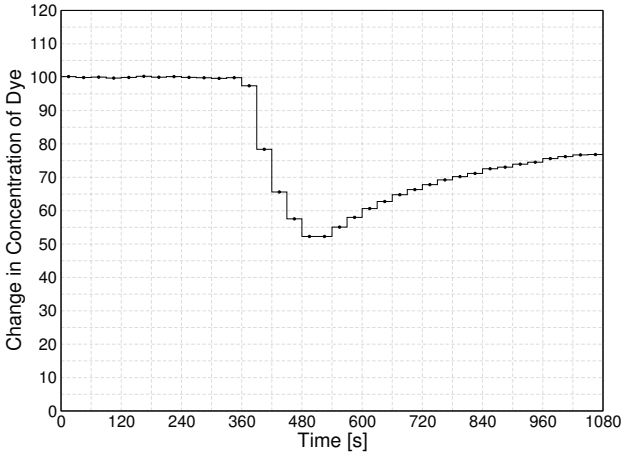

(d) *Concentration of the dye, calculated from the counts and contribution, measured at 10 µm from the electrode during the application of +2 V to a 100 nM sample of BODIPY-C10 in* $[C_4C_1im][NTf_2]$.

Figure 6.31: *Results from the fluorescence lifetime decay analysis of data collected at 10 µm from the electrode during the application of +2 V to a 100 nM solution of BODIPY-C10 in* $[C_4C_1im][NTf_2]$.

25 μm

From the counts collected at 25 μm (Figure 6.33a), a similar trend to that at 1 μm and 10 μm can be seen. There is a decrease in the counts immediately upon the application of the potential, and removal of the potential causes an immediate reversal and increase in the counts again.

Calculation of the fluorescence lifetime decay, and the components within the decay, shows that at all points within this experiment there is only one component present. This component has a similar lifetime to that of the BODIPY-C10 in Section 5.3.2 and at 1 μm and 10 μm, therefore it is assigned to the dye.

As with the data at 10 μm, the presence of only one component along with the significant concentration of the dye (Figure 6.33d), this component can be analysed. This component is shown in Figure 6.32.

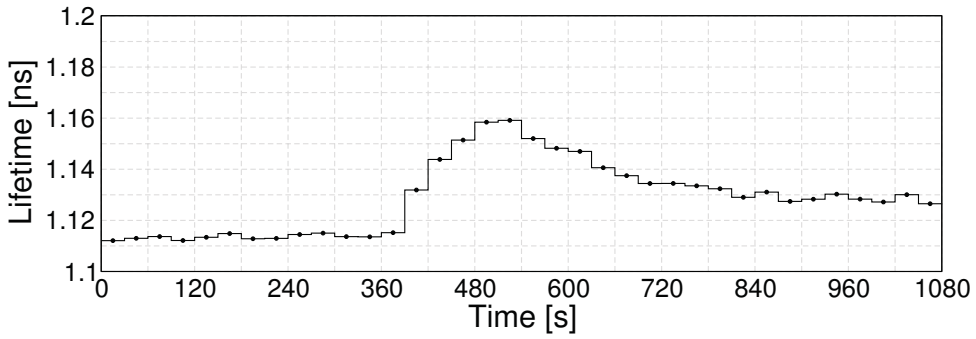

Figure 6.32: *Lifetime of BODIPY-C10 at 25 μm from the electrode during the application of +2 V to a 100 nM solution of BODIPY-C10 in $[C_4C_1im][NTf_2]$.*

This trend in the lifetime is remarkably similar to that at 10 μm. A clear increase in the lifetime of the dye is seen in the first bin which has the potential applied throughout. This increase continues beyond the time at which the potential was applied, reaching its maximum in the bin 30-60 seconds after the removal of the potential.

At its maximum, the lifetime of the dye has increased to ≈1.16 ns from ≈1.115 ns. Using the variable temperature calibration in Section 5.3.2 this corresponds to a 15.6 cP increase in viscosity, and using the variable cation calibration in Section 5.3.2 this corresponds to a 7.9 cP increase in viscosity. These are significantly lower increases in viscosity than those seen at 1 μm or 10 μm.

After the lifetime has reached its maximum (with the potential being removed at this point), there is a fairly quick decrease in the lifetime over the proceeding 180 seconds to 1.135 ns. This recovery then slows down and over the next 360 seconds only decreases by ≈0.005 ns, with the

lifetime of the dye being 1.13 ns at the end of the 10 minute application of 0 V of potential. As with the other distances, this is still higher than the pre-potential lifetime so does not constitute a full recovery of the lifetime.

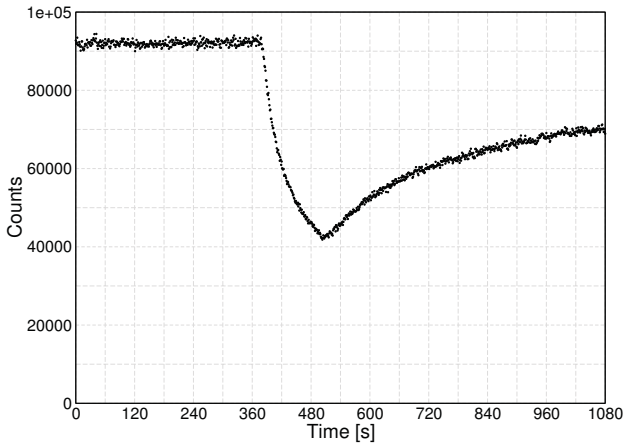

(a) *Counts collected at 25 µm from the electrode during the application of +2 V to a 100 nM sample of BODIPY-C10 in $[C_4C_1im][NTf_2]$.*

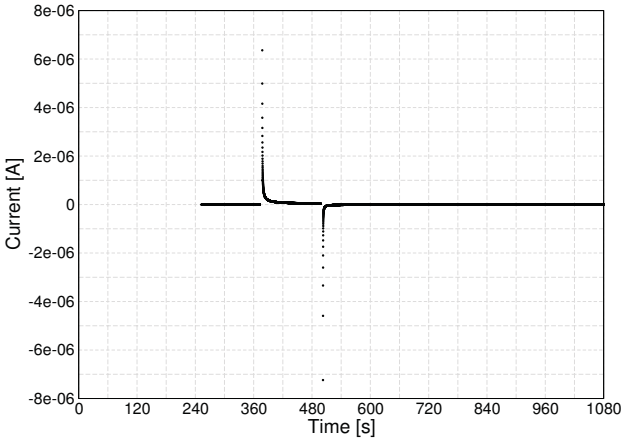

(b) *Current measured across the cell during the measurement of BODIPY-C10 at 25 µm from the electrode during the application of +2 V to a 100 nM sample of BODIPY-C10 in $[C_4C_1im][NTf_2]$. The OCP across the cell before the measurement was 25 mV.*

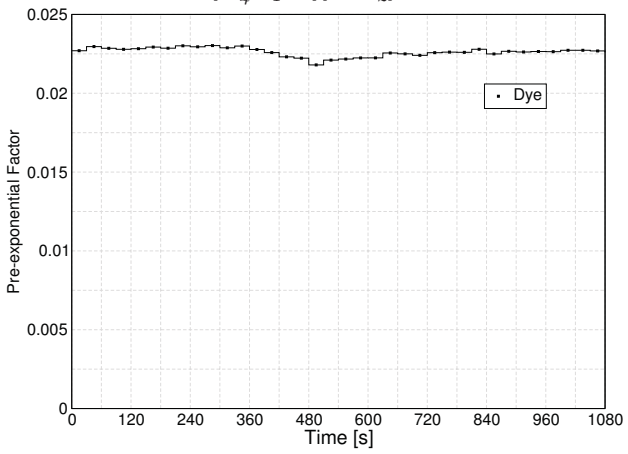

(c) *Pre-exponential factor of all of the components within the fluorescence lifetime decay measured at 25 µm from the electrode during the application of +2 V to a 100 nM sample of BODIPY-C10 in $[C_4C_1im][NTf_2]$.*

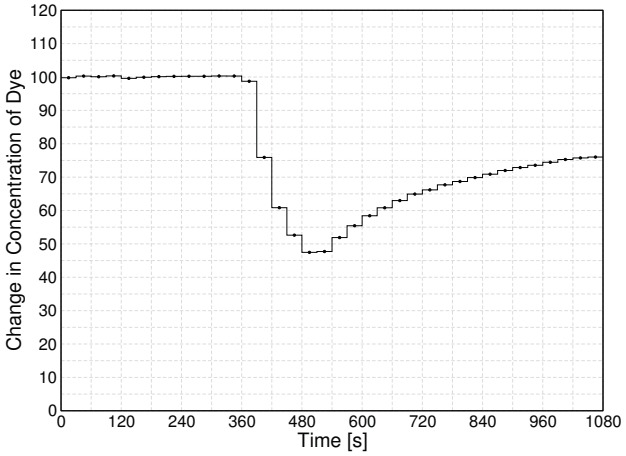

(d) *Concentration of the dye, calculated from the counts and contribution, measured at 25 µm from the electrode during the application of +2 V to a 100 nM sample of BODIPY-C10 in $[C_4C_1im][NTf_2]$.*

Figure 6.33: *Results from the fluorescence lifetime decay analysis of data collected at 25 µm from the electrode during the application of +2 V to a 100 nM solution of BODIPY-C10 in $[C_4C_1im][NTf_2]$.*

50 μm

The counts collected at 50 μm (Figure 6.35a) show a different trend to the rest of the samples. Upon application of the potential there is no change to the counts. It is only 60 seconds after the application of the potential that there is a decrease in the counts, and this is a very slow decrease.

This continues beyond the removal of the potential, with the counts only halting their decrease 180 seconds after the removal of the potential. After this point, there is an even slower increase in the counts over the remaining time in the experiment.

Calculation of the fluorescence lifetime decay, and the components within, shows that throughout the entirety of the experiment there is is only one component present in all of the decays. This component has a similar lifetime to that of the BODIPY-C10 seen in Section 5.3.2 and at 1 μm, 10 μm, and 25 μm, therefore it is assigned to BODIPY-C10.

As there is only one component, and a high concentration of the dye all of the time (Figure 6.35d), the lifetime of this component can be reasonably analysed, and this is shown in Figure 6.34.

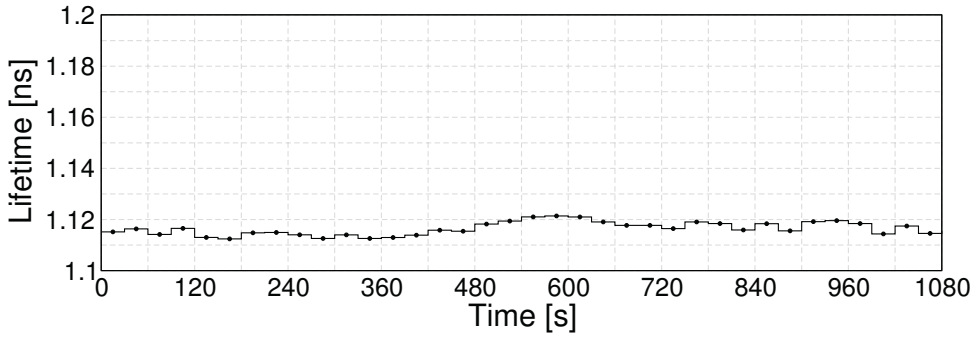

Figure 6.34: *Lifetime of BODIPY-C10 at 50 μm from the electrode during the application of +2 V to a 100 nM solution of BODIPY-C10 in $[C_4C_1im][NTf_2]$.*

Across this experiment, there is no major change in the lifetime, unlike the results at 1 μm, 10 μm, and 25 μm. Before the application of the potential, the lifetime remains constant at ≈1.115 ns. Upon application of the potential there is no change in the lifetime of the dye, however there does appear to be a slight increase in the lifetime at 480 seconds. This is the time at which the potential is removed.

If the increase is real, then this is only a small increase from ≈1.115 ns to ≈1.20 ns. Using the variable temperature calibration in Section 5.3.2 this would correspond to a 1.6 cP increase in viscosity, and using the variable cation calibration in Section 5.3.2 this would correspond to a 0.8 cP increase in viscosity. These are significantly lower increases in viscosity than those seen

at 1 µm, 10 µm, or 25 µm.

This lifetime appears to remain at a higher value for 120 seconds. The recovery of the lifetime is difficult to track however, as the noise in the data is similar to that of the increase. This is also why the increase in lifetime is less certain at 50 µm than that of other distances, where significant increases are seen.

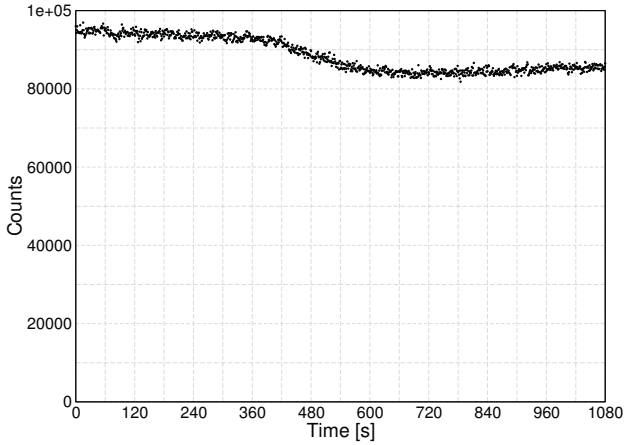

(a) *Counts collected at 50 µm from the electrode during the application of +2 V to a 100 nM sample of BODIPY-C10 in $[C_4C_1im][NTf_2]$.*

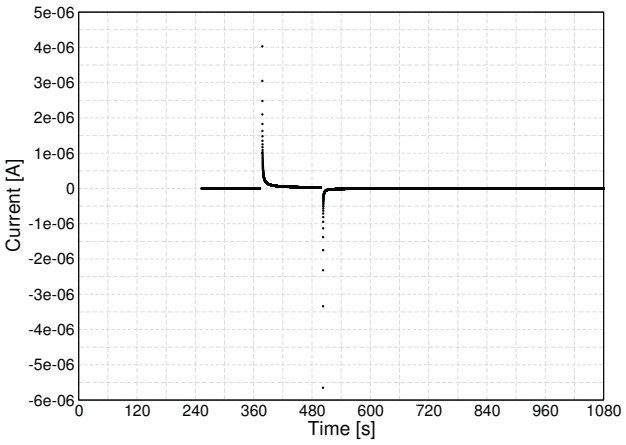

(b) *Current measured across the cell during the measurement of BODIPY-C10 at 50 µm from the electrode during the application of +2 V to a 100 nM sample of BODIPY-C10 in $[C_4C_1im][NTf_2]$. The OCP across the cell before the measurement was 6 mV.*

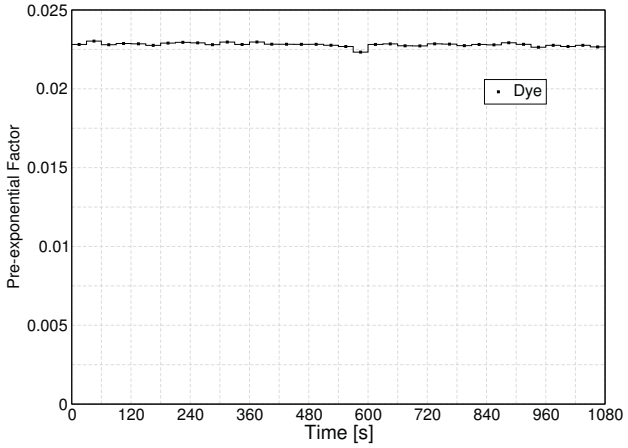

(c) *Pre-exponential factor of all of the components within the fluorescence lifetime decay measured at 50 µm from the electrode during the application of +2 V to a 100 nM sample of BODIPY-C10 in $[C_4C_1im][NTf_2]$.*

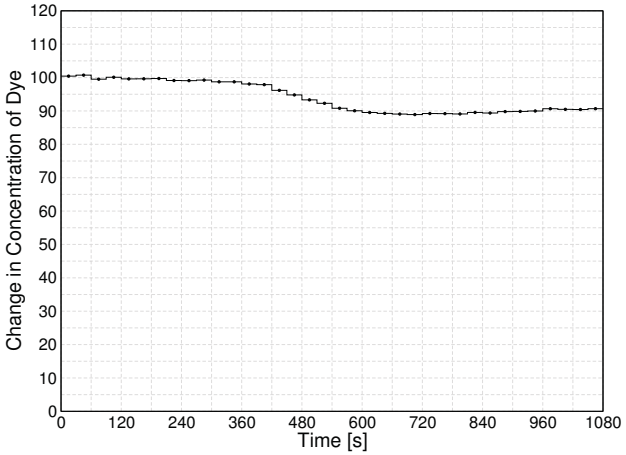

(d) *Concentration of the dye, calculated from the counts and contribution, measured at 50 µm from the electrode during the application of +2 V to a 100 nM sample of BODIPY-C10 in $[C_4C_1im][NTf_2]$.*

Figure 6.35: *Results from the fluorescence lifetime decay analysis of data collected at 50 µm from the electrode during the application of +2 V to a 100 nM solution of BODIPY-C10 in $[C_4C_1im][NTf_2]$.*

Discussion

Comparing all of the results, a significant increase to the lifetime of BODIPY-C10 can be seen at distances of 1-25 µm from an electrode upon application of +2 V. There is a small indication of an increase in the lifetime of the dye at 50 µm from the electrode, however this is not significant enough to conclusively prove that this occurs.

When considering the counts collected, as well as the concentration of the dye that can be estimated from the total counts and the dye component yield, there is a significant decrease in the counts and the concentration of the dye seen at all distances (Figure 6.36). However, in all of these samples, there is still enough dye within the focal volume to be able to analyse the lifetime of the dye.

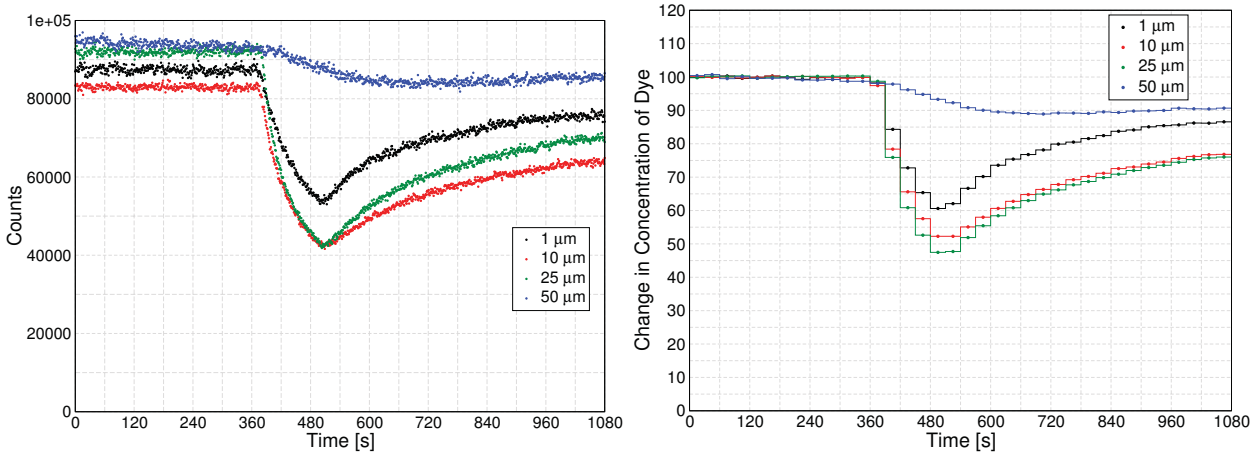

Figure 6.36: *Comparison of the changes to the counts (left), and the concentration of the dye (right), at 1 µm, 10 µm, 25 µm, and 50 µm when applying +2 V to a 100 nM solution of BODIPY-C10 in* $[C_4C_1im][NTf_2]$.

This decrease occurs almost instantly upon application of the potential, and recovers very slowly. For an explanation as to why the concentration of the dye decreases, a discussion on this for all dyes in all potentials is present in Section 6.4.1.

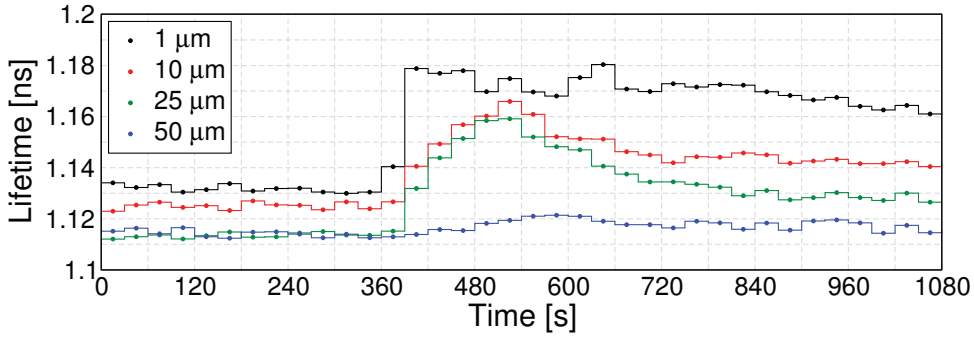

Figure 6.37: *Comparison of the lifetime of BODIPY-C10 at 1 µm, 10 µm, 25 µm, and 50 µm when applying +2 V to a 100 nM solution of BODIPY-C10 in* $[C_4C_1im][NTf_2]$.

When considering the differences in the lifetimes of the dye, there is a very clear trend. Upon application of the electric field, there are increases in the lifetime of the rotor. The magnitude of the increase in the lifetime is: 1 μm > 10 μm ≈ 25 μm > 50 μm. This shows that upon application of a potential, there is an increase in the viscosity experienced by the neutral BODIPY-C10 rotor.

This increase in the lifetime is a real effect, as the changes to the concentration have been accounted for. For a comprehensive discussion of the hypothesis behind the change in the lifetime of this dye see Section 6.4.2.

6.3.2 Negative 2 V

1 μm

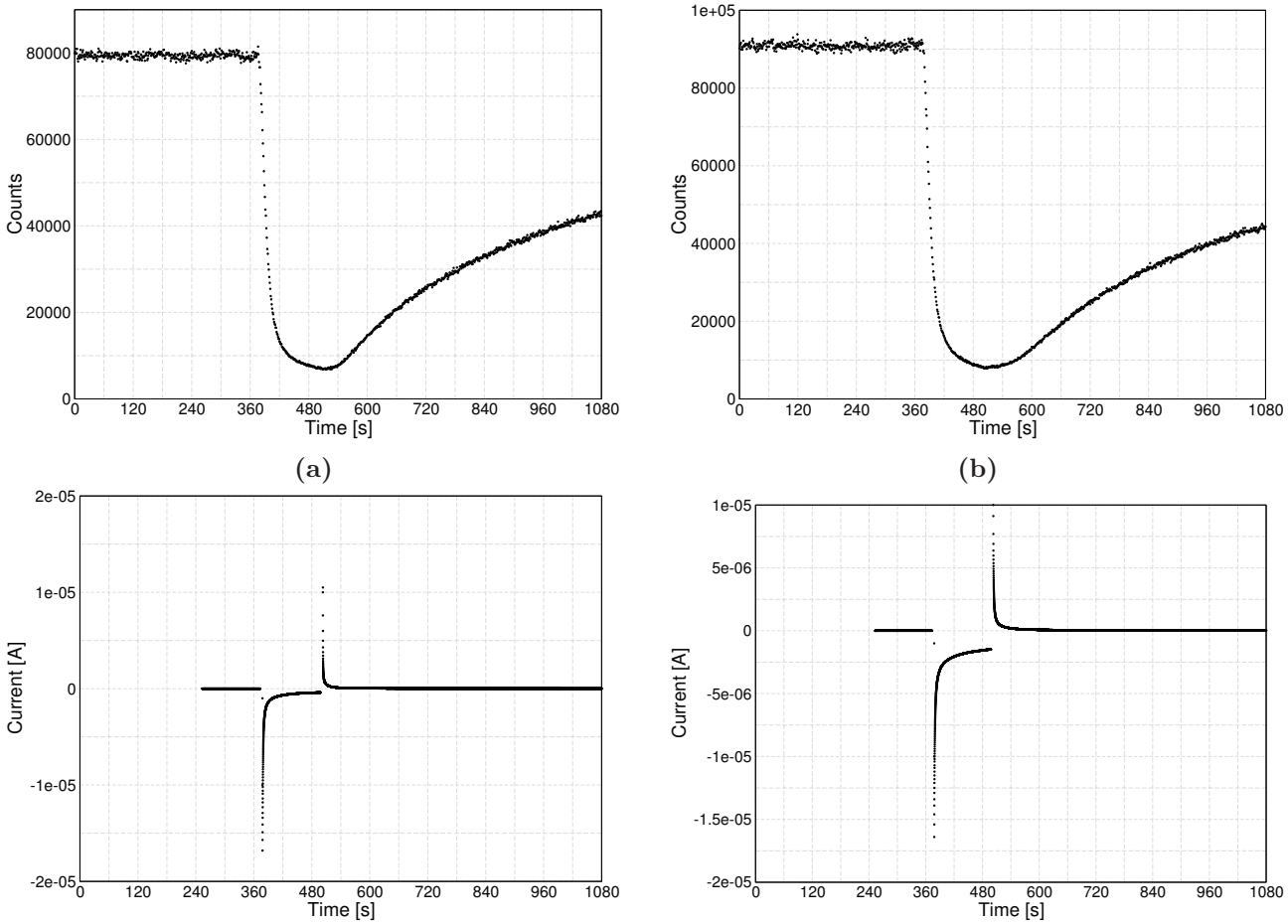

(a) **(b)**

(c) *OCP = -69 mV* **(d)** *OCP = -39 mV*

Figure 6.38: *(a) and (b): Counts per second collected at 1 μm from the electrode during the application of -2 V to a 100 nM solution of BODIPY-C10 in $[C_4C_1im][NTf_2]$. (c) and (d): Current across the cell during these measurements. OCP value is in the caption of the current graph.*

Upon application of -2 V to a 100 nM solution of BODIPY-C10 in $[C_4C_1im][NTf_2]$ there is a gradual decrease in the counts over ≈ 30 seconds down to the level of the counts arising from the ionic liquid (Figures 6.38a and 6.38b). This is a remarkable decrease, especially given that the dye is neutral molecule and would not be expected to be strongly affected by the electric field.

The recovery of the counts is relatively slow. While upon the release of the potential there is an immediate increase in the dye counts, this recovery proceeds very slow, only recovering 40% of the 'lost' dye signal within 10 minutes of 0 V application.

10 μm

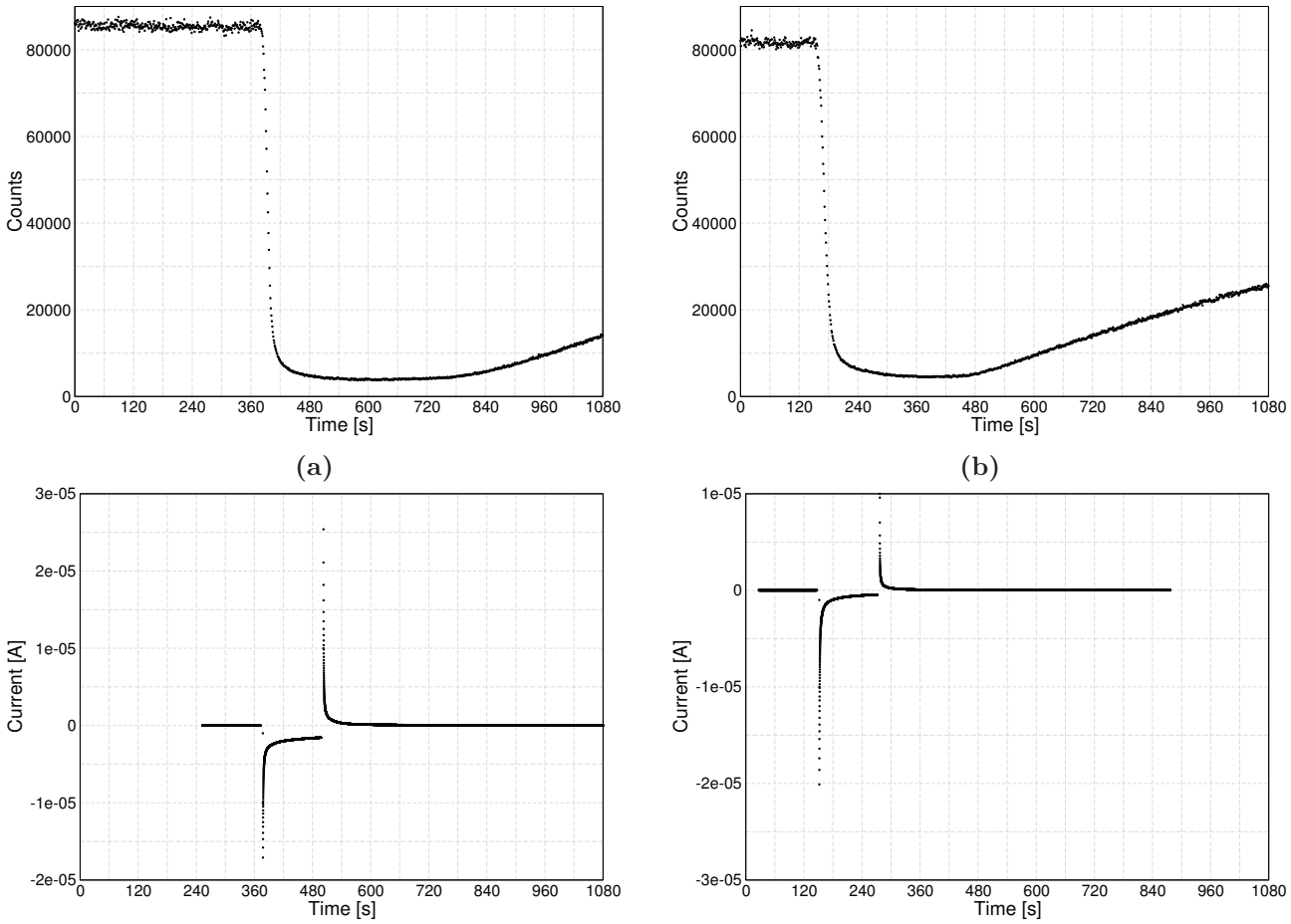

(a) **(b)**

(c) *OCP = 55 mV* **(d)** *OCP = 53 mV*

Figure 6.39: *(a) and (b): Counts per second collected at 10 μm from the electrode during the application of -2 V to a 100 nM solution of BODIPY-C10 in $[C_4C_1im][NTf_2]$. (c) and (d): Current across the cell during these measurements. OCP value is in the caption of the current graph.*

At 10 μm there is a similarly fast decrease in the counts as at 1 μm upon application of a potential of -2 V (Figures 6.39a and 6.39b). There is no delay between the application of the potential and the decrease in the counts down to the level of the ionic liquid.

Upon release of the potential, the counts remain at the level of the ionic liquid at 10 μm for ≈ 4 minutes. After this there is an increase in the counts again, similar to that seen at 1 μm, however given that there is a much longer delay between the removal of the potential and the increase, by the end of the experiment the counts have not recovered a lot and are still very low. 10 minutes after the removal of the potential, the counts have only increased to 15,000-20,000.

25 μm

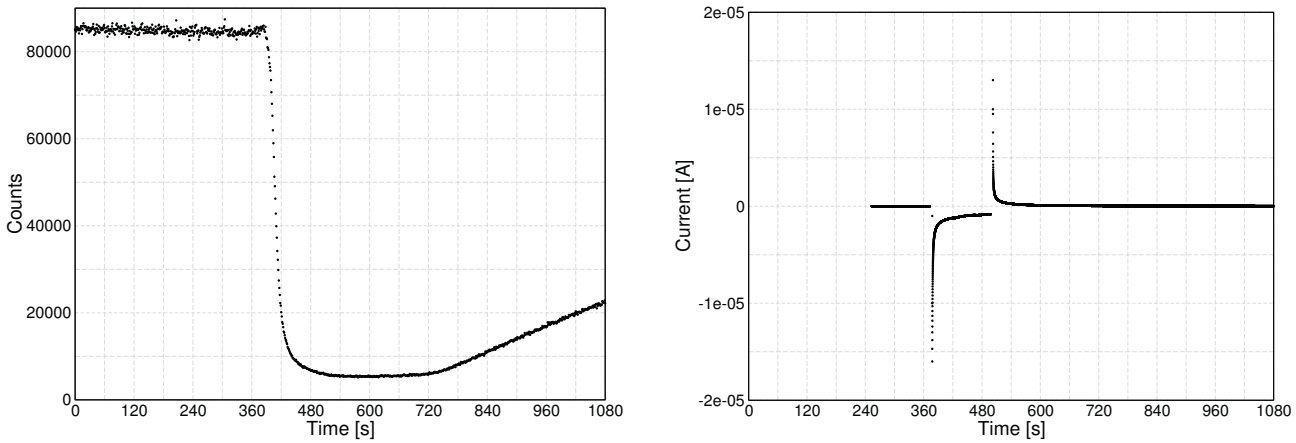

(a) **(b)** *OCP = -17 mV*

Figure 6.40: *(a): Counts per second collected at 25 μm from the electrode during the application of -2 V to a 100 nM solution of BODIPY-C10 in $[C_4C_1im][NTf_2]$. (b): Current across the cell during this measurements. OCP value is in the caption of the current graph.*

At 25 μm there is also a decrease in the counts to the level of the ionic liquid, however there is more of a delay between the application of the potential and the decrease in the counts (Figure 6.40a). At 1 μm and 10 μm the decrease is complete after 60 seconds, at 25 μm this requires 120 seconds, which is the total time the potential is applied for.

After the removal of the potential, in a similar way to the sample at 10 μm, the counts remain low and do not recover quickly. It is only 240 seconds after the removal of the potential that the counts begin to increase again.

This recovery is equally as slow as at 10 μm where even after 10 minutes with no potential being applied to the sample there are only ≈ 20,000 counts measured per second.

50 μm

The measurements at 50 μm are highly unusual as there are two measurements that have similar current traces and OCP values, however the number of counts per second are dramatically different.

In measurement 1 (Figures 6.41a and 6.41c), upon application of the potential there is a steady decrease in the counts to the level of the blank ionic liquid. In measurement 2 (Figures 6.41b and 6.41d), upon application of the potential there is a slight decrease in the counts, however this is very minor and does not decrease to the level of the blank ionic liquid.

In these measurements, there is a unusually large faradaic current present in both of the samples. Measurement 1, with the greater effect, has the larger faradaic current. However, this is present

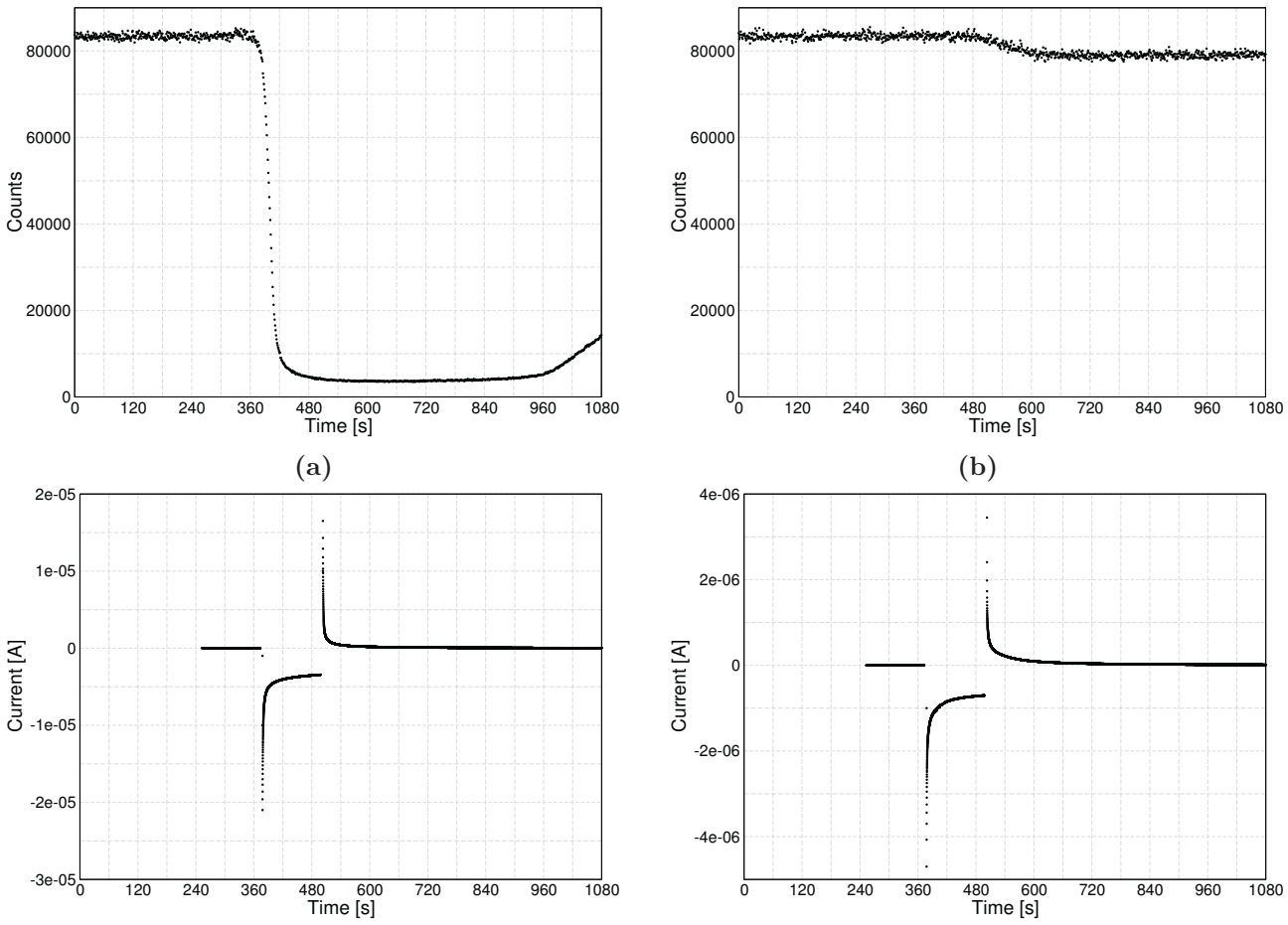

(a)

(b)

(c) *OCP = -34 mV*

(d) *OCP = -41 mV*

Figure 6.41: *(a) and (b): Counts per second collected at 50 µm from the electrode during the application of -2 V to a 100 nM solution of BODIPY-C10 in $[C_4C_1im][NTf_2]$. (c) and (d): Current across the cell during these measurements. OCP value is in the caption of the current graph.*

in both measurements, and is not present in any other measurements.

This large faradaic current suggests the presence of some impurities or a problem with the cell, which causes a constant high current flow. In order to determine if these measurements are a true reflection of what is occurring, these should be repeated.

Discussion

The measurements of the counts at 1 µm, 10 µm and 25 µm from an electrode show that upon application of -2 V to a sample of BODIPY-C10, there is a similar behaviour to that of Cy3 upon application of +2 V.

There is a decrease in the counts to the level of the blank ionic liquid, indicating a complete depletion of the dye at these distances from the electrode.

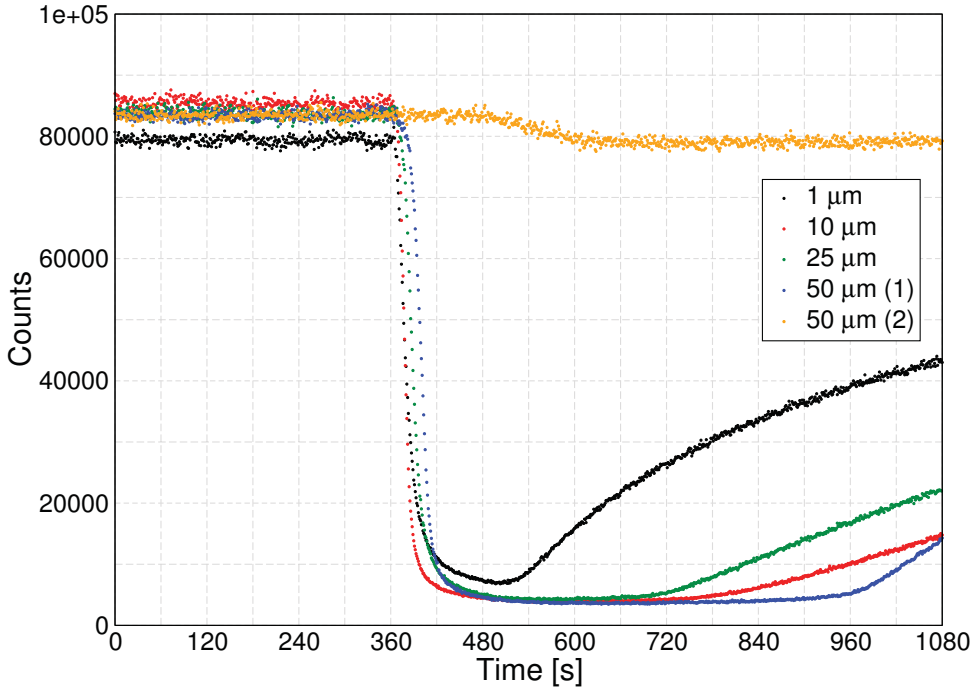

Figure 6.42: *Comparison of the changes to the counts at 1 µm, 10 µm, 25 µm, and both samples at 50 µm when applying -2 V to a 100 nM solution of BODIPY-C10 in* $[C_4C_1im][NTf_2]$.

Figure 6.42 shows that there is a distance dependence to the results, akin to that of the Cy3 positive potential results, wherein the distances closer to the electrode deplete and recover first. The two samples measured at 50 µm show vastly different results. Sample 1 (blue curve in Figure 6.42) takes 360 seconds after removal of the potential to begin the recovery of the counts. Sample 2 (orange curve in Figure 6.42) only takes 150 seconds after removal of the potential to begin the recovery of the counts, however the decrease is less severe for this sample.

The differences between these samples are unclear, as there is no significant differences between the OCP values of these measurements. Therefore, repeats of these measurements are needed to study why there are large differences between these samples.

6.4 Hypothesis for Changes to Counts and Lifetime in $[C_4C_1im][NTf_2]$

As both dyes have similar behaviours in different samples, this chapter will discuss the current best hypotheses behind the change in the counts/concentration of the dyes, as well as the change in the dye lifetimes.

6.4.1 Change in Dye Concentration

When considering the application of +1 V or +2 V to Cy3 in $[C_4C_1im][NTf_2]$ (Sections 6.2.2 and 6.2.1 respectively) and application of -2 V to BODIPY-C10 in $[C_4C_1im][NTf_2]$ (Section 6.3.2) there is a huge decrease in the number of counts collected in all of these samples. This decrease also occurs upon application of +2 V to BODIPY-C10 in $[C_4C_1im][NTf_2]$ (Section 6.3.1), however this is not as dramatic as the former samples and a lifetime of the dye can be extracted from the data. A similar effect is not seen upon application of -2 V to Cy3 in $[C_4C_1im][NTf_2]$ (Section 6.2.3).

When combining all of the results which show a decrease in counts, this decrease in counts is suspected to arise due to a decrease in the amount of dye in the focal volume upon application of the potential. It is unlikely that the ionic liquid ions could physically or chemically trap the dyes in a non-fluorescing state at such a large distance from a 'driving force' i.e. the electrode. A potential-driven quenching of the dyes is not likely, as this would require significant constant currently flow.

This means that there is significant electrophoresis of the dyes within the ionic liquid. Electrophoresis is the relative motion particles in the presence of an electric field.[47] While electrophoresis is a known phenomenon within ionic liquids it is not particularly well studied, especially with respect to longer time-scales or near electrodes.

Usually, electrophoresis is used to measure mobility of ions within an electric field,[168,169] transference numbers,[169,170] ion pairing and association,[171–173] and the diffusion of solutes within ionic liquids.[174] These are all achieved using electrophoretic NMR, which involves the measuring of diffusion using pulsed field gradient stimulated echo NMR while the sample has an electric field applied to it.

Each of these measurement takes <500 ms, and alternating current fields are often used in order to perform subsequent measurements. This means that electrophoresis is usually measured in

much shorter time-scales than the minutes that have been used in these experiments. Therefore the results require careful consideration in order to determine the nature of the electrophoresis as there is no precedent for the dynamics of ions in such conditions.

Due to the fact that depletion **and** recovery of the counts propagates from the electrode, the dyes are suspected to diffuse towards the electrode. The electrophoresis removes the dyes from the focal volume, which leads to the reduction in the counts. Once at the electrode, the dyes can be incorporated into the double layer structure, which can trap the dyes close enough to the electrode that they are not seen in these measurements.

Once the dyes have reached the electrodes, it is possible that the fluorescence can be quenched at the electrode. Quenching or modifying of the fluorescence of fluorophores near metal surfaces and nano-particles is a well known phenomenon.[175,176] Therefore it is possible that near the indium-tin oxide electrode, the proximity of the dye to the indium or tin could lead to a quenching of the fluorescence.

There is also a possibility that if the dyes are concentrating near the surface, self-quenching of the dye could be occurring too. Aggregation of cyanine dyes is known to lead to a quenching of the fluorescence of the dye due to formation of a dimer-triplet state.[177] Therefore a high concentration of dye at the electrode could lead to this type of quenching. This is not a problem in the bulk ionic liquid for two reasons: the dyes are in a low concentration, and solute ions in ionic liquid can be treated as *"completely separate, unrelated, highly screened species"*[178] and are "super-dissociated".[178]

The reason the dyes are postulated to move towards, rather than away from, the electrodes is mainly due to the way in which the counts from the dyes reappear. As the recovery of the counts proceeds first closer to the electrode, the dyes must be pulled towards the electrode, and upon release of the potential they diffuse away from the electrode upon release of the potential. If the dyes had been repelled from the electrode, then the recovery of the counts would occur first at greater distances from the electrode.

The Cy3 results at the same voltage shows a clear concentration dependence of the electrophoresis. Applying the same potential of +2 V and comparing the change in the counts shows that after the potential application, there is no Cy3 present 50 μm from the electrode in the 10 nM sample, however there is still dye present in the 100 nM sample.

Comparing the 10 nM Cy3 results with application of +1 V and +2 V, a voltage dependence of the electrophoresis can also be seen at all distances wherein a higher voltage leads to a quicker decrease in the counts at all distances.

This leads to the hypothesis that the long distance- and time-dependence of the results is be-

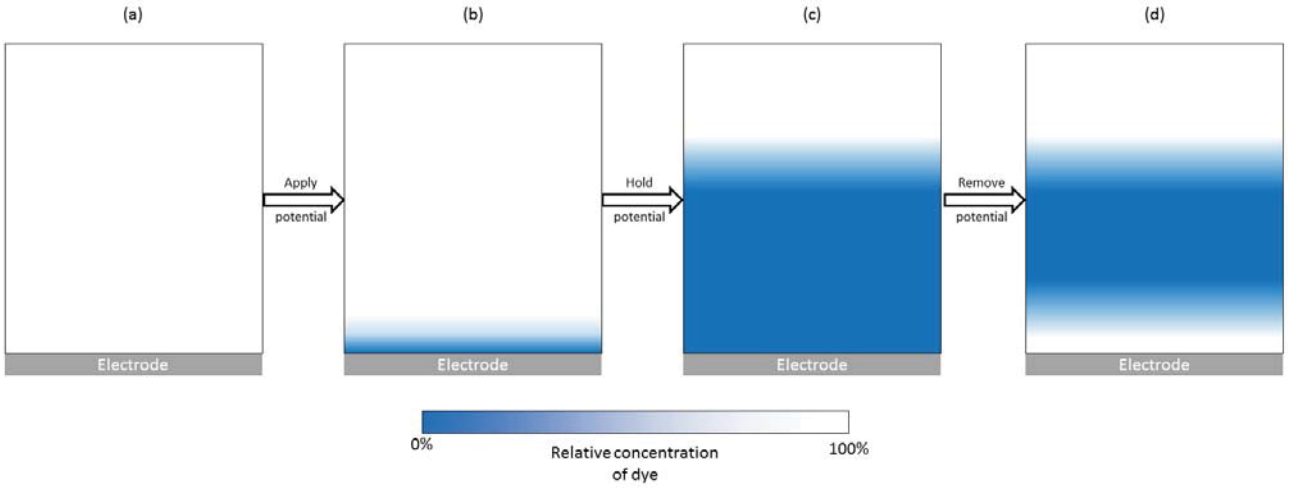

Figure 6.43: *Diagrammatic model of the proposed change in the counts through concentration changes.*

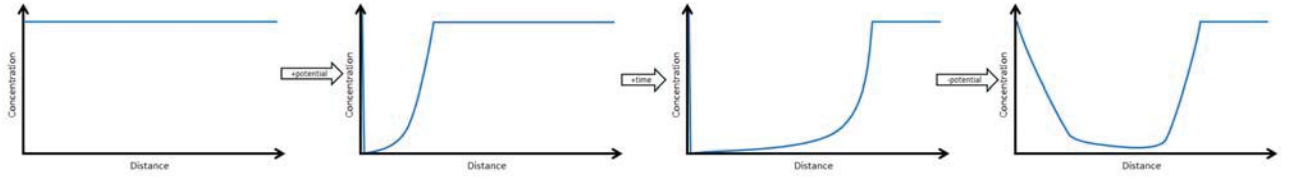

Figure 6.44: *Plots depicting the proposed concentration gradient over the experiment, with a darker colour meaning a greater decrease in the concentration.*

cause of a concentration gradient of the dye caused by the potential. This is shown as a diagram in Figure 6.43 and plotted in Figure 6.44.

Upon application of a potential, there is an immediate decrease in concentration close to the electrode, with the extent of the influence of this changing depending upon the voltage. Then, probably partially driven by the voltage, and partially driven by the low concentration of the dye near the electrode, dye at greater distances moves towards the electrode to replenish this absent dye. This dye is then pulled towards the electrode by the potential. This then extends the length of the concentration gradient, and thus pulls in more dye from further from the electrode.

The Cy3 results show that different concentrations lead to different scales of the effect. At higher concentrations, the concentration gradient does not extend as far away from the electrode, given a constant potential. The data from the different Cy3 concentrations at 50 µm after application of +2 V show this well. There is a decrease in counts which indicates electrophoresis of the dye occurs at 50 µm for 10 nM concentrations after ≈ 30 seconds, this is not seen as much in a concentration of 100 nM, where application of +2 V leads to a decrease in the concentration, but not down to the level of the blank ionic liquid.

Upon release of the potential, the dye is then in a high concentration at the electrode, and

begins to diffuse away. This gradually increases the counts again, with the increase occurring first at distances closer to the electrode. As the dye diffuses farther away and recovery is seen at greater distances, all distances show a similar rate of recovery of counts. This suggests that the concentration gradient for recovery is very shallow.

The conclusion that the dyes move towards the electrode under these conditions is unexpected. Cy3 is a positively charged dye, therefore should move away from a cathode and towards an anode; yet it is appears strongly attracted to a cathode, and not to an anode. BODIPY-C10 is a neutral dye, so should not be so strongly attracted to either an anode or a cathode; yet it is strongly attracted to an anode, and weakly to a cathode.

It is possible that the cause of this could be tied to the environment in which the dyes reside, however this seems unlikely. The results in Chapter 5 show that Cy3 lies within an anionic environment, therefore the movement of Cy3 could be tied to motion of the anions towards the cathode. Chapter 5 also shows that the BODIPY-C10 resides within the alkyl chains, which links the motion of the BODIPY-C10 to the cations. However, it is expected that the ions at the surface are not constantly being refreshed, due to a lack of significant faradaic current in the current traces. Therefore, motion of this kind should not occur, and the possible motion of the dyes should be considered.

The fact that the dyes are suspected to move towards electrodes also suggests that the dyes can be more preferentially incorporated into the double layer structure at the electrode than the ionic liquid ions. The reason as to why could be due to the lower charge density of the dyes. It is well known that the structure of ionic liquids at electrodes consists of multiple layers of alternating ions.[45] This is believed to be because the ions 'over-screen' the charge at the surface, therefore propagating the effect of the electrode further into the bulk than would be classically expected.

Incorporation of a less charge dense species could reduce the propagation of the charge into the bulk. A less charge dense species within the double layer will lead to less over-screening of the charge, and thus a lower propagation of the potential from the surface.

This is supported by research from Lynden-Bell *et al.* which shows that cationic species can have a negative free energy near a cathode in ionic liquids (see Figure 6.45).[179] This depends upon the size of the probe, as well as the charge at the cathode, but it can be seen that at a potential of +1 V there is an energy minimum at 0.4 nm and 1.1 nm for the larger probe. This shows that it is possible for a positive probe to be energetically favoured close to a cathode, with larger probes being *more* energetically favourable.

There was a slight energetic barrier found for the approach of a positive probe of $\approx 5kT$ for -1

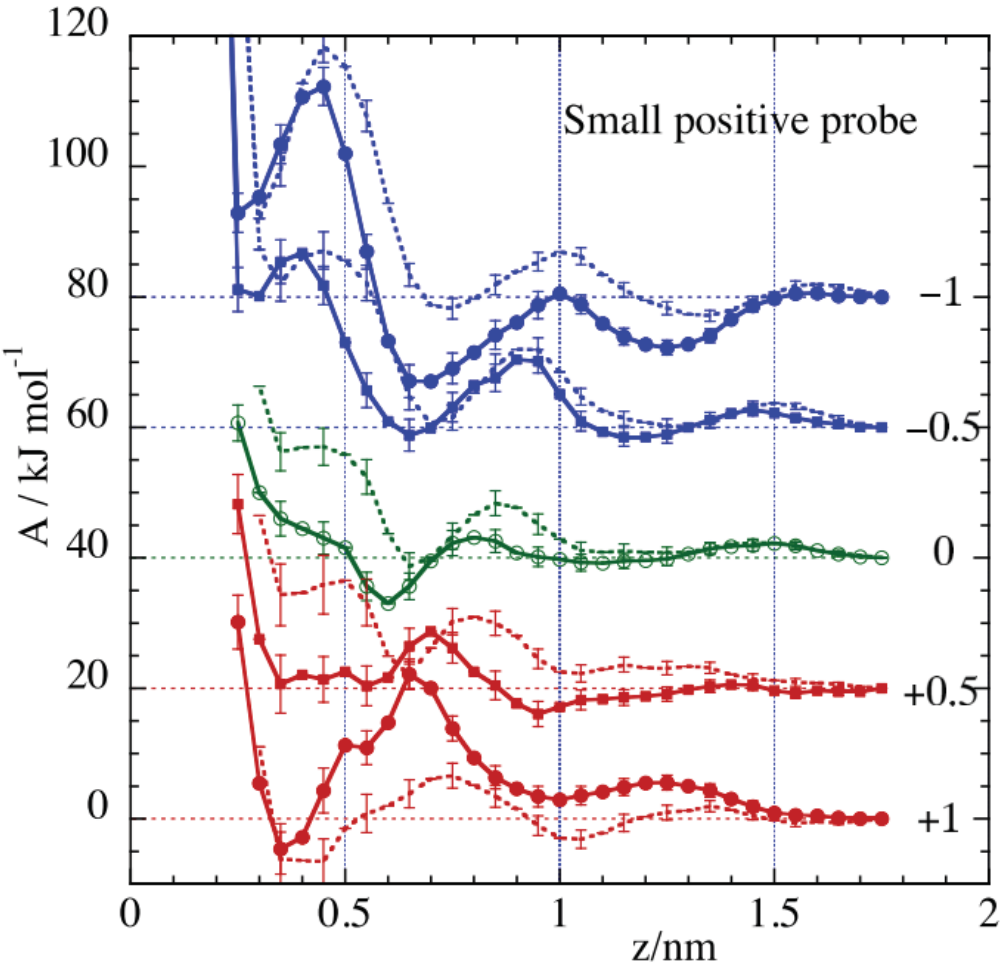

Figure 6.45: *Comparison of free energy profiles for small and large positively charged probes. The bold curves pertain to the small probes and the dashed curves to the large probes.*
Republished with permission of the PCCP Owner Societies, from Electrode screening by ionic liquids, R. M. Lynden-Bell, A. I. Frolov and M. V. Fedorov, Physical Chemistry Chemical Physics, 2012, ***14****, 2693; permission conveyed through Copyright Clearance Center, Inc.*

V, and $\approx 3kT$ for +1 V at the temperature of these calculations (298 K). This seems to increase with increasing probe size at an anode, and decrease with increasing probe size at a cathode. The existence of an energetic barrier at all could explain the slow accumulation of the effect, especially with regards to pulling in dye from greater distances.

The difference in the free energy at electrodes could explain the difference between the behaviour of Cy3 at anodes and cathodes, as for the large positively charged dyes, there is no energetic minimum at an anode, and there is one at a cathode.

When considering the neutral dye, BODIPY-C10, the 1-alkyl-3-methylimidazolium cations in ionic liquids are known to orient themselves perpendicular to an anode, with the alkyl chain stretched out away from the electrode.[179,180] Interestingly, Lynden-Bell *et al.* found that at an anode there was a minimum in the energy profile of a neutral probe (shown in Figure 6.46). This was found at a distance of 1 nm, the same distance at which the anion had an energy

minimum.[179] This suggests that instead of incorporating an anion into the second screening layer at the anode, it is possible that a neutral molecule can be incorporated, with little penalty to the energetics or screening.

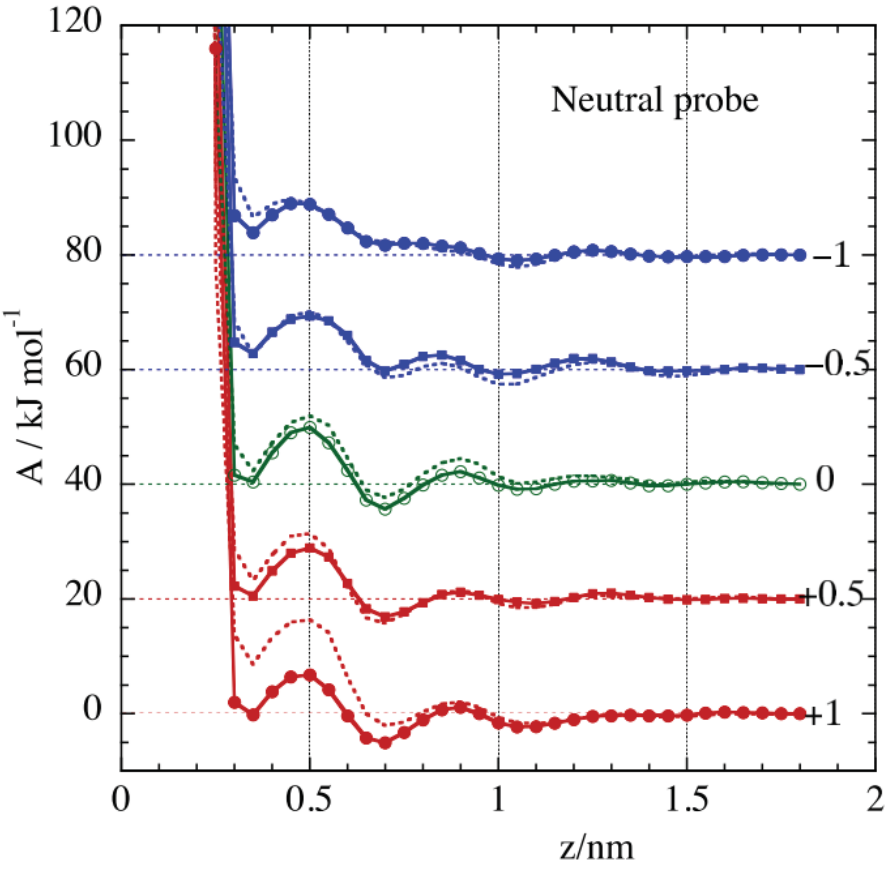

Figure 6.46: *Comparison of free energy profiles for small and large neutral probes. The bold curves pertain to the small probes and the dashed curves to the large probes.*
*Republished with permission of the PCCP Owner Societies, from Electrode screening by ionic liquids, R. M. Lynden-Bell, A. I. Frolov and M. V. Fedorov, Physical Chemistry Chemical Physics, 2012, **14**, 2693; permission conveyed through Copyright Clearance Center, Inc.*

The energetic barrier they found for approach of a neutral probe towards an anode was found to be $\approx 2kT$ at the temperature of these measurements (298 K), a relatively small energy barrier given the average kinetic energy of molecules is $\frac{3}{2}kT$.

The depth of this minimum also appears to decrease with increasing probe size, therefore for the large BODIPY-C10 there is a possibility that this could be a significant energy minimum to allow full incorporation of the BODIPY-C10 into the double layer structure at an anode.

At a cathode, there is a similar energetic barrier, however the depth of the minimum at $\approx$1.1 nm increases with increasing probe size. Therefore there is a lower energetic gain in the BODIPY-C10 incorporating into the double layer structure at a cathode, and the drop in counts is not as dramatic as for an anode.

Another possible hypothesis is that this aggregation of the dyes at the electrode is driven, at

least in part, due to the dye being an 'impurity' in the ionic liquid. It is well known that impurities in ionic liquids accumulate at surfaces, therefore the dyes could be pulled towards the surface due to some effect of the potential. However, as this does not occur for some dyes in some conditions, this is a less likely hypothesis.

Something that is consistent between dyes and is very interesting, is that there is a disconnect between what is occurring in the potential application/current measurement and what is happening with the counts i.e. changes in the potential show immediate changes to the current, but not immediate changes to the counts. This becomes more apparent with increasing distance between the measurement distance and the electrode.

This indicates that the current measurements are more indicative of the changes happening at the shorter distances, such as the formation of the double layer. The effects then propagate from the electrode, into the bulk of the ionic liquid. These take time to propagate, therefore there is a delay between changes to the potential and changes in the dye. Combined with the long time-scales, this is evidence of a diffusion controlled process.

This does not interfere with the hypothesis that the dye is slowly being incorporated into the double layer. This is because the incorporation of such low concentrations of dyes into the double layer would not lead to any measurable change in the current trace over time.

One interesting point to note is that the time-scale associated with the decrease in the counts upon application of the potential is always shorter than the time-scale associated to the recovery of the same magnitude. This suggests that the decrease during the potential application occurs with a strong force that is driving the system away from the initial, equilibrium state. The longer time-scale for the recovery of the counts indicates this is a slow diffusive change with no great driving force other than an entropic drive back to equilibrium.

What is consistently astounding is the extent to which this effect occurs. In all of the measurement conditions, changes to the counts propagate 50 μm from the electrode. Previous measurements of structures of ionic liquids at electrodes found these usually extend 10 nm away from the electrode, but some forces have been seen to extend up to 30 nm (Section 2.2.2).[56]

Here, depletion of the counts does extend to all distances measured, however changes to the lifetime (when they can be measured) do not. This also indicates that the cause in the change of counts is unrelated to the changes in the lifetime.

6.4.2 Change in Dye Lifetime

While the data on the lifetimes of the dyes cannot directly show what is causing an increase in the viscosity, based upon the knowledge of where the dye resides in the ionic liquid, as well as considering the trends in the lifetimes, hypotheses can be drawn.

When considering BODIPY-C10 in $[C_4C_1im][NTf_2]$, the dye lies between the polar and non-polar domains, though the decyl chain means this rotor should be more associated to the neutral, non-polar domain. In $[C_4C_1im][NTf_2]$ Cy3 partitions mostly into the anions, and although has to sample some non-polar moieties, the lifetime should be closely related to the flexibility of the mostly-anion cage around the rotor.

Application of a potential could lead to a minor increase in the interactions between the ions, thus leading to an increase in the viscosity. If this were the case, then the change in the viscosity reported would be more similar to that of a temperature-dependant effect, thus the change in viscosity would be taken from the variable temperature measurements in Sections 5.3.2 and 5.3.3.

There is also the possibility that the potential application causes a change in the partitioning of the dye between the polar and non-polar regions. If this were the case, then the change in the viscosity reported would be more similar to that of the viscosity changing due to a change in the ionic liquid cations, thus the change in viscosity would be taken from the variable cation measurements in Section 5.3.2 and 5.3.3.

Equally, the change could be due to a combination of these factors, and the choice of which 'calibration' should be used to report upon changes to viscosity is not clear.

Although the change in the lifetime of Cy3 leads to relatively large changes to the reported viscosity, the large amount of noise and uncertainty about the changes to the lifetime mean that this is not the best data to make predictions with.

Nevertheless, a hypothesis can be drawn. While the initial change in the lifetime is greater at closer distances to the electrode, the trend in the recovery appears to be approximately the same between the distances of 1-25 μm.

Unpublished results from a collaborator, who has studied Raman spectroscopy of neat ionic liquids near an electrode, provide a likely hypothesis.[181] They observe what appears to be an increase in the density of the ionic liquid near the electrode. An increase in the density would likely lead to a constriction of any ion cage-like structure, which would lead to a greater restriction to motion of the rotor, Cy3, and thus an increase in the lifetime and reported viscosity.

Assuming this hypothesis is correct, it appears that initially this increase is greater at distances

closer to the electrode, which is logical as the electrode can more easily affect distances closer to it. As the experiment continues, this effect manifests next at 10 μm and 25 μm. However, in the timescales of these experiments, no significant change to the lifetime of the Cy3 is observed at 50 μm, indicating this effect does not propagate that far away from the electrode. This leads to more ions crowded near the electrode, which becomes important when considering the recovery of the lifetime. A major reason the density increase seems reasonable is due to the increase in the contribution from the ionic liquid component. If the density of the ionic liquid does increase, and the long lifetime (≈5 ns) component is related to the cations and anions in the ionic liquid, then it is logical that this component would increase in its contribution to the overall lifetime decay. To re-iterate a statement from earlier, this component is definitely not related to Cy3, as the lifetime is far too long.

Upon release of the potential, after an initial equalisation of the lifetimes, the recovery appears to proceed at approximately the same rate regardless of the distance from the electrode. If an increase in density is present at all distances upon removal of the potential, there will be an 'easing' of the ionic liquid back towards its pre-potential, equilibrium density. The data suggest that this 'expansion' of the ionic liquid occurs simultaneously across the region where the density has increased i.e. the region which has an increased density expands equally at all distances from the electrode.

However, to confirm this, as mentioned in Section 6.2.3 more measurements would be needed in order to reduce the noise, and confirm if these trends are accurate. This could be achieved by either using Cy3 in higher concentrations or using a different, positively charged dye. A possibility that has been proposed for a new dye is to use an analogue of BODIPY, with a positively charged group e.g. a quaternised ammonium instead of a decyl chain. A negatively charged analogue could also be made using a carboxylate group instead of the decyl group, and this would lead to 3 dyes of similar structures but different charges.

Considering the BODIPY-C10 lifetime, the rate of recovery of the lifetime shows a different trend when comparing to the rate of recovery of the counts at different distances. The recovery in counts for these samples proceeds at a similar rate between 1 μm - 25 μm for BODIPY-C10, whereas the lifetime recovers faster at greater distances from the electrode. This is opposite to the trend seen in the recovery of the counts in other samples, wherein the recovery of the counts also occurs first at distances closer to the electrode.

What this means is that structural change in the ionic liquid, which causes the increase in the viscosity reported by BODIPY-C10, breaks down at greater distances from the electrode first. This 'recovery' then moves towards the electrode, causing the lifetime to decrease at greater

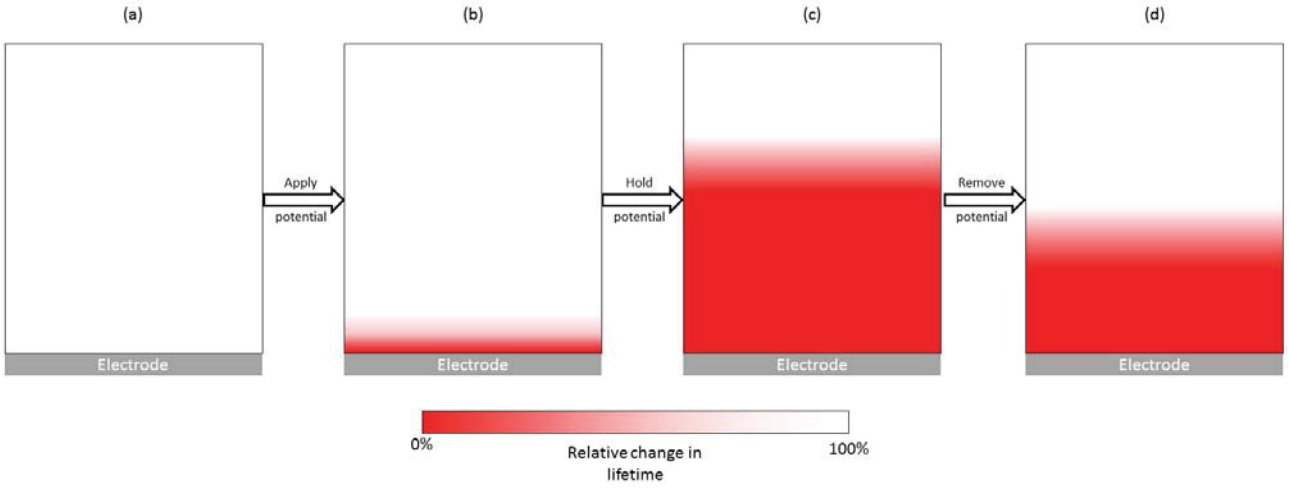

Figure 6.47: *Diagrammatic model of the proposed extent of the change in the structure which leads to an increased lifetime of the rotor, with a darker colour meaning a greater change in the lifetime.*

distances first, as shown in Figure 6.47.

The relatively constant, high lifetime at the electrode after removal of the potential also shows that there is a meta-stability to this structural change in the ionic liquid. If this were not the case, then the recovery would occur at a similar rate across all distances as is seen with the Cy3 data.

While the changes in the lifetime of BODIPY-C10 are less dramatic than the changes in the counts, they still occur at a similarly unexpected long distance from the electrode and persist for an immensely long time. This meta-stability could be the cause of the long time for which the changes to the lifetime persist, as a metastable structure can be formed quickly, but requires a long time to reverse back to the original structure.

An interesting observation from Figure 6.37 is that the pre-potential lifetime is greatest at 1 μm, then 10 μm, and constant at 25 μm and 50 μm. This is indicating that there is a possibility of a difference in the viscosity of the ionic liquid nearer to the electrode in the absence of an applied potential.

It is known that ionic liquid ions form structures at electrodes in the absence of potentials.[45] Therefore it is possible that these structures lead to a different viscosity reported by the molecular rotor. However, structures that have been measured at neutral surfaces (uncharged electrode interfaces) were previously not found to extend so far into the bulk. This further adds to the mystery of the phenomenally long-range propagation of effects of electrodes into the bulk reported here.

One possible hypothesis behind the increase in viscosity experienced by the BODIPY-C10 is that the potential causes a 'direct rotational alignment', or a 'preferential rotational alignment'

of the ions within the ionic liquid. As BODIPY-C10 reports on the microviscosity of the non-polar region, this would likely arise as a rotation that disrupts the non-polar region.

In a 'direct rotational alignment', the potential directly causes the ions to change their rotational alignment, and align with the electric field lines or with each other.

'Preferential rotational alignment' would be best described by considering ions as still rotating somewhat freely. However, instead of a strict alignment, the ions instead spend a slightly greater fraction of their time in a preferential rotational configuration (i.e. aligned with the electric field lines) than in other rotational configurations. Such a preferential rotational alignment has been seen before in experiments on ionic liquid mixtures, where the cations were seen to spend slightly more time in certain rotational orientations with the energies associated to this being very low ($<$2 kJ mol^{-1}).[182]

Equally, a combination of these effects could occur. Near the electrode, direct rotational alignment could be caused by the high potential. Further away, where the potential is weaker and more screened by the ions, there could be a preferential rotational alignment.

If this were the case, then more rotated ions near the surface can directly, or indirectly cause the propagation of the rotation further away from the electrode. A direct effect could be an ion-ion interaction wherein one ion aligns with the electric field lines causes a second, nearby ion to align with the first, similar to a dipole-dipole interaction.

Equally, a rotated ion could be much worse at properly screening the charge from the electrode, leading to further propagation of the potential into the system, causing more ions to align. This could either be due to a reduction in the screening, or a possible increase in over-screening.

This hypothesis of rotational alignment can also lead to the meta-stability of the system. Once an ion, or a group of ions, has aligned to a certain rotation through interactions with neighbouring ions, it could also hold the neighbouring ions in the rotated state. Thus it is the rotated ions which hold the rotation of the ions relative to each other.

Once the potential is removed, the propagation of this structure will slow down and eventually halt due to the lack of a driving force. There will then be an entropic drive for the system to return to a freely rotating state. This cannot easily occur near the electrode, as the ions are all holding each other in the rotation. However, at greater distances from the electrode, where direct rotational alignment has not occurred, the preferential rotational alignment can easily break down, reducing the viscosity.

As with the counts, the time-scale associated with any increase in the rotor lifetime is always shorter than the time-scale associated to a decrease of the same magnitude. This confirms that the increase of the lifetime occurs with a strong driving force, and the relaxation is a slow

change with an entropic drive back to equilibrium.

Comparing the hypotheses behind the proposed increases in viscosity for Cy3 and BODIPY-C10, these are very different in nature. It may be possible that they are not competing, and that simultaneously the density of the polar region could be increasing, which forces the non-polar region to also constrict and change the orientation of the ions. However, given the different structures of the dyes, and the uncertainty attached to the Cy3 results, it is possible that there are some subtle effects or trends missed here due to poor or missing data.

It does appear though, that with high certainty I would say that a viscosity change in the ionic liquid does occur near an electrode upon application of a potential. Given the conclusion that a change in the viscosity of the ionic liquids occurs, and that this could arise due to a change in the rotational orientations of the ions, there is one experiment within the literature that warrants discussion. Ma *et al.* observed changes in the rotational reorientation of dyes near to a charged surface (silica) in ionic liquids by studying the fluorescence anisotropy decay. This change in the rotational reorientation was shown to extend far into the bulk of the ionic liquid ($\approx$100 μm).[183,184]

The rotational diffusion dynamics can be calculated using the Debye-Stokes-Einstein model, Equation 6.3

$$\tau_{\mathrm{OR}} = \frac{\eta V f}{k_B T S} \tag{6.3}$$

where τ_{OR} is the decay time constant of rotational reorientation, η is the viscosity of the medium, V is the hydrodynamic volume of the reorienting entity, f is a frictional boundary condition term, k_BT is the thermal energy, and S is a shape factor to account for the ellipsoidal shape of the rotating species.

They concluded that changes they observed in τ_{OR} must come from a change in V due to changes in the ion pairing, as f, S, and k_BT are constants, and:

> *there is neither evidence nor precedence to suggest this term [viscosity] varies with proximity to a silica surface; it is a bulk property of the IL.*[183]

Here, evidence for a change in the viscosity of an ionic liquid near a charged surface has been presented. Not only is this a significant change in viscosity, but it has been measured by the study of the change in the rotational freedom of molecules, making these results especially important in the context of the rotational diffusion dynamics.

In order to confirm the results discussed here, a study of rotational orientation, and rotational dynamics at an electrode interface need to be conducted taking into account a possible change

in the viscosity of the ionic liquid. This could be complemented by studies of the structuring of the ions in the region of 10->25 μm away from an electrode to directly determine if such a rotational alignment exists.

Limitations with Lifetime Measurements

One of the limitations in these experiments is that they are not very time sensitive. This is due to the way that the data has to be processed before being analysed. When collecting the delay data to make the fluorescence lifetime decay, this is collected as one data point per repetition of the laser (20 MHz). Once collected, many of these delay data have to be combined into one histogram to create and fit the fluorescence lifetime decay.

The limitation with this technique is that, in order to generate a sufficiently good fluorescence lifetime decay that has a low enough amount of noise that it can be analysed, a lot of data points are needed. Even though 20 million data points are generated every second, this is not enough to make a high quality fluorescence lifetime decay, which is why each data point contains data from 30 seconds (one bin), as this is the shortest time which can create a good enough fluorescence lifetime decay that the data can be analysed.

The downside of these large bins is that changes to the lifetime which happen over a short period of time are not able to be measured. For example, if the lifetime of a rotor increases by 0.01 ns per second upon application of a potential, this cannot be observed using this technique. Instead, each bin contains a convolution of all of the values of the lifetime measured. If this lifetime is constant, then this is not a problem, but if it changes rapidly, then what is calculated is a convoluted average of all of these.

Therefore, while these results do show a change in the lifetime, the rapid build-up of this effect cannot be investigated using this technique. This means that if more precise measurements of the time-scales associated to these changes are required, then another technique which can measure on shorter time-scales is needed.

6.5 Post Field Application

Something that was noticed during the measurements involving electric fields was that post-experiment, there was a drift of the voltage towards the measurement voltage.

After the potential application, the cell is not shorted. Instead the potential difference between the electrodes is set to 0 V (the OCP) for 10 minutes in order to allow the cell to discharge. After this 10 minute period, the potentiostat was turned off i.e. the potential difference between the electrodes was no longer being forced to 0 V. Neither of these processes constitute a direct shorting of the cell.

Often the laser measurements would take longer than the electrochemical measurements to complete, and the potentiostat would still report the potential and current across the cell after the 10 minutes of holding the potential difference across the cell at the initial OCP. It was noticed that this voltage would slowly drift from the OCP towards the voltage which the measurements were run at, and this occurred with no noticeable current e.g. if the cell was set to -2 V during the measurement, the voltage after the 10 minutes of OCP would slowly decrease, with the current remaining <0.1 nA.

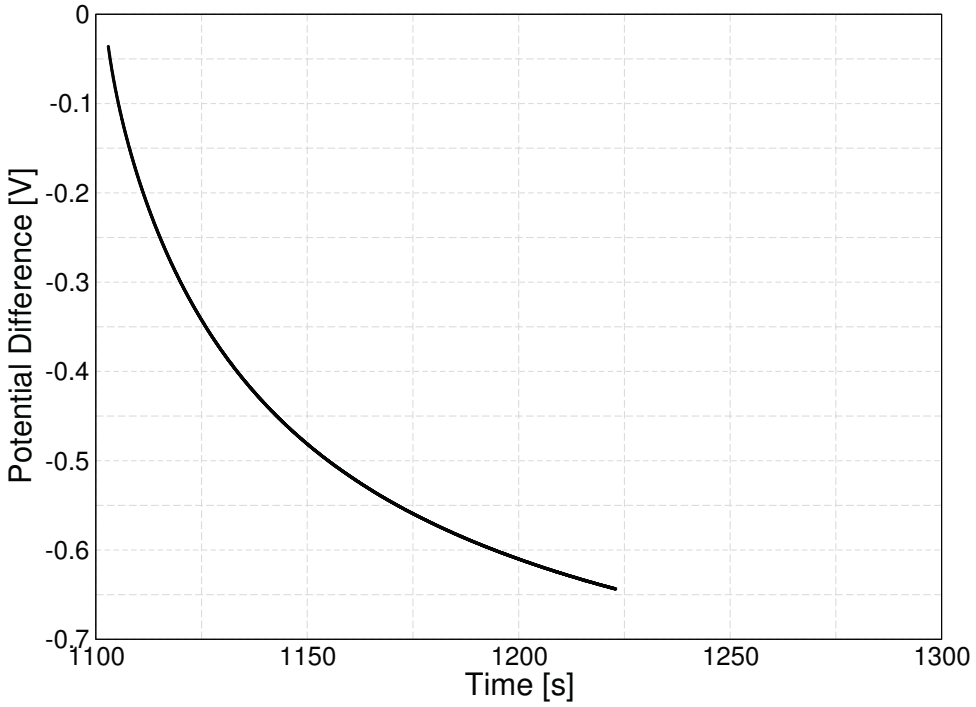

Figure 6.48: *Example of the drift of the voltage towards the measurement voltage after removal of the potential. This experiment is the application of -2 V to a 100 nM solution of BODIPY-C10 in* $[C_4C_1im][NTf_2]$ *shown in Figures 6.41a and 6.41c.*

What this is showing is that the changes occurring within the cell during the application of the potential lead to a different OCP, and these changes are stable enough to persist even after 10

minutes of holding at the previous OCP. What is strange about this is that, from the current traces from the measurements, it seems that the cells appear to charge and discharge very quickly.

A different OCP is not necessarily an unexpected result, given what is known to occur at an electrode-ionic liquid interface upon application of a potential. It is known that at such an interface, there is some structure formed, even in the absence of a potential.[46] Application of a potential causes ions of the opposite charge to move towards the electrode, and this causes a change of the structure at the interface. Immediately upon release of the potential, this different structure at the electrode is expected to persist for a short amount of time, and thus a measurement of the OCP will lead to a different result.

What is unexpected though is the time which this persists for. Given the fact that the current graph suggests the cell is almost completely discharged within the first 30-60 seconds, the fact that a different OCP is seen after 10 minutes of attempting to discharge the cell is further evidence towards the meta-stability of the effects of the potential. Not only does this manifest in delays and long time-scales to changes to the concentration and lifetime of the dye, but the electrochemical measurements too.

As the changes to the dye seem to be somewhat linked to the time-scale of the different OCP, the dye can be used to try to investigate the time-scales associated with this. One would expect that when the lifetime and counts reach their pre-potential values, the cell has completely discharged and the measured OCP at this time would be equal to the initial OCP value.

To investigate this, measurements of the dye were performed while holding the cell at 0 V for longer. Due to the time required for this, the measurement could only be performed once, so it was decided to probe the recovery of BODIPY-C10 at 25 μm after application of +2 V. This way, the recovery of the counts and the lifetime could be investigated at a long distance from the electrode.

Figure 6.49 shows the progression of the counts per second during this experiment. Due to the large file size this created, there is a gap in the middle of this graph where the file size limit was reached and the computer stopped recording. The recording was restarted when this was noticed and the time difference used to offset the measurements.

From this graph it can be seen that the recovery of the counts of the dye still does not fully complete, even after holding the cell at 0 V for nearly 3 hours. While initial recovery is slow, the rate of the recovery slows down with time, appearing asymptotical to the level of initial counts. As there are more data points here than in previous experiments, an equation can be found to describe the recovery of the counts.

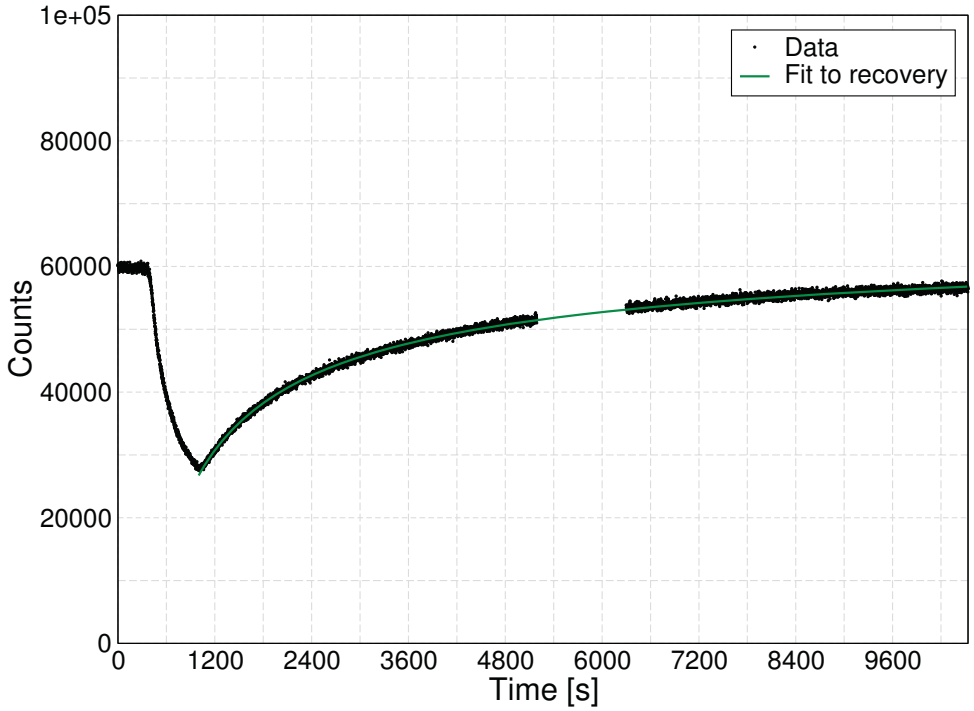

Figure 6.49: *Progression of the counts of a 75 nM sample of BODIPY-C10 in $[C_4C_1im][NTF_2]$ upon holding at 0 V after application of +2 V. The green line is the fit to the data after removal of the potential, shown in Equation 6.4.*

The recovery data, from the point at which the counts begin to increase onwards, can be fitted to a power law function. The green line in Figure 6.49 shows the fitted power law, which is:

$$C = -1.972 \times 10^6 \times t^{-0.5606} + 6.78 \times 10^4 \tag{6.4}$$

where C represents the counts, and t is the time.

When considering the lifetime, shown in Figure 6.50, there is a steady increase of the lifetime during the application of +2 V potential, as before. Upon setting the potential to 0 V, there is a decay of the lifetime towards the value of the lifetime before the application of the potential. As with the counts, there is more relaxation data than previously collected, therefore this data can be better fitted to an equation. The relationship between the lifetime and time also follows a power law. The green line in Figure 6.50 shows the fitted power law, which is:

$$\tau = 20.04 \times t^{-0.806} + 1.089 \tag{6.5}$$

where τ is the dye lifetime in ns, and t is time in seconds.

The recovery of the lifetime has a similarly long time-scale to that of the counts. However, from the equations of fit, these two do not occur at the same rate. The recovery of the lifetime has a greater power in its fit, therefore this shows that the lifetime recovers faster than the counts

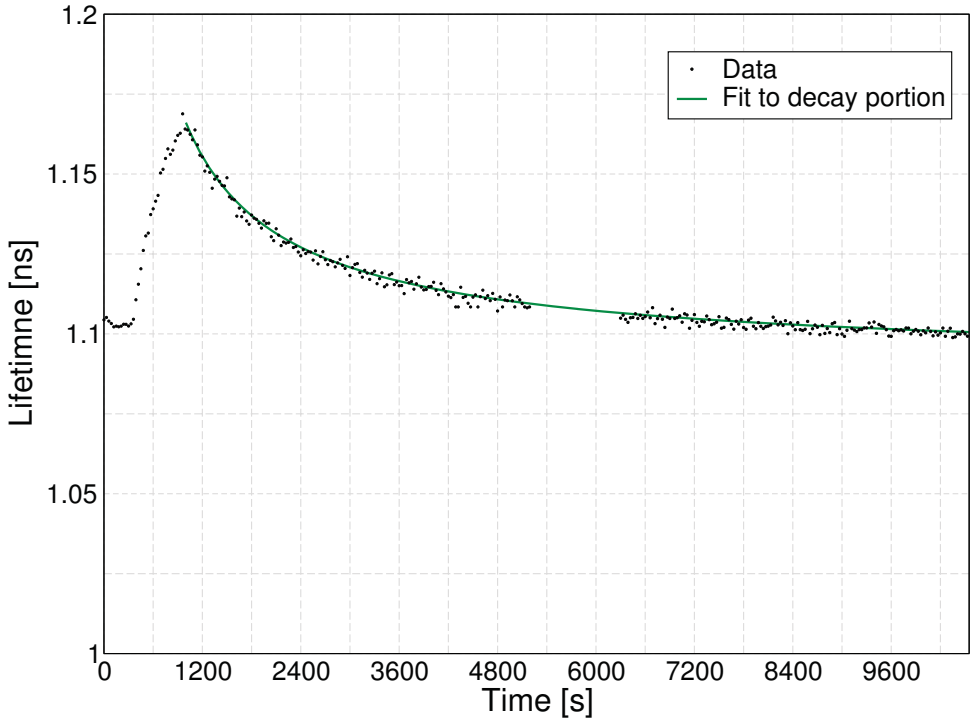

Figure 6.50: *Progression of the lifetime of a 75 nM sample of BODIPY-C10 in $[C_4C_1im][NTF_2]$ upon holding at 0 V after application of +2 V. The green line is the fit to the data after removal of the potential, shown in Equation 6.5.*

in this experiment.

Extrapolating the power law fit, the counts will reach the pre-potential level of counts (60,000) after ≈19,000 seconds. In contrast, the fit to the lifetime shows that the lifetime reaches its pre-potential average of 1.103 ns after ≈8,200 seconds.

The fact that both the lifetime and counts change over a much shorter time than the system recovers over confirms that the application of the potential leads to a strong driving force for change. Conversely, upon removal of the potential, there is no strong driving force for the system to return to equilibrium, so this occurs over a much longer time.

The consistent difference between the counts and lifetime is proof of a hypothesis alluded to in Section 6.4 but not explicitly stated. This hypothesis is that the change in the lifetime and the change in the counts must arise from **different** phenomena. Both of these have extremely long time-scales associated with them, however they are different in nature.

6.6 Holding Potential

Alongside the long time-scales associated with these measurements, it is possible that the distance to which the effect propagates is dependent upon the time for which the potential is applied.

To investigate this, fluorescence measurements were performed wherein the potential was applied for different amounts of time. These measurements were all compared at 50 μm in order to observe this effect at the longest distance which the setup could measure.

The compared experiments involved holding a cell containing BODIPY-C10 in $[C_4C_1im][NTf_2]$ at +2 V. The samples compared have the potential applied for 2 minutes (previously shown in Section 6.3.1), 10 minutes, and 60 minutes.

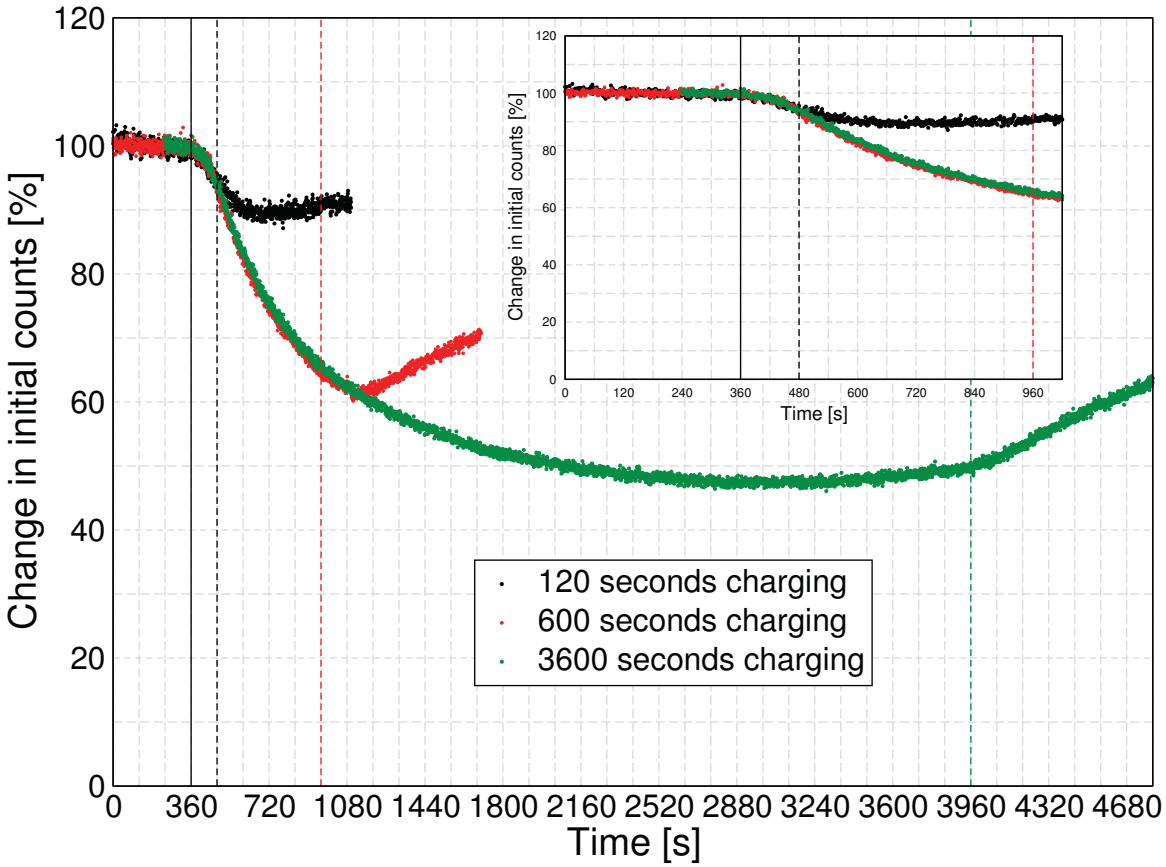

Figure 6.51: *Counts of samples of BODIPY-C10 in $[C_4C_1im][NTf_2]$, represented as a percentage of the initial counts, upon holding the potential for 2 minutes, 10 minutes, and 60 minutes. Plots are normalised in the x axis so the solid black line shows a consistent time for application of the potential. Dashed vertical coloured lines show the time at which the relevant coloured plot has its potential removed.*

Figure 6.51 shows the evolution of the counts over the different potential application time experiments. Due to a dilution error, the concentrations, and thus the number of counts differ between the samples. Therefore the samples are normalised to a percentage of the initial level

of counts, before the application of the potential.

This shows that the same trend is followed regardless of the time for which the potential is applied. Upon application of the potential there is a decease in the counts, with a slight delay between the application of the voltage and the beginning of the decrease of the counts.

All samples, regardless of the time for which the potential is applied, follow the same trend. During the application of the potential there is a steady decrease in the counts that gradually levels out at ≈3,000 seconds. Upon the potential being released and set to 0 V, each sample shows a subsequent increase in the counts after a delay.

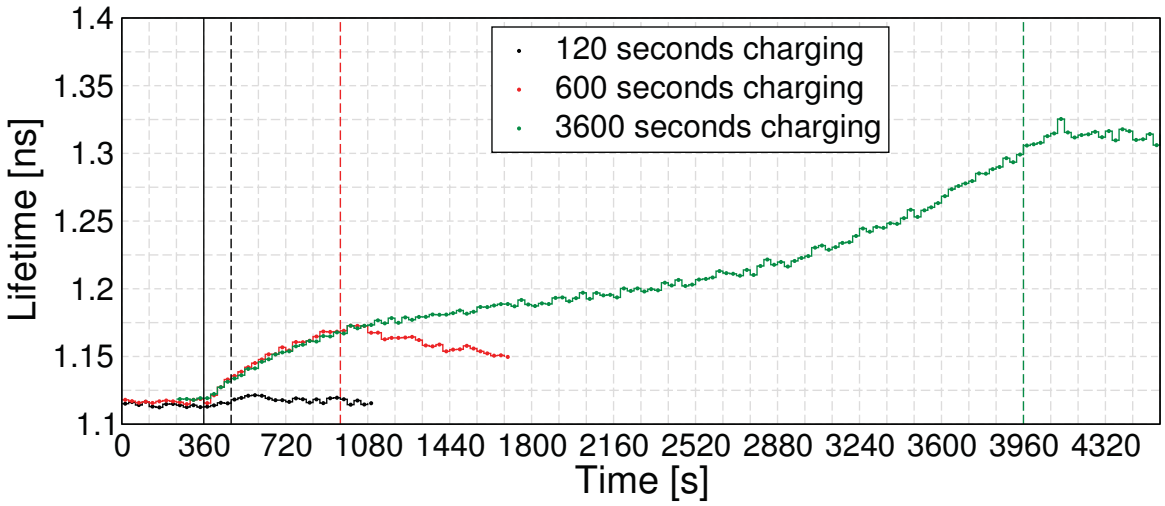

Figure 6.52: *Lifetime of samples of BODIPY-C10 in [C_4C_1im][NTf_2], upon holding the potential for 2 minutes, 10 minutes, and 60 minutes. Plots are normalised in the x axis so the solid black line shows a consistent time for application of the potential. Dashed vertical coloured lines show the time at which the relevant coloured plot has its potential removed.*

When considering the lifetime of BODIPY-C10 in these samples, shown in Figure 6.52, these show that application of the potential for a longer amount of time does cause increases in the dye lifetime where large changes are not previously seen. Holding the potential for a long time does cause large changes in the lifetime of the dye at 50 μm, however even after 1 hour of charging the lifetime hasn't fully plateaued.

What this does show is that, for the greater distances from the electrode, the magnitude of the effect seen is highly dependent upon the amount of time for which the potential is applied for. This is likely more of an important factor at longer distance from the electrode, although this has not been tested in this thesis.

This result does show that it may be possible to see some/more changes at longer distances if the potential is applied for longer. It is therefore important to note that the results presented and discussed in Sections 6.2-6.4 all have a caveat of "2 minutes of field application" attached, and may differ if this time is altered.

Chapter 7

Simulations of Ionic Liquids in Electric Fields

In this chapter, molecular dynamics simulations of two ionic liquids, 1-butyl-3-methylimdazolium bis(trifluoromethylsulfonyl)imide ($[C_4C_1im][NTf_2]$) and 1-octyl-3-methylimdazolium bis(trifluoromethylsulfonyl)imide ($[C_8C_1im][NTf_2]$) were performed to study changes in these ionic liquids in electric fields.

It must be noted that these results do not directly relate or replicate the experimental results, and they are not designed to do this. In the experiments, the phenomena seen involve build-up of an effect near a barrier, which is not present in these simulations due to the presence of periodic boundary conditions. In addition, the experimental effects occur over such long time- and length-scales that cannot be investigated using molecular dynamics. Instead these simulations are to be used to ascertain what *could* be occurring in an ionic liquid in an electric field, and these can then guide further experimental studies.

Some of the work presented here has already been published in the paper:

Effect of an External Electric Field on the Dynamics and Intramolecular Structures of Ions in an Ionic Liquid R. Clark, M. von Domaros, A. J. S. McIntosh, A. Luzar, B. Kirchner and T. Welton, *J. Chem. Phys.*, 2019, **151**, 164503.[2]

7.1 Introduction

While obviously very useful, there is a limitation to experimental studies in that, depending on the technique being used, it can be difficult to know everything that is occurring and affecting the experiment. Often, as with much of the work presented here in Chapters 5 and 6, measurements are made and then based upon the results, inferences are drawn about what is occurring. These ideas can then be tested by other means, and the cycle of the scientific process repeats. While very often these interpretations are correct, it can be useful to supplement this knowledge of what is occurring when rationalising experimental results with more concrete knowledge of the way molecules and ions can be affected by certain conditions.

This is where molecular dynamics simulations can be a very useful additional technique that can complement measurements. The molecular dynamics simulations, while also having limitations of their own, can give valuable insight into what *could* be occurring on a molecular level in experiments. Taking this approach and mindset, it is not necessary for molecular dynamics simulations to be able to replicate experimental conditions and results exactly. Close replications of experimental conditions can be good enough to give an idea as to what is occurring, and can aid in the design of new experiments to explore possible conclusions.

The difference between molecular dynamics and Monte Carlo methods should be noted. Both are methods to simulate equilibrium conditions, but approach the problem of how to find a thermodynamic equilibrium in different ways. Molecular dynamics involves a strict, sequential sampling method to find the time-dependent evolution of a system and does not require an assumption of ergodicity. Monte Carlo methods involve an aspect of pseudo-random sampling to generate the ensemble, assuming that the system being studied is ergodic. Herein, this thesis is only concerned with time-dependent molecular dynamics simulations.

Molecular dynamics involves using models which represent real atoms, and calculating how they interact to ascertain properties of materials. Perhaps the simplest of these systems is the Lennard-Jones fluid, a non-bonding fluid of particles interacting via the Lennard-Jones potential only. This is a very basic model and is not very useful for much more than teaching students how to run simulations and simulating noble gases.

Regardless of model choice, once an interaction potential is chosen, the motion of the particles needs to be calculated. The most basic method for this is to use the velocity-verlet algorithm (or other similar approaches such as the leapfrog algorithm), which calculates the motion of

bodies using Newton's equations of motion

$$\ddot{x}_i(t) = \frac{F_i(x(t))}{m_i} = a_i(t) \tag{7.1}$$

where the acceleration of a particle, $\ddot{x}_i(t)$ or $a_i(t)$, is calculated based upon the total force on a particle, $F_i(x(t))$, divided by its mass, m_i.

The basic principle of the verlet or velocity-verlet algorithm is to take a particle of known position at time t, $x(t)$, and calculate the new position at a small time later, $x(t + \delta t)$. This can be achieved by a Taylor expansion of the new position after the time-step, δt, as

$$\begin{aligned} x(t + \delta t) &= x(t) + \dot{x}(t)\delta t + \frac{1}{2!}\ddot{x}(t)\delta t^2 + ... \\ x(t + \delta t) &= x(t) + v(t)\delta t + \frac{1}{2}a(t)\delta t^2 + ... \end{aligned} \tag{7.2}$$

therefore with knowledge of a particle position, velocity, $v(t)$, and the net total force on the particle, the movement of said particle can be modelled over time.

Implementations in software packages vary depending on the complexities of implementation in order to minimise errors or increase customisation of the algorithm, so will not be discussed. What is clear, even in this simplistic example, is that accurate knowledge and modelling of the force on a particle is a key step in order to produce accurate simulations.

This is discussed in detail in Section 7.1.2 with regards to ionic liquids, but briefly, molecular dynamics simulations employ a 'force field' to parametrise the interactions between particles in a simulation. What the simulation software will do is, given an initial configuration of the simulation (which can easily be built with open-access software), use a version of this style of equation to propagate the initial conditions until the system has reached a thermodynamic equilibrium.

As molecular dynamics simulations are inherently time-dependent, they assume that the simulation is in a thermodynamic equilibrium. This means that when sampling a molecular dynamics simulation, data points are assumed to represent a thermodynamic/statistical ensemble. An ensemble is an ergodic (time-independent), isotropic (direction-independent) representation of a system.

In practice, molecular dynamics simulations cannot sample 100% of an ensemble. The amount of data required for this is massive, therefore simulations are run for a period of time and independent data points collected from this. Enough data points need to be collected that the sampled trajectory can be representative of the ensemble, and significant conclusions drawn

from this.

Knowledge of what makes a 'good' set-up for a molecular dynamics simulation of an ionic liquid is vital, in terms of the force field, the simulation parameters for an ensemble and some experimental results with which to compare the simulation results. These will be explored in the rest of the introduction to this chapter, along with some development and discussion on thermostatting procedures (Sections 7.2 and 7.3).

7.1.1 Literature Simulations of Ionic Liquids in Electric Fields

As ionic liquids are conducting liquids which have high ion concentrations, a number of studies on ionic liquids have focused on possible electrochemical uses.[10,185,186] In these particular applications, it is important to understand how ions within the ionic liquids behave under the effect of external electric fields. This leads to molecular dynamics studies being the best way to understand the motion of the ions on an atomic level in an electric field.

As a relatively new field, there is still a lot of progress in both simulation techniques and studies of the fundamentals.

There is a study by Petravic and Delhommelle on molten NaCl, which although is not on an 'ionic liquid', is useful as it brings forth some important concerns which need to be addressed when studying high ion concentrations in electric fields. They consider a few different types of thermostats that could be used when performing simulations of ions in electric fields.

They see that when applying electric field strengths greater than 0.25 $V Å^{-1}$, there are differences in the current density, conductivity, potential energy and kinetic temperature depending on which thermostat was chosen.[187] While they were unable to directly compare these results to experimental results to determine a 'best' thermostat, they did make some interesting observations.

They discovered that a configuration-based thermostat gave the most consistently logical results, mainly due to the fact that this method of calculating temperature does not have any consideration of ion motion. This means that the increase in motion of the ions forced by the electric field did not interfere with the thermostat directly.[187]

The thermostats they tested that did consider some kind of kinetic temperature showed a smaller response to an electric field than the configurational thermostat. A 'global' thermostat showed a much weaker response to an electric field and even showed a decrease in the temperature relative to the thermostatted value in directions perpendicular to the field.[187]

This was due to a 'freezing effect' where the motion of the electric field is included in the temperature passed to the thermostat. The thermostat then took the increase in motion caused by the electric field (which is the exact response that was desired) and attempted to compensate by cooling the whole simulation, without any consideration of the anisotropy, hence incorrectly overcompensating.

The other two kinetic thermostats they investigated involved accounting for this anisotropic increase in ion motion calculating flow temperature and removing it from the temperature (creating a new moving reference frame for thermostatting), and by ignoring the direction of flow and calculating temperature using the motion perpendicular to the field only.[187]

A discussion comparing these thermostatting methods and how they apply to this system is present in Sections 7.2 and 7.3.

One other useful observation they made was that when being affected by the electric field, the momentum of the cation and the anion must remain exactly opposite in order to allow for conservation of momentum *and* charge neutrality.[187] This is the Sundheim rule, that the ratio between the masses of the ions is the same as the ratios between the velocities of the ions, and must necessarily be followed.[188]

Surprisingly, a large number of the studies in the literature do not appear to take these considerations of anisotropic motion, thermostatting, or even the fact that the ions within the system will have a different motion to equilibrium, into account. Nevertheless, the results can be a useful representation, as long as the limitations of the conditions to which they are attached are considered. These could be effects such as the 'freezing' effect of a global thermostat, or that measured time-scales of processes might only be changing due to an increase in ion motion.

When considering ionic liquids in electric fields, simulations have been conducted that focus on the electrical double layers formed in ionic liquids,[53,61,76,189–192] along with simulations of the properties of IL/solvent mixtures in electric fields.[193–195]

Interfacial simulations do not have the same problems as bulk simulations when thermostatting in an electric field, in that the electrode/barrier stops the ions from being able to accelerate indefinitely. This means that the ion motion has an inherent barrier and restriction of the motion is not explicitly required by the simulation.

A review by Fedorov and Kornyshev summarises the main findings of simulations of ionic liquids at electrified interfaces very well. These are that[76]

- The electrode/molten salt interface has a multilayer structure with several layers that penetrate to the bulk up to several nanometers from the interface.

- The effects of ion size are important.
- Mixtures (other salts, solvent, etc.) strongly affect properties of the electrical double layer.

A select few examples of interesting results of ionic liquids at electrodes are discussed below. It should be noted that no simulations to date have been able to replicate some of the experimental results seen in this thesis, and other work, that show incredibly long distances and long time-scale effects when applying electric fields to ionic liquids (see Section 2.2.2 for details).
Uysal *et al.* simulated the structure and dynamics of the ionic liquid $[C_9C_1im][NTf_2]$ at a graphene electrode to attempt to understand the hysteresis that has been seen in electrochemical measurements for various ionic liquids.[61,189] From the simulations they carried out, they found that the electrode surface was completely covered with either cations or anions, and never a combination of the two. They attribute this to the hysteresis in the experimental measurements, as distinct layers of ions at an interface would be very stable, thus requiring long times to break down.[61,189]
A possible explanation for the exclusively cationic or anionic coverage of an electrode could come from a study by Fedorov *et al.* on a bead-type model of ionic liquids.[196] Their results could be interpreted as suggesting that when crossing over from positive to negative potentials, the neutral moieties are what displace the negative moieties from the surface. But going from negative to positive potentials, the neutral moieties could block the negative moieties from accessing the surface. This would lead to a hysteresis of the potential for anionic and cationic coverage, as well as explain the exclusive coverage of each ion.
In a recent study, Mao *et al.* looked at the effect of very large anions (1,4-bis(2-ethylhexoxy)-1,4-dioxobutane-2-sulfonate, [AOT], and various dodecylsulfonate anions) on the structure of the ionic liquid/electrode interface using the $[C_4C_1im]^+$ cation. They saw that in the presence of an electric field, large anions showed a weaker double layer structure, seen in a faster decay of the radial distribution functions of the large ions relative to smaller ($[BF_4]^-$) anions.[53] This agrees with the second main finding in the review by Fedorov and Kornyshev and suggests that the structure of the double layer is influenced not by the number of layers, but the distance of the layers from the electrode.
An interesting result from a simulation of ionic liquid/solvent mixtures in an electric field is that the hydrophobicity of the ionic liquid can be controlled using an electric field.[193] This required huge electric fields to be applied, of up to 6 $VÅ^{-1}$.
Studies by English and Mooney have also compared the response of the ions in an ionic liquid

and water in binary mixtures.[194,195] They found that the ions in an ionic liquid had a much slower response to a change in polarity of electric field than water, and also a lesser magnitude of response. This muted response was consistent, regardless of the mole fraction of water used, indicating that the ionic liquid response was decoupled from the co-solvent.[194,195]

When considering simulations of pure, neat ionic liquids in electric fields, there are very few simulations present in the literature.[197–202]

Using coarse grain simulations of the 1-dodecyl-3-methylimidazolium cation ($[C_{12}C_1im]^+$), Wang showed the elongation of the alkyl chain to form a 'nematic like' structure in $[C_{12}C_1im][NO_3]$ in an electric field of 1 VÅ^{-1}.[199] The volume of the simulation box was found to significantly decrease when this structure formed, whereas at electric fields below this, the simulation box was found to expand. The diffusion of the ions normal to the field lines was also found to increase at electric fields of 0.05 VÅ^{-1}. The reduction in simulation box size was attributed to the formation of the nematic structure, although reasons for the formation of this structure, as well as the expansion of the box and change in diffusion of the ions were not discussed in this study.

Simulations of 1-ethyl-3-methylimidazolium tetrafluroborate ($[C_2C_1im][BF_4]$) in electric fields by Zhao *et al.* showed that above a 'critical value' of 1.14 VÅ^{-1} the ions formed a 'lane-like' ordered structure as shown in Figure 7.1.[198] They found that this structure led to a decrease in the diffusion of the ions perpendicular to the field, but led to an increase in the diffusion of a probe Argon atom placed within the simulation box in the direction of the field.

When using a coarse grain model, Shi and Wang looked into changes to the ion cage of $[C_2C_1im][NO_3]$ in different electric fields. They saw that under strong electric fields of > 0.01 VÅ^{-1} the ion cage structure began to break down. They saw this both in structural analyses (radial and spacial distribution functions), and in the dynamics (ion cage correlation functions). They also found that this breakdown of the ion cage led to an increase in the diffusion of the ions.[200]

With regards to the way the ion cage broke down, they found that there was an anisotropy to this breakdown. The ion cage expanded greatly in the direction parallel to the vector of the electric field and much less so perpendicular to the vector of the electric field. They also found that in the absence of the electric field, the ion average position was in the centre of the cage, but in the presence of the electric field the average ion position was shifted more to one side of the ion cage.[200]

Daily and Micci also used a coarse grain model to investigate the ion dynamics of $[C_2C_1im][BF_4]$ in an electric field. They found an increase in ion velocity, kinetic temperature and conductivity

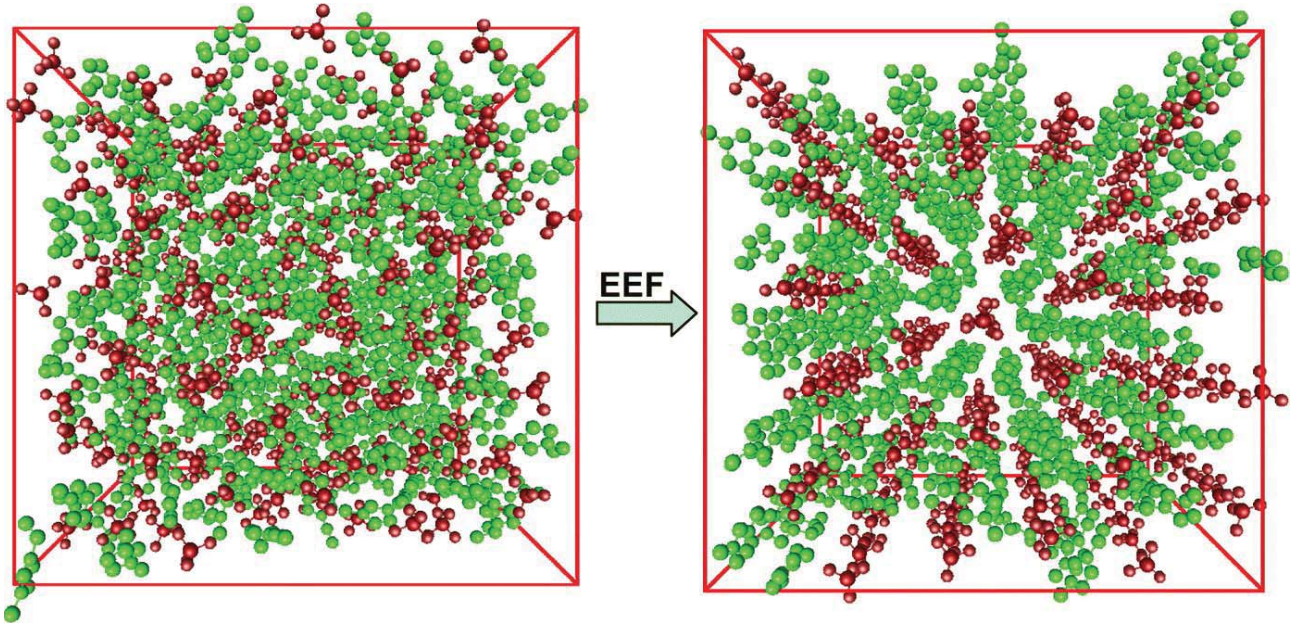

Figure 7.1: *A snapshot of the structure of the ionic liquid $[C_2C_1im][BF_4]$ under different electric fields. The green balls are cations and the red balls are anions. The left picture shows the state of ionic liquid without an electric field and the right picture depicts an organised state where electric field is 1.14 VÅ^{-1}. Figure taken from Zhao* et al.[198] *reprinted with permission from Taylor and Francis; Copyright 2012 https://www.taylorandfrancis.com.*

with increasing electric field.[197] They attempted to rationalise these results with conventional theories for conductivity, but encountered issues with higher electric fields, as they found a similar ion-lane formation as was later seen by Zhao *et al.*[198] which led to a breakdown of the theory.[197]

When considering fine structure, Atilhan and Aparicio investigated mixtures of choline chloride with glycerol, urea, malonic acid, levulinic acid and phenylacetic acid. They observed elongation of the dipole of the hydrogen bond donors and acceptors parallel to the direction of the field, along with changes to the diffusion of the ions/molecules normal to the field.[202]

Rather than using a direct current field (as all of the previously mentioned literature uses), English *et al.* investigated the frequency and amplitude dependence of alternating current electric fields on the properties of $[C_1C_1im][PF_6]$ and $[C_4C_1im][PF_6]$. They found that these ionic liquids had the strongest response to alternating fields with frequencies of 2.45 to 10 GHz when studying self-diffusion coefficients and dipole alignment.[201]

Their results also showed that electric field strength had more of an effect on ion dynamics than the frequency did, with the diffusion coefficient having almost no dependence on frequency until very high frequencies were reached (200 GHz). Their results also show that frequency dependence decreased with increasing electric field strength.[201]

7.1.2 Force Fields

In molecular dynamics simulations, a set of parameters which dictate how the particles in the simulations interact is needed; this is known as the "force field". Contained within the force field are parameters such as the number of particles in each molecule/ion, the charges on each particle, the type of interactions they have, interaction parameters, bonds, bond information, dihedral information etc.

The choice of force field is very important as this can change the accuracy, limitations and the computational cost of the experiment being performed. The greater detail in the model, the more information can be gained from the simulations and the closer the simulations are to real experiments, however this comes at a greater computational cost.

There are a few criteria for these simulations that dictate the choice of force field:

1. The desire to accurately observe changes to the structure *and* dynamics of the ions.
2. The accuracy of the model in high ionic concentrations.
3. The response of the model to the application of an external electric field.

The first point leads to the requirement for an all-atom, atomistic model. The force field developed by Canongia-Lopes and Padua (CL&P) is probably the most widely used and thoroughly maintained force field for ionic liquids.[203] The CLP force field uses an optimised potential for liquid simulations. This force field is based upon the OPLS all atom (OPLS-AA) type force field, which splits the total energy of the system into multiple components[204]

$$E_{\text{Total}} = E_{\text{ab}} + E_{\text{Bond}} + E_{\text{Angle}} + E_{\text{Torsion}} \tag{7.3}$$

The interaction energy (E_{ab}) between two particles a and b is modelled using combined Coulomb plus Lennard-Jones terms

$$E_{\text{ab}} = \sum_{a}^{i} \sum_{b}^{j} \left[k_e \frac{q_a q_b}{r_{ab}} + 4\epsilon_{ab} \left(\frac{\sigma_{ab}^{12}}{r_{ab}^{12}} - \frac{\sigma_{ab}^{6}}{r_{ab}^{6}} \right) \right] f_{ab} \tag{7.4}$$

where k_e is Coulomb's constant, q_a and q_b represent the charges on particles a and b, r_{ab} is the distance between the particles, ϵ_{ab} is the depth of the Lennard-Jones potential well, σ_{ab} is the distance at which the potential well is at its minima, and f_{ij} is a scaling factor used for modifying different types of interactions.[204]

The energies of bond stretching (E_{Bond}) and angle bending (E_{Angle}) are represented by harmonic oscillators

$$E_{\text{Bond}} = \sum_{\text{Bonds}} K_r(r - r_{\text{eq}})^2 \tag{7.5}$$

$$E_{\text{Angle}} = \sum_{\text{Angles}} K_\theta(\theta - \theta_{\text{eq}})^2 \tag{7.6}$$

where K_r and K_θ are the spring constants of the harmonic oscillators, r_{eq} is the equilibrium bond distance, and θ_{eq} is the equilibrium bond angle.

Dihedral torsion (E_{Torsion}) is represented by a sum of cosine waves

$$E_{\text{Torsion}} = \sum_i \frac{V_1^i}{2}\left[1 + \cos\left(\phi_{\text{i}} + \text{f}_{\text{i}}1\right)\right] + \frac{V_2^i}{2}\left[1 + \cos\left(2\phi_{\text{i}} + \text{f}_{\text{i}}2\right)\right] + \frac{V_3^i}{2}\left[1 + \cos\left(3\phi_{\text{i}} + \text{f}_{\text{i}}3\right)\right] \tag{7.7}$$

where This force field is well established in its ability to predict structural properties of ionic liquids, and was the force field used to predict the micro-heterogeneity of ionic liquids.[21,23]

Where this force field is less accurate is the prediction of the ion dynamics.[205] This was established to be due to the intermolecular interactions being too strong, so some authors have compensated for this by scaling the charge on the ions down to $\approx 0.8e$.[206] This was found to more accurately reproduce the dynamical properties of the system, however this reduced the accuracy of the static properties.

Another way that has been found to account for the slower than experimental dynamics is to include polarisability within the force field. Schröder and Steinhauser found that addition of polarisability increased the dynamics of 1-ethyl-3-methylimidazolium trifluoromethanesulfonate ($[C_2C_1im][OTf]$) closer to experimental values, without changing the ion centre distribution.[207]

In a follow-up study which compared the polarisable force field with various charge scaled force fields for $[C_2C_1im][OTf]$, it was also found that a polarisable force field more accurately reproduced experimental results than any scaled charge model.[208] In particular, the scaled charge models suffered in their prediction of 'fine' properties i.e. rotation, configuration and hydrogen bonding were found to change drastically with scaled charges.[208]

Schmollngruber *et al.* compared two types of polarisation methods (induced point dipole and Drude oscillators) to non-polarisable models, as well as looking at the impact of implicit or explicit inclusion of hydrogen polarisability on the properties of $[C_2C_1im][OTf]$. What they discovered was that having a polarisable force field was important to get accurate results, however the methods they tested showed no difference between a Drude oscillator method and an induced point dipole method; nor did their results show a difference between implicit or explicit inclusion of hydrogen polarisability.[209] All that mattered for accurate results was that

a polarisable force field was used with an appropriate level of polarisability to the atoms.

The use of a polarisable force field allows for the fulfilment of requirements 2 & 3. It is well known that for simulations on or containing water, the polarisability of the water molecule must be taken into account in order to generate meaningful results. In a recent review of polarisation in simulations, Bedrov *et al.* concluded that polarisable force fields are required when attempting to study any material with a high concentration of ions, which obviously includes ionic liquids. This is due to the high proximity of ions to each other resulting in strong local electric fields, which cause strong polarisation effects on a molecular level. Their review shows that in turn this requires either explicit or mean-field inclusion of polarisation in order for any model to be accurate.[210]

Further confirmation of the need for a polarisable force field comes from a review by English and Waldren.[211] Their general conclusion in the force field requirements for molecular dynamics simulation in electric fields was to use the best possible force field i.e. the most accurate force field with respect to replicating experimental measurements. It was also specified that this force field will be, in the most ideal scenario, one that implicitly or explicitly includes considerations of polarisablity. They point to studies which show that under the influence of an external electric field, polarisable models work better when predicting crystal growth in methane hydrate,[212] hydrogen bonding kinetics and molecular mobility of water,[213] and microwave heating of water.[214]

They also review various types of systems from very polar to non-polar and concluded, based upon the closeness of the results to experimental values, that having a polarisable force field was important when considering any highly charged or highly dielectric medium, especially in the presence of an external electric field.[211] Because of these reasons, it was decided to use a polarisable force field for all of the simulations here.

The force field used for the work in this thesis uses the charges and modified OPLS parameters from the CL&P force field for the atoms. Due to the all-atom nature of this force field, and the available tools (namely the `polarizer` tool built into `fftool`), Drude oscillators were used as the method for polarisation.

The Drude model attaches auxiliary particles to each atom, with the additional particle taking charge to model the polarisability of the atom. The Drude particle motion is decoupled from the main atom, although the two are bound together by a harmonic oscillator with a high spring constant and equilibrium distance of zero. This leads to a pair of particles modelling each atom, the Drude core (D_C) and the Drude particle (D_P).

This split means that the D_C models how the centre of mass of the Drude pair moves, and the

D_P models how the electron cloud moves. Because of this, the charge on D_P is usually set to a negative value. This is not a literal method for modelling electron cloud motion, nevertheless it is a reasonable approximation that can be implemented into many molecular dynamics simulation packages.[210]

This has advantages over other models, such as the fluctuating charge model, as D_C and D_P can both be treated as classical particles in the velocity-verlet algorithm, assuming that careful consideration of the D_P properties and appropriate screening is applied to the Drude pair.

There are various ways to implement a Drude model into a simulation, each with different ways to determine the masses, charges and spring constants for the Drude pair. Here, the method proposed by Lamoureux and Roux is used. This uses a constant mass for D_P of 0.4 amu, and a constant spring constant for the Drude pair of 1000 kcal mol^{-1} Å^{-2}.[80]

As the mass of the Drude pair needs to be equal to the mass of the atom before addition of D_P, the mass of each D_C is reduced such that

$$m_A = m_{D_P} + m_{D_C} \tag{7.8}$$

This presents a problem when considering hydrogen atoms. For hydrogen, a reduction of 0.4 amu means that D_P carries a significant proportion of the mass of the Drude pair and thus the assumption that D_P models only the electron cloud breaks down. Luckily, as discussed earlier, Schmollngruber *et al.*[209] found that explicit inclusion of hydrogen polarisability is not necessary, and implicit inclusion gives the same result. Therefore the polarisability of hydrogen is accounted for on the D_P of the adjacent atom in this model.

To simulate the different polarisabilities of each atom, each D_P is assigned a different charge. The charge of each D_P (q_D) is calculated from the polarisability of the atom by[80]

$$q_D^2 = \alpha k_D \tag{7.9}$$

Implicit hydrogen polarisability was included by addition of α_H to α of the adjacent atom. For example in the terminal CH_3 group, $\alpha_C = 1.081$ Å^3 and $\alpha_H = 0.389$ Å^3, therefore one D_P was attached to the carbon atom with the charge calculated using $\alpha = 1.081 + 3 \times 0.389 = 2.248$ Å^3. As addition of too many extra D_P can drastically increase computation time, the same additive method was used to account for the polarisability of fluorine atoms too.

The polarisabilties used here are those calculated by Bernardes *et al.* which were the most recent and deemed most accurate at the beginning of this project.[81]

Very recently, a more substantial piece of work from Goloviznina *et al.* has looked into making a more general Drude-polarised ionic liquid force field.[215] They consider not only the addition of Drude particles, but also a rescaling of the Lennard-Jones parameters (ϵ_{ij} and σ_{ij} in Equation 7.4). They find that while some scaling was required to achieve optimum parameters, the optimum they found was to modify all of the parameters by a factor of 0.985.[215] As this is a small factor, the force field chosen and developed here can be determined to be satisfactory to get accurate results, given the availability of force fields at the time.

7.2 Anisotropic Considerations When Thermostatting

In molecular dynamics simulations the temperature (in one dimension) is defined from the average kinetic energy of the particles, per Equation 7.10.[216]

$$E_K = \frac{1}{2}K_B T,\ E_K = \frac{1}{2}mv^2 \therefore \langle T \rangle = \sum_{i=1}^{N} \frac{m_i \langle v_i^2 \rangle}{K_B} \tag{7.10}$$

where E_K is the kinetic energy, K_B is the Boltzmann constant, T is the temperature, m is the mass of a particle, v is velocity of a particle, N is the number of particles in the system and the brackets $\langle\rangle$ denote the ensemble average.

When running molecular dynamics simulations the temperature will inherently fluctuate, with a variance of $\frac{2}{3N}$ in a canonical (fixed number of molecules, volume and temperature: NVT) ensemble.[216] This variance is expected, however the accumulation of numerical, round off errors from calculations of energy and the equations of motion can lead to a larger drift. While the kinetic energy of an individual particle should be allowed to drift, the ensemble average and distribution of kinetic energies should remain constant, and the accumulation of too many rounding errors leads to a drift of this average and distribution from the initial values.[216,217]

As when simulating a canonical ensemble (fixed number of molecules, volume and temperature: NVT) or an isobaric-isothermic ensemble (fixed number of molecules, pressure and temperature: NPT) the temperature should remain around a fixed value, so a method to control the average and variance in the temperature is needed. The numerical algorithms applied during the simulation to achieve this are called thermostats.

Thermostats are numerical algorithms that are applied to loosely control the kinetic temperature of the simulation box, so the temperature of an individual particle can change, as long as the ensemble remains within the set parameters.

There are various methods used to control the kinetic energy and hence the temperature; constrained formulation approaches (e.g. Berendsen and Langevin thermostats) use a global friction factor to slow the dynamics of the particles, extended system methods (e.g. a Nosé-Hoover thermostat) add fictitious degrees of freedom to use as a pseudo heat bath, and constraint methods forcibly scale the velocity of particles to fit the temperature.[218,219]

Many of the algorithms for these thermostats were developed with the assumption that the simulation box is in a thermodynamic equilibrium, so there is no external influence on the simulation box and all the laws of thermodynamics are satisfied.

When applying an external electric field to a simulation there is not a thermodynamic equilib-

rium as there exists an anisotropic flow of matter driven by an external influence, thus violating the assumption of an isolated system. However, given sufficient time under the effect of the electric field, the system can reach a steady-state where the flow of matter is constant. This is the principle behind non-equilibrium molecular dynamics and means that an accurate representation of the system can still be simulated.

Application of a global thermostat to an anisotropic system can lead to a 'freezing' effect, where the increase in motion in one direction can lead to 'over-damping' of the simulation. Taking the example of an electric field, the thermostat would recognise an increase in temperature parallel to the applied field and increase the total damping of the system to compensate for this (e.g. by removing kinetic energy, increasing the friction etc.). Unmodified thermostats will incorrectly apply this increased dampening to the whole system, and this will decrease the temperature perpendicular to the electric field, which is not expected to change. The kinetic energy should be allowed to increase parallel to the field, without affecting the temperature perpendicular to the field.

In an ideal scenario, the increase in the temperature parallel to the field could be calculated and compensated for before calculating the temperature to use to adjust the thermostatting parameters. However, this relies upon the system being thermostatted appropriately for the temperature calculation to be correct, which is a circular dependence. This could in theory be done with an iterative approach but would be very expensive and time consuming.

An easier way to avoid the thermostat over-compensating for the increase in kinetic energy parallel to anisotropic disturbances would be to ignore the anisotropy when calculating temperature. This means that as the electric field is applied in the z direction, only the kinetic energies in the x and y directions are passed to the thermostat algorithm to calculate the temperature.

This does require the assumption that application of anisotropic disturbance in one direction has no effect on the other directions. This is a reasonable assumption to make, especially as within `LAMMPS` the application of an electric field is achieved by adding a force to each particle in the direction of the electric field (see Chapter 4 for details).

This also has the advantage of being a very simple and inexpensive approach. As the electric field is applied along the z vector of the simulation box, the temperature perpendicular to this (in the xy plane) can be calculated with the command

```
compute TRESOLVEDXY ATOMS temp/partial 1 1 0
```

where the group `ATOMS` includes all of the non-Drude particles in the simulation box. The

standard thermostat for the atoms is set with the command

```
fix THERMOSTAT ATOMS nvt temp 400.0 400.0 20.0
```

and then the thermostat can then be modified easily with the command

```
fix_modify THERMOSTAT temp TRESOLVEDXY
```

From herein, simulations run with this `fix_modify` command are referred to as using a 'modified' thermostat, and simulations without this command are referred to as using a 'global' thermostat.

The modify command does increase the simulation time slightly, with the `LAMMPS` log file showing an increase in the `Modify` computation time from $\approx$ 12000 s (7 % of total time) to $\approx$ 24000 s (12 % of total time) in the simulation. However, given that there is an extra `compute` command that is run at every time-step and that the extra computation required for the electric field is much more than this, this is still an acceptable computational time for a polarisable force field and speeds of up to 1 ns/day can be achieved on the high performance computer at Imperial College.

7.2.1 Thermostatting in the XY vs XYZ directions

What this method relies upon is that in a simulation without anisotropy, "ignoring" the temperature in one direction when thermostatting leads to accurate temperatures in all directions, and doesn't affect the outcome of the simulations significantly.

The easiest way to see this is by looking at the variations in the temperature in each direction. The fluctuations in the temperature in the x and y directions can be used as a guide for acceptable fluctuations, and the average temperatures in each direction gives an idea behind how well the system is maintained at a constant temperature.

In this section, the use of two thermostats will be compared with regard to anisotropic thermostatting: the Nosé-Hoover thermostat and the canonical sampling by velocity rescaling (CSVR) thermostat. These will be compared to each other, and to the expected temperature to ascertain which is the better thermostat for these simulations.

For the Noseé-Hoover thermostat, the default settings in LAMMPS were used (which uses a chain of 3 thermostats [according to the documentation].[82]), and for the CSVR thermostat the time integration had to be performed using the `fix nve` command, then the thermostatting performed using the CSVR thermostat using the following commands:

```
fix POSITIONINTEGRATION ATOMS nve
fix CSVRTEMPATOMS ATOMS temp/csvr 400.0 400.0 20.0 12345
```

The data presented below from this investigation was all collected on simulation of the ionic liquid $[C_4C_1im][NTf_2]$.

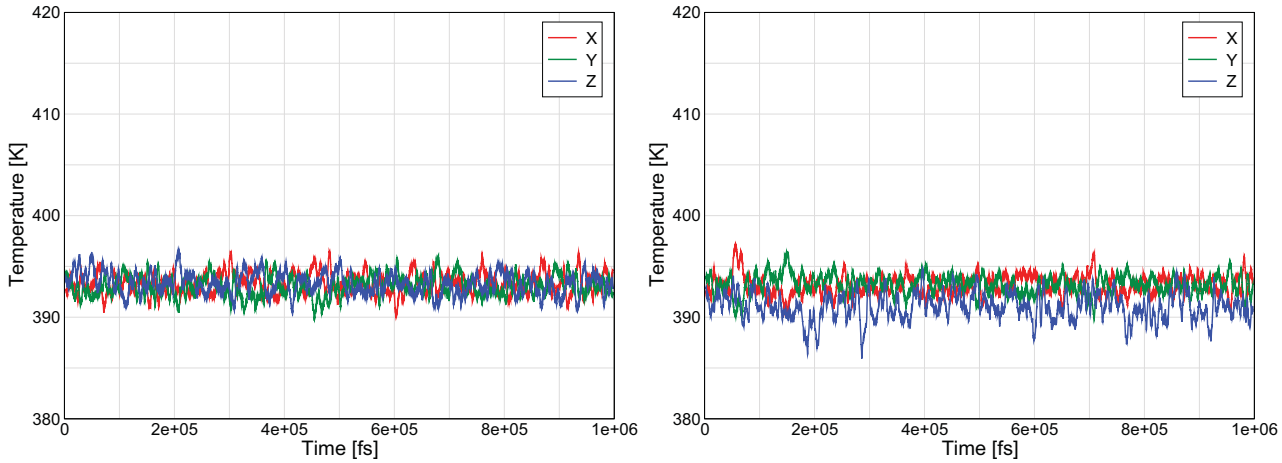

Figure 7.2: *Temperature in the x, y and z directions in 1 ns production runs of $[C_4C_1im][NTf_2]$ with no electric fields using the Nosé-Hoover thermostat to hold the temperature at 400 K. Left shows a simulation run with a global thermostat, right shows the same simulation but run with a modified thermostat.*

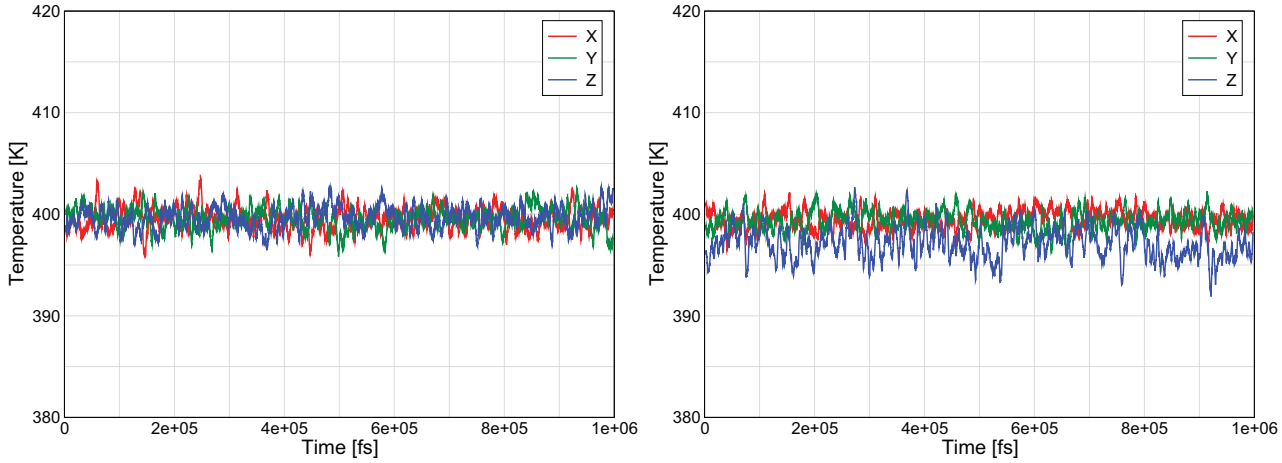

Figure 7.3: *Temperature in the x, y and z directions in 1 ns production runs of $[C_4C_1im][NTf_2]$ with no electric fields using the CSVR thermostat to hold the temperature at 400 K. Left shows a simulation run with a global thermostat, right shows the same simulation but run with a modified thermostat.*

The graphs in Figures 7.2 and 7.3 and the data in Table 7.1 show that when using a global thermostat, the temperature is (unsurprisingly) equal in all directions.

Oddly, while the temperature in the CSVR thermostat fluctuates around 400 K, the temperature the simulations were set to, the temperature of the Nosé-Hoover thermostat fluctuates around a lower temperature of approximately 393 K. Both do keep the temperature relatively steady with a standard deviation of approximately 5.9 K.

Table 7.1: *Average temperature in the x, y and z direction of simulations of $[C_4C_1im][NTf_2]$ run with the Nosé-Hoover thermostat and the CSVR thermostat. Errors are the standard deviation of the data. Raw data is that plotted in Figures 7.2 and 7.3.*

Thermostat	Nosé-Hoover		CSVR	
Directions considered	Global	Modified	Global	Modified
Avg. temp. in x direction (K)	393.33±5.89	393.14±5.91	399.56±5.97	399.49±5.92
Avg. temp. in y direction (K)	393.06±5.91	393.23±5.87	399.59±5.96	399.34±5.95
Avg. temp. in z direction (K)	393.32±5.92	391.03±5.98	399.66±5.98	397.09±6.06

When using the modified thermostat, the temperatures in the x and y directions remain the same temperature that the relevant thermostat held the temperature at using a global thermostat, as expected.

The average temperature in the z direction reduces slightly, by approximately 2 K when using either thermostat. As this is less than the standard deviation of the temperature in the x or y direction, this can be deemed an acceptable change in temperature and the temperature remains constant despite the thermostat not explicitly including the temperature in this direction.

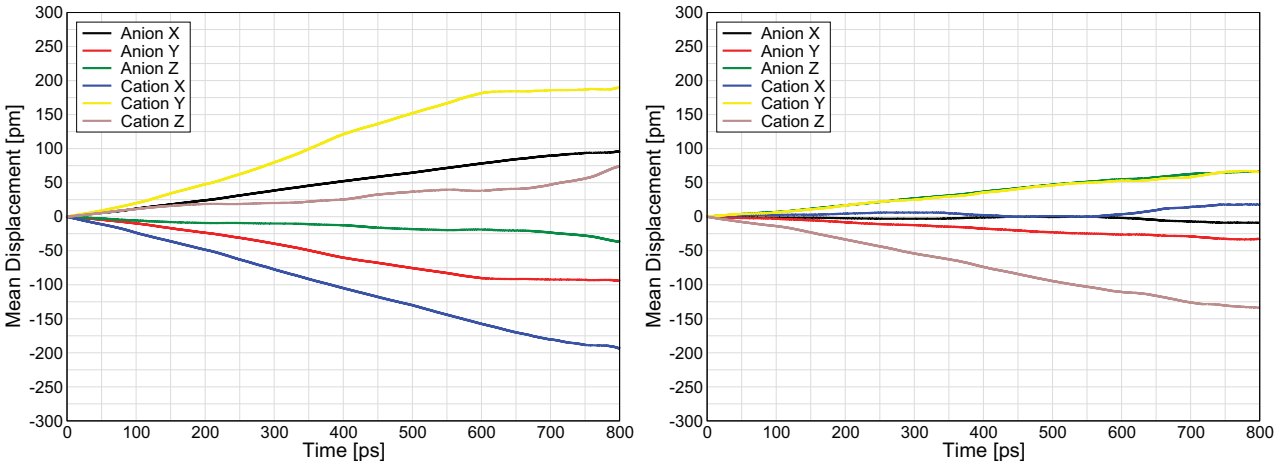

Figure 7.4: *Drift in the x, y and z directions in 1 ns production runs of $[C_4C_1im][NTf_2]$ with no electric fields using the Nosé-Hoover thermostat. Left shows a simulation run with a global thermostat, right shows the same simulation but run with a modified thermostat.*

When considering the implications of the modified thermostats, another concern beyond a change in temperature was that the ions could drift along the directions not controlled by the thermostat. Figures 7.4 and 7.5 show that this is not a serious concern.

For the Nosé-Hoover thermostat (Figure 7.4) the simulation with a global thermostat seems to show a higher drift in the ions than the simulation with the modified thermostat. Conversely, the CSVR thermostat (Figure 7.5) has very little drift of the ions using a global thermostat, and a larger drift of the ions in the z direction than the x and y direction when using the modified thermostat.

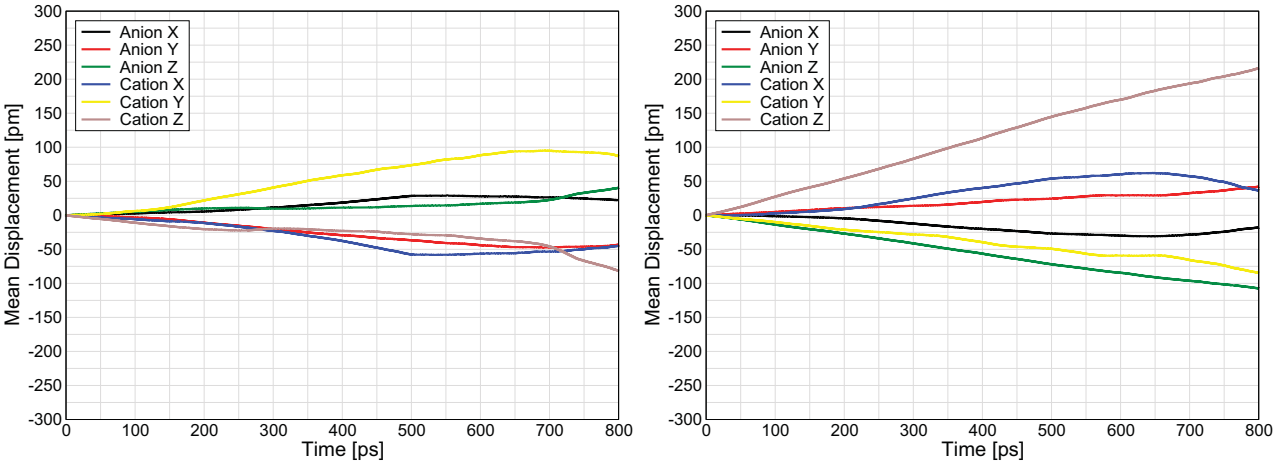

Figure 7.5: *Drift in the x, y and z directions in 1 ns production runs of $[C_4C_1im][NTf_2]$ with no electric fields using the CSVR thermostat. Left shows a simulation run with a global thermostat, right shows the same simulation but run with a modified thermostat.*

Given the 'benchmark' of the drift in the x and y directions, there can reasonably be said to be no difference in the drift when applying the modified thermostat.

One thing that should be noted is that the ratio of the mean displacement of the cation to the mean displacement of the anion is always *exactly* 2.0122:1 and the ions move in the opposite directions. This holds true for all of the simulations, regardless of the direction considered, regardless of the strength of the electric field applied. This is a consequence of conservation of momentum by the command

```
fix MOMENTUM all momentum 1000 linear 1 1 1
```

which zeroes the linear momentum of the whole simulation box in all directions every 1000 time-steps by adjusting the velocities. The ratio is exactly the same as the mass ratio of the cation and anion.

This command is used ubiquitously across all of these simulations, and is required to compensate for any centre of mass translation of the box that may occur due to random fluctuations.

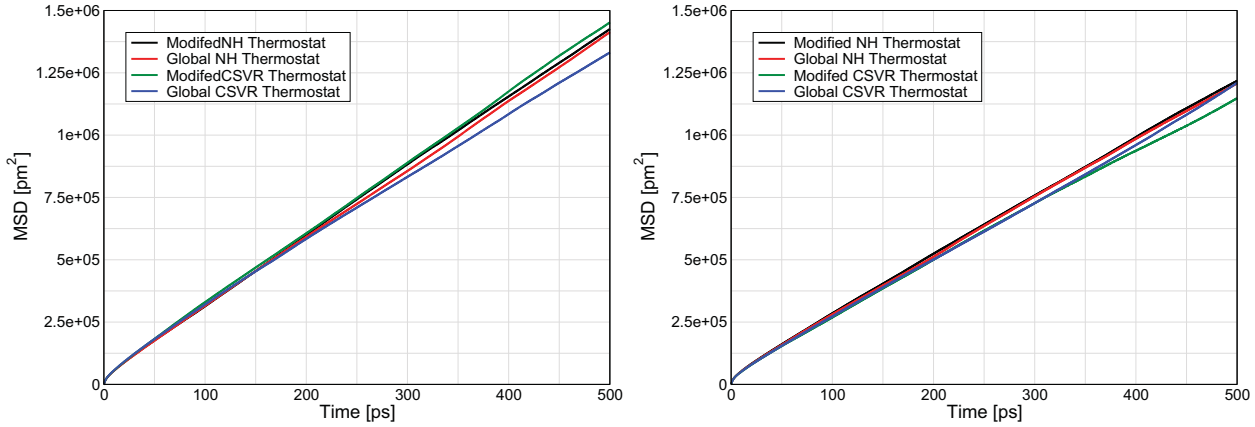

Figure 7.6: *Total average (in all directions) mean square displacement for the cation (left) and anion (right) in all of the zero electric field simulations of $[C_4C_1im][NTf_2]$.*

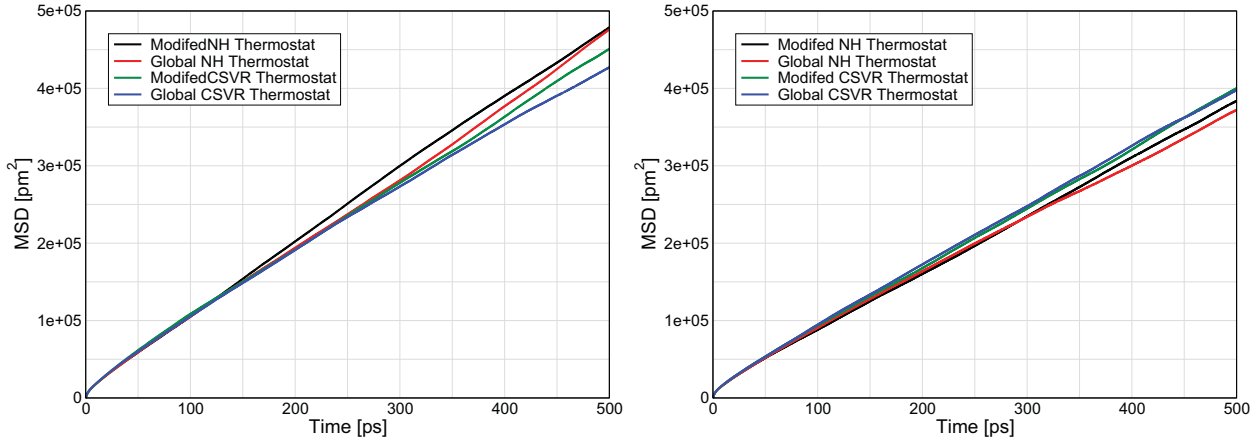

Figure 7.7: *Mean square displacement for the cation (left) and anion (right) in the x direction in all of the zero electric field simulations of $[C_4C_1im][NTf_2]$.*

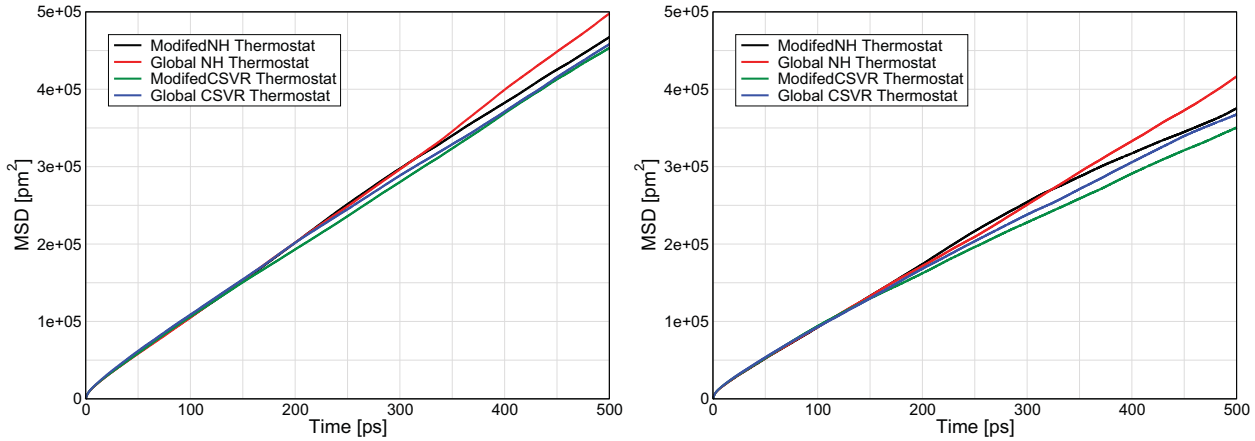

Figure 7.8: *Mean square displacement for the cation (left) and anion (right) in the y direction in all of the zero electric field simulations of $[C_4C_1im][NTf_2]$.*

The mean squared displacements of the ions remain very similar for both ions in the x and y directions, as well as in all directions (Figures 7.7, 7.8 and 7.6 respectively). Changing the thermostat from a global to modified thermostat should not affect the control of the dynamics in the x and y directions, so the fact that these remain constant is expected.

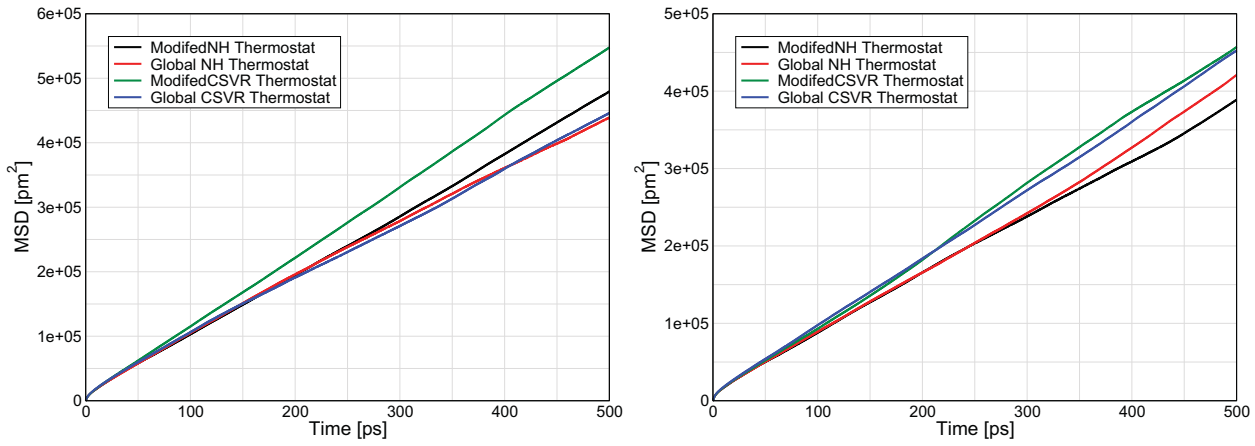

Figure 7.9: *Mean square displacement for the cation (left) and anion (right) in the z direction in all of the zero electric field simulations of* $[C_4C_1im][NTf_2]$.

An assumption of the modified thermostat is that it should not affect the total mean squared displacement of the ion, so the fact that this remains constant is a good indicator that the modified thermostat is performing as hoped.

The mean squared displacement in the z direction does change a little with thermostat and method, however diffusion coefficients need to be calculated to see if this is significant.

When using a modified or global Nosé Hoover thermostat, the mean squared displacement remains similar for both of the ions. When using a CSVR thermostat, the choice of using either a modified or global thermostat affects the mean squared displacement of the cation, but not the anion.

The anion remains consistent within the CSVR thermostat, but slightly different to that of the Nosé-Hoover thermostat. From the calculation of diffusion coefficients below this does not seem to be significant.

In contrast, cation mean squared displacement is very different when changing between a modified and global thermostat. This suggests that some process invoked in this thermostat affects the cation differently when including or excluding one dimension in the thermostat. What this process is, the cause of it and the reason it changes the mean squared displacement of the cation is not clear.

When considering the diffusion coefficient of the anion, shown in Table 7.3, the anion diffusion does not change significantly with the different thermostatting methods across both thermostats.

The diffusion coefficient of the cation (Table 7.2) is very similar in the Nosé-Hoover thermostat with both thermostatting methods, but is significantly different with the different thermostatting methods using the CSVR thermostat. This was determined through a p-value < 0.05 in a

Table 7.2: *Diffusion coefficient of the cation from the mean square displacement in the x, y and z direction of simulations of $[C_4C_1im][NTf_2]$ run with the Nosé-Hoover thermostat and the CSVR thermostat. Error is the standard deviation of the combined analysis of the data from the first half, second half and whole of the trajectory.*

Cation

Thermostat	Nosé-Hoover		CSVR	
Directions considered	xyz	xy	xyz	xy
D	4.52±0.21	4.87±0.31	4.16±0.17	4.76±0.16
D_x	4.55±0.17	4.63±0.13	4.06±0.28	4.23±0.14
D_y	4.52±0.60	4.79±0.36	4.50±0.49	4.35±0.04
D_z	4.49±0.35	4.67±0.12	3.91±0.39	5.68±0.37

Table 7.3: *Diffusion coefficient of the anion from the mean square displacement in the x, y and z direction of simulations of $[C_4C_1im][NTf_2]$ run with the Nosé-Hoover thermostat and the CSVR thermostat. Error is the standard deviation of the combined analysis of the data from the first half, second half and whole of the trajectory.*

Anion

Thermostat	Nosé-Hoover		CSVR	
Directions considered	xyz	xy	xyz	xy
D	3.84±0.59	3.89±0.29	4.04±0.13	4.01±0.35
D_x	3.58±0.54	3.69±0.14	3.92±0.14	3.92±0.17
D_y	3.80±0.76	4.01±0.73	3.70±0.28	3.24±0.20
D_z	4.16±0.53	3.98±0.44	4.51±0.15	4.90±0.68

two tailed t-test comparing the sets of diffusion values from each thermostat (Table 7.4).

Table 7.4: *P-values of a two-tailed t-test comparing the diffusion coefficient of the cation and anion when using the global and modified Nosé-Hoover and CSVR thermostats. In all cases the statistical degrees of freedom was 11. A p-value < 0.05 indicates a significant difference between the diffusion coefficients when changing the thermostatting method.*

Thermostat	Cation	Anion
Nosé-Hoover	0.131	0.844
CSVR	0.014	0.910

Looking at the data, it is the simulation using the global, unmodified thermostat that is significantly different to the modified thermostat, and it is also significantly different to the global ($p = 0.043$) and modified ($p = 0.001$) Nosé-Hoover thermostat.

This is unexpected as it suggests that when using the global CSVR thermostat, the cation velocity is rescaled to a lower value than when the temperature in the z direction is excluded. As discussed above, the graph of the mean squared displacement of the cation in the z direction also suggests the cation is affected differently in the global and modified thermostat. However, the mean squared displacement graph suggested that the modified thermostat led to a larger mean squared displacement in the z direction, and the modified thermostat had a similar mean squared displacement to the other methods of thermostatting.

While this is reflected in the diffusion coefficients, the statistical analysis in Table 7.4 uses the data in all directions in order to have enough data to reach statistically significant conclusions. Attempting to perform a t-test using only the diffusion coefficients in the z direction does not provide enough data to suggest the results are statistically different. This is because there are only three data points for each thermostat, therefore the t-value threshold to reject the null hypothesis (that the mean diffusion in the z direction is the same) is much higher.
The cause for this mismatch is uncertain, but the fact that there are conflicting results lowers the trust in the results from the CSVR thermostat.

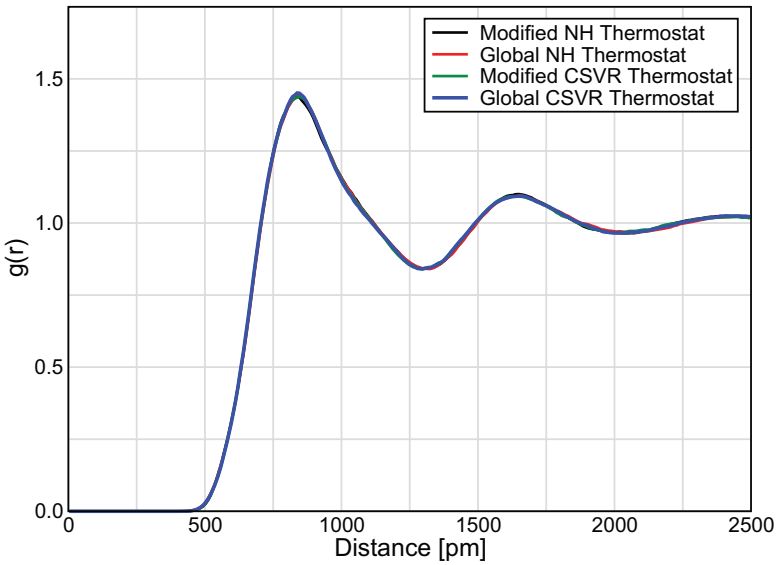

Figure 7.10: *The radial distribution of the anion centre of mass with respect to the anion centre of mass.*

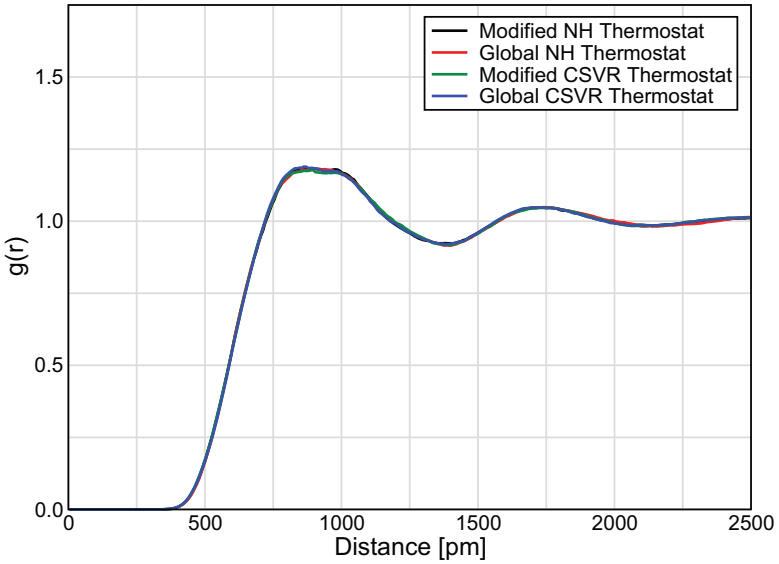

Figure 7.11: *The the radial distribution of the cation centre of mass with respect to the cation centre of mass.*

When comparing the bulk and some of the inter-ion structuring, all of the thermostats perform

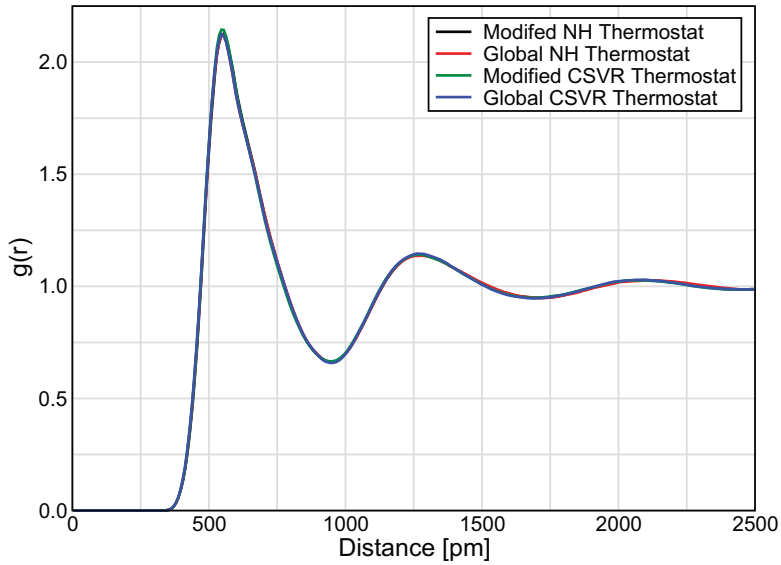

Figure 7.12: *The radial distribution of the anion centre of mass with respect to the cation centre of mass.*

very similarly. Changing between global and modified thermostat has no effect on the radial distribution of the ion centres of mass either with respect to themselves (Figures 7.10 and 7.11) or each other (Figure 7.12).

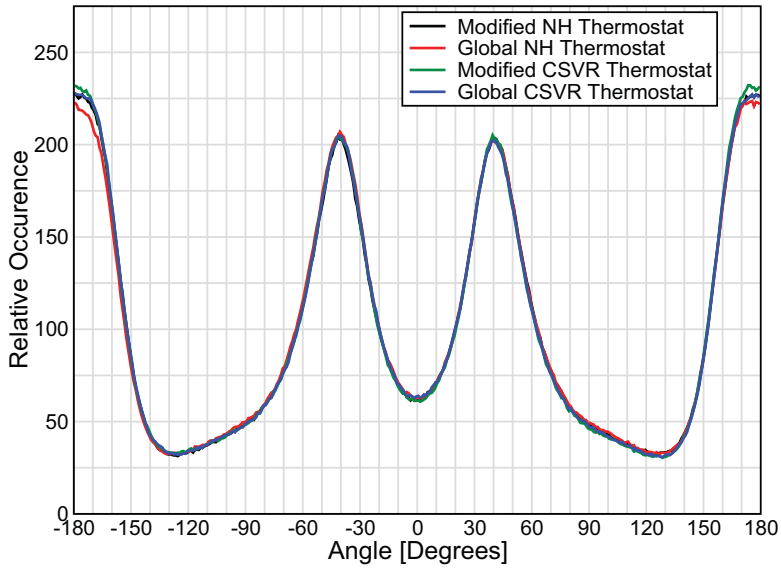

Figure 7.13: *The dihedral distribution of the anion C-S-S-C dihedral, indicative of the cis/trans isomer.*

Figures 7.13 and 7.14 show the distribution of some intramolecular vectors, which were calculated in order to check that the thermostats and modifications did not affect the ions themselves. These show that there is little effect of the thermostat or method to the structure of the ions, as would be expected.

In summary, this section shows that when using either thermostat, the temperature of the simulation box is adequately thermostatted when only considering temperature in two out of

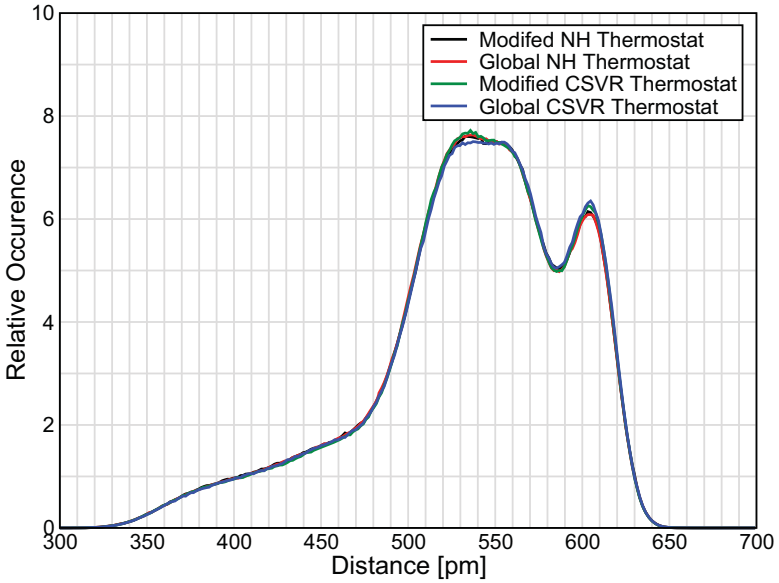

Figure 7.14: *The radial distribution of the distance between centre of the imidazolium ring and the terminal carbon on the butyl chain.*

three directions. The CSVR thermostat seems to hold the temperature closer to the set value, and while the Nosé-Hoover thermostat still holds the temperature constant, the temperature is a few degrees Kelvin below the set value.

Further analysis of mean squared displacement and diffusion coefficients shows that these are consistent for the Nosé-Hoover thermostat between the global and modified thermostat, but statistical analysis showed that they are different in the global and modified CSVR thermostat. There is no significant difference in either the bulk structure or ion structure by the methods tested here, although it is well known that the CL&P force field is very good at predicting structural properties of ionic liquids so they were not expected to be different.

The modified method of thermostatting allows application of anisotropic disturbances to the system whilst still being able to control temperature in the directions not affected by the applied disturbance. Therefore, the next step is to study the performance of the modified thermostats in the presence of an electric field. This will be used to determine which thermostat will be used from herein.

7.3 Applying Thermostatting to Simulations in Electric Fields

Now that the modified thermostatting method has been shown to be an acceptable way to control the temperature of a simulation in an isotropic system, the performance of this methodology in an anisotropic system with an electric field will be evaluated.

Simulations were run according to the procedure in Chapter 4 where a pre-equilibrated simulation at 400 K has an electric field applied in the z direction by a force of $F = EQ$.

The resultant temperatures in these simulations are shown in Table 7.5.

Table 7.5: *Average temperature in the x, y and z direction of simulations of $[C_4C_1im][NTf_2]$ using a Nosé-Hoover and a CSVR thermostat with an electric field applied in the z direction. Errors are the standard deviation of the data.*

Electric Field Strength VÅ^{-1}	Temperature (K)					
	Nosé-Hoover			CSVR		
	x	y	z	x	y	z
0.000	393.1±5.9	393.2±5.9	391.0±6.0	399.5±5.9	399.3±5.9	397.1±6.1
0.001	393.1±5.9	393.3±5.9	391.0±6.0	399.4±5.9	399.4±6.0	397.4±6.0
0.002	393.2±5.9	393.2±5.9	391.3±6.0	399.3±5.9	399.5±6.0	397.8±6.1
0.005	393.3±5.9	393.1±5.9	391.3±6.1	399.4±6.0	399.4±6.0	397.4±6.1
0.010	393.2±5.9	393.2±5.9	391.2±6.0	399.3±6.0	399.6±6.0	397.5±6.0
0.020	393.2±5.9	393.2±5.9	391.9±6.0	399.5±5.9	399.3±6.0	398.4±6.1
0.050	393.2±5.9	393.2±5.9	393.5±6.0	399.4±5.9	399.4±6.0	399.7±6.1
0.100	393.3±5.9	393.4±5.9	397.0±6.0	399.5±6.0	399.6±6.0	403.1±6.1
0.200	393.8±6.0	393.8±6.0	406.4±6.5	400.8±6.1	400.6±6.1	413.7±6.5
0.300	394.5±6.1	394.6±6.1	425.0±7.9	403.5±6.4	403.7±6.4	434.4±8.1
0.400	397.4±6.1	397.3±6.1	462.3±10.6	408.5±6.8	408.3±6.8	473.6±11.0
0.500	400.7±6.5	400.9±6.6	522.8±15.2	415.2±7.3	415.5±7.3	538.4±15.8

For both thermostats, the temperature in every direction remains approximately constant in electric fields $\leq$0.02 VÅ^{-1} indicating that kinetic energy does not change in these electric fields, despite the presence of an electric field.

Considering the direction of the electric field (z), the average temperature increases slightly with an electric field of 0.02 VÅ^{-1}. However this is not a significant increase in either thermostat.

Electric fields of $\geq$0.05 VÅ^{-1} cause significant increases in the temperature. This increase is expected as the additional force from the electric field should increase the kinetic energy in the z direction and thus the temperature. The fact that the temperatures remain stable with a standard deviation of $\approx$ 3% means that the simulations have reached a steady state, meaning they are properly equilibrated.

Along the x and y dimensions, where the temperature is thermostatted, there is a slight increase in the temperature. For the Nosé-Hoover thermostat, this increase is small and seems to be well controlled by the thermostat across the range of electric fields tested here. For the CSVR thermostat, the thermostat seems to be able to control the temperature relatively well at electric fields < 0.4 VÅ^{-1}. When applying electric fields $\geq$0.4 VÅ^{-1} the thermostat keeps the temperature relatively constant across the simulations, however the average temperatures in the x and y axis are significantly higher than the temperatures they should be.

This is unexpected, as the CSVR method uses Equation 7.10 to calculate an actual kinetic energy (K) and an expected kinetic energy distribution ($\bar{K}$). Then, the thermostat uses these to calculate a scaling factor (α) which is used to scale the velocity by

$$\alpha = \sqrt{\frac{\bar{K}}{K}} \tag{7.11}$$

The problem with this may lie in the stochastic nature of the choice of $\bar{K}$. The CSVR method relies upon the randomness of a collection of variables unlike the Nosé-Hoover thermostat. Other than that, the methods should produce the same results so the reason behind the difference is unclear.

The end result is that the Nosé-Hoover thermostat is better at regulating temperature than the CSVR thermostat at high electric fields with this method of thermostatting in this system. Not only that, it is also more efficient. Running the simulations in the same queue on the Imperial HPC using the same resources (1 node, 16 cpus, 64 GB memory), both thermostats perform comparably when no electric field is applied, computing 0.558 ns/day (12.9 time-steps/s). However, when an electric field is added to the computation, the Nosé-Hoover thermostat can achieve similar computational efficiency of 0.539 ns/day (12.5 time-steps/s) while the performance of the CSVR thermostat falls slightly to 0.491 ns/day (11.4 time-steps/s). This may seem like a small drop, but when longer simulations are run this can add a significant amount of time needed for the simulations to complete.

Because of the accuracy and to a lesser extent the computation time, for the second set of simulations on 1-octyl-3-methylimidazolium bis(trifluoromethylsufonyl)imide ($[C_8C_1im][NTf_2]$) only a Nosé-Hoover thermostat was used. This was also because, due to the size of the simulation files and limitations on the computation of the simulations, obtaining as few files as possible was preferred.

The temperature of the simulations of $[C_8C_1im][NTf_2]$ in electric fields, shown in Table 7.6, follow the same trend as that of the simulations of $[C_4C_1im][NTf_2]$, in that the temperature in

Table 7.6: *Average temperature in the x, y and z direction of the simulations of [C_8C_1im][NTf_2] with an electric field applied in the z direction. Errors are the standard deviation of the data.*

Electric Field Strength (VÅ^{-1})	Temperature (K)		
	x	y	z
0.000	393.9±5.2	393.0±5.1	392.6±5.3
0.001	393.1±5.2	393.8±5.2	391.8±5.3
0.002	393.3±5.2	393.6±5.2	392.2±5.2
0.005	393.7±5.2	393.3±5.2	391.1±5.3
0.010	393.0±5.2	393.9±5.2	391.6±5.5
0.020	393.4±5.2	393.5±5.2	394.0±5.3
0.050	393.5±5.2	393.3±5.2	398.4±5.4
0.100	393.5±5.2	393.4±5.2	406.0±5.4
0.200	393.7±5.2	393.6±5.2	412.5±5.6
0.300	394.1±5.3	394.2±5.3	423.0±6.5
0.400	395.8±5.2	395.9±5.2	449.5±8.6
0.500	402.2±11.8	423.6±12.7	3319.7±316.7

the x and y directions remains approximately constant, and the temperature in the z direction remaining constant at electric fields up to 0.05 VÅ^{-1} and increasing at electric fields above this. There is an obvious difference for simulations of [C_8C_1im][NTf_2] compared to [C_4C_1im][NTf_2] in that at 0.5 VÅ^{-1} the temperature in the z direction increases dramatically to over 3000 K. Upon analysis of this trajectory, it was found that this led to multiple problems, meaning this simulation could not be used. This is discussed more in Appendix C.

Choice of Thermostatting Method in an Electric Field

In conclusion, the data from these simulations seems to be representative of an anisotropic system. For all of the simulations of [C_4C_1im][NTf_2] and all of the simulations of [C_8C_1im][NTf_2] <0.5 VÅ^{-1}, the simulations are well thermostatted in the x and y directions and there is no obvious freezing of the motion in the z direction given the temperature increase that occurs at 0.05 VÅ^{-1}. Later analysis in Section 7.4 shows the reason behind this electric field causing an increase in the temperature.

Between the two thermostats tested on [C_4C_1im][NTf_2], the Nosé-Hoover thermostat seems to control the temperature the best when applying an electric field, despite the CSVR thermostat giving a more accurate temperature value. This shows that while the CSVR thermostat can be more accurate, the Nosé-Hoover thermostat is more reliable. This conclusion is backed up by the analysis in Section 7.2.1 which shows that while there are not many differences between the two thermostats or methods of thermostatting, the Nosé-Hoover global and modified ther-

mostats agree more often than the global and modified CSVR thermostats.

From hereon, all results presented are from simulations are performed with a modified Nosé-Hoover thermostat, as this has been determined to be the most reliable thermostat. This is because this thermostat has been shown to be a valid way to control the temperature perpendicular to the direction along which the electric field is applied.

7.4 Dynamics in an Electric Field

7.4.1 Theory

Assuming that the ions move randomly with Brownian motion, the diffusion of an ion within an ensemble can be studied using the mean squared displacement

$$\langle x^2(\tau)\rangle = \langle (x(t+\tau) - x(t))^2\rangle \tag{7.12}$$

where $\langle x^2(\tau)\rangle$ is the ensemble mean squared displacement (MSD), τ is the lag time, $x(t)$ and $x(t+\tau)$ are the ion position at time t and $t+\tau$ respectively and the angled brackets $\langle\rangle$ denote the average over the whole ensemble.

Mean squared displacement is used as it is a good descriptor of the "exploration" of a system from a particle undergoing a random walk.

Diffusion coefficients can be used to relate the diffusivity (the rate at which a particle moves) of one species to another. This is a direct relationship, where a greater diffusion coefficient means the species is moving further in the same time step.

The diffusion coefficient can be calculated using the Einstein relation

$$\lim_{\tau\to\infty}\langle x^2(\tau)\rangle = 2nD\tau^{\alpha} + C, \text{where } \alpha = 1 \tag{7.13}$$

where n is the number of dimensions being considered, D is the diffusion coefficient, α is an indicator of the type of diffusion (sub-, normal or super-) and C is a constant.

It should be noted that lag time is used, not "real time" in the simulation, and the data for any given lag time is taken from all data-points which are separated by the lag time i.e. from any two positions separated in time by τ. This is due to the ergodicity of an ensemble, meaning that the choice of a "zero time" is arbitrary.

At short lag times, before enough averaging of ion motion occurs, the ion motion is within the ballistic regime and is undergoing super-diffusion (Equation 7.13 where $1 < \alpha < 2$). At longer lag times, if the ion is diffusing with true Brownian motion, Equation 7.13 can be used to calculate the diffusion coefficient ($\alpha = 1$). In order for Brownian motion to occur, the ion motion must be random in nature with no external effect influencing the motion.

An applied external electric field causes non-Brownian motion by forcing a constant flow of ions, a current. This means that Equation 7.13 cannot be used to explain ion motion parallel

to the electric field i.e. along the z vector.

When considering the motion along the z vector, the ions are subjected to constant force from the field. This force on the ions causes them to accelerate until the frictional force from surrounding ions balances out the force from the electric field at equilibrium, leading to the ions migrating through the liquid at a constant velocity, the drift velocity v_d.

Assuming the drift velocity of the ions caused by the electric field is constant, a drift corrected diffusion coefficient, also known as an effective diffusion coefficient, may be calculated by removing the drift from the MSD

$$D_{\text{eff}} = \frac{\langle x(\tau)^2 \rangle - \langle x(\tau) \rangle^2}{2n\tau} \tag{7.14}$$

where D_{eff} is the effective diffusion coefficient and $\langle x(\tau) \rangle$ is the ensemble mean displacement

$$\langle x(\tau) \rangle = \langle (x(t+\tau) - x(t)) \rangle \tag{7.15}$$

Calculations of D_{eff} can also check if the increase in diffusion is related exclusively to an increase in the drift. If D_{eff} in an electric field is equal to D (Equation 7.13) under no field conditions, then the drift is solely responsible for the change in diffusion. Thus, the electric field causes no changes to the system that affect the random nature of the diffusion, other than the drift.

However, if D_{eff} is not equal to D in zero field then the electric field is affecting the random nature of the fluctuations causing diffusion.

Considering the drift velocity, assuming a linear response, this should be related to the electric field strength by

$$v_d = \frac{\langle x(\tau) \rangle}{\tau} = \mu E \tag{7.16}$$

where v_d is the drift velocity, μ is the electrical mobility and E the electric field strength. Assuming Equation 7.16 is valid and the system is at a steady state, drift diffusion coefficients are accessible from the electrical mobility through the Einstein-Smoluchowski relation

$$D_{\text{drift}} = \frac{\mu k_B T}{q} = \frac{v_d k_B T}{qE} \tag{7.17}$$

where D_{drift} is the drift inclusive diffusion coefficient, q is the ion charge and k_B is Boltzmann's constant.

It has been demonstrated before that particles diffusing in the presence of a constant perturbation force can have a non-linear response to the applied force.[220] A general approach cannot

be found for each system, as the deviation from linear behaviour depends on the nature and strength of the interactions within the system in equilibrium, and also how the perturbation affects and interacts with these.

Here, the electric fields are defined as belonging to one of three groups depending on their effect on the inter-particle interactions in the system. According to their definitions, 'weak' electric fields are defined as those whose forces are not strong enough to change the interactions between the particles. 'Moderate' electric fields have strong enough forces to interfere with and change the interactions between particles, but are not strong enough to completely overcome the inter-particle interactions. 'Strong' electric field completely overcome the inter-particle interactions and the electric field forces become the dominant forces in the system.

Blickle *et. al* found that, as per the definitions above for their system, moderate perturbations were those that gave rise to non-linear responses.[220] Weak perturbations did not cause changes in the interactions so non-linearity was not observed, and strong perturbations led to the behaviour being dictated by the perturbations, which was a linear response.

In molecular solvents, inter-particle interactions are weak, arising mainly from dispersion forces, so non-linear responses are rarely encountered. In contrast to this, inter-particle interactions in ionic liquids are dominated by strong coulombic interactions. If the electric field changes the interaction between ions while also applying an accelerating force there will be a change in the frictional forces and a non-linear response to changes in the electric field.

A non-linear response of the drift velocity to changes in the strength of the electric field leads to μ changing with the electric field strength. As the relationship between the mobility and electric field strength is not linear, a calculation of D_{drift} is impossible.

7.4.2 Diffusion of Ions Parallel to the Electric Field

The greatest effect of the electric field should be seen parallel to the electric field.

$[\mathbf{C_4C_1im}][\mathbf{NTf_2}]$

As seen in Table 7.5 in Section 7.3, the temperature of the simulation box along the z vector increases noticeably at 0.05 VÅ^{-1}, therefore one would expect that the dynamics would remain the same in electric fields below this threshold. The mean square displacement is shown for $[C_4C_1im]^+$ (Figure 7.15) and $[NTf_2]^-$ (Figure 7.16) in $[C_4C_1im][NTf_2]$.

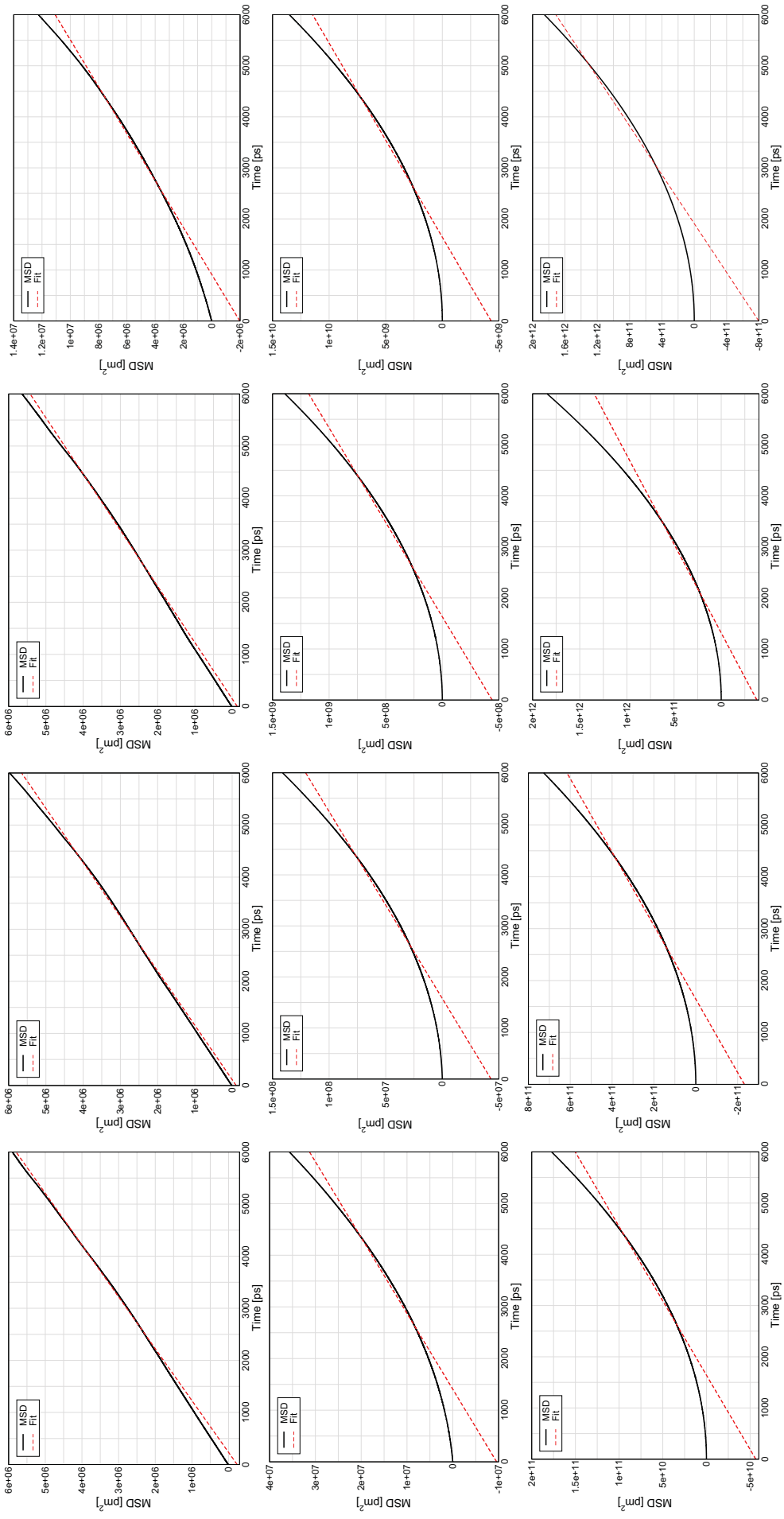

Figure 7.15: *Mean square displacement of $[C_4C_1im]^+$ along the z vector in $[C_4C_1im][NTf_2]$ in electric field simulations of (from top left reading across) 0.000 VÅ^{-1}, 0.001 VÅ^{-1}, 0.002 VÅ^{-1}, 0.005 VÅ^{-1}, 0.010 VÅ^{-1}, 0.020 VÅ^{-1}, 0.050 VÅ^{-1}, 0.100 VÅ^{-1}, 0.200 VÅ^{-1}, 0.300 VÅ^{-1}, 0.400 VÅ^{-1}, 0.500 VÅ^{-1}.*

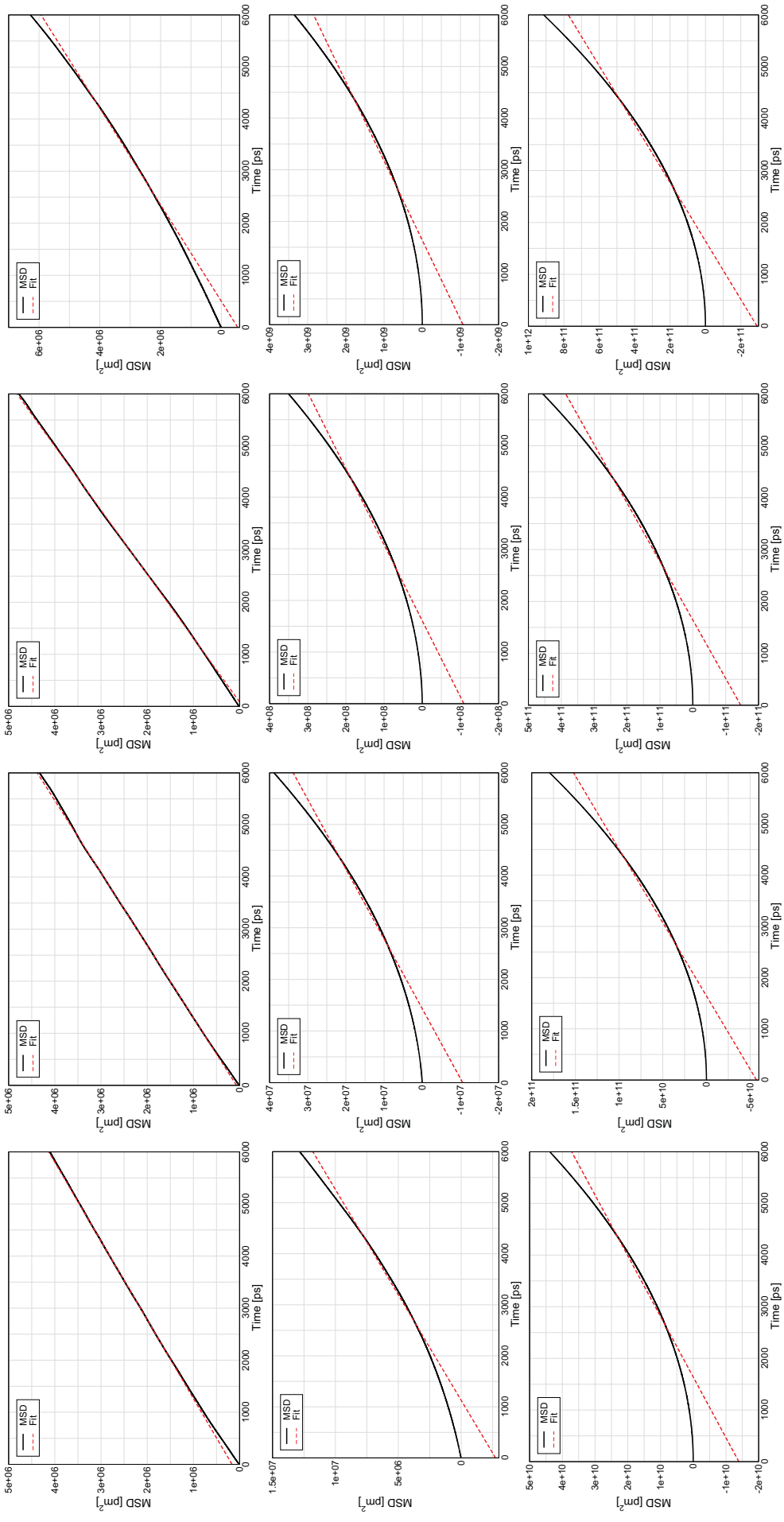

Figure 7.16: *Mean square displacement of $[NTf_2]^-$ along the z vector in $[C_4C_1im][NTf_2]$ in electric field simulations of (from top left reading across) 0.000 VÅ^{-1}, 0.001 VÅ^{-1}, 0.002 VÅ^{-1}, 0.005 VÅ^{-1}, 0.010 VÅ^{-1}, 0.020 VÅ^{-1}, 0.050 VÅ^{-1}, 0.100 VÅ^{-1}, 0.200 VÅ^{-1}, 0.300 VÅ^{-1}, 0.400 VÅ^{-1}, 0.500 VÅ^{-1}.*

Table 7.7: *Diffusion coefficients (D) and effective diffusion coefficients (D_{eff}) of $[C_4C_1im]^+$ and $[NTf_2]^-$ in the z direction in simulations of $[C_4C_1im][NTf_2]$ in electric fields.*

Field Strength [VÅ^{-1}]	D [$\times 10^{-10}$ m^{2}s^{-1}]		D_{eff} [$\times 10^{-10}$ m^{2}s^{-1}]	
	$[C_4C_1im]^+$	$[NTf_2]^-$	$[C_4C_1im]^+$	$[NTf_2]^-$
0.000	5.02	3.31	5.02	3.31
0.001	4.80	3.59	4.61	3.52
0.002	4.63	4.07	4.32	3.85
0.005	-	-	4.30	3.77
0.010	-	-	4.32	4.77
0.020	-	-	5.51	4.64
0.050	-	-	11.1	8.34
0.100	-	-	26.3	19.4
0.200	-	-	111	47.6
0.300	-	-	213	109
0.400	-	-	365	181
0.500	-	-	777	263

These show clearly that even though the temperature remains constant in electric fields of <0.05 VÅ^{-1}, there is a change in the MSD. The only electric fields that have a linear relationship between MSD and lag time are 0.000 VÅ^{-1}, 0.001 VÅ^{-1} and 0.002 VÅ^{-1}. In these electric fields the ions are undergoing normal diffusion, so Equation 7.13 can be used to calculate the diffusion coefficients. For completeness, drift corrected diffusion coefficients were calculated for these electric fields too.

For electric fields of ≥0.005 VÅ^{-1}, the relationship between MSD and lag time is non-linear and $\alpha > 1$. This means that Equation 7.13 cannot be used to find the diffusion coefficient, and instead a drift corrected diffusion coefficient should be found using Equation 7.14. These are shown in Table 7.7.

In electric fields ≤0.02 VÅ^{-1}, the D and D_{eff} of $[C_4C_1im]^+$ and $[NTf_2]^-$ remain approximately the same as D(zero field). This indicates that the induction of a drift is the only change in the system, which causes the change in the MSD, and this change is not due to a change in the diffusive character of the ions.

In electric fields >0.02 VÅ^{-1}, removing the drift does not fully compensate for the change in the MSD and leads to D_{eff} increasing to greater than D(zero field). This shows that at these electric fields there are other effects upon the diffusion of the ions occurring, i.e. the diffusive character of the ions is now being affected by the electric field.

To investigate this further, the drift velocities of $[C_4C_1im]^+$ and $[NTf_2]^-$ in $[C_4C_1im][NTf_2]$ were calculated from the mean displacement using Equation 7.16. These are shown in Table 7.8 and plotted against electric field strength in Figure 7.17.

Table 7.8 shows that there is drift of both of the ions in every electric field, even though at

Table 7.8: *Drift velocity of $[C_4C_1im]^+$ and $[NTf_2]^-$ in the z direction in simulations of $[C_4C_1im][NTf_2]$ in electric fields.*

Field Strength [VÅ^{-1}]	Drift Velocity [pm ps^{-1}] $[C_4C_1im]^+$	$[NTf_2]^-$
0.001	0.09	-0.04
0.002	0.16	-0.08
0.005	0.43	-0.21
0.010	0.92	-0.46
0.020	1.94	-0.96
0.050	6.19	-3.08
0.100	19.4	-9.63
0.200	70.1	-34.8
0.300	142	-70.6
0.400	227	-113
0.500	321	-159

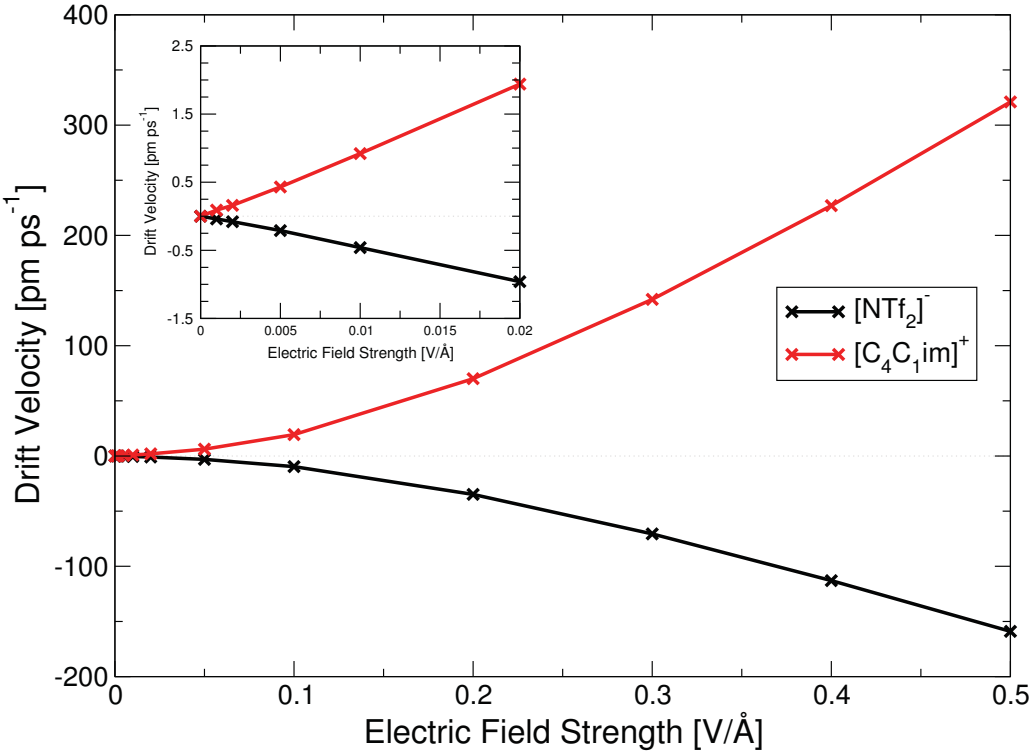

Figure 7.17: *Drift velocities of the centre of mass of $[C_4C_1im]^+$ and $[NTf_2]^-$ in the z direction in simulations of $[C_4C_1im][NTf_2]$ in electric fields. Inset shows the drift velocities for electric fields below 0.05 VÅ^{-1}.*

0.001 VÅ^{-1} and 0.002 VÅ^{-1} this drift does not seem to be large enough to affect the MSD and $D \approx D_{\text{eff}}$. The drift can be seen to increase with the electric field strength, which is expected as higher electric fields apply a larger force to the ions.

The drift velocities and graphs of mean displacement (Figure 7.18 and Figure 7.19) show that $[C_4C_1im]^+$ drifts in the positive z direction and $[NTf_2]^-$ drifts in the negative z direction, which are the directions expected from the direction of the force from the electric field.

In weak electric fields (<0.05 VÅ^{-1}), the drift velocity of $[C_4C_1im]^+$ and $[NTf_2]^-$ changes linearly with electric field strength (see inset in Figure 7.17). Using Equation 7.16 a mobility of 9.0 × 10^{-9} m^2 s^{-1} V^{-1} can be calculated for $[C_4C_1im]^+$, and a mobility of -4.5 × 10^{-9} m^2 s^{-1} V^{-1} for $[NTf_2]^-$ in this range. The Einstein-Smoluchowski relation (Equation 7.17) gives drift diffusion coefficients of 3.10 × 10^{-10} m^2 s^{-1} for $[C_4C_1im]^+$ and 1.55 × 10^{-10} m^2 s^{-1} for $[NTf_2]^-$.
In moderate electric fields ($\geq$ 0.05 VÅ^{-1}) the relationship between v_d and E breaks down. Here, v_d changes more than expected when increasing E, thus the mobility is not the same. It can be seen that the magnitude of the mobility increases with electric field strength, indicating that the ions appear to be more susceptible to the electric field the stronger the electric field is.
Considering the changing trend between the drift velocity (and thus mobility) with electric field strength, as well as the fact that D_{eff} increases with electric field strength, it can be seen that this is not a simple system to investigate. This is discussed more in Section 7.4.4.

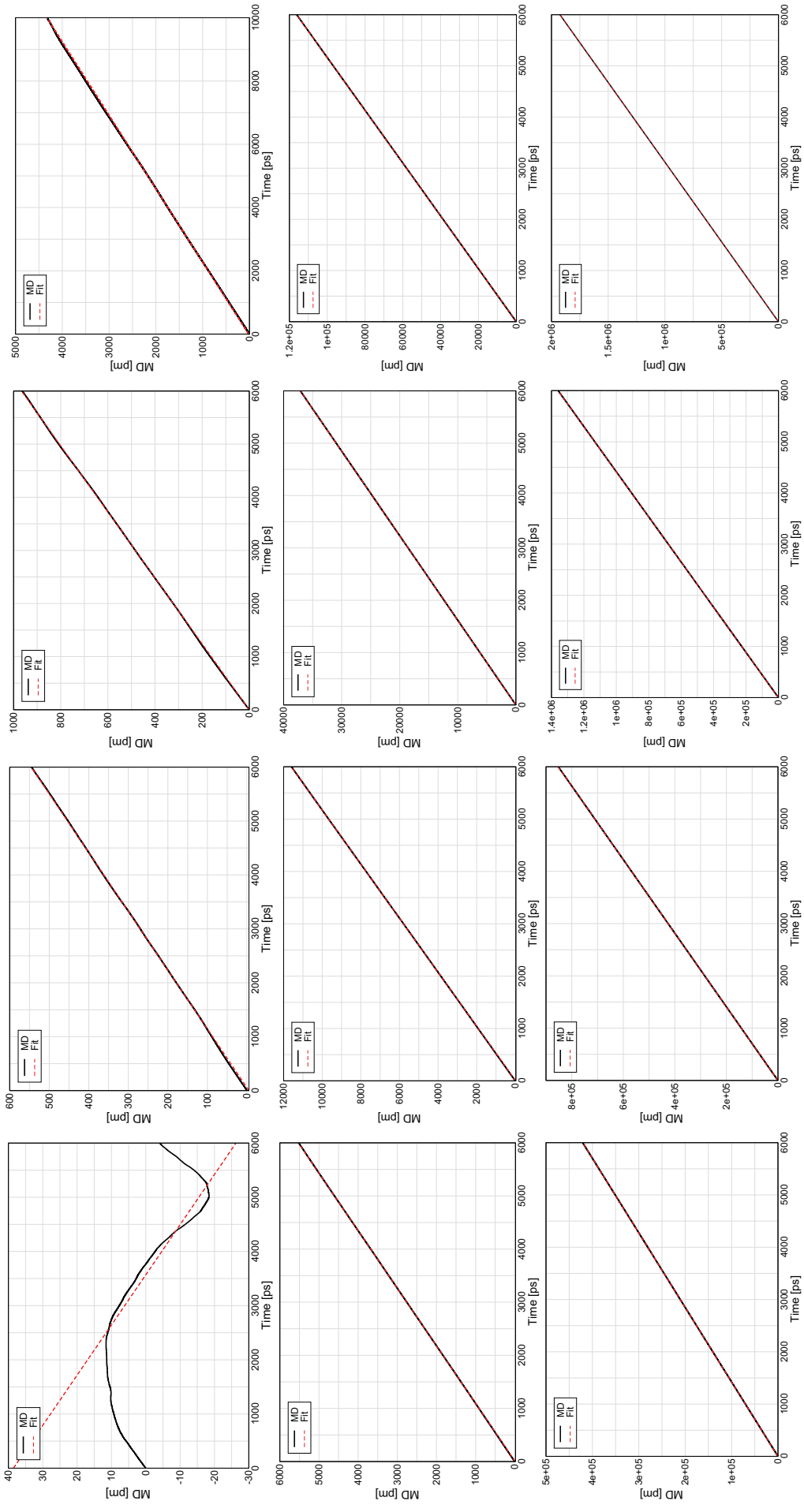

Figure 7.18: *Mean displacement against lag time for $[C_4C_1im]^+$ along the z direction in simulations of $[C_4C_1im][NTf_2]$ in electric fields of (from top left reading across) 0.000 $VÅ^{-1}$, 0.001 $VÅ^{-1}$, 0.002 $VÅ^{-1}$, 0.005 $VÅ^{-1}$, 0.010 $VÅ^{-1}$, 0.020 $VÅ^{-1}$, 0.050 $VÅ^{-1}$, 0.100 $VÅ^{-1}$, 0.200 $VÅ^{-1}$, 0.300 $VÅ^{-1}$, 0.400 $VÅ^{-1}$, 0.500 $VÅ^{-1}$.*

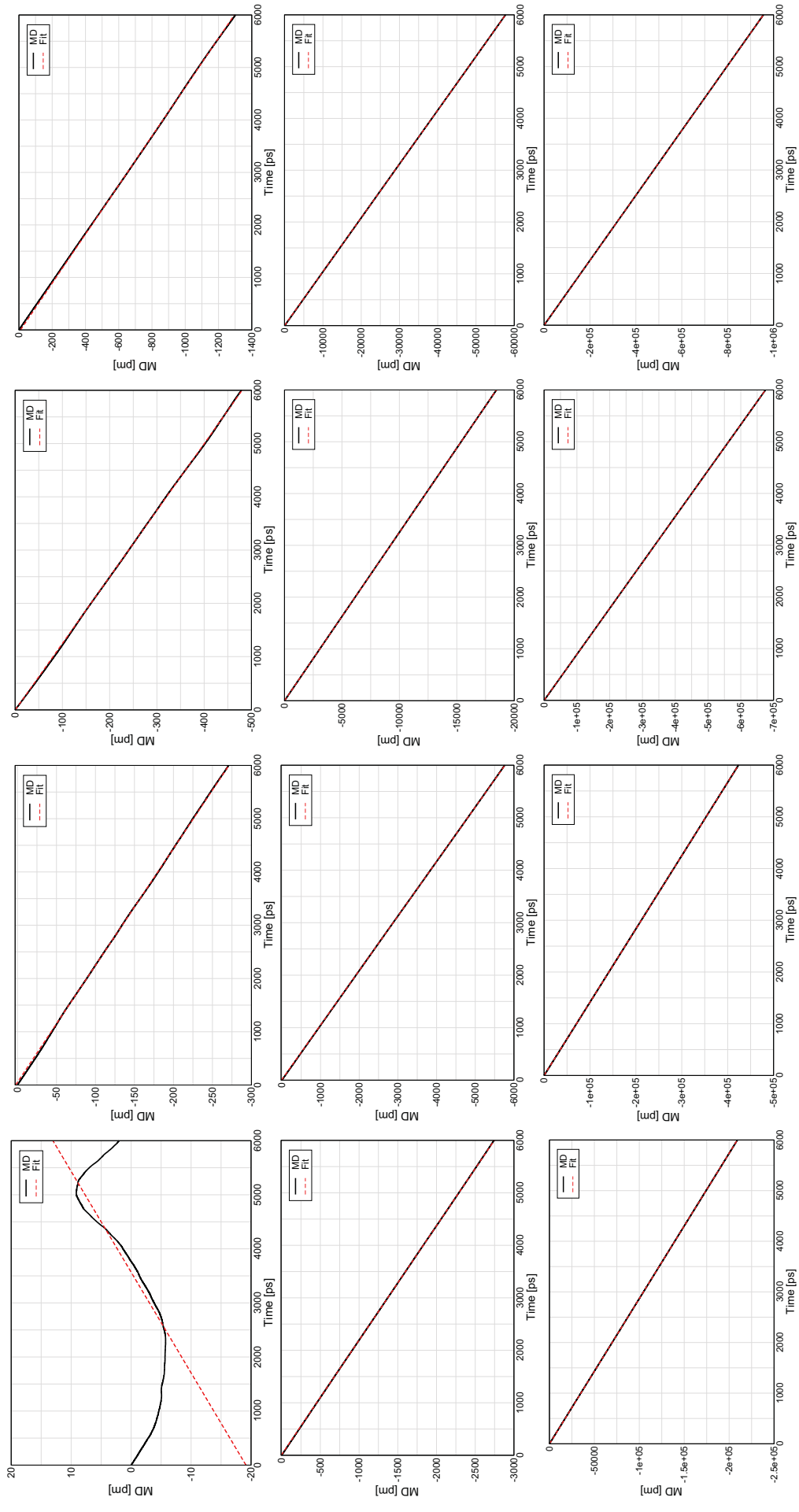

Figure 7.19: *Mean displacement against lag time of $[NTf_2]^-$ along the z direction in simulations of $[C_4C_1im][NTf_2]$ in electric fields of (from top left reading across) 0.000 VÅ^{-1}, 0.001 VÅ^{-1}, 0.002 VÅ^{-1}, 0.005 VÅ^{-1}, 0.010 VÅ^{-1}, 0.020 VÅ^{-1}, 0.050 VÅ^{-1}, 0.100 VÅ^{-1}, 0.200 VÅ^{-1}, 0.300 VÅ^{-1}, 0.400 VÅ^{-1}, 0.500 VÅ^{-1}.*

$[C_8C_1im][NTf_2]$

Table 7.6 shows that the temperature of the simulation box of $[C_8C_1im][NTf_2]$ along the z vector increases significantly at 0.05 VÅ^{-1}. Therefore, the MSD of the ions along the z direction in electric fields with constant temperature are shown in Figures 7.20 and 7.21.
Similarly to $[C_4C_1im][NTf_2]$, the MSD changes in electric fields of >0.002 VÅ^{-1}, despite a constant temperature being observed <0.05 VÅ^{-1}, which indicates that there is a drift in these electric fields that affects the MSD. Therefore Equation 7.13 can only be used to calculate the diffusion of the ions in electric fields of ≤0.002 VÅ^{-1}. For the rest of the electric fields, Equation 7.14 can be used to calculate the effective diffusion coefficient. These are all shown in Table 7.9.

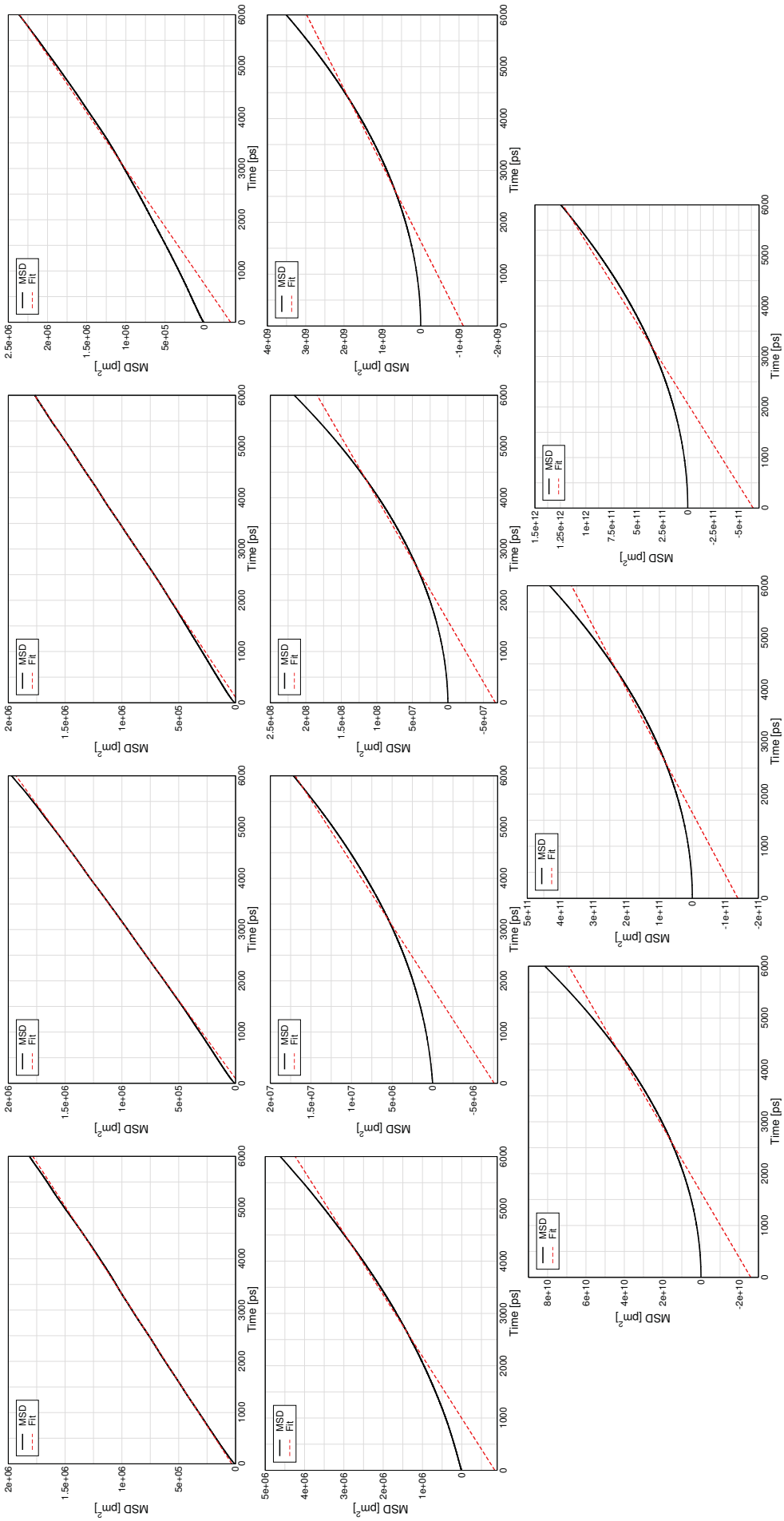

Figure 7.20: *Mean square displacement of $[C_8C_1im]^+$ along the z vector in $[C_8C_1im][NTf_2]$ in electric field simulations of (from top left reading across) 0.000 VÅ^{-1}, 0.001 VÅ^{-1}, 0.002 VÅ^{-1}, 0.005 VÅ^{-1}, 0.010 VÅ^{-1}, 0.020 VÅ^{-1}, 0.050 VÅ^{-1}, 0.100 VÅ^{-1}, 0.200 VÅ^{-1}, 0.300 VÅ^{-1}, 0.400 VÅ^{-1}.*

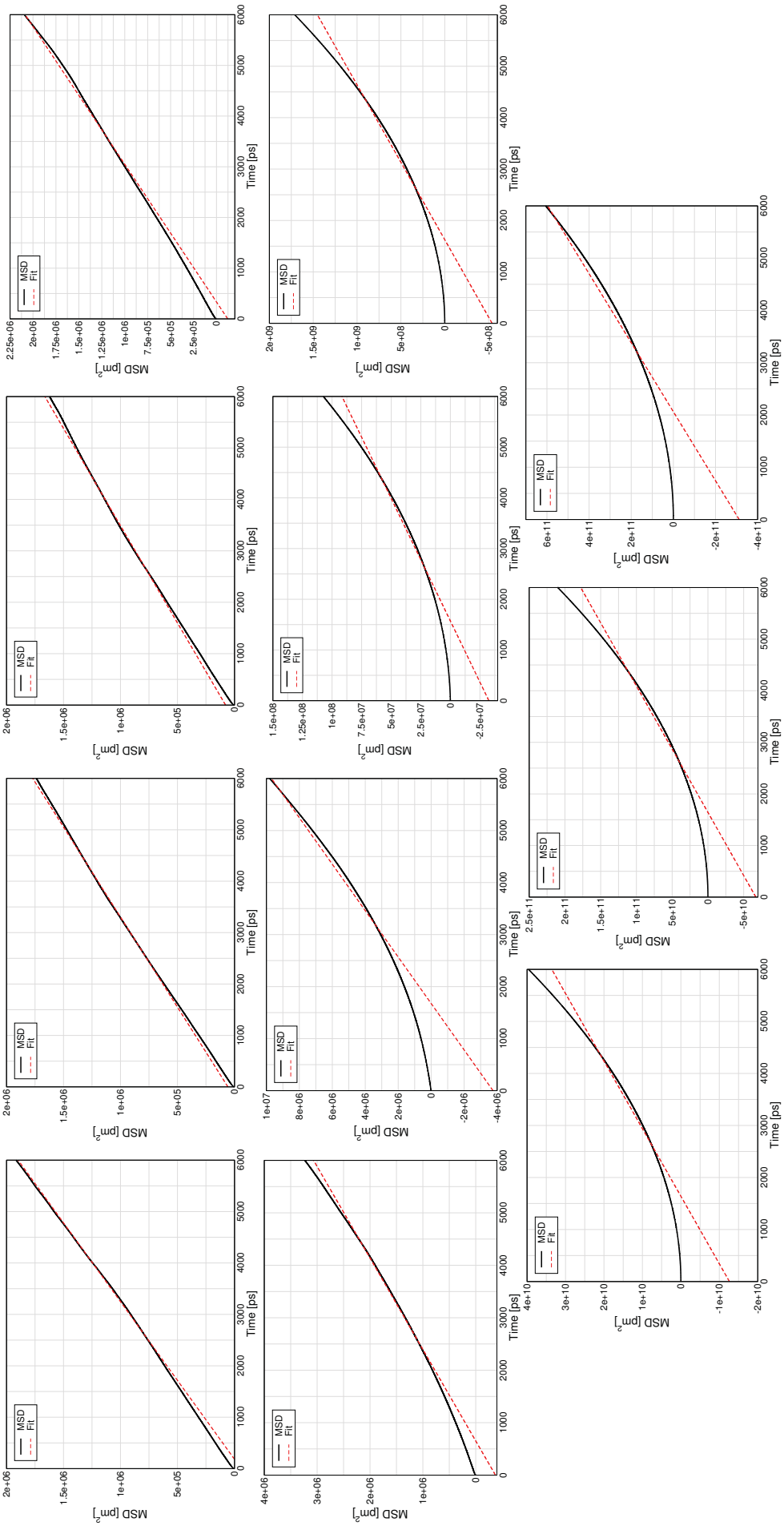

Figure 7.21: *Mean square displacement of $[NTf_2]^-$ along the z vector in $[C_8C_1im][NTf_2]$ in electric field simulations of (from top left reading across) 0.000 VÅ^{-1}, 0.001 VÅ^{-1}, 0.002 VÅ^{-1}, 0.005 VÅ^{-1}, 0.010 VÅ^{-1}, 0.020 VÅ^{-1}, 0.050 VÅ^{-1}, 0.100 VÅ^{-1}, 0.200 VÅ^{-1}, 0.300 VÅ^{-1}, 0.400 VÅ^{-1}.*

Table 7.9: *Diffusion coefficients (D) and effective diffusion coefficients (D_{eff}) of $[C_8C_1im]^+$ and $[NTf_2]^-$ in the z direction in simulations of $[C_8C_1im][NTf_2]$ in electric fields.*

Field Strength [VÅ^{-1}]	D [$\times 10^{-10}$ m^{2}s^{-1}]		D_{eff} [$\times 10^{-10}$ m^{2}s^{-1}]	
	$[C_8C_1im]^+$	$[NTf_2]^-$	$[C_8C_1im]^+$	$[NTf_2]^-$
0.000	1.50	1.67	1.50	1.67
0.001	1.72	1.38	1.70	1.37
0.002	1.49	1.25	1.49	1.25
0.005	-	-	1.51	1.49
0.010	-	-	1.62	1.57
0.020	-	-	2.12	2.30
0.050	-	-	4.42	4.10
0.100	-	-	24.4	14.7
0.200	-	-	121	62.8
0.300	-	-	346	116
0.400	-	-	576	250

It can be seen from this table that the diffusion coefficients of the ions remain constant in electric fields of $\leq$0.01 VÅ^{-1}. Above this, there is a steady increase in the diffusion coefficient of both ions. It can also be seen that the cation and anion have approximately similar diffusion coefficients in electric fields of $\leq$0.05 VÅ^{-1}. Above this, there is deviation of the two.

To investigate this further, the drift velocities of $[C_8C_1im]^+$ and $[NTf_2]^-$ were calculated and are shown in Table 7.10 and plotted against electric field strength in Figure 7.22.

Table 7.10: *Drift velocity of $[C_8C_1im]^+$ and $[NTf_2]^-$ in the z direction in simulations of $[C_8C_1im][NTf_2]$ in electric fields.*

Field Strength [VÅ^{-1}]	Drift Velocity [pm ps^{-1}]	
	$[C_8C_1im]^+$	$[NTf_2]^-$
0.001	0.02	-0.02
0.002	-	-
0.005	0.13	-0.09
0.010	0.27	-0.19
0.020	0.64	-0.45
0.050	2.42	-1.69
0.100	9.83	-6.85
0.200	47.5	-33.1
0.300	110	-76.4
0.400	186	-130

Unexpectedly, for the simulation at 0.002 VÅ^{-1} there is no significant drift, despite there being a drift at 0.001 VÅ^{-1}. The plot of MD against lag time for both ions (shown in Figure 7.23 and 7.24) shows that there is a weak drift of the ions, but this is similar to that of zero field. Therefore there is a negligible drift in this simulation.

The inset in Figure 7.22 shows that the drift velocities for the simulations $\leq$0.01 VÅ^{-1} a linear relationship between the electric field strength and the drift velocity of the ions is observed.

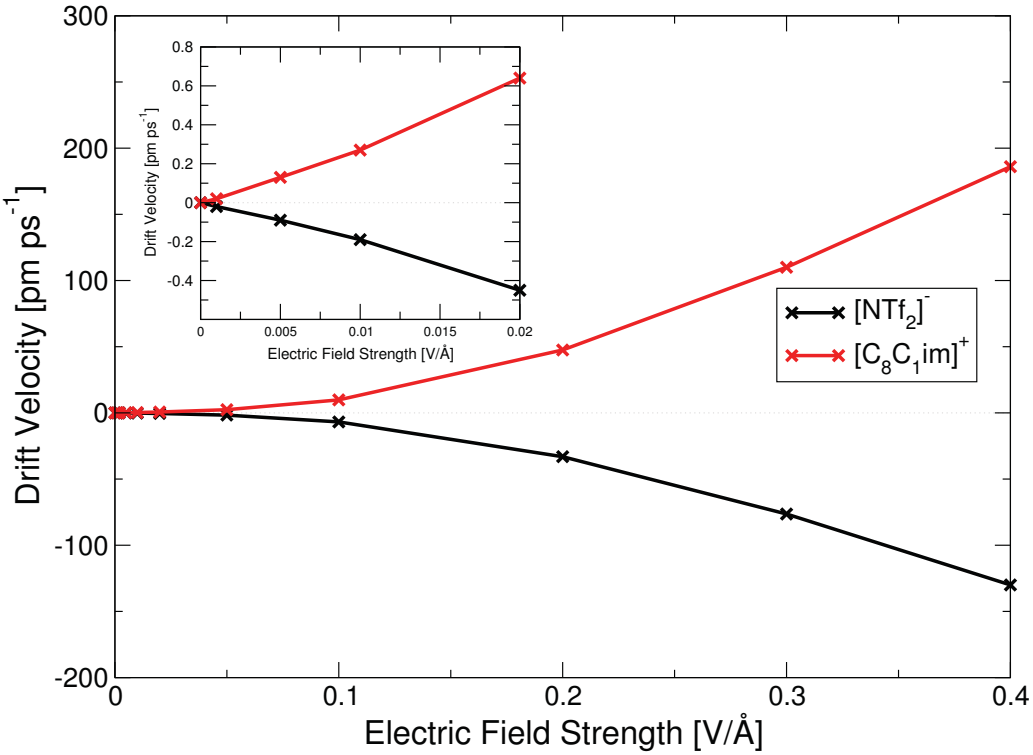

Figure 7.22: *Drift velocities of the centre of mass of $[C_8C_1im]^+$ and $[NTf_2]^-$ in the z direction in simulations of $[C_8C_1im][NTf_2]$ in electric fields. Inset shows the drift velocities for electric fields below 0.05 VÅ^{-1}.*

Using Equation 7.16, a mobility of 2.53 × 10^{-9} m^2 s^{-1} V^{-1} can be calculated for $[C_8C_1im]^+$, and a mobility of -1.76 × 10^{-9} m^2 s^{-1} V^{-1} for $[NTf_2]^-$ in this range. The Einstein-Smoluchowski relation (Equation 7.17) gives drift diffusion coefficients of 8.72 × 10^{-11} m^2 s^{-1} for $[C_8C_1im]^+$ and 6.41 × 10^{-11} m^2 s^{-1} for $[NTf_2]^-$. The values for the mobility and drift diffusion coefficients are lower for $[C_8C_1im][NTf_2]$ than $[C_4C_1im][NTf_2]$, which follows the same trend as the diffusion coefficients.

In electric fields of ≥0.02 VÅ^{-1} this relationship between electric field strength and drift velocity breaks down, and the drift velocity increases more than would be expected from the mobility, which becomes dependent upon the electric field strength.

In these electric fields, $D_{\text{eff}} > D$ as well, therefore the breakdown of the Einstein-Smoluchowski relation again coincides with an increase in the diffusive character of the ions.

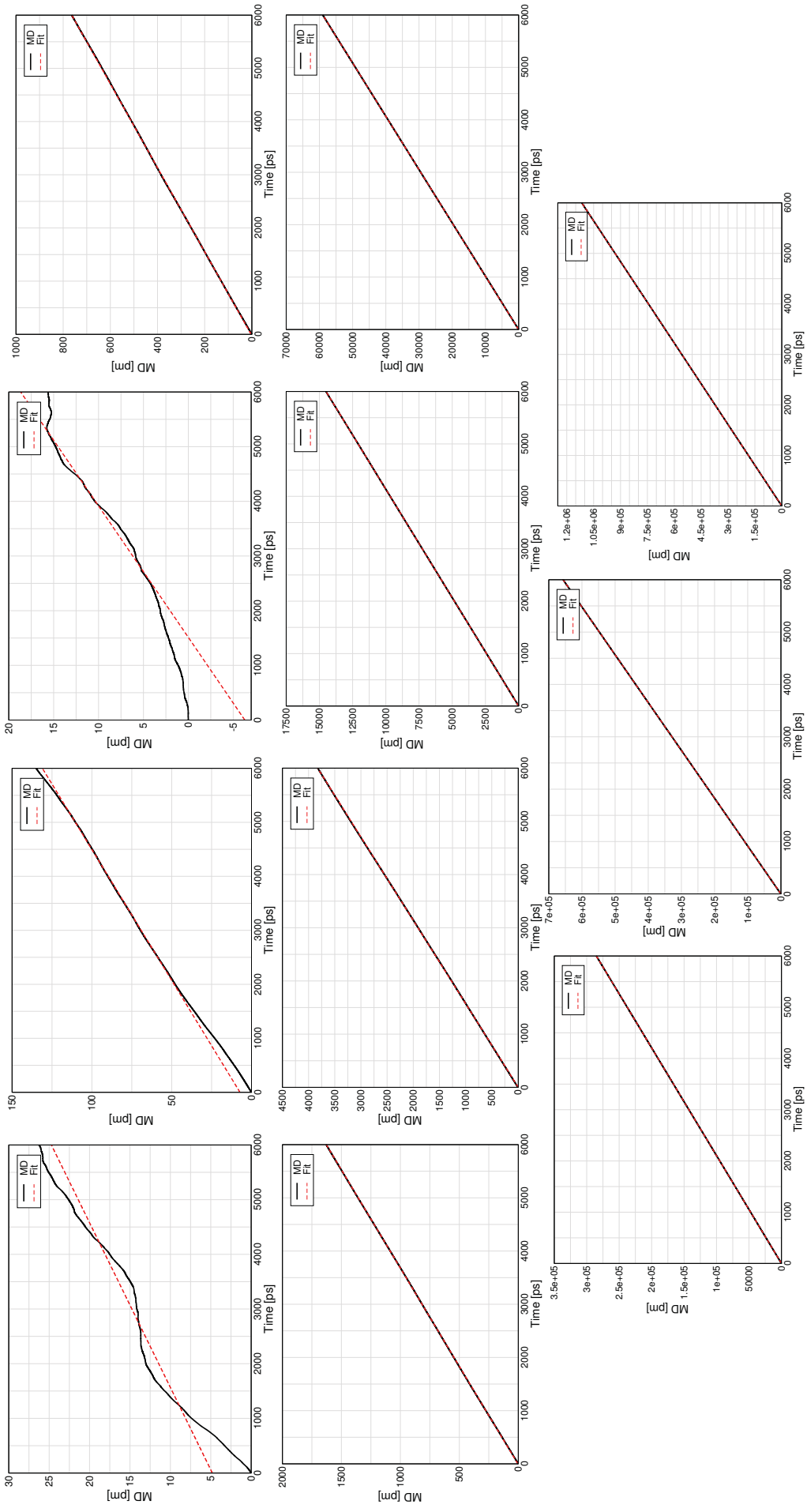

Figure 7.23: *Mean displacement against lag time for $[C_8C_1im]^+$ along the z direction in simulations of $[C_8C_1im][NTf_2]$ in electric fields of (from top left reading across) 0.000 VÅ^{-1}, 0.001 VÅ^{-1}, 0.002 VÅ^{-1}, 0.005 VÅ^{-1}, 0.010 VÅ^{-1}, 0.020 VÅ^{-1}, 0.050 VÅ^{-1}, 0.100 VÅ^{-1}, 0.200 VÅ^{-1}, 0.300 VÅ^{-1}, 0.400 VÅ^{-1}.*

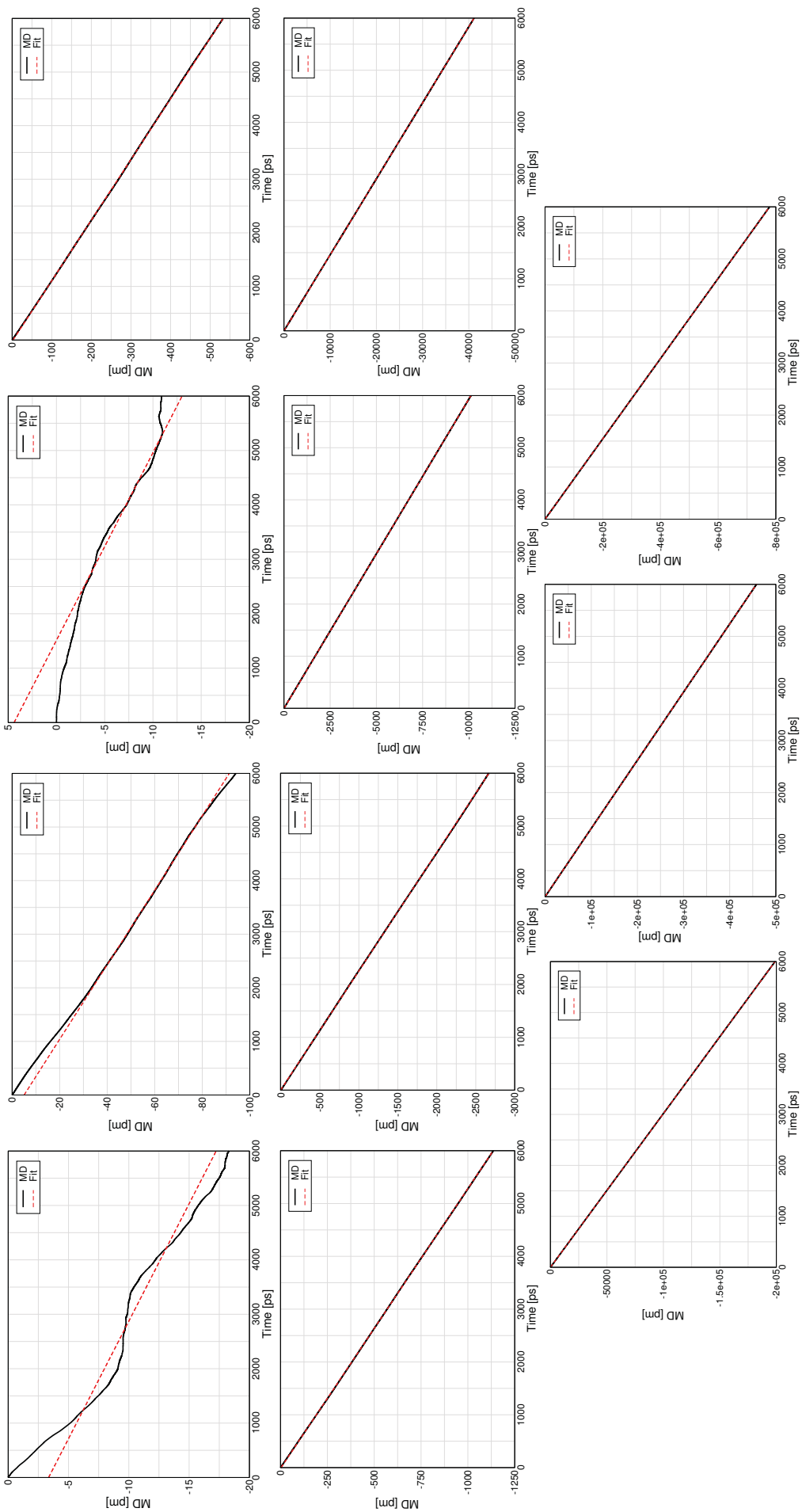

Figure 7.24: *Mean displacement against lag time of $[NTf_2]^-$ along the z direction in simulations of $[C_8C_1im][NTf_2]$ in electric fields of (from top left reading across) 0.000 VÅ^{-1}, 0.001 VÅ^{-1}, 0.002 VÅ^{-1}, 0.005 VÅ^{-1}, 0.010 VÅ^{-1}, 0.020 VÅ^{-1}, 0.050 VÅ^{-1}, 0.100 VÅ^{-1}, 0.200 VÅ^{-1}, 0.300 VÅ^{-1}, 0.400 VÅ^{-1}.*

7.4.3 Diffusion of Ions Perpendicular to the Electric Field

An assumption of the thermostatting method in the electric field was that because there was no external force perpendicular to the field, the motion will be unaffected by the field and can be used to control the temperature. Indeed the temperatures in these directions remain relatively constant, increasing by just a few degrees Kelvin at the higher electric field strengths (≥ 0.3 VÅ^{-1} in Tables 7.5 and 7.6), but remaining near the set temperature. To investigate this, the mean squared displacements of the ions perpendicular to the electric field were investigated in both $[C_4C_1im][NTf_2]$ and $[C_8C_1im][NTf_2]$ in all electric field strengths.

$[\mathbf{C_4C_1im}][\mathbf{NTf_2}]$

The mean squared displacements of the cation and anion in $[C_4C_1im][NTf_2]$ were calculated along the x and y vectors, and are shown in Figures 7.25, 7.26, 7.27, 7.28. The relationship between mean squared displacement and lag time was found to be linear for all of the electric fields tested here, so the Einstein relation (Equation 7.13) was used to calculate the diffusion coefficients of the cation and anion in these directions. These are shown in Table 7.11.

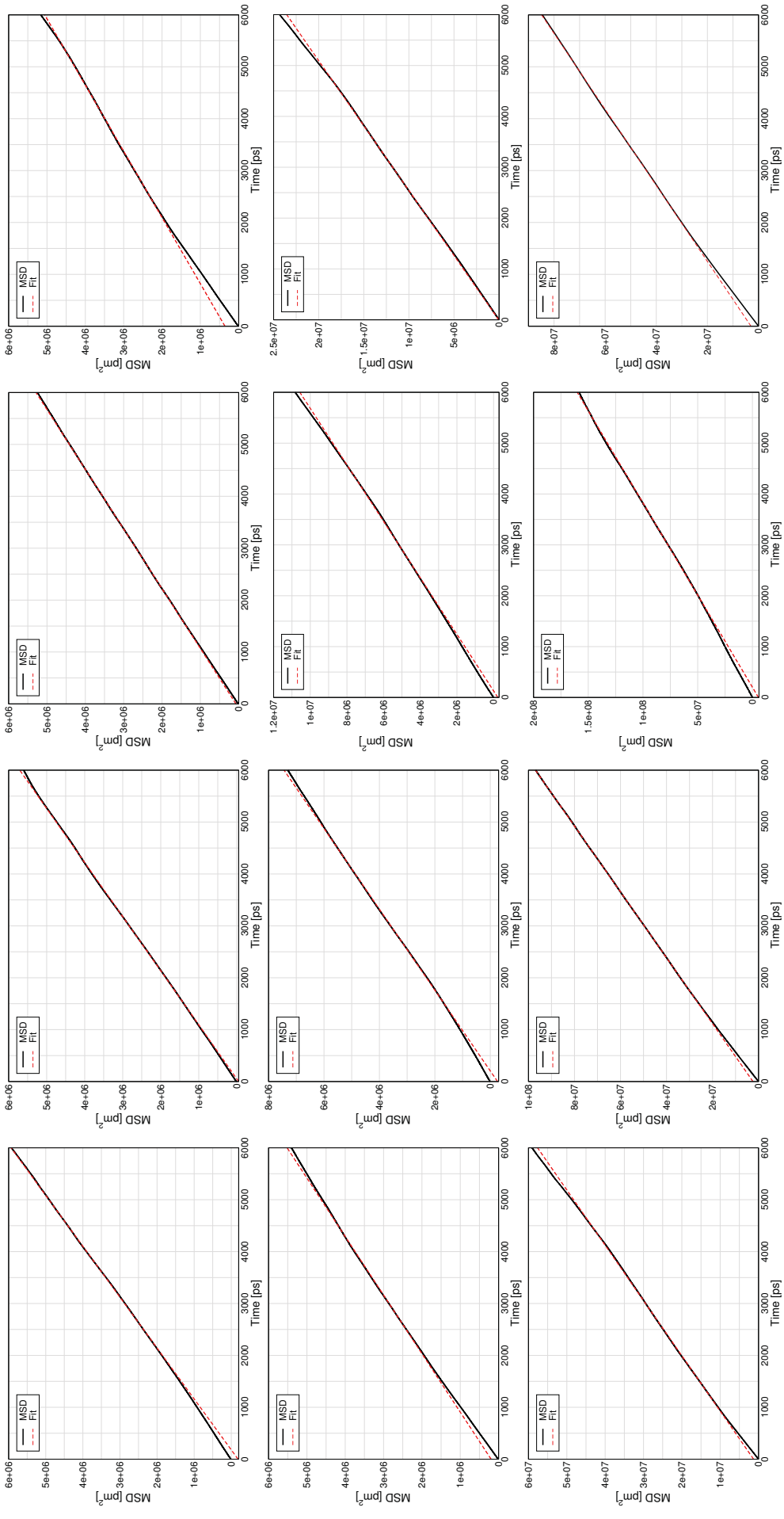

Figure 7.25: *Mean squared displacement against lag time for the centre of mass of $[C_4C_1im]^+$ in $[C_4C_1im][NTf_2]$ along the x vector. The electric fields are, from top left reading across, 0.000 VÅ^{-1}, 0.001 VÅ^{-1}, 0.002 VÅ^{-1}, 0.005 VÅ^{-1}, 0.010 VÅ^{-1}, 0.020 VÅ^{-1}, 0.050 VÅ^{-1}, 0.100 VÅ^{-1}, 0.200 VÅ^{-1}, 0.300 VÅ^{-1}, 0.400 VÅ^{-1}, 0.500 VÅ^{-1}.*

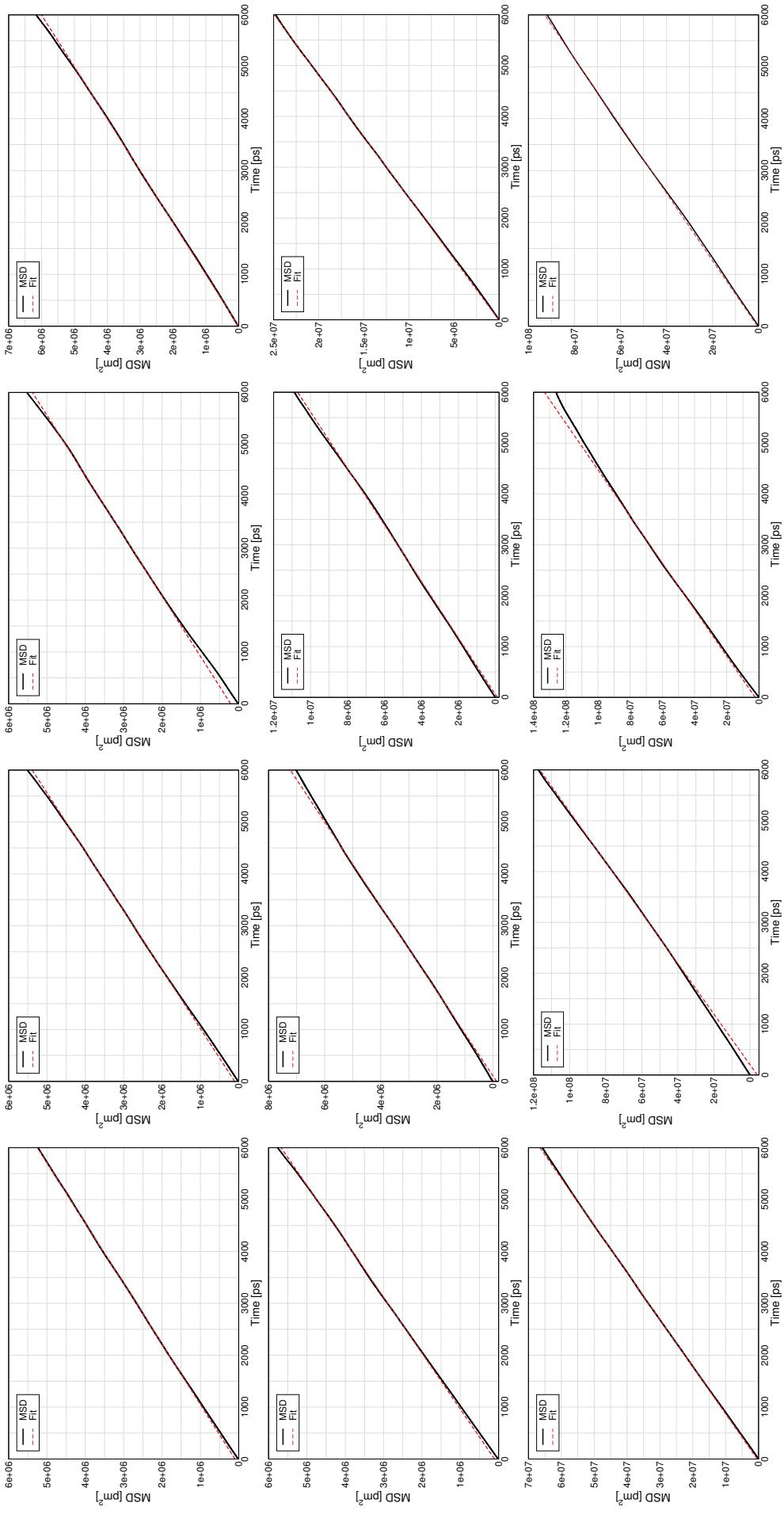

Figure 7.26: *Mean squared displacement against lag time for the centre of mass of $[C_4C_1im]^+$ in $[C_4C_1im][NTf_2]$ along the y vector. The electric fields are, from top left reading across, 0.000 VÅ^{-1}, 0.001 VÅ^{-1}, 0.002 VÅ^{-1}, 0.005 VÅ^{-1}, 0.010 VÅ^{-1}, 0.020 VÅ^{-1}, 0.050 VÅ^{-1}, 0.100 VÅ^{-1}, 0.200 VÅ^{-1}, 0.300 VÅ^{-1}, 0.400 VÅ^{-1}, 0.500 VÅ^{-1}.*

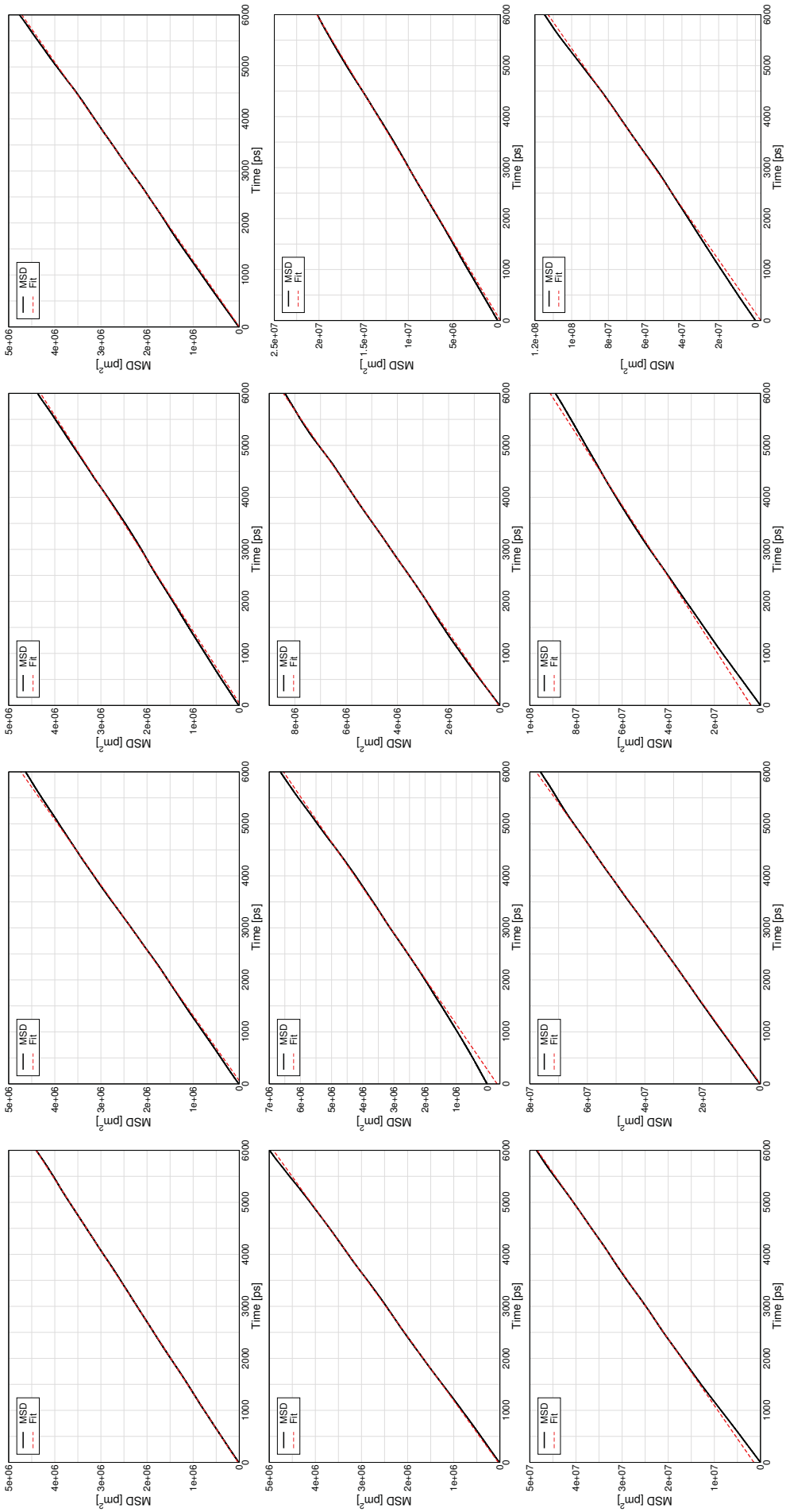

Figure 7.27: *Mean squared displacement against lag time for the centre of mass of $[NTf_2]^-$ in $[C_4C_1im][NTf_2]$ along the x vector. The electric fields are, from top left reading across, 0.000 VÅ^{-1}, 0.001 VÅ^{-1}, 0.002 VÅ^{-1}, 0.005 VÅ^{-1}, 0.010 VÅ^{-1}, 0.020 VÅ^{-1}, 0.050 VÅ^{-1}, 0.100 VÅ^{-1}, 0.200 VÅ^{-1}, 0.300 VÅ^{-1}, 0.400 VÅ^{-1}, 0.500 VÅ^{-1}.*

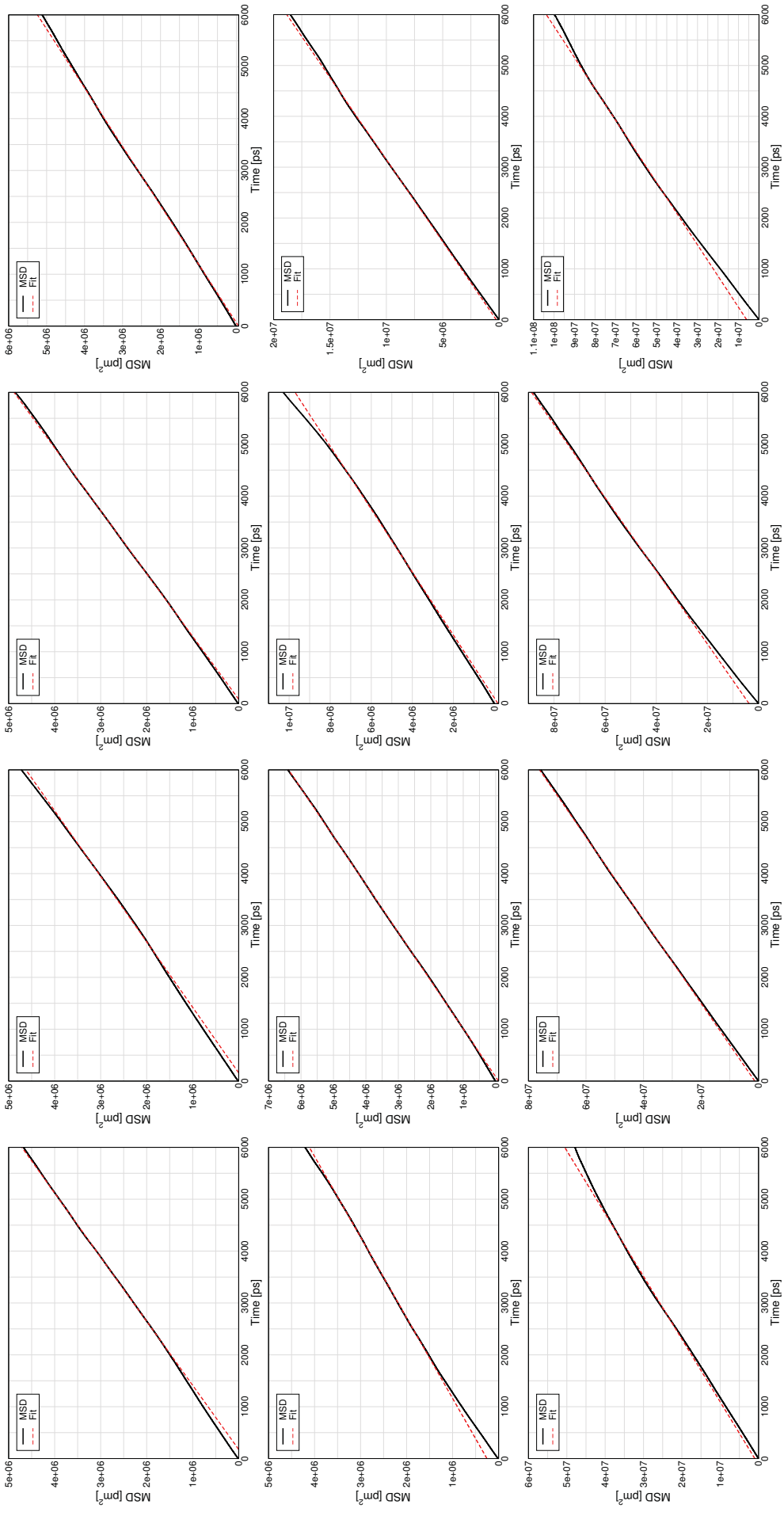

Figure 7.28: *Mean squared displacement against lag time for the centre of mass of $[NTf_2]^-$ in $[C_4C_1im][NTf_2]$ along the y vector. The electric fields are, from top left reading across, 0.000 VÅ^{-1}, 0.001 VÅ^{-1}, 0.002 VÅ^{-1}, 0.005 VÅ^{-1}, 0.010 VÅ^{-1}, 0.020 VÅ^{-1}, 0.050 VÅ^{-1}, 0.100 VÅ^{-1}, 0.200 VÅ^{-1}, 0.300 VÅ^{-1}, 0.400 VÅ^{-1}, 0.500 VÅ^{-1}.*

Table 7.11: *Diffusion coefficients of the cation and anion in [C_4C_1im][NTf_2] in all electric fields along the x and y directions calculated using Equation 7.13.*

Field Strength [VÅ^{-1}]	Diffusion Coefficient [$\times 10^{-10}$ m^{2}s^{-1}]					
	$[C_4C_1im]^+$			$[NTf_2]^-$		
	x	y	xy	x	y	xy
0.000	4.90	4.29	4.60	3.65	4.04	3.84
0.001	4.80	4.40	4.60	3.99	3.96	3.97
0.002	4.35	4.31	4.32	3.62	4.13	3.88
0.005	3.92	5.00	4.39	3.93	4.41	4.17
0.010	4.43	4.64	4.55	4.06	3.22	3.64
0.020	6.42	6.12	6.27	5.71	5.39	5.55
0.050	9.00	9.01	9.00	7.01	8.23	7.62
0.100	19.6	20.7	20.2	17.1	15.5	16.3
0.200	47.0	55.1	51.0	39.1	41.3	40.2
0.300	78.8	100	89.7	65.0	62.4	63.7
0.400	138	119	129	72.6	70.9	71.7
0.500	147	154	151	96.4	91.4	93.9

Table 7.11 shows that the diffusion coefficients of $[C_4C_1im]^+$ and $[NTf_2]^-$ remain constant up to 0.01 VÅ^{-1} matching the constant temperature values in Table 7.5.

Electric fields of $\geq$0.02 VÅ^{-1} cause an increase in the diffusion coefficients of the ions perpendicular to the field direction, with the magnitude increasing with electric field strength. At $\geq$0.3 VÅ^{-1}, this is accompanied by an increase in temperature but not at electric fields below this.

The increase in diffusion is not due to a drift of the ions, as the mean displacement along the x and y axis is negligible (shown in Figures 7.29 and 7.30), and the relationship between the MSD and lag time is linear ($\alpha = 1$).

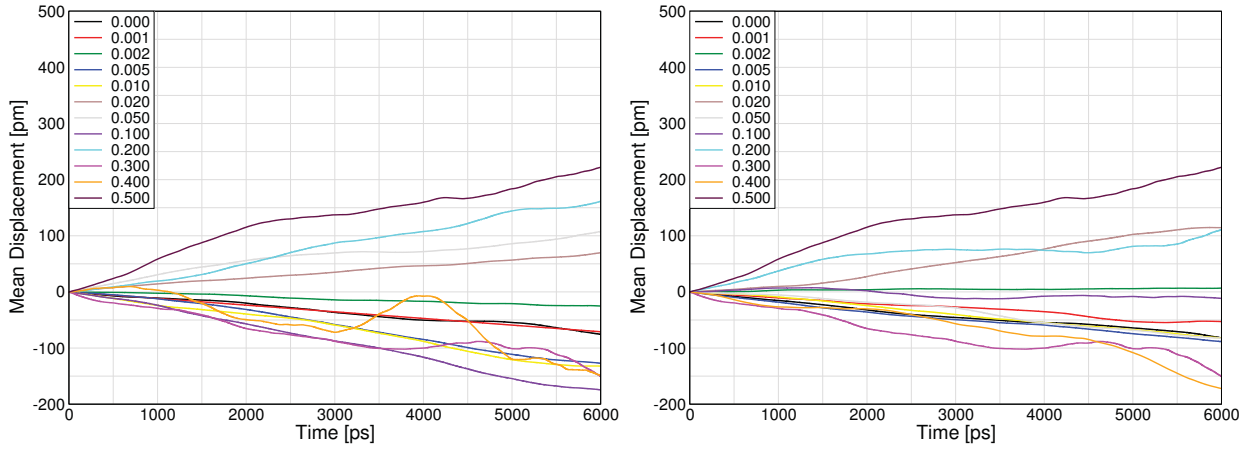

Figure 7.29: *Mean displacement of [C_4C_1im]$^+$ along the x (left) and y (right) vectors. Electric fields are shown in the legend in VÅ^{-1}.*

The lack of drift or changes to the temperature of the simulation with an increase in the diffusion coefficient further highlights the complexity of the diffusion of ions in an electric field in

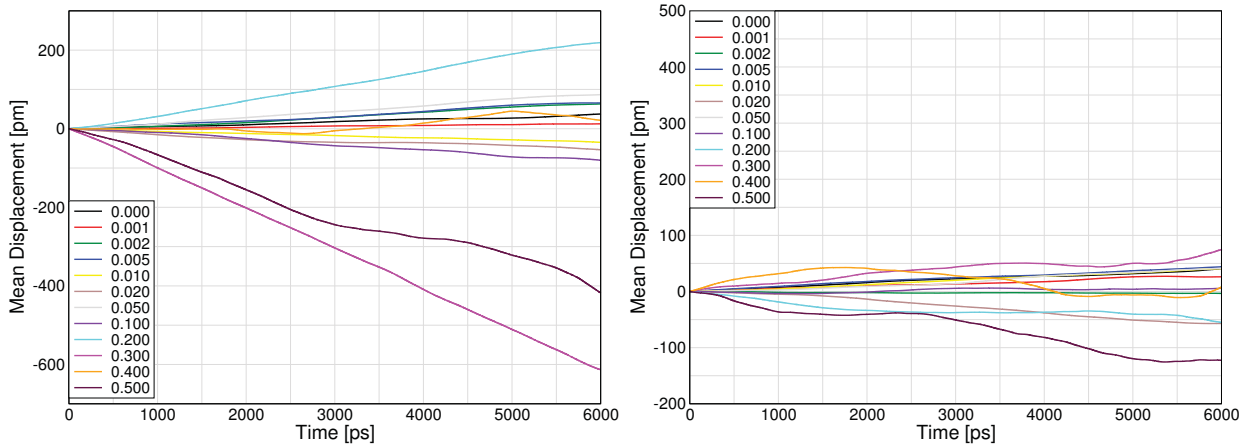

Figure 7.30: *Mean displacement of $[NTf_2]^-$ along the x (left) and y (right) vectors. Electric fields are shown in the legend in VÅ^{-1}.*

ionic liquids. This is discussed more below.

$[C_8C_1im][NTf_2]$

The mean squared displacement of the cation and anion in $[C_8C_1im][NTf_2]$ were calculated along the x and y vectors of the simulation box and are shown in Figures 7.31, 7.32, 7.33, 7.34. The relationship between mean squared displacement and lag time was found to be linear for all of the electric fields tested here, so the Einstein relation (Equation 7.13) was used to calculate the diffusion coefficients of the cation and anion in these directions. These are shown in Table 7.12.

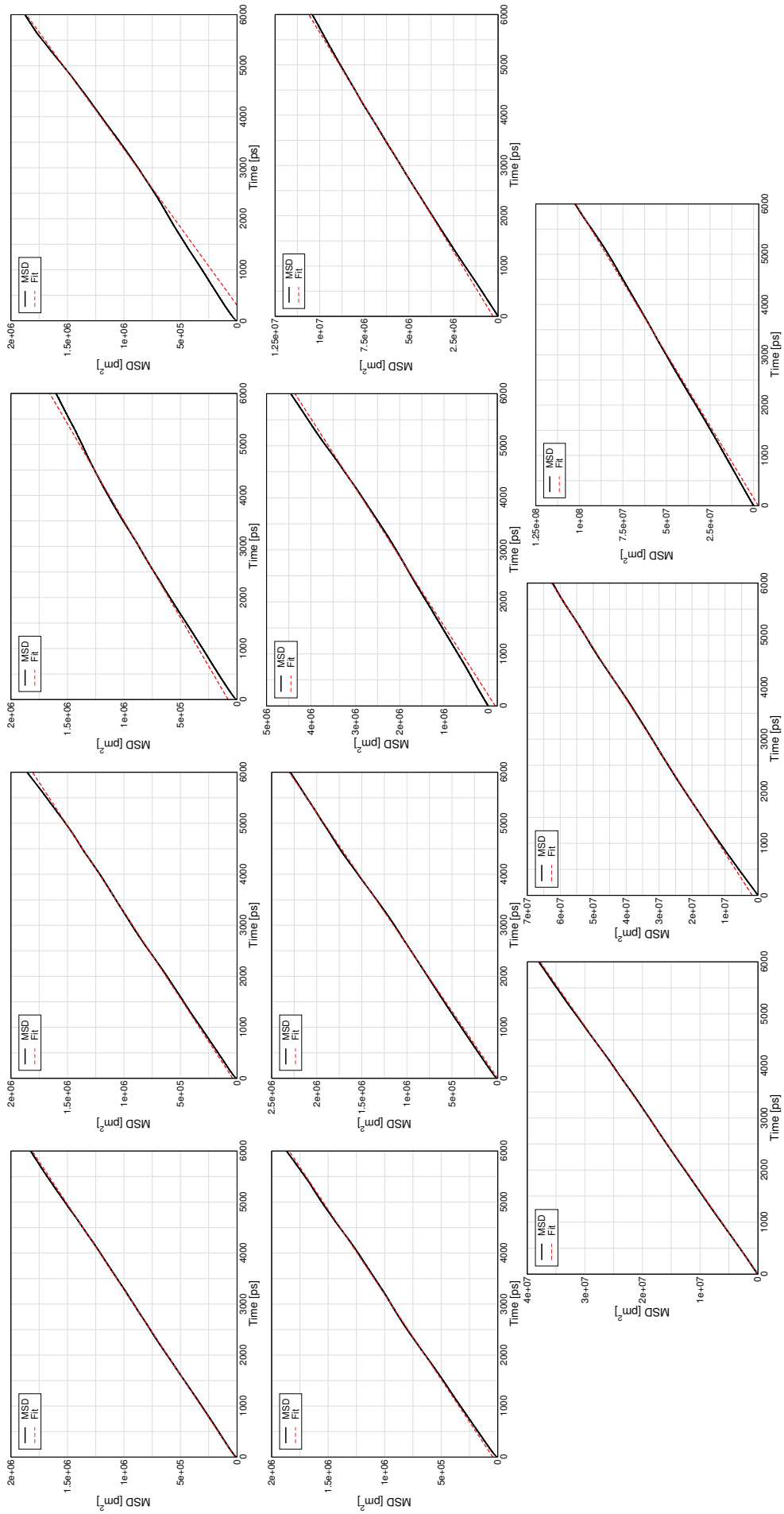

Figure 7.31: *Mean squared displacement against lag time for the centre of mass of $[C_8C_1im]^+$ in $[C_8C_1im][NTf_2]$ along the x vector. The electric fields are, from top left reading across, 0.000 VÅ^{-1}, 0.001 VÅ^{-1}, 0.002 VÅ^{-1}, 0.005 VÅ^{-1}, 0.010 VÅ^{-1}, 0.020 VÅ^{-1}, 0.050 VÅ^{-1}, 0.100 VÅ^{-1}, 0.200 VÅ^{-1}, 0.300 VÅ^{-1}, 0.400 VÅ^{-1}.*

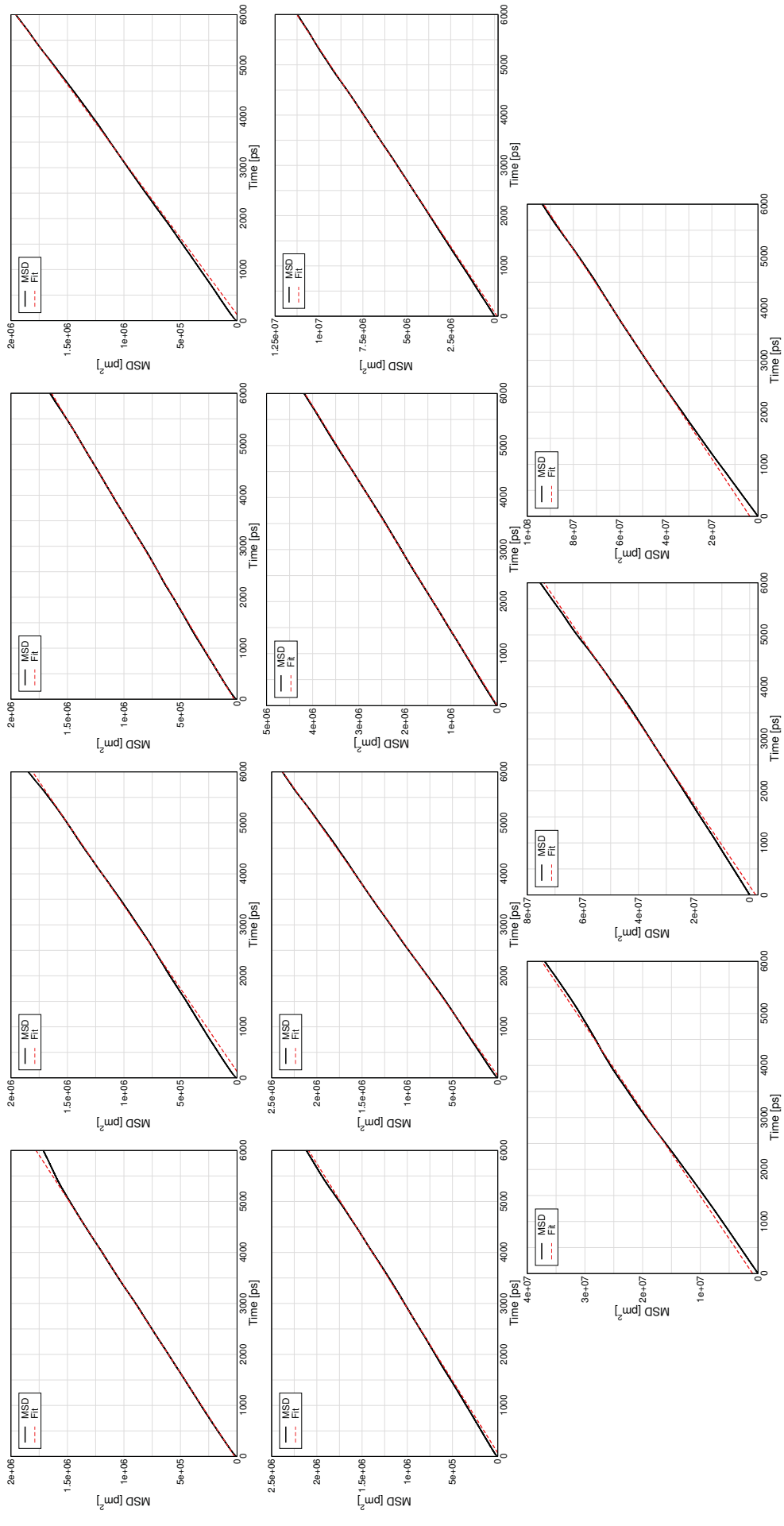

Figure 7.32: *Mean squared displacement against lag time for the centre of mass of $[C_8C_1im]^+$ in $[C_8C_1im][NTf_2]$ along the y vector. The electric fields are, from top left reading across, 0.000 VÅ^{-1}, 0.001 VÅ^{-1}, 0.002 VÅ^{-1}, 0.005 VÅ^{-1}, 0.010 VÅ^{-1}, 0.020 VÅ^{-1}, 0.050 VÅ^{-1}, 0.100 VÅ^{-1}, 0.200 VÅ^{-1}, 0.300 VÅ^{-1}, 0.400 VÅ^{-1}.*

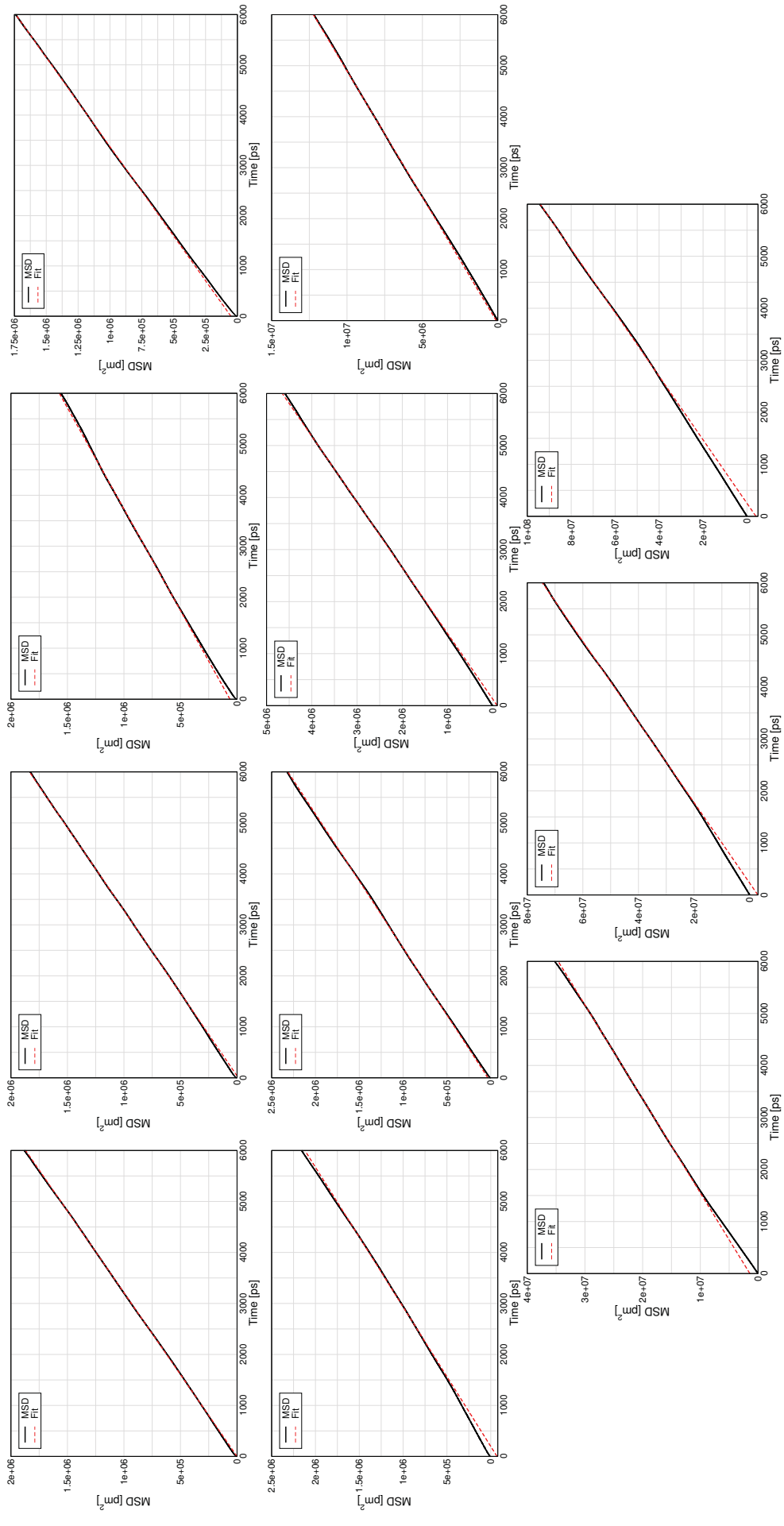

Figure 7.33: *Mean squared displacement against lag time for the centre of mass of $[NTf_2]^-$ in $[C_8C_1im][NTf_2]$ along the x vector. The electric fields are, from top left reading across, 0.000 VÅ^{-1}, 0.001 VÅ^{-1}, 0.002 VÅ^{-1}, 0.005 VÅ^{-1}, 0.010 VÅ^{-1}, 0.020 VÅ^{-1}, 0.050 VÅ^{-1}, 0.100 VÅ^{-1}, 0.200 VÅ^{-1}, 0.300 VÅ^{-1}, 0.400 VÅ^{-1}.*

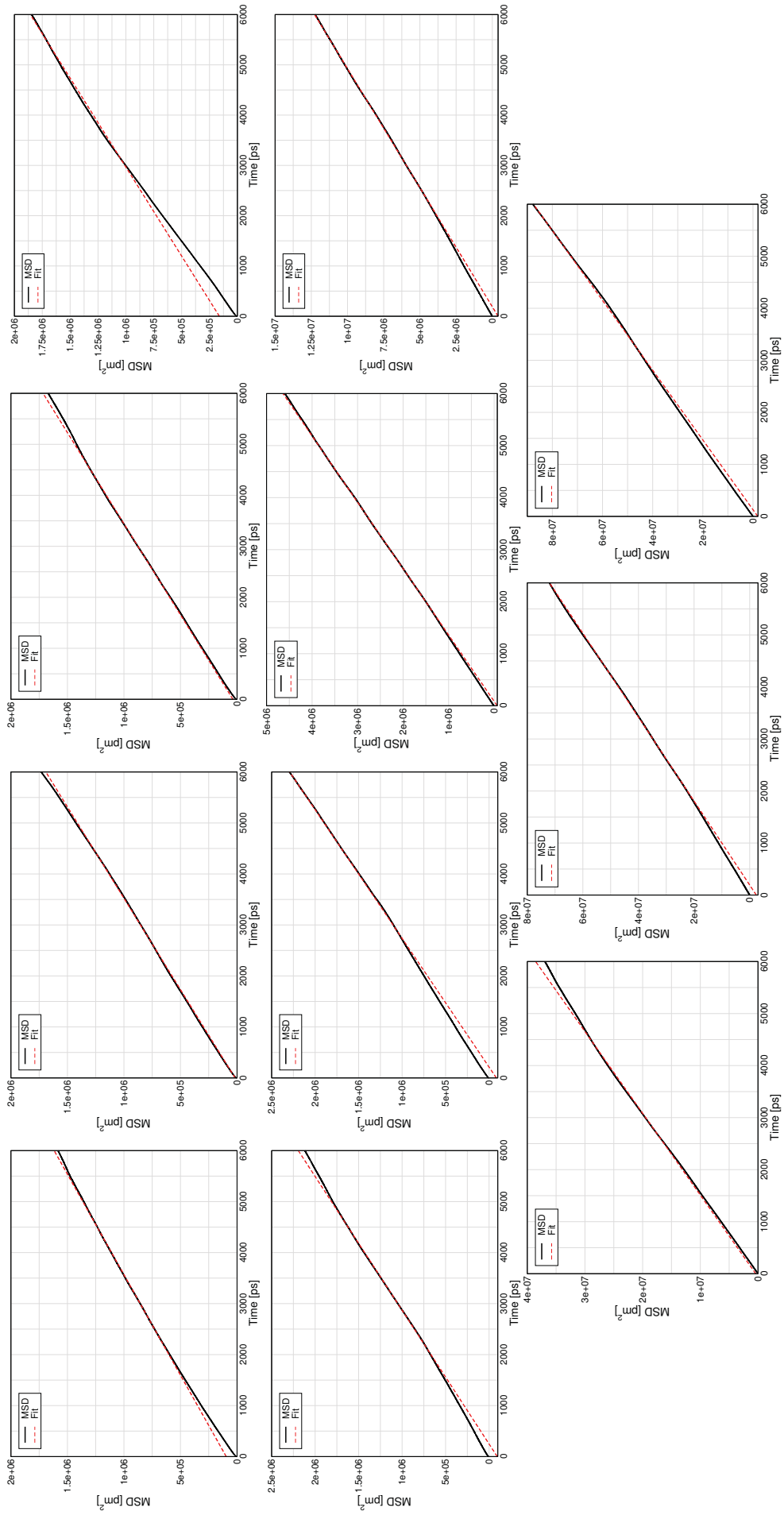

Figure 7.34: *Mean squared displacement against lag time for the centre of mass of $[NTf_2]^-$ in $[C_8C_1im][NTf_2]$ along the y vector. The electric fields are, from top left reading across, 0.000 VÅ^{-1}, 0.001 VÅ^{-1}, 0.002 VÅ^{-1}, 0.005 VÅ^{-1}, 0.010 VÅ^{-1}, 0.020 VÅ^{-1}, 0.050 VÅ^{-1}, 0.100 VÅ^{-1}, 0.200 VÅ^{-1}, 0.300 VÅ^{-1}, 0.400 VÅ^{-1}.*

Table 7.12: *Diffusion coefficients of the cation and anion in $[C_8C_1im][NTf_2]$ in all electric fields along the x and y directions calculated using Equation 7.13.*

Field Strength [VÅ^{-1}]	Diffusion Coefficient [$\times 10^{-10}$ m^{2}s^{-1}]					
	$[C_8C_1im]^+$			$[NTf_2]$		
	x	y	xy	x	y	xy
0.000	1.51	1.36	1.44	1.57	1.21	1.39
0.001	1.55	1.52	1.53	1.53	1.47	1.50
0.002	1.24	1.36	1.30	1.23	1.32	1.27
0.005	1.64	1.66	1.65	1.41	1.41	1.41
0.010	1.56	1.79	1.67	1.48	1.79	1.84
0.020	1.93	2.00	1.96	1.90	1.98	1.94
0.050	3.93	3.51	3.72	3.87	3.88	3.88
0.100	8.26	9.41	8.84	10.0	10.5	10.3
0.200	31.8	29.5	30.7	28.7	29.3	29.0
0.300	50.4	66.1	58.3	63.7	61.4	62.5
0.400	87.3	74.6	80.9	81.9	74.6	78.2

Similarly to $[C_4C_1im][NTf_2]$, in $[C_8C_1im][NTf_2]$ there is a disconnect between the electric fields which cause changes in temperature and ones that cause a change in diffusion.

The diffusion coefficients of $[C_8C_1im]^+$ and $[NTf_2]^-$ remain constant in electric fields of $\leq$0.01 VÅ^{-1}, matching the constant temperature values (Table 7.6). Electric fields of $\geq$0.02 VÅ^{-1} cause an increase in the diffusion coefficients of the ions perpendicular to the field direction, with the magnitude increasing with electric field strength. At $\geq$0.3 VÅ^{-1}, this is accompanied by an increase in temperature but not at electric fields below this.

In the x and y directions, changes in diffusion are not due to drift of the ions, as the mean displacement is negligible (shown in Figures 7.35 and 7.36), and the relationship between the MSD and lag time is linear ($\alpha = 1$).

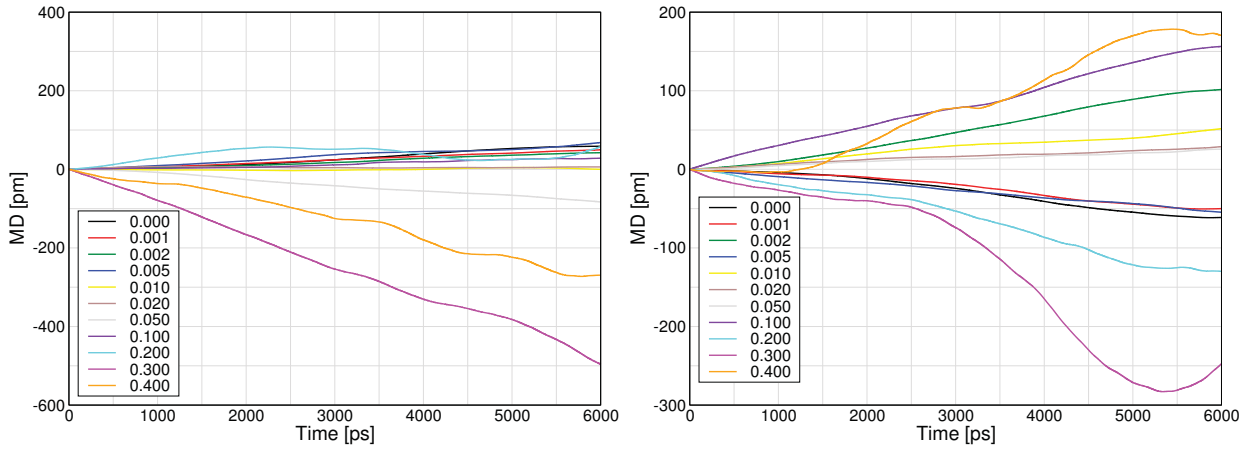

Figure 7.35: *Mean displacement of $[C_8C_1im]^+$ along the x (left) and y (right) vectors. Electric fields are shown in the legend in VÅ^{-1}.*

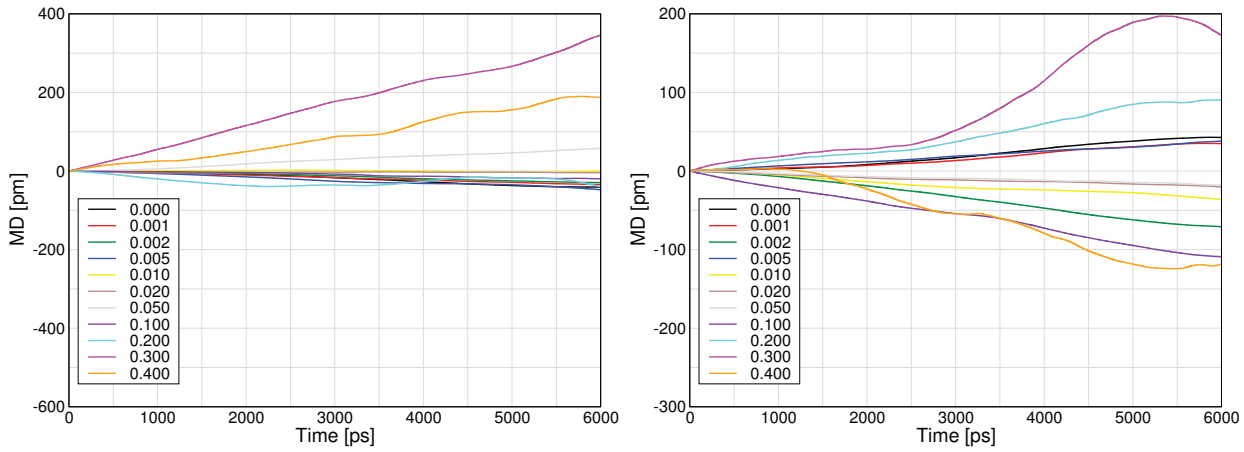

Figure 7.36: *Mean displacement of $[NTf_2]^-$ along the x (left) and y (right) vectors. Electric fields are shown in the legend in VÅ^{-1}.*

7.4.4 Discussion

First considering the diffusion of the ions parallel to the electric field, both $[C_4C_1im][NTf_2]$ and $[C_8C_1im][NTf_2]$ show remarkably similar trends. The trend between MSD and lag time remains linear only in electric fields of $\leq$0.002 VÅ^{-1}, and above this becomes non-linear with $1 < \alpha < 2$. In all electric fields (except 0.002 VÅ^{-1} for $[C_8C_1im][NTf_2]$) there is a drift of the ions, with the cation drifting in the positive direction and the anion in the negative direction. This drift is so small in electric fields of $\leq$0.002 VÅ^{-1} that it does not affect α.

For both ionic liquids $D_{\text{eff}} \approx D$ and $v_d \propto E$ up to a threshold electric field strength. For $[C_4C_1im][NTf_2]$ this threshold is 0.05 VÅ^{-1} and for $[C_8C_1im][NTf_2]$ this is 0.02 VÅ^{-1}. This difference in the electric field threshold is the major difference between the diffusion of the ionic liquids parallel to the electric field.

Above the threshold electric fields, D_{eff} increases with electric field and v_d is greater than expected from the trends below the threshold. Combined, these suggest that these electric fields cause a change in the diffusive character (i.e. the random diffusion) of the ions, alongside an induction of drift.

Considering the diffusion of the ions perpendicular to the electric field, there is no significant drift of any of the ions in any electric field. Therefore this change in these values must come from a change in the nature of the diffusion.

Above 0.3 VÅ^{-1} the increase in diffusion likely comes from joule heating (a.k.a. ohmic heating). This is the process by which thermal energy supplied to molecules in a system by a voltage difference is redistributed perpendicular to the direction of the applied voltage. This is due to collisions of the molecules leading to a scattering of the directions of motion, randomising the direction of motion with respect to the field lines and distributing thermal energy perpendicular

to the direction of the electric field. This would not lead to a drift, but to an increase in the diffusion and the temperature, which occurs in electric fields of $\geq$0.3 VÅ^{-1}.

Below this electric field strength another explanation is needed, and to understand this the 'normal' motion of ions needs to be discussed. Ionic liquids are well known to be structurally heterogeneous (Section 2.1.1), and have been shown to be dynamically heterogeneous as well.[221] This was discovered when solutes within an ionic liquid were found to experience two dynamically heterogeneous regions, a 'cage' and a 'jump' region.[33,200,222]

In the cage region the ion was trapped within an ion cage, composed of counter ions in the liquid. The cage keeps the ion trapped in the same average position, thus its net diffusion is zero, although it does have a velocity. In the jump region the ion is not bound by any species and diffuses freely through the liquid until it becomes trapped in another cage. Therefore within the jump region there is net diffusion of the ion.

This model was first described based upon the study of solutes in ionic liquids,[33,222] however it has been found that this model can be applied to ions of an ionic liquid. Feng *et al.* found that the diffusion of the ions of $[C_4C_1im][NTf_2]$ was composed of two regimes of diffusion, which they described as 'free' and 'bound' regions.[35] These are two distinct regimes of ion diffusion where ion motion in the free regime is highly correlated to itself and fast diffusion occurs. Oppositely, in the bound regime the ion motion is highly anti-correlated to itself and the ion remains in the same average position. This description of a free and bound regime is analogous to that of a jump and cage region respectively, therefore the same model can be used to describe motion of solute and solvent ions in ionic liquids.[33,35,200,222]

Using this model, the diffusion of an ion within an ionic liquid will depend upon its ability to leave the cage/bound region and remain in the jump/free region. This can be related to a number of factors including the size and charge of the ion, along with the ability of the cage to keep the ion trapped. The latter can be thought of as a kinetic barrier to leave the cage i.e. an activation energy to diffusive motion. If the ion has enough kinetic energy to overcome this activation barrier, it can escape the cage and enter the jump/free region.

In both ionic liquids, electric fields of $\leq$0.01 VÅ^{-1} induce a drift in the z direction. However, the inherent random motion in the system does not change ($D_{\text{eff}} = D$(zero field)), and the diffusion perpendicular to the electric field remains constant. The drift of the ions in the z direction can also be linearly correlated to the electric field strength in these electric fields.

This means that the activation energy required to leave the cage/bound region remains the same in these electric fields, and the underlying ion diffusion and trapping ability of the ion cage is unaffected. Instead it seems that these electric fields cause preferential 'hopping' of the

ions parallel to the field, i.e. the electric field influences the direction in which the ions leave the cage/bound region.

This does not affect the underlying random nature of diffusion, i.e. the probability of the ions leaving the cage/bound region. Instead it means that the ion enters into, and diffuses within, the jump/free region more often in the direction dictated by the electric field. This effect is limited to diffusion parallel to the electric field, and diffusion perpendicular to the electric field is unaffected.

This effect persists in $[C_4C_1im][NTf_2]$ in 0.02 VÅ^{-1}, but not for $[C_8C_1im][NTf_2]$, indicating that the ion cage may be more difficult to disrupt in $[C_4C_1im][NTf_2]$. There is an increase in the diffusion perpendicular to the electric field in $[C_4C_1im][NTf_2]$ at 0.02 VÅ^{-1}, however, indicating that the cage may be disrupted at this electric field.

Higher electric fields ($\geq$ 0.05 VÅ^{-1}) lead to the drift of the ions being no longer linearly correlated to electric field strength and D_{eff} increases. There is also a significant increase in the diffusion coefficients perpendicular to the electric field. The combination of these effects show that the change in the diffusion of the ions at these electric field strengths cannot be explained entirely by a change in the drift as in lower electric fields. Therefore there must be a change in the underlying diffusion of the ions compared to that in weak electric fields.

As shown later (Section 7.5.1), these changes to the underlying diffusion occur at the same electric fields that cause changes to the bulk/neighbouring liquid structure, and this is directly linked to the cage/bound and jump/free regions. It is not immediately clear whether an increase in the drift of the ions causes changes to the bulk structure, or whether there are changes in the structure which lead to changes in the diffusion.

One needs to remember that while each ion is bound within its own ion cage, it also forms part of the cage for its neighbouring ions. Hence moving one ion into the jump/free region leads to a modification of the cage region for its neighbouring ions. If this movement is rare then the average ion cage around any given ion will be approximately consistent. Thus, the ions can drift slowly without causing changes to the cage/bound regions.

It is possible that, as the electric field strength increases the number of ions entering the jump/free region, the average ion cage around each ion will be different. Equally it is possible that changes to the bulk liquid structure lead to break-down of the ion cage, which in turn leads to the changes to the diffusion of the ions. It cannot be determined from these data which of these is the correct cause, or if they occur simultaneously. All that can be determined is that these effects (change in the nature of diffusion and structural changes) occur together.

Regardless, it seems clear that this change in the diffusive nature of the ions can be associ-

ated with the breakdown of the ion cage structure. The ion cage breakdown leads to a lower energy required to leave the cage/bound region and remain within the jump/free region, allowing greater diffusion of the ions to occur. The combination between this breakdown, and the electric field adding an extra accelerating force upon the ions, leads to the change in the diffusive nature of the ions. The breakdown of the ion cage also explains the increase in the diffusion perpendicular to the field. As all of the ion cages are connected in the bulk structure, the collapse of one ion cage can cascade throughout the liquid structure, leading to ion cage breakdown perpendicular to the electric field.

To explain why the diffusion of the ions increases while temperature remains constant, one must remeber the different time-scales over which these properties are calculated. The temperature in a simulation is calculated using the instantaneous velocity of all particles at one time step (Equation 7.10), while the diffusion is calculated as an average squared displacement over a long range of time steps (Equation 7.13). Therefore, when trapped in an ion cage, the instantaneous velocity of an ion can be high while the net diffusion is low. However, if the cage weakens and the ion spends less time in the cage/bound region, with the same velocity it can travel further over longer periods of time, allowing ions to diffuse further with the same velocity.

What can be seen is that D_{eff} is greater parallel to the electric field than D perpendicular to the electric field for all ions in all electric fields for both ionic liquids. This indicates that, as expected, the breakdown of the ion cage is greater parallel to the electric field, than perpendicular to it.

This phenomenon also demonstrates that the electric field affects the whole ionic liquid, whether through direct or indirect effects. The ion cage breakdown perpendicular to the electric field is a secondary effect of the electric field due to the fact that it occurs in directions in which the electric field is not applied.

Ion cage structure breakdown in ionic liquids in electric fields has been observed before.[200] Expansion of the ion cage in electric fields was discovered, and this was found to be more pronounced parallel to the electric field. However, the drift of the ions in all electric fields was not observed/reported to occur before the breakdown of the ion cage, and the breakdown was not seen to occur in such low fields as reported herein.

This greater level of detail could be due to the all-atom or polarisable nature of the force field used in this work, opposed to the coarse grain model used before.[200]

The change in the ion cage at these electric fields is supported by changes to the velocity autocorrelation functions, shown in Figures 7.37, 7.38, 7.39, and 7.40.

The velocity autocorrelation function shows the trapping of the ions within the ion cage, through

the correlation of the velocities to themselves. A negative correlation indicates motion in the opposite direction to the initial velocity, which if strong enough is evidence of a rattling backwards and forwards type of motion.

These show that for both ionic liquids, there is a negative autocorrelation for both ions in low electric fields, which is from the ion cage trapping the ion. In greater electric fields, the correlation becomes more positive. This shows that the motion of the ion becomes more correlated with itself, i.e. the ion velocity is more constant and there is less rattling motion within the ion cage.

In the x and y directions, the autocorrelations always decay to zero, which is more evidence that there is no drift, as the limit of the velocity autocorrelation function is the square of the drift velocity.

In the z direction, the raw autocorrelation does not decay to zero in longer time-steps (bottom left). Correcting for this drift shows that the correlation is more positive for all ions in the higher electric fields, indicating that as expected from the drift corrected diffusion coefficients, the ion cage breaks down more in the direction parallel to the electric field.

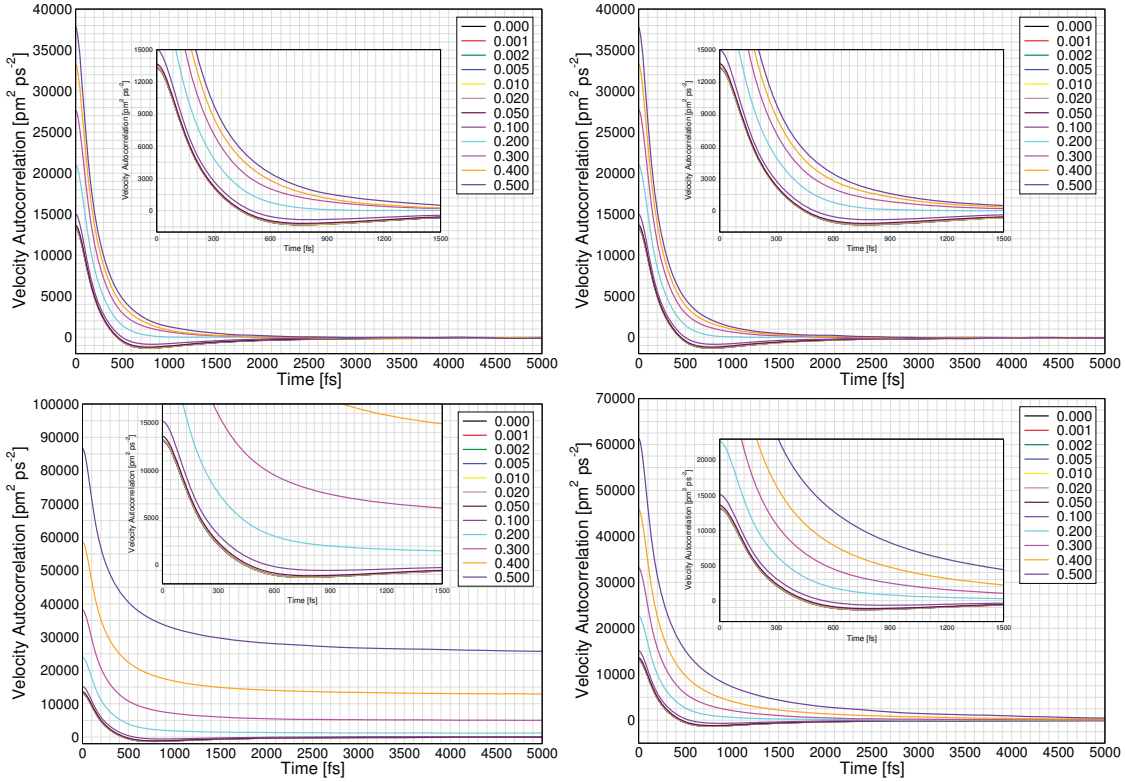

Figure 7.37: *Velocity autocorrelation function of $[NTf_2]^-$ in $[C_4C_1im][NTf_2]$ along the x (top left), y (top right), z (bottom left) directions, and drift corrected z (bottom right). Electric fields are shown in the legend in VÅ^{-1}.*

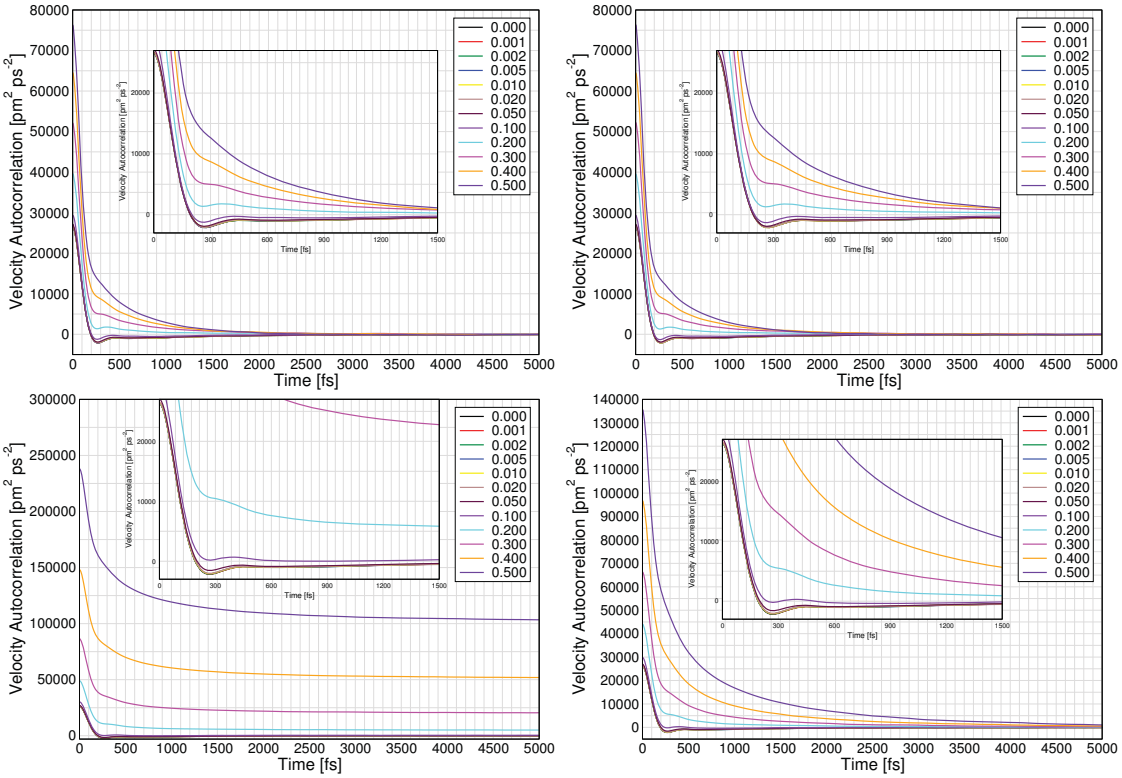

Figure 7.38: *Velocity autocorrelation function of $[C_4C_1im]^+$ in $[C_4C_1im][NTf_2]$ along the x (top left), y (top right), z (bottom left) directions, and drift corrected z (bottom right). Electric fields are shown in the legend in VÅ^{-1}.*

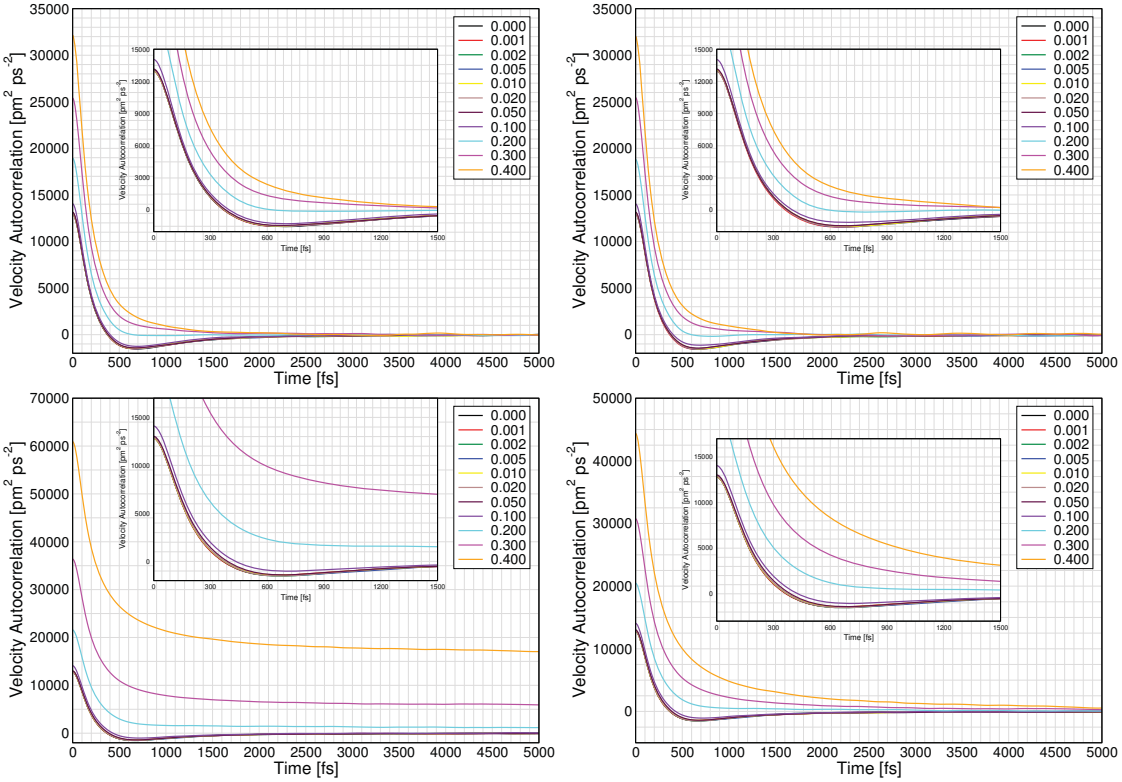

Figure 7.39: *Velocity autocorrelation function of $[NTf_2]^-$ in $[C_8C_1im][NTf_2]$ along the x (top left), y (top right) vectors, raw z (bottom left) and drift corrected z (bottom right). Electric fields are shown in the legend in VÅ^{-1}.*

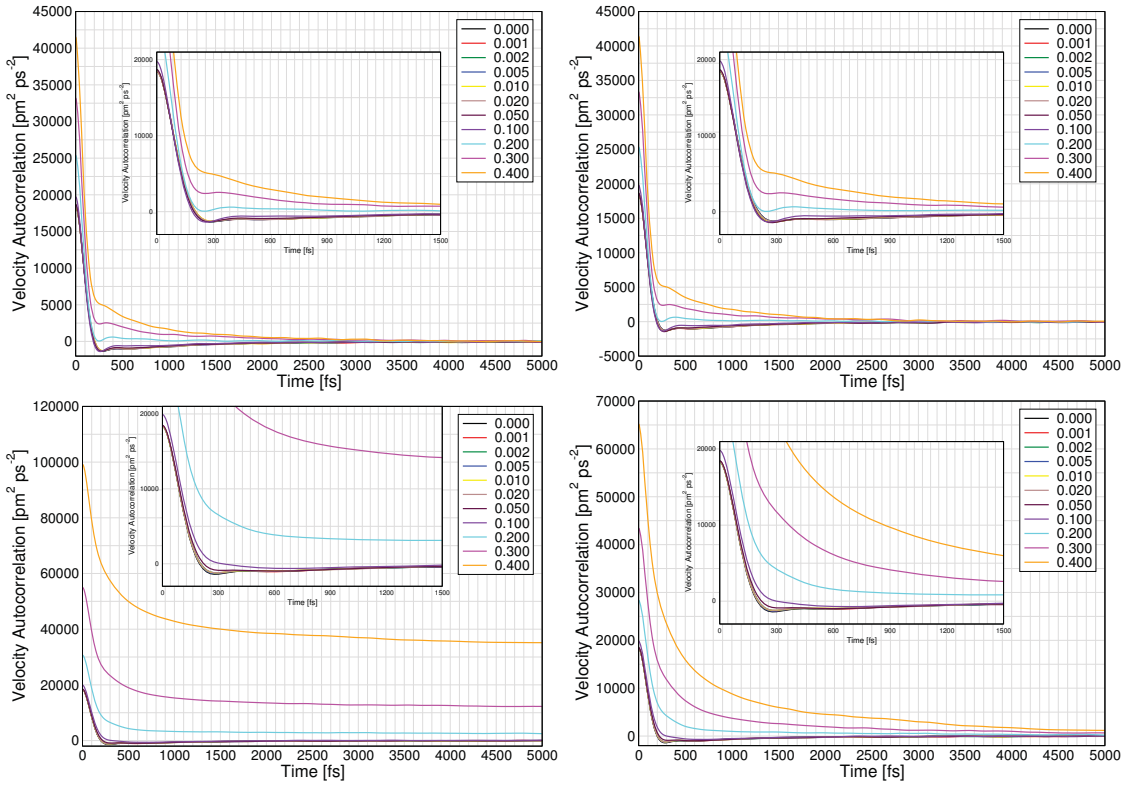

Figure 7.40: *Velocity autocorrelation function of $[C_8C_1im]^+$ in $[C_8C_1im][NTf_2]$ along the x (top left), y (top right) vectors, raw z (bottom left) and drift corrected z (bottom right). Electric fields are shown in the legend in $VÅ^{-1}$.*

7.5 Structure of Ionic Liquids in Electric Fields

When considering structural features of ionic liquids, these can be grouped into three categories. Firstly, there are 'bulk structures'. These are defined as structural properties that are related the liquid as a whole and includes analyses of properties such as analysis of the ionic liquids domains through Voronoi tessellation, or ion correlation through analysis of radial distribution functions. The results and analysis for $[C_4C_1im][NTf_2]$ and $[C_8C_1im][NTf_2]$ are presented in Section 7.5.1.

Along with this, there are neighbour structures. This includes any structural feature that arises within or as a consequence of a change to the first and second solvation shells of the ions in the liquid. This includes analyses such as the spatial distribution functions, hydrogen bonding structures and related dynamics. The results and analysis for $[C_4C_1im][NTf_2]$ and $[C_8C_1im][NTf_2]$ are presented in Section 7.5.2.

There is also the structures of the ions themselves. Unique to ionic liquids when compared to 'classic' inorganic salts is that the ions are not spherical, and the conformation of the ions can change. The results and analysis for $[C_4C_1im][NTf_2]$ and $[C_8C_1im][NTf_2]$ are presented in Section 7.5.3.

7.5.1 Changes to Bulk Structuring of Ionic Liquids in Electric Fields

Radial Distribution Functions

The most common analysis performed to investigate structures in molecular dynamics simulations are calculations of radial distribution functions (RDFs). A RDF describes how the density of an observed particle (ρ_{P}) changes as a function of distance from a reference particle (r). This density is expressed in terms of $g(r)$, which is the density normalised by the bulk density of the particle in the system (ρ^{bulk}) such that

$$\rho_{\mathrm{P}}(r) = \rho^{bulk} g(r) \tag{7.18}$$

It then follows that $g(r) = 1$ indicates that the density of the observed particle at the distance r is equal to that of the bulk density. This is the value that the RDF should converge towards in liquids and gases, as larger r leads to a more homogeneous structure, with heterogeneity in the structure being what leads to $g(r) \neq 1$.

From the RDF the coordination number of the observed particles within a sphere of radius x from the reference particle can be found by integration of $g(r)$. This is often referred to as the Number Integral (NI) and is calculated by

$$NI(x) = 4\pi\rho^{bulk} \int_0^x g(r) r^2 dr \tag{7.19}$$

Where care needs to be taken with the normalisation is when looking at intermolecular RDFs. This is because the bulk density of an intermolecular distance is very low, therefore normalisation of the RDF using bulk density leads to very high $g(r)$ values that do not converge towards $g(r) = 1$ as they should. Instead these converge to $g(r) = 0$ as intermolecular distances do not extend to distances greater than the molecule itself. Therefore all intermolecular RDFs are either an un-normalised histogram, or use a "modified $g(r)$" where the normalisation has been applied, but $g(r)$ is not the same as an intramolecular $g(r)$.

When considering simulations of ionic liquids, one can look at the RDF of the cation and anion centres of mass with respect to each other to gain information about the bulk structure of the simulation. These are shown in Figure 7.41 for $[C_4C_1im][NTf_2]$, and in Figure 7.42 for $[C_8C_1im][NTf_2]$.

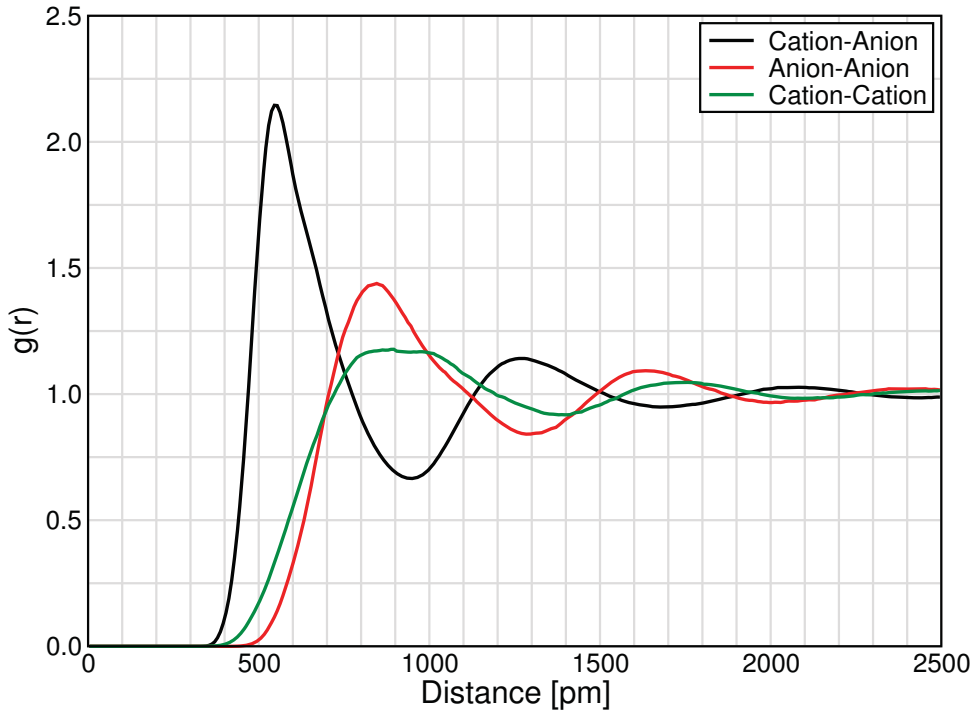

Figure 7.41: *Radial distribution function of the centre of mass of the cation and the centre of mass anion from each other and themselves in the simulation of $[C_4C_1im][NTf_2]$ with no electric field.*

For $[C_4C_1im][NTf_2]$ there is a very strong structuring of the anion and cation centres of mass around each other, with a peak $g(r)$ of around 2.2 at 550 pm. This shows that each ion has a

first solvation shell containing counter ions, preserving local electrical neutrality. The cation-cation and anion-anion RDFs also confirm this, as they both have very low $g(r)$ values at $r =$ 550 pm.

The anion centre of mass RDF from other anion centres of mass shows that after the shell of cations there is a fairly well defined secondary solvation shell of anions at 850 pm. The same cannot be said for the secondary solvation shell of the cations. This has a very broad peak around the same r value as the anion second solvation shell. Although this means that the solvation shells are at approximately the same distance, the density of the secondary solvation shell of cations around cations is much lower, and the structure of this shell less well defined. Interestingly, the cation secondary shell has what appear to be two peaks at slightly different r values. This indicates that there are two positions in the secondary solvation shell that the cation can take. Although this can't be investigated using these RDFs, this will be looked at when analysing the spatial distribution functions in Section 7.5.2.

The next solvation shells proceed as would be expected for an ordered liquid, with a tertiary solvation shell, shown by a peak of slightly higher than average density of counter ions at 1275 pm. There is also evidence of a quaternary solvation shell of the same ion appearing at 1625 pm for the anion and 1800 pm for the cation, and even a quinternary solvation shell of counter ions at 2100 pm.

This shows that while $[C_4C_1im][NTf_2]$ is a liquid, the bulk/long range structure of the liquid is a very regular lattice-like structure with solvation shells persisting for rather long distances. This indicates that the non-polar region has little effect on the bulk structure, and it is dominated by long-range strong coulombic interactions.

Despite being very similar to $[C_4C_1im][NTf_2]$, the ion centre of mass RDFs in $[C_8C_1im][NTf_2]$ are significantly different (Figure 7.42).

$[C_8C_1im][NTf_2]$ also has a peak in the cation-anion RDF, however this is at a slightly higher r (575 pm compared to 550 pm), meaning the first solvation shell is slightly larger, but not significantly. What is significantly different is that this first shell has a much lower $g(r)$ value at the peak of $g(r) = 1.6$ compared to 2.2 for $[C_4C_1im][NTf_2]$. Along with the lower $g(r)$ value, the coordination number within the first solvation shell is different, being 6.9 for $[C_4C_1im][NTf_2]$ and 5.8 for $[C_8C_1im][NTf_2]$.

This means that the first shell is less dense in $[C_8C_1im][NTf_2]$ than in $[C_4C_1im][NTf_2]$. This is probably due to the larger alkyl chains on the cation in $[C_8C_1im][NTf_2]$ leading to fewer cations being packed around anions, while the number of anions could be reduced due to the alkyl chains excluding more volume around the cation.

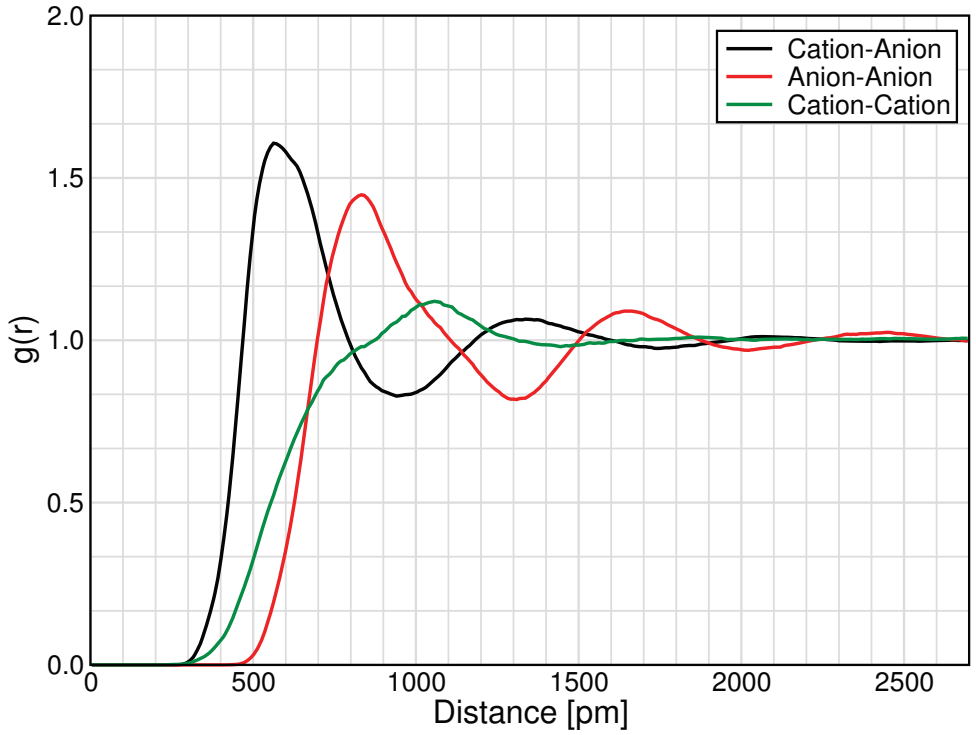

Figure 7.42: *Radial distribution function of the centre of mass of the cation and the centre of mass anion from each other and themselves in the simulation of [C_8C_1im][NTf_2] with no electric field.*

For the anion secondary shell there is a fairly well defined peak at 850 pm. This is exactly the same as the secondary solvation shell for the anion in [C_4C_1im][NTf_2], indicating that the anion structure is unaffected by this change in alkyl chain length. This is the same for the quaternary solvation shell of the anion.

The cation secondary solvation shell for the cation in [C_8C_1im][NTf_2] is very different to that in [C_4C_1im][NTf_2]. While this peak for [C_4C_1im][NTf_2] is broad, the peak for [C_8C_1im][NTf_2] is even more broad, with a peak around 1050 pm with a maximum $g(r)$ of 1.1. This indicates a disordered secondary coordination shell for the cation, with only 10 % more cations in the solvation shell than in the bulk liquid. There is also no strong correlation of the cation to itself beyond this shell, with no quaternary solvation shell being present.

The difference between [C_8C_1im][NTf_2] and [C_4C_1im][NTf_2] is in the alkyl chains of the cations, which leads to the disruption to the secondary shell of cations.

Now that the structure as determined from the RDFs has been established in the absence of an electric field, how the RDFs change in an electric field will be investigated.

For [C_4C_1im][NTf_2] in an electric field of up to 0.02 VÅ^{-1} there is no change in this RDF (Figure 7.43). Electric fields of 0.05 VÅ^{-1} and above lead to an increasingly more homogeneous structure with the peaks at 1275 pm and 2100 pm, as well as the troughs at 1700 pm and 950 pm moving towards $g(r) = 1$. This indicates that in these stronger electric fields, the ions are

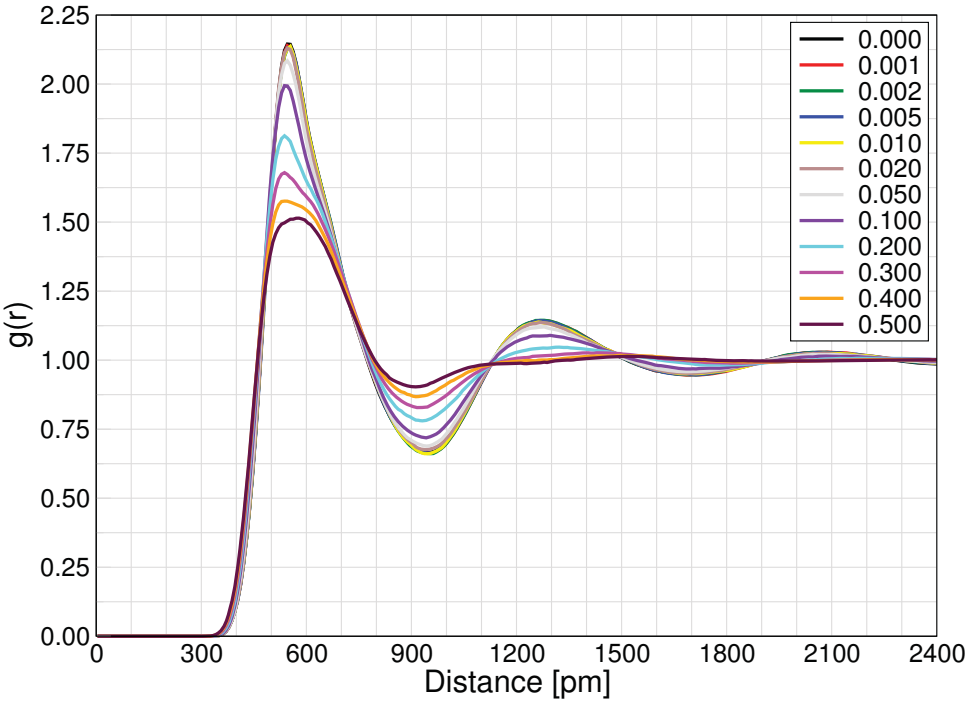

Figure 7.43: *Radial distribution function of the centre of mass of the cation to the centre of mass anion in the simulations of $[C_4C_1im][NTf_2]$ in electric fields. Field strength is shown in the legend in $VÅ^{-1}$.*

no longer in organised solvation shells.

Despite this, there appears to be a cation-anion distance at approximately 700 pm which does not move towards $g(r) = 1$ with electric fields, indicating some structure does still remain at higher electric fields. There is a reduction in the $g(r)$ value of the peak at 550 pm, indicating some reduction in the density of counterions in the first solvation shell.

The anion-anion centre of mass RDF in $[C_4C_1im][NTf_2]$ (Figure 7.44) also shows a shifting of the peaks and troughs towards $g(r) = 1$ with increasing electric fields; further indicating a loss of structure i.e. solvation shells. As with the cation-anion RDF, the anion-anion RDF is unaffected by electric fields up to 0.02 $VÅ^{-1}$, then increasingly larger changes occur with electric fields of 0.05 $VÅ^{-1}$ and above.

For this RDF, the first peak splits into two features at 0.2 $VÅ^{-1}$. The spatial distribution functions (Section 7.5.2) show that the lower distance peak arises from a depletion of the cation on one side of the anion, with the space being filled by another anion. The larger distance peak comes from anions with a cation spacer, with the increase in anion-anion distance arising from an increase in the cation-anion distance (seen in Figure 7.43).

The cation-cation centre of mass RDF for $[C_4C_1im][NTf_2]$ (Figure 7.43) shows very little change in electric fields of up to 0.05 $VÅ^{-1}$. Above this there is a homogenisation of the structure with increasing electric field. Obvious changes in this RDF come from a loss of the second solvation

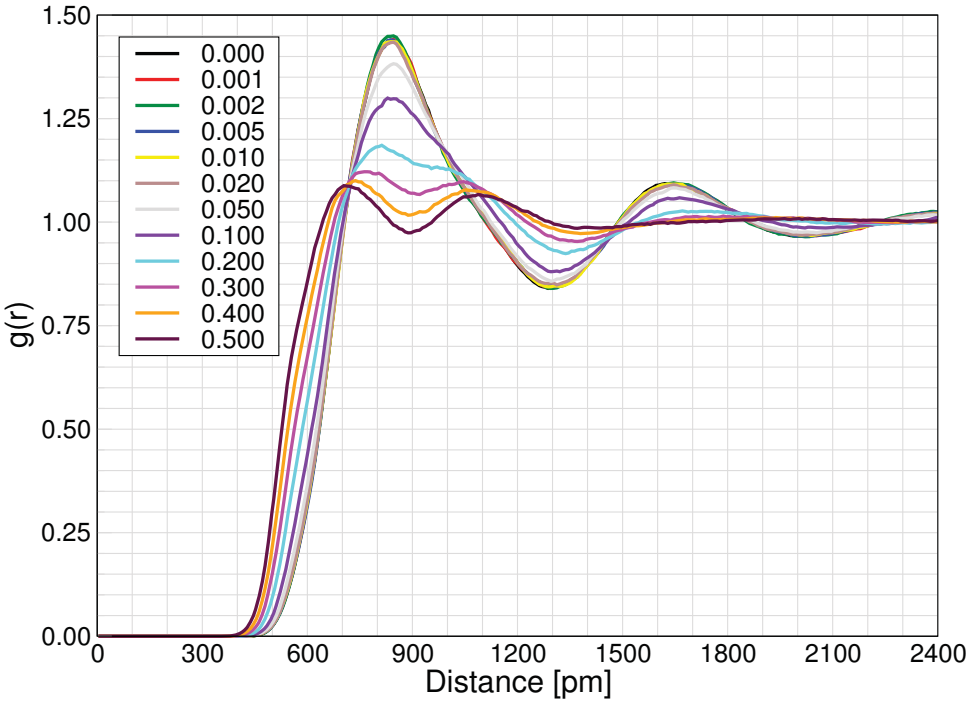

Figure 7.44: *Radial distribution function of the centre of mass of the anion to the centre of mass anion in the simulations of $[C_4C_1im][NTf_2]$ in electric fields. Field strength is shown in the legend in $VÅ^{-1}$.*

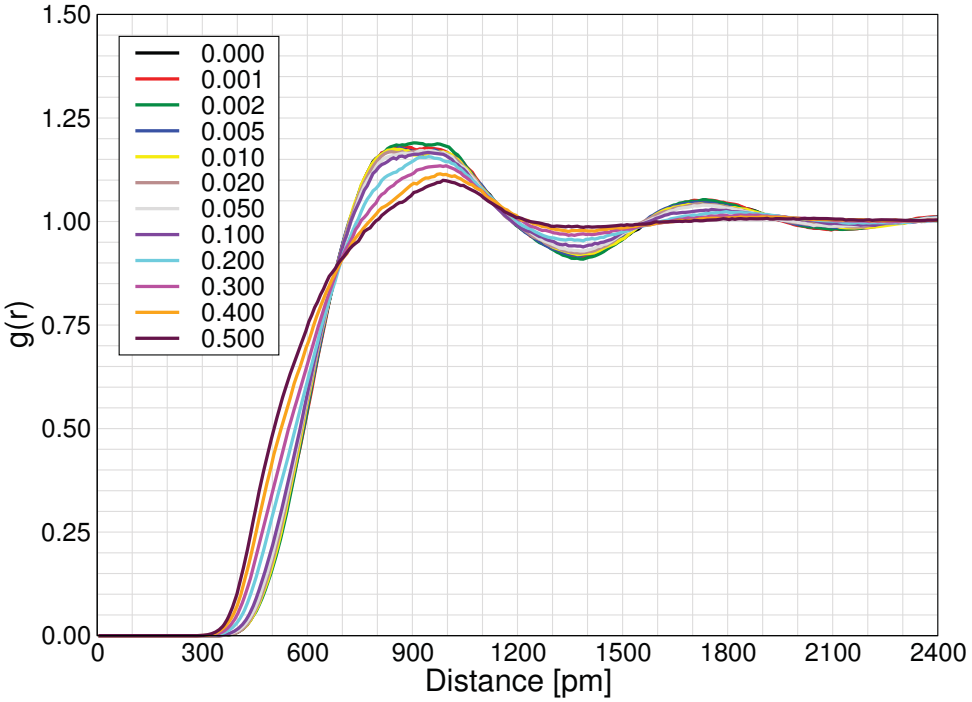

Figure 7.45: *Radial distribution function of the centre of mass of the cation to the centre of mass cation in the simulations of $[C_4C_1im][NTf_2]$ in electric fields. Field strength is shown in the legend in $VÅ^{-1}$.*

shell of cations, with these moving closer to fill in the 'free' space caused by the loss of the second solvation shell of anions.

In electric fields of 0.2 $VÅ^{-1}$ and above, there is also a change in the first peak with a loss in

the density of cations at ≈700-1000 pm. The spatial distribution functions (Figure 7.52) show that this is due to a shift in the position of the nearest cation from around the imidazolium ring towards the terminal carbon on the butyl chain. As the centre of mass is closer to the imidazolium ring than the terminal carbon, this shifts the peak to larger distances.

This also explains why the cation-cation peak is broader than the anion-anion or cation-anion peak. As the centre of mass of the cation is around the imidazolium ring, there are a lot of positions around each cation the neighbouring cation can take, broadening the peak in the RDF.

In summary for $[C_4C_1im][NTf_2]$, the cation-anion and anion-anion RDFs are unaffected by electric fields up to and including 0.02 VÅ^{-1}, while the cation-cation RDF is unaffected by electric fields up to and including 0.05 VÅ^{-1}.

Above these electric fields, there is a homogenisation of the structure, which becomes greater with increasing electric field strength and the outer solvation shells are more affected than the inner.

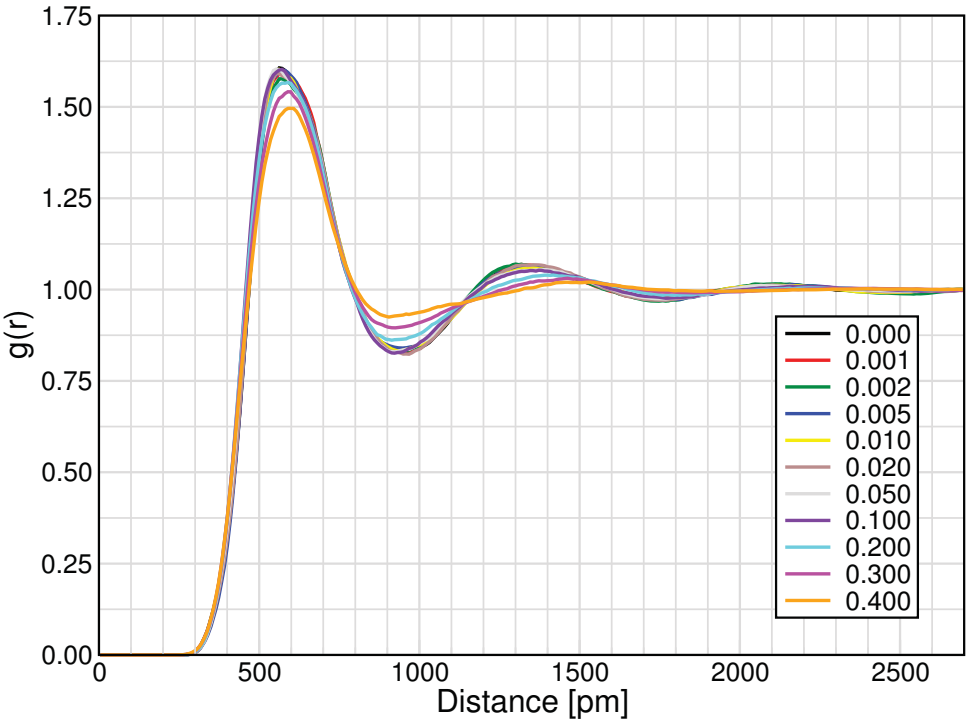

Figure 7.46: *Radial distribution function of the centre of mass of the cation to the centre of mass anion in the simulations of $[C_8C_1im][NTf_2]$ in electric fields. Field strength is shown in the legend in VÅ^{-1}.*

The cation-anion RDF in $[C_8C_1im][NTf_2]$ (Figure 7.46) has few changes with electric field, especially with regards to the first peak. The number integrals remain the same, varying by only 0.06 between all the electric field strengths, and the peak position remains between 560-580 pm. This shows that the position of the first solvation shell is not affected by the electric field.

The structures of the RDF beyond that of the first peak do shift towards $g(r) = 1$ at electric fields of 0.2 VÅ^{-1} and above. However this structuring is not very strong to begin with, and the shift is not as large as that in $[C_4C_1im][NTf_2]$.

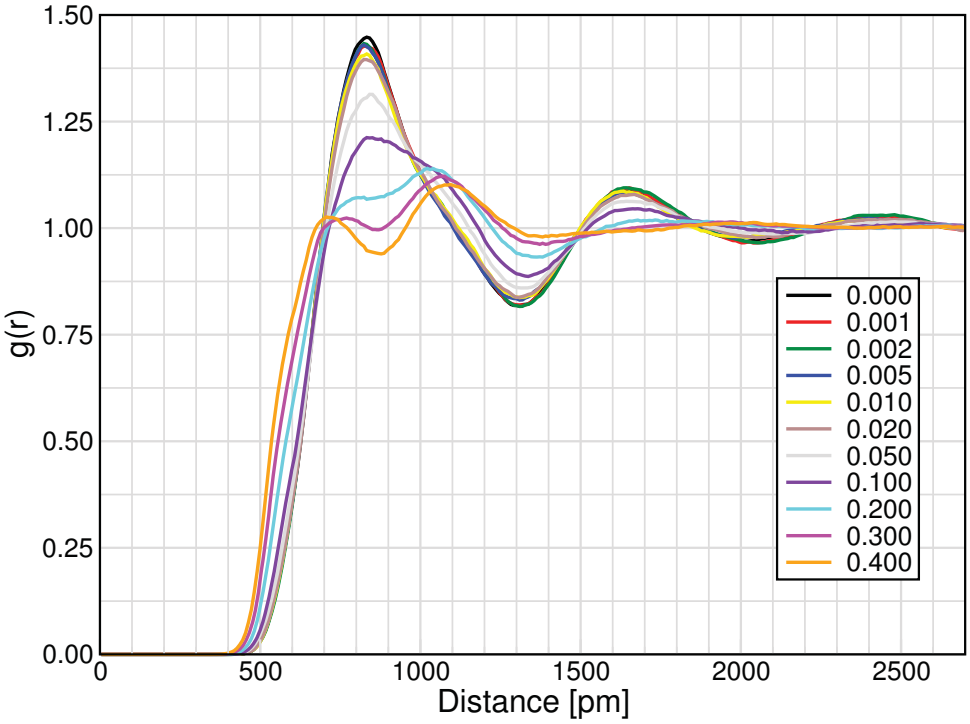

Figure 7.47: *Radial distribution function of the centre of mass of the anion to the centre of mass anion in the simulations of $[C_8C_1im][NTf_2]$ in electric fields. Field strength is shown in the legend in VÅ^{-1}.*

The anion-anion RDF in $[C_8C_1im][NTf_2]$ (Figure 7.47) is very similar to that of $[C_4C_1im][NTf_2]$. This indicates that the bulk distribution of the anions are very similar in the two ionic liquids and that an electric field has the same effect.

The cation-cation RDF in $[C_8C_1im][NTf_2]$ (Figure 7.48) does not change much in different electric fields. There is only one peak in this RDF, so it is not possible to observe changes in structure beyond the first cation-cation shell.

There is a slight shift in the position of the cation-cation peak with electric field, however this is inconsistent with the electric field, meaning a trend is not extractable.

In summary for $[C_8C_1im][NTf_2]$, the anion-anion RDF changes in a similar manner to that of the anion-anion RDF in $[C_4C_1im][NTf_2]$.

Oppositely, cation-cation and cation-anion RDFs are not affected by the electric field as much, however there is less structure present in $[C_8C_1im][NTf_2]$ to begin with.

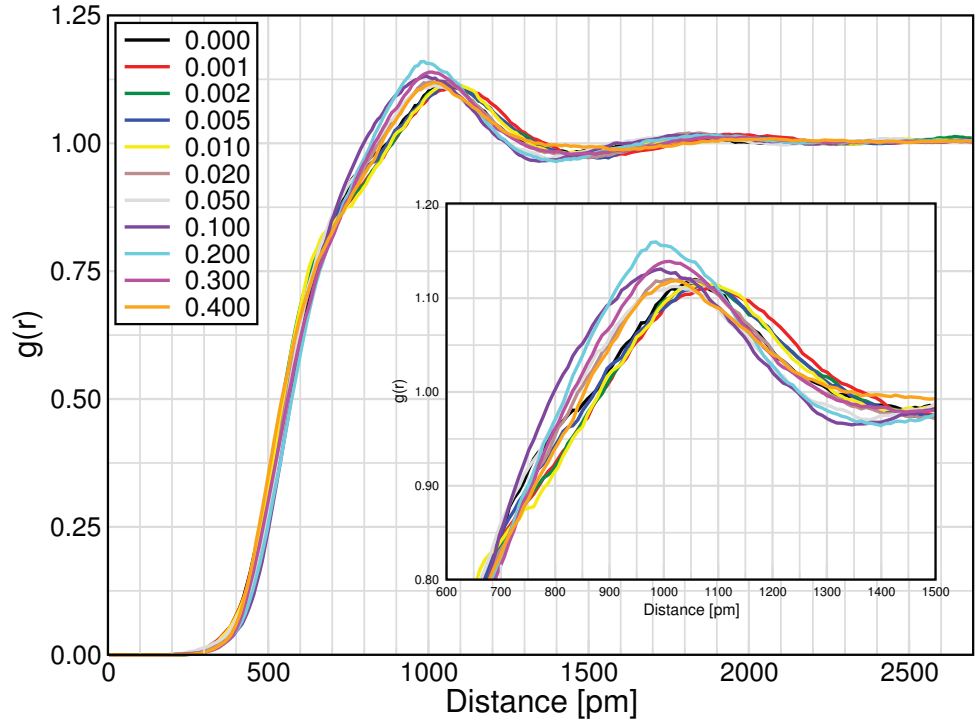

Figure 7.48: *Radial distribution function of the centre of mass of the cation to the centre of mass cation in the simulations of $[C_8C_1im][NTf_2]$ in electric fields. Field strength is shown in the legend in $VÅ^{-1}$.*

Domain Analysis

The micro-heterogeneity in ionic liquids is an important feature which leads to a lot of their important properties, for example the behaviour of solutes depends upon which domain they partition into.[34] Therefore when discussing structural changes in an ionic liquid in an electric field, attention should be paid to change in the domains.

TRAVIS,[88] the analysis software used in much of this thesis, contains a package which performs Voronoi tessellation in order to analyse domains.[158] In this method, each atom is defined as a Voronoi centre, and the van der Waals radii are used to calculate the Voronoi volume. Neighbouring particles with overlapping Voronoi volumes have their overlap removed by modifying the volume so they are cut-off by a plane, which is equidistant from both of the Voronoi centres. Then the rest of the empty space is filled by expanding the Voronoi spheres until the whole of the box has been filled.

Once this has been completed, a full description of the volume in the system has been achieved and neighbouring volumes within the same domain (as defined by the user) can be combined into box-wide domains. Using $[C_4C_1im][NTf_2]$ and $[C_8C_1im][NTf_2]$ as examples, the definitions of atoms in each domain for these ionic liquids are shown in Figure 7.49. The anion, cation ring and adjacent CH_n groups are defined as the polar domain, and the remaining CH_n groups

are defined as the non-polar domain.

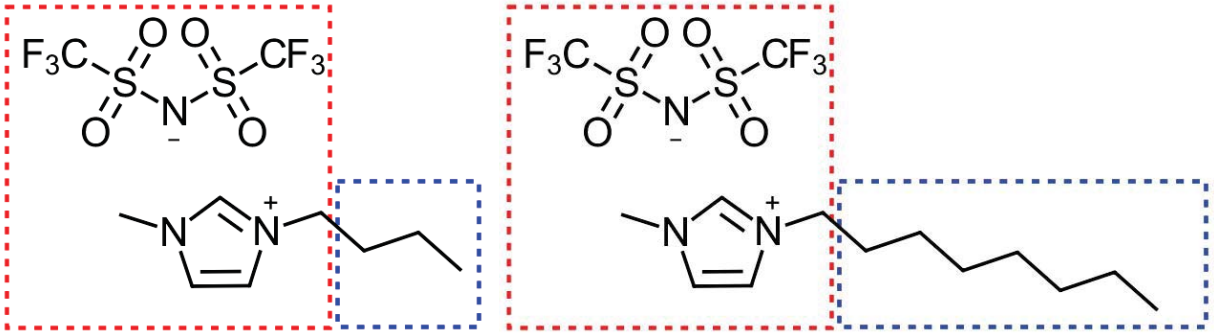

Figure 7.49: *Definitions of the atoms in each domain used for the Voronoi tessellation. Red square contains all the atoms defined as belonging to the polar domain. Blue square contains all atoms used for the non-polar domain.*

Using these definitions, some of the parameters of the Voronoi domains for $[C_4C_1im][NTf_2]$ without an electric field are shown in Table 7.13, and for $[C_8C_1im][NTf_2]$ in Table 7.14.

Table 7.13: *Voronoi statistics for the polar and non-polar domain in $[C_4C_1im][NTf_2]$ averaged over the whole simulation.*

Domain Type	No. of Domains	Volume [Å^3]	Surface Area [Å^2]	Isoperimetric Quotient
Polar	1.00 ± 0.00	108374 ± 200	29177 ± 273	0.231 ± 0.003
Non-Polar	10.26 ± 2.89	3020 ± 1064	3115 ± 1094	0.561 ± 0.043

Table 7.14: *Voronoi statistics for the polar and non-polar domain in $[C_8C_1im][NTf_2]$ averaged over the whole simulation.*

Domain Type	No. of Domains	Volume [Å^3]	Surface Area [Å^2]	Isoperimetric Quotient
Polar	1.00 ± 0.00	102883 ± 212	37258 ± 561	0.152 ± 0.003
Non-Polar	1.14 ± 0.36	53133 ± 9849	34743 ± 6415	0.122 ± 0.098

For the polar and non-polar domains in $[C_4C_1im][NTf_2]$ and $[C_8C_1im][NTf_2]$ the parameters calculated were the number of domains, the volumes of each domain, the surface area of each domain, and the isoperimetric quotient. The latter is a measure of the deviation from a spherical shape, with lower isoperimetric quotients indicating a larger deviation from a spherical shape.[158]

The Voronoi analysis for $[C_4C_1im][NTf_2]$ without an electric field (Table 7.13) shows clearly that this ionic liquid contains one continuous polar domain, with dispersed non-polar domains. This matches with the expected micro-heterogeneity that has been seen before with these ionic liquids, explained more in Section 2.1.1.

Every time-step within the simulation has one continuous polar domain, and between 1 and

24 non-polar domains. The polar domains have very large and relatively constant parameters, with the deviation between the smallest and largest volume and surface area being 2000 Å^3 and 2000 Å^2 respectively. The isoperimetric quotient is quite low, however this is due to the non-polar domains disrupting the structure of the polar domain, giving a sponge-like structure. The distribution of the number of non-polar domains is interesting because there is one time-step which contains a continuous non-polar domain, although as a percentage this occurs in 0.005% of the time-steps sampled in this simulation. Both the mean and mode average number of non-polar domains is 10, showing that there are a large number of dispersed domains within the liquid.

There is also a large distribution of the size and surface areas of the non-polar domains, with the maximum and minimum area being 29558 Å^2 and 105 Å^2 respectively, and the maximum and minimum volume being 28553 Å^3 and 72 Å^3 respectively. This shows a very high surface-to-volume ratio indicating that while there is some 'aggregation' of the non-polar domains within the Voronoi analysis, they are not fully coalescing, and are instead forming a sponge- or strand-like structure.

This is backed up by the isoperimetric quotient for these domains where larger non-polar domains have a very small isoperimetric quotient of ≈0.05, indicating a high deviation from a sphere. The smaller domains have much higher isoperimetric quotient of ≈0.7, and are likely one or more isolated alkyl chains with a near-spherical shape.

Considering the Vornoi analysis for $[C_8C_1im][NTf_2]$ and comparing to $[C_4C_1im][NTf_2]$, $[C_8C_1im][NTf_2]$ has one polar domain, and fewer non-polar domains than $[C_4C_1im][NTf_2]$. This is to be expected given what is known about the micro-heterogeneities of these ionic liquids.

The average volume of the polar domain in $[C_8C_1im][NTf_2]$ is similar to that of $[C_4C_1im][NTf_2]$ as there are the same number of atoms in the system defined as belonging to the polar domain. The surface area is larger, and the isoperimetric quotient smaller than that of $[C_4C_1im][NTf_2]$. This can be rationalised due to there being more atoms defined in the non-polar domain, which disrupt the aggregation of the moieties in the polar domain, giving the polar domain a larger surface area and a smaller isoperimetric quotient.

Focussing on the number of non-polar domains in $[C_8C_1im][NTf_2]$, this ionic liquid lies beyond the chain length which has been shown to cause micro-heterogeneity in the $[C_nC_1im][NTf_2]$ ionic liquids. However, in these simulations there is not always a single continuous non-polar domain. In 87% of the time-steps sampled in this simulation there is one continuous non-polar domain, but this is not an unchanging feature of this liquid. 12% of the time-steps contained two non-polar domains, and 1% of the time-steps contained three non-polar domains.

When two or three non-polar domains are present, there is always one large domain with one or two smaller domains. The small domains are around either 200 Å^3 or 500 Å^3 in volume, indicating that they are likely one or two alkyl chains that have become isolated from the main non-polar domain. This is supported by high isoperimetric quotients for the isolated domains, with the smaller isolated domains having isoperimetric quotients of around 0.6, and the larger isolated domains having isoperimetric quotients of around 0.4. These are larger than those seen in $[C_4C_1im][NTf_2]$ as the alkyl chain groups in $[C_8C_1im][NTf_2]$ are longer and therefore more oblique. Nevertheless, it is interesting that, at least with these definitions of polar and non-polar domains, one continuous non-polar domain is not a permanent feature of $[C_8C_1im][NTf_2]$. The lack of a continuous non-polar domain also leads into the large error in the average volume and surface area of the non-polar domains. Ignoring time-steps with two or more domains reduces the error in volume to 211 Å^3 and the error in surface area to 562 Å^2, which demonstrates that the large non-polar domains remain relatively similar.

The change in the Voronoi analysis of $[C_4C_1im][NTf_2]$ and $[C_8C_1im][NTf_2]$ will be studied when changing the electric field strength.

Table 7.15: *Voronoi statistics for the polar domain in $[C_4C_1im][NTf_2]$ in various electric fields.*

Field Strength [VÅ^{-1}]	No. of Domains	Volume [Å^3]	Surface Area [Å^2]	Isoperimetric Quotient
0.000	1.00 ± 0.00	108374 ± 200	29177 ± 273	0.231 ± 0.003
0.001	1.00 ± 0.00	108377 ± 202	29157 ± 268	0.232 ± 0.003
0.002	1.00 ± 0.00	108373 ± 179	29143 ± 284	0.232 ± 0.003
0.005	1.00 ± 0.00	108396 ± 169	29187 ± 301	0.231 ± 0.004
0.010	1.00 ± 0.00	108382 ± 191	29195 ± 283	0.231 ± 0.003
0.020	1.00 ± 0.00	108435 ± 169	29316 ± 289	0.230 ± 0.003
0.050	1.00 ± 0.00	108526 ± 175	29558 ± 277	0.227 ± 0.003
0.100	1.00 ± 0.00	108682 ± 170	29967 ± 259	0.223 ± 0.003
0.200	1.00 ± 0.00	108850 ± 168	30434 ± 256	0.218 ± 0.003
0.300	1.00 ± 0.00	108888 ± 167	30671 ± 265	0.216 ± 0.003
0.400	1.00 ± 0.00	108872 ± 176	30757 ± 263	0.215 ± 0.003
0.500	1.00 ± 0.00	108802 ± 183	30727 ± 262	0.215 ± 0.003

The polar domain in $[C_4C_1im][NTf_2]$ shows some small changes as the electric field increases (Table 7.15). However, a continuous polar domains remains a feature of this ionic liquid in every electric field investigated.

There is an increase in the average volume of the polar region when the electric field strength is $\geq$0.02 VÅ^{-1}. This increase in volume cannot be due to an increase in the number of polar particles in the simulation as this is constant. Instead this can only come from an change in the ions which would increase in the Voronoi tessellation volume of the domain.

Table 7.16: *Voronoi statistics for the non-polar domain in $[C_4C_1im][NTf_2]$ in various electric fields.*

Field Strength [VÅ^{-1}]	No. of Domains	Volume [Å^3]	Surface Area [Å^2]	Isoperimetric Quotient
0.000	10.26 ± 2.89	3020 ± 1064	3115 ± 1094	0.561 ± 0.043
0.001	9.72 ± 2.94	3237 ± 1267	3335 ± 1299	0.561 ± 0.047
0.002	10.03 ± 2.97	3124 ± 1204	3217 ± 1233	0.561 ± 0.046
0.005	9.81 ± 2.96	3218 ± 1289	3323 ± 1329	0.556 ± 0.047
0.010	10.06 ± 3.14	3148 ± 1250	3247 ± 1282	0.560 ± 0.046
0.020	10.61 ± 3.09	2937 ± 1085	3051 ± 1125	0.559 ± 0.042
0.050	11.10 ± 3.27	2795 ± 1012	2936 ± 1060	0.563 ± 0.043
0.100	12.35 ± 3.34	2457 ± 787	2631 ± 837	0.558 ± 0.041
0.200	13.22 ± 3.60	2284 ± 740	2499 ± 806	0.557 ± 0.040
0.300	13.30 ± 3.54	2263 ± 736	2498 ± 809	0.557 ± 0.039
0.400	12.85 ± 3.52	2358 ± 805	2609 ± 887	0.557 ± 0.039
0.500	12.04 ± 3.36	2530 ± 887	2790 ± 971	0.557 ± 0.040

Considering the cation moieties in the polar domain, this imidazolium ring with its attached CH_n groups is very rigid and therefore would not be expected to be the cause of the volume change.

Considering the anion, later results in this thesis show that the anion has a greater preference for the *cis* isomer in electric fields (Section 7.5.3). Calculations performed by Clough *et al.*[223] show that the *cis* isomer is slightly larger (≈2 Å), however this is not enough to account for the large increase of the polar domain. The cause of this domain volume increase is thus not obvious.

The non-polar domain in $[C_4C_1im][NTf_2]$ shows much larger changes in the presence of an electric field than the polar domain (Table 7.16).

The mean (and mode) average number of non-polar domains decreases slightly in electric fields of 0.001-0.01 VÅ^{-1}, then increases in electric fields of 0.02-0.3 VÅ^{-1}, then decreases at 0.4 and 0.5 VÅ^{-1}. This change is mirrored by changes to the volume and the surface area.

As the average isoperimetric quotient does not change in the initial change in domain properties between 0.001 and 0.01 VÅ^{-1}, it seems that application of these electric fields cause a slight increase in the aggregation of the non-polar domains without any change to the bulk structure.

The change in the number of non-polar domains can be well visualised in Figure 7.50, which shows a 2D histogram of the number of domains in different electric field strength. This shows the shift from 0 to 0.001 VÅ^{-1}, then the relatively constant domain distribution from 0.001 to 0.01 VÅ^{-1}.

From 0.01 to 0.3 VÅ^{-1} the distribution of domains widens and the position of the peak shifts to

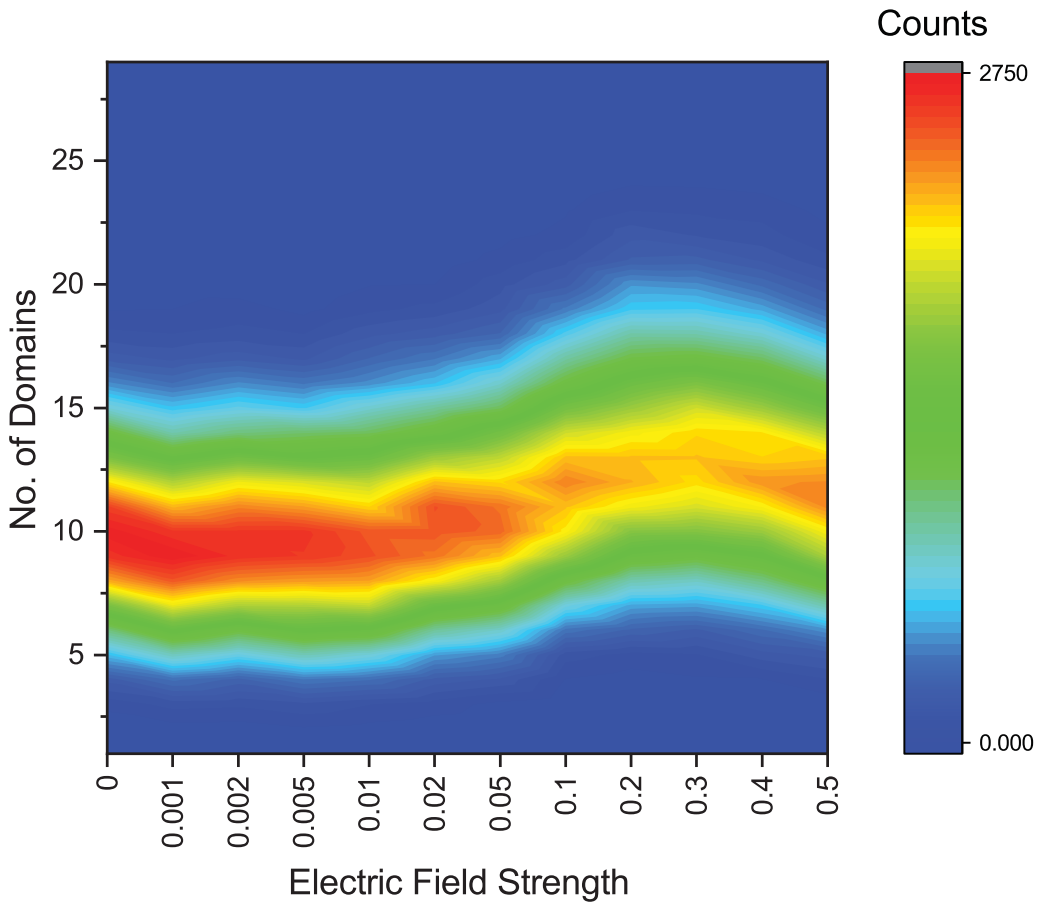

Figure 7.50: *2D histogram of the number of non-polar domains in [C_4C_1im][NTf_2] at each time-step at different electric fields. Electric field strength is given in VÅ^{-1}.*

a larger number of domains. As the average volume of the domains decreases and the surface area decreases, the non-polar domains are more dispersed. At 0.4 and 0.5 VÅ^{-1} this trend reverses and the domains start to coalesce again.

In [C_4C_1im][NTf_2] the non-polar domains are comprised entirely of the alkyl chains on the cations. Later in this thesis, the alkyl chains are shown to stretch out and the cations take a more stretched conformer, increasing the terminal carbon on the alkyl chain to imidazolium ring distances (Section 7.5.3). However as this trend does not match the trend in the domains, it is suspected not to be the reason behind these changes.

The polar domain in [C_8C_1im][NTf_2] in the presence of an electric field (Table 7.17), has a continuous polar domain regardless of the electric field investigated. In [C_8C_1im][NTf_2], as opposed to [C_4C_1im][NTf_2], the volume and surface area of the polar domain increases across the electric fields, while the isoperimetric quotient decreases across the same range.

As with [C_4C_1im][NTf_2], this increase is due to an unknown change in the structure as the polar cation moieties do not change in volume, and the anion increase in volume is not enough

Table 7.17: *Voronoi statistics for the polar domain in $[C_8C_1im][NTf_2]$ in various electric fields.*

Field Strength [VÅ^{-1}]	No. of Domains	Volume [Å^3]	Surface Area [Å^2]	Isoperimetric Quotient
0.000	1.00 ± 0.00	102883 ± 212	37258 ± 561	0.152 ± 0.003
0.001	1.00 ± 0.00	102903 ± 246	37527 ± 466	0.151 ± 0.003
0.002	1.00 ± 0.00	102984 ± 208	37631 ± 541	0.150 ± 0.003
0.005	1.00 ± 0.00	103027 ± 205	37665 ± 419	0.150 ± 0.004
0.010	1.00 ± 0.00	103033 ± 205	38100 ± 474	0.147 ± 0.003
0.020	1.00 ± 0.00	103119 ± 190	38526 ± 548	0.145 ± 0.003
0.050	1.00 ± 0.00	103363 ± 190	40524 ± 490	0.135 ± 0.002
0.100	1.00 ± 0.00	103682 ± 174	42805 ± 416	0.125 ± 0.002
0.200	1.00 ± 0.00	103982 ± 190	44316 ± 378	0.119 ± 0.002
0.300	1.00 ± 0.00	104132 ± 185	44930 ± 402	0.116 ± 0.002
0.400	1.00 ± 0.00	104163 ± 196	45179 ± 420	0.115 ± 0.002

Table 7.18: *Voronoi statistics for the non-polar domain in $[C_8C_1im][NTf_2]$ in various electric fields.*

Field Strength [VÅ^{-1}]	No. of Domains	Volume [Å^3]	Surface Area [Å^2]	Isoperimetric Quotient
0.000	1.14 ± 0.36	53133 ± 9849	34743 ± 6415	0.122 ± 0.098
0.001	1.14 ± 0.36	53116 ± 9811	35014 ± 6493	0.121 ± 0.098
0.002	1.14 ± 0.35	52924 ± 9848	35047 ± 6590	0.122 ± 0.100
0.005	1.11 ± 0.33	53923 ± 8738	35754 ± 5021	0.111 ± 0.086
0.010	1.22 ± 0.45	50836 ± 11811	34102 ± 7948	0.140 ± 0.117
0.020	1.08 ± 0.27	54615 ± 7484	37095 ± 5104	0.101 ± 0.074
0.050	1.12 ± 0.32	53199 ± 9080	38167 ± 6510	0.107 ± 0.091
0.100	1.08 ± 0.28	53970 ± 7575	41140 ± 5789	0.090 ± 0.077
0.200	1.04 ± 0.21	54613 ± 5780	43330 ± 4600	0.076 ± 0.058
0.300	1.04 ± 0.21	54526 ± 5628	43981 ± 4568	0.074 ± 0.057
0.400	1.04 ± 0.19	54651 ± 5256	44349 ± 4286	0.072 ± 0.052

to account for this increase.

The non-polar domain in $[C_8C_1im][NTf_2]$ follows a general trend where increasing electric field leads to fewer, larger non-polar domains, with a few exceptions (see Table 7.18).

As the average number of non-polar domains decreases, and the average volume and surface area of the non-polar domains increases with electric field, then there is coalescing of the non-polar domains into fewer, larger domains.

As with $[C_4C_1im][NTf_2]$, there is a stretching of the alkyl chains into longer conformations. Whether this is the cause of this change in the non-polar domain, or how it leads to less domains is not clear.

In summary for $[C_8C_1im][NTf_2]$, there is an aggregation of the non-polar domains into fewer larger domains, with these having a larger surface area. The polar domain gains a small amount of average volume, but increases significantly in its surface area.

7.5.2 Changes to Neighbour Structuring of Ionic Liquids in Electric Fields

Spatial Distribution Functions

Complementary to radial distribution functions are spatial distribution functions (SDFs). While RDFs describe how the radial distribution of an observed particle changes from a reference point, SDFs give information on the spatial positions of the observed particle around the reference particle change at a given distance.

To investigate how the distribution of cation and anions around each other change, the SDFs were calculated for both of the ions around themselves and each other. These are shown using $[NTf_2]^-$ as the reference molecule in $[C_4C_1im][NTf_2]$ in Figure 7.51, using $[C_4C_1im]^+$ as the reference molecule in $[C_4C_1im][NTf_2]$ in Figure 7.52, using $[NTf_2]^-$ as the reference molecule in $[C_8C_1im][NTf_2]$ in Figure 7.53 and using $[C_8C_1im]^+$ as the reference molecule in $[C_8C_1im][NTf_2]$ in Figure 7.54.

The anion centred SDF in $[C_4C_1im][NTf_2]$ shows that under no electric field, the cation is spatially distributed approximately evenly in a toroidal shape, centred around the nitrogen of the anion. There appears to be no preference for any specific site for the cation to coordinate to the anion. This SDF remains unchanged in electric fields ≤ 0.1 VÅ^{-1}. At 0.2 VÅ^{-1} and above, the cation shifts from being in the toroidal shape to being clustered near the nitrogen of the anion. This is the same electric field which causes a change to the shape of the RDF, therefore it can be determined that cations found at 550 pm from the anion are near the CF_3 groups, and the cations found 700 pm away from the anion are near the nitrogen atom.

Considering the spatial distribution of the anion around itself, in zero electric field there is a relatively even spatial distribution of anions, with no preference for clustering around one part of the reference anion.

This SDF remains constant in electric fields of ≤ 0.02 VÅ^{-1}, matching with the RDFs showing no change in the bulk radial structuring of the ion centres of mass. In electric fields of ≥ 0.05 VÅ^{-1} there is a spatial redistribution of the anion around itself towards the CF_3 groups. There is also a distribution of $[NTf_2]^-$ above and below the C-S-N-S-C plane that appears at 0.4 VÅ^{-1}.

Changes in the spatial distribution of the anions occur only in electric fields ≥ 0.02 VÅ^{-1}, whereas changes to the spatial distribution of the cation occur at ≥ 0.2 VÅ^{-1}.

The cation centred SDF in $[C_4C_1im][NTf_2]$ shows that under no electric field, the anion is spa-

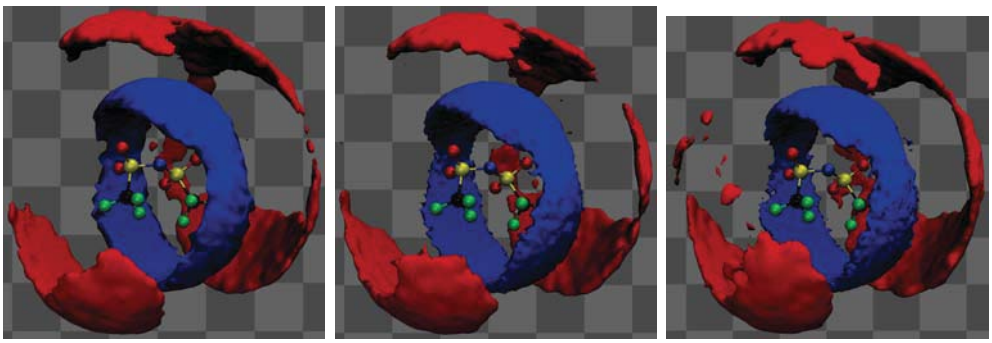

Red: 5.7 nm^{-3}
Blue: 2.9 nm^{-3}

Red: 5.7 nm^{-3}
Blue: 2.9 nm^{-3}

Red: 5.7 nm^{-3}
Blue: 2.9 nm^{-3}

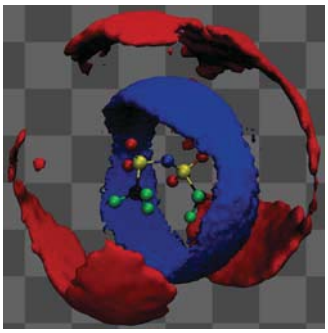

Red: 5.7 nm^{-3}
Blue: 2.9 nm^{-3}

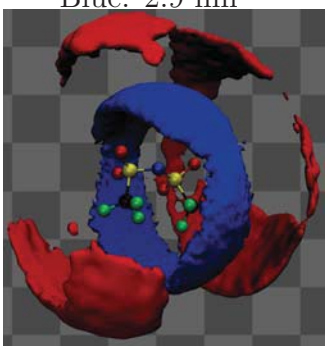

Red: 5.7 nm^{-3}
Blue: 2.9 nm^{-3}

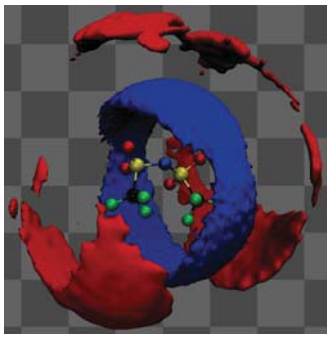

Red: 5.7 nm^{-3}
Blue: 2.9 nm^{-3}

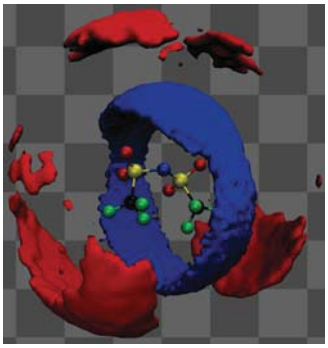

Red: 5.7 nm^{-3}
Blue: 2.85 nm^{-3}

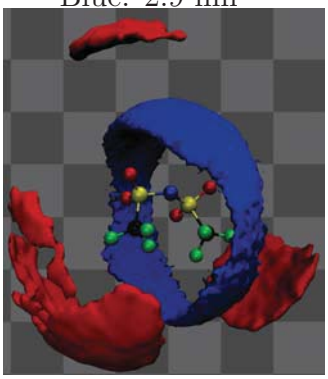

Red: 5.6 nm^{-3}
Blue: 2.8 nm^{-3}

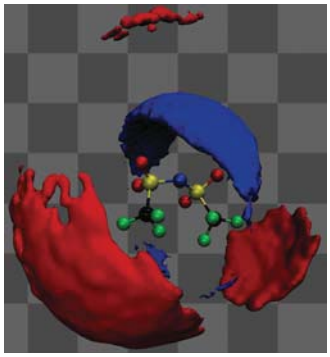

Red: 5.6 nm^{-3}
Blue: 2.6 nm^{-3}

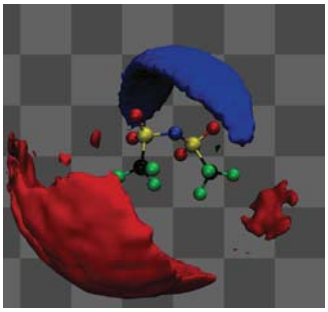

Red: 5.5 nm^{-3}
Blue: 2.6 nm^{-3}

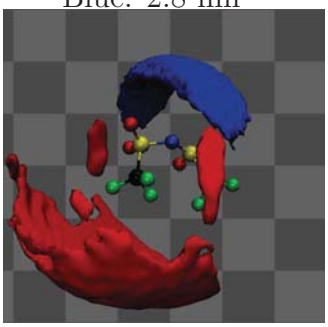

Red: 5.5 nm^{-3}
Blue: 2.6 nm^{-3}

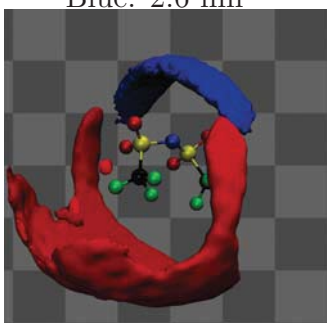

Red: 5.5 nm^{-3}
Blue: 2.6 nm^{-3}

Figure 7.51: *Spatial distribution of the cation (blue surface) and anion (red surface) around a reference anion in [C_4C_1im][NTf_2]. Isovalues for the surfaces are shown below the digram. The electric fields are, from top left reading across: 0.000 VÅ^{-1}, 0.001 VÅ^{-1}, 0.002 VÅ^{-1}, 0.005 VÅ^{-1}, 0.010 VÅ^{-1}, 0.020 VÅ^{-1}, 0.050 VÅ^{-1}, 0.100 VÅ^{-1}, 0.200 VÅ^{-1}, 0.300 VÅ^{-1}, 0.400 VÅ^{-1}, 0.500 VÅ^{-1}.*

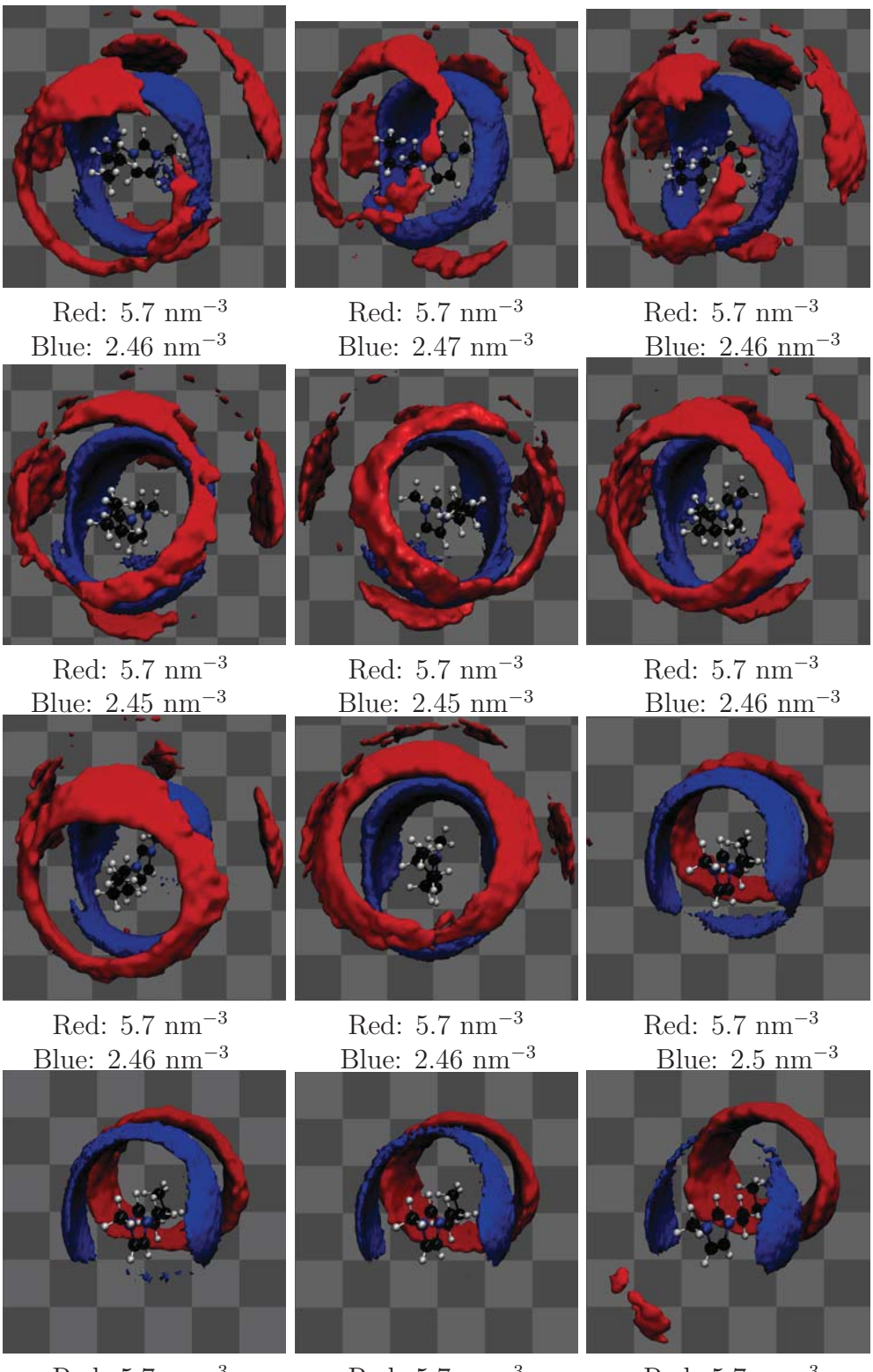

Figure 7.52: *Spatial distribution of the anion (blue surface) and cation (red surface) around a reference cation in [C_4C_1im][NTf_2]. Isovalues for the surfaces are shown below the digram. The electric fields are, from top left reading across: 0.000 VÅ^{-1}, 0.001 VÅ^{-1}, 0.002 VÅ^{-1}, 0.005 VÅ^{-1}, 0.010 VÅ^{-1}, 0.020 VÅ^{-1}, 0.050 VÅ^{-1}, 0.100 VÅ^{-1}, 0.200 VÅ^{-1}, 0.300 VÅ^{-1}, 0.400 VÅ^{-1}, 0.500 VÅ^{-1}.*

tially distributed in a near toroidal shape around the imidazolium ring. The exception to this is around the C4/5 position, the toroid is distorted towards the butyl chain. There is also a small distribution of anions in a similar position, but towards the methyl group.

These are common positions in which hydrogen bonding occurs,[224] indicating the presence of some hydrogen bonding. However when comparing these SDFs with those of stronger hydrogen bonding anions (e.g. bromide, acetate), these anions show a much greater preference for these spatial positions than the $[NTf_2]^-$ anion does. This indicates that in accordance with the literature $[NTf_2]^-$ is a weakly hydrogen bonding anion.[224]

This SDF remains constant in electric fields of $\leq$ 0.02 VÅ^{-1}. Electric fields of $\geq$0.05 VÅ^{-1} have a loss of the anion at the C4/5-methyl group, $\geq$0.3 VÅ^{-1} have a loss of the anion at the C4/5-butyl group, and $\geq$0.4 VÅ^{-1} shows a reduction in the anions positioned around the C2 group. This means any hydrogen bonding present is being disrupted by the electric field. This is discussed more in the next section.

The cation in the SDF with no electric field is very dispersed around the reference cation, with no position in which the cation prefers to reside. This explains why the cation-cation RDF in Section 7.5.1 has a very broad peak. It is due to a lack of sites in which the cation prefers to reside. Combined with the very changeable nature of the cation centre of mass with the motion of the butyl chain, this leads to a large range of possible values for the cation-cation distance. This SDF remains constant in electric fields of $\leq$0.02 VÅ^{-1}. This is not very obvious, but when calculating the difference between the SDFs this is easier to see.

The spatial distribution of the cations becomes *more* organised as the electric field increases $\geq$0.02 VÅ^{-1}. There is a reduction of cations around the imidazolium ring, and an increase in cations around the butyl chain. At 0.5 VÅ^{-1} there is also a small distribution of cations positioned near the methyl group. When viewing the simulations the cations diffuse with their methyl groups leading the molecule, hence the appearance of cations in this position means that there are cations directly in front of other cations as they diffuse.

This, along with a similar phenomena with the anions, suggests the ions are beginning to line up and starting to form of channels, like those reported by Zhao *et al.* for $[C_2C_1im][NO_3]$ in electric fields of 1.14 VÅ^{-1}.[198]

The anion centred SDF in $[C_8C_1im][NTf_2]$ with no electric field shows that the cation resides in three distinct positions, near the nitrogen atom as well as above and below the C-S-S-C plane. In electric fields of $\geq$0.05 VÅ^{-1} there is a shift of the cations into a more homogeneous distribution, positions between the three no-field positions being occupied. These join into a horse-shoe shape in electric fields of 0.1-0.3 VÅ^{-1} and re-separate at 0.4 VÅ^{-1}. As the cation-anion RDF

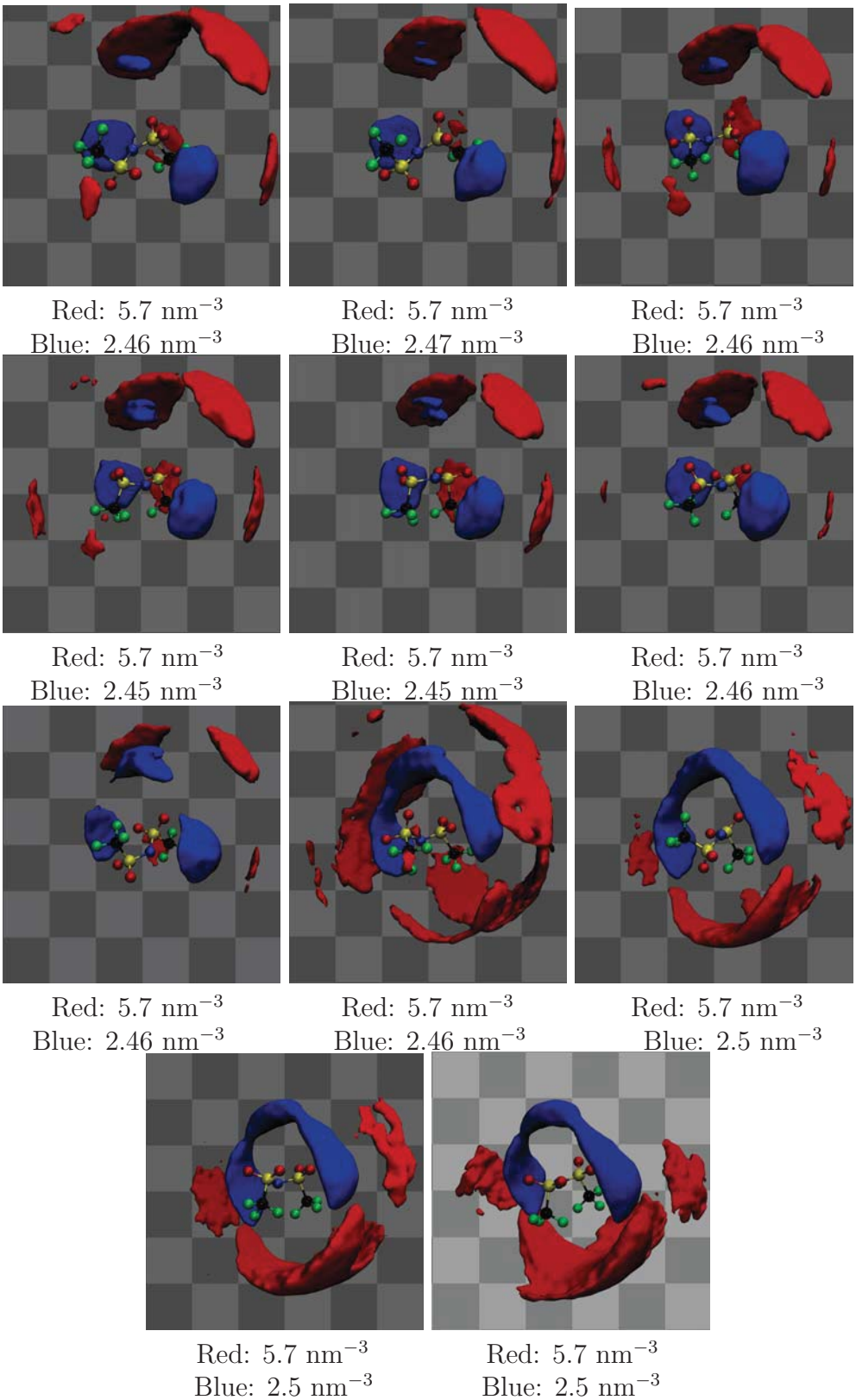

Figure 7.53: *Spatial distribution of the anion (blue surface) and cation (red surface) around a reference anion in [C_8C_1im][NTf_2]. Isovalues for the surfaces are shown below the digram. The electric fields are, from top left reading across: 0.000 VÅ^{-1}, 0.001 VÅ^{-1}, 0.002 VÅ^{-1}, 0.005 VÅ^{-1}, 0.010 VÅ^{-1}, 0.020 VÅ^{-1}, 0.050 VÅ^{-1}, 0.100 VÅ^{-1}, 0.200 VÅ^{-1}, 0.300 VÅ^{-1}, 0.400 VÅ^{-1}.*

remains constant in these electric fields (Figure 7.46), changes in the anion-cation structure involve only a spatial re-distribution of the cation around the anion, with no change in the

radial distribution.

The distribution of the anion around a reference anion is fairly uniform, with the observed anion mostly occupying spatial positions which the cation does not. This remains the same in electric fields of $\leq$0.02 VÅ^{-1}. Electric fields of 0.05 and 0.1 VÅ^{-1} cause the spatial distribution to become more diffuse. Electric fields of $\geq$0.2 VÅ^{-1} have two spatial positions in which the anion can be found. The first is near the CF_3 groups, and the second is above and below the C-S-S-C plane.

Using the SDFs, the shorter distance peak in the RDFs can be assigned to anions near the CF_3 group. The longer distance peak is due to anion-anion distances that have a cation between them.

The spatial distribution of the anion around the cation in $[C_8C_1im][NTf_2]$ with no electric field has a concentration of the anion near the C2 position, extending to either side of the plane of the imidazolium ring, similar to $[C_4C_1im][NTf_2]$. There is also a small concentration near the C4/5 protons towards the methyl group, however the concentration towards the alkyl chain is missing. This could be because the octyl chain is larger than the butyl, therefore the excluded volume created by motion of the octyl chain is greater than the butyl chain in $[C_4C_1im][NTf_2]$. This distribution remains constant in electric fields of $\leq$0.1 VÅ^{-1}. Above this, there is a loss of the concentrations of anions at the C2 and C4/5-methyl positions. As the RDFs remain constant, the anions must be moving from these positions towards the positions above and below the plane of the imidazolium ring.

The spatial distribution of the cation around the cation is different to that of $[C_4C_1im][NTf_2]$. The cation occupies the same spatial positions as the anion around the imidazolium ring, but at a greater radial distance. There are also small concentrations of cations towards the methyl groups present in this SDF.

This distribution also remains constant in electric fields of $\leq$0.1 VÅ^{-1}. Above this, the SDFs show the cations move towards spatial positions above and below the plane of the imidazolium ring.

These results in particular highlight the importance of SDFs. The RDFs show no change in the radial distribution of the ions relative to each other when considering the cation in $[C_8C_1im][NTf_2]$, therefore one could conclude that the structure in $[C_8C_1im][NTf_2]$ is unaffected by an electric field. However the SDFs show that there is a spatial reorganisation of the ions instead of a change in the radial distribution.

Both the cation and anion SDFs around a central cation remain constant in electric fields $\leq$ 0.1 VÅ^{-1}. This is a stronger electric field than that which caused changes in the SDFs in

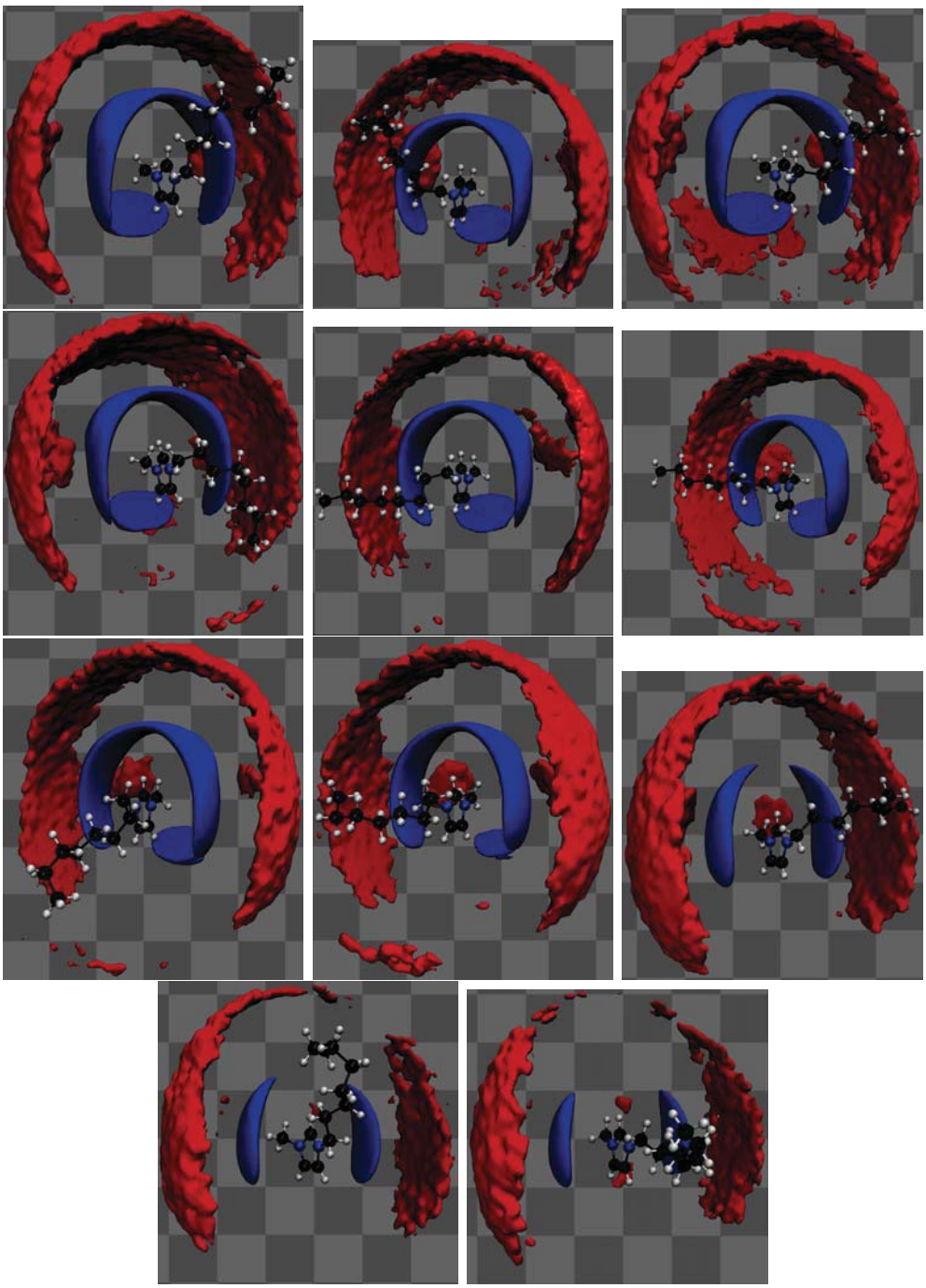

Figure 7.54: *Spatial distribution of the anion (blue surface) and cation (red surface) around a reference cation in [C_8C_1im][NTf_2]. Isovalues for the anion surface are all 7.0 nm^{-3}, and for the cation surfaces are all 2.0 nm^{-3}. The electric fields are, from top left reading across: 0.000 VÅ^{-1}, 0.001 VÅ^{-1}, 0.002 VÅ^{-1}, 0.005 VÅ^{-1}, 0.010 VÅ^{-1}, 0.020 VÅ^{-1}, 0.050 VÅ^{-1}, 0.100 VÅ^{-1}, 0.200 VÅ^{-1}, 0.300 VÅ^{-1}, 0.400 VÅ^{-1}.*

[C_4C_1im][NTf_2] or the anion centred SDF in [C_8C_1im][NTf_2]. This, along with the constant cation-containing RDFs in [C_8C_1im][NTf_2] (Figures 7.46 and 7.48) indicates that the neighbouring structures around the cation in [C_8C_1im][NTf_2] are less affected by electric fields than [C_4C_1im][NTf_2] or the anion-anion structuring in [C_8C_1im][NTf_2]. This could be due to some property of the ionic liquids, or may be due to the lack of strong structuring to begin with.

This would need to be tested with other ionic liquids.

In summary, the SDFs show that in $[C_4C_1im][NTf_2]$ there are large spatial reorganisations in the ionic liquid at high electric fields that are accompanied by changes in the radial distribution of the ionic liquid. For example, the anion RDF splits into two peaks in the highest electric fields, and the SDF shows that this can be attributed to some anions moving away from having a cation 'spacer' between them and moving closer to one-another. There is also a slight change in the cation RDF, which the SDF shows is due to a movement of the spatial distribution of the cation from an isotropic distribution to being more clustered around the butyl chain.

The same can be said for the anion centred structural analyses in $[C_8C_1im][NTf_2]$, however the cation is slightly different. The RDFs show no change in any electric field, however from the SDFs it can be seen that the cation structures undergo a spatial redistribution.

Hydrogen Bonding Structure

From the SDFs it can be seen that hydrogen bonding may somewhat influence the distribution and orientation of anions and cations around each other. This is expected to be a weak hydrogen bond, as $[NTf_2]^-$ is known to be a weak hydrogen bonding anion.[224]

In order to quantify this, the combined distribution function (CDF) of the distance between the hydrogen atom and hydrogen bond acceptor is histogrammed against angular distribution of the hydrogen bond (donor-hydrogen-acceptor).

The hydrogen bond donors used are the C2 and C4/5 positions, as these are the positions on imidazolium ionic liquids where the strongest hydrogen bonds occur.[224] The acceptor used is the oxygen on the $[NTf_2]^-$ anion, as again this is the strongest hydrogen bond acceptor.[224]

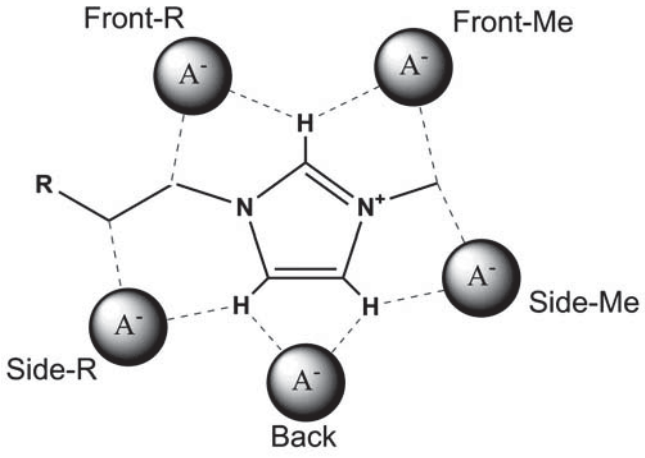

Figure 7.55: *Hydrogen bonding positions and names around an imidazolium ring, plus the nomenclature used in this thesis.*

In this thesis, the naming scheme used by Hunt *et al.* will be used for the positions of the anion around the cation. A schematic of this is shown in Figure 7.55. The definition of Hunt *et al.* of the strengths of hydrogen bonds will also be used. This involves using a distance and angle criteria, which was determined for di-ionic hydrogen bonds, to give the relative strength of the hydrogen bond.[224]

Per this definition, a 'strong' hydrogen bond has a proton-acceptor distance of 120-150 pm and a donor-proton-acceptor angle of 0-10°. A 'moderate' hydrogen bond has a proton-acceptor distance of 150-220 pm and a donor-proton-acceptor angle of 10-50°. A 'weak' hydrogen bond has a proton-acceptor distance of >220 pm and a donor-proton-acceptor angle of 50-90°.

Figure 7.56 shows the combined distribution function for the hydrogen bond at the C2 position in $[C_4C_1im][NTf_2]$. The CDF in 0.000 VÅ^{-1} confirms that hydrogen bonding in the C2 position in $[C_4C_1im][NTf_2]$ is a weak hydrogen bond. There is a peak in the CDF at ≈240 pm and 40°. The 40° is due to the anions being positioned slightly towards the methyl/butyl groups in the front-R and front-Me positions, common positions for weak hydrogen bonds in $[C_nC_1im][NTf_2]$ ionic liquids.[224]

Although this meets the angle criteria for a moderate hydrogen bond, the distance criteria is that of a weak hydrogen bond. As the distribution is very broad, especially in terms of angles, the hydrogen bond should be classified as a weak hydrogen bond.

There are also two smaller peaks in the CDF at 640 pm and 180°, and 580 pm and 140°. This cannot be due to the C2 hydrogen bond. Instead, it could be due to anions at the opposite side of the imidazolium ring in the side-R, side-Me or back positions. There is also the possibility that this can come from anions above and below the plane of the imidazolium ring, a position present in the SDFs.

Considering the C2 peak in the CDF in different electric fields, this peak remains at a constant position and density in electric fields up to and including 0.05 VÅ^{-1}. This shows that the weak hydrogen bonding in this position is not affected by these electric fields.

At 0.05 VÅ^{-1} there is a change in the SDF, but not a major change. Therefore the hydrogen bond is at least strong enough to resist the minor changes at these electric field strengths.

Above 0.05 VÅ^{-1} there is no change in the length of the hydrogen bond. However, there is a decrease in the density of the hydrogen bonds, alongside an increase in the angle. These combined show a decrease in the number of hydrogen bonds, showing that these electric fields are interfering with the hydrogen bonds.

Remaining with $[C_4C_1im][NTf_2]$, Figure 7.57 shows the combined distribution function for the hydrogen bond at the C4/5 positions in $[C_4C_1im][NTf_2]$. As with the hydrogen bonds in the

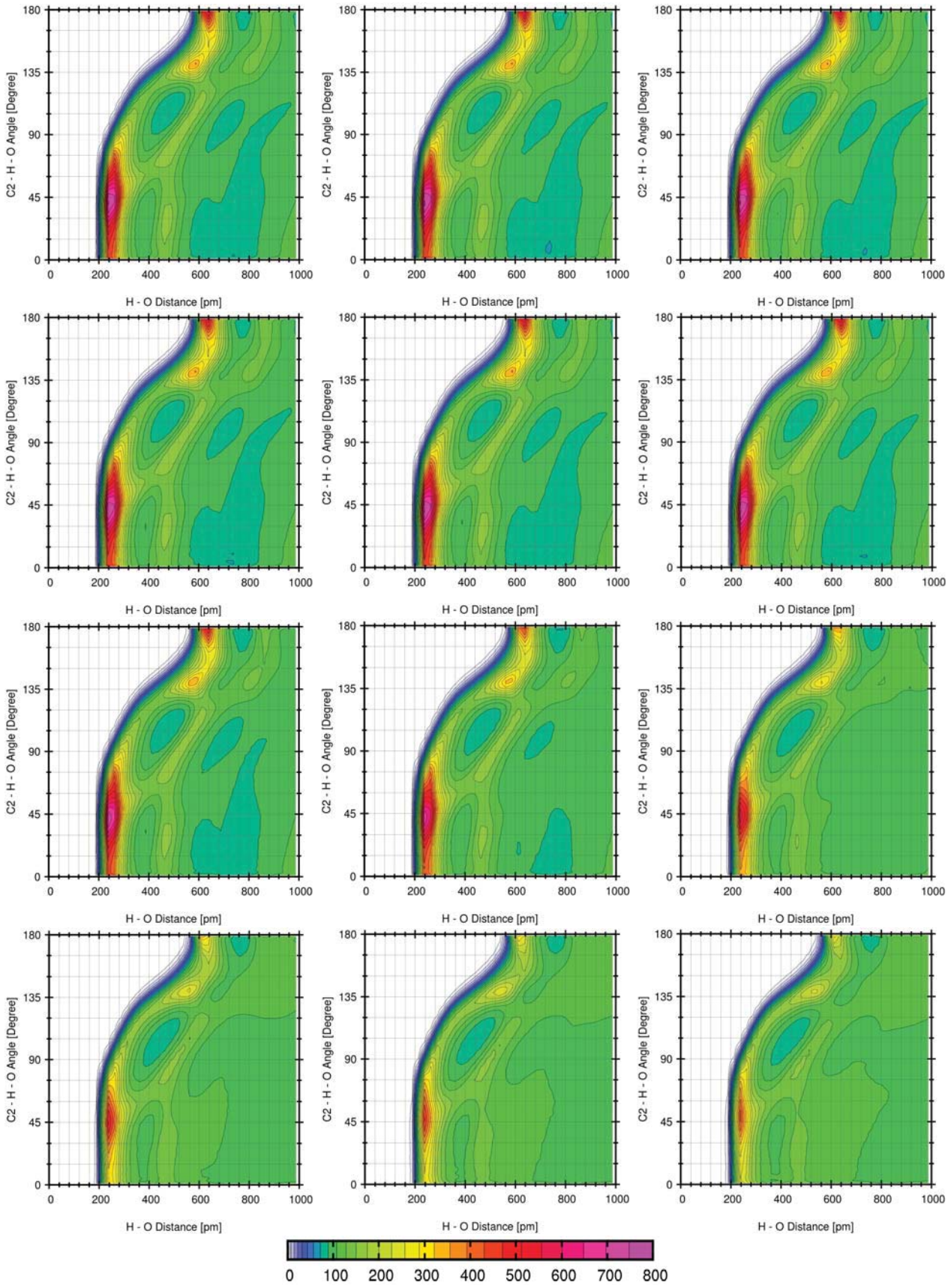

Figure 7.56: *Combined distribution function showing the distance and angle dependence of the C2 proton to the oxygen of the anion in $[C_4C_1im][NTf_2]$. The electric fields are, from top left reading across: 0.000 VÅ^{-1}, 0.001 VÅ^{-1}, 0.002 VÅ^{-1}, 0.005 VÅ^{-1}, 0.010 VÅ^{-1}, 0.020 VÅ^{-1}, 0.050 VÅ^{-1}, 0.100 VÅ^{-1}, 0.200 VÅ^{-1}, 0.300 VÅ^{-1}, 0.400 VÅ^{-1}, 0.500 VÅ^{-1}.*

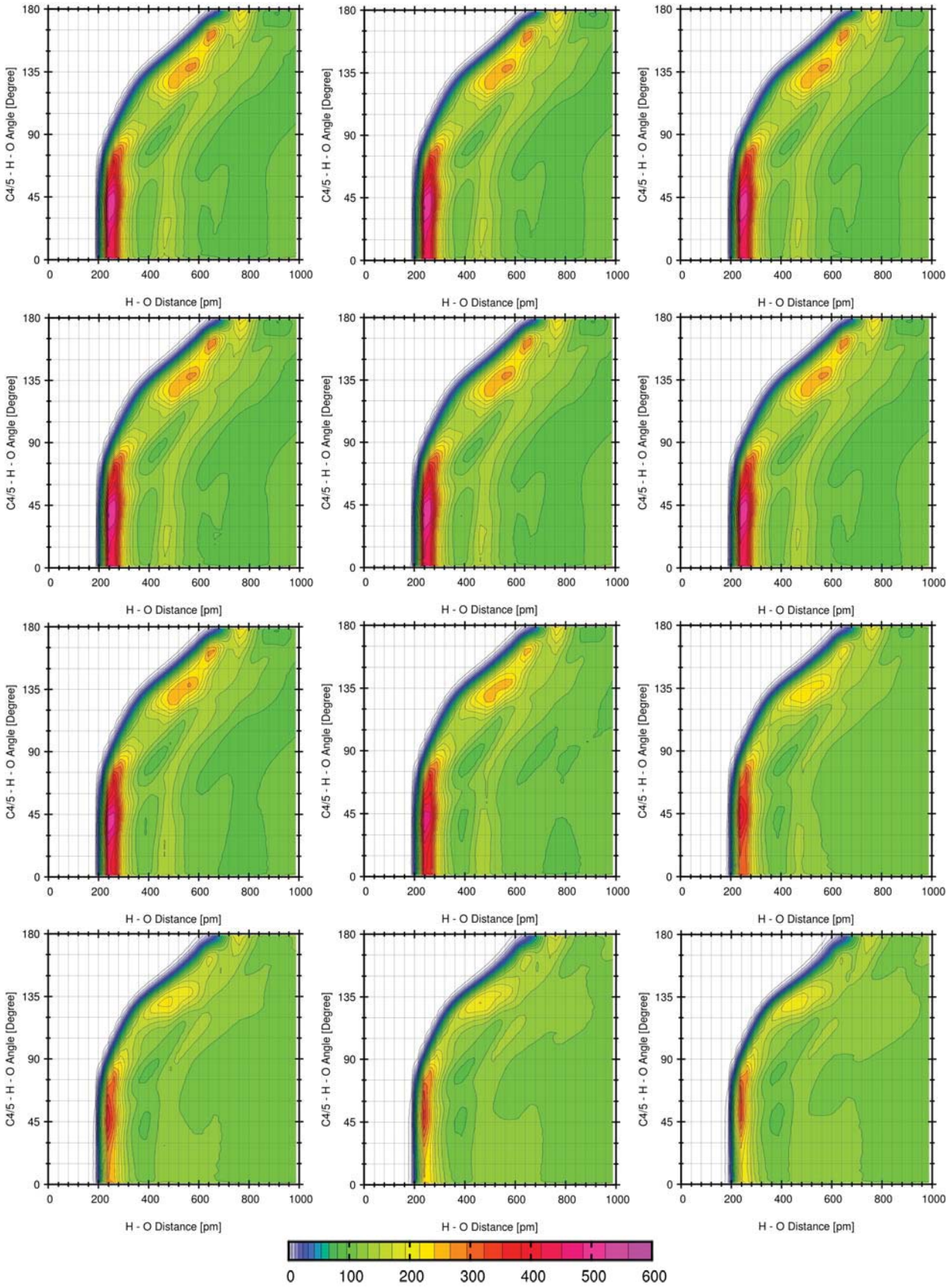

Figure 7.57: *Combined distribution function showing the distance and angle dependence of the C4 and C5 proton to the oxygen of the anion in $[C_4C_1im][NTf_2]$. The electric fields are, from top left reading across: 0.000 VÅ^{-1}, 0.001 VÅ^{-1}, 0.002 VÅ^{-1}, 0.005 VÅ^{-1}, 0.010 VÅ^{-1}, 0.020 VÅ^{-1}, 0.050 VÅ^{-1}, 0.100 VÅ^{-1}, 0.200 VÅ^{-1}, 0.300 VÅ^{-1}, 0.400 VÅ^{-1}, 0.500 VÅ^{-1}.*

C2 position, the CDF in 0.000 VÅ^{-1} confirms that hydrogen bonds in the C4/5 position in $[C_4C_1im][NTf_2]$ are weak hydrogen bonds. There is a peak in the CDF at ≈240-260 pm and 40° which is a moderate hydrogen bond in terms of the angle, and weak in terms of distance. As with C2, the broad angular distribution means that this hydrogen bond should be classified as weak.

The peak height in the C4/5 hydrogen bond CDF in 0.000 VÅ^{-1} is lower than that of the C2 position in 0.000 VÅ^{-1}, therefore there are fewer hydrogen bonds at the C4/5 position.

The main peak corresponds to anions hydrogen bonding in one of the side or back positions. While the CDFs cannot distinguish between these, the SDFs for $[C_4C_1im][NTf_2]$ suggest that the anions are mainly in the side-R and back positions. This is because there is no concentration of anions near the C4 proton, which is where they would be to hydrogen bond in the side-Me position.

This distribution has two secondary peaks: one at 560 pm and 135°, and one at 620 pm and 165°. These two peaks correspond to the oxygen atoms hydrogen bonding in the C2 position, and confirms that the C2 position hydrogen bonds in the front-Me and front-R positions. Each of these peaks corresponds to anions hydrogen bonding on the same side and opposite side respectively (i.e. 135° corresponds to front-R anions to the C5 position, 165° corresponds to front-Me anions to the C5 position). Considering how the SDFs change in different electric fields, there is no change in the peak height, distance at the peak or angle at the peak in electric fields up to and including 0.02 VÅ^{-1}.

In electric fields of 0.05 VÅ^{-1} and above, there is a reduction in the peak height. This indicates a loss of ions in the hydrogen bonding position, and therefore a loss of hydrogen bonds. Like for the C2 position, this is accompanied by an increase in the angle of the hydrogen bond, further reinforcing the weakening of the hydrogen bond. The lower electric field required to change the distribution when considering these hydrogen bonds further confirms that this hydrogen bond is weaker than the one in the C2 position.

Moving to $[C_8C_1im][NTf_2]$, Figure 7.58 shows the combined distribution function for the hydrogen bond at the C2 position in $[C_8C_1im][NTf_2]$. Considering the CDF at 0.000 VÅ^{-1}, this looks very similar to the CDF of the C2 position in $[C_4C_1im][NTf_2]$. There is one major peak at a low distance and angle, and two secondary peaks at greater distances and angles.

The main peak is at a distance of 260 pm and an angle of 45°. This is a greater distance and angle than for the hydrogen bonds in the C2 position in $[C_4C_1im][NTf_2]$, indicating that hydrogen bonding in this position is weaker in $[C_8C_1im][NTf_2]$. The distribution is also broader in terms of angles and distances, further confirming a weaker hydrogen bond.

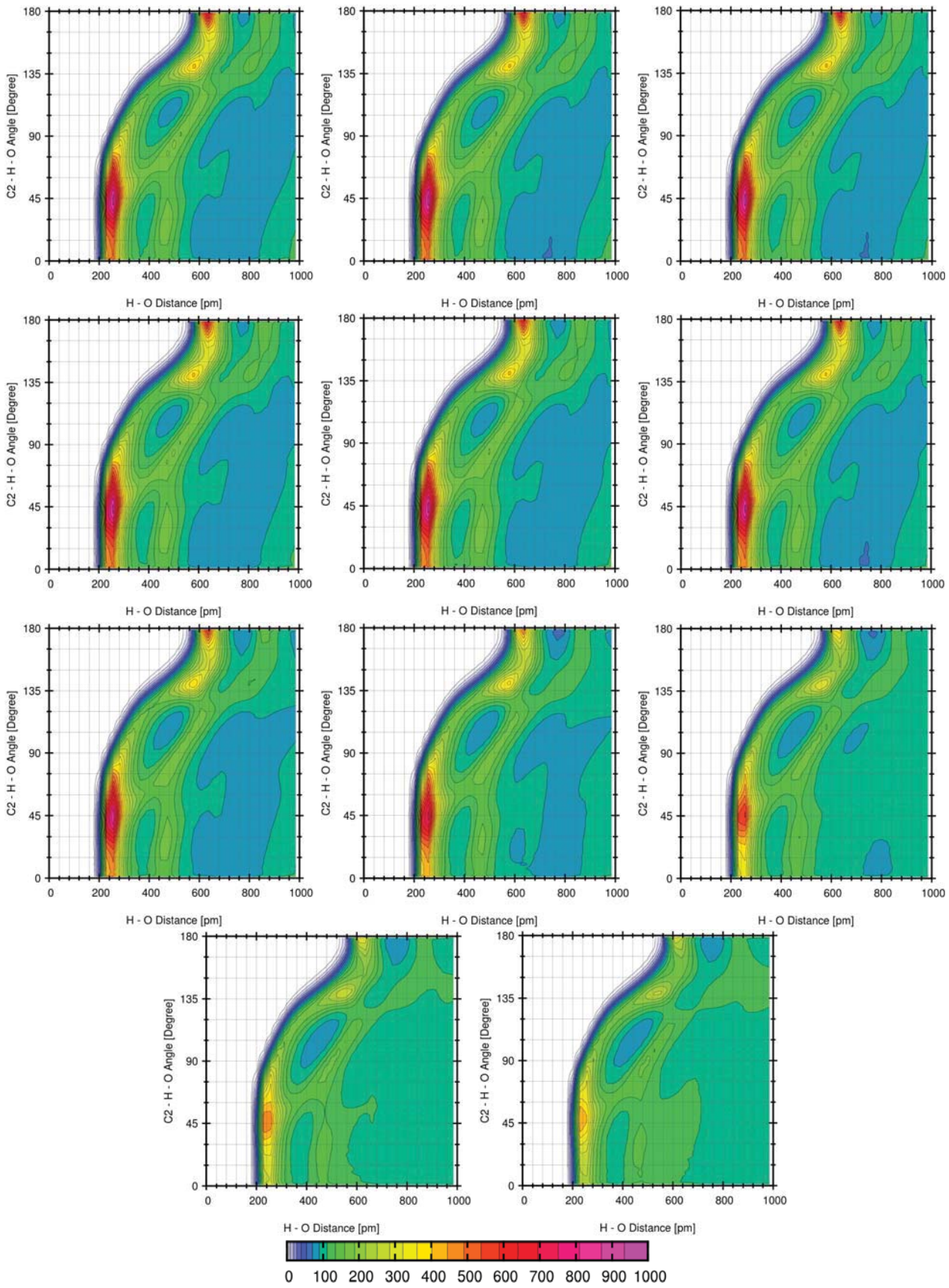

Figure 7.58: *Combined distribution function showing the distance and angle dependence of the C2 proton to the oxygen of the anion in $[C_8C_1im][NTf_2]$. The electric fields are, from top left reading across: 0.000 VÅ^{-1}, 0.001 VÅ^{-1}, 0.002 VÅ^{-1}, 0.005 VÅ^{-1}, 0.010 VÅ^{-1}, 0.020 VÅ^{-1}, 0.050 VÅ^{-1}, 0.100 VÅ^{-1}, 0.200 VÅ^{-1}, 0.300 VÅ^{-1}, 0.400 VÅ^{-1}.*

The secondary peaks are at 580 pm and 140°, and 640 pm and 180°. As the cation-centred SDF for this ionic liquid shows no anions are positioned in the back or side-R positions, these peaks must come from anions in the side-Me position or above and below the imidazolium ring. Considering how the distributions change in electric fields, this CDF remains constant in electric fields up to and including 0.01 VÅ^{-1}. At 0.02 VÅ^{-1} there is a slight reduction in the density of oxygen atoms at the peak, but the distribution remains the same otherwise.

At 0.05 VÅ^{-1} and above, the decrease in the density at the peak continues but there is also an increase in the angle at the peak. Increasing electric fields cause a further decrease in the peak intensity and a larger increase in the angle at the peak.

The lower threshold electric field required to cause changes to the distribution is further evidence that this hydrogen bond in $[C_8C_1im][NTf_2]$ is weaker than the same hydrogen bond in $[C_4C_1im][NTf_2]$.

Remaining with $[C_8C_1im][NTf_2]$, Figure 7.59 shows the combined distribution function for the hydrogen bonds at the C4/5 position in $[C_8C_1im][NTf_2]$. This is very different to all the other CDFs in this thesis. There is a main peak, however the angle is at 135° instead of 45°. The secondary peak corresponding to anions hydrogen bonding in the C2 position is still present, and in approximately the same location as the same peak in $[C_4C_1im][NTf_2]$.

Looking at the SDF of the anion around the cation in $[C_8C_1im][NTf_2]$, there is a small concentration of anions in the side-Me position that could be the cause of the distribution in this position. However this is not a position which forms hydrogen bonds.

The absence of a peak at a low angle (<50°) and short distance (<250 pm) indicates that hydrogen bonding at this position of the imidazolium ring does not occur for $[C_8C_1im][NTf_2]$.

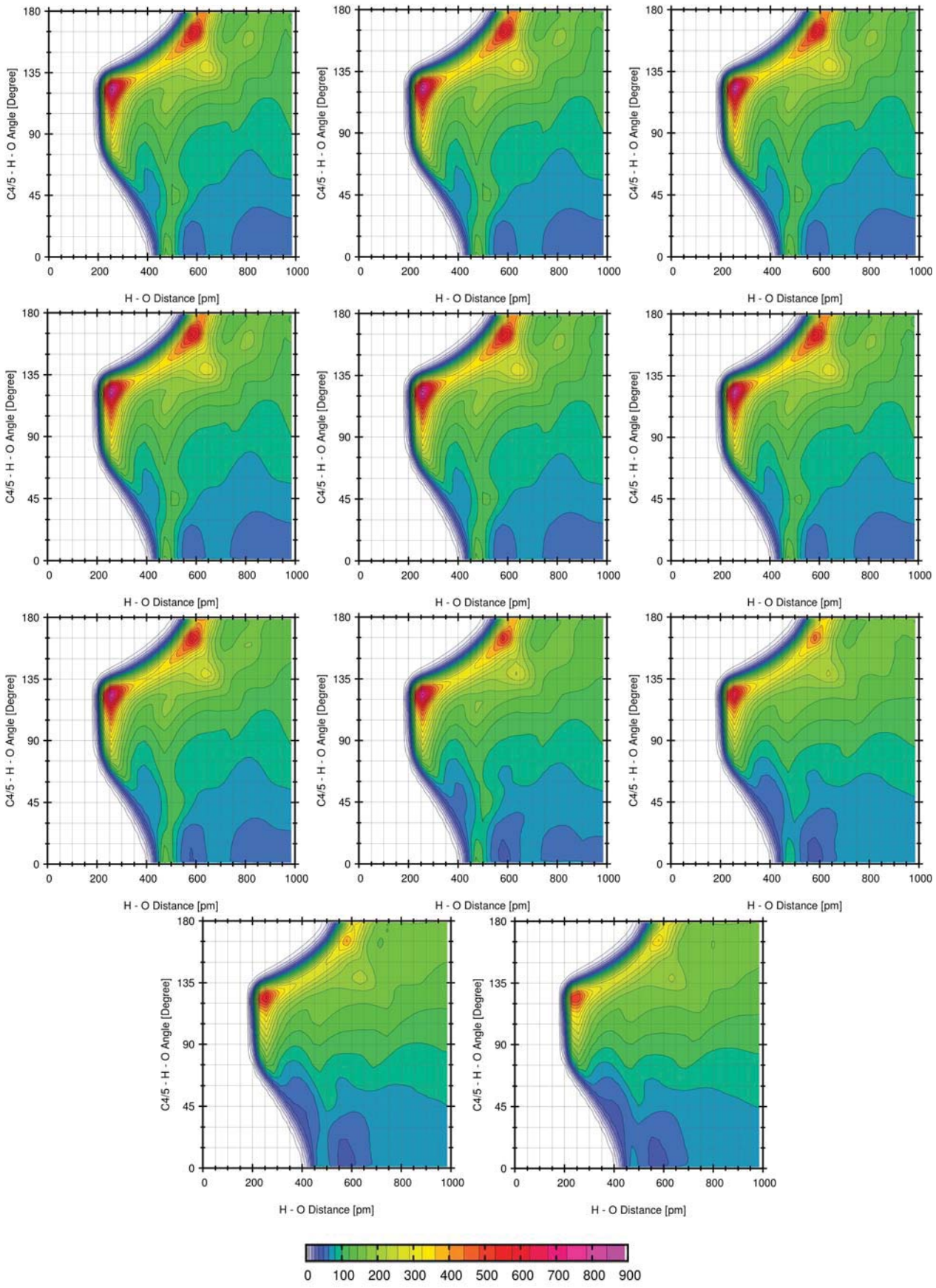

Figure 7.59: *Combined distribution function showing the distance and angle dependence of the C4 and C5 proton to the oxygen of the anion in* $[C_8C_1im][NTf_2]$. *The electric fields are, from top left reading across: 0.000* $VÅ^{-1}$, *0.001* $VÅ^{-1}$, *0.002* $VÅ^{-1}$, *0.005* $VÅ^{-1}$, *0.010* $VÅ^{-1}$, *0.020* $VÅ^{-1}$, *0.050* $VÅ^{-1}$, *0.100* $VÅ^{-1}$, *0.200* $VÅ^{-1}$, *0.300* $VÅ^{-1}$, *0.400* $VÅ^{-1}$.

7.5.3 Changes to Ion Structure of Ionic Liquids in Electric Fields

Changes to the bulk and neighbouring ion structure have been established in electric fields. Alongside this, there is the possibility that the internal structures of the ions can change in electric fields. This could be the cause of, or result of the larger scale structural changes in the ionic liquids, so will be investigated here.

Cation Structure

A major way to cause large changes to the structure of the cation is by changing the conformation of the longer alkyl chain: the butyl chain in $[C_4C_1im][NTf_2]$ and the octyl chain in $[C_8C_1im][NTf_2]$.

Therefore a vector that can be analysed in order to observe changes to the cation structure is the distance between the centre of the imidazolium ring and the terminal carbon atom on the long alkyl chain. This will give a simple representation of how stretched the alkyl chain is in all electric fields. This is shown diagrammatically in Figure 7.60.

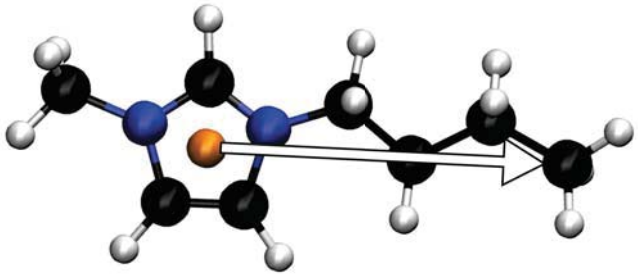

Figure 7.60: *Diagram showing the vector from the centre of the imidazolium ring (orange sphere) to the terminal carbon on the butyl alkyl chain ($[C_4C_1im][NTf_2]$ used as an example).*

For $[C_4C_1im][NTf_2]$, the histograms of the lengths of this vector in all electric fields are shown in Figure 7.61.

There are two main regions of interest in this histogram, a peak at 600 pm and a region from 500 pm - 565 pm. The peak at 600 pm corresponds to the length of fully extended butyl chain, where all bonds are in the *anti* conformation. The region between 500 pm - 565 pm corresponds to a partially bent butyl chain, where one or more bonds are in the *gauche* conformation. Conformations with butyl chains which are fully *gauche* are not observed, however the histogram does have a 'fronting' tail, indicating that there are some cations having multiple bonds *gauche*. When looking at the different electric fields, this histogram remains the same in electric fields of up to 0.02 $VÅ^{-1}$ showing that these electric fields do not affect the distribution of the lengths

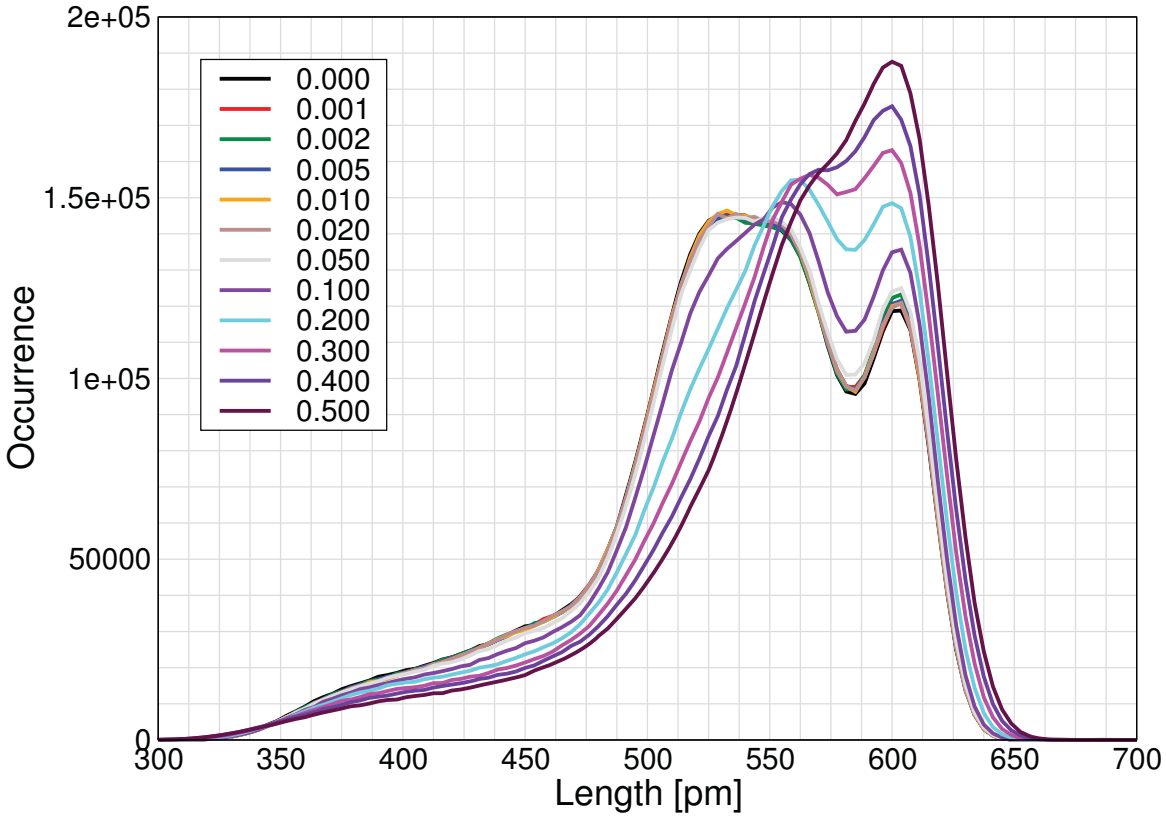

Figure 7.61: *Histogram of the distance from the centre of the imidazolium ring in $[C_4C_1im][NTf_2]$ to the terminal carbon on the butyl chain in different electric fields. Electric fields are in the legend in $VÅ^{-1}$.*

of this vector.

At 0.05 $VÅ^{-1}$ there is a slight shift in the distribution. This is most obvious in the all-*anti* peak, which increases in height by ≈4%.

Changes to the distribution become more obvious at higher electric field strengths. There is a decrease in the number of cations with more 'curled up' conformations which give shorter distances, and an increase in the number of cations with more 'stretched out' conformations which give longer distances.

In an electric field of 0.3 $VÅ^{-1}$ there is a transition from the >1 bonds *gauche* conformer being the most common, to the all-*anti* conformation being the most common conformation for the cation.

For $[C_8C_1im][NTf_2]$, the histograms of the distributions of the lengths of the same vector in all electric fields are shown in Figure 7.62.

Like in $[C_4C_1im][NTf_2]$, there is a region which represents an all-*anti* alkyl chain, and one for alkyl chains with partial-*gauche* bonds. The all-*anti* region is the shoulder in the distribution at 1100 pm, and the partial-*gauche* bonds correspond to lengths of $\lesssim$1075 pm.

This distribution being broader is a product of the octyl chain having more bonds, around

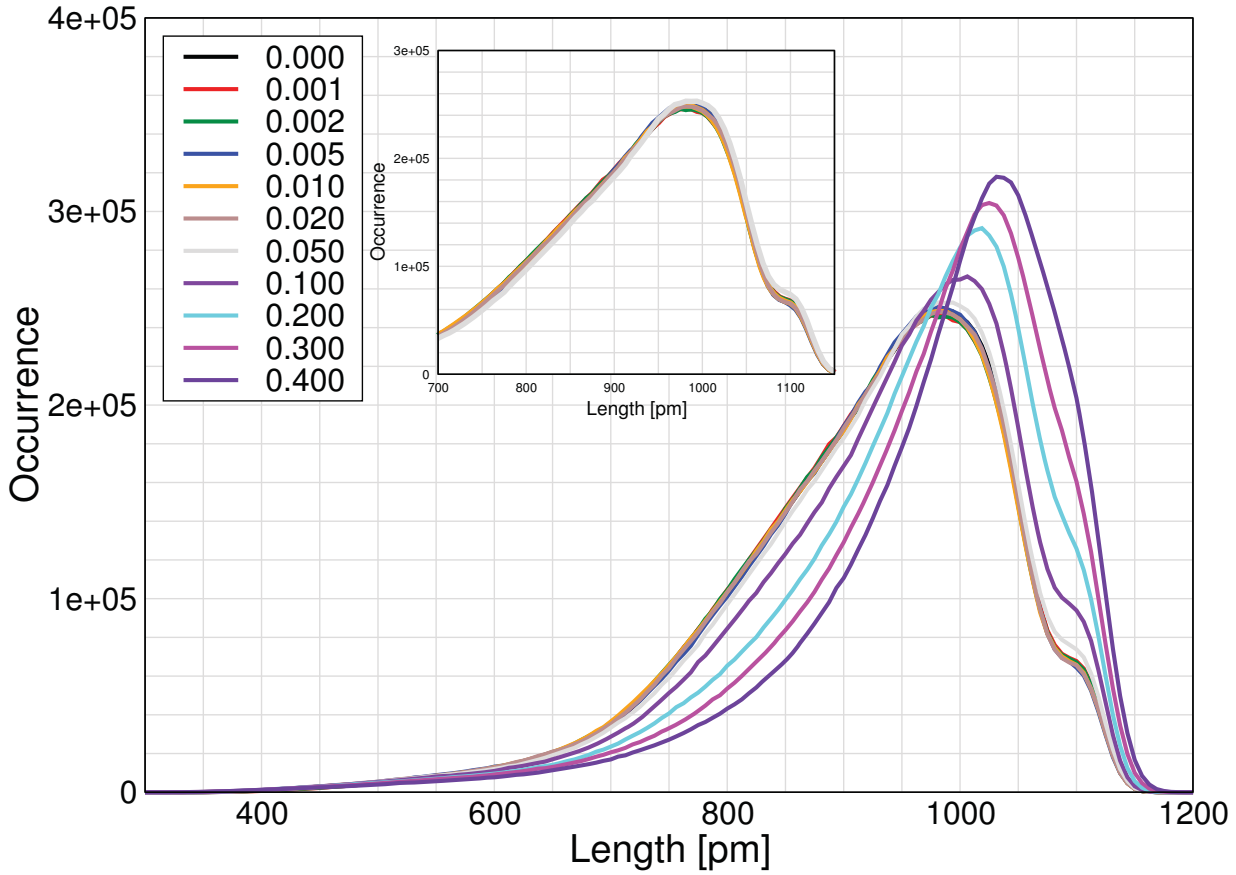

Figure 7.62: *Histogram of the distance from the centre of the imidazolium ring in $[C_8C_1im][NTf_2]$ to the terminal carbon on the octyl chain in different electric fields. Electric fields are in the legend in VÅ^{-1}. Inset is a close up of the distributions in electric fields of 0-0.05 VÅ^{-1}.*

which rotation changes the length of this vector. This leads to more possible conformations, and hence a broader distribution.

As with $[C_4C_1im][NTf_2]$, this histogram remains the same in electric fields of up to 0.02 VÅ^{-1} and shifts slightly at 0.05 VÅ^{-1}. For the cation in $[C_8C_1im][NTf_2]$, the increase in the height of the histogram at 1100 pm is ≈13%.

Further increases to the electric field cause greater changes to the distribution, with an increase in the number of cations with longer lengths, and a decrease of the number of cations with shorter lengths. This is matched with a shift in the peak position to longer lengths, in line with the octyl chain taking longer configurations in higher electric fields.

In summary, the cation alkyl chain does not seem to be affected significantly by electric fields up to 0.02 VÅ^{-1}. In an electric field of 0.05 VÅ^{-1} there is a slight increase in the number of cations having the longest ring centre-terminal carbon distance i.e. all-*anti* conformer. Above this, there are large changes to the distribution with larger electric fields causing a greater stretching of the alkyl chains.

It is possible that this is related to the changes in the dynamics, seen in Section 7.4, as they

occur at the same electric field. It is possible that this change in the cation ring centre-terminal carbon distance is related to an increase in motion. Though there is no way to confirm this from these simulations, changes to structure not caused by a increase in motion will be discussed later in this thesis.

Anion Structure

Alongside changes to the structure of the cations, the anion can also undergo a change to its structure.

It is well known that the $[NTf_2]$ anion has two conformers, a *cis*-like isomer (a.k.a. Z isomer or C_1 isomer) and a *trans*-like isomer (a.k.a. E isomer or C_2 isomer), both shown in Figure 7.63.

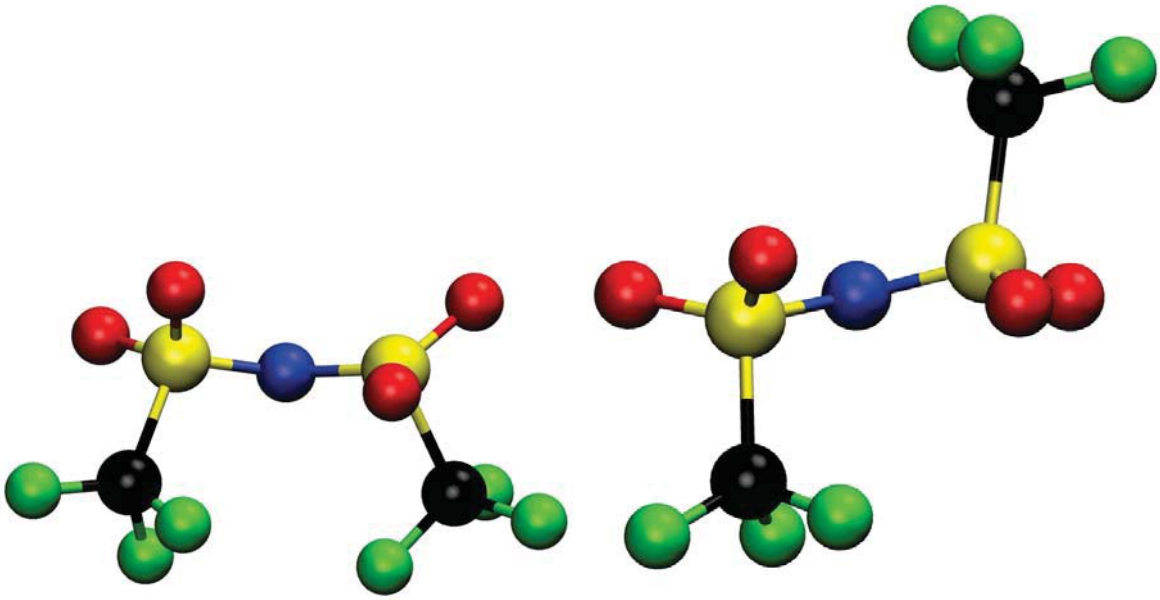

Figure 7.63: *The cis (left) and trans (right) isomer of the [NTf$_2$] anion.*

To distinguish between these, the C-S-S-C dihedral angle can be analysed (see Figure 7.64). The *cis* isomer has a small C-S-S-C dihedral angle (0-50°), and the *trans* has a large C-S-S-C dihedral angle (160-180°).

The distribution of these dihedrals in $[C_4C_1im][NTf_2]$ and $[C_8C_1im][NTf_2]$ in various electric fields are shown in Figures 7.65 and 7.66 respectively.

For $[NTf_2]$ in $[C_4C_1im][NTf_2]$ in low electric fields, there are obvious peaks at ±40° for the *cis* isomer, and ±170-180° for the *trans* isomer.

Increasing the electric field up to 0.02 VÅ^{-1} has no visible effect on the distribution, with the peaks remaining at the same height and position.

Above 0.02 VÅ^{-1} there are changes in the distribution, with a decrease in the occurrence of

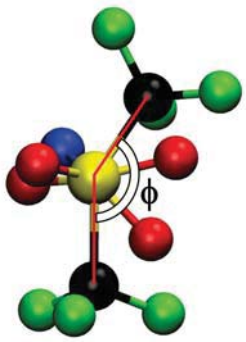

Figure 7.64: *The C-S-S-C dihedral, which can be used to distinguish the cis and trans isomers of [NTf_2].*

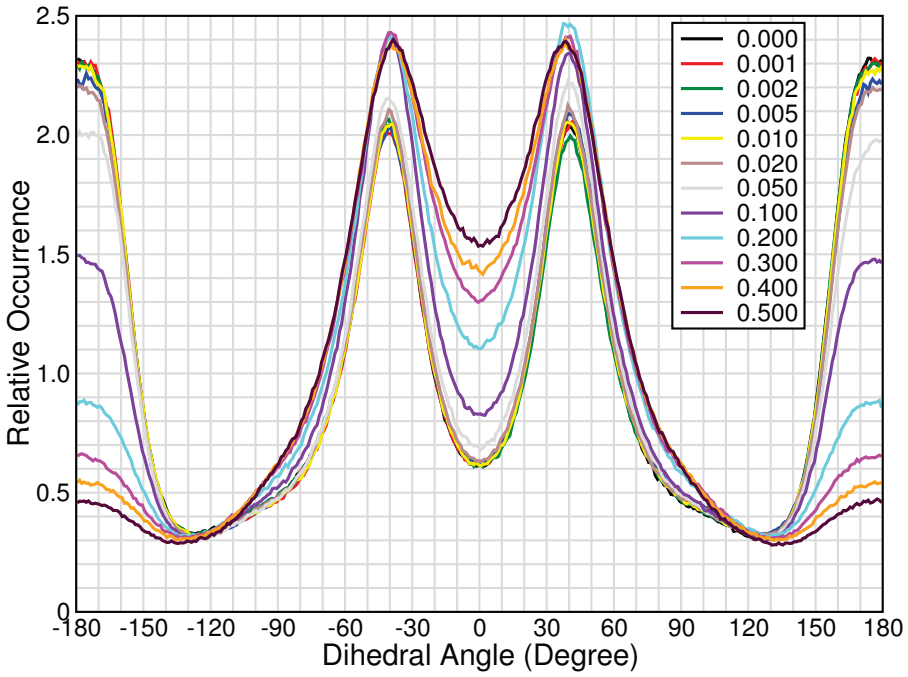

Figure 7.65: *Distribution of the C-S-S-C dihedral in different electric fields in [C_4C_1im][NTf_2]. Electric fields are in the legend in VÅ^{-1}.*

dihedral angles representing the *trans* isomer, and an increase in the occurrence of dihedral angles representing the *cis* isomer. This is showing that in electric fields greater than 0.02 VÅ^{-1} there is a preference for the anion to be in the *cis* isomer.

For [NTf_2] in [C_8C_1im][NTf_2] there is a remarkably similar trend to [NTf_2] in [C_4C_1im][NTf_2]. The distribution remains the same in electric fields $\leq$0.02 VÅ^{-1}, and above this the distribution shows that there is a preference for the *cis* isomer.

To analyse this more, the *cis*/*trans* isomer ratio can be found from each dihedral distribution by integration of the dihedral. Using the range -125° - 125° as representing the *cis* isomer, the percentage of *cis* isomer is shown in Table 7.19.

This shows a remarkable agreement between the anions across the two ionic liquids. In electric fields of $\leq$0.01 VÅ^{-1} there is $\approx$ 63% *cis* isomer across both ionic liquids. There is an exception

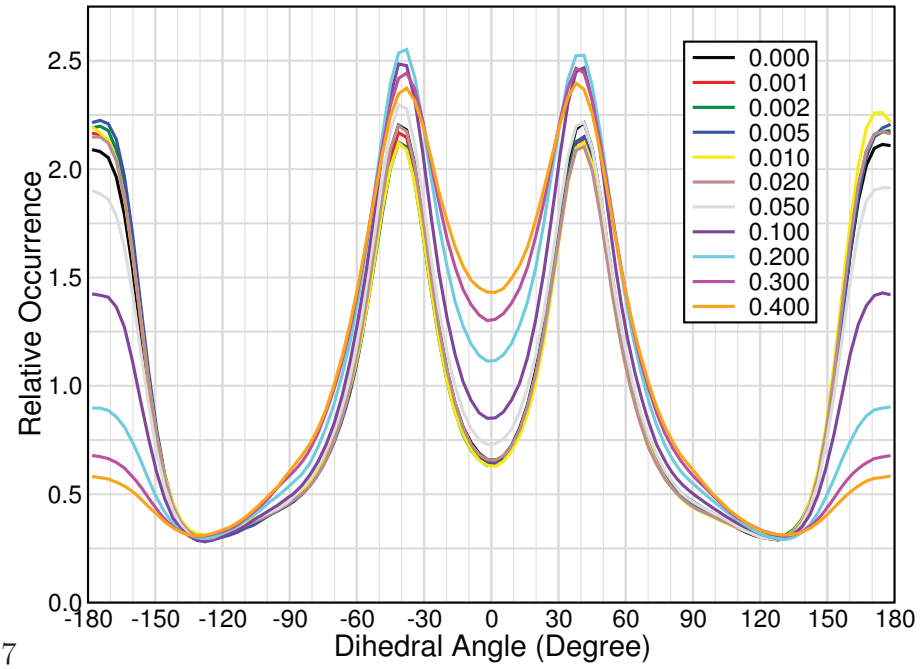

7

Figure 7.66: *Distribution of the C-S-S-C dihedral in different electric fields in $[C_8C_1im][NTf_2]$. Electric fields are in the legend in VÅ^{-1}.*

for the simulation of $[C_8C_1im][NTf_2]$ in zero electric field, which appears to have an anomalously large amount of *cis* isomer.

At 0.02 VÅ^{-1} there is a slight increase of $\approx 1\%$ in the amount of *cis* isomer that is not obvious in the distribution, suggesting that this electric field may have some influence on the *cis*/*trans* ratio.

In electric fields of $\geq$0.05 VÅ^{-1} there are further increases in the amount of *cis* isomer in both ionic liquids. Across the ionic liquids, the amount of *cis* isomer remains within 0.5% of each other. This suggests that the cause of the isomerisation into the *cis* isomer is related to an inherent property of the anion interacting with the electric field, and not to the cation, or any other bulk property, such as viscosity or density.

Cation Orientation

Alongside changes to the structure of the ions, there is also the possibility of the orientation of the ions changing in electric fields. For the cation, the orientation can be investigated through the orientation of the imidazolium ring. This was performed looking at the vector originating at the nitrogen attached to the long alkyl chain, and ending at the nitrogen attached to the methyl group (see Figure 7.67).

The imidazolium ring was found to remain the same, even with changes in the alkyl chain, therefore the angular distribution can be used to provide information into the orientation of

Table 7.19: *Percentage of $[NTf_2]^-$ in the cis isomer in $[C_4C_1im][NTf_2]$ and $[C_8C_1im][NTf_2]$ in various electric fields strengths. A cis anion is defined as having a dihedral angle between -125° and 125° in Figures 7.65 and 7.66.*

Electric Field Strength	% *cis* isomer	
[VÅ^{-1}]	[C_4C_1im][NTf_2]	[C_8C_1im][NTf_2]
0.000	62.9	65.5
0.001	63.0	63.4
0.002	63.0	63.1
0.005	63.5	63.9
0.010	63.2	63.5
0.020	64.5	64.3
0.050	67.7	68.0
0.100	73.9	74.4
0.200	82.1	82.4
0.300	85.6	85.4
0.400	87.3	86.7
0.500	88.8	-

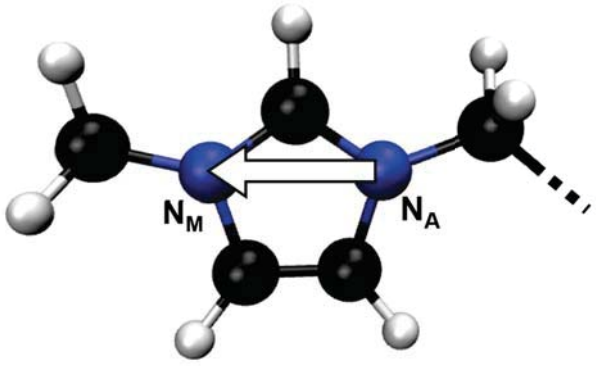

Figure 7.67: *Diagram showing the vector from the nitrogen attached to the long alkyl chain (N_A) and the nitrogen attached to the methyl group (N_M).*

the imidazolium ring. For [C_4C_1im][NTf_2] the angular distribution is shown in Figure 7.68, and for [C_8C_1im][NTf_2] in Figure 7.70.

In [C_4C_1im][NTf_2], there is an approximately even distribution (i.e. random orientation) of this angle in electric fields of ≤ 0.005 VÅ^{-1}.

At 0.01 VÅ^{-1} there is a slight increase in the number of these vectors aligning with this direction i.e. pointing so the vector is in the positive z direction. This is easier to see in Figure 7.69, which shows the cumulative integral of the distribution, expressed as a percentage.

This shows more clearly that the alignmentof the vector with the electric field does start to occur at 0.01 VÅ^{-1}, with a slightly higher amount of vectors with an angle of <90°. The alignment increases further in higher electric fields, with more of this vector pointing in the positive z direction, and less in the negative z direction in higher electric fields.

In [C_8C_1im][NTf_2], the trend is very similar (Figure 7.70). Low electric fields have random

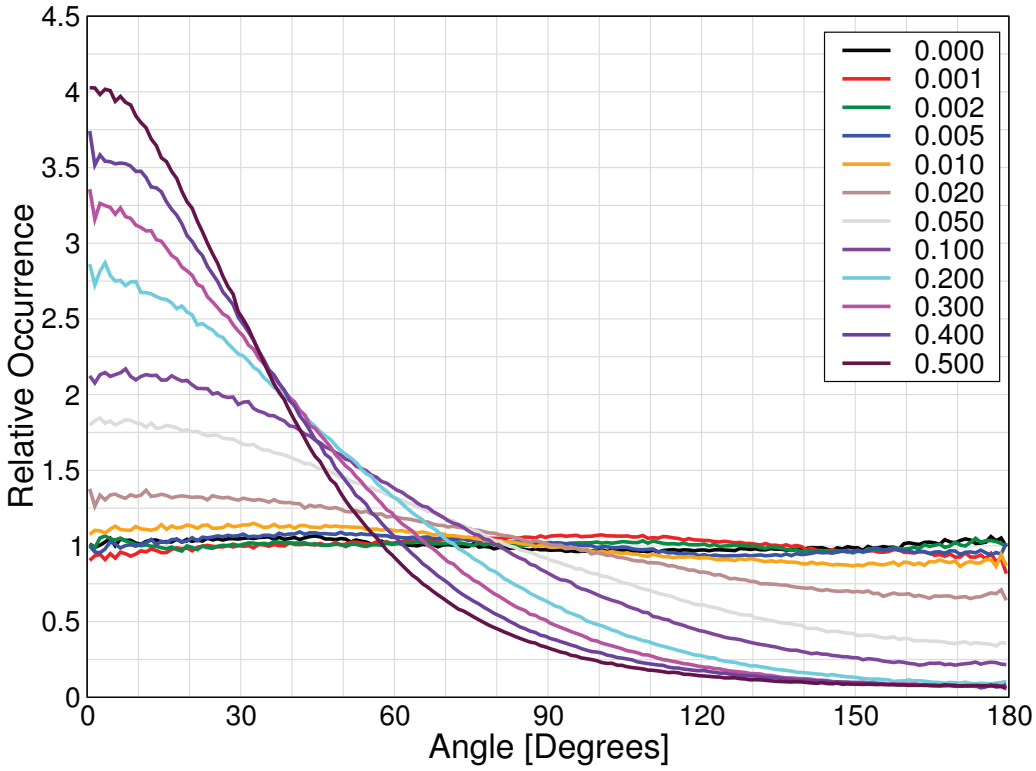

Figure 7.68: *Normalised angular distribution of the $N_A \rightarrow N_M$ vector to the z vector of the simulation box in various electric fields in [C_4C_1im][NTf_2]. Electric fields are in the legend in VÅ^{-1}.*

orienations. There is some slight orientation in 0.01 VÅ^{-1} which is more obvious in the integral (Figure 7.71), and the orientation increases as the electric field does.

When comparing the two cations at the same electric field, it can be seen that this vector in [C_8C_1im][NTf_2] aligns more with the electric field than the same vector in [C_4C_1im][NTf_2]. This is unexpected as the forces on the ions from the electric fields will be the same. There must be some property of the cation/ionic liquid, other than the charge, that leads to this difference.

For both cations, the change in orientation has a tendency towards 0°. As the cation has been established to diffuse in the positive z direction, then the cation diffuses with the methyl group leading the cation, followed by the imidazolium ring, and then the alkyl chain.

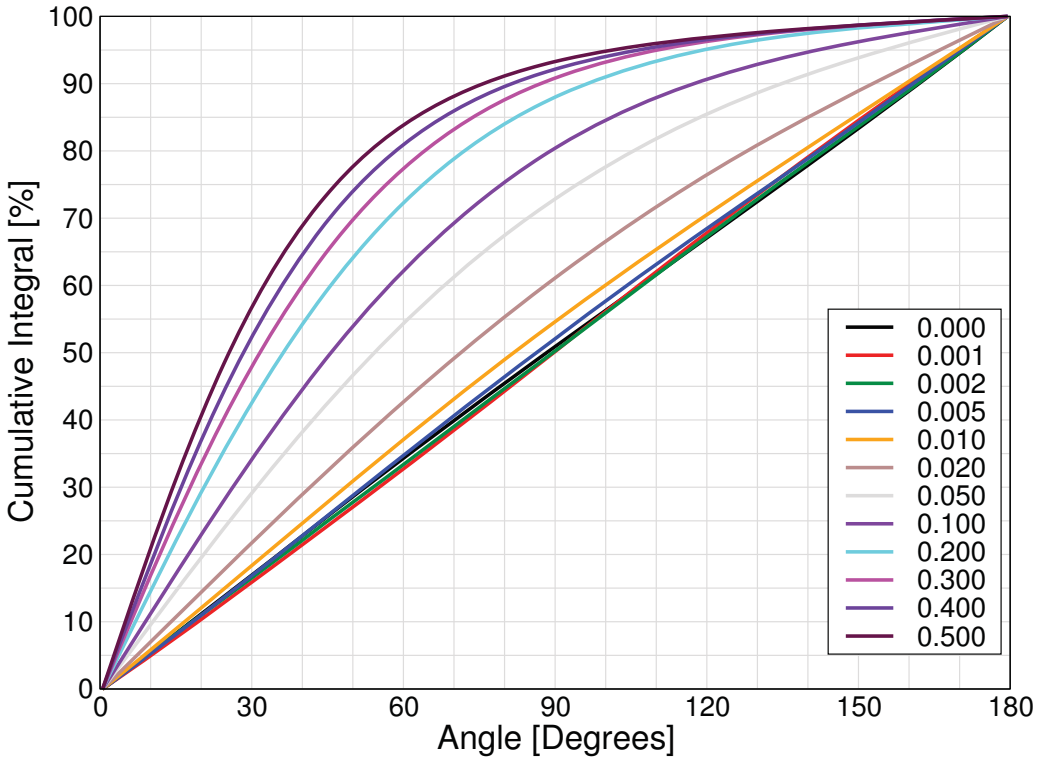

Figure 7.69: *Normalised integral of the angular distribution of the $N_A \rightarrow N_M$ vector to the z vector of the simulation box in various electric fields in $[C_4C_1im][NTf_2]$. Electric fields are in the legend in $V\text{Å}^{-1}$.*

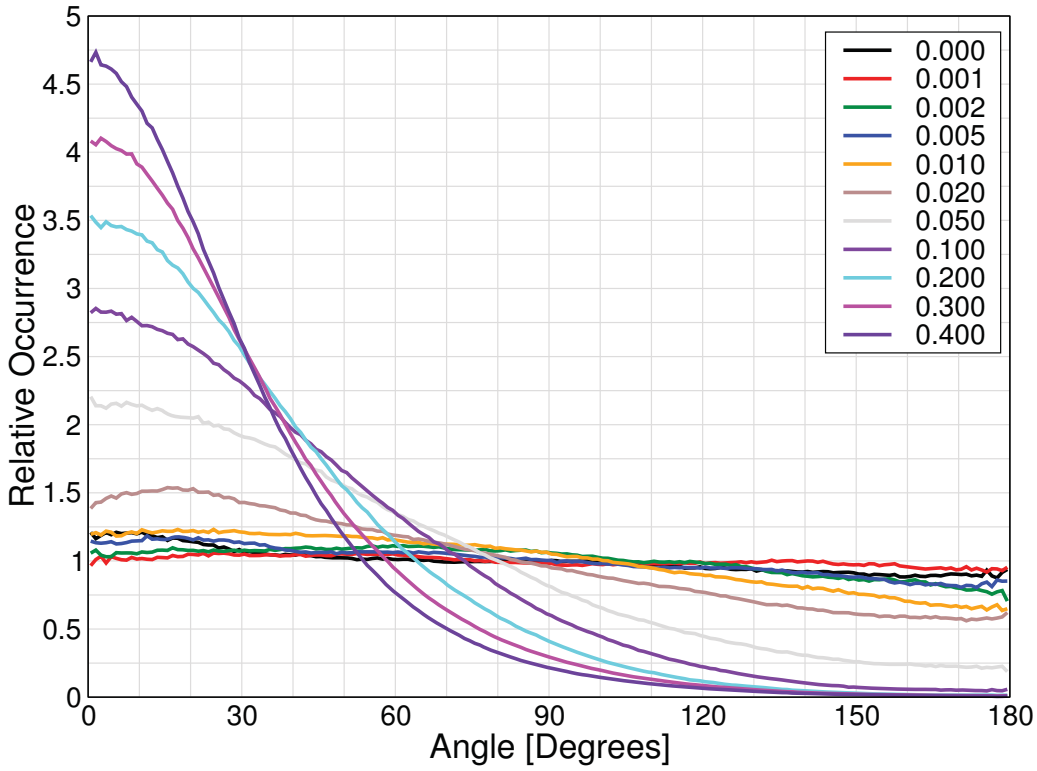

Figure 7.70: *Normalised angular distribution of the $N_A \rightarrow N_{Me}$ vector to the z vector of the simulation box in various electric fields in $[C_8C_1im][NTf_2]$. Electric fields are in the legend in $V\text{Å}^{-1}$*

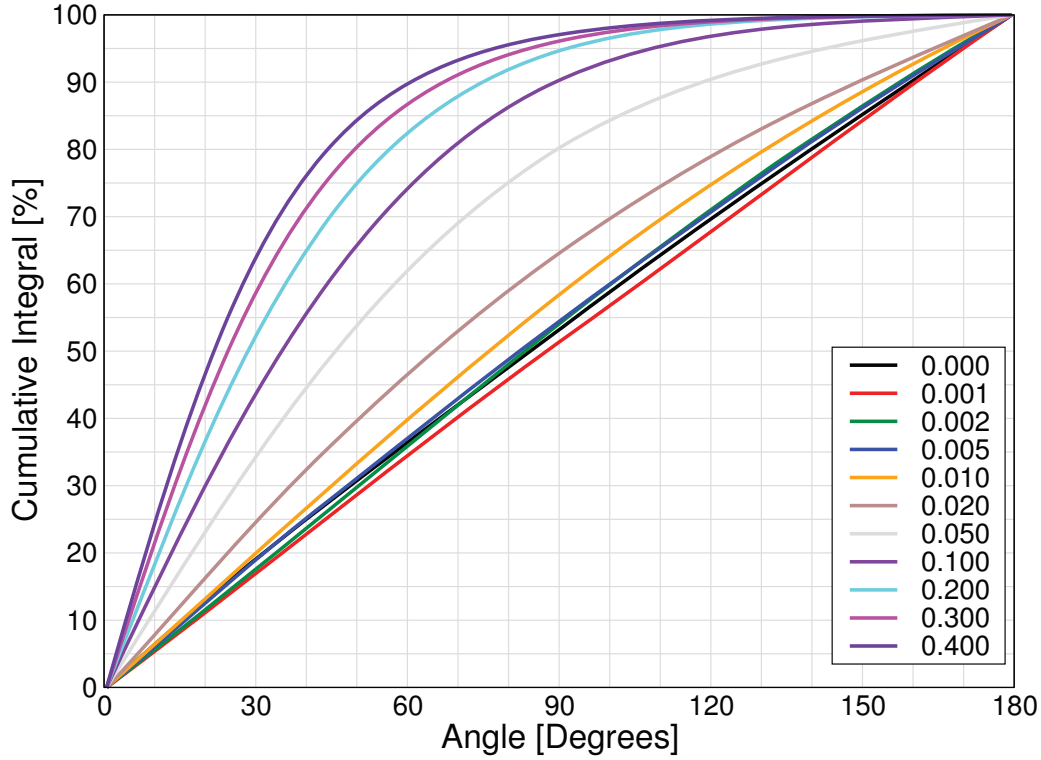

Figure 7.71: *Normalised integral of the angular distribution of the* $N_A \rightarrow N_M$ *vector to the z vector of the simulation box in various electric fields in* $[C_8C_1im][NTf_2]$. *Electric fields are in the legend in* $V\text{Å}^{-1}$.

Anion Orientation

For the anion, there is difficulty defining a vector to investigate the orientation, due to the large differences between the *cis* and *trans* isomers. Several vectors were tested on their suitability for monitoring anion orientation, and it was found that the best vector originated from the geometrical centre of the sulfur atoms and ended on the nitrogen atom (Figure 7.72).

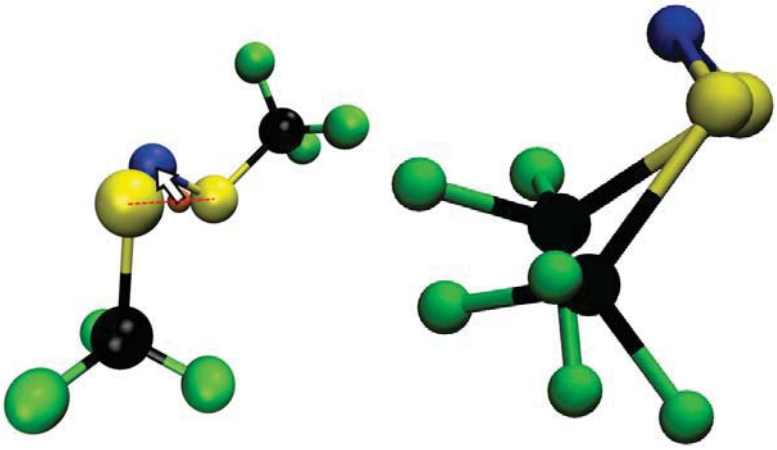

Figure 7.72: *Diagram showing the vector from the geometrical centre of the sulfur atoms to the nitrogen atom. Oxygen atoms excluded for clarity.*

It should be noted there is a slight change in the relative positions of the sulfur atoms with the *cis/trans* isomerisation. Nevertheless, the orientation of this vector in $[C_4C_1im][NTf_2]$ and $[C_8C_1im][NTf_2]$ in different electric fields is shown in Figures 7.73 and 7.74 respectively.
Even with the limitation of the vector not being perfect, an orientation can be seen to occur as the electric field increases. In both ionic liquids there is an increase in the number of anions having this vector at 60-90°. This is the angle at which the nitrogen atom sticks out of the C-S-S-C plane in the *cis* isomer, as on the right in Figure 7.72. Observation of the whole trajectory confirms this, meaning that the increase of anions with the observed vector at this angle suggests the C-S-S-C plane is now orienting itself in a more planar angle to the z vector. As it has already been established that the anion diffuses in the negative z direction, it can be deduced that the C-S-S-C plane is orientated approximately parallel to the z vector of the simulation box. The CF_3 groups are pointing in the positive z direction, while the anion is diffusing in the negative z direction with the sulfur and nitrogen atoms leading the anion.

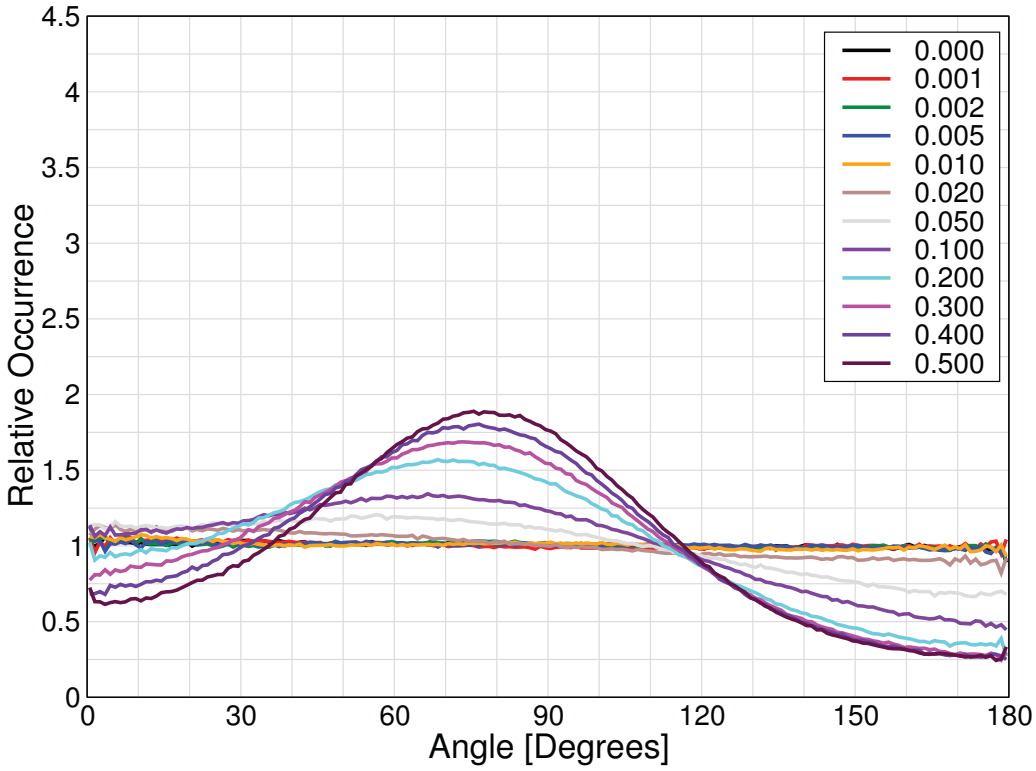

Figure 7.73: *Normalised angular distribution of the sulfur centre to nitrogen vector to the z vector of the simulation box in various electric fields in $[C_4C_1im][NTf_2]$. Electric fields are in the legend in $VÅ^{-1}$.*

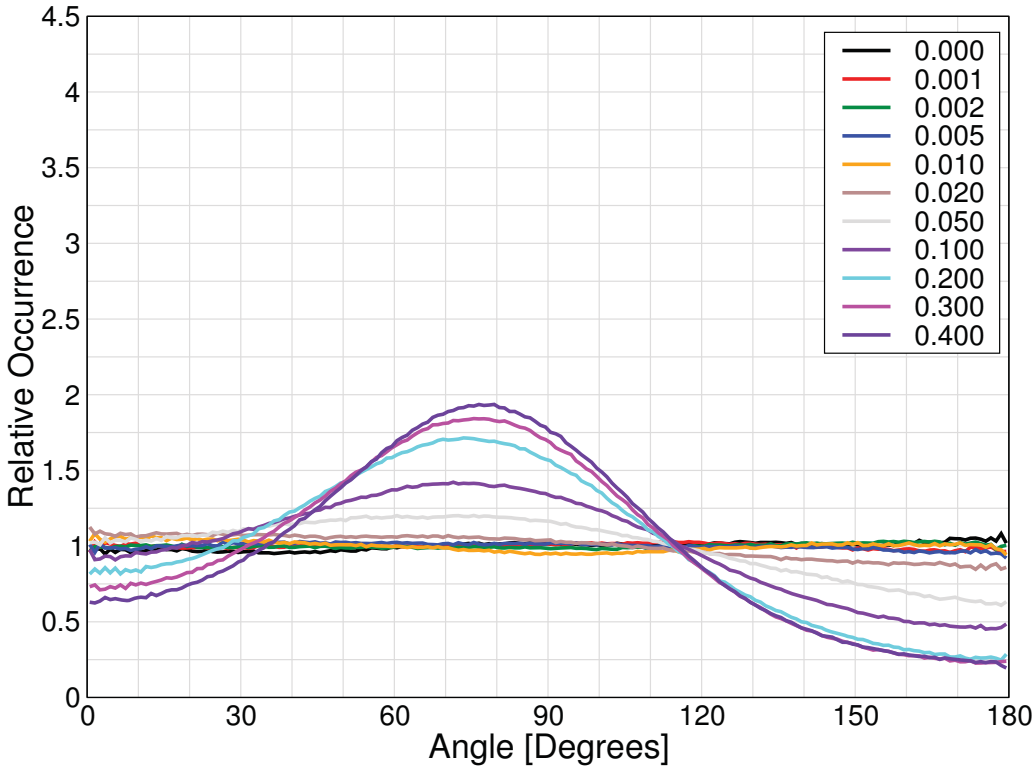

Figure 7.74: *Normalised angular distribution of the sulfur centre to nitrogen vector to the z vector of the simulation box in various electric fields in $[C_8C_1im][NTf_2]$. Electric fields are in the legend in $VÅ^{-1}$.*

Chapter 8

Charge Arms in Ionic Liquids

When considering the results in Chapter 7, there are some interesting phenomena seen in high electric fields that do not fit simple explanations e.g. a preference for the *cis* isomer of the $[NTf_2]^-$ anion.

In classic molecular solvents, results such as this would be discussed with respect to a dipole i.e. the slightly more negative and slightly more positive parts of the molecule that can be affected and moved with an electric field. Strictly speaking, a dipole is a property of a neutral molecule, defined as the separation of two charges of $+q$ and $-q$.[47] However, dipoles are poorly defined for ions. Instead of being a consistent vector, the dipole moment changes depending upon the position at which it is measured. A full derivation of this is included in Appendix D. In lieu of a dipole, Kobrak and Sandalow proposed a new quantity, the "charge arm".[225] This vector is defined using two centres of the ion, with one being the centre of charge, $\overrightarrow{R_{\mathrm{cq}}}$ (the geometrical centre of all of the atoms in the ion, weighted according to their charges) mathematically defined as

$$\overrightarrow{R_{\mathrm{cq}}} = \sum_{i=1}^{N} \frac{q_i \overrightarrow{r_i}}{q_{\mathrm{total}}} \tag{8.1}$$

where N is the number of atoms, q_i the atomic charges, $\overrightarrow{r_i}$ the position of the atoms, and q_{total} the total charge on the ion.

The other centre is the centre of mass, $\overrightarrow{R_{\mathrm{cm}}}$ (the geometrical centre of all of the atoms in the ion, weighted according to their charges), mathematically defined as

$$\overrightarrow{R_{\mathrm{cm}}} = \sum_{i=1}^{N} \frac{m_i \overrightarrow{r_i}}{M_{\mathrm{total}}} \tag{8.2}$$

where m_i is the atomic mass, and M_{total} the total mass of the ion.

The charge arm is defined as beginning at the centre of mass, and ending at the centre of charge, as represented in Figure 8.1.

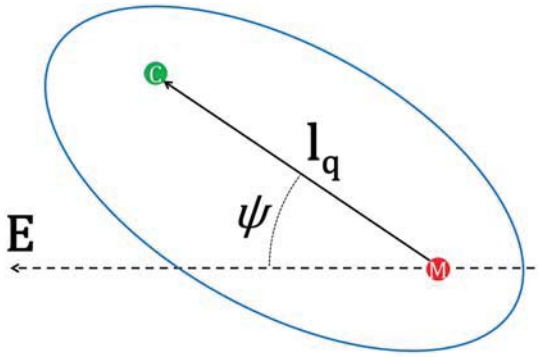

Figure 8.1: *Schematic for the charge arm (l_q) in a non-symmetric ion, represented by the blue oval. The red centre labelled 'M' is the centre of mass and the green centre labelled 'C' is the centre of charge. E is representative of an electric field line, and ψ is the angle between the charge arm and field line.*

It is important to note that the charge arm is not the same as a dipole, as it cannot describe dielectric constants. However it is a property of an ion, and it should be relevant to the orientation and the dynamics of the ions. This is especially true in the presence of an electric field,[225] hence the interest in this work.

There was an idea that an electric field should produce a torque upon the charge arm, which was introduced by Kobrak and Sandalow.[225] If an electric field of strength E is applied to an ion at an angle ψ relative to the charge arm of length l_q, there should be a torque upon the ion of

$$T = E \cdot l_q \cdot Q_{\text{total}} \cdot sin\,(\psi) \tag{8.3}$$

This torque applied along the charge arm suggests that an alignment of the charge arms of the ions along the electric field lines should occur. This is because the torque pulls the charge arm vector into alignment with the electric field lines, and will increase in force the more 'mis-aligned' the charge arm is with respect to the field lines.

Due to the direct dependence of this torque upon the electric field strength, this distribution of charge arms should shift towards a greater alignment at higher electric field strengths. Alongside this, there is also a direct dependence of the torque force on the charge arm length. Therefore, the torque will be greater, and thus the alignment with the electric field lines should be greater, with a longer charge arm.

There will also be another component of the force, perpendicular to the torque, which pulls the

charge arm along the electric field line, and this will be equal to

$$F_{\perp T} = E \cdot l_q \cdot Q_{\text{total}} \cdot cos\,(\psi) \tag{8.4}$$

This force will cause a stretching of the charge arms into longer lengths, and will also dictate the direction in which the charge arms are pulled. As with T, $F_{\perp T}$ is dependent upon the electric field field strength, so the charge arms should be stretched more in higher electric fields. As $F_{\perp T}$ is dependent upon the charge arm length, so longer charge arms should be stretched more. One factor not considered by Kobrak and Sandalow was that the charge arm of the ions can change with changes to the conformation of the ions. The reason many ionic liquids are liquid at room temperature is due to the flexibility of their constituent ions. This flexibility, especially for an ion such as $[NTf_2]^-$ that changes drastically upon conformational changes, can lead to very different lengths of charge arms. Therefore, it could be predicted that ions will change their conformation, if possible, in an electric field due to the torque force.
As far as I am aware, no work has gone into a mathematically rigorous explanation of the charge arm. The hope is that the results presented herein can inspire such work to take place.

8.1 Charge Arms of Ions in the Absence of an Electric Field

First, the charge arms of the ions in the ionic liquids will be established in the absence of an electric field, before the charge arms are analysed in an electric field.
As the anion is consistent between both ionic liquids studied here, it will be considered in both liquids together.
As is already established, the anion has two conformers: a *cis* isomer and a *trans* isomer.
The *cis* isomer, shown in Figure 8.2, has a centre of charge (purple sphere) near to the nitrogen atom, offset slightly towards the oxygen atoms. The centre of mass (orange sphere) is positioned towards the centre of the square defined by the carbon and sulfur atoms. The charge arm of the *cis* isomer of the anion is relatively long, and stretches towards the nitrogen atom.
The *trans* isomer, shown in Figure 8.3, has a centre of charge (purple sphere) near the nitrogen atom, similar to the *cis* isomer. This shows that the charge in the $[NTf_2]^-$ anion is concentrated around the $SO_2{-}N{-}SO_2$ region in the anion, as movement of the CF_3 groups does not affect the centre of charge.

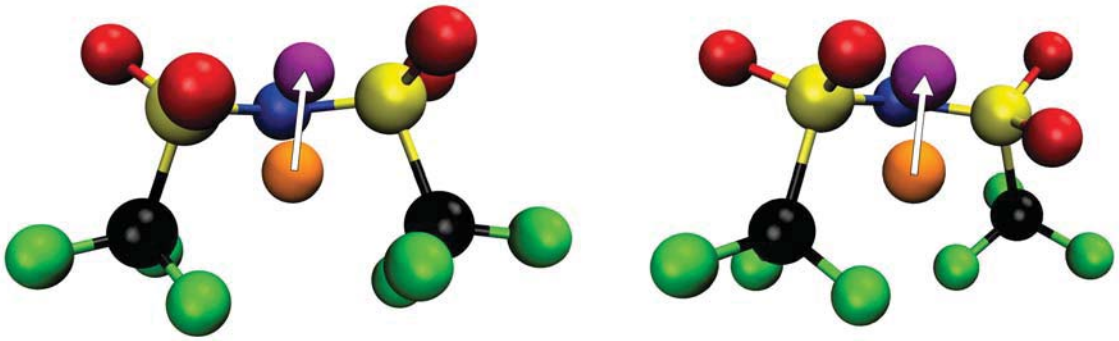

Figure 8.2: *Anion centre of charge (purple sphere) and centre of mass (orange sphere) in the cis isomer. Left shows an example in $[C_4C_1im][NTf_2]$, right is an example in $[C_8C_1im][NTf_2]$. White arrow with black outline denotes the charge arm.*

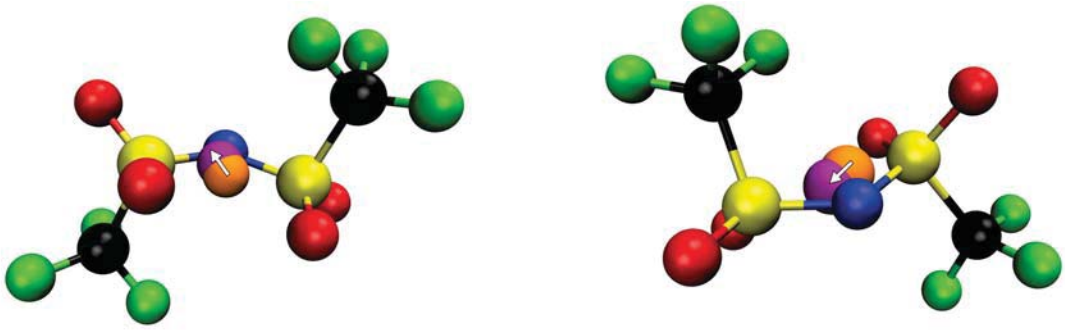

Figure 8.3: *Anion centre of charge (purple sphere) and centre of mass (orange sphere) in the trans isomer. Left shows an example in $[C_4C_1im][NTf_2]$, right is an example in $[C_8C_1im][NTf_2]$. White arrow with black outline denotes the charge arm.*

However the *trans* isomer has a centre of mass (orange sphere) in an almost coincident position to the centre of charge. This is because rotation of one of the $S-CF_3$ groups brings the centre of mass closer to the nitrogen atom. The result of this is that the charge arm in the *trans* isomer being very short.

This difference between the conformers can be seen in the distribution of the lengths of the charge arm in $[NTf_2]^-$, shown in Figure 8.4. This clearly shows two peaks with a distinct minimum between them, one shorter length peak at approximately 30 pm corresponding to the *trans* isomer, and another peak at approximately 125 pm corresponding to the *cis* isomer.

By integration of the areas underneath the normalised histograms, the percentage of the anion in each conformer can be found. Using the minimum at 73 pm as the cutoff and integrating above this, 62.0% of the anions in $[C_4C_1im][NTf_2]$ are in the *cis* isomer, with 65.3% of the anions in the *cis* isomer in $[C_8C_1im][NTf_2]$.

Despite the mismatch, as is discussed later when looking at the electric field data, the anion in $[C_8C_1im][NTf_2]$ seems to have a slightly inflated amount of the *cis* isomer, as other simulations of $[C_8C_1im][NTf_2]$ show a much closer match to $[C_4C_1im][NTf_2]$. The cause of this is unknown. What this does show though is that the charge arms are easily distinguishable in a plot of this

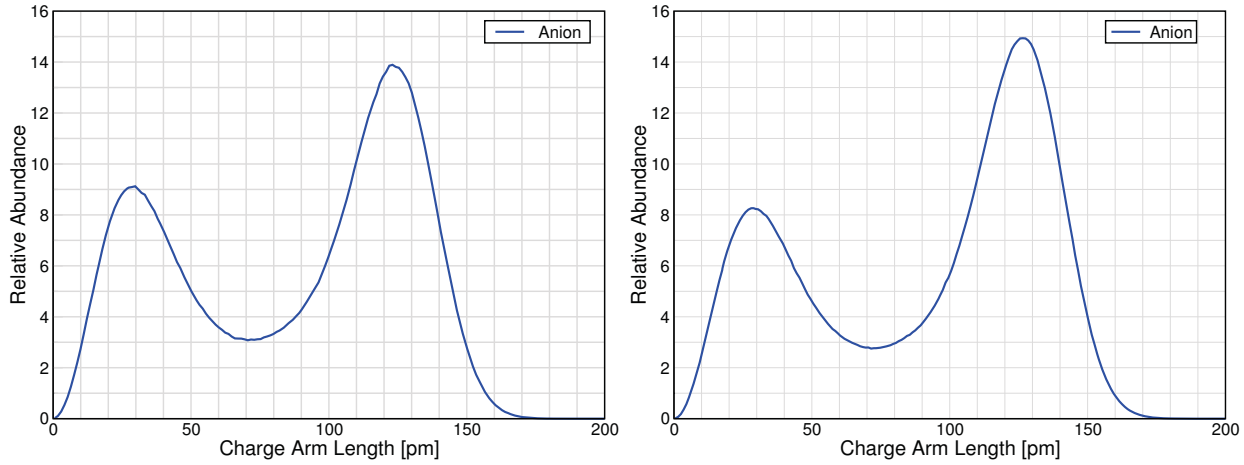

Figure 8.4: *Distribution of lengths of the anion charge arm in the simulations with no electric fields. Left shows the distribution in $[C_4C_1im][NTf_2]$, right shows the distribution in $[C_8C_1im][NTf_2]$.*

kind, and from this plot the ratio of *cis* to *trans* isomers can be found, as was in Section 7.5.3 from the dihedrals.

The cations are different to the anions in that there are not distinct different conformers. Instead the cations have an flexible alkyl chain which can curl up or stretch out to change the conformation. Two conformations of $[C_4C_1im]^+$ are shown in Figure 8.5 with their charge arms highlighted.

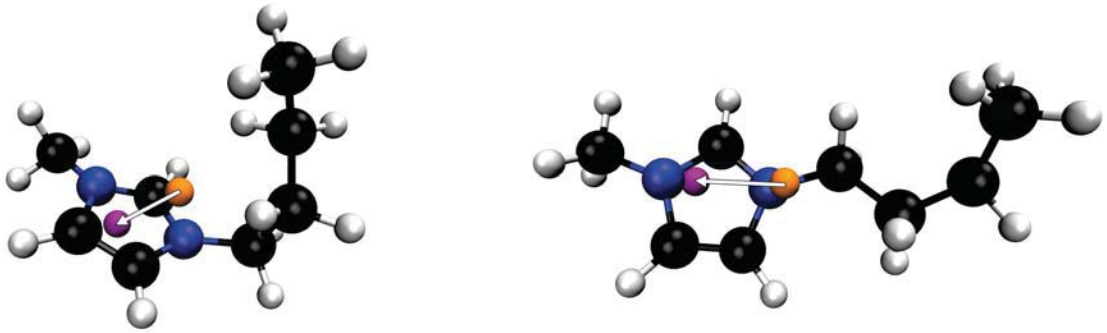

Figure 8.5: *Centre of charge (purple sphere) and centre of mass (orange sphere) in the $[C_4C_1im]^+$ in different conformations. White arrow with black outline denotes the charge arm.*

As the butyl chain is relatively short, there are few conformations it can take. However, even with this limited motion there are significantly different charge arms as the butyl chain flexes. With the butyl chain in a stretched conformer, the centre of mass is almost coincident to the nitrogen attached to the butyl chain, while the centre of charge resides slightly closer to the centre of the ring, and near the nitrogen attached to the methyl group. Both of these centres lie approximately in the plane of the imidazolium ring.

As the butyl chain flexes, the center of charge stays in approximately the same position relative to the nitrogen atom in the imidaozlium ring, but moves slightly above or below the plane of

the ring in the opposite direction to the butyl chain i.e. if the chain bends above the ring, the centre of charge shifts below.

The centre of mass is more mobile with changes to the butyl chain conformation. As the chain flexes, the centre of mass moves with the chain in the same direction the chain is flexing i.e. if the butyl chain bends upwards, curling towards the middle of the imidazolium ring, the centre of mass also shifts significantly up and towards the middle of the imidazolium ring.

Due to the shape of the cation, curling of the butyl chain always involves motion towards the imidazolium ring. Therefore, the longest charge arm occurs when the butyl chain is fully stretched out (similar to the right hand side of Figure 8.5), with shorter charge arms corresponding to increasingly bent butyl chains.

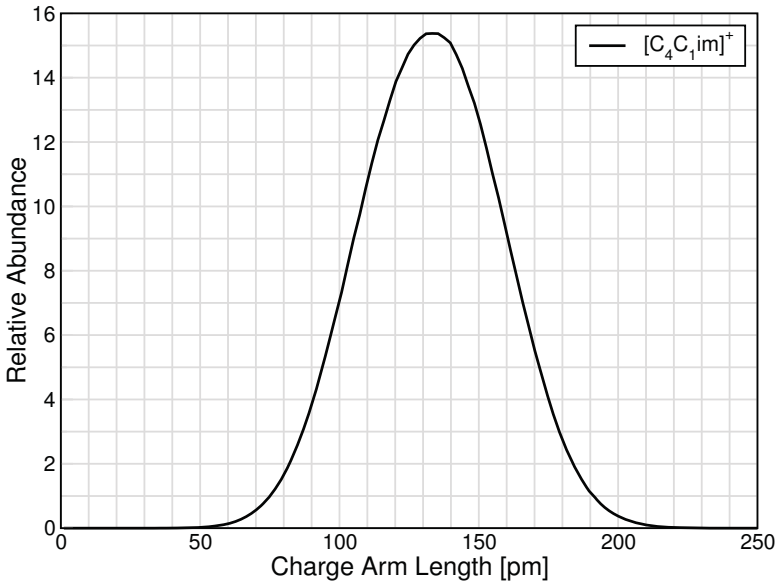

Figure 8.6: *Distribution of lengths of the charge arm of $[C_4C_1im]^+$ in $[C_4C_1im][NTf_2]$ with no electric fields.*

The distribution of charge arm lengths in Figure 8.6 shows the stretching and bending of the butyl chain as a smooth distribution with charge arm lengths for $[C_4C_1im]^+$ ranging from ≈ 50 pm to ≈ 220 pm, with a peak in the distribution at 135 pm.

This shows that for $[C_4C_1im]^+$ there is no preference for one conformation/orientation of the alkyl chain over another, and there is a smooth distribution over all possible lengths. This is opposite to $[NTf_2]^-$ which has distinct conformers present in its distribution of charge arms.

$[C_8C_1im]^+$ is similar to $[C_4C_1im]^+$, however this has a much longer alkyl chain attached to the imidazolium ring, leading to many more possible conformations for this alkyl chain, a selection of which are shown in Figure 8.7.

Similar to $[C_4C_1im]^+$ the centre of charge in $[C_8C_1im]^+$ is around the nitrogen attached to the methyl group when the alkyl chain is fully extended. However, the centre of charge moves more

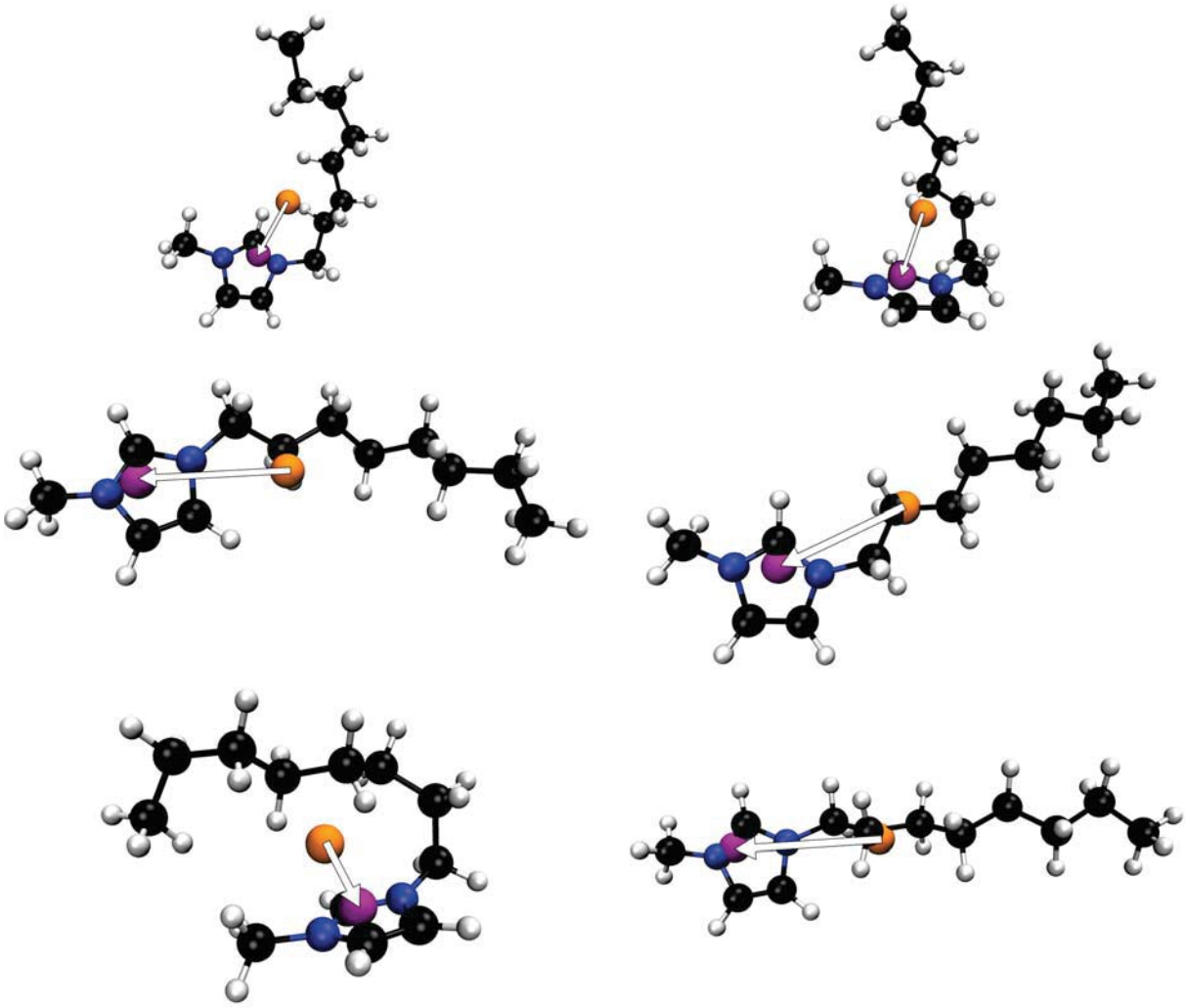

Figure 8.7: *Centre of charge (purple sphere) and centre of mass (orange sphere) in the $[C_8C_1im]^+$ in various different conformations. White arrow with black outline denotes the charge arm.*

in $[C_8C_1im]^+$ with flexing of the octyl chain. With the different conformations of the octyl chain, the centre of charge can be found anywhere in a region approximately lying between the nitrogen adjacent to the methyl group and the C2 carbon atom.

The larger change in $[C_8C_1im]^+$ is in the centre of mass. In the fully stretched conformation the centre of mass resides around the second carbon atom on the octyl chain. Similarly to $[C_4C_1im]^+$, as the octyl chain curls up, the centre of mass moves towards the middle of the imidazolium ring, towards the centre of charge with the centre of mass moving in the same direction the alkyl chain is flexing. Due to the octyl chain having more curled conformations that it can take (i.e. the number of dihedrals around which the chain can rotate is higher), there is greater variation of the position of the centre of mass.

What is seen exclusively in $[C_8C_1im]^+$, that is not in $[C_4C_1im]^+$, is the existence of conformations where the alkyl chain has bent towards the C2 or C4/5 positions on the imidazolium ring, like those in the top left of Figure 8.7. In these conformations, the centre of charge remains in

the same approximate position near the C2 carbon/nitrogen near the methyl group, and the centre of mass moves around the imidazolium ring with the octyl chain.

Another conformation seen in $[C_8C_1im]^+$ is a 'scorpion' configuration, where the alkyl chain has fully curled back so that the terminal CH_3 on the alkyl chain is near the methyl group,[25] as shown in the bottom left conformation in Figure 8.7. In this conformation the centre of mass lies above the imidazolium ring on the same side the chain has folded over.

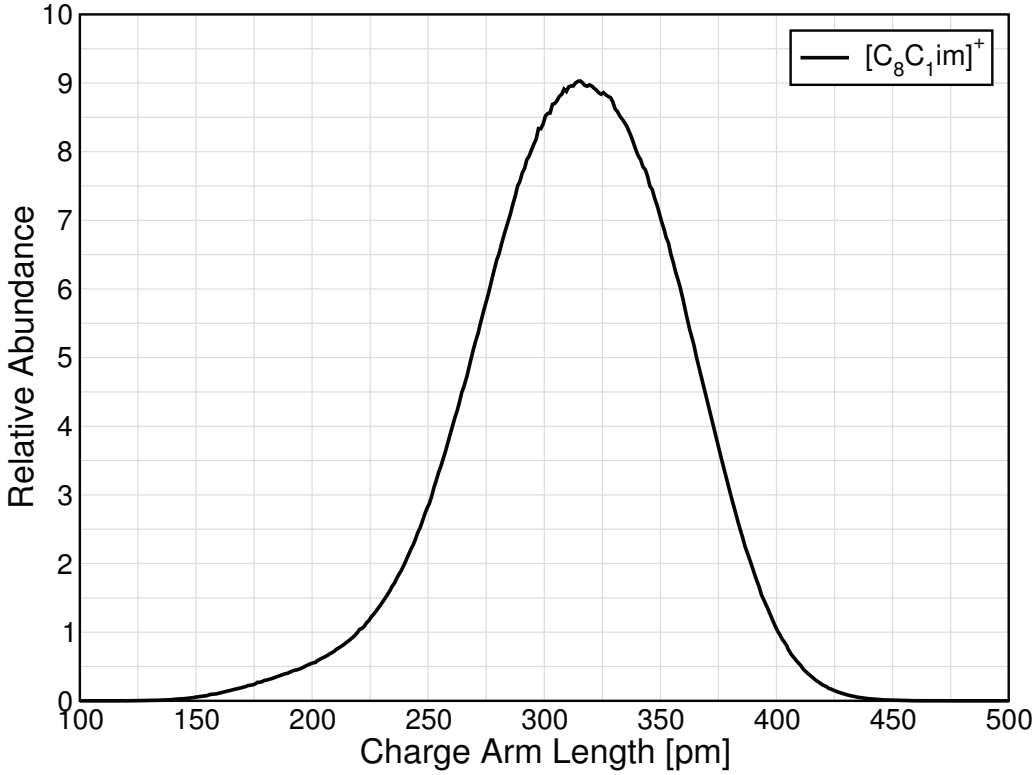

Figure 8.8: *Distribution of lengths of the charge arm of $[C_8C_1im]^+$ in $[C_8C_1im][NTf_2]$ with no electric fields.*

The distribution of charge arm lengths for $[C_8C_1im]^+$ (Figure 8.8) is a smooth distribution with a peak at 315 pm. As with $[C_4C_1im]^+$ there is no preference for any conformation and the distribution is relatively uniform. The distribution for $[C_8C_1im]^+$ has a slight tail on the lower length side of the distribution from 150 pm-225 pm. This is likely due to charge arms from the scorpion conformation, as this brings the centre of mass closer to the centre of charge than the other conformations can.

In summary, the charge arm of the anion reports on the amount of anion in each isomer. While the cation charge arm does not give the same level of detailed information, it does represent the variety of conformations the cations take, from a fully stretched out alkyl chain to a more curled up conformation. Both cations have their longest charge arm when the alkyl chains are fully extended.

8.2 Charge Arms in Ionic Liquids in Electric Fields

Beginning with the lengths of the charge arms, then moving on to the orientation of the charge arms, how an electric field affects the charge arm is investigated here.

8.2.1 Cation Charge Arm Length

The distribution of the lengths of the charge arms of $[C_4C_1im]^+$ in $[C_4C_1im][NTf_2]$ are shown in all electric fields studied in Figure 8.9.

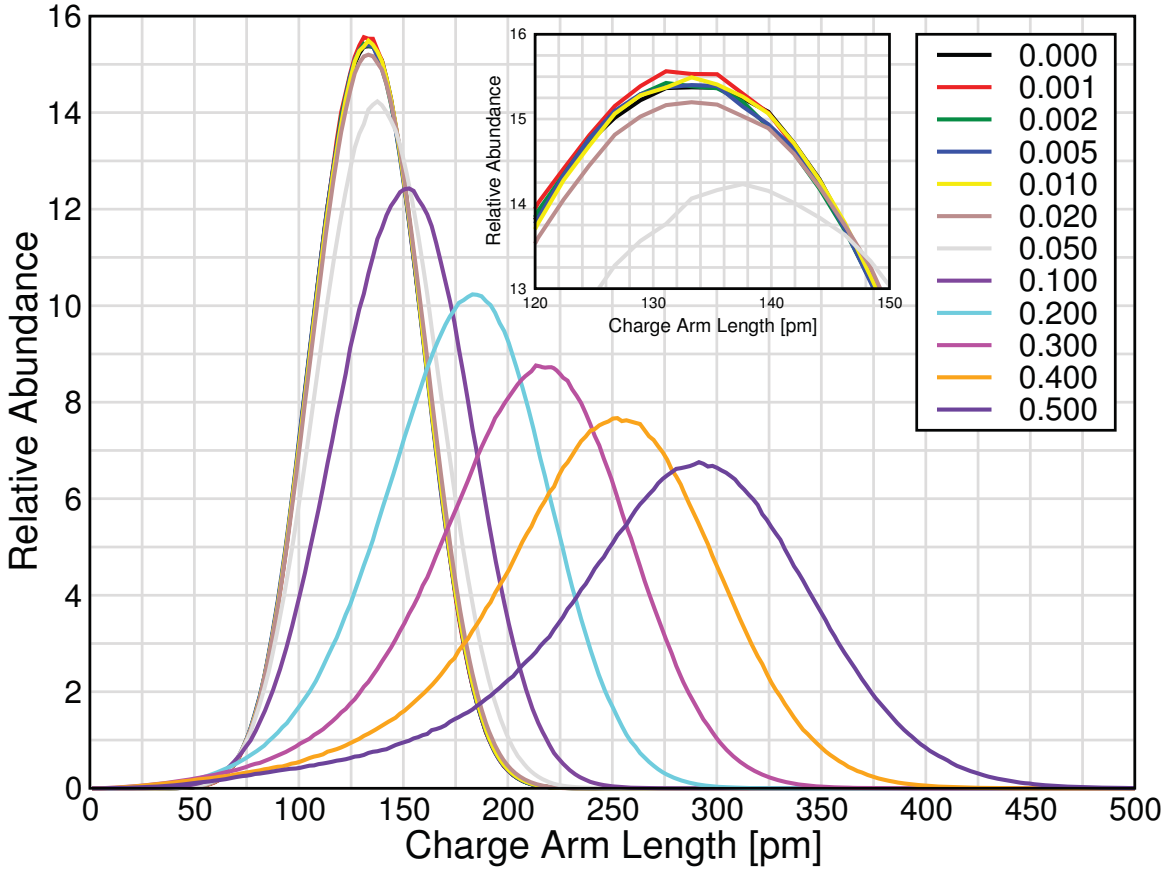

Figure 8.9: *Distribution of lengths of the charge arm of $[C_4C_1im]^+$ in $[C_4C_1im][NTf_2]$ in various electric fields. Electric field strength is shown in the legend in VÅ^{-1}. Inset is a close up of the peak.*

From the inset it can be seen that the distribution of charge arm lengths remains constant in electric fields of up to and including 0.01 VÅ^{-1} and the peak position remains around 135 pm. In an electric field of 0.02 VÅ^{-1} there is a slight shift in the distribution, and while the peak position remains in the same place, the distribution shifts from 50% of the lengths greater than the peak position, to 48% of the lengths greater than the peak position.

In electric fields of 0.05 VÅ^{-1} and above there is a shift in the distribution, with the distribution shifting towards longer charge arms in stronger electric fields. This is seen in the peak position,

which shifts from 135 pm in ≤0.02 VÅ^{-1} to 138 pm in 0.05 VÅ^{-1}, 152 pm in 0.1 VÅ^{-1}, 183 pm in 0.2 VÅ^{-1}, 213 pm in 0.3 VÅ^{-1}, 252 pm in 0.4 VÅ^{-1}, and 291 pm in 0.5 VÅ^{-1}.

In addition to the shift of the peak, the distortion of the distribution persists, with <45% of the cations having a charge arm of length greater than the peak position in electric fields of 0.05 VÅ^{-1} and above. This 'fronting' of the peak shows that while stronger electric fields cause an increase in the charge arm length, there are still some cations with very short charge arms present.

The distribution of the length of the charge arms of $[C_8C_1im]^+$ in $[C_8C_1im][NTf_2]$ are shown in all electric fields studied here in Figure 8.10.

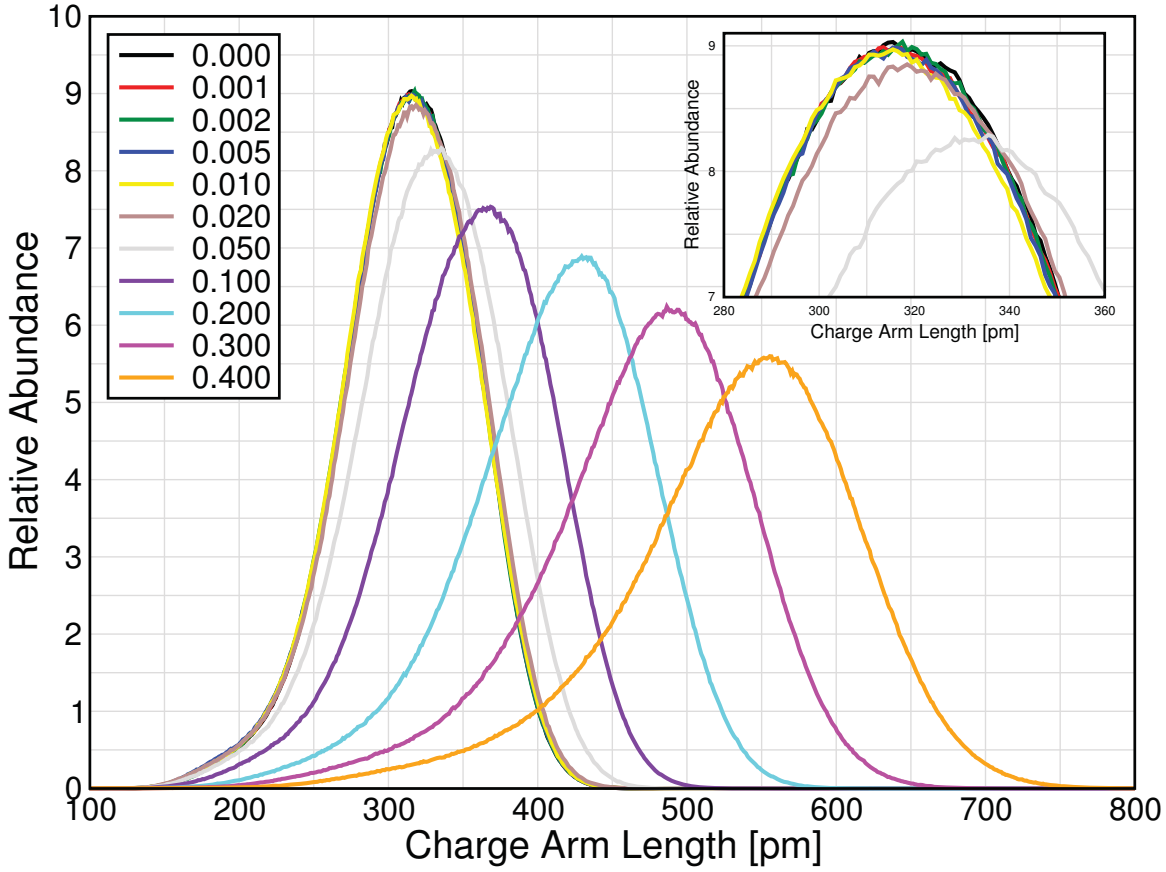

Figure 8.10: *Distribution of lengths of the charge arm of $[C_8C_1im]^+$ in $[C_8C_1im][NTf_2]$ in various electric fields, electric field strength is shown in the legend in VÅ^{-1}. Inset is a close up of the peak.*

The inset in Figure 8.10 shows that there is no change to the distribution of charge arm lengths in electric fields of up to and including 0.01 VÅ^{-1}, similar to what was seen for $[C_4C_1im]^+$. The peak position remains at 315 pm and there is also an approximately even distribution of charge arm lengths, with ≈51% of the cations having charge arms shorter than the peak value.

The shift of the distribution in an electric field of 0.02 VÅ^{-1} is more pronounced in $[C_8C_1im]^+$ than $[C_4C_1im]^+$. In $[C_8C_1im]^+$ there is an increase in the peak position to 319 pm.

Stronger electric fields of ≥0.05 VÅ^{-1} cause larger changes in the distribution, with a shift

towards longer charge arms with increasing electric field strength. The peak position shifts from 315 pm in ≤0.01 VÅ^{-1} to 138 pm in 0.05 VÅ^{-1}, 152 pm in 0.1 VÅ^{-1}, 183 pm in 0.2 VÅ^{-1}, 213 pm in 0.3 VÅ^{-1}, 252 pm in 0.4 VÅ^{-1}, and 291 pm in 0.5 VÅ^{-1}.

There is also a 'fronting' distortion of the distribution, leading to <45% of the cations having a charge arm longer than the peak position in fields of 0.02 VÅ^{-1} and above.

When comparing the distributions of charge arms in $[C_4C_1im]^+$ and $[C_8C_1im]^+$ there are clear similarities in the trends, in that they remain constant up to 0.01 VÅ^{-1}, with a slight shift at 0.02 VÅ^{-1}, and then greater shift with increasing electric field strength above this.

There are however some differences in these. For $[C_8C_1im]^+$ there is a shift in the peak position in an electric field of 0.02 VÅ^{-1} but not for $[C_4C_1im]^+$. This is possibly due to the longer inherent charge arm in $[C_8C_1im]^+$ meaning the same percentage change to the charge arm is smaller. This is backed up by the histogram average data in Table 8.1 which shows a slight increase in the mean length of $[C_4C_1im]^+$ at 0.02 VÅ^{-1}.

Table 8.1: *Mean and standard deviation of the histogram of charge arm lengths $[C_4C_1im]^+$ and $[C_8C_1im]^+$ in $[C_4C_1im][NTf_2]$ and $[C_8C_1im][NTf_2]$.*

Electric Field Strength VÅ^{-1}	$[C_4C_1im]^+$		$[C_8C_1im]^+$	
	Mean [pm]	Std. Dev. [pm]	Mean [pm]	Std. Dev. [pm]
0.000	133.0	24.8	312.6	44.4
0.001	132.9	24.7	312.8	44.3
0.002	132.9	24.9	312.3	44.2
0.005	132.8	24.9	312.2	44.9
0.010	133.0	24.9	312.1	44.8
0.020	133.6	25.2	314.1	45.4
0.050	137.8	27.2	325.9	48.6
0.100	149.0	31.5	354.2	53.9
0.200	176.5	40.4	411.0	62.3
0.300	206.8	49.0	469.9	71.6
0.400	241.0	57.6	533.4	81.0
0.500	277.5	67.0	-	-

The mean length also shows that up to 0.1 VÅ^{-1} the percentage change in the longer charge arm ($[C_8C_1im]^+$) is greater than the percentage change in the shorter charge arm. Above 0.1 VÅ^{-1} though, this reverses and $[C_4C_1im]^+$ has a greater percentage increase in the charge arm length.

If Equation 8.4 was followed, then the force on the charge arm in $[C_8C_1im]^+$ should be ≈ 2.3 times higher than the force on $[C_4C_1im]^+$. Therefore the increase in charge arm in $[C_8C_1im]^+$ should always be greater. Hence, it appears that this model does not fully explain the observed behaviour.

8.2.2 Anion Charge Arm Length

The distribution of charge arm lengths for $[NTf_2]^-$ in $[C_4C_1im][NTf_2]$ is shown in Figure 8.11.

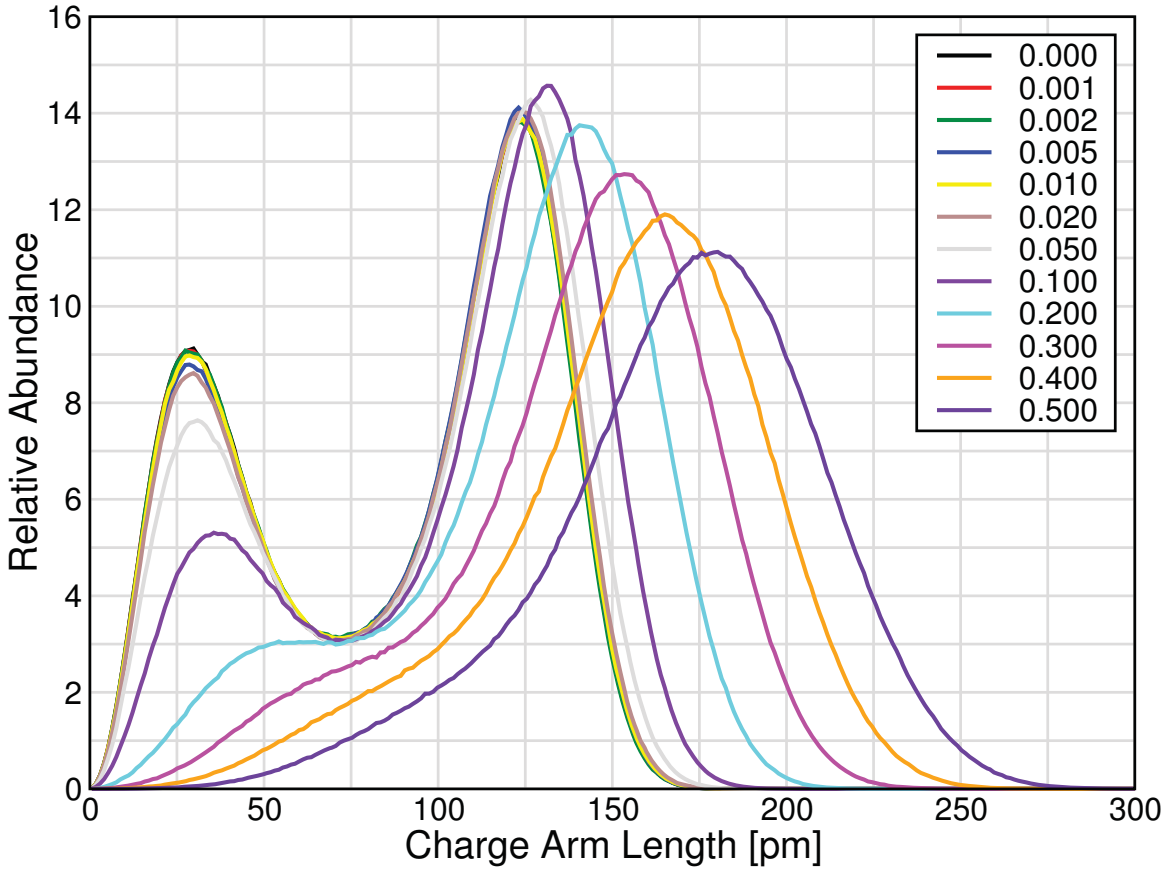

Figure 8.11: *Distribution of lengths of the charge arm of $[NTf_2]^-$ in $[C_4C_1im][NTf_2]$ in various electric fields, electric field strength is shown in the legend in VÅ^{-1}.*

From this there is a clear shift of the distribution of charge arm lengths of $[NTf_2]^-$ to longer lengths as the electric field strength increases. There is a decrease in the peak representative of the *trans* isomer (0-75 pm), and an increase in the amount of anions in the *cis* isomer. The percentage of anions in the *cis* isomer can be calculated by integrating the distribution from the minima, and is shown in Table 8.2.

Table 8.2: *Percentage of $[NTf_2]^-$ in the cis isomer in $[C_4C_1im][NTf_2]$ in various electric fields strengths. A cis anion is defined as having a charge arm longer than 75 pm in the charge arm length distribution (Figure 8.11). This definition of the cis and trans isomers is difficult above 0.2 VÅ^{-1}.*

Electric Field [VÅ^{-1}]	0.000	0.001	0.002	0.005	0.01	0.02	0.05	0.1	0.2	>0.2
percent *cis* isomer	62.7	62.8	62.3	63.1	62.6	64.8	67.2	75.0	86.3	-

This data shows a clear increase in the amount of *cis* isomer present, in agreement with the dihedral measurements in Section 7.5.3. For the charge arm of $[NTf_2]^-$ in $[C_4C_1im][NTf_2]$, the distribution remains approximately the same up to electric fields of 0.01 VÅ^{-1}. This is sup-

ported by the % *cis* isomer, which remains around 63% up to 0.01 VÅ^{-1}.

As with the charge arm of $[C_4C_1im]^+$, there is a slight shift in the distribution at 0.02 VÅ^{-1}. This is most obvious in the *cis* isomer percentage, which increases by 2% in this electric field. Above this, the percentage of cis isomers continues to increase with electric fields, up to 86.3% at 0.2 VÅ^{-1}. Above this, the definition of a *cis* and a *trans* isomer is not possible as the minimum which is used to define this disappears.

The distribution of the anion C-S-S-C dihedral angles show there is still a small amount of *trans* isomer present. The C-S-S-C dihedral is a better measure of the *cis*/*trans* ratio as it directly relates to this.

For $[NTf_2]^-$ in $[C_8C_1im][NTf_2]$, the distribution of charge arm lengths is plotted in Figure 8.12.

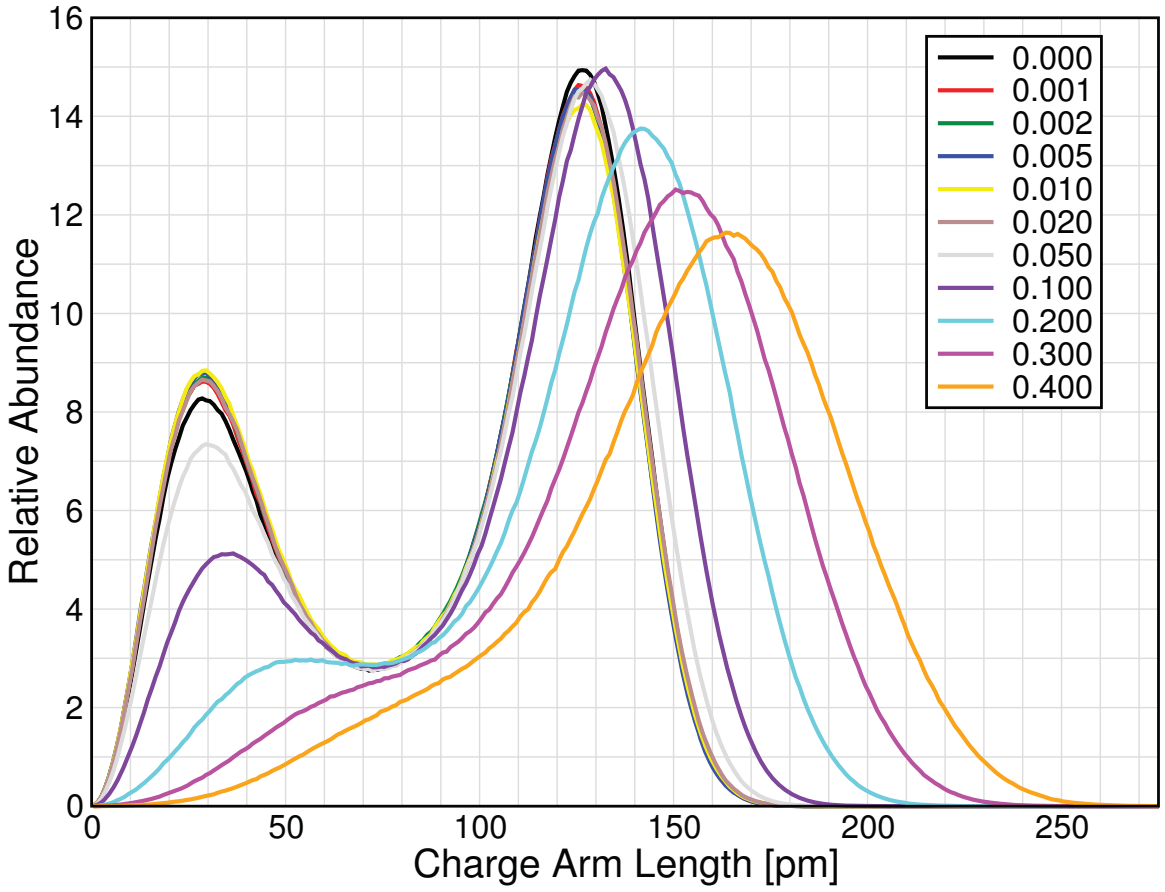

Figure 8.12: *Distribution of lengths of the charge arm of $[NTf_2]^-$ in $[C_8C_1im][NTf_2]$ in various electric fields, electric field strength is shown in the legend in VÅ^{-1}.*

As for $[NTf_2]^-$ in $[C_4C_1im][NTf_2]$, the distribution of lengths of the charge arm of $[NTf_2]^-$ in $[C_8C_1im][NTf_2]$ remains constant up to electric fields of 0.01 VÅ^{-1}, with the exception of 0.000 VÅ^{-1}.

At 0.000 VÅ^{-1} the distribution of charge arms does not match with other low electric field data, with $\approx$ 1.5% more *cis* isomer. This is matched by the dihedral data, wherein the no electric

field dihedral angle distribution has ≈ 1% more *cis* isomer. Due to the percent of *cis* isomer in $[C_4C_1im][NTf_2]$ being around 63%, it is assumed that for some unknown reason the 0.000 VÅ^{-1} simulation for $[C_8C_1im][NTf_2]$ has an inconsistently high percentage of *cis* isomer.

Returning to the data for $[C_8C_1im][NTf_2]$ in electric fields, there is a slight increase in the percentage of $[NTf_2]^-$ in the *cis* isomer at 0.02 VÅ^{-1}, although the distribution does not look like it shifts much (Table 8.3).

Table 8.3: *Percentage of $[NTf_2]^-$ in the cis isomer in $[C_8C_1im][NTf_2]$ in various electric fields strengths. A cis anion is defined as having a charge arm longer than 75 pm in the charge arm length distribution (Figure 8.12). This definition of the cis and trans isomers is difficult above 0.2 VÅ^{-1}.*

Electric Field [VÅ^{-1}]	0.000	0.001	0.002	0.005	0.01	0.02	0.05	0.1	0.2	>0.2
% *cis* isomer	65.0	63.6	63.6	63.4	62.9	64.8	67.9	75.3	85.5	-

Above 0.02 VÅ^{-1} there is a clear increase in the percentage of *cis* isomer up to 0.2 VÅ^{-1}, above which there is a difficulty defining the isomers due to the lack of a minimum. As with $[NTf_2]^-$ in $[C_4C_1im][NTf_2]$, the C-S-S-C dihedral still shows the presence of some *trans* isomer.

As opposed to the dihedral data in the previous section (7.5.3), there is now a reasonable explanation behind the isomerisation of the anion in large electric fields. This isomerisation comes as a result of the cis isomer having a longer charge arm than the *trans*. As electric fields cause a preference for a longer charge arm, the anion undergoes a *trans*→*cis* isomerisation.

What can also be seen is a remarkable agreement between the *cis* percentage from the charge arms in $[C_4C_1im][NTf_2]$ and $[C_8C_1im][NTf_2]$, with at most 1% difference between the values in all electric fields. Even though these are the same anions, there was a possibility that there could be some cation-dependent effect that leads to a difference. However, this is not the case for the charge arm lengths. This will be discussed more in Section 8.5.

What is somewhat expected given the conclusion that longer charge arm are preferred in stronger electric fields, the $[NTf_2]^-$ dihedral data shows that, in both ionic liquids, the anion never fully isomerises into the *cis* isomer. This is despite the *cis* isomer having a much longer charge arm than the *trans*, and the electric field causing isomerisation to the longer charge arms. The percentage *cis* isomer increases greatly in the range of 0.05-0.3 VÅ^{-1} but then less so at greater electric fields, and the maximum from the dihedrals is 89% *cis* isomer in 0.5 VÅ^{-1} in $[C_4C_1imNTf_2]$.

The charge arm data shows that any *trans* isomer present has its Drude particles oriented in such a way to increase the charge arm. This confirms that longer charge arms are preferred, so the existence of the shorter charge arm *trans* isomer is not a simple feature.

8.2.3 Cation Charge Arm Orientation

From Equation 8.3, there will be a torque upon the charge arms pulling them parallel to the electric field lines. Section 7.5.3 shows that there is a change in the orientation of the imidazolium ring, for which the charge arm is suspected to be the cause of this and needs to be investigated.

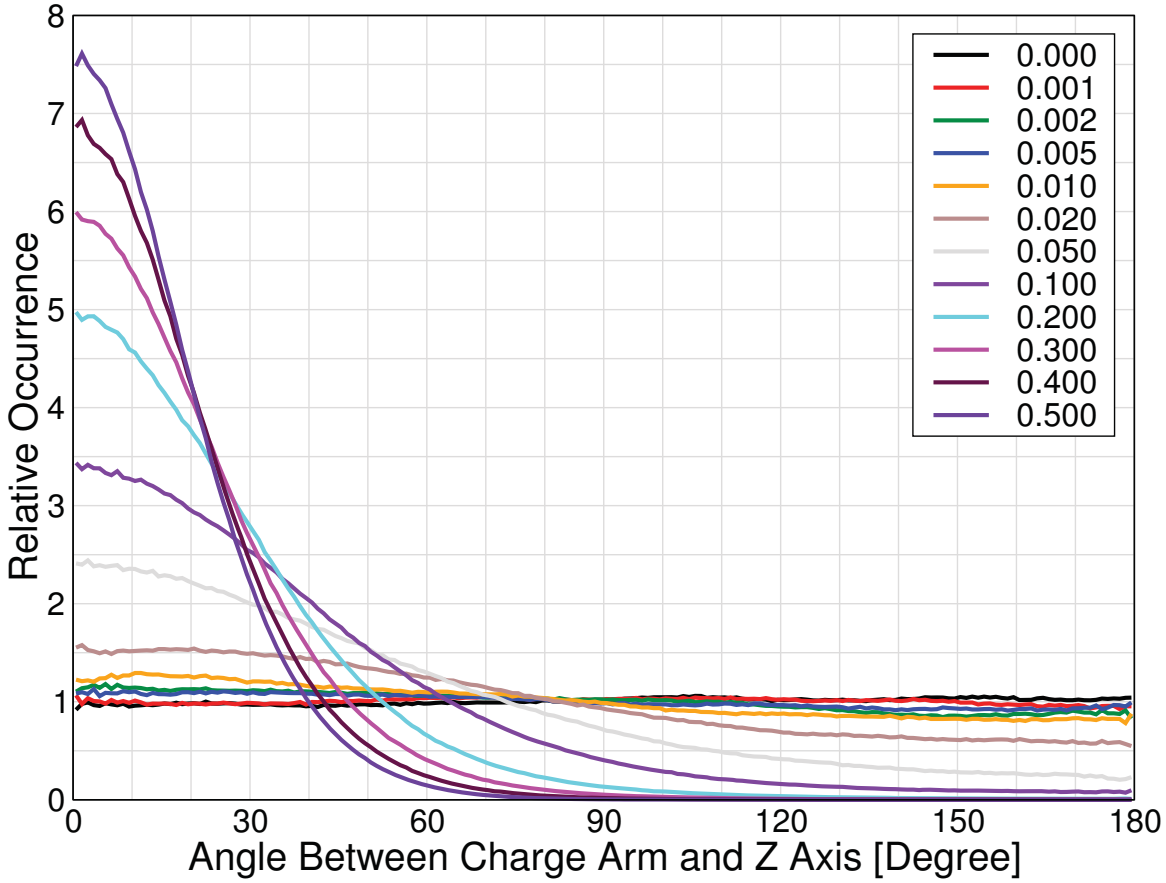

Figure 8.13: *Angular distribution of the charge arms of $[C_4C_1im]^+$ in $[C_4C_1im][NTf_2]$ in various electric fields with respect to the positive z vector of the simulation box. Electric field strength is shown in the legend in VÅ^{-1}.*

Figure 8.13 shows the orientation of the cation charge arm to the electric field vector (along the z axis) in $[C_4C_1im][NTf_2]$. This shows a clear aligning of the charge arms with the electric field, which increases with the electric field strength.

This alignment is towards 0°, which means the charge arm vector points along the z axis in the positive direction. This is the direction in which the centre of charge is pulled by the electric field, so is the expected way the charge arm should align.

This alignment is fairly obvious at 0.02 VÅ^{-1} and above from the distribution, but this data is too noisy to see any alignment below this. To see if there is alignment of the charge arms in electric fields below this, the integral of the angular distribution can give a better representation

of this. This is shown for $[C_4C_1im]^+$ in $[C_4C_1im][NTf_2]$ in Figure 8.14.

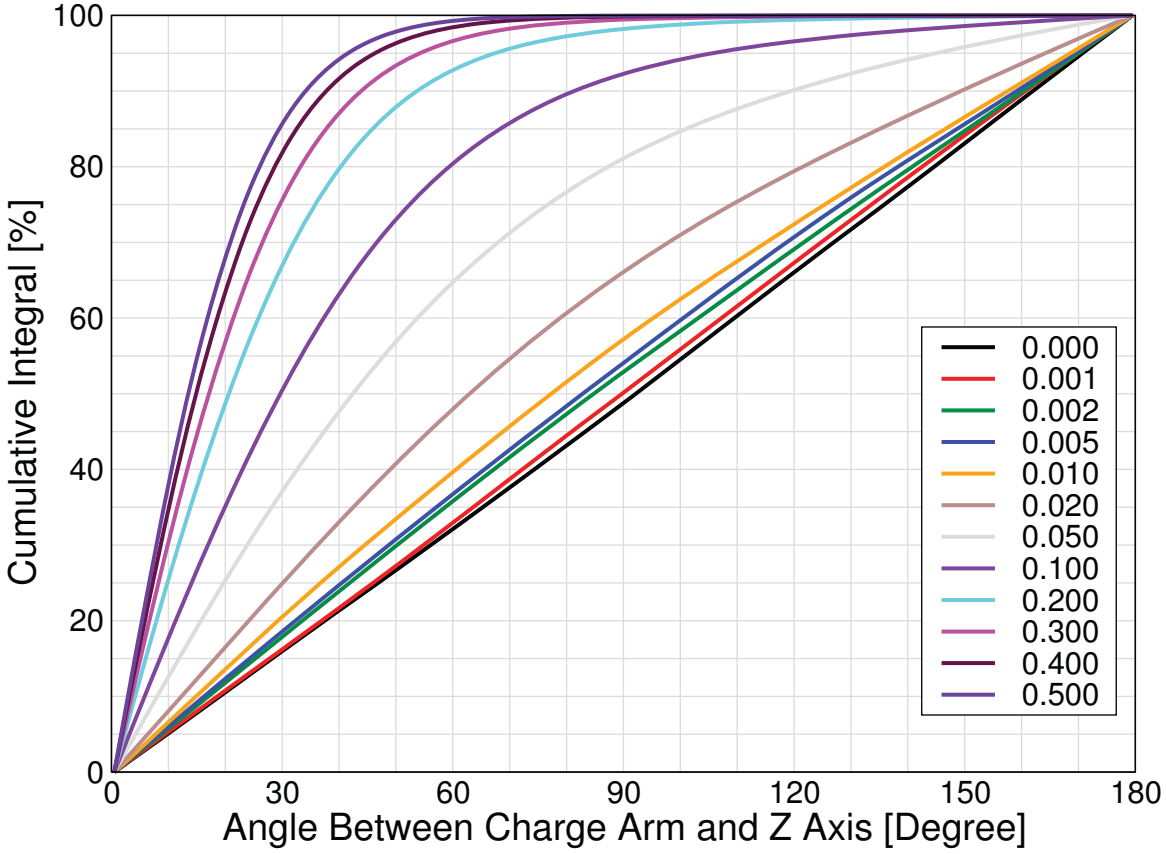

Figure 8.14: *Integral of the angular distribution of the charge arms of $[C_4C_1im]^+$ in $[C_4C_1im][NTf_2]$ in various electric fields with respect to the positive z vector of the simulation box. Electric field strength is shown in the legend in VÅ^{-1}.*

This analysis shows that there is a change in the orientation of the charge arms in lower electric fields. This is not a true alignment, as the charge arms are not fully orienting with the field. Instead there is a greater amount of $[C_4C_1im]^+$ being found on average with angles less than 90° with respect to the z vector of the box. This is best seen when considering the cumulative integral at certain angles in the distribution, shown in Table 8.4.

Table 8.4: *Percentage of $[C_4C_1im]^+$ in $[C_4C_1im][NTf_2]$ with a charge arm less than 30°, 90°, and 120° in each electric field.*

Field [VÅ^{-1}]	0.000	0.001	0.002	0.005	0.01	0.02	0.05	0.1	0.2	0.3	0.4	0.5
<30°[%]	15.7	15.9	17.6	18.2	20.2	24.5	36.5	49.7	66.1	74.9	81.2	85.0
<90°[%]	49.5	50.4	53.2	54.3	57.5	66.3	81.3	92.4	98.2	99.5	99.9	99.97
<120°[%]	65.8	67.0	68.8	70.4	72.2	79.2	90.0	96.5	99.4	99.9	99.97	100.00

By integrating the normalised angular distribution to a specific angle, the cumulative integral (from $0 \rightarrow \theta$) gives the relative number of ions with a charge arm of less than that angle. This integral shows that the preference for $[C_4C_1im]^+$ to take angles closer to alignment with the electric field lines begins at 0.002 VÅ^{-1}, and this preference becomes more pronounced with stronger electric fields. This proves the torque force in Equation 8.3 exists, and affects the ions

even at such low electric field strength as 0.002 VÅ^{-1} where other effects of the electric field are not seen.

From Equation 8.3, the torque, and thus the effect, from the electric field should be stronger on $[C_8C_1im]^+$ as this has a longer charge arm. To see if this is true, the normalised angular distribution is shown in Figure 8.15.

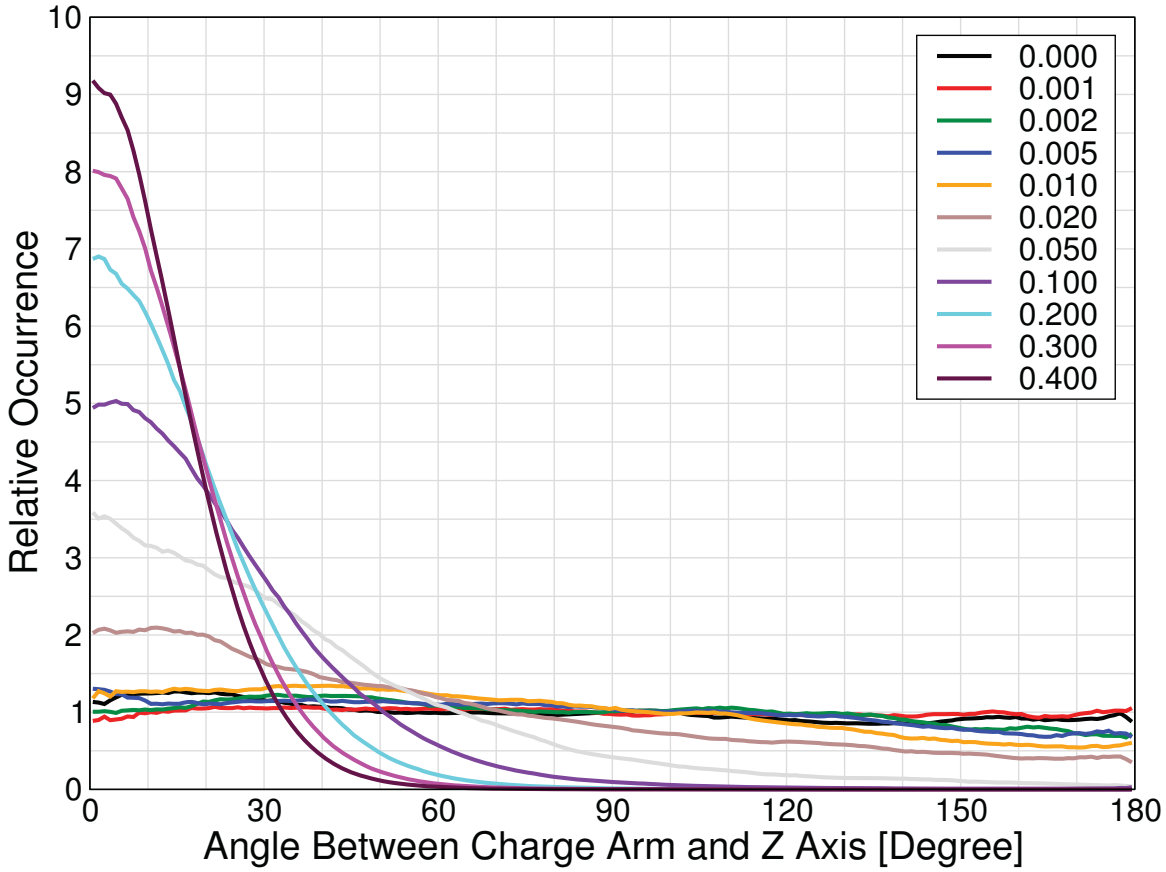

Figure 8.15: *Angular distribution of the charge arms of $[C_8C_1im]^+$ in $[C_8C_1im][NTf_2]$ in various electric fields with respect to the positive z vector of the simulation box. Electric field strength is shown in the legend in VÅ^{-1}.*

The distribution of $[C_8C_1im]^+$ shows a clear alignment with the electric field, with the degree of orientation with the electric field increasing with electric field strength. This orientation occurs as a preference towards 0° with respect to the direction of the electric field, as expected from the charge.

It is immediately obvious from the angular distribution that $[C_8C_1im]^+$ has a stronger orientation than $[C_4C_1im]^+$. Taking the orientation at 0.4 VÅ^{-1} as an example, for $[C_8C_1im]^+$ a 9× higher than expected occurrence is seen at 0° than would occur if the charge arm vectors were randomly orientated. The same electric field and the same bin for $[C_4C_1im]^+$ shows a 7× higher occurrence at 0° than would be seen if the charge arm vectors were randomly orientated. This rudimentary comparison shows that for all electric fields in the range 0.02-0.4 VÅ^{-1} inclu-

sive, there is a greater occurrence of $[C_8C_1im]^+$ having smaller angles to the electric field lines. To see if this is the case below 0.02 VÅ^{-1}, the cumulative integrals can be used (Figure 8.16, Table 8.5).

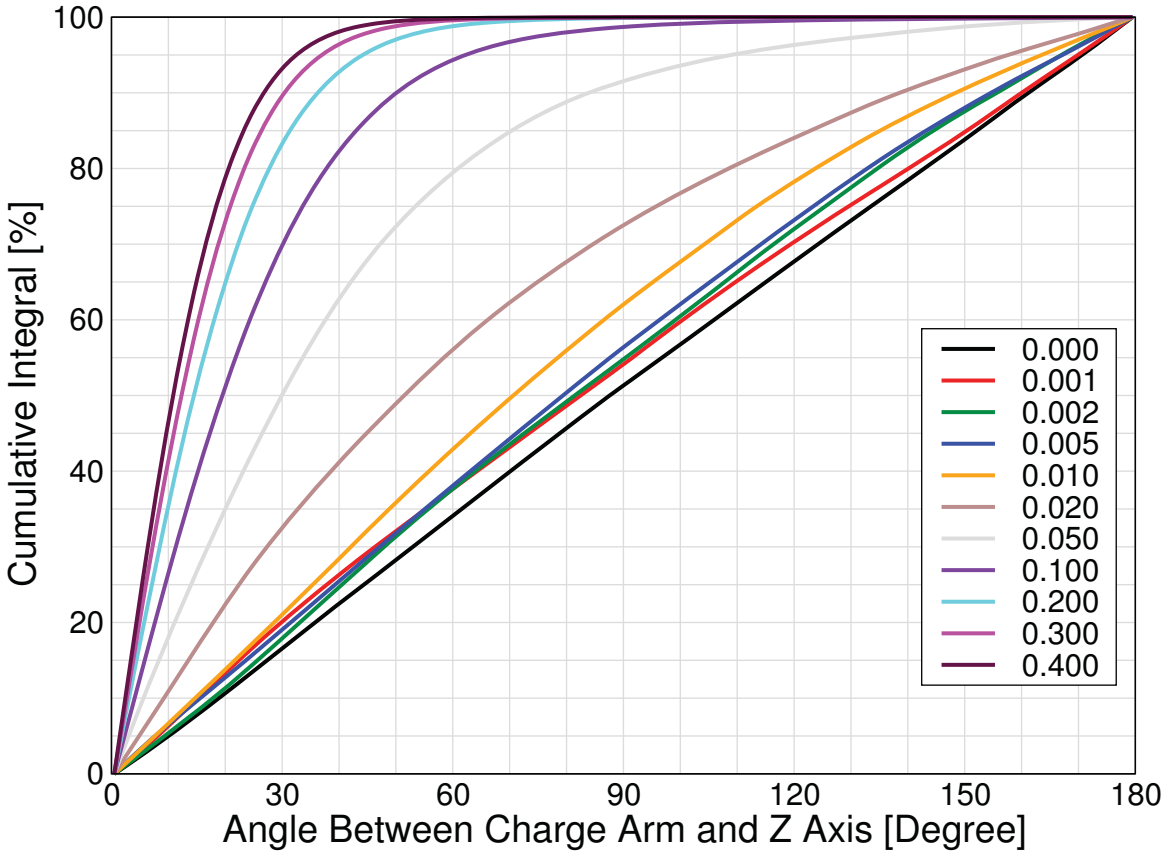

Figure 8.16: *Integral of the angular distribution of the charge arms of $[C_8C_1im]^+$ in $[C_8C_1im][NTf_2]$ in various electric fields with respect to the positive z vector of the simulation box. Electric field strength is shown in the legend in VÅ^{-1}.*

Table 8.5: *Percentage of $[C_8C_1im]^+$ in $[C_8C_1im][NTf_2]$ with a charge arm less than 30°, 90°, and 120° in each electric field.*

Field [VÅ^{-1}]	0.000	0.001	0.002	0.005	0.01	0.02	0.05	0.1	0.2	0.3	0.4
<30°[%]	15.8	19.8	17.6	18.7	20.6	32.1	49.4	69.0	82.6	89.0	92.76
<90°[%]	51.6	54.4	55.1	56.7	62.3	72.7	91.7	98.8	99.9	99.96	99.98
<120°[%]	67.4	70.0	71.7	72.3	78.0	83.9	96.3	99.5	99.98	99.99	100.00

The integrals show that the greater alignment of $[C_8C_1im]^+$ occurs in all of the electric fields which show a significant orientation ($\geq$0.002 VÅ^{-1}). Comparing any of the integrals in Table 8.5 to those in Table 8.4 shows that the longer charge arm in $[C_8C_1im]^+$ does align more strongly with the electric field lines in all electric field strengths.

This confirms what was expected from the theory of charge arms, that a longer charge arm leads to a greater preference for orientation with the electric field lines due to a stronger torque force on the charge arms.

8.2.4 Anion Charge Arm Orientation

Given that the cations have been shown to follow the theory that a longer charge arm leads to a greater alignment with the field, the orientation of the anion can be looked at to see if the orientation is ion dependent.

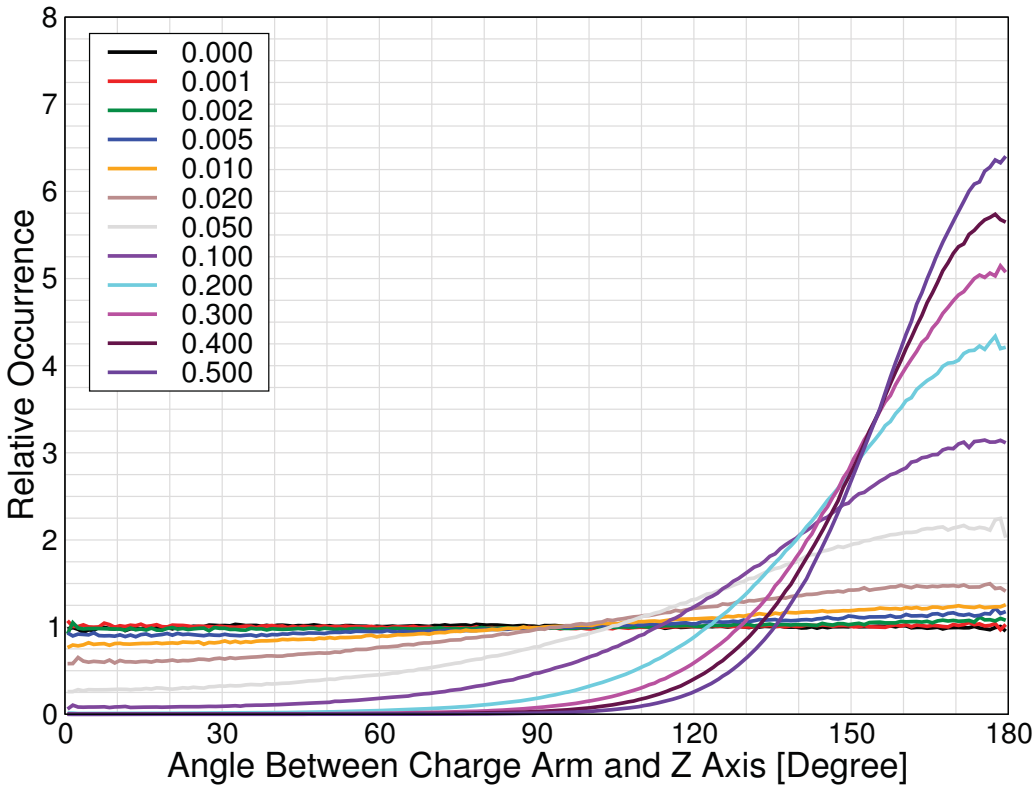

Figure 8.17: *Normalised angular distribution of the charge arms of $[NTf_2]^-$ in $[C_4C_1im][NTf_2]$ in various electric fields with respect to the positive z vector of the simulation box. Electric field strength is shown in the legend in VÅ^{-1}.*

Comparing Figures 8.17 and 8.18 there is a remarkable similarity between the two distributions, as with the distribution of the charge arm lengths.

In both ionic liquids, the charge arm of $[NTf_2]^-$ orients so it is pointing along the electric field lines in the negative direction, as would be expected from the direction the electric field pulls the centre of charge. As with the cations, stronger electric fields cause a greater alignment of the charge arms with the electric field lines.

Obvious changes in the orientation occur at 0.01 VÅ^{-1}, but are possible below this. Therefore in order to better compare the charge arms of the anions in the two ionic liquids, the distributions were integrated to find the cumulative integral. The plots are shown in Figures 8.19 and 8.20, and the percentage of anions above a selected few angles are shown in Tables 8.6 and 8.7.

These data show that in both $[C_4C_1im][NTf_2]$ and $[C_8C_1im][NTf_2]$, the orientation of $[NTf_2]^-$ is different in electric fields of 0.005 VÅ^{-1} and above. There is a possibility that there is a slight

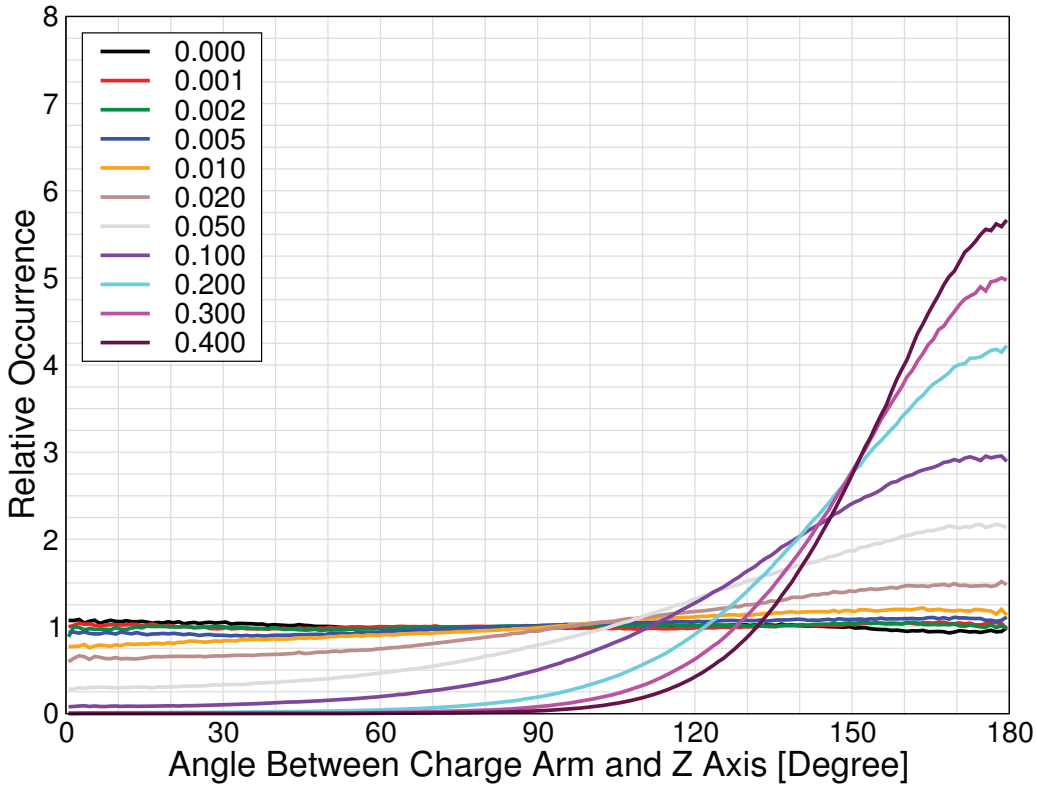

Figure 8.18: *Normalised angular distribution of the charge arms of $[NTf_2]^-$ in $[C_8C_1im][NTf_2]$ in various electric fields with respect to the positive z vector of the simulation box. Electric field strength is shown in the legend in VÅ^{-1}.*

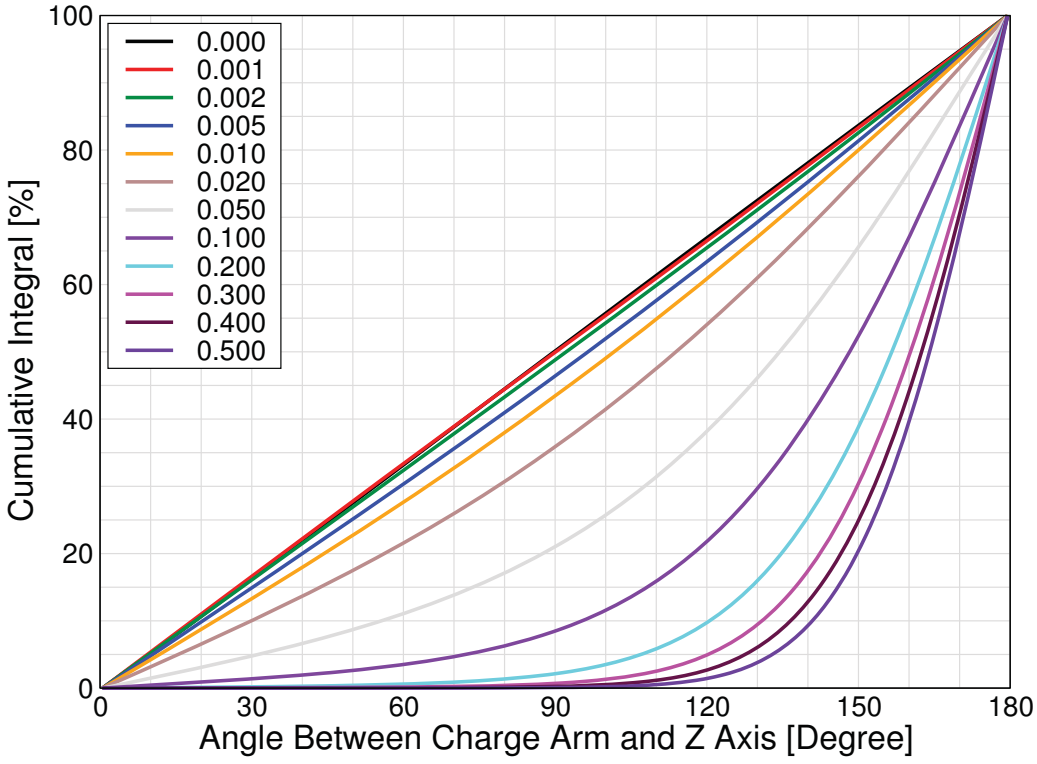

Figure 8.19: *Integral of the angular distribution of the charge arms of $[NTf_2]^-$ in $[C_4C_1im][NTf_2]$ in various electric fields with respect to the positive z vector of the simulation box. Electric field strength is shown in the legend in VÅ^{-1}.*

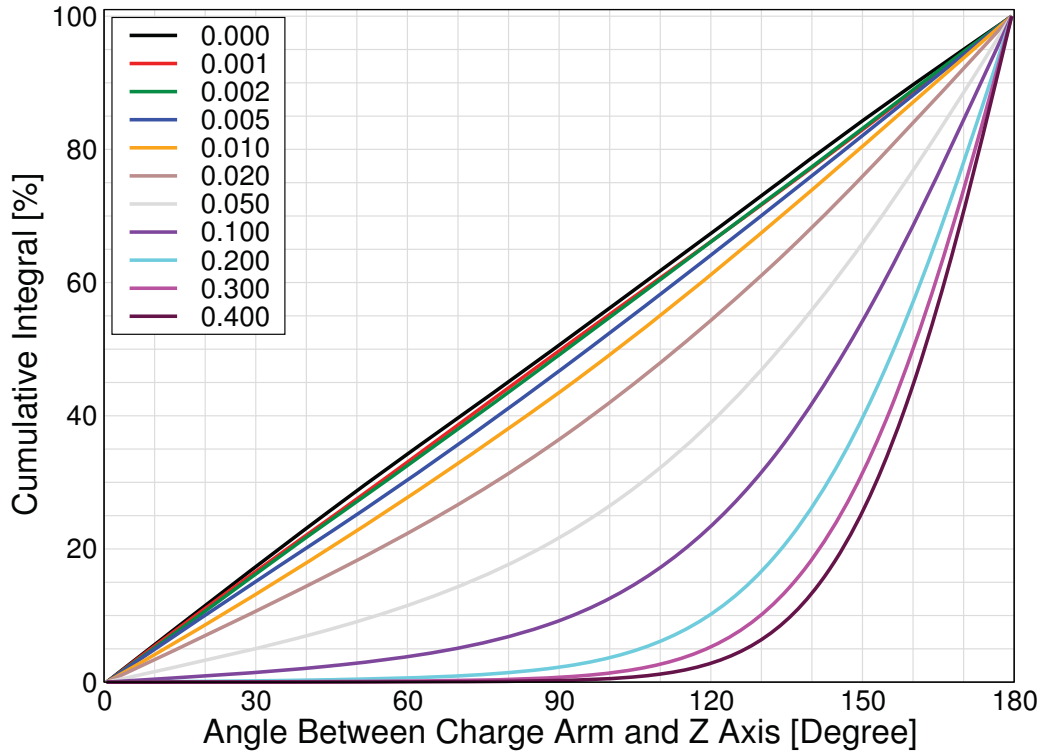

Figure 8.20: *Integral of the angular distribution of the charge arms of $[NTf_2]^-$ in $[C_8C_1im][NTf_2]$ in various electric fields with respect to the positive z vector of the simulation box. Electric field strength is shown in the legend in VÅ^{-1}.*

Table 8.6: *Percentage of $[NTf_2]^-$ in $[C_4C_1im][NTf_2]$ with a charge arm greater than 30°, 90°, and 120° in each electric field.*

Field [VÅ^{-1}]	0.000	0.001	0.002	0.005	0.01	0.02	0.05	0.1	0.2	0.3	0.4	0.5
>30°[%]	84.0	83.7	84.2	85.3	86.9	90.1	95.3	98.6	99.8	99.95	99.99	100.00
>90°[%]	49.6	49.8	50.9	53.3	56.3	63.8	78.8	91.4	97.8	99.3	99.8	99.9
>120°[%]	33.4	33.8	34.8	36.9	39.4	46.3	62.2	78.5	90.5	95.2	97.4	98.6

Table 8.7: *Percentage of $[NTf_2]^-$ in $[C_8C_1im][NTf_2]$ with a charge arm greater than 30°, 90°, and 120° in each electric field.*

Field [VÅ^{-1}]	0.000	0.001	0.002	0.005	0.01	0.02	0.05	0.1	0.2	0.3	0.4
>30°[%]	83.0	83.7	84.1	85.1	87.0	89.5	95.1	98.6	99.8	99.95	99.99
>90°[%]	49.7	50.5	51.1	53.6	56.8	63.8	78.5	90.9	97.8	99.3	99.8
>120°[%]	32.9	34.1	34.2	36.2	39.1	46.0	61.4	76.9	90.1	94.9	97.3

preference in 0.002 VÅ^{-1} however this is not as obvious as in the cation angular distributions. What is clear is that the alignment of the anion is almost identical, especially at higher electric field strengths where the integrals differ by less than 0.5%. This makes it clear that the effect of the torque force upon each ion is independent of the ionic liquid in which the ion sits, at least within the $[C_nC_1im][NTf_2]$ series.

8.3 Charge Arm Length Against Orientation

So far it has been shown that the charge arms increase in length and orient themselves to the electric field in the direction that the electric field pulls the charge arm. Although it is implied that longer charge arms lead to a greater orientation with the field, this has only been seen as a general trend between electric fields.

To confirm if longer ions do align more strongly with the electric field, a direct comparison in the form of a combined distribution function was calculated for the cation and anion charge arms in both ionic liquids. These are presented in Figures 8.21, 8.22, 8.23 and 8.24.

These confirm that it is the case that longer charge arms do prefer aligning more with the electric fields than shorter charge arms. This is most obvious in the mid-range electric fields, where there is still a significant number of charge arms of all lengths. In these electric fields, there is a strong correlation between the length of the charge arm and the angle which it takes, with longer charge arms having a greater distribution of ions with the angle the electric field is causing the ions to rotate towards (0° for cations, 180° for anions).

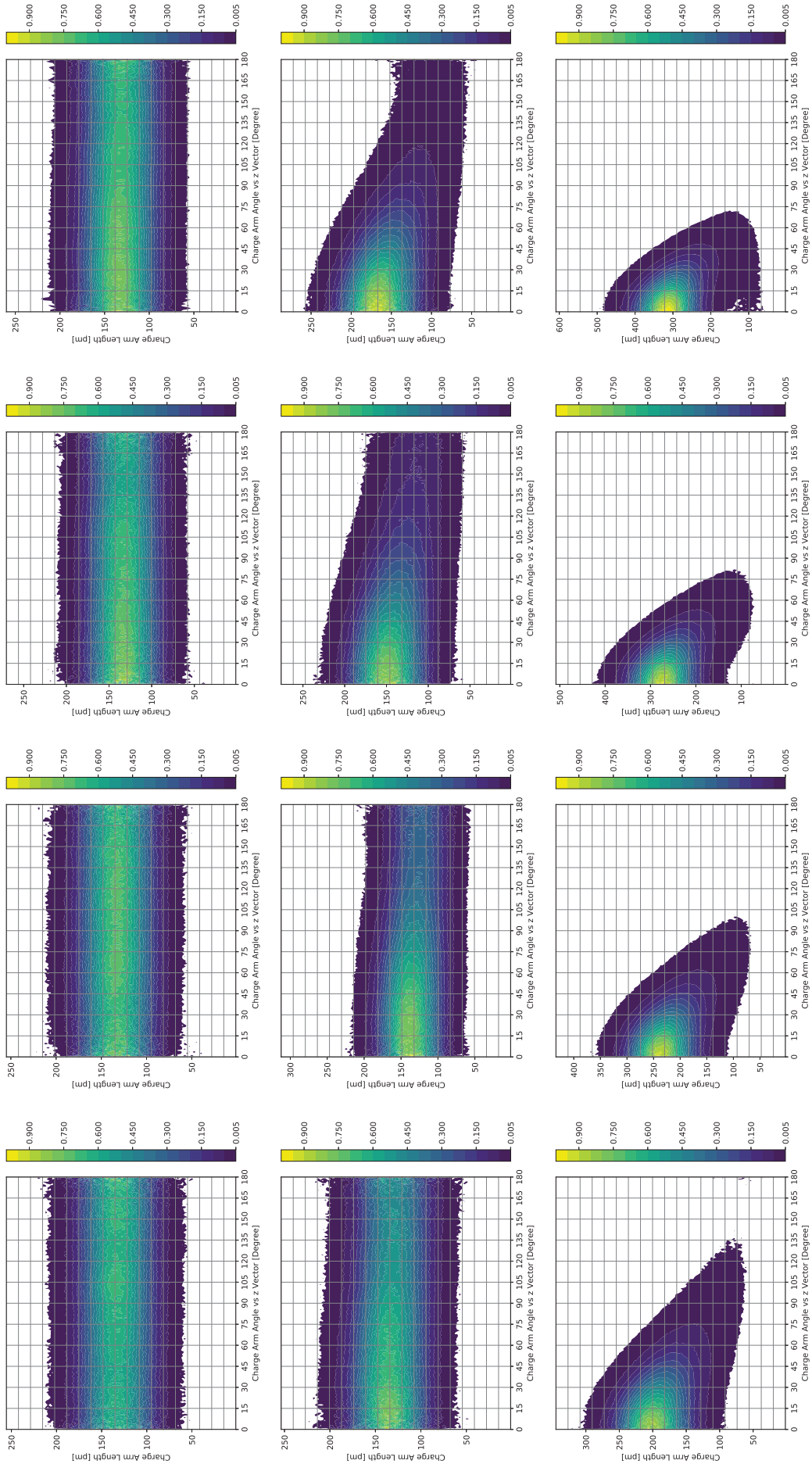

Figure 8.21: *2D histogram of the length of the charge arm $[C_4C_1im]^+$ in $[C_4C_1im][NTf_2]$ against its angle to the z vector. Histograms are normalised to a maximum of 1, and density values of <0.005 are masked for clarity. The electric fields are, from top left reading across, 0.000 VÅ^{-1}, 0.001 VÅ^{-1}, 0.002 VÅ^{-1}, 0.005 VÅ^{-1}, 0.01 VÅ^{-1}, 0.02 VÅ^{-1}, 0.05 VÅ^{-1}, 0.1 VÅ^{-1}, 0.2 VÅ^{-1}, 0.3 VÅ^{-1}, 0.4 VÅ^{-1}, 0.5 VÅ^{-1}.*

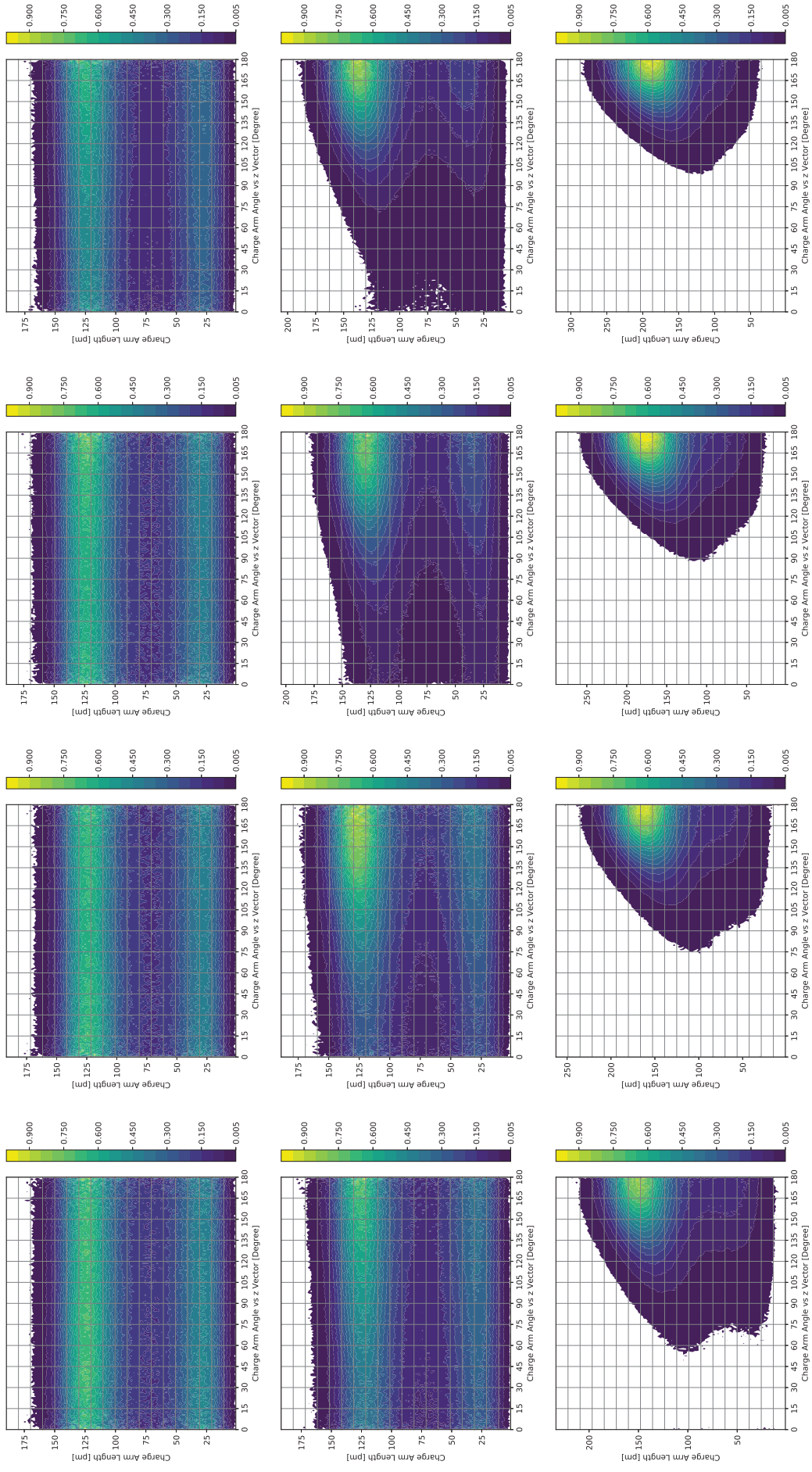

Figure 8.22: *2D histogram of the length of the charge arm $[NTf_2]^-$ in $[C_4C_1im][NTf_2]$ against its angle to the z vector. Histograms are normalised to a maximum of 1, and density values of <0.005 are masked for clarity. The electric fields are, from top left reading across, 0.000 VÅ^{-1}, 0.001 VÅ^{-1}, 0.002 VÅ^{-1}, 0.005 VÅ^{-1}, 0.01 VÅ^{-1}, 0.02 VÅ^{-1}, 0.05 VÅ^{-1}, 0.1 VÅ^{-1}, 0.2 VÅ^{-1}, 0.3 VÅ^{-1}, 0.4 VÅ^{-1}, 0.5 VÅ^{-1}.*

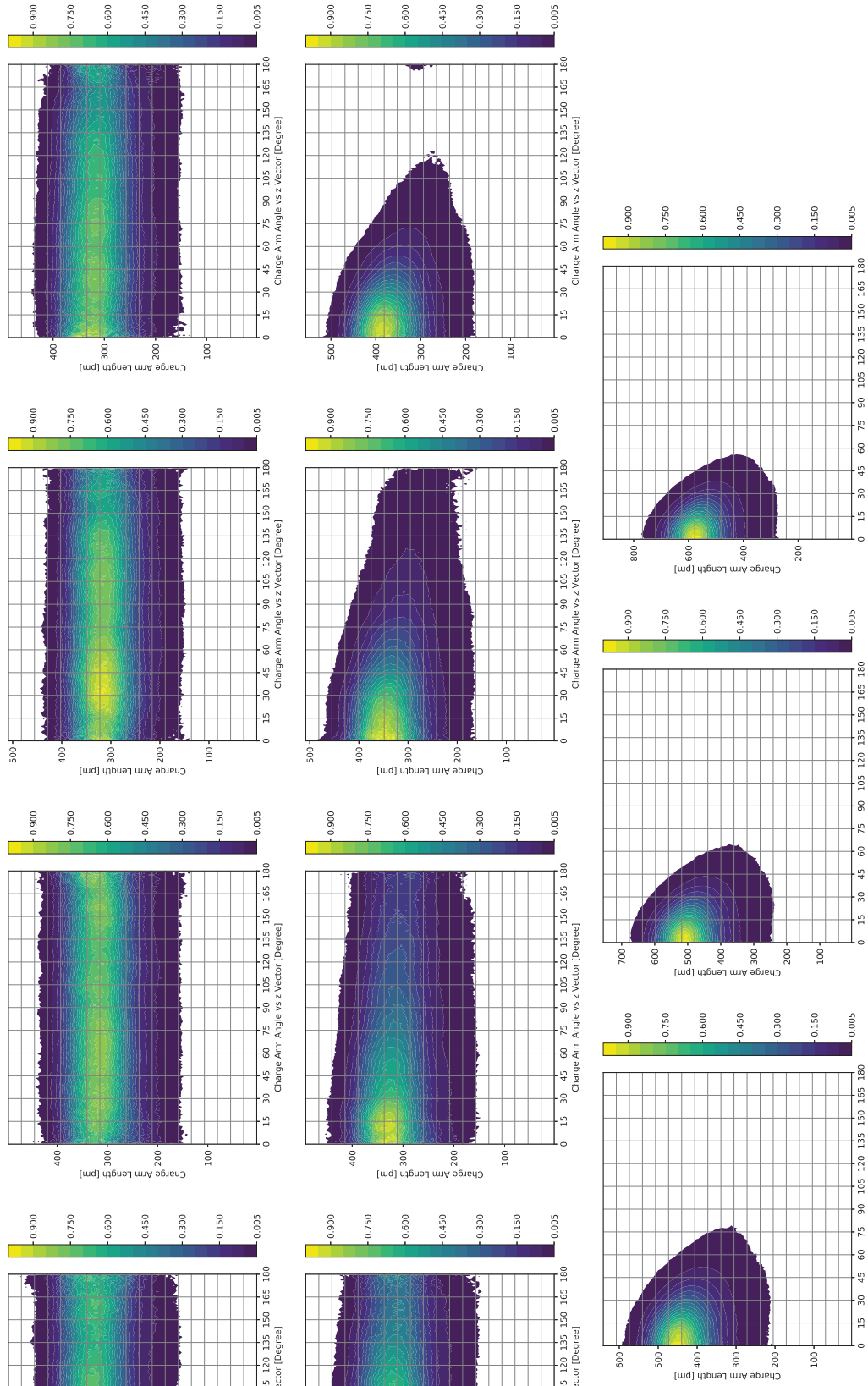

Figure 8.23: *2D histogram of the length of the charge arm $[C_8C_1im]^+$ in $[C_8C_1im][NTf_2]$ against its angle to the z vector. Histograms are normalised to a maximum of 1, and density values of <0.005 are masked for clarity. The electric fields are, from top left reading across, 0.000 VÅ^{-1}, 0.001 VÅ^{-1}, 0.002 VÅ^{-1}, 0.005 VÅ^{-1}, 0.01 VÅ^{-1}, 0.02 VÅ^{-1}, 0.05 VÅ^{-1}, 0.1 VÅ^{-1}, 0.2 VÅ^{-1}, 0.3 VÅ^{-1}, 0.4 VÅ^{-1}.*

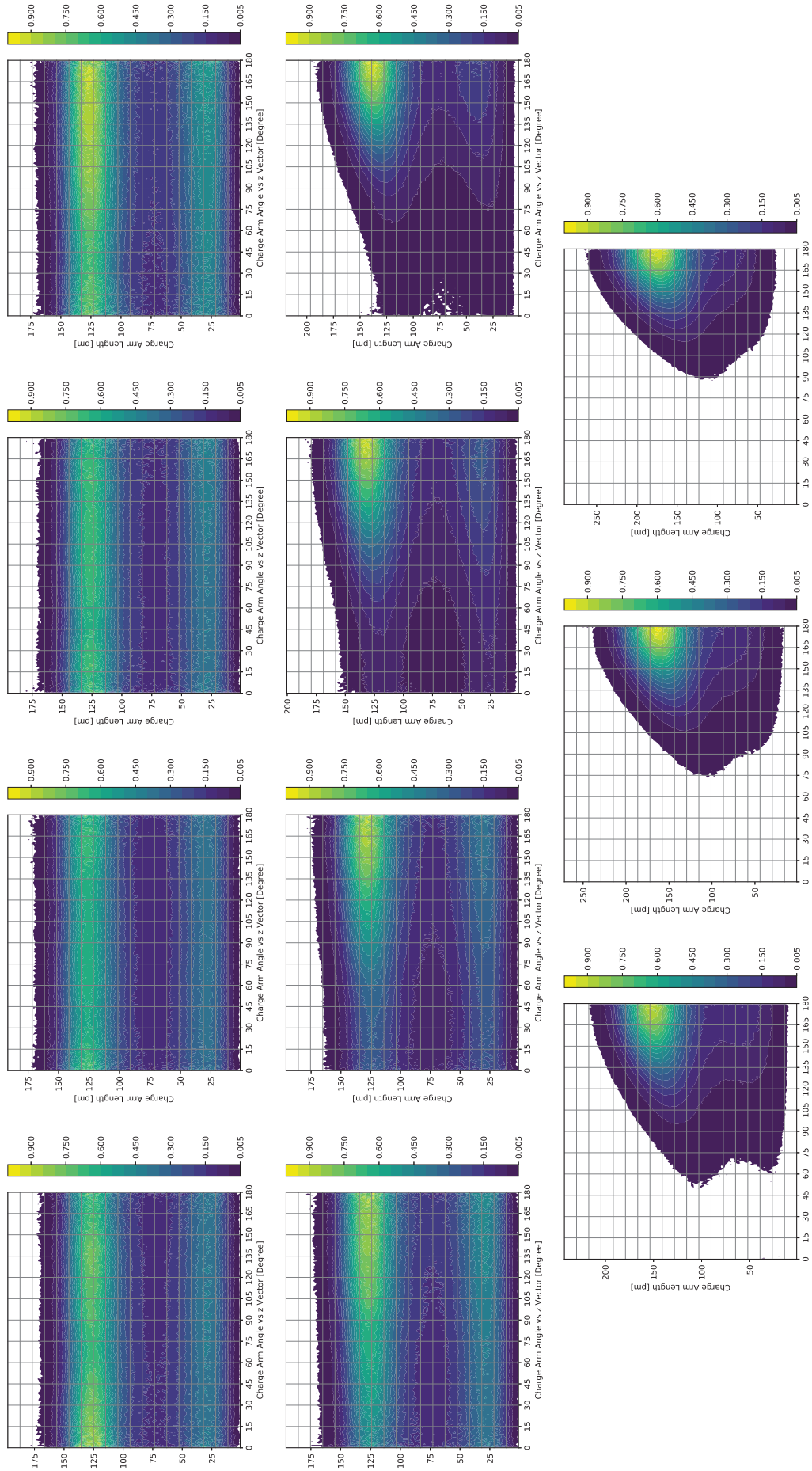

Figure 8.24: *2D histogram of the length of the charge arm $[NTf_2]^-$ in $[C_8C_1im][NTf_2]$ against its angle to the z vector. Histograms are normalised to a maximum of 1, and density values of <0.005 are masked for clarity. The electric fields are, from top left reading across, 0.000 VÅ^{-1}, 0.001 VÅ^{-1}, 0.002 VÅ^{-1}, 0.005 VÅ^{-1}, 0.01 VÅ^{-1}, 0.02 VÅ^{-1}, 0.05 VÅ^{-1}, 0.1 VÅ^{-1}, 0.2 VÅ^{-1}, 0.3 VÅ^{-1}, 0.4 VÅ^{-1}.*

8.4 Charge Arms to Charge Arms

8.4.1 Comparing Ionic Liquids

From the theory of the forces upon the charge arms, introduced in beginning of this chapter, upon application of an electric field there is an 'aligning force' upon the ions. Equation 8.4 (repeated below) shows that the magnitude of this alignment should be directly proportional to the length of the charge arm.

$$F_{\perp T} = E \cdot l_q \cdot Q_{\text{total}} \cdot cos\,(\psi)$$

To see if this is the case, the different charge arms in the two ionic liquids can be investigated. This can easily be done with the orientation of the cations and anions, as well as the length of the anionic charge arm. However, the lengths of the cationic charge arms are more difficult to compare due their different inherent lengths, as well as the difficulty in finding a way to 'normalise' the plots. In the absence of a reliable way to compare these the relative lengths of, and the changes to, the cation charge arms will not be compared here.

Considering the cations in the ionic liquids, these each have different charge arm lengths, with the charge arm of $[C_4C_1im]^+$ being shorter than that of $[C_8C_1im]^+$.

Equation 8.4 states that $[C_8C_1im]^+$ should be more affected (i.e. align more with the electric field) by the same electric field strength than $[C_4C_1im]^+$.

Figure 8.25 shows that greater alignment of $[C_8C_1im]^+$ does occur in all electric fields $\geq$0.020 VÅ^{-1}, where alignment is obvious.

Interestingly, an overlap of the charge arm distribution can be seen under some electric fields. This overlap occurs at: 0.05 VÅ^{-1} for $[C_8C_1im]^+$ and 0.1 VÅ^{-1} for $[C_4C_1im]^+$; 0.1 VÅ^{-1} for $[C_8C_1im]^+$ and 0.2 VÅ^{-1} for $[C_4C_1im]^+$; and 0.2 VÅ^{-1} for $[C_8C_1im]^+$ and 0.4 VÅ^{-1} for $[C_4C_1im]^+$.

What this demonstrates is that doubling the electric field strength has the same effect on the alignment of both cations, independent of their different lengths (Table 8.1).

This brings forward the question of: do ions with the same length charge arms in different ionic liquids behave the same? This can be found in these ionic liquids by comparing the anion between the simulations of the different ionic liquids. While the evidence in the previous sections has shown that the anion has the same *cis*:*trans* ratio in different ionic liquids, a direct comparison is welcome.

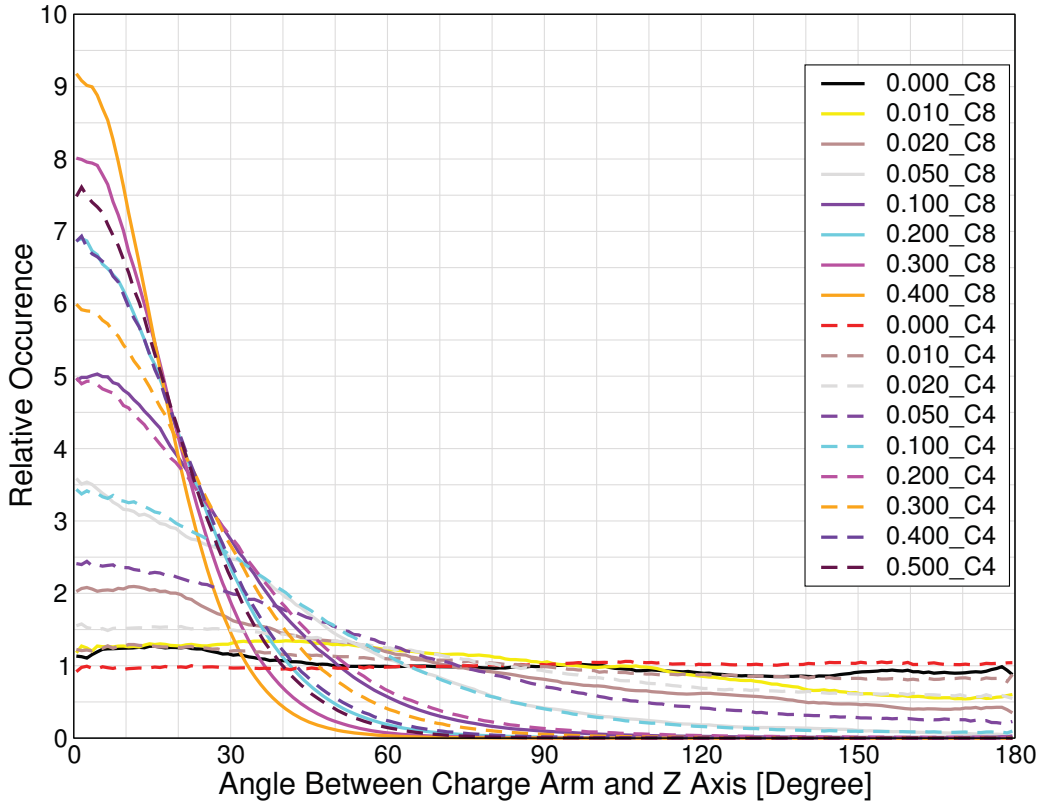

Figure 8.25: *Comparison of the relative alignment of the charge arm of $[C_4C_1im]^+$ in $[C_4C_1im][NTf_2]$ (dashed line) and $[C_8C_1im]^+$ in $[C_8C_1im][NTf_2]$ (solid line) in various electric fields with respect to the positive z vector of the simulation box. Electric field strength is shown in the legend in $VÅ^{-1}$.*

Figure 8.26 shows this direct comparison of the distribution of the lengths of the anionic charge arm between two ionic liquids. This shows conclusively that the behaviour of the lengths of the charge arms of the anions is exactly the same in both ionic liquids.

Figure 8.27 shows that the orientation of the anions is also the same between the different ionic liquids.

Altogether, these results show that, regardless of the ionic liquid in which ions reside, charge arms of the same ion have the same length, and changes to their length and orientation are the same when equivalent electric fields are applied to the ionic liquid. When the charge arms are of different lengths, the response of these to the same electric field are different, with longer charge arms aligning more with the electric field at the same electric field strength. However, the changes in these charge arms are still directly proportional to the applied electric field strength.

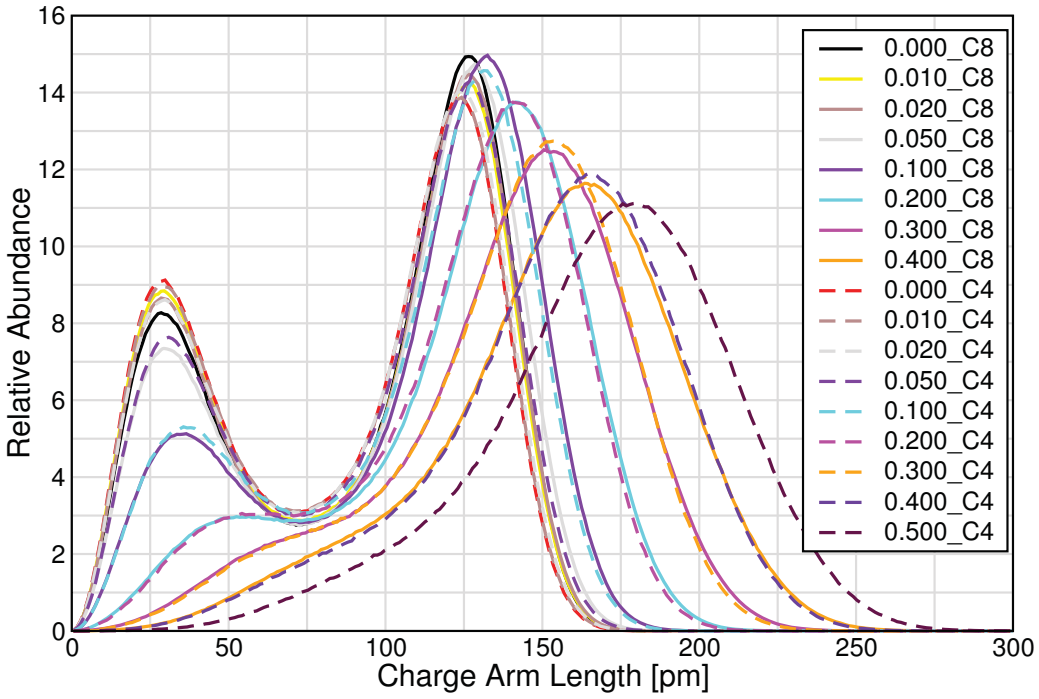

Figure 8.26: *Comparison of the length distrobutions of the charge arm of $[NTf_2]^-$ in $[C_4C_1im][NTf_2]$ (dashed line) and $[NTf_2]^-$ in $[C_8C_1im][NTf_2]$ (solid line) in various electric fields with respect to the positive z vector of the simulation box. Electric field strength is shown in the legend in VÅ^{-1}.*

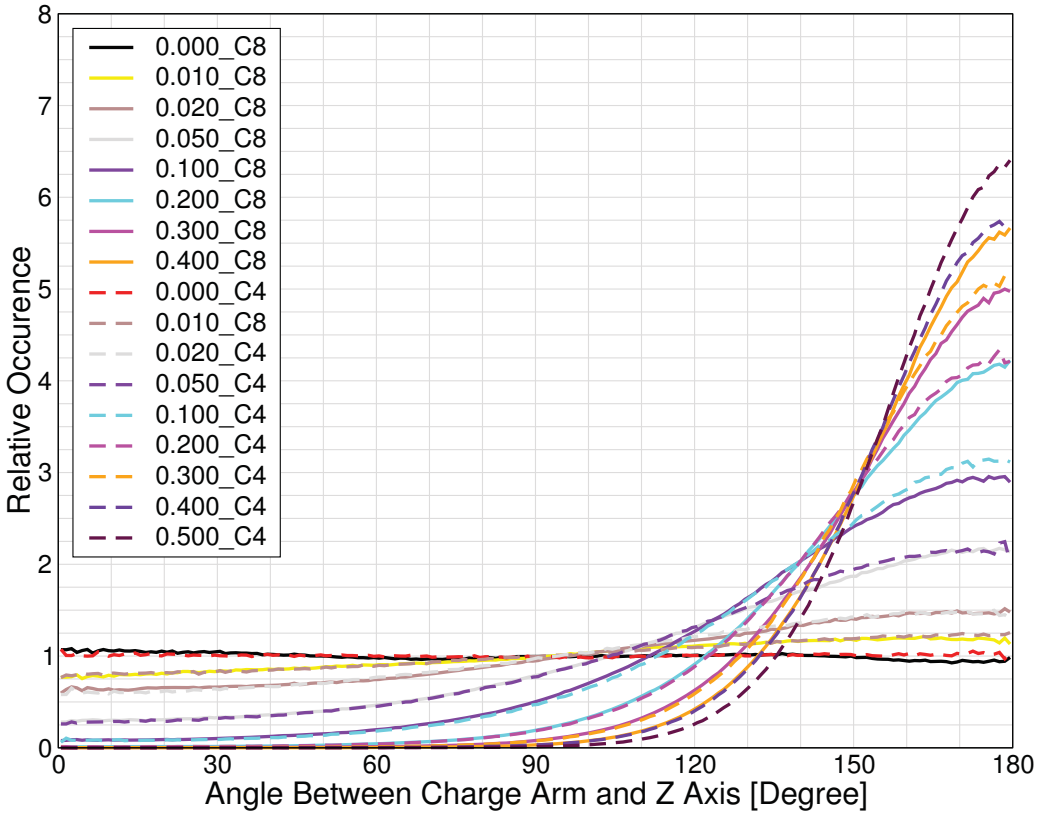

Figure 8.27: *Comparison of the relative alignment of the charge arm of $[NTf_2]^-$ in $[C_4C_1im][NTf_2]$ (dashed line) and $[NTf_2]^-$ in $[C_8C_1im][NTf_2]$ (solid line) in various electric fields with respect to the positive z vector of the simulation box. Electric field strength is shown in the legend in VÅ^{-1}.*

8.4.2 Comparing Anion Isomers

Whilst an easy comparison can be drawn between the different ions in the ionic liquids to observe the effect of different charge arm lengths, in these ionic liquids the behaviours of the different anion isomers can also be compared.

The *cis* and *trans* isomers of the anion have previously been identified to have different length charge arms, with the *cis* isomer having a significantly longer charge arm than the *trans* isomer. Therefore, the orientations of the *cis* and *trans* isomers were compared in every electric field strength. In every electric field the isomers were defined by their C-S-S-C dihedral angles, with the *cis* isomer defined as having a dihedral angle <60°, and the *trans* isomer having a dihedral angle >135°. Any anion with a dihedral between these two was excluded from the *cis*/*trans* analysis, but was included for the analysis of all anions. The relative amount of anions labelled as each isomer are shown in Table 8.8.

Table 8.8: *Percentage of $[NTf_2]^-$ anions labelled as cis (dihedral<60°), trans (dihedral>135°) and neither (60°<dihedral<135°) in $[C_4C_1im][NTf_2]$ in each electric field.*

Field [VÅ^{-1}]	0.000	0.001	0.002	0.005	0.01	0.02	0.05	0.1	0.2	0.3	0.4	0.5
cis [%]	44.2	44.5	44.3	44.2	44.1	44.5	48.1	53.6	58.7	61.2	63.0	64.9
trans [%]	34.7	34.3	34.7	34.9	34.7	34.3	30.3	23.7	16.4	13.1	11.0	9.5
neither [%]	21.1	21.2	21.0	20.9	21.2	21.2	21.6	22.7	24.9	25.7	26.0	25.6

This was only carried out on trajectories for $[C_4C_1im][NTf_2]$ due to the time, storage and compute required for this analysis, which was limited due to the university being shut down because of COVID-19. Due to the similarity of the anions in all other analyses, the same analysis on $[C_8C_1im][NTf_2]$ would be expected to show the same results.

The angular distributions of the charge arms of the anions to the z vector in the simulation box are shown in Figure 8.28. These are split into the anions labelled as *cis*, *trans*, as well as the overall average for anions in the simulation box.

In electric field strengths of $\leq$0.005 VÅ^{-1} there are no large differences in the orientation of the different isomers of the anion.

In electric field strengths of 0.01 VÅ^{-1}-0.2 VÅ^{-1} there is a clear difference in the alignment of the different isomers, with the *cis* isomer aligning more strongly with the electric field than the *trans* isomer.

This is due to the *cis* isomer having a longer charge arm than the *trans* isomer. Equation 8.4 states the torque force should be greater on the *cis* isomer, therefore at any given electric field, the force on the *cis* isomer to rotate and align with the electric field will be greater.

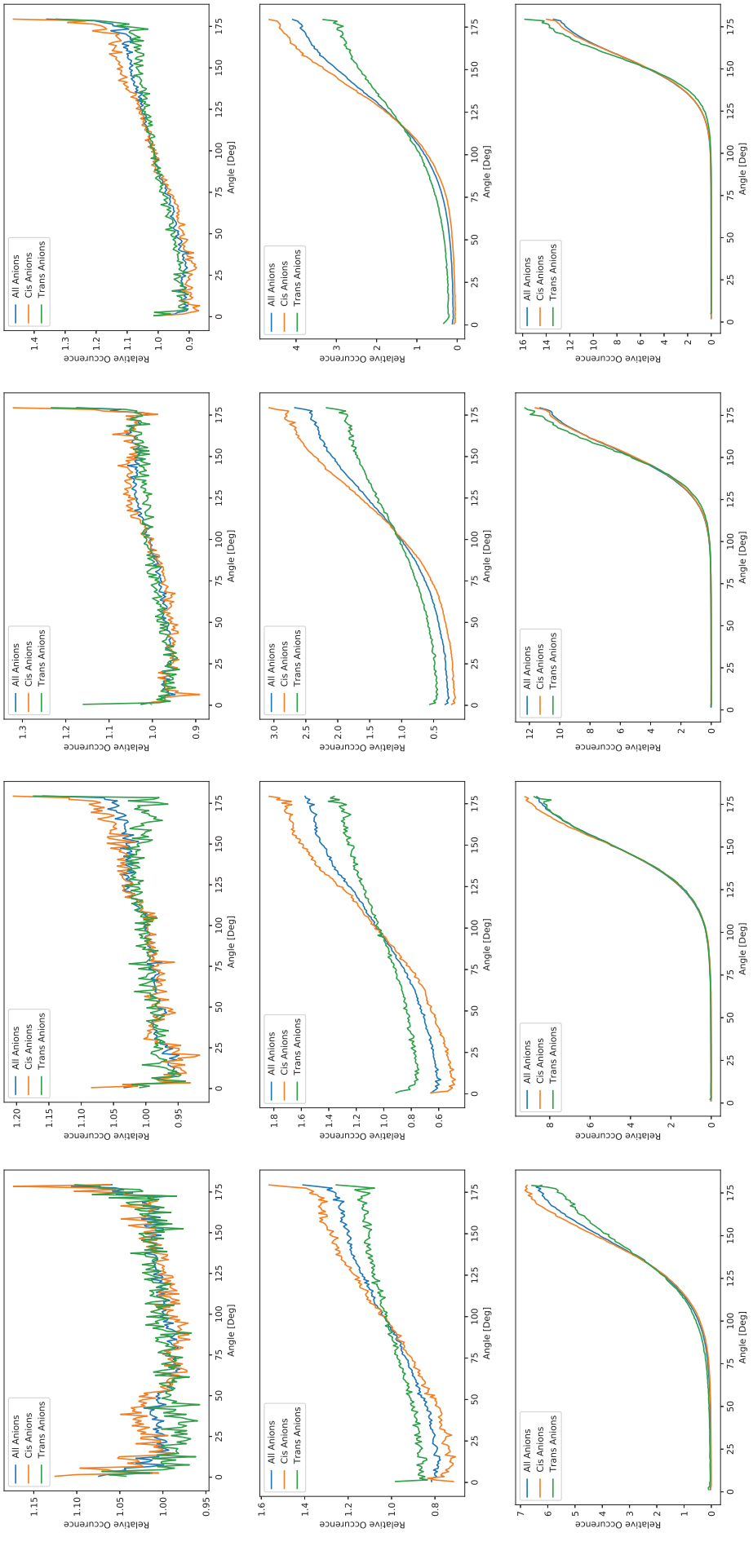

Figure 8.28: *Normalised angular distribution of the angle between the charge arm of $[NTf_2]^-$ in $[C_4C_1im][NTf_2]$ split between the cis and trans isomers. The electric fields in which they are measured are, from top left reading across, 0.000 $VÅ^{-1}$, 0.001 $VÅ^{-1}$, 0.002 $VÅ^{-1}$, 0.005 $VÅ^{-1}$, 0.01 $VÅ^{-1}$, 0.02 $VÅ^{-1}$, 0.05 $VÅ^{-1}$, 0.1 $VÅ^{-1}$, 0.2 $VÅ^{-1}$, 0.3 $VÅ^{-1}$, 0.4 $VÅ^{-1}$, 0.5 $VÅ^{-1}$.*

In electric field strengths of $\geq$0.3 VÅ^{-1} both isomers align very strongly with the electric field, and the alignments of the different isomers are approximately the same. Looking at the distribution of charge arm lengths in these electric fields (Figure 8.11), these are the electric field strengths at which assignment of the isomers by charge arm length is not possible. This suggests that, even though there is some anion in the *trans* isomer, the charge arm has been stretched out, causing a smearing in the length distribution.

Table 8.8 (and Table 7.19) show there is an increase in the amount of *cis* isomer and a decrease in the amount of *trans* isomer as the electric field strength increases, however there is still a significant amount of *trans* isomer in higher electric fields. Given the significantly longer charge arm in the *cis* isomer, and the strong force applied from the electric fields, it was expected that there should be a greater preference for the anion to be in its *cis* isomer, especially at the very high electric field strengths. Therefore there must be a reason behind the presence of *trans* anions in high electric fields.

This is hypothesised to come not from a direct effect of the electric field upon the charge arm, but instead from the motion of the anions caused by the electric field. To investigate this, the motion of an anion along the z vector of the simulation box in the *cis* and *trans* isomers can be compared.

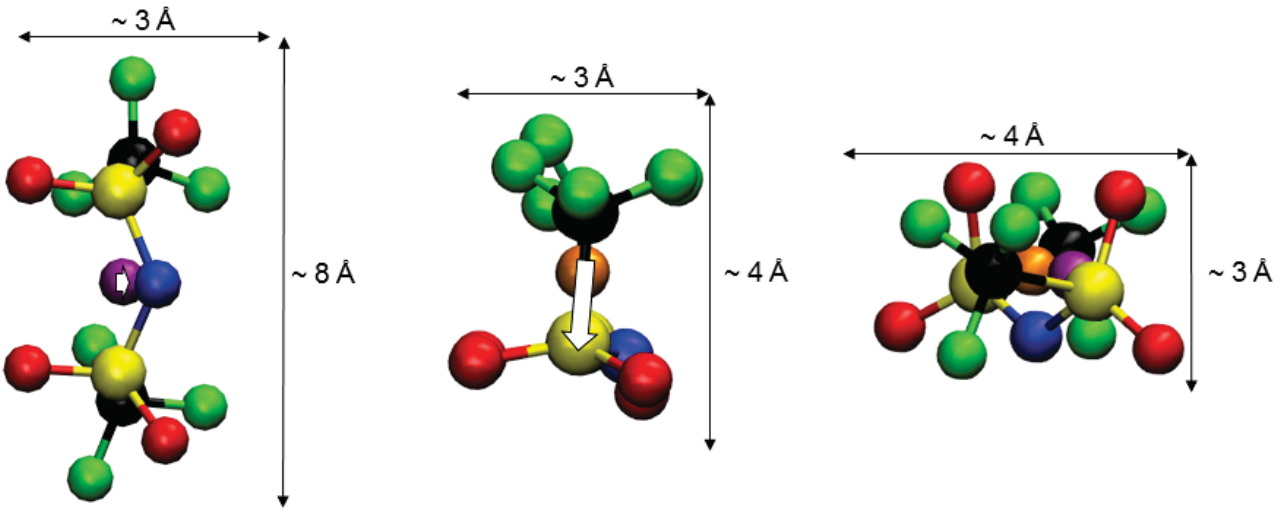

Figure 8.29: *Comparison of the leading surface and the area of this surface of: the cis isomer when diffusing parallel to the charge arm (left), the cis isomer when diffusing perpendicular to the charge arm (centre), and trans isomer (right).*

For the *cis* isomer, having its charge arm aligned with the electric field means the electric field is causing the anion to diffuse with its O, S, and N atoms facing the direction of motion, as shown on the left in Figure 8.29. While this does mean the torque from the electric field is minimised, this leads to a relatively large cross section of 24 Å^3, which will provide a significant

retardation force to motion in this manner.

Remaining in the *cis* isomer, the anion has a smaller cross section of 12 Å^3 on the face perpendicular to the S-N-S bonds, shown in the centre in Figure 8.29. If the electric field causes diffusion in this direction, the charge arm would be perpendicular to the electric field, therefore there will be a high torque on the anion from the electric field.

Considering the *trans* isomer, the charge arm is shorter which is not necessarily favourable in large electric field strengths. However, this means that there will be a lower torque force 'penalty' upon mis-alignment of the charge arm with the electric field. This means the ion can rotate so that it can have a smaller cross section (12 Å^3) along its direction of motion, without having a large torque force.

In summary, while the *cis* isomer has a long charge arm, when the electric field pulls the ion along the direction of the charge arm, there is a large surface area and thus retardation force to motion. Rotating to present a smaller surface area will lead to a large torque upon the charge arm, so is also unfavourable. For the *trans* isomer, while the charge arm is short, this means that there is a lower torque force upon rotation of the charge arm to present a smaller surface area. Therefore it is possible that a significant amount of *trans* isomer is present as it can diffuse faster.

Table 8.9: *Average displacement along the z direction per timestep (50 fs) of $[NTf_2]^-$ anions labelled as cis (dihedral<60°), trans (dihedral>135°) and the overall average in $[C_4C_1im][NTf_2]$ in each electric field.*

Field [VÅ^{-1}]	≤0.005	0.01	0.02	0.05	0.1	0.2	0.3	0.4	0.5
cis [pm]	≈0	-0.0173	-0.0434	-0.142	-0.442	-1.63	-3.33	-5.32	-7.60
trans [pm]	≈0	-0.0262	-0.0553	-0.167	-0.540	-2.01	-4.21	-6.63	-9.30
All [pm]	≈0	-0.0245	-0.0493	-0.153	-0.478	-1.74	-3.53	-5.61	-7.95

Table 8.10: *Average velocity along the z direction of $[NTf_2]^-$ anions labelled as cis (dihedral<60°), trans (dihedral>135°) and the overall average in $[C_4C_1im][NTf_2]$ in each electric field.*

Field [VÅ^{-1}]	≤0.005	0.01	0.02	0.05	0.1	0.2	0.3	0.4	0.5
cis [pm/ps]	≈0	-0.347	-0.870	-2.84	-8.84	-32.6	-66.7	-106.4	-152.1
trans [pm/ps]	≈0	-0.514	-1.10	-3.34	-10.8	-40.2	-84.2	-132.6	-185.8
All [pm/ps]	≈0	-0.487	-0.983	-3.05	-9.56	-34.9	-70.6	-112.2	-159.1

When calculating the average distance moved along the z direction in one timestep (Table 8.9), and the velocity in the z direction (Table 8.10), the *trans* isomer moves further and faster than the *cis* isomer in all electric fields. This means that it is more preferential for the anion to diffuse in the direction the electric field is pulling it in its *trans* isomer.

This leads to a 'competition' between the *cis* and *trans* isomers. In the *cis* isomer, the anion has a longer charge arm, which is preferable, however the anion diffuses slower. In the *trans* isomer,

the ion diffuses faster, which is preferable, however it has a shorter charge arm. Therefore there is a balance between the most favourable static orientation, and the most favourable dynamic orientation.

This does not occur in the absence of an electric field as the system is isotropic, and there is no force to dictate the direction in which the ions must rotate or diffuse along. Therefore the competition between favouring longer charge arms, a certain charge arm orientation and minimising surface area does not occur and the *cis* and *trans* isomers have the same velocity.

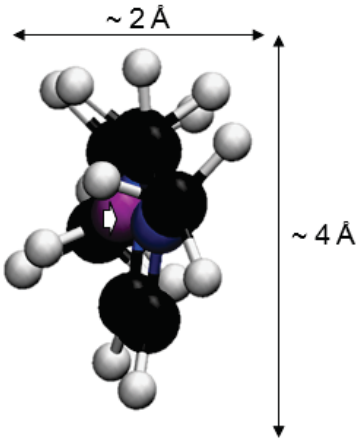

Figure 8.30: *Leading surface and the area of this surface for the cation when diffusing parallel to its charge arm.*

This does not occur in the cation as when diffusing parallel to the charge arm, both $[C_4C_1im]^+$ and $[C_8C_1im]^+$ have very small surface areas of $\approx$8 Å^3 (see Figure 8.30), therefore there is no competition between the charge arm torque force and a smaller surface area.

8.5 Charge Arms vs Dipoles

Due to the 'replacement' of a dipole with the charge arm, naturally the question arises of whether the charge arms act in a similar way to dipoles.

The results from the previous sections in this chapter suggest that this is not the case. In particular, the results in Section 8.4.1 on the similarity between the anions in the different ionic liquids support this. If the charge arms did act like dipoles, differences would be expected between the behaviour of the anions in electric fields.

Alongside this, when considering the different possible interactions between dipoles, and similar interactions in charge arms, there are some fairly obvious differences.

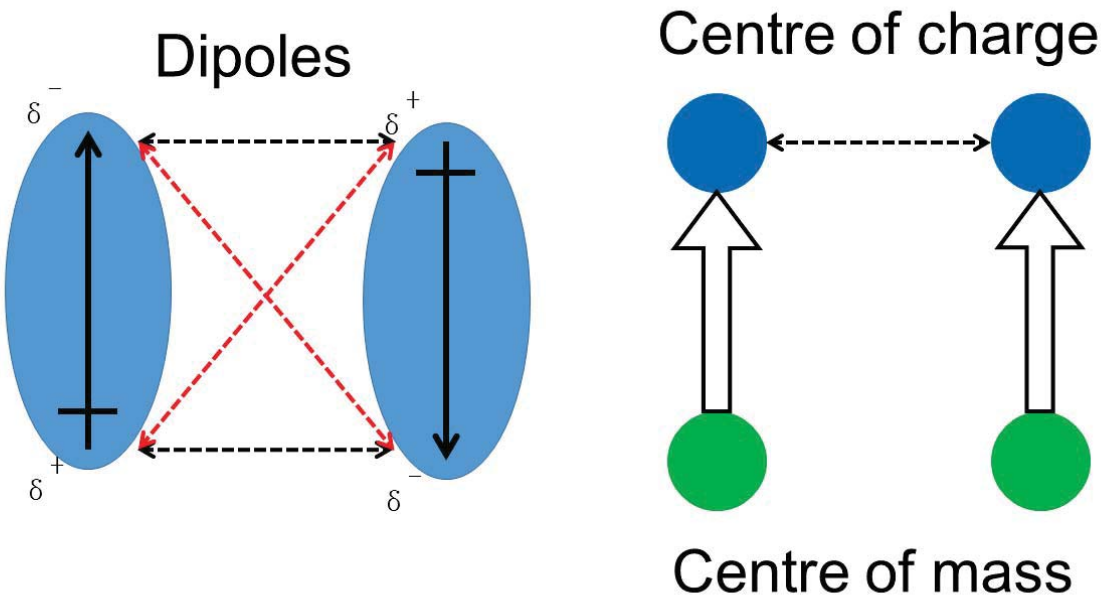

Figure 8.31: *Comparison of the types of interactions in dipoles and charge arms. Green circles represent the centres of mass, blue circles the centres of charge, and light blue ovals the dipoles. Black dashed lines indicate attractive interactions, red dashed lines indicate repulsive interactions.*

Using a very simple model, shown in Figure 8.31, dipole interactions can be broken down into four components. There are two attractive δ^+-δ^- components, one repulsive δ^+-δ^+ component and one repulsive δ^--δ^- component. These are all electrostatic interactions so are relatively strong intermolecular interactions, despite the low charge on the dipole. It is the combination of these attractive and repulsive interactions that leads to a favourable orientation of the dipoles, as shown in Figure 8.31.

Considering the charge arm interactions, unlike the interactions between the δ^+ and δ^- on different dipoles, there are no direct interactions between the centre of charge and the centre of

mass on different ions. In charge arm-charge arm interactions, only the strong coulombic interactions between the centres of charge are significant. These is much stronger than dipole-dipole interactions, however without the complementary interactions, it is unlikely that there will be a 'dipole-like' interaction between charge arms that would lead to an ion-ion orientational effect. It is possible that there is some slight preferential orientation of ions that are in close proximity, which then averages out in longer distances to a net-zero orientation across the bulk ionic liquid. This is likely to occur if the centres of mass are near each other, therefore the centres of charge are close enough to interact e.g. if two ions have their centres of mass close together then their centres of charge will interact. In this case, the attraction/repulsion of the centres of charge can lead to a preferential alignment/misalignment respectively.

To investigate this, the distance between the ion centres of mass, and the angles of the charge arms with respect to each other are show in histograms against each other in Figures 8.32-8.37. It must be noted that, within these results, there is a possibility that there is also a complementary or competing steric effect. For example, it may be case that a 'dipole-like' charge arm interaction exists and prefers two ions to align with each other, with an angle of 0°. However, there may be a competing steric effect that prefers the same two ions to mis-align with each other, with an angle of 180°. This would lead to an enhancing or dampening of the charge arm interaction, depending upon whether the steric effect was complementary or competing respectively.

Equally, such an effect could lead to the appearance of an apparent dipole-like charge arm interaction that does not exist.

Unfortunately, it is not possible to determine if such a steric effect exists in these ionic liquids with these simulations, how strong these may be, or what effect this has. Therefore the results will be discussed assuming that there are no steric effects.

The way to determine if a steric effects exist, would be to run a simulation of these ionic liquids without a charge arm. This would be difficult to achieve as to remove the charge arms, the charges should be adjusted so that the overall charge on both ions is zero. However this would lead to completely different system, therefore any steric effect seen in this simulation may not be relevant to the ionic liquids.

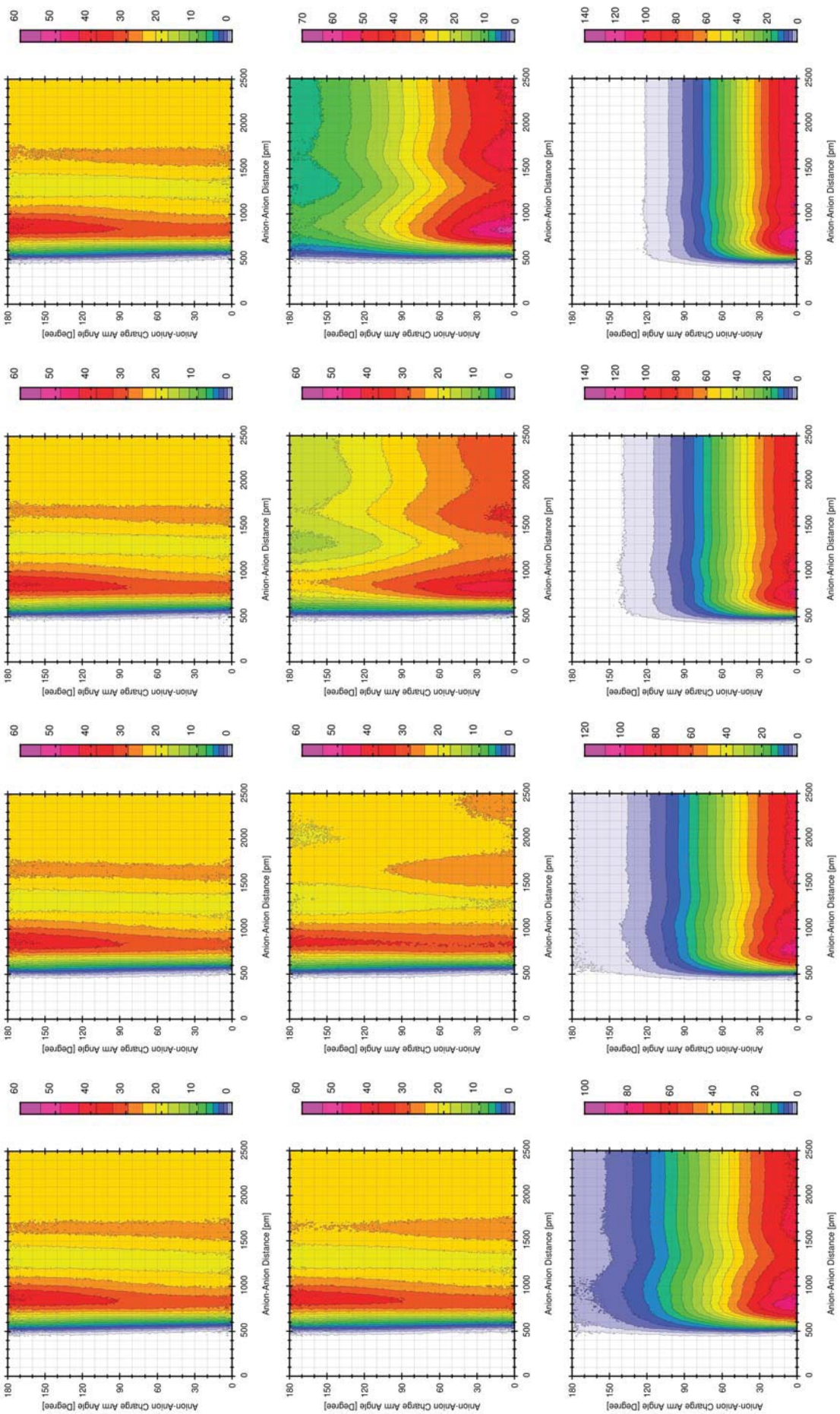

Figure 8.32: *2D histogram of the distance between the centres of mass of two $[NTf_2]^-$ and the angle between their charge arms in $[C_4C_1im][NTf_2]$. Histograms are normalised to an integral of 10000. The electric fields are, from top left reading across, 0.000 VÅ^{-1}, 0.001 VÅ^{-1}, 0.002 VÅ^{-1}, 0.005 VÅ^{-1}, 0.01 VÅ^{-1}, 0.02 VÅ^{-1}, 0.05 VÅ^{-1}, 0.1 VÅ^{-1}, 0.2 VÅ^{-1}, 0.3 VÅ^{-1}, 0.4 VÅ^{-1}, 0.5 VÅ^{-1}.*

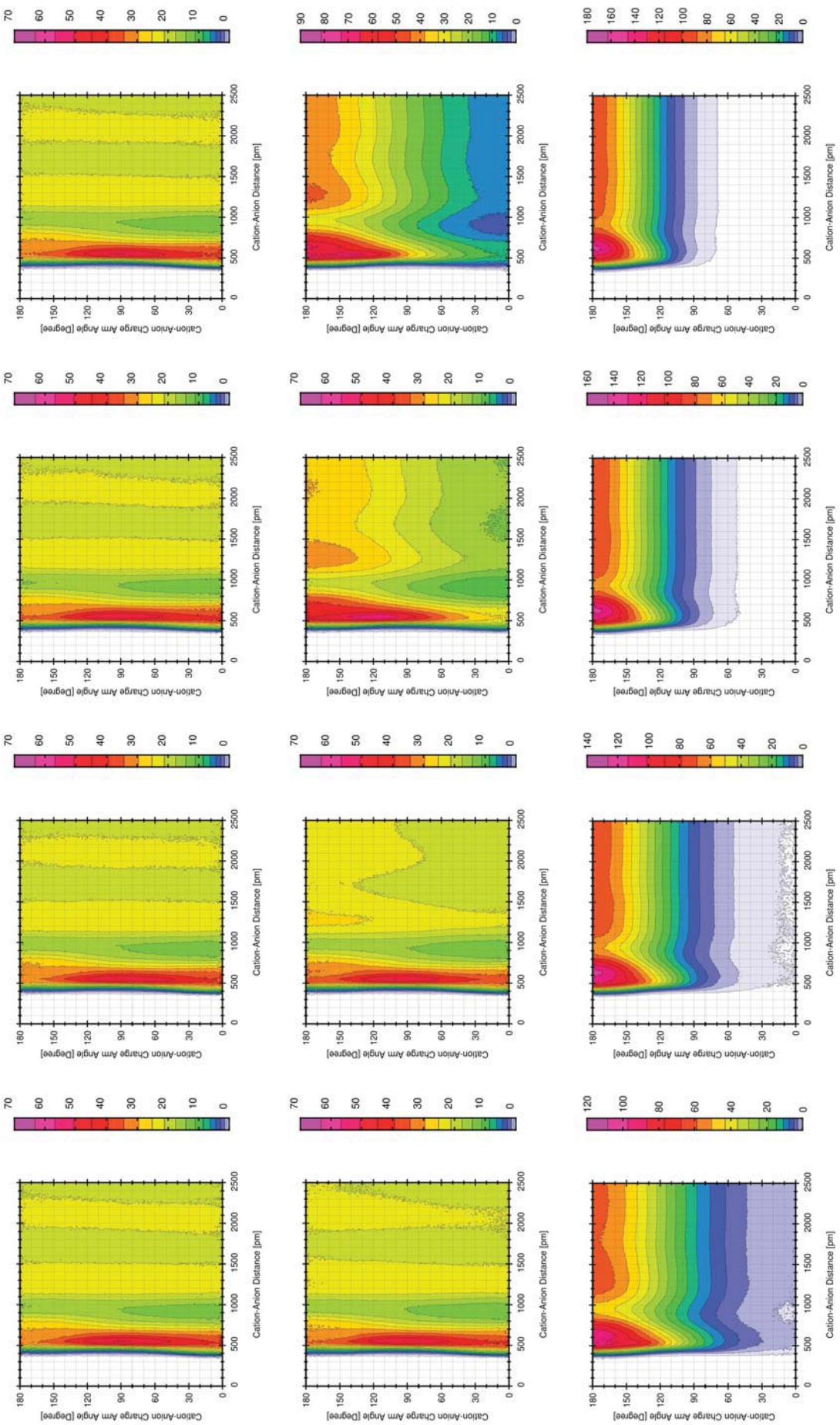

Figure 8.33: *2D histogram of the distance between the centres of mass of a $[NTf_2]^-$ and a $[C_4C_1im]^+$ and the angle between their charge arms in $[C_4C_1im][NTf_2]$. Histograms are normalised to an integral of 10000. The electric fields are, from top left reading across, 0.000 VÅ^{-1}, 0.001 VÅ^{-1}, 0.002 VÅ^{-1}, 0.005 VÅ^{-1}, 0.01 VÅ^{-1}, 0.02 VÅ^{-1}, 0.05 VÅ^{-1}, 0.1 VÅ^{-1}, 0.2 VÅ^{-1}, 0.3 VÅ^{-1}, 0.4 VÅ^{-1}, 0.5 VÅ^{-1}.*

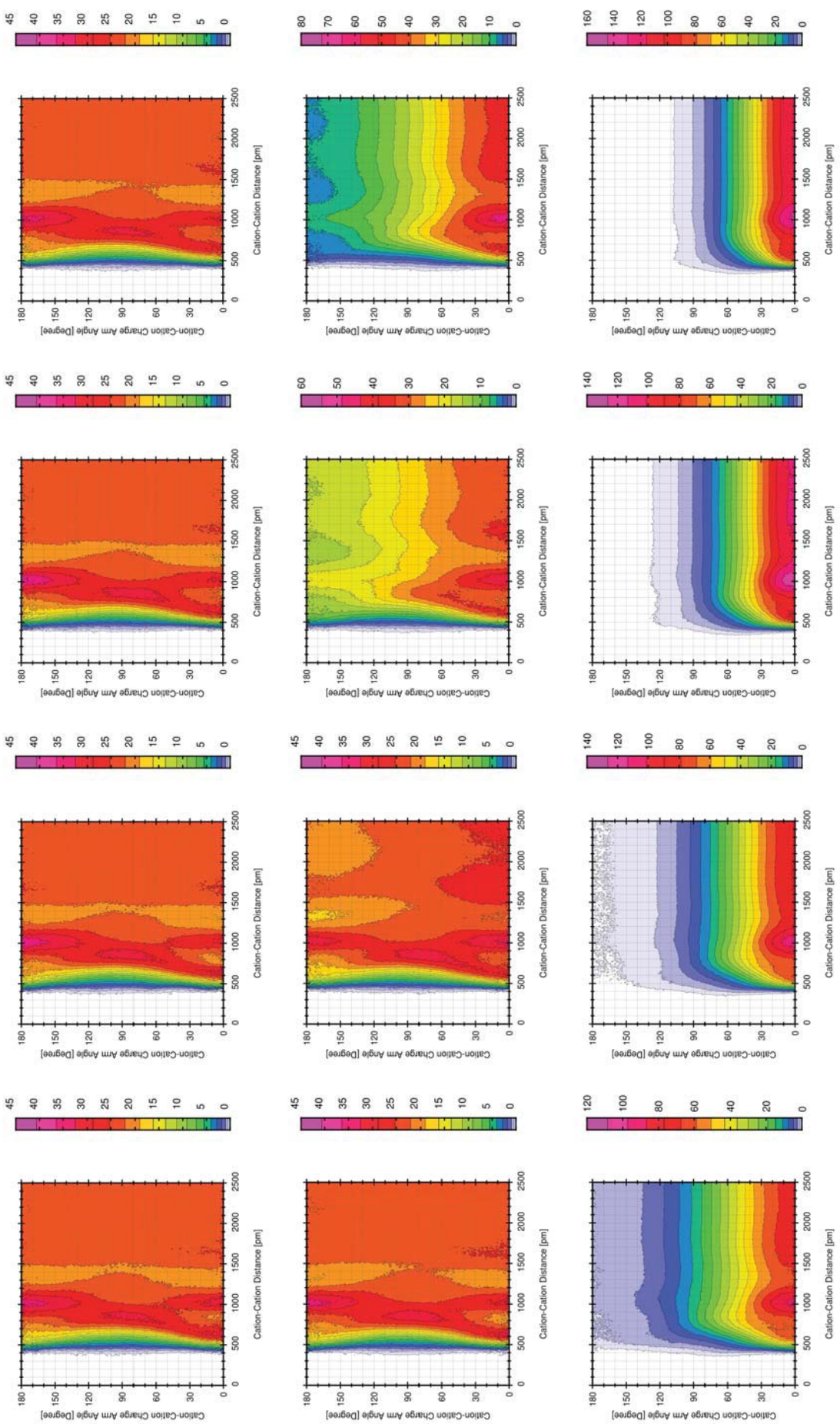

Figure 8.34: *2D histogram of the distance between the centres of mass of two $[C_4C_1im]^+$ and the angle between their charge arms in $[C_4C_1im][NTf_2]$. Histograms are normalised to an integral of 10000. The electric fields are, from top left reading across, 0.000 VÅ^{-1}, 0.001 VÅ^{-1}, 0.002 VÅ^{-1}, 0.005 VÅ^{-1}, 0.01 VÅ^{-1}, 0.02 VÅ^{-1}, 0.05 VÅ^{-1}, 0.1 VÅ^{-1}, 0.2 VÅ^{-1}, 0.3 VÅ^{-1}, 0.4 VÅ^{-1}, 0.5 VÅ^{-1}.*

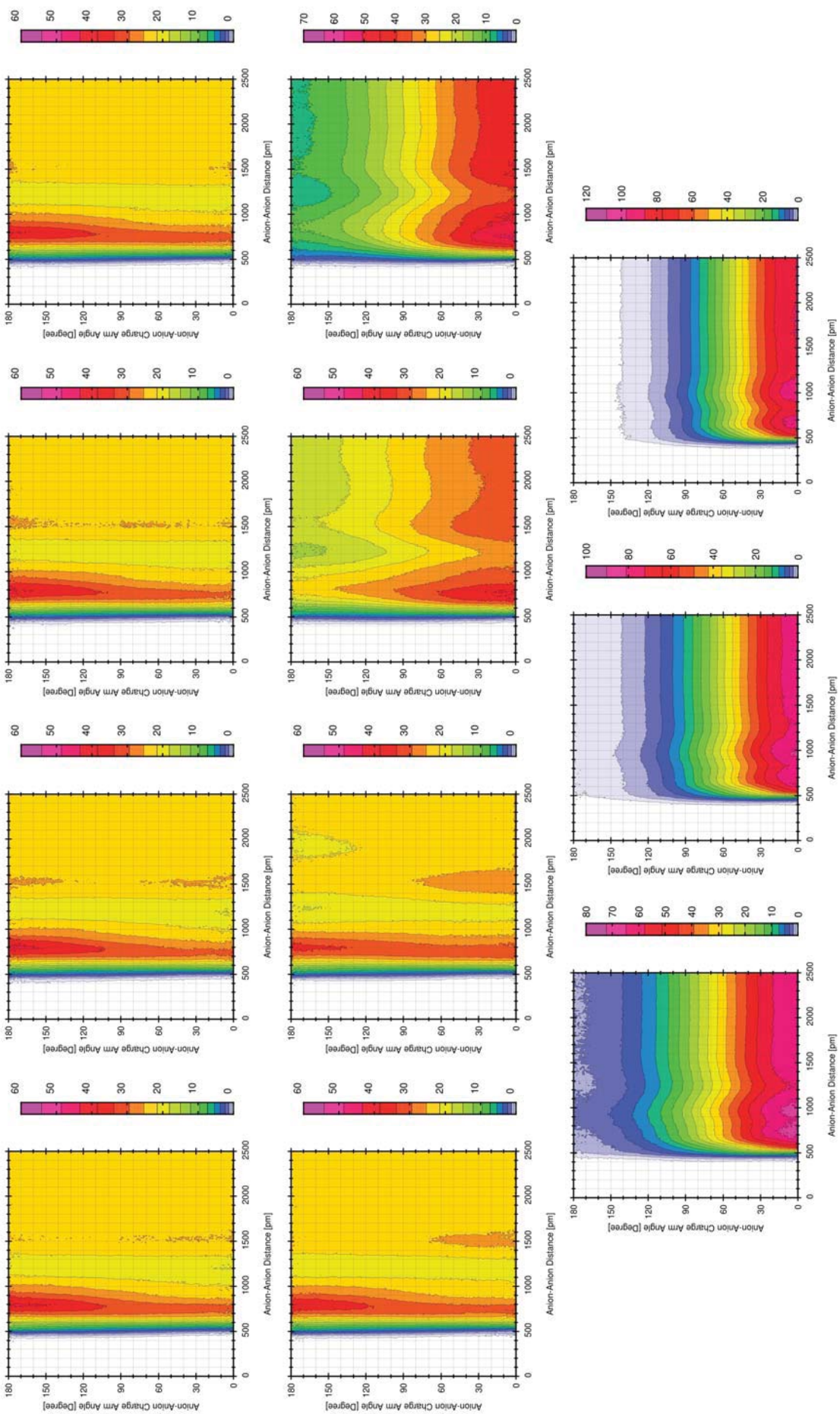

Figure 8.35: *2D histogram of the distance between the centres of mass of two $[NTf_2]^-$ and the angle between their charge arms in $[C_8C_1im][NTf_2]$. Histograms are normalised to an integral of 10000. The electric fields are, from top left reading across, 0.000 VÅ^{-1}, 0.001 VÅ^{-1}, 0.002 VÅ^{-1}, 0.005 VÅ^{-1}, 0.01 VÅ^{-1}, 0.02 VÅ^{-1}, 0.05 VÅ^{-1}, 0.1 VÅ^{-1}, 0.2 VÅ^{-1}, 0.3 VÅ^{-1}, 0.4 VÅ^{-1}.*

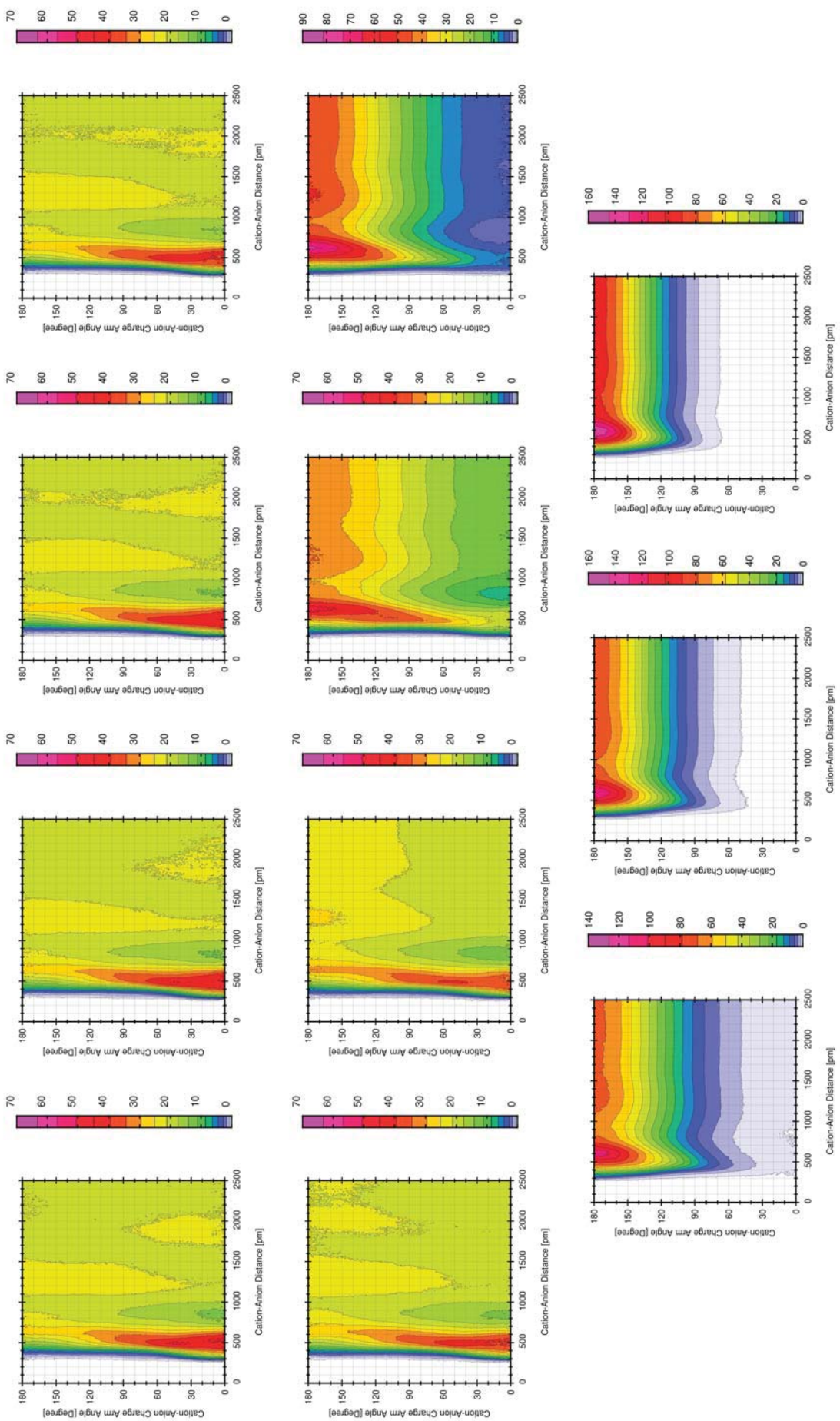

Figure 8.36: *2D histogram of the distance between the centres of mass of a $[NTf_2]^-$ and a $[C_8C_1im]^+$ and the angle between their charge arms in $[C_8C_1im][NTf_2]$. Histograms are normalised to an integral of 10000. The electric fields are, from top left reading across, 0.000 VÅ^{-1}, 0.001 VÅ^{-1}, 0.002 VÅ^{-1}, 0.005 VÅ^{-1}, 0.01 VÅ^{-1}, 0.02 VÅ^{-1}, 0.05 VÅ^{-1}, 0.1 VÅ^{-1}, 0.2 VÅ^{-1}, 0.3 VÅ^{-1}, 0.4 VÅ^{-1}.*

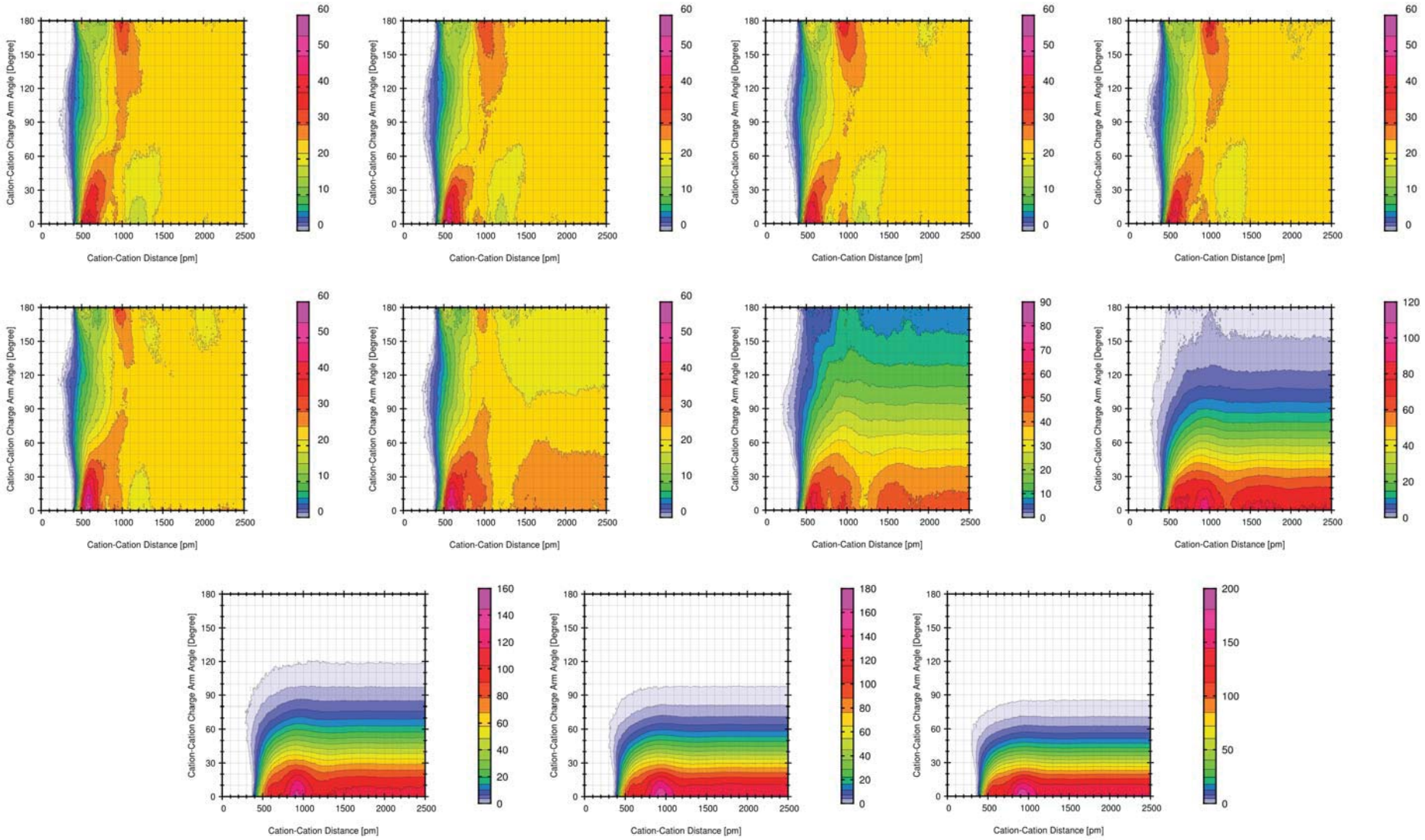

Figure 8.37: *2D histogram of the distance between the centres of mass of two $[C_8C_1im]^+$ and the angle between their charge arms in $[C_8C_1im][NTf_2]$. Histograms are normalised to an integral of 10000. The electric fields are, from top left reading across, 0.000 VÅ^{-1}, 0.001 VÅ^{-1}, 0.002 VÅ^{-1}, 0.005 VÅ^{-1}, 0.01 VÅ^{-1}, 0.02 VÅ^{-1}, 0.05 VÅ^{-1}, 0.1 VÅ^{-1}, 0.2 VÅ^{-1}, 0.3 VÅ^{-1}, 0.4 VÅ^{-1}.*

From these graphs, it can be seen that in electric fields of 0.05 VÅ^{-1} and above the distribution and alignment of the charge arms is strongly influenced by the electric field. Therefore this discussion and comparison will be concerned with only the electric fields <0.05 VÅ^{-1}.

Looking at the histograms between two $[NTf_2]^-$ anions, these are very similar between the two ionic liquids (Figures 8.32 and 8.35). There is no preferential angular orientation of the charge arm vectors when the centres of mass are >1200 pm apart in both ionic liquids. When the centres of mass are <1200 pm apart, there is a greater distribution of charge arms with angles between them of 180°. This shows that, in both ionic liquids, when the centres of mass of two anions are near each other, their charge arms more likely point in opposite directions.

When increasing the electric field to 0.02 VÅ^{-1}, there is an increase in the number of charge arms aligning in the same direction, which is an effect of the electric field (Figure 8.27). These 2D histograms show that this alignment occurs in anions whose centres of mass are >1200 pm apart, and anions whose centres of mass are <1200 pm apart remain pointing in opposite directions in both ionic liquids.

The histograms between cations and anions are slightly different to each other. For the relationship between $[C_4C_1im]^+$ and $[NTf_2]^-$ (Figure 8.33), there is no preferential angular orientation of the charge arm vectors when the centres of mass are >700 pm apart. When the centres of mass are <700 pm apart, there is a preference for the charge arms of $[C_4C_1im]^+$ and $[NTf_2]^-$ to be at an angle of 90°. The reason as to why they prefer to be at 90° is not obvious, however this is not expected to be an effect of charge arm.

For the relationship between the charge arms of $[C_8C_1im]^+$ and $[NTf_2]^-$ (Figure 8.36), there is a more complex relationship between the distance between the centres of mass and angle between the charge arm. When the centre of masses of $[C_8C_1im]^+$ and $[NTf_2]^-$ are <700 pm apart, there is also a preferential angular orientation of the charge arm vectors, however the preferential angle between the charge arms is <60°, indicating a preference for the charge arms to align with each other when their centres of mass are closer.

When the distance between the centres of mass is 700-1600 pm the preference shifts, and the charge arms seem to more likely misalign, with the most common angles being >90°. Then at distances of >1600 pm this changes again and the charge arms more often have angles <90°.

For both of the cation-anion charge arm histograms, the shorter centre of mass distance orientations are less affected by the electric field than the centres of mass that are at greater distances. This is similar to the $[NTf_2]^-$ ions with respect to themselves, where the overall change in the distribution of charge arm orientation comes from charge arms with greater separation between their centres of mass.

The histograms between cations are very different in the different ionic liquids. Considering the relationship between the centre of mass and angle distribution for two $[C_4C_1im]^+$ ions (Figure 8.34), there is a maximum in the histogram at 1000 pm and 180°. This indicates that some repulsion of the centres of charge is possible, however this is not a very strong maximum, as the overall distribution is very shallow. There are also another maxima at ≈800 pm and 90°, and at 1000 pm and 0°, therefore the correlation between the centre of mass and centre of charge is very weak for this cation overall.

Increasing the electric field causes a greater amount of charge arms to take angles of 0°, and this effect is more pronounced in charge arms with greater centre of mass distances. However, there is also a decrease in the charge arms at shorter distances having angles of 180 °, further evidence that the charge arm-charge arm interaction is weak between two $[C_4C_1im]^+$ ions.

The centre of mass distance against charge arm orientation for two $[C_8C_1im]^+$ ions (Figure 8.37) shows that when the centres of mass are closer, the charge arms for $[C_8C_1im]^+$ are more likely to be aligned with each other (angle of 0°) than mis-aligned (angle of 180°). This is the opposite of what would be expected if the centres of charge where to repel each other. There is a peak at 180°, however this occurs at a greater separation of centres of mass than the peak at 0°, and is smaller in height.

In summary, there is some evidence of dipole-like behaviour in the ions in $[C_4C_1im][NTf_2]$ and $[C_8C_1im][NTf_2]$. This comes from the $[NTf_2]^-$ charge arms pointing in opposite directions when the centres of mass are close together, i.e. the centres of charge repel each other. The charge arms of $[C_8C_1im]^+]$ and $[NTf_2]^-$ show a similar interaction, where if the centres of mass are close enough, the ions align with each other i.e. the centres of charge attract each other. This is not a long distance interaction, as expected, with centres of mass at distances of >1200 pm not showing a preferential alignment.

There are also some charge arms that show little or no evidence of charge arm-charge arm interactions, such as between $[C_4C_1im]^+$ and $[NTf_2]^-$ as well as between two $[C_8C_1im]^+$ ions. This presents an interesting avenue for future work, wherein the relationship between ions with different charge arm lengths can be more thoroughly investigated to determine how much, if any, impact potential dipole-like charge arm interactions affect short range structuring in ionic liquids.

Chapter 9

Thesis Summary

When considering the entirety of this thesis, there are a few important conclusions across the chapters which warrant summarising herein.

When studying molecular rotors in ionic liquids, there is not a simple explanations behind the trends observed between the rotor lifetime and bulk viscosity. This is due to the molecular rotors reporting upon the microviscosity of the ionic liquids (the viscosity of the different regions of the ionic liquids) instead of the bulk viscosity. Therefore the region where the rotor resides within the ionic liquid is very important, hence why a systematic study of the relationship between the change in the lifetime of the rotor and bulk viscosity of various ionic liquids was performed.

It was found that the neutral rotor preferred to segregate into the non-polar domain of the ionic liquids. When a large enough non-polar domain was present to fully encapsulate the rotor, the lifetime of the rotor was less sensitive to changes in the bulk viscosity than when the rotor could not segregate. This also indicates that when the rotor could not segregate, it had to sample some polar domains. The positive rotor was found to prefer to segregate into the polar region, specifically into the anions. This led to no correlation between rotor lifetime and bulk viscosity when modifying the bulk viscosity by changing the anion and keeping the cation constant. However, changing the bulk viscosity by changing the cation with a constant anion, as well as changing the temperature led to correlations. These indicated partial sampling of the cationic/non-polar domains in ionic liquids where the dye could not segregate into the anionic domain, as well as an indication of a temperature-dependence of the dye lifetime that has not been investigated yet.

When observing the same rotors in ionic liquids in an electric field, some very peculiar behaviour

was observed. In some cases, there was depletion of the rotors from the focal volume, even at 50 μm away from the electrode, and persisting for hours in time. This was attributed to electrophoresis of the rotors towards the electrodes, due to the way that recovery occurred as well as there being literature precedence for favourable incorporation of molecules larger than the ionic liquid near electrodes. This electrophoresis explains the slow nature behind the change in counts, as it is a diffusive process and rotors in ionic liquids have very slow diffusion coefficients.[77,144]

When there was enough measurable rotor in the focal volume, an increase in the viscosity, as reported by both of the rotors, was observed up to 25 μm, and this persisted for similarly long times as the electrophoresis. This was hypothesised to come from an increase in the density of the ionic liquid, or a change in the rotational dynamics of the ions in the ionic liquid, or perhaps both.

When performing molecular dynamics simulations on ionic liquids in uniform electric fields to find explanations behind these results, large changes in the diffusion and drift of the ions are observed, due to the large electric fields which need to be applied to see effects of the electric field and the lack of a boundary upon which structure could build up. In low electric field strengths there is only a drift of the ions, and no change to the diffusive nature of the ions. In higher electric fields the diffusive nature of the ions changed, and this was attributed to a breakdown of the the ion cages which led to less retardation to the motion of the ions.

The structure of the ionic liquid as a whole changes in the stronger electric fields (which cause the change to the diffusive nature of the ions) with a homogenisation of the structure i.e. a loss of structural features. However, these changes are not large changes. Large structural changes are seen in the conformation and orientation of the ions.

The rationalisation of the orientational and rotational behaviour of the ions is explained through the charge arm. This is a relatively new concept, introduced to replace a dipole in ions. Through the charge arm, the conformational changes in the ions as well as the change to their rotational alignment with electric fields are explained. There is also a discussion of the differences between a dipole and a charge arm, with the hopes that this can lead to a more thorough investigation of the charge arm, specifically possible applications of the charge arms, and any potential intrinsic properties of ions described by this concept.

Bibliography

[1] R. Clark, M. A. Nawawi, A. Dobre, D. Pugh, Q. Liu, A. P. Ivanov, A. J. P. White, J. B. Edel, M. K. Kuimova, A. J. S. McIntosh and T. Welton, *Chemical Science*, 2020, **68**, 6121 – 6133.

[2] R. Clark, M. von Domaros, A. J. S. McIntosh, A. Luzar, B. Kirchner and T. Welton, *The Journal of Chemical Physics*, 2019, **151**, 164503.

[3] S. Gehrke, M. von Domaros, R. Clark, O. Hollóczki, M. Brehm, T. Welton, A. Luzar and B. Kirchner, *Faraday Discussions*, 2018, **206**, 219–245.

[4] J. S. Wilkes, J. A. Levisky, R. A. Wilson and C. L. Hussey, *Inorganic Chemistry*, 1982, **21**, 1263–1264.

[5] J. S. Wilkes and M. J. Zaworotko, *Journal of the Chemical Society, Chemical Communications*, 1992, 965.

[6] M. G. Freire, C. M. S. S. Neves, I. M. Marrucho, J. A. P. Coutinho and A. M. Fernandes, *The Journal of Physical Chemistry A*, 2010, **114**, 3744–3749.

[7] M. Freemantle, *Chemical & Engineering News*, 1998, **76**, 32–37.

[8] M. Bier and S. Dietrich, *Molecular Physics*, 2010, **108**, 211–214.

[9] Y. U. Paulechka, D. H. Zaitsau, G. J. Kabo and A. A. Strechan, *Thermochimica Acta*, 2005, **439**, 158–160.

[10] M. Galiński, A. Lewandowski and I. Stępniak, *Electrochimica Acta*, 2006, **51**, 5567–5580.

[11] Z. Lei, C. Dai and B. Chen, *Chemical Reviews*, 2014, **114**, 1289–1326.

[12] T. Schubert, S. Zein El Abedin, A. P. Abbott, K. J. McKenzie, K. S. Ryder and F. Endres, *Electrodeposition from Ionic Liquids*, 2008, 83–123.

[13] T. Welton, *Chemical Reviews*, 1999, **99**, 2071–2084.

[14] J. F. Wishart, *Energy & Environmental Science*, 2009, **2**, 956.

[15] U. Schröder, J. D. Wadhawan, R. G. Compton, F. Marken, P. A. Z. Suarez, C. S. Consorti, R. F. de Souza and J. Dupont, *New Journal of Chemistry*, 2000, **24**, 1009–1015.

[16] H. Tokuda, K. Hayamizu, K. Ishii, M. A. B. H. Susan and M. Watanabe, *The Journal of Physical Chemistry B*, 2005, **109**, 6103–6110.

[17] Z. Hu and C. J. Margulis, *Proceedings of the National Academy of Sciences*, 2006, **103**, 831–836.

[18] S. M. Urahata and M. C. C. Ribeiro, *The Journal of Chemical Physics*, 2004, **120**, 1855–1863.

[19] C. J. Margulis, *Molecular Physics*, 2004, **102**, 829–838.

[20] Y. Wang and G. A. Voth, *Journal of the American Chemical Society*, 2005, **127**, 12192–12193.

[21] J. N. Canongia Lopes and A. A. Pádua, *Journal of Physical Chemistry B*, 2006, **110**, 3330–3335.

[22] J. N. Canongia Lopes, M. F. Costa Gomes and A. A. H. Pádua, *The Journal of Physical Chemistry B*, 2006, **110**, 16816–16818.

[23] L. M. N. B. F. Santos, J. N. Canongia Lopes, J. A. P. Coutinho, J. M. S. S. Esperança, L. R. Gomes, I. M. Marrucho and L. P. N. Rebelo, *Journal of the American Chemical Society*, 2007, **129**, 284–285.

[24] K. Shimizu, C. E. Bernardes and J. N. Canongia Lopes, *Journal of Physical Chemistry B*, 2014, **118**, 567–576.

[25] K. Shimizu, C. E. S. Bernardes, A. Triolo and J. N. Canongia Lopes, *Physical Chemistry Chemical Physics*, 2013, **15**, 16256.

[26] H. K. Kashyap, C. S. Santos, H. V. R. Annapureddy, N. S. Murthy, C. J. Margulis and E. W. Castner, Jr, *Faraday Discuss.*, 2012, **154**, 133–143.

[27] A. Triolo, O. Russina, H. J. Bleif and E. Di Cola, *Journal of Physical Chemistry B*, 2007, **111**, 4641–4644.

[28] A. Triolo, O. Russina, R. Caminiti, H. Shirota, H. Y. Lee, C. S. Santos, N. S. Murthy and E. W. Castner, Jr, *Chemical Communications*, 2012, **48**, 4959.

[29] Y. Shen, D. F. Kennedy, T. L. Greaves, A. Weerawardena, R. J. Mulder, N. Kirby, G. Song and C. J. Drummond, *Physical Chemistry Chemical Physics*, 2012, **14**, 7981.

[30] O. Hollõczki, M. Macchiagodena, H. Weber, M. Thomas, M. Brehm, A. Stark, O. Russina, A. Triolo and B. Kirchner, *ChemPhysChem*, 2015, **16**, 3325–3333.

[31] M. A. A. Rocha, C. F. R. A. C. Lima, L. R. Gomes, B. Schröder, J. A. P. Coutinho, I. M. Marrucho, J. M. S. S. Esperança, L. P. N. Rebelo, K. Shimizu, J. N. C. Lopes and L. M. N. B. F. Santos, *Journal of Physical Chemistry B*, 2011, **115**, 10919–10926.

[32] A. M. Moschovi and V. Dracopoulos, *Journal of Molecular Liquids*, 2015, **210**, 189–199.

[33] A. Kaintz, G. Baker, A. Benesi and M. Maroncelli, *Journal of Physical Chemistry B*, 2013, **117**, 11697–11708.

[34] J. C. Araque, S. K. Yadav, M. Shadeck, M. Maroncelli and C. J. Margulis, *Journal of Physical Chemistry B*, 2015, **119**, 7015–7029.

[35] G. Feng, M. Chen, S. Bi, Z. A. H. Goodwin, E. B. Postnikov, N. Brilliantov, M. Urbakh and A. A. Kornyshev, *Physical Review X*, 2019, **9**, 021024.

[36] M. Sha, X. Ma, N. Li, F. Luo, G. Zhu and M. D. Fayer, *The Journal of Chemical Physics*, 2019, **151**, 154502.

[37] W. D. Amith, J. C. Araque and C. J. Margulis, *The Journal of Physical Chemistry Letters*, 2020, **11**, 2062–2066.

[38] A. Elbourne, K. Voïtchovsky, G. G. Warr and R. Atkin, *Chemical Science*, 2015, **6**, 527–536.

[39] R. Hagiwara, K. Matsumoto, J. Hwang and T. Nohira, *The Chemical Record*, 2019, **19**, 758–770.

[40] H.-M. Kwon, M. L. Thomas, R. Tatara, Y. Oda, Y. Kobayashi, A. Nakanishi, K. Ueno, K. Dokko and M. Watanabe, *ACS Applied Materials & Interfaces*, 2017, **9**, 6014–6021.

[41] A. Balducci, U. Bardi, S. Caporali, M. Mastragostino and F. Soavi, *Electrochemistry Communications*, 2004, **6**, 566–570.

[42] A. Eftekhari, *Energy Storage Materials*, 2017, **9**, 47–69.

[43] Z. Lei, Z. Liu, H. Wang, X. Sun, L. Lu and X. S. Zhao, *Journal of Materials Chemistry A*, 2013, **1**, 2313–2321.

[44] T. Romann, E. Anderson, P. Pikma, H. Tamme, P. Möller and E. Lust, *Electrochemistry Communications*, 2017, **74**, 38–41.

[45] R. Hayes, N. Borisenko, M. K. Tam, P. C. Howlett, F. Endres and R. Atkin, *The Journal of Physical Chemistry C*, 2011, **115**, 6855–6863.

[46] R. Atkin, N. Borisenko, M. Drüschler, S. Z. El Abedin, F. Endres, R. Hayes, B. Huber and B. Roling, *Physical Chemistry Chemical Physics*, 2011, **13**, 6849.

[47] P. Atkins and J. De Paula, *Atkins' Physical Chemistry*, Oxford University Press, 10th edn, 2014, p. 1008.

[48] M. A. Gebbie, M. Valtiner, X. Banquy, E. T. Fox, W. A. Henderson and J. N. Israelachvili, *Proceedings of the National Academy of Sciences*, 2013, **110**, 9674–9679.

[49] M. A. Gebbie, H. A. Dobbs, M. Valtiner and J. N. Israelachvili, *Proceedings of the National Academy of Sciences*, 2015, **112**, 7432–7437.

[50] A. M. Smith, A. A. Lee and S. Perkin, *Journal of Physical Chemistry Letters*, 2016, **7**, 2157–2163.

[51] R. M. Espinosa-Marzal, A. Arcifa, A. Rossi and N. D. Spencer, *The Journal of Physical Chemistry Letters*, 2014, **5**, 179–184.

[52] H.-W. Cheng, P. Stock, B. Moeremans, T. Baimpos, X. Banquy, F. U. Renner and M. Valtiner, *Advanced Materials Interfaces*, 2015, **2**, 1500159.

[53] X. Mao, P. Brown, C. Červinka, G. Hazell, H. Li, Y. Ren, D. Chen, R. Atkin, J. Eastoe, I. Grillo, A. A. H. Padua, M. F. Costa Gomes and T. A. Hatton, *Nature Materials*, 2019, **18**, 1350–1357.

[54] M. Han and R. M. Espinosa-Marzal, *The Journal of Physical Chemistry C*, 2018, **122**, 21344–21355.

[55] M. A. Gebbie, M. Valtiner, X. Banquy, W. A. Henderson and J. N. Israelachvili, *Proceedings of the National Academy of Sciences*, 2013, **110**, E4122–E4122.

[56] M. A. Gebbie, A. M. Smith, H. A. Dobbs, A. A. Lee, G. G. Warr, X. Banquy, M. Valtiner, M. W. Rutland, J. N. Israelachvili, S. Perkin and R. Atkin, *Chemical Communications*, 2017, **53**, 1214–1224.

[57] A. A. Lee, C. S. Perez-Martinez, A. M. Smith and S. Perkin, *Physical Review Letters*, 2017, **119**, 026002.

[58] A. A. Lee, D. Vella, S. Perkin and A. Goriely, *Journal of Physical Chemistry Letters*, 2015, **6**, 159–163.

[59] N. Nishi, Y. Hirano, T. Motokawa and T. Kakiuchi, *Physical Chemistry Chemical Physics*, 2013, **15**, 11615.

[60] M. Chu, M. Miller, T. Douglas and P. Dutta, *Journal of Physical Chemistry C*, 2017, **121**, 3841–3845.

[61] A. Uysal, H. Zhou, G. Feng, S. S. Lee, S. Li, P. Fenter, P. T. Cummings, P. F. Fulvio, S. Dai, J. K. McDonough and Y. Gogotsi, *The Journal of Physical Chemistry C*, 2014, **118**, 569–574.

[62] Y. Yasui, Y. Kitazumi, R. Ishimatsu, N. Nishi and T. Kakiuchi, *The Journal of Physical Chemistry B*, 2009, **113**, 3273–3276.

[63] C. S. Perez-Martinez and S. Perkin, *Soft Matter*, 2019, **15**, 4255–4265.

[64] R. S. Anaredy and S. K. Shaw, *Langmuir*, 2016, **32**, 5147–5154.

[65] C. Merlet, B. Rotenberg, P. A. Madden and M. Salanne, *Physical Chemistry Chemical Physics*, 2013, **15**, 15781.

[66] J. Jiang, D. Cao, D.-e. Jiang and J. Wu, *Journal of Physics: Condensed Matter*, 2014, **26**, 284102.

[67] C. Péan, C. Merlet, B. Rotenberg, P. A. Madden, P. L. Taberna, B. Daffos, M. Salanne and P. Simon, *ACS Nano*, 2014, **8**, 1576–1583.

[68] J. Comtet, A. Niguès, V. Kaiser, B. Coasne, L. Bocquet and A. Siria, *Nature Materials*, 2017, **16**, 634–639.

[69] L. Kong, W. Huang and X. Wang, *Journal of Physics D: Applied Physics*, 2016, **49**, 225301.

[70] K. Motobayashi, K. Minami, N. Nishi, T. Sakka and M. Osawa, *The Journal of Physical Chemistry Letters*, 2013, **4**, 3110–3114.

[71] M. Drüschler, N. Borisenko, J. Wallauer, C. Winter, B. Huber, F. Endres and B. Roling, *Physical Chemistry Chemical Physics*, 2012, **14**, 5090.

[72] W. Zhou, Y. Xu and Y. Ouchi, *ECS Transactions*, 2013, **50**, 339–348.

[73] S. Makino, Y. Kitazumi, N. Nishi and T. Kakiuchi, *Electrochemistry Communications*, 2011, **13**, 1365–1368.

[74] A. J. Lucio and S. K. Shaw, *Analytical and Bioanalytical Chemistry*, 2018, 1–12.

[75] F. B. Sillars, S. I. Fletcher, M. Mirzaeian and P. J. Hall, *Physical Chemistry Chemical Physics*, 2012, **14**, 6094.

[76] M. V. Fedorov and A. A. Kornyshev, *Chemical Reviews*, 2014, **114**, 2978–3036.

[77] M. A. Nawawi, *PhD thesis*, Imperial College London, 2019.

[78] A. Dequidt, J. Devémy and A. A. Pádua, *Journal of Chemical Information and Modeling*, 2016, **56**, 260–268.

[79] J. N. Canongia Lopes, J. Deschamps and A. A. Pádua, *The Journal of Physical Chemistry B*, 2004, **108**, 2038–2047.

[80] G. Lamoureux and B. Roux, *Journal of Chemical Physics*, 2003, **119**, 3025–3039.

[81] C. E. S. Bernardes, K. Shimizu, J. N. C. Lopes, P. Marquetand, E. Heid, O. Steinhauser and C. Schröder, *Physical Chemistry Chemical Physics*, 2016, **18**, 1665–1670.

[82] S. Plimpton, *Journal of Computational Physics*, 1995, **117**, 1–19.

[83] W. Shinoda, M. Shiga and M. Mikami, *Physical Review B - Condensed Matter and Materials Physics*, 2004, **69**, 134103.

[84] G. Bussi, D. Donadio and M. Parrinello, *The Journal of Chemical Physics*, 2007, **126**, 014101.

[85] A. A. Pádua, *Fftool V1.0.0*, 2015, `https://www.zenodo.org/record/18618`.

[86] L. Martinez, R. Andrade, E. G. Birgin and J. M. Martínez, *Journal of Computational Chemistry*, 2009, **30**, 2157–2164.

[87] M. Vranes, S. Dozic, V. Djeric and S. Gadzuric, *Journal of Chemical and Engineering Data*, 2012, **57**, 1072–1077.

[88] M. Brehm and B. Kirchner, *Journal of Chemical Information and Modeling*, 2011, **51**, 2007–2023.

[89] W. Humphrey, A. Dalke and K. Schulten, *Journal of Molecular Graphics*, 1996, **14**, 33–38.

[90] Q. G. Zheng, H. Liu, Q. Xia, Q. S. Liu and L. Mou, *Acta Physico-Chimica Sinica*, 2017, **33**, 736–744.

[91] H. Tokuda, K. Hayamizu, K. Ishii, M. A. B. H. Susan and M. Watanabe, *Journal of Physical Chemistry B*, 2004, **108**, 16593–16600.

[92] H. Tokuda, K. Ishii, M. A. Susan, S. Tsuzuki, K. Hayamizu and M. Watanabe, *Journal of Physical Chemistry B*, 2006, **110**, 2833–2839.

[93] M. K. Kuimova, *Physical Chemistry Chemical Physics*, 2012, **14**, 12671.

[94] M. A. Haidekker and E. A. Theodorakis, *Journal of Biological Engineering*, 2010, **4**, 11.

[95] N. A. Hosny, C. Fitzgerald, A. Vyšniauskas, A. Athanasiadis, T. Berkemeier, N. Uygur, U. Pöschl, M. Shiraiwa, M. Kalberer, F. D. Pope and M. K. Kuimova, *Chemical Science*, 2016, **7**, 1357–1367.

[96] C. Rumble, K. Rich, G. He and M. Maroncelli, *The Journal of Physical Chemistry A*, 2012, **116**, 10786–10792.

[97] R. Guo, J. Yin, Y. Ma, Q. Wang and W. Lin, *Journal of Materials Chemistry B*, 2018, **6**, 2894–2900.

[98] L. A. Ernst, R. K. Gupta, R. B. Mujumdar and A. S. Waggoner, *Cytometry*, 1989, **10**, 3–10.

[99] W. West, S. Lovell and W. Cooper, *Photographic Science and Engineering*, 1970, **14**, 52–62.

[100] W. Cooper, S. Lovell and W. West, *Photographic Science and Engineering*, 1970, **14**, 184–191.

[101] D. O'Brien, T. Kelly and L. Costa, *Photographic Science and Engineering*, 1974, **18**, 76–84.

[102] S. Ghelli and G. Ponterini, *Journal of Molecular Structure*, 1995, **355**, 193–200.

[103] I. Baraldi, A. Carnevali, F. Momicchioli and G. Ponterini, *Spectrochimica Acta Part A: Molecular Spectroscopy*, 1993, **49**, 471–495.

[104] F. Momicchioli, I. Baraldi and G. Berthier, *Chemical Physics*, 1988, **123**, 103–112.

[105] K. G. Vladimirova, A. Y. Freidzon, A. A. Bagatur'yants, G. V. Zakharova, A. K. Chibisov and M. V. Alfimov, *High Energy Chemistry*, 2008, **42**, 275–282.

[106] R. Ziessel and A. Harriman, *Chemical Communications*, 2011, **47**, 611–631.

[107] A. Harriman, G. Izzet and R. Ziessel, *Journal of the American Chemical Society*, 2006, **128**, 10868–10875.

[108] A. Harriman, L. J. Mallon, S. Goeb, G. Ulrich and R. Ziessel, *Chemistry - A European Journal*, 2009, **15**, 4553–4564.

[109] T. Bura, P. Retailleau and R. Ziessel, *Angewandte Chemie International Edition*, 2010, **49**, 6659–6663.

[110] Z.-N. Sun, H.-L. Wang, F.-Q. Liu, Y. Chen, P. K. H. Tam and D. Yang, *Organic Letters*, 2009, **11**, 1887–1890.

[111] Z. Ekmekci, M. D. Yilmaz and E. U. Akkaya, *Organic Letters*, 2008, **10**, 461–464.

[112] R. Guliyev, S. Ozturk, E. Sahin and E. U. Akkaya, *Organic Letters*, 2012, **14**, 1528–1531.

[113] X. Cao, W. Lin, Q. Yu and J. Wang, *Organic Letters*, 2011, **13**, 6098–6101.

[114] T. W. Hudnall and F. P. Gabbaï, *Chemical Communications*, 2008, 4596.

[115] M. R. Rao, S. M. Mobin and M. Ravikanth, *Tetrahedron*, 2010, **66**, 1728–1734.

[116] S. Atilgan, T. Ozdemir and E. U. Akkaya, *Organic Letters*, 2008, **10**, 4065–4067.

[117] H. Chen, W. Gao, M. Zhu, H. Gao, J. Xue and Y. Li, *Chemical Communications*, 2010, **46**, 8389.

[118] S. C. Dodani, Q. He and C. J. Chang, *Journal of the American Chemical Society*, 2009, **131**, 18020–18021.

[119] X. Qi, E. J. Jun, L. Xu, S.-J. Kim, J. S. Joong Hong, Y. J. Yoon and J. Yoon, *The Journal of Organic Chemistry*, 2006, **71**, 2881–2884.

[120] S. C. Dodani, S. C. Leary, P. A. Cobine, D. R. Winge and C. J. Chang, *Journal of the American Chemical Society*, 2011, **133**, 8606–8616.

[121] S. Madhu, R. Kalaiyarasi, S. K. Basu, S. Jadhav and M. Ravikanth, *Journal of Materials Chemistry C*, 2014, **2**, 2534.

[122] N. Heiland, C. Cidarér, C. Rohr, M. Piescheck, J. Ahrens, M. Bröring and U. Schröder, *ChemSusChem*, 2017, **10**, 4215–4222.

[123] H. Lim, S. Seo, S. Pascal, Q. Bellier, S. Rigaut, C. Park, H. Shin, O. Maury, C. Andraud and E. Kim, *Scientific Reports*, 2016, **6**, 18867.

[124] P. Loison, N. A. Hosny, P. Gervais, D. Champion, M. K. Kuimova and J.-M. Perrier-Cornet, *Biochimica et Biophysica Acta*, 2013, **1828**, 2436–2443.

[125] Y. Wu, M. Štefl, A. Olzyńska, M. Hof, G. Yahioglu, P. Yip, D. R. Casey, O. Ces, J. Humpolíčková and M. K. Kuimova, *Physical Chemistry Chemical Physics*, 2013, **15**, 14986.

[126] M. Olšinová, P. Jurkiewicz, M. Pozník, R. Šachl, T. Prausová, M. Hof, V. Kozmík, F. Teplý, J. Svoboda and M. Cebecauer, *Physical Chemistry Chemical Physics*, 2014, **16**, 10688–10697.

[127] M. R. Dent, I. López-Duarte, C. J. Dickson, N. D. Geoghegan, J. M. Cooper, I. R. Gould, R. Krams, J. A. Bull, N. J. Brooks and M. K. Kuimova, *Physical Chemistry Chemical Physics*, 2015, **17**, 18393–18402.

[128] F. Bergström, I. Mikhalyov, P. Hägglöf, R. Wortmann, T. Ny and L. B. Johansson, *Journal of the American Chemical Society*, 2002, **124**, 196–204.

[129] M. A. H. Alamiry, E. Bahaidarah, A. Harriman, T. Bura and R. Ziessel, *RSC Advances*, 2012, **2**, 9851.

[130] M. A. H. Alamiry, A. C. Benniston, G. Copley, K. J. Elliott, A. Harriman, B. Stewart and Y.-G. Zhi, *Chemistry of Materials*, 2008, **20**, 4024–4032.

[131] M. K. Kuimova, G. Yahioglu, J. A. Levitt and K. Suhling, *Journal of the American Chemical Society*, 2008, **130**, 6672–6673.

[132] J. A. Levitt, M. K. Kuimova, G. Yahioglu, P.-h. Chung, K. Suhling and D. Phillips, *Journal of Physical Chemistry C*, 2009, **113**, 11634–11642.

[133] H. L. Kee, C. Kirmaier, L. Yu, P. Thamyongkit, W. J. Youngblood, M. E. Calder, L. Ramos, B. C. Noll, D. F. Bocian, W. R. Scheidt, R. R. Birge, J. S. Lindsey and D. Holten, *The Journal of Physical Chemistry B*, 2005, **109**, 20433–20443.

[134] A. C. Benniston, A. Harriman, V. L. Whittle and M. Zelzer, *European Journal of Organic Chemistry*, 2010, **2010**, 523–530.

[135] E. Bahaidarah, A. Harriman, P. Stachelek, S. Rihn, E. Heyer and R. Ziessel, *Photochemical & Photobiological Sciences*, 2014, **13**, 1397–1401.

[136] A. Polita, S. Toliautas, R. Žvirblis and A. Vyšniauskas, *Physical Chemistry Chemical Physics*, 2020, **22**, 8296–8303.

[137] R. E. Scalise, P. A. Caradonna, H. J. Tracy, J. L. Mullin and A. E. Keirstead, *Journal of Inorganic and Organometallic Polymers and Materials*, 2014, **24**, 431–441.

[138] P. K. Singh, A. K. Mora and S. Nath, *Chemical Physics Letters*, 2016, **644**, 296–301.

[139] A. Paul and A. Samanta, *The Journal of Physical Chemistry B*, 2008, **112**, 16626–16632.

[140] J. D. Kimball, S. Raut, L. P. Jameson, N. W. Smith, Z. Gryczynski and S. V. Dzyuba, *RSC Advances*, 2015, **5**, 19508–19511.

[141] A. Paul, P. K. Mandal and A. Samanta, *Chemical Physics Letters*, 2005, **402**, 375–379.

[142] A. Paul, P. K. Mandal and A. Samanta, *Journal of Physical Chemistry B*, 2005, **109**, 9148–9153.

[143] A. Paul and A. Samanta, *Journal of Chemical Sciences*, 2006, **118**, 335–340.

[144] A. J. S. Mcintosh, *PhD thesis*, Imperial College London, 2015.

[145] M. J. Earle, C. M. Gordon, N. V. Plechkova, K. R. Seddon and T. Welton, *Analytical Chemistry*, 2007, **79**, 758–764.

[146] M. Tariq, P. J. Carvalho, J. A. Coutinho, I. M. Marrucho, J. N. C. Lopes and L. P. Rebelo, *Fluid Phase Equilibria*, 2011, **301**, 22–32.

[147] A. Skrzypczak and P. Neta, *Journal of Physical Chemistry A*, 2003, 7800–7803.

[148] Y. Nishiyama, M. Terazima and Y. Kimura, *The Journal of Physical Chemistry B*, 2009, **113**, 5188–5193.

[149] R. G. Evans, O. V. Klymenko, P. D. Price, S. G. Davies, C. Hardacre and R. G. Compton, *ChemPhysChem*, 2005, **6**, 526–533.

[150] R. P. Daly, J. C. Araque and C. J. Margulis, *The Journal of Chemical Physics*, 2017, **147**, 061102.

[151] C. A. Rumble, C. Uitvlugt, B. Conway and M. Maroncelli, *Journal of Physical Chemistry B*, 2017, **121**, 5094–5109.

[152] A. Vyšniauskas, M. Qurashi, N. Gallop, M. Balaz, H. L. Anderson and M. K. Kuimova, *Chemical Science*, 2015, **6**, 5773–5778.

[153] A. Vyšniauskas, I. López-Duarte, N. Duchemin, T.-T. Vu, Y. Wu, E. M. Budynina, Y. A. Volkova, E. Peña Cabrera, D. E. Ramírez-Ornelas and M. K. Kuimova, *Physical Chemistry Chemical Physics*, 2017, **19**, 25252–25259.

[154] M. A. Ab Rani, A. Brant, L. Crowhurst, A. Dolan, M. Lui, N. H. Hassan, J. P. Hallett, P. A. Hunt, H. Niedermeyer, J. M. Perez-Arlandis, M. Schrems, T. Welton and R. Wilding, *Physical Chemistry Chemical Physics*, 2011, **13**, 16831.

[155] O. Russina, A. Triolo, L. Gontrani, R. Caminiti, D. Xiao, L. G. Hines, R. A. Bartsch, E. L. Quitevis, N. Plechkova and K. R. Seddon, *Journal of Physics Condensed Matter*, 2009, **21**, 424121.

[156] D. Pontoni, J. Haddad, M. Di Michiel and M. Deutsch, *Soft Matter*, 2017, **13**, 6947–6955.

[157] R. Elfgen, O. Hollóczki and B. Kirchner, *Accounts of Chemical Research*, 2017, **50**, 2949–2957.

[158] M. Brehm, H. Weber, M. Thomas, O. Hollõczki and B. Kirchner, *ChemPhysChem*, 2015, **16**, 3271–3277.

[159] K. Bica, M. Deetlefs, C. Schröder and K. R. Seddon, *Physical Chemistry Chemical Physics*, 2013, **15**, 2703.

[160] Y. Marcus, *Journal of Molecular Liquids*, 2015, **209**, 289–293.

[161] M. G. Del Pópolo and G. A. Voth, *The Journal of Physical Chemistry B*, 2004, **108**, 1744–1752.

[162] S. Zahn, J. Thar and B. Kirchner, *The Journal of Chemical Physics*, 2010, **132**, 124506.

[163] T. Burankova, R. Hempelmann, A. Wildes and J. P. Embs, *The Journal of Physical Chemistry B*, 2014, **118**, 14452–14460.

[164] F. Ferdeghini, Q. Berrod, J.-M. Zanotti, P. Judeinstein, V. G. Sakai, O. Czakkel, P. Fouquet and D. Constantin, *Nanoscale*, 2017, **9**, 1901–1908.

[165] M. Casalegno, G. Raos, G. B. Appetecchi, S. Passerini, F. Castiglione and A. Mele, *The Journal of Physical Chemistry Letters*, 2017, **8**, 5196–5202.

[166] M. E. Sanborn, B. K. Connolly, K. Gurunathan and M. Levitus, *Journal of Physical Chemistry B*, 2007, **111**, 11064–11074.

[167] F. Philippi, A. Quinten, D. Rauber, M. Springborg and R. Hempelmann, *The Journal of Physical Chemistry A*, 2019, **123**, 4188–4200.

[168] Z. Zhang and L. A. Madsen, *The Journal of Chemical Physics*, 2014, **140**, 084204.

[169] M. Gouverneur, F. Schmidt and M. Schönhoff, *Physical Chemistry Chemical Physics*, 2018, **20**, 7470–7478.

[170] M. Gouverneur, J. Kopp, L. van Wüllen and M. Schönhoff, *Physical Chemistry Chemical Physics*, 2015, **17**, 30680–30686.

[171] F. Schmidt and M. Schönhoff, *The Journal of Physical Chemistry B*, 2020, **124**, 1245–1252.

[172] K. Zhao and D. Li, *Journal of Chromatography A*, 2018, **1558**, 96–106.

[173] M. Brinkkötter, G. A. Giffin, A. Moretti, S. Jeong, S. Passerini and M. Schönhoff, *Chemical Communications*, 2018, **54**, 4278–4281.

[174] T. J. Simons, P. M. Bayley, Z. Zhang, P. C. Howlett, D. R. MacFarlane, L. A. Madsen and M. Forsyth, *The Journal of Physical Chemistry B*, 2014, **118**, 4895–4905.

[175] J. R. Lakowicz, *Principles of fluorescence spectroscopy*, Springer US, Boston, MA, 2006, pp. 1–954.

[176] S. S. Tan, S. J. Kim and E. T. Kool, *Journal of the American Chemical Society*, 2011, **133**, 2664–2671.

[177] A. K. Chibisov, G. V. Zakharova and H. Görner, *Physical Chemistry Chemical Physics*, 1999, **1**, 1455–1460.

[178] M. Y. Lui, L. Crowhurst, J. P. Hallett, P. A. Hunt, H. Niedermeyer and T. Welton, *Chemical Science*, 2011, **2**, 1491.

[179] R. M. Lynden-Bell, A. I. Frolov and M. V. Fedorov, *Physical Chemistry Chemical Physics*, 2012, **14**, 2693.

[180] C. Aliaga, C. S. Santos and S. Baldelli, *Physical Chemistry Chemical Physics*, 2007, **9**, 3683.

[181] S. Shigeto and T. Shogo, *No Title*, 2019.

[182] R. P. Matthews, I. J. Villar-Garcia, C. C. Weber, J. Griffith, F. Cameron, J. P. Hallett, P. A. Hunt and T. Welton, *Physical Chemistry Chemical Physics*, 2016, **18**, 8608–8624.

[183] K. Ma, R. Jarosova, G. M. Swain and G. J. Blanchard, *Langmuir*, 2016, **32**, 9507–9512.

[184] Y. Wang, R. Jarošová, G. M. Swain and G. J. Blanchard, *Langmuir*, 2020, **36**, 3038–3045.

[185] D. R. MacFarlane, M. Forsyth, P. C. Howlett, J. M. Pringle, J. Sun, G. Annat, W. Neil and E. I. Izgorodina, *Accounts of Chemical Research*, 2007, **40**, 1165–1173.

[186] M. J. Shiddiky and A. A. Torriero, *Biosensors and Bioelectronics*, 2011, **26**, 1775–1787.

[187] J. Petravic and J. Delhommelle, *Journal of Chemical Physics*, 2003, **118**, 7477–7485.

[188] B. R. Sundheim, *The Journal of Physical Chemistry*, 1956, **60**, 1381–1383.

[189] A. Uysal, H. Zhou, G. Feng, S. S. Lee, S. Li, P. T. Cummings, P. F. Fulvio, S. Dai, J. K. McDonough, Y. Gogotsi and P. Fenter, *Journal of Physics Condensed Matter*, 2015, **27**, 032101.

[190] H. Zhao, *Physical Review E - Statistical, Nonlinear, and Soft Matter Physics*, 2011, **84**, 051504.

[191] M. Chen, S. Li, G. Feng and H. Zhao, *Molecules*, 2017, **22**, 241.

[192] C. Lian, S. Zhao, H. Liu and J. Wu, *The Journal of Chemical Physics*, 2016, **145**, 204707.

[193] M. Sha, D. Niu, Q. Dou, G. Wu, H. Fang and J. Hu, *Soft Matter*, 2011, **7**, 4228.

[194] N. J. English and D. A. Mooney, *Physical Chemistry Chemical Physics*, 2009, **11**, 9370–9374.

[195] N. J. English and D. A. Mooney, *Journal of Physical Chemistry B*, 2009, **113**, 10128–10134.

[196] M. Fedorov, N. Georgi and A. Kornyshev, *Electrochemistry Communications*, 2010, **12**, 296–299.

[197] J. W. Daily and M. M. Micci, *The Journal of Chemical Physics*, 2009, **131**, 094501.

[198] Y. Zhao, K. Dong, X. Liu, S. Zhang, J. Zhu and J. Wang, *Molecular Simulation*, 2012, **38**, 172–178.

[199] Y. Wang, *Journal of Physical Chemistry B*, 2009, **113**, 11058–11060.

[200] R. Shi and Y. Wang, *The Journal of Physical Chemistry B*, 2013, **117**, 5102–5112.

[201] N. J. English, D. A. Mooney and S. O'Brien, *Molecular Physics*, 2011, **109**, 625–638.

[202] M. Atilhan and S. Aparicio, *The Journal of Physical Chemistry B*, 2017, **121**, 221–232.

[203] J. N. C. Lopes and A. A. H. Padua, *CLP Force Field*.

[204] W. L. Jorgensen, D. S. Maxwell and J. Tirado-Rives, *Journal of the American Chemical Society*, 1996, **118**, 11225–11236.

[205] A. A. Pádua, *Journal of Chemical Physics*, 2017, **146**, 204501.

[206] B. L. Bhargava and S. Balasubramanian, *The Journal of Chemical Physics*, 2007, **127**, 114510.

[207] C. Schröder and O. Steinhauser, *Journal of Chemical Physics*, 2010, **133**, 154511.

[208] C. Schröder, *Physical Chemistry Chemical Physics*, 2012, **14**, 3089.

[209] M. Schmollngruber, V. Lesch, C. Schröder, A. Heuer and O. Steinhauser, *Physical Chemistry Chemical Physics*, 2015, **17**, 14297–14306.

[210] D. Bedrov, J.-P. Piquemal, O. Borodin, A. D. MacKerell, B. Roux and C. Schröder, *Chemical Reviews*, 2019, **119**, 7940–7995.

[211] N. J. English and C. J. Waldron, *Physical Chemistry Chemical Physics*, 2015, **17**, 12407–12440.

[212] N. J. English and J. M. D. MacElroy, *The Journal of Chemical Physics*, 2004, **120**, 10247–10256.

[213] N. J. English and J. M. D. MacElroy, *The Journal of Chemical Physics*, 2003, **119**, 11806–11813.

[214] N. J. English and J. M. D. MacElroy, *The Journal of Chemical Physics*, 2003, **118**, 1589–1592.

[215] K. Goloviznina, J. N. Canongia Lopes, M. Costa Gomes and A. A. H. Pádua, *Journal of Chemical Theory and Computation*, 2019, **15**, 5858–5871.

[216] D. Frenkel and B. Smith, *Understanding Molecular Simulations*, Academic Press, 2008, p. 638.

[217] P. H. Hünenberger, *Advances in Polymer Science*, Springer, Berlin, 2005, vol. 173, pp. 105–147.

[218] T. Schlick, *Molecular Modeling and Simulation: An Interdisciplinary Guide*, Springer New York, New York, NY, 2nd edn, 2010, vol. 21, pp. 425–461.

[219] M. P. Allen and D. J. Tildesley, *Computer Simulations of Liquids*, Oxford University Press, Oxford, 1st edn, 1991, p. 400.

[220] V. Blickle, T. Speck, C. Lutz, U. Seifert and C. Bechinger, *Physical Review Letters*, 2007, **98**, 210601.

[221] Y.-L. Wang, B. Li, S. Sarman, F. Mocci, Z.-Y. Lu, J. Yuan, A. Laaksonen and M. D. Fayer, *Chemical Reviews*, 2020, acs.chemrev.9b00693.

[222] J. C. Araque, J. J. Hettige and C. J. Margulis, *Journal of Physical Chemistry B*, 2015, **119**, 12727–12740.

[223] M. T. Clough, C. R. Crick, J. Gräsvik, P. A. Hunt, H. Niedermeyer, T. Welton and O. P. Whitaker, *Chemical Science*, 2015, **6**, 1101–1114.

[224] P. A. Hunt, C. R. Ashworth and R. P. Matthews, *Chemical Society Reviews*, 2015, **44**, 1257–1288.

[225] M. N. Kobrak and N. Sandalow, *ECS Proceedings Volumes*, 2004, **2004-24**, 417–425.

[226] R. K. Wangsness, *Electromagnetic Fields*, John Wiley & Sons, Inc., New York, NY, 2nd edn, 1986, p. 587.

Appendix A

Fluorescence Lifetime Decays of Cy3 and BODIPY-C10 in Various Ionic Liquids

A.1 Fluorescence lifetime Decay of Neat Ionic Liquids

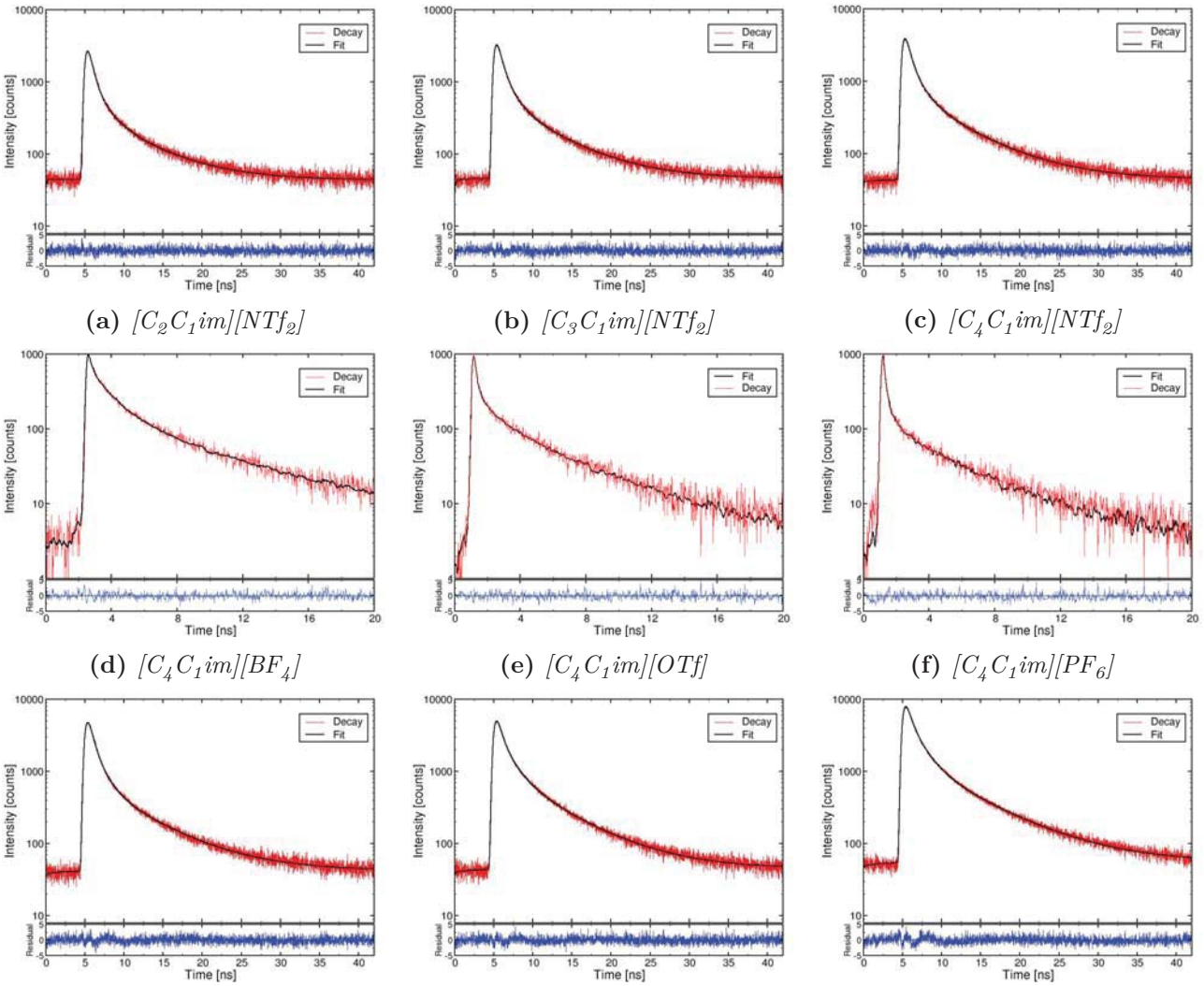

(a) $[C_2C_1im][NTf_2]$ **(b)** $[C_3C_1im][NTf_2]$ **(c)** $[C_4C_1im][NTf_2]$

(d) $[C_4C_1im][BF_4]$ **(e)** $[C_4C_1im][OTf]$ **(f)** $[C_4C_1im][PF_6]$

(g) $[C_6C_1im][NTf_2]$ **(h)** $[C_8C_1im][NTf_2]$ **(i)** $[C_{12}C_1im][NTf_2]$

Figure A.1: *Fluorescence lifetime decays and fits of blank ionic liquids.*

A.2 Fluorescence Lifetime Decay of BODIPY-C10 in Ionic Liquids

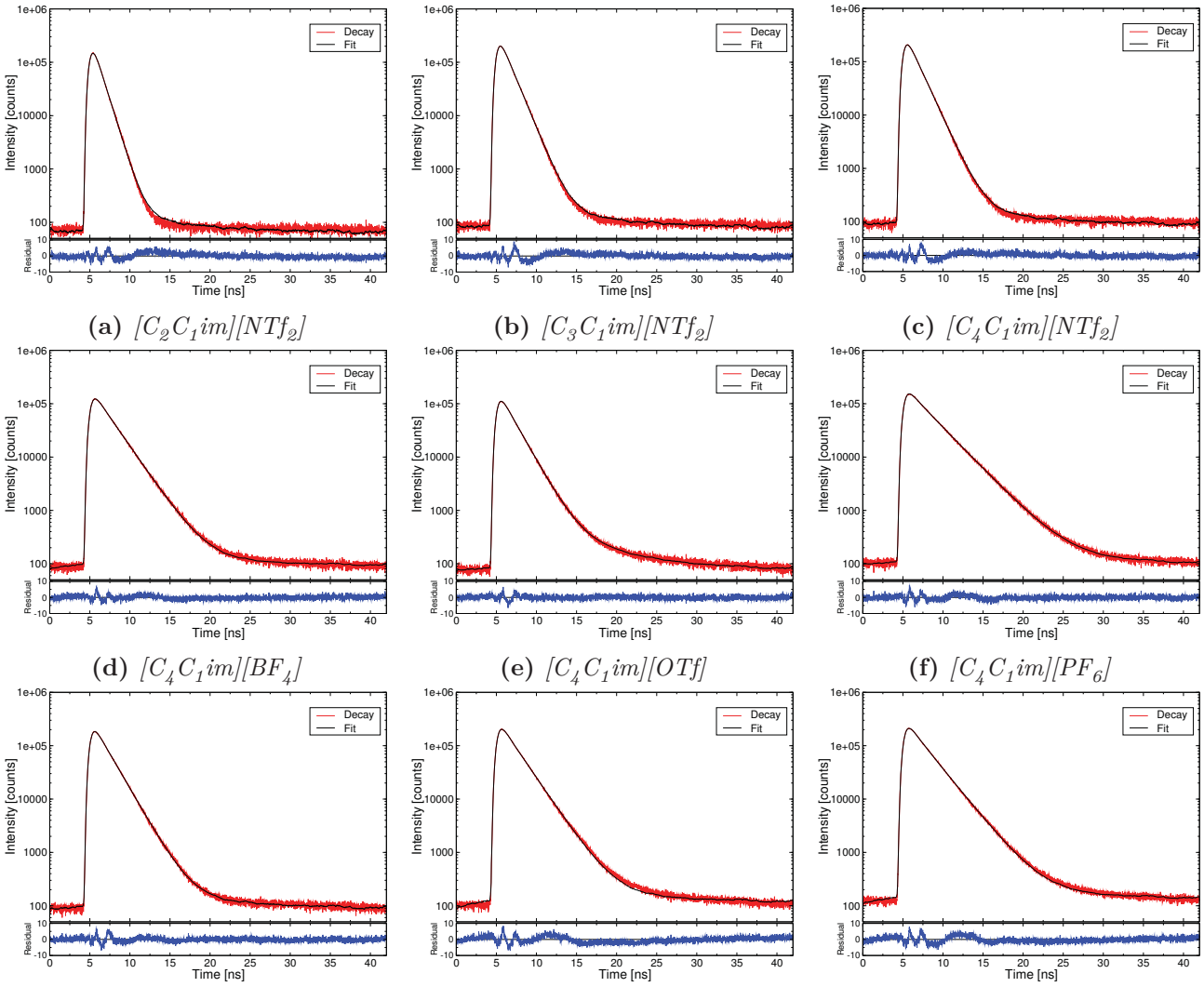

(a) $[C_2C_1im][NTf_2]$ (b) $[C_3C_1im][NTf_2]$ (c) $[C_4C_1im][NTf_2]$

(d) $[C_4C_1im][BF_4]$ (e) $[C_4C_1im][OTf]$ (f) $[C_4C_1im][PF_6]$

(g) $[C_6C_1im][NTf_2]$ (h) $[C_8C_1im][NTf_2]$ (i) $[C_{12}C_1im][NTf_2]$

Figure A.2: *Fluorescence lifetime decays and fits of BODIPY-C10 in ionic liquids.*

A.3 Fluorescence Lifetime Decay of BODIPY-C10 in Various Temperatures in [C_4C_1im] [NTf_2]

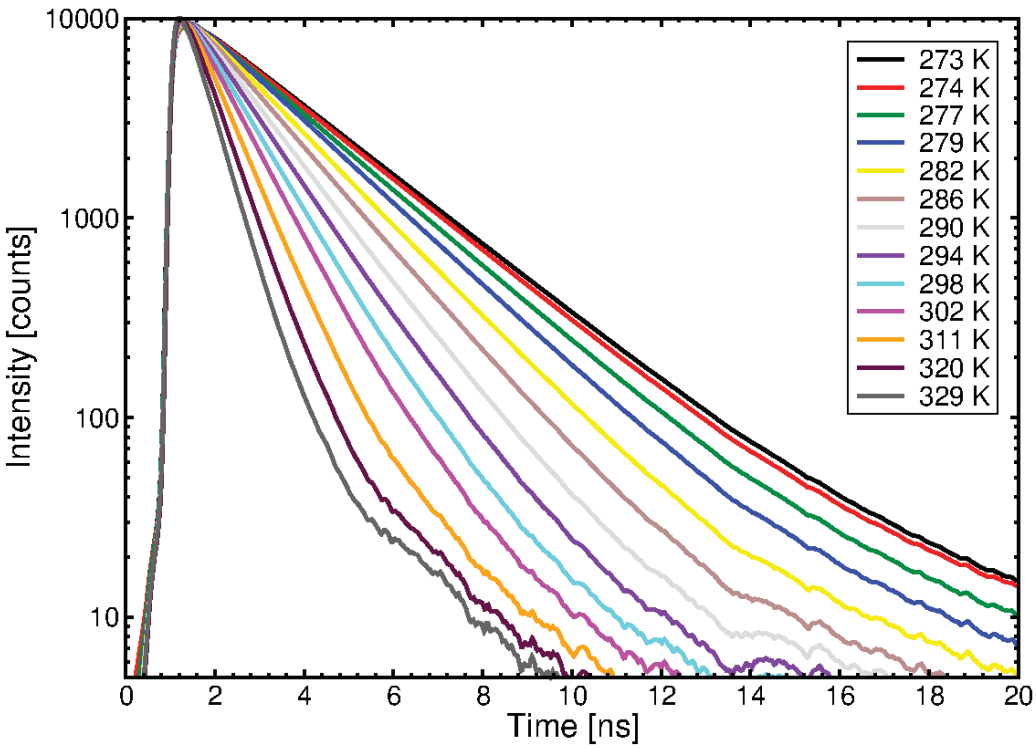

Figure A.3: *Fluorescence lifetime decay of BODIPY-C10 in [C_4C_1im][NTf_2] at various temperatures.*

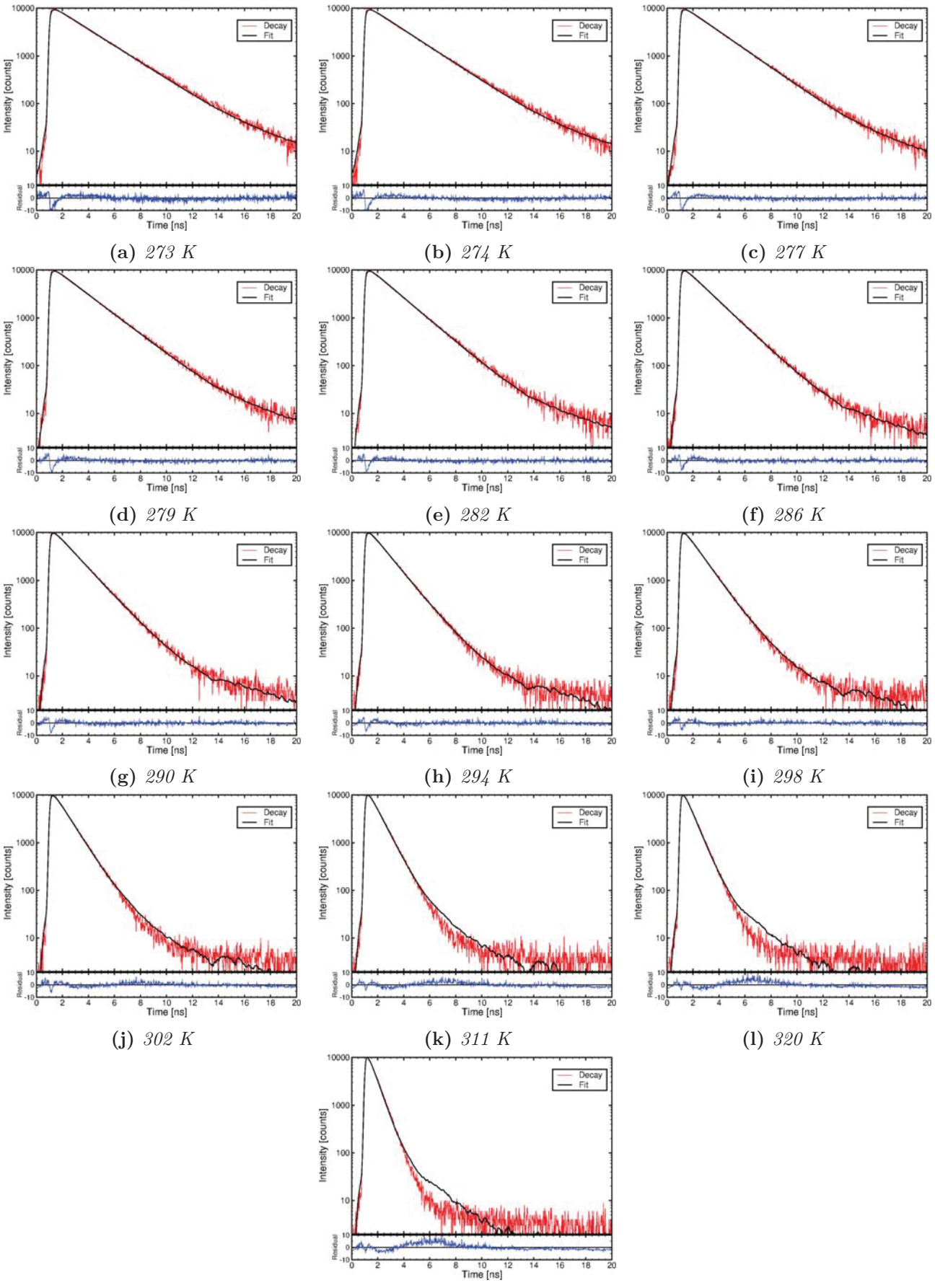

(a) *273 K* **(b)** *274 K* **(c)** *277 K*

(d) *279 K* **(e)** *282 K* **(f)** *286 K*

(g) *290 K* **(h)** *294 K* **(i)** *298 K*

(j) *302 K* **(k)** *311 K* **(l)** *320 K*

(m) *329 K*

Figure A.4: *Fluorescence lifetime decays and fits of of BODIPY-C10 in $[C_4C_1im][NTf_2]$ at various temperatures.*

A.4 Fluorescence Lifetime Decay of Cy3 in Ionic Liquids

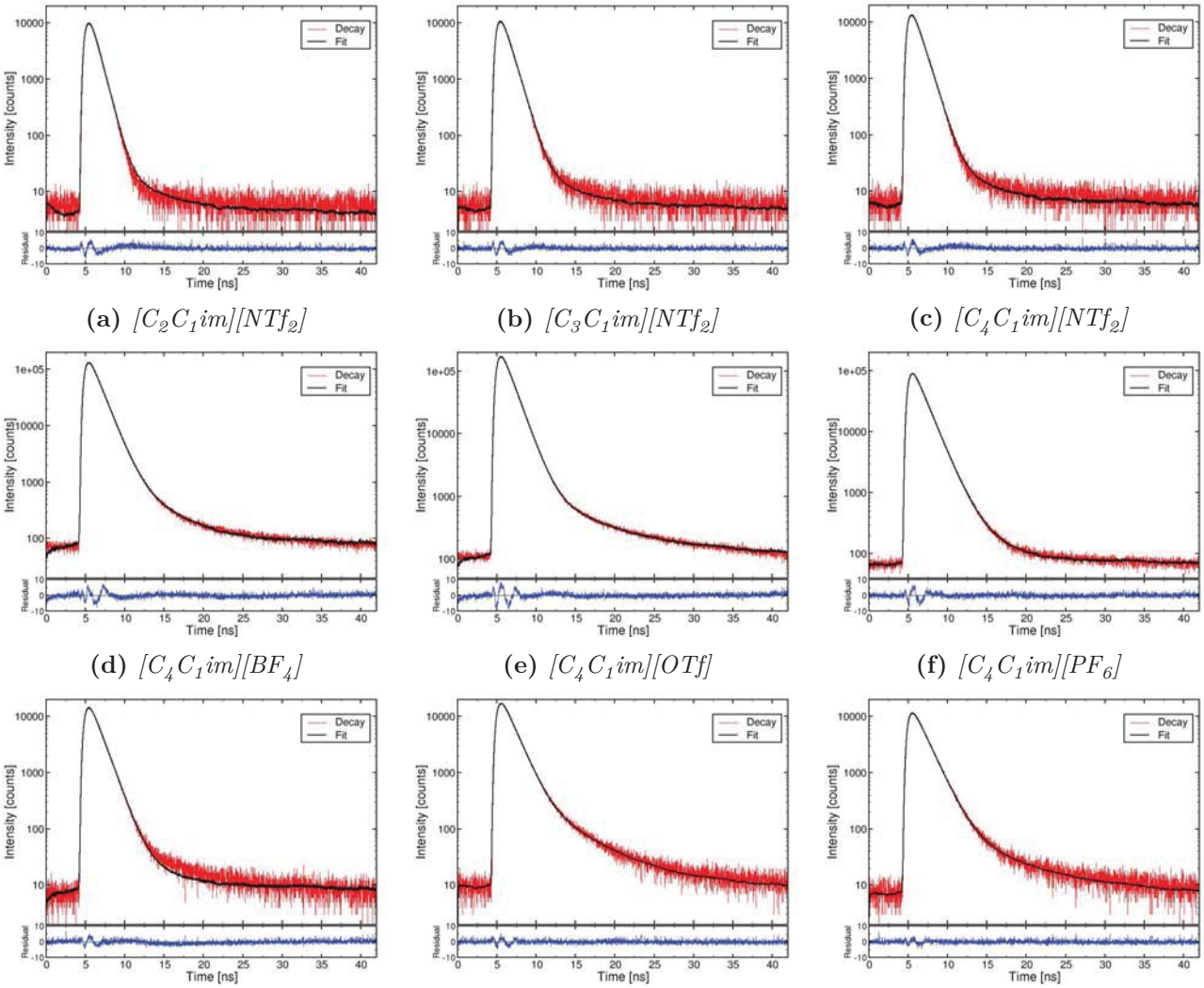

(a) $[C_2C_1im][NTf_2]$ **(b)** $[C_3C_1im][NTf_2]$ **(c)** $[C_4C_1im][NTf_2]$

(d) $[C_4C_1im][BF_4]$ **(e)** $[C_4C_1im][OTf]$ **(f)** $[C_4C_1im][PF_6]$

(g) $[C_6C_1im][NTf_2]$ **(h)** $[C_8C_1im][NTf_2]$ **(i)** $[C_{12}C_1im][NTf_2]$

Figure A.5: *Fluorescence lifetime decays and fits of Cy3 in ionic liquids.*

A.5 Fluorescence Lifetime Decay of Cy3 in Various Temperatures in $[C_4C_1im][NTf_2]$

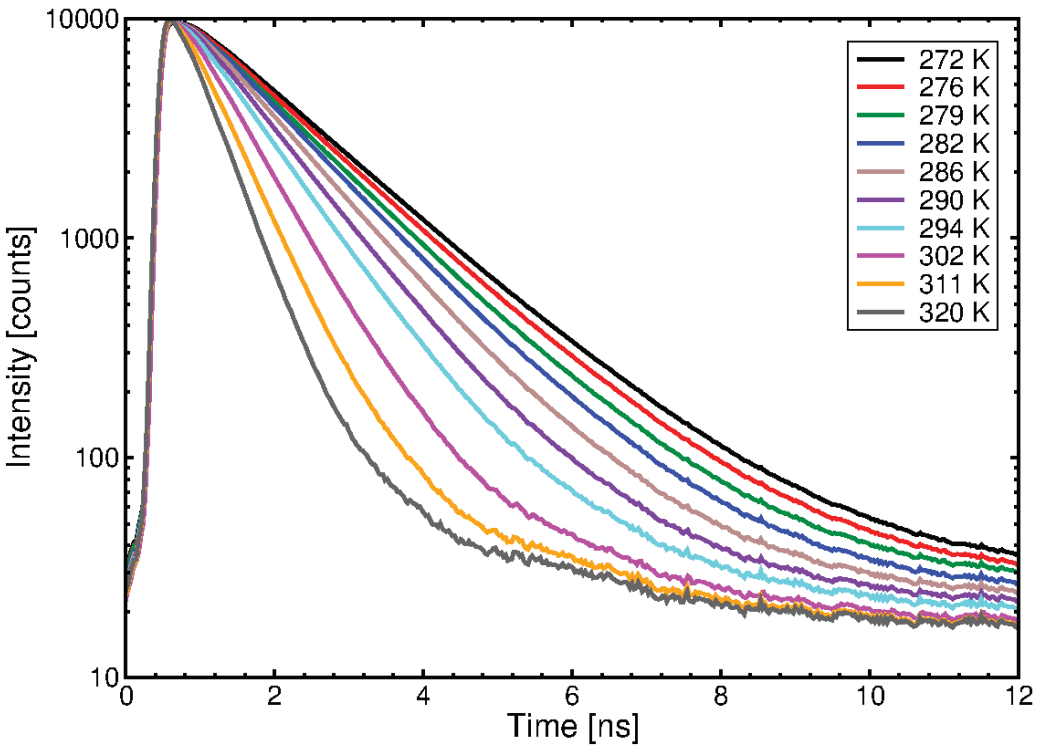

Figure A.6: *Fluorescence lifetime decay of Cy3 in $[C_4C_1im][NTf_2]$ at various temperatures.*

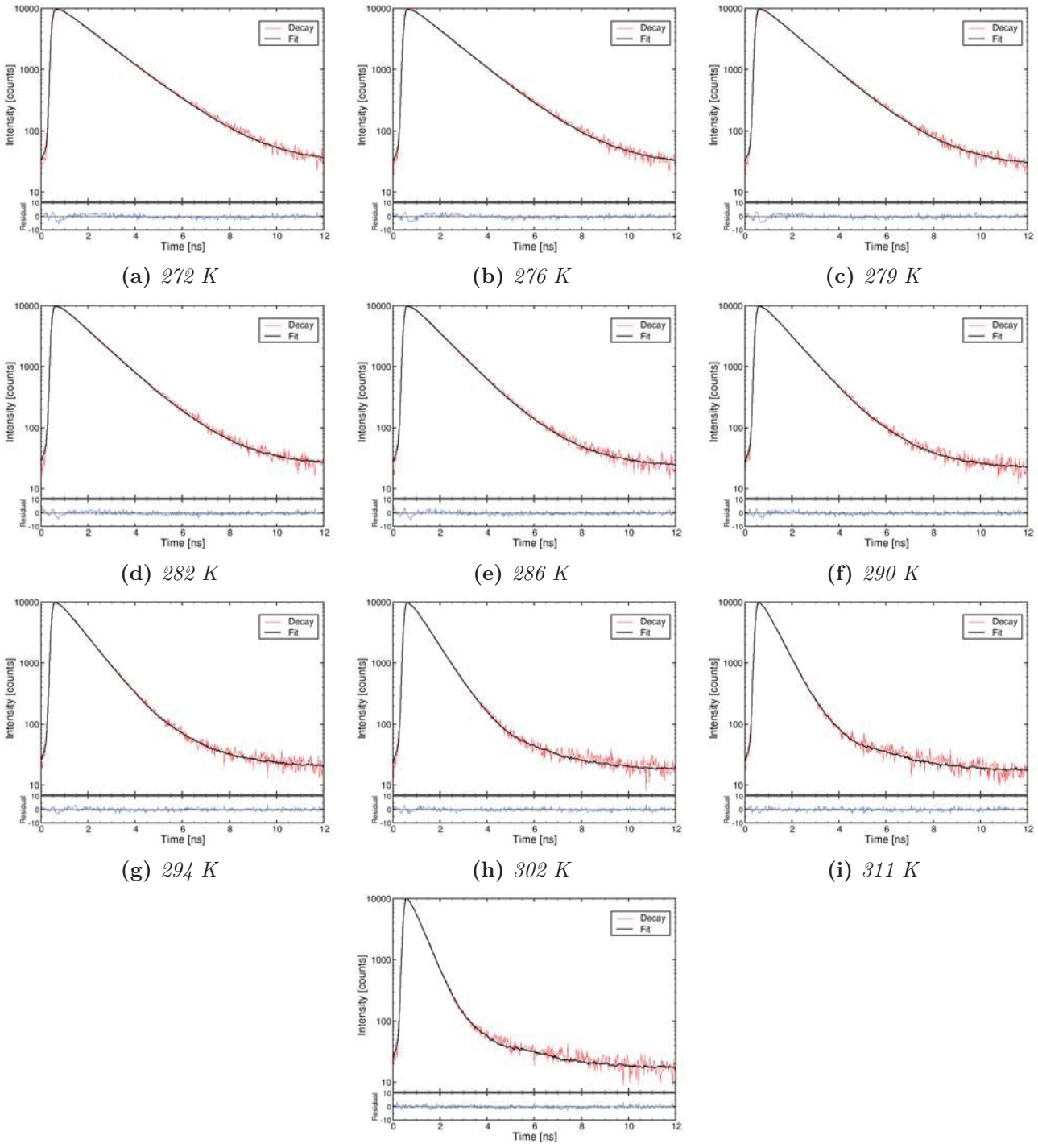

(a) *272 K* **(b)** *276 K* **(c)** *279 K*

(d) *282 K* **(e)** *286 K* **(f)** *290 K*

(g) *294 K* **(h)** *302 K* **(i)** *311 K*

(j) *320 K*

Figure A.7: *Fluorescence lifetime decays and fits of of Cy3 in $[C_4C_1im][NTf_2]$ at various temperatures.*

Appendix B

Cyclic Voltammogram of Dyes in $[C_4C_1im][NTf_2]$

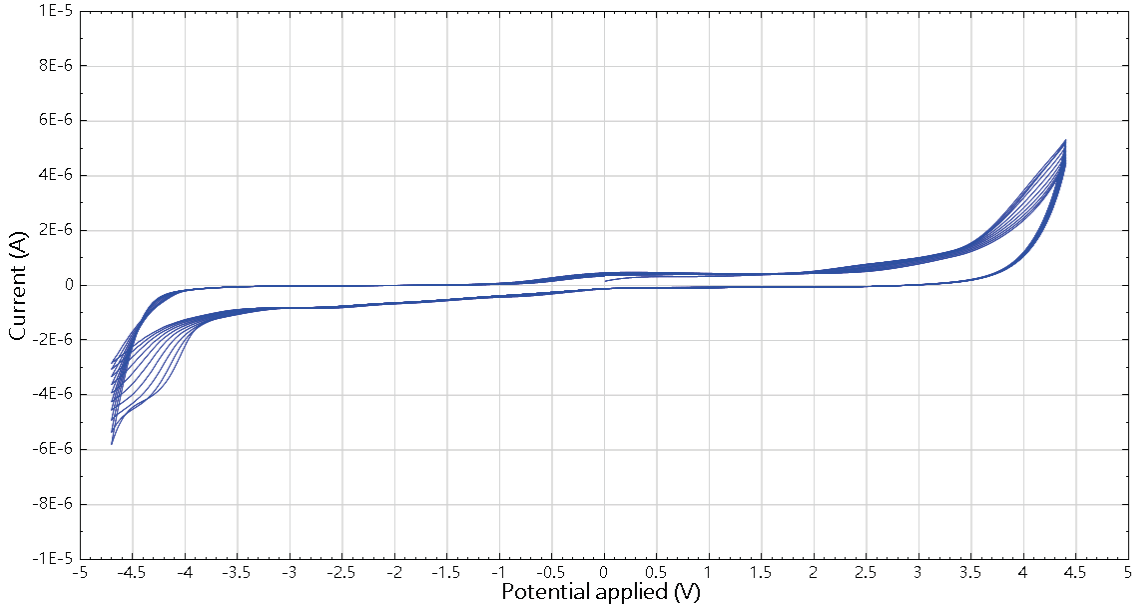

Figure B.1: *CV of neat ultra-pure $[C_4C_1im][NTf_2]$ measured within the indium-tin oxide cell. Scan rate used was 100 mV/s.*

The CV of the neat ionic liquid $[C_4C_1im][NTf_2]$ (Figure B.1) shows no large features in the range +3.5 V to -3.5 V, below and above which (respectively) there is decomposition.

The CV of Cy3 (Figure B.2) shows repeating reduction peaks around -2.3 V and -2.9 V. These are irreversible peaks with no oxidation, indicating that they involve electrochemical decomposition of the Cy3 molecule. The cause of these are unknown, but the fact that they are outside the measurement voltages used in this thesis, the dye can be said to be stable in the ionic liquid in the measurement voltage ranges.

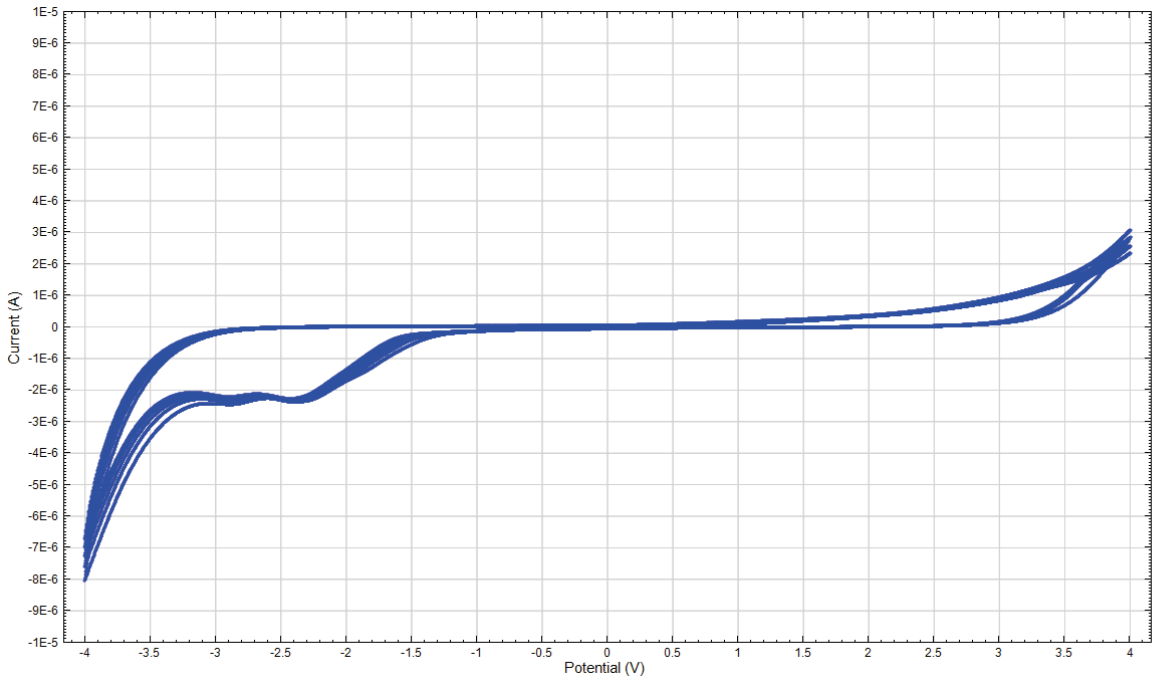

Figure B.2: *CV of 1 mM Cy3 in $[C_4C_1im][NTf_2]$ measured within the indium-tin oxide cell. Scan rate was 100 mV/s.*

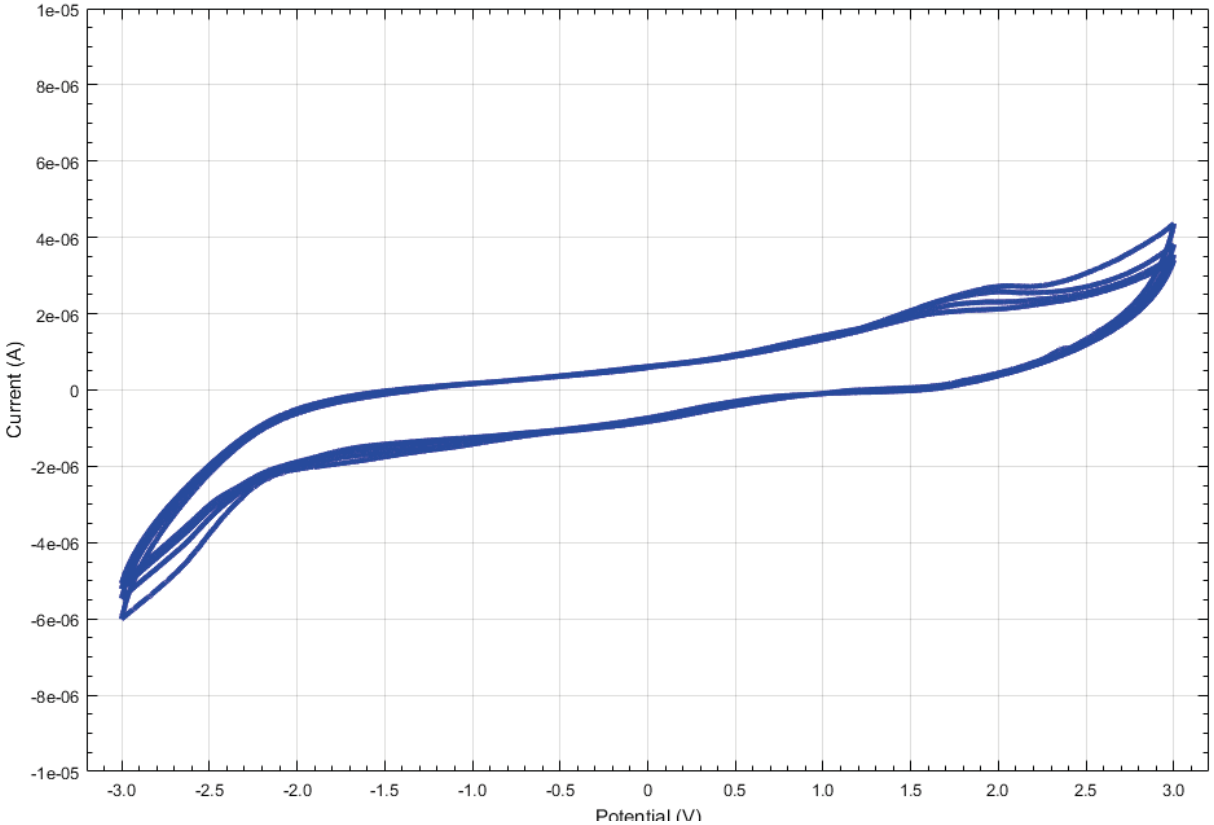

Figure B.3: *CV of 20 mM BODIPY-C10 in $[C_4C_1im][NTf_2]$ measured within the indium-tin oxide cell. Scan rate was 25 mV/s.*

The CV of BODIPY-C10 (Figure B.3) has a much larger nonfaradaic current, and the scan rate had to be decreased to account for this. Still, this dye also appears stable in the measurement

voltage ranges used in this thesis. There is a small peak around 1.6 V, however this is suspected to arise due to trace water impurities, as previous CVs of BODIPY have also shown that BODIPY-C10 is relatively stable up to 2.5 V,[134] the point at which decomposition appears to begin in this CV.

Appendix C

Simulation of $[C_8C_1im][NTf_2]$ in

For the simulation of $[C_8C_1im][NTf_2]$ in an electric fields strength of 0.5 VÅ^{-1}, the thermostat holds the temperatures in the x and y directions relatively constant. However the temperature in the z direction in this simulation is dramatically higher than below 0.5 VÅ^{-1}. This Appendix discusses the reasons behind this, and problems caused by this.

C.1 Temperature of $[C_8C_1im][NTf_2]$ in 0.5 VÅ^{-1}

Given the large temperatures in this simulation, there are some concerns about the validity of the thermostatting method that need to be evaluated for this simulation. Figure C.1 shows the temperature in each direction during this simulation.

When observing the trajectory, the structure seen in Figure C.2 shows the the cause of the very high temperature in the z direction, is the formation of channels within the bulk structure of the liquid. The channels allow the ions, particularly the cations, to move without any other ions blocking their motion. This, in combination with the force applied by the electric field, means the ions move extremely fast along the channels leading to a high kinetic temperature. This high kinetic temperature is not necessarily a problem for the thermostat, as we exclude the kinetic temperature in this direction from the thermostatting. However, the formation of the channels could cause problems for the thermostat as the channels could lead to a freezing of the motion in the x and y directions, if the channels are rigid and restrict the motion in these directions. This freezing of motion was observed by Zhao *et al.*[198] using $[C_2C_1im][NO_3]$. In these simulations, the channels seem to be somewhat flexible and they move around the

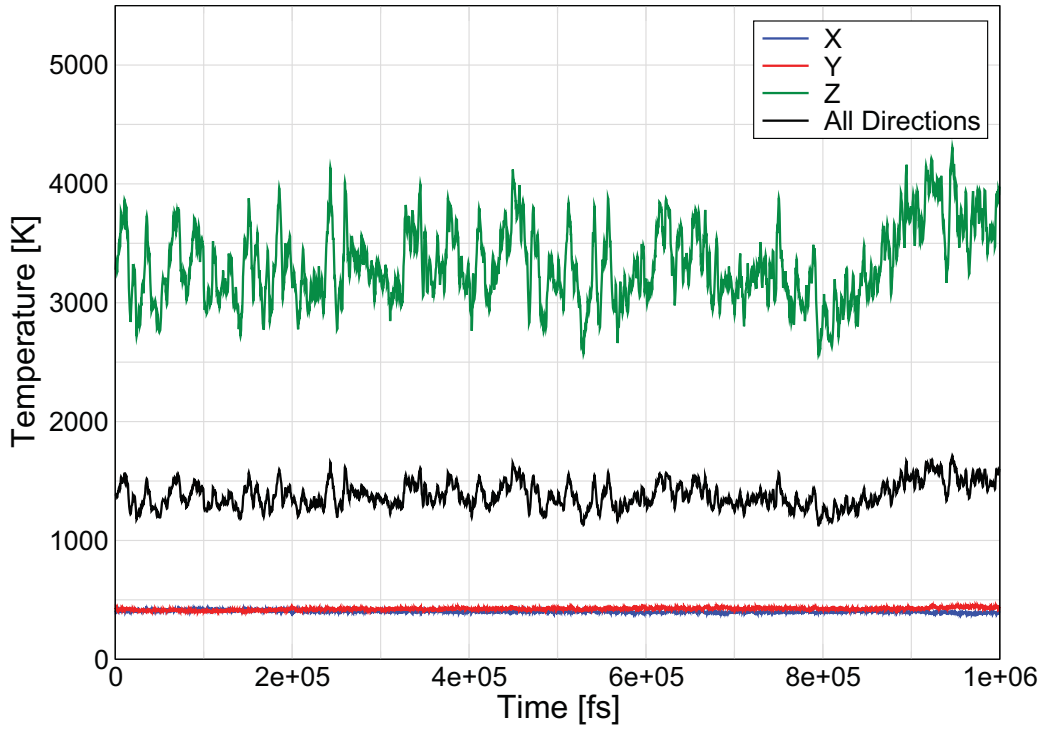

Figure C.1: *Temperature in the x, y and z directions as well as the average temperature of the simulation box of the simulation of $[C_8C_1im][NTf_2]$ with an applied electric field of 0.5 VÅ^{-1}.*

liquid in the x and y directions (snapshots from the simulation in Figure C.3). This means that there is still some motion in the x and y directions that the thermostat can use to control temperature.

There is also some obvious lateral motion of the ions within the channels that can be observed when viewing the simulation (i.e. oscillating back and forth), so this combined with the movement of the channels suggests that there could be enough motion within the channels to thermostat the simulation in a valid way.

There is, however, a possibility that this motion perpendicular to the field comes from an artificial increase in the motion. This would occur if formation of these channels does cause a freezing of the motion perpendicular to the field. This would decrease the speed, and therefore the temperature, so in order to compensate for this the thermostats would relax their constrains in order to increase the kinetic temperature to the desired value. There is no way to reasonably test for this with an analysis, therefore it cannot be explicitly excluded that the lateral motion seen is an artefact of the thermostat from the temperature.

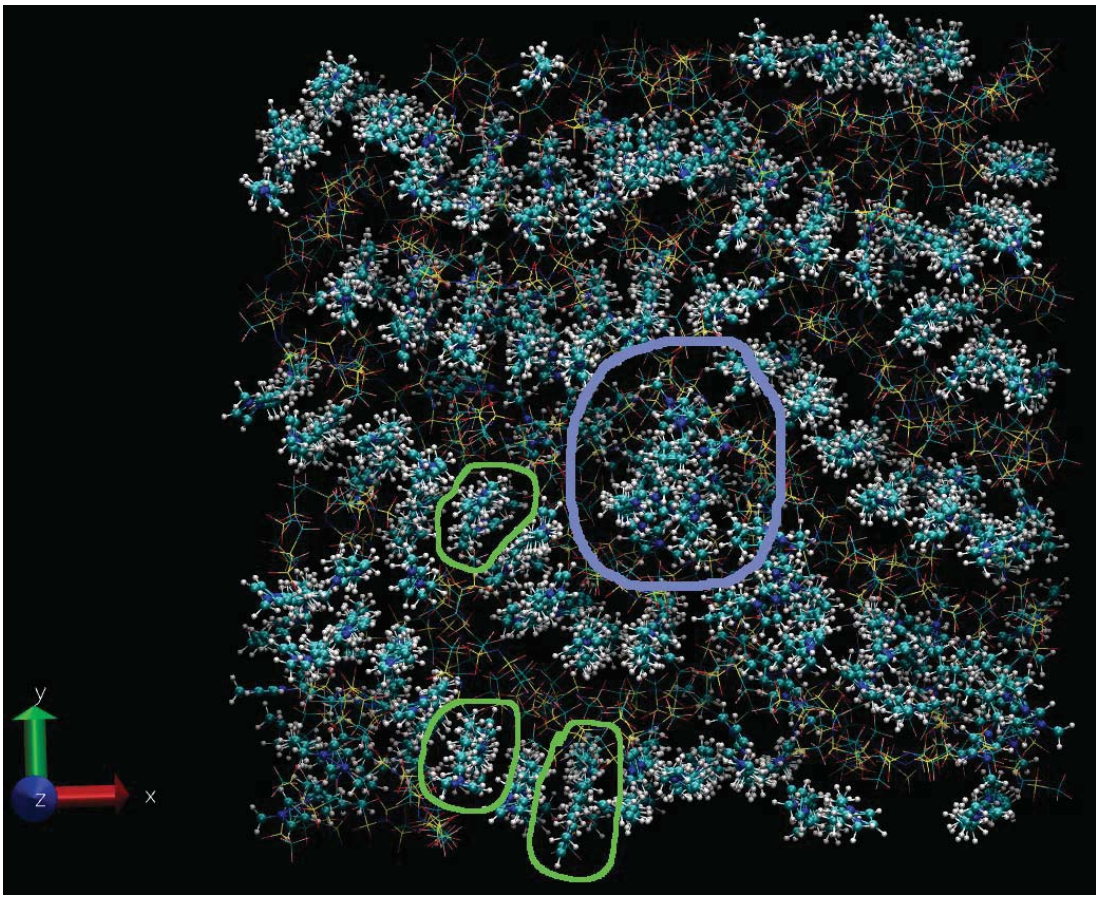

Figure C.2: *Snapshot of the simulation box of the simulation of $[C_8C_1im][NTf_2]$ with an applied electric field of 0.5 VÅ^{-1} showing examples of channel formation. Anions are represented by the lines, cations by the sticks and balls. Some of the channels are highlighted in green for clarity. The region of interest in Section C.2 is highlighted in light blue.*

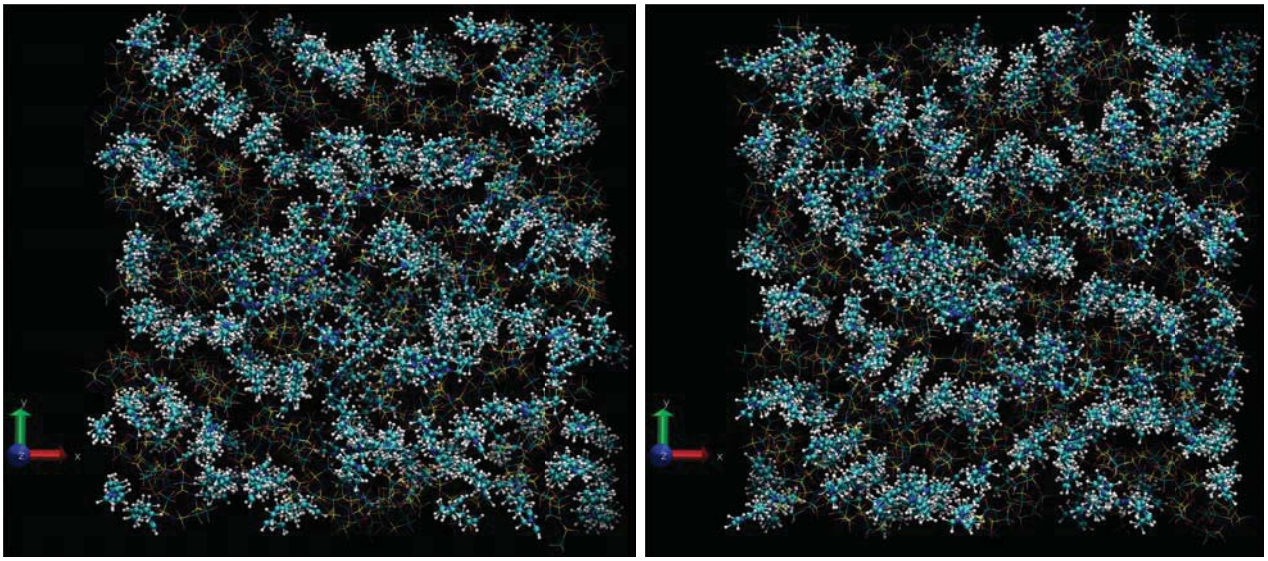

Figure C.3: *Snapshots of the simulation box of $[C_8C_1im][NTf_2]$ with an applied electric field of 0.5 VÅ^{-1} along the z direction showing different channel positions in the x and y directions. Snapshots taken approximately 2 ps apart.*

C.2 Problems With This Simulation

While investigating these channels, several problems were found with this simulation that meant that it was not possible to use it in this thesis.

Firstly, the assignment of a Drude particle to one Drude core provided difficult. While in other simulations the average Drude-atom distances were <1 pm, in this simulation this increased to ≈30 pm and varied by ±25 pm. This meant that at any given time-step it was difficult to assign all Drude particles so that there was one Drude particle to one Drude core. This must be a consequence of the high temperature and fast motion, as the charges on the Drude particles and Drude cores are identical to that of $[C_4C_1im][NTf_2]$, and the equivalent simulation at 0.5 $VÅ^{-1}$ does not show a similar effect.

Another problem that was noticed when viewing the trajectories was that in the centre of the simulation box, there was a region (highlighted in light blue in Figure C.2) where there were anions and cations undergoing some abnormal behaviour. Within this region the cations and anions were moving along **both** directions of the z vector i.e. some cations were diffusing in the negative z direction and some anions were diffusing in the positive z direction. Even more abnormal was the presence of atoms and molecules that would apparently 'teleport' around the box, jumping from one part of the simulation box to another.

The reason suspected to be behind all of these results is that the large kinetic energy and electric potential energy caused the ions to dissociate into individual atoms and Drude particles, in a 'plasma-like' soup. One needs to remember that the Drude particles, and the Drude cores to which they are attached, are highly charged (up to $3e$). Therefore in a sufficiently strong electric field, the force on the Drude particles and cores will be strong enough, and in opposite directions, that the electric field can strip the Drude particles from the Drude cores.

If the ions are dissociating into a plasma-like state, LAMMPS will try to assign this particle soup to molecules, and then attempt to order the trajectory by molecule when outputting. As LAMMPS is expecting a set number of molecules, if the program is having trouble assigning the correct number of molecules, this will cause a crash due to the program "losing molecules". This would explain why, when running these simulations, they regularly crashed and had to be restarted 4-5 times every nanosecond.

This only seems to be a problem using Drude particles, as other measurements in the literature using coarse-grain or all-atom non-polarisable models have been able to exceed 0.5 $VÅ^{-1}$ with no reported problems.[194,199]

Due to the difficulty in running these simulations, it was decided to exclude them from the

work in this thesis.

Appendix D

Electric Multipole Definition

In order to understand dipoles and the impossibility of using this method to rationalise these results, a full derivation of the electric multiple moment of an ion/molecule is included hern. This is very well understood and precedented,[226] and there is no claim to the novelty of this derivation in this work. The electric potential energy in a system comprised of point charges

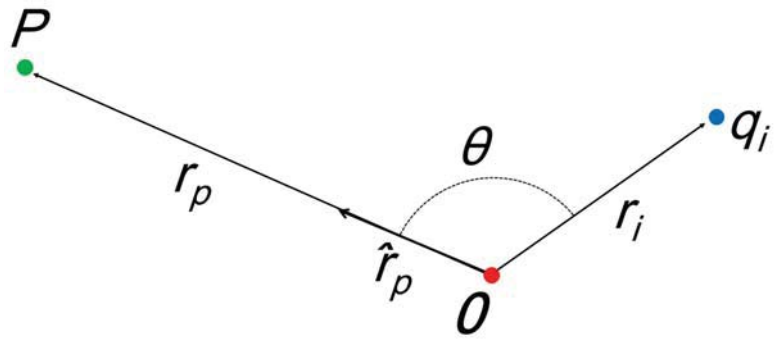

Figure D.1: *Coordinate geometry for multipole calculation. Red dot represents the origin in the coordinate system. Blue dot represents a particle with charge q_i at a distance of r_i from the origin. Green dot represents the measurement point P at a distance r_p from the origin, with a direction $\hat{r}_p$, and an angle θ from the vector r_i.*

can be calculated using

$$\phi(r) = \sum_{i=1}^{N} \frac{q_i}{4\pi\epsilon_0 R_i} \tag{D.1}$$

When considering ions or molecules, Equation D.1 can be used to calculate the electrical potential energy of the compound at an arbitrary point in space. The potential is calculated at an arbitrary point P, using the charges of the atoms, q_i, and their distance from the origin, r_i, as represented in Figure D.1.

In this case the distance from each atom i to P can be calculated by

$$R_i^2 = r_p^2 + r_i^2 - 2r_i r_p cos\theta_i \tag{D.2}$$

and Equation D.1 can be written as

$$\phi(r) = \sum_{i=1}^{N} \frac{q_i}{4\pi\epsilon_0} \cdot \frac{1}{\left[r_p^2 + r_i^2 - 2r_i r_p cos\theta_i\right]^{\frac{1}{2}}} \tag{D.3}$$

Now, let us assume that the point P is sufficiently far enough away from the compound that the distance r_p is greater than any and all r_i. This means the fraction r_i/r_p is always less than unity.

We can take advantage of this assumption by removing a factor of r_p^2 from R_i and writing this as

$$R_i^2 = r_p^2 \left[1 + \frac{r_i^2}{r_p^2} - 2\frac{r_i}{r_p} cos\theta_i\right] \tag{D.4}$$

$$R_i = r_p \left[1 + \frac{r_i^2}{r_p^2} - 2\frac{r_i}{r_p} cos\theta_i\right]^{\frac{1}{2}} \tag{D.5}$$

This can be factored to get

$$R_i = r_p(1+t)^{\frac{1}{2}} \tag{D.6}$$

where

$$t = \frac{r_i^2}{r_p^2} - 2\frac{r_i}{r_p} cos\theta_i \tag{D.7}$$

Now, Equation D.3 can be written as

$$\phi(r) = \sum_{i=1}^{N} \frac{q_i}{4\pi\epsilon_0} \cdot \frac{1}{r_p(1+t)^{\frac{1}{2}}} \tag{D.8}$$

$$\phi(r) = \frac{1}{4\pi\epsilon_0 r_p} \sum_{i=1}^{N} \frac{q_i}{(1+t)^{\frac{1}{2}}} \tag{D.9}$$

This means the power series

$$(1 \pm t)^{-1/2} = 1 \mp \frac{1}{2}t + \frac{3}{8}t^2 \mp \frac{5}{16}t^3 + ... \tag{D.10}$$

can be used to expand the sum in Equation D.9. As we have already stated that $r_P > r_i$ for all i, the terms containing $(r_i/r_p)^n$ where $n \geq 3$ will be very small so will be neglected in the expansion as they will have a minimal contribution to the result. Thus, the t^3 term does not

need to be included, as it contains only $(r_i/r_p)^3$ and higher terms. Performing the expansion and inserting t from Equation D.7 gives

$$(1 \pm t)^{-1/2} = 1 - \frac{1}{2}\left[\frac{r_i^2}{r_p^2} - 2\frac{r_i}{r_p}cos\theta_i\right] + \frac{3}{8}\left[\frac{r_i^2}{r_p^2} - 2\frac{r_i}{r_p}cos\theta_i\right]^2 + O\left(t^3\right) \tag{D.11}$$

$$(1\pm t)^{-1/2} = 1-\frac{1}{2}\left(\frac{r_i}{r_p}\right)^2+\frac{r_i}{r_p}cos\theta_i+\frac{3}{8}\left(\frac{r_i}{r_p}\right)^4-\frac{3}{2}\left(\frac{r_i}{r_p}\right)^3 cos\theta_i+\frac{3}{2}\left(\frac{r_i}{r_p}\right)^2 cos^2\theta_i+O\left(t^3\right) \tag{D.12}$$

Dropping $(r_i/r_p)^n$ where $n \geq 3$ terms gives the final result of the expansion as

$$(1 \pm t)^{-1/2} = 1 + \frac{r_i}{r_p}cos\theta_i + \frac{1}{2}\left(\frac{r_i^2}{r_p^2}\right)^2\left(cos^2\theta_i - 1\right) + O\left(t^3\right) \tag{D.13}$$

Substituting this expansion into Equation D.9 transforms the electrical potential equation into

$$\phi(r) = \frac{1}{4\pi\epsilon_0 r_p}\sum_{i=1}^{N} q_i\left[1 + \frac{r_i}{r_p}cos\theta_i + \frac{1}{2}\left(\frac{r_i^2}{r_p^2}\right)^2\left(3cos^2\theta_i - 1\right)\right] \tag{D.14}$$

This equation can then be expanded and split into multiple sums by collecting the powers of r_i

$$\begin{aligned}\phi(r) = &\frac{1}{4\pi\epsilon_0 r_p}\sum_{i=1}^{N} q_i + \frac{1}{4\pi\epsilon_0 r_p^2}\sum_{i=1}^{N} q_i r_i cos\theta_i + \\ &\frac{1}{4\pi\epsilon_0 r_p^3}\sum_{i=1}^{N}\frac{q_i r_i^2}{2}(3cos^2\theta_i - 1) + O\left(t^3\right)\end{aligned} \tag{D.15}$$

These three sums are the first three terms of the multipole expansion of the electric potential. It allows the breakdown of the electric potential into multiple terms, each of which contributes to the overall electric potential. The three terms calculated here are called, respectively, the monopole term, the dipole term, and the quadrupole term. Each of the summations in the terms are referred to as the 'moments' of the multipole i.e. the monopole moment is $\sum_{i=1}^{N} q_i$.
It can be seen that these terms increasing depend on the reciprocal of the distance of the measured point, r_p, as $1/r_p$, $1/r_p^2$, $1/r_p^3$, and so on, so as that when increasing the distance from the compound, the higher order terms become less important.
For convenience in the upcoming discussion, the multipole expansion of the electric potential can be written as

$$\phi(r) = \phi_M(r) + \phi_D(r) + \phi_Q(r) + ... \tag{D.16}$$

D.1 The Monopole Term

When considering the monopole term,

$$\phi_M(r) = \frac{1}{4\pi\epsilon_0 r_p} \sum_{i=1}^{N} q_i \tag{D.17}$$

the monopole moment is easily recognisable as

$$\sum_{i=1}^{N} q_i = Q_{\text{total}} = Q \tag{D.18}$$

where Q is the net total charge on the compound. Thus the monopole term has the form

$$\phi_M(r) = \frac{Q}{4\pi\epsilon_0 r_p} \tag{D.19}$$

and the electric potential arising from the monopole depends only upon the total charge in the system. As the monopole moment (Equation D.18) does not depend upon r_i or r_p the monopole is a unique property of the system, meaning the moment arising from the monopole is not affected by a change in the origin.

The monopole is where the first obvious difference between a neutral molecule and an ion arises. As molecules are neutral the electric potential from a molecule contains no contribution from a monopole moment, therefore molecules do not have a monopole moment. Conversely, ions do have a net charge, therefore their electric potential does contain a significant contribution from the monopole moment, and ions do contain a monopole.

D.2 The Dipole Term

When considering the dipole term,

$$\phi_D(r) = \frac{1}{4\pi\epsilon_0 r_p^2} \sum_{i=1}^{N} q_i r_i cos\theta_i \tag{D.20}$$

Wangsness showed that the sum in this term can be rearranged to

$$\sum_{i=1}^{N} q_i r_i cos\theta_i = \hat{r}_p \sum_{i=1}^{N} q_i r_i \tag{D.21}$$

The dipole moment, **p**, can then be defined as

$$\mathbf{p} = \sum_{\mathrm{i=1}}^{\mathrm{N}} \mathrm{q_i r_i} \tag{D.22}$$

and the dipole term written as

$$\phi_D(r) = \frac{\hat{r}_p \cdot \mathbf{p}}{4\pi\epsilon_0 r_p^2} \tag{D.23}$$

Since the dipole moment (Equation D.22) depends upon r_i, but is independent of r_p, the dipole moment is an individual property of the distribution of charge, and is not affected by the location of the measurement point.

While not immediately obvious, this is where the second difference between a neutral molecule and a charged ion.

Equation D.22 shows that the dipole moment depends upon the value of r_i. This means that shifting the reference frame causes a change to r_i.

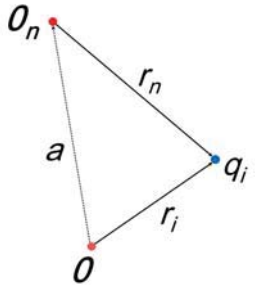

Figure D.2: *New coordinate geometry for multipole calculation. Filled red dot represents the origin in the new coordinate system, and r_n the new distance to each charge q_i. a is the vector which describes the shift in the origin.*

Considering this, a translation of the origin described by the vector a causes a change in the vector r_i (represented by Figure D.2), which can be expressed as

$$r_n = r_i - a \tag{D.24}$$

Inserting this into the dipole moment to define the new dipole moment, **p'**, gives

$$\begin{aligned} \mathbf{p'} = \sum_{\mathrm{i=1}}^{\mathrm{N}} \mathrm{q_i r_n} &= \sum_{i=1}^{N} q_i \left(r_i - a\right) \\ &= \sum_{i=1}^{N} q_i r_i - a \sum_{i=1}^{N} q_i \\ &= \mathbf{p} - \mathrm{a} \cdot \mathrm{Q_{total}} \end{aligned} \tag{D.25}$$

This removes the dependence upon the origin of the system on the dipole moment, however means that the total charge must now be accounted for. As for neutral systems (e.g. molecules) $Q_{\text{total}} = 0$, the dipole moment is independent of origin choice, therefore the description of a dipole moment in Equation D.22 is a valid dipole moment.[226]

For a system with an overall charge (e.g. ions) as $Q_{\text{total}} \neq 0$ the dipole moment is dependant upon the definition of the origin, which is a purely arbitrary choice. This leads to an inability to define a unique dipole moment for an ion.[225,226]

This can be somewhat circumvented by defining the origin as the "centre of charge".[225] This is the geometrical centre of the system, with the contribution of each point weighed by the charge on the point. Mathematically this is represented as

$$R_{\text{cq}} = \sum_{j=1}^{N} \frac{q_j r_j}{Q_{\text{total}}} \tag{D.26}$$

When shifting the origin to the centre of charge, the new dipole moment (**p'**) can be calculated using Equation D.25, with a describing the motion from the origin to the centre of charge

$$\begin{aligned} \mathbf{p'} &= \mathbf{p} - \mathrm{a} \cdot \mathrm{Q}_{\text{total}} \\ &= \sum_{i=1}^{N} q_i r_i - R_{\text{cq}} \cdot Q_{\text{total}} \\ &= \sum_{i=1}^{N} q_i r_i - \sum_{i=1}^{N} \frac{q_i r_i}{Q_{\text{total}}} \cdot Q_{\text{total}} \\ &= 0 \end{aligned} \tag{D.27}$$

This shows that moving from any arbitrarily defined origin to the centre of charge leads to the dipole moment being equal to 0 and not contributing to the electric potential.

While using the centre of charge as the origin removes the problem of a changing dipole by zeroing contributions from the dipole moment, however this also removes the possibility of using the dipole to study changes to ions in an electric field.